Forschungszentrum Jülich
in der Helmholtz-Gemeinschaft

Thomas Brückel, Gernot Heger, Dieter Richter and Reiner Zorn (Editors)

Laboratory Course

Neutron Scattering

Lectures

RWTH Aachen
University of Münster

Materie und Material
Matter and Materials

Schriften des Forschungszentrums Jülich
Reihe Materie und Material/Matter and Materials Band/Volume 38

Forschungszentrum Jülich GmbH
Institut für Festkörperforschung

Thomas Brückel, Gernot Heger, Dieter Richter, Reiner Zorn (Editors)

Neutron Scattering

Lectures of the JCNS Laboratory Course held at Forschungszentrum Jülich and the research reactor FRM II of TU Munich

In cooperation with

RWTH Aachen and University of Münster

Schriften des Forschungszentrums Jülich
Reihe Materie und Material/Matter and Materials Band/Volume 38

ISSN 1433-5506 ISBN 978-3-89336-489-3

Bibliographic information published by the Deutsche Nationalbibliothek.
The Deutsche Nationalbibliothek lists this publication in the Deutsche
Nationalbibliografie; detailed bibliographic data are available in the
Internet at http://dnb.d-nb.de.

Publisher and Distributor:	Forschungszentrum Jülich GmbH Zentralbibliothek, Verlag D-52425 Jülich Telefon (02461) 61-5368 · Telefax (02461) 61-6103 e-mail: zb-publikation@fz-juelich.de Internet: http://www.fz-juelich.de/zb
Cover Design:	Grafische Medien, Forschungszentrum Jülich GmbH
Printer:	Grafische Medien, Forschungszentrum Jülich GmbH
Copyright:	Forschungszentrum Jülich 2007

Schriften des Forschungszentrums Jülich
Reihe Materie und Material/Matter and Materials Band/Volume 38

ISSN 1433-5506
ISBN 978-3-89336-489-3

The complete volume is freely available on the Internet on the Jülicher Open Access Server (JUWEL)
at http://www.fz-juelich.de/zb/juwel

Contents

I

Fourier Transform

Reiner Zorn

I. Fourier Transform

Reiner Zorn

In this lecture a short introduction to Fourier transforms (FTs), their application, and useful theorems will be given. Emphasis will be put on the application for scattering problems although some of the theorems have more widespread importance. The proofs of the theorems will mostly only be sketched. For the mathematically more inclined reader refs. 1–3 are recommended.

I.1 Definitions

The most straightforward definition of Fourier transforms (FTs) is that given by the Fourier sine and cosine transform, respectively[1]:

$$F_{\mathrm{c}}(X) = \int_0^\infty f(x)\cos(2\pi X x)\mathrm{d}x\,, \tag{I.1}$$

$$F_{\mathrm{s}}(X) = \int_0^\infty f(x)\sin(2\pi X x)\mathrm{d}x\,. \tag{I.2}$$

Here, we will preferentially use the exponential two-sided Fourier transform which results from combining the sine and cosine FT using the Euler formula, $\exp(\mathrm{i}z) = \cos z + \mathrm{i}\sin z$ with $\mathrm{i} = \sqrt{-1}$:

$$F(X) = \int_{-\infty}^\infty f(x)\exp(\mathrm{i}Xx)\mathrm{d}x\,. \tag{I.3}$$

The advantage of this definition is that once the exponential FT is known the sine and cosine FT can be obtained as the imaginary and real part. Also it turns out that the integral in (I.3) is often easier to calculate than those containing trigonometric functions. Of course, the imaginary part has to be considered with some care in physical applications. Its significance depends on the context in which the the exponential FT occurs.

[1] Wherever no physical meaning is associated with the functions and variables, we will write the original function and argument in lowercase letters, e.g. $f(x)$, and the Fourier transformed function and argument by its uppercase counterparts, e.g. $F(X)$.

In classical applications where it is just a completion of the cosine FT it may be discarded. In quantum-mechanical calculations it usually represents the phase of a quantity like the wave function which is not observable. Nevertheless, it has its importance when calculating interference phenomena.

Wherever possible we will use the functional notation

$$\mathcal{F}_{X|x}[f(x)] = \int_{-\infty}^{\infty} f(x)\exp(\mathrm{i}Xx)\mathrm{d}x\,. \tag{I.4}$$

to abbreviate the Fourier integral.

The inversion of the FT (I.3) is:

$$f(x) = \mathcal{F}^{-1}_{x|X}[F(X)] = \frac{1}{2\pi}\int_{-\infty}^{\infty} F(X)\exp(-\mathrm{i}Xx)\mathrm{d}X\,. \tag{I.5}$$

The proof that (I.5) is the inverse of (I.3) is not simple and can be found in ref. 1.

Note that the inverted FT (iFT) is not much different from the FT, in shorthand:

$$\mathcal{F}^{-1}_{X|x} = \frac{1}{2\pi}\mathcal{F}_{-X|x}\,. \tag{I.6}$$

In order to make this symmetry more obvious, some authors include 2π in the argument of the exponential or "symmetrise" the pre-factors in equations (I.3) and (I.5) to $1/\sqrt{2\pi}$. In both variant definitions the iFT is just the FT at negative argument $-X$. Also it is clear at this point that the FT may have a minus sign in the argument of the exponential instead of the iFT without any change of their relation. This variant is also often found in the literature.

The so-called near-equivalence expressed by (I.6) has the consequence that most of the theorems derived hold in similar ways for FT and iFT, at most only differing in a factor 2π or a minus sign.

If one of the functions, say $f(x)$, is periodic, i.e. $f(x+a) = f(x)$, it can be expressed as a Fourier series

$$f(x) = \sum_{K=-\infty}^{\infty} F_K \exp(-2\pi\mathrm{i}Kx/a)\,. \tag{I.7}$$

This means that the Fourier transform $F(X)$ reduces to a sequence of complex numbers F_K. These coefficients F_K result from the relation

$$F_K = \frac{1}{a}\int_{-a/2}^{a/2} f(x)\exp(2\pi\mathrm{i}Kx/a)\mathrm{d}x\,. \tag{I.8}$$

A third variant is the completely discrete FT where both f_k and F_K are sequences of complex numbers. In this case the FT is

$$F_K = \frac{1}{N} \sum_{k=0}^{N-1} f_k \exp(2\pi \mathrm{i} K k/N) \tag{I.9}$$

with the inverse

$$f_k = \sum_{K=0}^{N-1} F_K \exp(-2\pi \mathrm{i} K k/N)\,. \tag{I.10}$$

(Again, different definitions with $1/N$ for the iFT or $1/\sqrt{N}$ for both may be found in the literature.)

A straightforward generalisation of the FT is that to multiple dimensions. The most important case of three dimensions is:

$$F(X,Y,Z) = \int_{-\infty}^{\infty} \mathrm{d}x \int_{-\infty}^{\infty} \mathrm{d}y \int_{-\infty}^{\infty} \mathrm{d}z \exp(\mathrm{i}Xx) \exp(\mathrm{i}Yy) \exp(\mathrm{i}Zz) f(x,y,z)\,. \tag{I.11}$$

The arguments of the exponentials can be grouped together and replaced by the scalar product of the vector $\underline{r} = (x,y,z)$ and the 'reciprocal space' vector $\underline{R} = (X,Y,Z)$:

$$F(\underline{R}) = \int \exp(\mathrm{i}\underline{R} \cdot \underline{r}) f(\underline{r}) \mathrm{d}^3 r\,. \tag{I.12}$$

The inversion is obviously

$$f(\underline{r}) = \frac{1}{(2\pi)^3} \int \exp(-\mathrm{i}\underline{R} \cdot \underline{r}) F(\underline{R}) \mathrm{d}^3 r \tag{I.13}$$

with one $1/2\pi$ pre-factor for each of the individual coordinates' transform.

An important special case of the 3D FT is that of isotropic functions, where the functions only depend on the absolute values $r = \|\underline{r}\| = \sqrt{x^2+y^2+z^2}$ and $R = \|\underline{R}\|$. In spherical polar coordinates (I.12) reads:

$$F(R) = \int_0^{\infty} \mathrm{d}r \int_0^{\pi} \mathrm{d}\theta \int_0^{2\pi} \mathrm{d}\phi\; r^2 \sin\theta \exp(\mathrm{i}\underline{R} \cdot \underline{r}) f(\underline{r}) =$$

Because of the symmetry one can assume $\underline{R} = (0,0,R)$ without loss of generality[2]. Then $\underline{R} \cdot \underline{r} = Rr\cos\theta$. In addition, because $f(\underline{r})$ does not depend on ϕ the integral over this angle can be carried out: $\int_0^{2\pi} \mathrm{d}\phi = 2\pi$. With this we get:

$$= \int_0^{\infty} \mathrm{d}r \int_0^{\pi} \mathrm{d}\theta\; 2\pi r^2 \sin\theta \exp(\mathrm{i}Rr\cos\theta) f(r) =$$

[2] German: ohne Beschränkung der Allgemeinheit

Here, we substitute $\cos\theta \to t$ with the consequence that $\mathrm{d}t = -\sin\theta \mathrm{d}\theta$:

$$= -\int_0^\infty \mathrm{d}r\; 2\pi r^2 \int_1^{-1} \mathrm{d}t \exp(\mathrm{i}Rrt) f(r) =$$

Because only $\exp(\mathrm{i}Rrt)$ depends on t the integration can be carried out resulting in

$$= \int_0^\infty \frac{\sin(Rr)}{Rr} f(r) 4\pi r^2 \mathrm{d}r = \frac{4\pi}{R} \int_0^\infty f(r) r \sin(Rr) \mathrm{d}r \,. \tag{I.14}$$

From the definition of the exponential FT and relation (I.71) shown later one can see that alternatively the FT of an isotropic function can be written as

$$F(R) = -\frac{2\pi\mathrm{i}}{R} \mathcal{F}_{R|\,r}[r f(|r|)] = \frac{2\pi}{R} \frac{\mathrm{d}}{\mathrm{d}R} \mathcal{F}_{R|\,r}[f(|r|)] \,. \tag{I.15}$$

Similarly it can be shown that the inverse FT is

$$f(r) = \frac{1}{2\pi^2 r} \int_0^\infty F(R) R \sin(Rr) \mathrm{d}R \,. \tag{I.16}$$

Finally, the Laplace transform (LT) which is closely related to the FT should be mentioned in passing:

$$\mathcal{L}_{X|\,x}[f(x)] = \int_0^\infty f(x) \exp(-Xx) \mathrm{d}x \,. \tag{I.17}$$

It can be seen that with the change of variables $X \to -\mathrm{i}X$ this becomes the one-sided variant of the exponential FT. The inverse of the Laplace transform is

$$\mathcal{L}^{-1}_{x|\,X}[F(X)] = \frac{1}{2\pi\mathrm{i}} \int_{\gamma-\mathrm{i}\infty}^{\gamma+\mathrm{i}\infty} F(X) \exp(Xx) \mathrm{d}X \tag{I.18}$$

where γ is chosen such that all singularities of $F(X)$ lie to the left of the integration line. Because of the similarity between FT and LT some of the rules mentioned in the following (e.g. the convolution theorem) hold in an only slightly modified way for the LT too.

I.2 Motivation from Physics

I.2.1 Fraunhofer diffraction

For light scattering the situation that light source and detection are both in a sufficient distance that for the incident as well as the scattered light plane waves can be assumed, is called *Fraunhofer diffraction*. For the set-up shown in Fig. I.1 we will show that then the diffraction pattern visible on the screen basically is the squared Fourier transform of

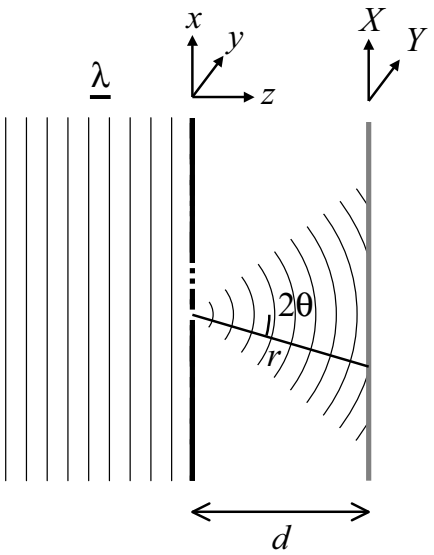

Figure I.1: Fraunhofer diffraction. For simplicity only one partial wave is shown.

the pattern in the object plane. In this discussion we will neglect the vector character of the electromagnetic field but just deal with a scalar field $a(\underline{r}, t)$.

Let the amplitude in the object plane be $f(x, y)$, e.g. by variation of the transparency of the screen. Then the amplitude of the partial wave starting at (x, y) in the observation plane at (X, Y) is proportional to $f(x, y)/r$ where $r = \sqrt{(X-x)^2 + (Y-y)^2 + d^2}$. Because the object screen is illuminated by wave fronts parallel to it all partial waves start with the same phase but arrive in the observation plane with phase

$$\delta = 2\pi \frac{r}{\lambda} = \frac{2\pi}{\lambda} \sqrt{(X-x)^2 + (Y-y)^2 + d^2}\,. \tag{I.19}$$

(The frequency of the waves be ν and the wave length $\lambda = c/\nu$.) The situation of Fraunhofer diffraction requires that $x, y \ll X, Y \ll d$. The first conditions lead to the approximation

$$\delta \approx \frac{2\pi}{\lambda} \sqrt{X^2 - 2Xx + Y^2 - 2Yy + d^2} \tag{I.20}$$

and the second allows the square root to be approximated:

$$\delta = \frac{2\pi d}{\lambda} \sqrt{1 + \frac{X^2}{d^2} - \frac{2Xx}{d^2} + \frac{Y^2}{d^2} - \frac{2Yy}{d^2}} \approx \frac{2\pi d}{\lambda} \left(1 + \frac{X^2}{2d^2} - \frac{Xx}{d^2} + \frac{Y^2}{2d^2} - \frac{Yy}{d^2}\right)\,. \tag{I.21}$$

The field in the observation plane at (X, Y) is the integral over the contributions of all

partial waves:

$$\begin{aligned} a(X,Y,t) &= \int_{-\infty}^{\infty} \mathrm{d}x \int_{-\infty}^{\infty} \mathrm{d}y \frac{f(x,y)}{r} \cos(\delta + 2\pi\nu t) \\ &= \Re \int_{-\infty}^{\infty} \mathrm{d}x \int_{-\infty}^{\infty} \mathrm{d}y \frac{f(x,y)}{r} \exp(\mathrm{i}(\delta + 2\pi\nu t)) \end{aligned} \tag{I.22}$$

In first order approximation $r \approx d$ and one can insert the approximation (I.21) for δ to obtain

$$\begin{aligned} a(X,Y,t) &= \Re \frac{1}{d} \exp\left(\mathrm{i}\left(2\pi\nu t + \frac{2\pi d}{\lambda}\left(1 + \frac{X^2}{2d^2} + \frac{Y^2}{2d^2}\right)\right)\right) \\ &\quad \times \int_{-\infty}^{\infty} \mathrm{d}x \int_{-\infty}^{\infty} \mathrm{d}y\, f(x,y) \exp\left(-\mathrm{i}\frac{2\pi}{\lambda d}(Xx + Yy)\right) . \end{aligned} \tag{I.23}$$

We note that this is still a simple oscillating field

$$a(X,Y,t) = \Re A \exp(\mathrm{i}2\pi\nu t) \tag{I.24}$$

with a complex amplitude $A = A' + \mathrm{i}A''$

$$A = \frac{1}{d} \exp\left(\frac{2\pi\mathrm{i}d}{\lambda}\left(1 + \frac{X^2}{2d^2} + \frac{Y^2}{2d^2}\right)\right) \mathcal{F}_{2\pi X/\lambda d, 2\pi Y/\lambda d|\, x,y}[f(x,y)] \tag{I.25}$$

proportional to the two-dimensional FT of $f(x,y)$. The target value of the FT, $Q_{[x,y]} = 2\pi[X,Y]/\lambda d$ is the small-angle approximation of the scattering vector which for higher angles is $Q = \frac{4\pi}{\lambda}\sin\theta$ where θ is half the angle between the incident and the scattered beam.

The observed intensity is the average of the squared field, i.e.

$$I(X,Y) = \nu \int_0^{1/\nu} a^2(X,Y,t)\mathrm{d}t\,. \tag{I.26}$$

By inserting (I.24) one obtains

$$\begin{aligned} I(X,Y) &= \nu \int_0^{1/\nu} \left(A'\cos(2\pi\nu t) - A''\sin(2\pi\nu t)\right)^2 \mathrm{d}t \\ &= A'^2\nu \int_0^{1/\nu} \cos^2(2\pi\nu t)\mathrm{d}t \\ &\qquad -2A'A''\nu \int_0^{1/\nu} \cos(2\pi\nu t)\sin(2\pi\nu t)\mathrm{d}t + A''^2\nu \int_0^{1/\nu} \sin^2(2\pi\nu t)\mathrm{d}t \\ &= \frac{A'^2 + A''^2}{2} = \frac{|A|^2}{2} \end{aligned} \tag{I.27}$$

Because $|\exp(\mathrm{i}x)| = 1$ for any real x inserting A from (I.25) simply yields:

$$I(X,Y) = \frac{1}{2d^2}\left|\mathcal{F}_{2\pi X/\lambda d, 2\pi Y/\lambda d|\, x,y}[f(x,y)]\right|^2 . \tag{I.28}$$

This result—that the scattered intensity pattern is the squared FT of the scattering object density—is a general feature of scattering processes (light, neutrons, x-rays...).

I.2.2 Complex conductance

To give a non-scattering example too we will consider the derivation of the complex conductance in electronics. For a simple resistor Ohm's law states that

$$I = G \cdot U \tag{I.29}$$

where $G = 1/R$ is the reciprocal value of the resistance, the conductance. For a simple resistor this equation remains valid if current I and voltage U are replaced by time-dependent quantities $i(t)$ and $u(t)$.

This is not more the case if the resistor is replaced by a two-terminal circuit which contains capacitors and inductors. In this case by virtue of the charges of capacitors and fields in the coils the circuit has a "memory" which allows past voltages to affect the current at a certain time. Despite this more complex behaviour the circuit often still responds *linear*, i.e. the current resulting from a sum of voltages $u_1(t) + u_2(t)$ is simply the sum of the currents resulting from each of the single stimuli: $i_1(t) + i_2(t)$. In this case the response current to an arbitrary voltage signal $u(t)$ can be expressed as

$$i(t) = \int_{-\infty}^{t} g(t, \tilde{t}) u(\tilde{t}) \mathrm{d}\tilde{t}\,. \tag{I.30}$$

The idea behind this expression is that one can decompose $u(t)$ into individual pulses. $g(t, \tilde{t})$ describes the current at time t resulting from a unit pulse at time $\tilde{t}$. Because of linearity all the contributions to the current can be simply summed up. The response of the circuit usually does not depend on the absolute time. Therefore, g does only depend on the time difference $t - \tilde{t}$ in most cases:

$$i(t) = \int_{-\infty}^{t} g(t - \tilde{t}) u(\tilde{t}) \mathrm{d}\tilde{t} = \int_{0}^{\infty} g(\hat{t}) u(t - \hat{t}) \mathrm{d}\hat{t}\,. \tag{I.31}$$

The integrals can be extended to infinity if one defines $g(t) = 0$ for $t < 0$.

The most interesting practical case is that the voltage depends sinusoidally on time, $u(t) = U_0 \cos(\omega t)$. Inserting this into equation (I.31) yields:

$$\begin{aligned} i(t) &= \int_{-\infty}^{\infty} g(\hat{t}) U_0 \cos(\omega(t - \hat{t})) \mathrm{d}\hat{t} \\ &= \int_{-\infty}^{\infty} g(\hat{t}) U_0 \Re \exp(-\mathrm{i}\omega(t - \hat{t})) \mathrm{d}\hat{t} \\ &= U_0 \Re \exp(-\mathrm{i}\omega t) \int_{-\infty}^{\infty} g(\hat{t}) \exp(\mathrm{i}\omega \hat{t}) \mathrm{d}\hat{t} \end{aligned}$$

$$= \quad U_0 \Re \left(\exp(-\mathrm{i}\omega t) G(\omega) \right) . \tag{I.32}$$

Here, $G(\omega)$ emerges naturally as the FT of the response function $g(t)$. It is in general complex. Denoting the real and complex parts with primes and double-primes one obtains

$$i(t) = U_0 (G'(\omega) \cos(\omega t) + G''(\omega) \sin(\omega t)) . \tag{I.33}$$

Thus, $i(t)$ is sum of a sine and a cosine function (i.e. phase shifted with respect to $u(t)$) $I'_0 \cos(\omega t) + I''_0 \sin(\omega t)$ with

$$I'_0 = G'(\omega) \cdot U_0 \text{ and } I''_0 = G''(\omega) \cdot U_0 \tag{I.34}$$

which is the analogue of Ohm's law for AC conductance.

I.3 Some examples

Only two concrete examples of FTs will be presented here, the exponential/Lorentzian FT pair and the Gaussian function. Interestingly, together with clever use of the rules and the delta function presented in the following sections these may cover 90 % of all physical problems. If there is really the necessity to obtain the FT of other functions they may be found in table books as [4]. In some cases it may even be more effective to look up the Fourier integrals (I.1–I.3) in a table of definite integrals. The (according to the experience of the author) most extensive compilation of such integrals can be found in [5].

Exponential decay: Because the exponential $\exp(-ax)$ diverges for x going to negative infinity one cannot FT it with the two-sided transform. One has either to use a one sided transform or define a function

$$f(x) = \begin{cases} 0 & \text{for } x < 0 \\ \exp(-ax) & \text{for } x > 0 \end{cases} \tag{I.35}$$

which is cut-off at $x = 0$. This makes also sense in most of the physical contexts, e.g. thinking of the current of a capacitor which is discharged by closing a circuit with a resistor at time zero. The Fourier integral (I.3) becomes then

$$\int_0^\infty \exp(\mathrm{i}Xx) \exp(-ax) \mathrm{d}x = \int_0^\infty \exp((\mathrm{i}X - a)x) \mathrm{d}x = \tag{I.36}$$

The indefinite integral of the exponential is known, $\int \exp(Ax) = \exp(Ax)/A$, thus one continues the calculation

$$= \frac{\exp((\mathrm{i}X - a)x)}{\mathrm{i}X - a}\bigg|_0^\infty = \frac{1}{a - \mathrm{i}X} = \frac{a}{a^2 + X^2} + \frac{X}{a^2 + X^2}\,\mathrm{i}\,.$$

The real part (which is usually the physically relevant) is a so-called Lorentzian function which peaks at $X = 0$ and has a full width at half maximum of $2a$. Reverting to the interpretation as a decay in time, a is related to the time constant by $a = 1/\tau$. This means that the decay time and the width of the Lorentzian in frequency are inversely proportional.

Gaussian: The bell-shaped curve of the Gaussian (or 'normal') distribution

$$f(x) = \frac{1}{\sqrt{2\pi}\sigma} \exp\left(-\frac{x^2}{2\sigma^2}\right) \tag{I.37}$$

decays to both sides rapidly enough and can thus be FTed two-sidedly. The Fourier integral is:

$$\int_{-\infty}^{\infty} \exp(\mathrm{i}Xx) \frac{1}{\sqrt{2\pi}\sigma} \exp\left(-\frac{x^2}{2\sigma^2}\right) \mathrm{d}x = \frac{1}{\sqrt{2\pi}\sigma} \int_{-\infty}^{\infty} \exp\left(\mathrm{i}Xx - \frac{x^2}{2\sigma^2}\right) \mathrm{d}x =$$

In order to simplify the integral we are going to 'complete the square'[3] inside the exponential by adding $\sigma^2 X^2/2$ and compensating this by a factor in front of the integral:

$$\begin{aligned} &= \frac{1}{\sqrt{2\pi}\sigma} \exp\left(-\frac{\sigma^2 X^2}{2}\right) \int_{-\infty}^{\infty} \exp\left(-\frac{x^2}{2\sigma^2} + \mathrm{i}Xx + \frac{\sigma^2 X^2}{2}\right) \mathrm{d}x \\ &= \frac{1}{\sqrt{2\pi}\sigma} \exp\left(-\frac{\sigma^2 X^2}{2}\right) \int_{-\infty}^{\infty} \exp\left(-\frac{(x - \mathrm{i}\sigma^2 X)^2}{2\sigma^2}\right) \mathrm{d}x = \end{aligned}$$

The definite integral of the Gaussian distribution always fulfills the normalisation property $(1/\sqrt{2\pi}\sigma) \int_{-\infty}^{\infty} \exp(-(x - A)^2/2\sigma^2)\mathrm{d}x = 1$, irrespectively of its centre A. Therefore, the simple result is:

$$= \exp\left(-\frac{\sigma^2 X^2}{2}\right)\,. \tag{I.38}$$

This means that the FT of a Gaussian is a Gaussian, a property which is called 'self-reciprocity'. It is shared by all Hermite functions of which the Gaussian is the simplest [2]. Nevertheless, the Fourier transform is not the *same* Gaussian but one with the reciprocal standard deviation $1/\sigma$ of the original Gaussian. Also the FT is not normalised to one but its maximum is fixed to one. This in turn causes that the area under the FT Gaussian is $\int_{-\infty}^{\infty} \exp(-\sigma^2 X^2/2)\mathrm{d}x = \sqrt{2\pi}/\sigma$.

[3] German: quadratische Ergänzung

I.4 The delta 'function'

We are now coming to a topic which may create nausea to mathematicians because we are going to define a function with infinite value. This may be justified by the mathematical concept of *distributions* (in contrast to functions). But because this lecture is addressed to physicists we will simply define the delta function as the following limit:

$$\delta(x) = \lim_{a\to 0} \begin{cases} 1/a & \text{for } |x| < a/2 \\ 0 & \text{everwhere else} \end{cases} . \tag{I.39}$$

When the limit is carried out the delta function is everywhere zero except for $x = 0$ where it has an infinite value. What is important is that the area under the function is always one during the whole limiting process. Therefore, we conclude that $\int_{-\infty}^{\infty} \delta(x)\mathrm{d}x = 1$. This integral condition and the fact that only the value at $x = 0$ does not vanish is the only characteristics of the delta function. Therefore, different definitions by limits are possible, e.g. by narrowing Gaussian functions, equation (I.37) with $\sigma \to 0$. It is somehow justified to say that the delta function is the Black Hole of mathematics, where every individuality of the function is lost as that of a star when it collapses.

The property making the delta function interesting is that it is able to pull out a single value of a function from a definite integral:

$$\int_{-\infty}^{\infty} \delta(x) f(x)\mathrm{d}x = \lim_{a\to 0} \frac{1}{a} \int_{-a/2}^{a/2} f(x)\mathrm{d}x =$$

Because in the limit of small a the function does not vary much over the interval $[-a/2, a/2]$ it can be replaced by its value at the centre, $f(0)$:

$$= \lim_{a\to 0} \frac{1}{a}\, a f(0) = f(0)\,. \tag{I.40}$$

Formally, it is also possible to use derivatives of the delta function in integrals which are calculated by application of the rule of integration by parts:

$$\int_{-\infty}^{\infty} \delta'(x) f(x)\mathrm{d}x = \delta(x) f(x)|_{-\infty}^{\infty} - \int_{-\infty}^{\infty} \delta(x) f'(x)\mathrm{d}x = -f'(0)\,. \tag{I.41}$$

(The product $\delta(x)f(x)$ vanishes for any $x \neq 0$ therefore also in the limit $x \to \pm\infty$) This means that the derivatives of the delta function have the characteristic property to pick the derivatives of a function at $x = 0$ below an integral.

From the basic property of the delta function (I.40) follows that the FT as the integral (I.3) is

$$\mathcal{F}_{X|\,x}[\delta(x)] = \int_{-\infty}^{\infty} \exp(\mathrm{i}Xx)\delta(x)\mathrm{d}x = 1\,, \tag{I.42}$$

i.e. the FT of the delta function is the constant function $F(X) = 1$. By writing down the inversion formula (I.5) one obtains that the iFT of a constant is a delta function:

$$\mathcal{F}^{-1}_{x|\,X}[1] = \frac{1}{2\pi}\int_{-\infty}^{\infty} \exp(-\mathrm{i}Xx)\mathrm{d}x = \delta(x)\,. \tag{I.43}$$

(At this point it is important not to forget the 2π!) Because in the last two formulae $\mathrm{i}Xx$ can be replaced by $-\mathrm{i}Xx$ it is of course also true that the iFT of the delta function is a constant $(1/2\pi)$ and the FT of a constant a delta function:

$$\mathcal{F}^{-1}_{x|\,X}[\delta(X)] = \frac{1}{2\pi}\,, \tag{I.44}$$

$$\mathcal{F}_{X|\,x}[1] = 2\pi\delta(x)\,. \tag{I.45}$$

As a typical application we will now use the delta function to show that the Fourier series is a special case of the continuous FT. Let $F(X)$ be a function which consists of delta functions at discrete values $X = 2\pi K/a$, $K \in \mathbb{Z}$ with 'weights' $2\pi F_K$:

$$F(X) = \sum_{K=-\infty}^{\infty} 2\pi F_K \delta\left(X - \frac{2\pi K}{a}\right)\,. \tag{I.46}$$

The iFT of this function is

$$\begin{aligned} f(x) &= \frac{1}{2\pi}\int_{-\infty}^{\infty}\sum_{K=-\infty}^{\infty} 2\pi F_K \delta\left(X - \frac{2\pi K}{a}\right)\exp(-\mathrm{i}Xx)\mathrm{d}x \\ &= \sum_{K=-\infty}^{\infty} F_K \int_{-\infty}^{\infty}\delta\left(X - \frac{2\pi K}{a}\right)\exp(-\mathrm{i}Xx)\mathrm{d}x \\ &= \sum_{K=-\infty}^{\infty} F_K \exp\left(-\frac{2\pi\mathrm{i}Kx}{a}\right) \end{aligned} \tag{I.47}$$

which is just the Fourier series (I.7).

Without demonstrating this we mention that in a similar way the completely discrete FT (I.9) can be derived from the continuous FT.

I.5 Some useful theorems

I.5.1 Linearity

From the definition it is clear that the FT is a linear operation, i.e.:

$$\mathcal{F}_{X|x}[af(x)] = a\mathcal{F}_{X|x}[f(x)] \tag{I.48}$$

$$\mathcal{F}_{X|x}[f(x)+g(x)] = \mathcal{F}_{X|x}[f(x)] + \mathcal{F}_{X|x}[g(x)]\,. \tag{I.49}$$

Obviously, this is also true for the iFT. The physical significance of this property is that (in a linear medium) waves superimpose without influencing each other.

I.5.2 Scaling theorem

Let a be a non-zero real number. Then

$$\mathcal{F}_{X|x}[f(ax)] = \frac{1}{|a|}\mathcal{F}_{X/a|x}[f(x)]\,. \tag{I.50}$$

Proof: If $a > 0$ we write out the left-hand FT as an integral and substitute $ax \to t$:

$$\int_{-\infty}^{\infty} \exp(\mathrm{i}Xx) f(ax)\mathrm{d}x = \int_{-\infty}^{\infty} \exp(\mathrm{i}Xt/a) f(t)\frac{\mathrm{d}t}{a} = \frac{1}{a}\int_{-\infty}^{\infty} \exp(\mathrm{i}(X/a)t) f(t)\mathrm{d}t\,.$$

If $a < 0$ we have to multiply the infinite bounds by a negative number effectively exchanging them and thus introducing a minus sign:

$$\int_{-\infty}^{\infty} \exp(\mathrm{i}Xx) f(ax)\mathrm{d}x = \int_{\infty}^{-\infty} \exp(\mathrm{i}Xt/a) f(t)\frac{\mathrm{d}t}{a} = -\frac{1}{a}\int_{-\infty}^{\infty} \exp(\mathrm{i}(X/a)t) f(t)\mathrm{d}t\,.$$

It is clear that both cases are represented if the absolute value $|a|$ is used in the denominator.

The physical phenomenon related to this property of the FT is the change of diffraction patterns with the change of the scattering object. If an object is scaled down affinely the diffraction pattern becomes larger in an inverse proportional way without changing its shape but just by a scaling factor.

An important special case of the scaling theorem is that of $a = -1$ and a real function $f(x) \in \mathbb{R}$:

$$\mathcal{F}_{X|x}[f(-x)] = \mathcal{F}_{-X|x}[f(x)] = \left(\mathcal{F}_{X|x}[f(x)]\right)^* \tag{I.51}$$

where the star denotes the complex conjugate defined as $(a+b\mathrm{i})^* = a-b\mathrm{i}$. In words: The Fourier transform of the mirror image of a *real* function is the complex conjugate of the original function.

I.5.3 Shifting theorem

The shifting theorem can be written in two ways:

$$\mathcal{F}_{X|x}[f(x+a)] = \exp(-\mathrm{i}Xa)\mathcal{F}_{X|x}[f(x)] \quad \text{and} \tag{I.52}$$

$$\mathcal{F}_{X+A|x}[f(x)] = \mathcal{F}_{X|x}[\exp(\mathrm{i}xA)f(x)]\,. \tag{I.53}$$

The proof of the second relation is trivial by insertion into the definition. To prove the first line, which is the more common statement, one has to substitute $x + a \to t$ in the Fourier integral.

Because $|\exp(-\mathrm{i}Xa)| = 1$ this implies that the complex absolute of a FT does not change if its argument function $f(x)$ is shifted. For scattering experiments, which usually only observe the absolute value but not the phase, this means that the diffraction pattern is not changed when the sample is displaced within the beam.

I.5.4 Symmetries

If a function shows certain symmetries its FT may have properties reflecting that symmetry. One example is the periodicity (or translational symmetry) of $f(x)$ which—as shown above—causes the FT to be a sum of equidistant delta functions. Others are mirror symmetries which cause the FT to be purely real or imaginary. In summary, the symmetry

relations for one-dimensional FT are:

$f(x)$	$F(X)$
periodic: $f(x+a) = f(x)$	discrete, stepsize $\Delta X = 2\pi/a$
discrete, stepsize $\Delta x = 2\pi/A$	periodic: $F(X+A) = F(X)$
real: $\forall_{x\in\mathbb{R}}\, f(x) \in \mathbb{R}$	$F(-X) = F^*(X)$
$f(-x) = f^*(x)$	real: $\forall_{X\in\mathbb{R}}\, F(X) \in \mathbb{R}$
especially:	
real and even	real and even
real and odd	imaginary and odd
imaginary and even	imaginary and even
imaginary and odd	real and odd

A consequence is that if $f(x)$ and $F(X)$ are both real functions (which has to be the case if both have a physically observable meaning) both have to be even functions. In this case it makes not much difference whether one uses the one-sided cosine FT (I.1) or the two-sided exponential FT (I.3) because they only differ by a constant factor of two.

A more subtle case of "symmetry" arises if a function is not mirrored at zero but cut-off. Such functions are called *causal* because in physics they usually describe the response of a system to a stimulus at time zero, e.g. the electric displacement $\underline{D}(t)$ for a electric field pulse $\underline{E}(t) = \delta(t)$ (or $g(t)$ in the example of subsection I.2.2). If one does not believe in precognition, clairvoyance or related effects one may safely assume that the past remains unaffected by the stimulus at $t = 0$ and thus the response function vanishes for $t < 0$. The FT of the response function

$$F(\omega) = \int_0^\infty f(t) \exp(\mathrm{i}\omega t)\mathrm{d}t \tag{I.54}$$

is the *susceptibility*[4]. In the example above it is related to the dielectric constant by $\epsilon(\omega) = 1 + F(\omega)$. The susceptibility has both a real and an imaginary part because $f(t)$ is neither even nor odd. Nevertheless, from causality, $f(t) = 0$ for $t < 0$, follows that the real and imaginary part are not independent but can be calculated from each other via the Kramers-Kronig relations[11]. The sketch of the proof of the Kramers-Kronig

[4] Here, we specify t and ω as arguments because only the interpretation as time and frequency make sense.

relations is as follows: Firstly, $F(\omega)$ is interpreted in the sense of complex analysis[5] as a function of complex argument. Because the integral in (I.54) is not extended to negative t it converges for any ω with positive imaginary part. Thus, $F(\omega)$ is analytic in the upper half plane of ω values. For this reason Cauchy's theorem

$$F(\omega) = \frac{1}{2\pi \mathrm{i}} \oint_{\mathcal{C}} \frac{F(\tilde{\omega})}{\tilde{\omega} - \omega} \mathrm{d}\tilde{\omega} \tag{I.55}$$

can be invoked where $\mathcal{C}$ is a contour comprising the real ω axis and a semicircle at infinity in the upper half plane. By some straightforward mathematics follows that the real and imaginary part of $F(\omega) = F'(\omega) + F''(\omega)\mathrm{i}$ are related by

$$F'(\omega) = \frac{1}{\pi} \mathcal{P} \int_{-\infty}^{\infty} \frac{F''(\tilde{\omega})}{\tilde{\omega} - \omega} \mathrm{d}\tilde{\omega} \text{ and} \tag{I.56}$$

$$F''(\omega) = -\frac{1}{\pi} \mathcal{P} \int_{-\infty}^{\infty} \frac{F'(\tilde{\omega})}{\tilde{\omega} - \omega} \mathrm{d}\tilde{\omega} \,. \tag{I.57}$$

Here, $\mathcal{P}$ denotes the *(Cauchy) principal value* of the integral: Actually the integrand diverges at $\tilde{\omega} = \omega$ in a way that is not integrable. Nevertheless the limits

$$\lim_{\epsilon \to 0} \left(\int_{-\infty}^{\omega - \epsilon} \ldots \mathrm{d}\tilde{\omega} + \int_{\omega + \epsilon}^{\infty} \ldots \mathrm{d}\tilde{\omega} \right)$$

exist and are called principal values. Equations (I.56) and (I.57) are of not much use in the theoretical calculation of susceptibilities because it is much easier to calculate them as real and imaginary part of the FT (I.54). Nevertheless, they have some importance for experiments where only one of the quantities $F'(\omega)$ or $F''(\omega)$ is accessible and the other has to be calculated. For this purpose one usually invokes the symmetries resulting from the fact that $f(t)$ is a real function, $F'(-\omega) = F'(\omega)$ and $F''(-\omega) = -F''(\omega)$, and obtains:

$$F'(\omega) = \frac{2}{\pi} \mathcal{P} \int_{0}^{\infty} \frac{\tilde{\omega} F''(\tilde{\omega})}{\tilde{\omega}^2 - \omega^2} \mathrm{d}\tilde{\omega} \,. \tag{I.58}$$

$$F''(\omega) = -\frac{2\omega}{\pi} \mathcal{P} \int_{0}^{\infty} \frac{F'(\tilde{\omega})}{\tilde{\omega}^2 - \omega^2} \mathrm{d}\tilde{\omega} \,, \tag{I.59}$$

equations which only include the susceptibility at positive frequencies.

---

[5] German: Funktionentheorie

I.5.5 Convolution theorem

The *convolution*[6] of two functions is defined as follows:

$$f \otimes g(x) = \int_{-\infty}^{\infty} f(t)g(x-t)\mathrm{d}t\,. \tag{I.60}$$

One of the most important occurrences of the convolution and its two- and three-dimensional generalisations in Physics is the consideration of limited instrumental resolution. E.g. if $f(x,y)$ is the ideal two-dimensional picture of a scene and $g(x,y)$ is the picture of a single light spot by a camera, then $f \otimes g(x,y)$ is the blurred picture of the scene you obtain from the camera. Actually, most of the "optical" effects included in programs like Adobe PhotoShop® are realised mathematically as convolutions.

One of the most important theorems on FTs is now that the FT of a convolution is the product of the individual FTs:

$$\mathcal{F}_{X|x}[f \otimes g(x)] = \mathcal{F}_{X|x}[f(x)] \cdot \mathcal{F}_{X|x}[g(x)] = F(X)G(X) \tag{I.61}$$

or vice versa:

$$\mathcal{F}_{X|x}[f(x)g(x)] = \mathcal{F}_{X|x}[f(x)] \otimes \mathcal{F}_{X|x}[g(x)] = F(X) \otimes G(X)\,. \tag{I.62}$$

Proof of relation (I.61): From the definition (I.3) follows straightforwardly:

$$\begin{aligned}
\mathcal{F}_{X|x}[f \otimes g(x)] &= \int_{-\infty}^{\infty} \exp(\mathrm{i}Xx) \left(\int_{-\infty}^{\infty} f(t)g(x-t)\mathrm{d}t \right) \mathrm{d}x \\
&= \int_{-\infty}^{\infty} \mathrm{d}x \int_{-\infty}^{\infty} \mathrm{d}t \exp(\mathrm{i}Xx) f(t)g(x-t) \\
&= \int_{-\infty}^{\infty} \mathrm{d}x \int_{-\infty}^{\infty} \mathrm{d}t \exp(\mathrm{i}X(x-t)) \exp(\mathrm{i}Xt) f(t)g(x-t) \\
&= \int_{-\infty}^{\infty} \mathrm{d}t \int_{-\infty}^{\infty} \mathrm{d}x \exp(\mathrm{i}X(x-t)) \exp(\mathrm{i}Xt) f(t)g(x-t)
\end{aligned} \tag{I.63}$$

Substituting $x - t \to x'$ leaves the infinite bounds of the first integral unchanged:

$$\begin{aligned}
&= \int_{-\infty}^{\infty} \mathrm{d}t \int_{-\infty}^{\infty} \mathrm{d}x' \exp(\mathrm{i}Xx') \exp(\mathrm{i}Xt) f(t)g(x') \\
&= \int_{-\infty}^{\infty} \exp(\mathrm{i}Xt) f(t)\mathrm{d}t \int_{-\infty}^{\infty} \exp(\mathrm{i}Xx') g(x')\mathrm{d}x' \\
&= \mathcal{F}_{X|x}[f(x)] \cdot \mathcal{F}_{X|x}[g(x)]
\end{aligned} \tag{I.64}$$

---

[6] German: Faltung (sometimes also used in English)

Note that the critical step of this proof is the exchange of integrations at line (I.63). For some "crazy" functions this may not be allowed and in consequence the convolution theorem does not hold. Nevertheless, for "physical" functions this is usually no issue.

In addition to numerous applications to derive FTs analytically—of which some will be discussed in section I.6—the convolution theorem is also exploited in numerical calculations, e.g.:

- Discretisation of (I.60) with N points for f and g each means for a numerical calculation of $f \otimes g$ that N sums of N summands have to be calculated. Thus the complexity rises proportional to N^2 with the number of points. At the first glance it seems more complicated to use the convolution theorem, i.e. calculate the FTs of f and g first, multiply them, and Fourier backtransform the product. Nevertheless, because fast FT algorithms [6] have a complexity only proportional to $N \log N$ and only N products have to be calculated the aggregate computational effort may be smaller via FT for sufficiently large N.

- With regard to the significance of the convolution as influence of the limited instrumental resolution it is clearly of interest to reconstruct the function $f(x)$ (physical quantity) from the convolution product $f \otimes g(x)$ (measured quantity) and $g(x)$ (instrumental resolution function). Because the inverse integral transform of (I.60) is usually not known it is not possible to calculate $f(x)$ directly. Nevertheless, using the convolution theorem it is easy to calculate $F(X)$ by dividing the FT of the measured quantity by that of the resolution function[7]:

$$F(X) = \frac{\mathcal{F}_{X|x}[f \otimes g(x)]}{\mathcal{F}_{X|x}[g(x)]} \,. \tag{I.65}$$

[7] It should be mentioned that if experimental errors are considered the result may be ambiguous, i.e. depend strongly on the particular realisation of errors. The inversion of (I.60) is an "ill-defined" problem, even a small difference in the errors of the measured quantity may cause a largely different $f(x)$. This means that in order to select a physically meaningful $f(x)$ one has to introduce additional criteria, e.g. smoothness of the result. This leads to various empirical techniques as indirect Fourier transform [7], Tikhonov regularisation [8, 9], or Maximum Entropy methods [10]

In principle, the thus obtained $F(X)$ could be back-transformed to yield $f(x)$ but the accumulation of numerical errors usually prohibits this in practice.

Closely related to the convolution is the correlator or correlation function of two functions:

$$\langle f(0)g(x)\rangle = \int_{-\infty}^{\infty} f(t)g(x+t)\mathrm{d}t\,. \tag{I.66}$$

By a substitution $t \to -t'$ it is easy to show that

$$\langle f(0)g(x)\rangle = f(-x) \otimes g(x) \tag{I.67}$$

so that the correlator is just the convolution with one of the functions mirrored. Using the convolution theorem and scaling theorem in succession, it follows that the FT of the correlation function is the product of the FTs of the correlated functions with one FT mirrored, i.e.

$$\mathcal{F}_{X|x}[\langle f(0)g(x)\rangle] = \mathcal{F}_{-X|x}[f(x)]\mathcal{F}_{X|x}[g(x)] = F(-X)G(X)\,. \tag{I.68}$$

For a real function $f(x)$ from (I.51) follows that the FT of the correlation function is the product of the complex conjugate of the FT of that function multiplied with the FT of the other function:

$$\mathcal{F}_{X|x}[\langle f(0)g(x)\rangle] = F^*(X)G(X)\,. \tag{I.69}$$

In physics the most important special case is the autocorrelation function where $f = g$:

$$\mathcal{F}_{X|x}[\langle f(0)f(x)\rangle] = F^*(X)F(X) = |F(X)|^2\,. \tag{I.70}$$

This relation, which expresses that the autocorrelation function $\langle f(0)f(t)\rangle$ and the power spectrum $|F(\omega)|^2$ of a signal $f(t)$ are related by a FT, is known as the Wiener-Khinchine theorem.

Note that the right-hand side is just the typical result for the scattered intensity as in (I.28). The Wiener-Khinchine theorem thus allows the scattered intensity to be calculated in two ways: (1) The object density can be FTed to obtain an amplitude of which subsequently the absolute squared is calculated. (2) One can construct the autocorrelation function of the object density (called Patterson function, pair correlation function, van-Hove function etc. depending on context) and FT it.

I.5.6 Differentials, integrals

By differentiating (I.3) one obtains directly:

$$\begin{aligned}\frac{\mathrm{d}}{\mathrm{d}X}\mathcal{F}_{X|x}[f(x)] &= \frac{\mathrm{d}}{\mathrm{d}X}\int_{-\infty}^{\infty}\exp(\mathrm{i}Xx)f(x)\mathrm{d}x \\ &= \int_{-\infty}^{\infty}\mathrm{i}x\exp(\mathrm{i}Xx)f(x)\mathrm{d}x \\ &= \mathrm{i}\mathcal{F}_{X|x}[xf(x)]\,. \end{aligned} \tag{I.71}$$

Analogously, for the iFT holds:

$$\frac{\mathrm{d}}{\mathrm{d}x}\mathcal{F}^{-1}_{x|X}[F(X)] = -\mathrm{i}\mathcal{F}^{-1}_{x|X}[XF(X)]\,. \tag{I.72}$$

By FTing the last equation and inserting $F(X) = \mathcal{F}_{X|x}[f(x)]$ one obtains the more common form of the differentiation theorem:

$$\mathcal{F}_{X|x}\left[\frac{\mathrm{d}f}{\mathrm{d}x}\right] = -\mathrm{i}X\mathcal{F}_{X|x}[f(x)]\,. \tag{I.73}$$

Thus, the FT of the derivative is the FT of the original function multiplied by $-\mathrm{i}X$ [8].

In signal processing differentiation of a signal $f(t)$ is realised by a high pass filter. Expressed in frequency domain, $f(\omega)$, this filter has the effect of pronouncing the high frequencies and shifting the phase by 90°. This is exactly what is mathematically expressed by a multiplication with $-\mathrm{i}\omega$.

By induction[9] it is easy to prove that the FT of derivatives of arbitrary order n can be easily calculated:

$$\mathcal{F}_{X|x}\left[\frac{\mathrm{d}^n f}{\mathrm{d}x^n}\right] = (-\mathrm{i}X)^n\mathcal{F}_{X|x}[f(x)]\,. \tag{I.74}$$

Since the integral is a kind of inverse operation to the derivative, similar theorems hold for integration. Namely, the definite integral of a FT is:

$$\begin{aligned}\int_A^X \mathcal{F}_{T|x}[f(x)]\mathrm{d}T &= \int_A^X \mathrm{d}T\int_{-\infty}^{\infty}\mathrm{d}x\exp(\mathrm{i}Tx)f(x) \\ &= \int_{-\infty}^{\infty}\mathrm{d}x\int_A^X \mathrm{d}T\exp(\mathrm{i}Tx)f(x)\end{aligned}$$

[8] Note that for alternative definitions of the FT this factor may by $+\mathrm{i}X$ or $\pm 2\pi\mathrm{i}X$.

[9] German: vollständige Induktion

$$= \int_{-\infty}^{\infty} \left(\frac{\exp(\mathrm{i}Xx)}{\mathrm{i}x} - \frac{\exp(\mathrm{i}Ax)}{\mathrm{i}x} \right) f(x)\mathrm{d}x$$
$$= \mathrm{i}\mathcal{F}_{A|\,x}\left[\frac{f(x)}{x}\right] - \mathrm{i}\mathcal{F}_{X|\,x}\left[\frac{f(x)}{x}\right] . \qquad \text{(I.75)}$$

With respect to X the first term is a constant and therefore an indefinite integral or primitive[10] of a FT is

$$\int \mathcal{F}_{X|\,x}[f(x)]\mathrm{d}X = -\mathrm{i}\mathcal{F}_{X|\,x}\left[\frac{f(x)}{x}\right] , \qquad \text{(I.76)}$$

i.e. the FT of the function divided by ix.

The corresponding theorem for the iFT is:

$$\int_a^x \mathcal{F}^{-1}_{t|\,X}[F(X)]\mathrm{d}t = \mathrm{i}\mathcal{F}^{-1}_{x|\,X}\left[\frac{F(X)}{X}\right] - \mathrm{i}\mathcal{F}^{-1}_{a|\,X}\left[\frac{F(X)}{X}\right] . \qquad \text{(I.77)}$$

As above, by FTing the last equation and inserting $F(X) = \mathcal{F}_{X|\,x}[f(x)]$ the FT of an integral is obtained:

$$\mathcal{F}_{X|\,x}\left[\int_a^x f(t)\mathrm{d}t\right] = \mathrm{i}\frac{F(X)}{X} - \mathrm{i}\mathcal{F}^{-1}_{a|\,X}\left[\frac{F(X)}{X}\right] 2\pi\delta(X)$$
$$= \mathrm{i}\frac{\mathcal{F}_{X|\,x}[f(x)]}{X} - 2\pi\mathrm{i}\mathcal{F}^{-1}_{a|\,X}\left[\frac{\mathcal{F}_{X|\,x}[f(x)]}{X}\right]\delta(X) \qquad \text{(I.78)}$$

This expression seems to be impracticably complicated. But one has to notice that the second term is just a delta function. Therefore, up to the value at $X = 0$ it can be omitted for the result. For the same reason the integration constant of the indefinite integral does not play a rôle except for the delta function strength at $X = 0$ and

$$\forall_{X\neq 0} \quad \mathcal{F}_{X|\,x}\left[\int f(x)\mathrm{d}x\right] = \mathrm{i}\frac{\mathcal{F}_{X|\,x}[f(x)]}{X} . \qquad \text{(I.79)}$$

Note that this result is included in the general expression (I.74) if the integration is interpreted as the -1^{th} derivative[11].

Obviously, the integration corresponds to the low pass filter in signal processing as the derivative did for the high pass.

---

[10] German: Stammfunktion

[11] If the definitions of *fractional calculus* [12] are used rule (I.74) is even valid for any real n.

I.5.7 Sum rules

The title of this subsection is actually a misnomer since it deals with infinite integrals over FTs which only in the discrete version can be expressed by sums. Nevertheless, it is the term most used in the Physics literature.

The simplest sum rule is that for the infinite integral of the FT itself:

$$\begin{aligned}\int_{-\infty}^{\infty} \mathcal{F}_{X|\,x}[f(x)]\mathrm{d}X &= \int_{-\infty}^{\infty} \mathrm{d}X \int_{-\infty}^{\infty} \mathrm{d}x \exp(iXx) f(x) \\ &= \int_{-\infty}^{\infty} f(x) 2\pi\delta(x)\mathrm{d}x = 2\pi f(0)\,. \end{aligned} \tag{I.80}$$

(We use that $\int_{-\infty}^{\infty} \mathrm{d}x \exp(iXx)$ is the FT of one, see (I.45).) Here again, we assume that the integrals over X and x are interchangeable which may cause problems for certain functions. Often (e.g. for a simple function as (I.35)) it may be necessary to interpret the integral over X as Cauchy principal value and handle discontinuities in $f(x)$ by imposing Dirichlet's condition, $f(a) = (\lim_{x\searrow a} f(x) + \lim_{x\nearrow a} f(x))/2$.

The complementary sum rule is even simpler to derive:

$$\mathcal{F}_{0|\,x}[f(x)] = \int_{-\infty}^{\infty} f(x) \exp(\mathrm{i}0x)\mathrm{d}x = \int_{-\infty}^{\infty} f(x)\mathrm{d}x\,. \tag{I.81}$$

We see that the infinite integral of a FT corresponds to the value of the original function at zero (up to a factor 2π) and vice versa.

We define the equivalent width of a function $f(x)$ as

$$\Delta x = \frac{\int_{-\infty}^{\infty} f(x)\mathrm{d}x}{f(0)}\,. \tag{I.82}$$

i.e. by the area under the function reshaped into a rectangle of width Δx and the height of the function at $x = 0$. If $F(X)$ is the FT of $f(x)$ using (I.81) one can write

$$\Delta x = \frac{F(0)}{f(0)}\,. \tag{I.83}$$

Analogously, with (I.80) one obtains

$$\Delta X = \frac{\int_{-\infty}^{\infty} F(X)\mathrm{d}X}{F(0)} = \frac{2\pi f(0)}{F(0)}\,. \tag{I.84}$$

Multiplying the last two equations yields

$$\Delta X \cdot \Delta x = 2\pi \tag{I.85}$$

which is the *uncertainty relation* of Fourier transforms. It expresses in a mathematically exact way the notion "If the function is narrower the FT is wider and vice versa." It is also the mathematical origin of the uncertainty relation in quantum mechanics. For scattering experiments its consequence is that an object of dimension Δx causes a scattering pattern of size $\Delta Q = 2\pi/\Delta x$ where $Q = \frac{4\pi}{\lambda}\sin\theta$ is the scattering vector.

The sum rules (I.80) and (I.81) are a special case of general rules to calculate the moments of a FT. The n^{th} moment of a function is defined as

$$[x^n]_f = \int_{-\infty}^{\infty} x^n f(x)\mathrm{d}x\,. \tag{I.86}$$

These moments are of special importance if $f(x)$ has the meaning of a probability distribution (e.g. in the example of a Gaussian (I.37) above). Then the moments enter into statistical quantities as average, variance, skewness, and kurtosis. Using the differentiation rule (I.74) the n^{th} ($n \in \mathbb{N}$) moment of a FT can be calculated in a simple way:

$$[X^n]_F = \int_{-\infty}^{\infty} X^n F(X)\mathrm{d}X = \int_{-\infty}^{\infty} \mathrm{i}^n \mathcal{F}_{X|\,x}\left[\frac{\mathrm{d}^n f}{\mathrm{d}x^n}\right]\mathrm{d}X = 2\pi\mathrm{i}^n \left.\frac{\mathrm{d}^n f}{\mathrm{d}x^n}\right|_{x=0} \tag{I.87}$$

or complementarily:

$$[x^n]_f = (-\mathrm{i})^n \left.\frac{\mathrm{d}^n F}{\mathrm{d}X^n}\right|_{X=0} \tag{I.88}$$

This means that all moments of $f(x)$ are characterised by the behaviour of the FT, viz its derivatives, close to zero. For this reason the FT of a probability distribution is called *characteristic function* in probability theory.

There are also sum rules concerning quadratic expressions in the FTs. E.g. by integrating (I.69) and applying sum rule (I.80) one obtains

$$\int_{-\infty}^{\infty} F^*(X)G(X)\mathrm{d}X = \int_{-\infty}^{\infty} \mathcal{F}_{X|\,x}\left[\langle f(0)g(x)\rangle\right]\mathrm{d}X = 2\pi\langle f(0)g(0)\rangle = 2\pi\int_{-\infty}^{\infty} f(x)g(x)\mathrm{d}x\,.$$

One has to note that this equation is only valid for real $f(x)$ since (I.69) is restricted to this (in physics most important) case. Without proof we note that the generalisation to complex $f(x)$ (and $g(x)$) is

$$\int_{-\infty}^{\infty} F^*(X)G(X)\mathrm{d}X = 2\pi\int_{-\infty}^{\infty} f^*(x)g(x)\mathrm{d}x\,. \tag{I.89}$$

This is usually called the *power-* or *Plancherel's theorem* because if f and g are interpreted as voltage $u(t)$ and current $i(t)$ of a signal the right hand side is the electrical power of

that signal. The power theorem now states that the power can also be calculated by integrating the product of the voltage and current spectra, $U(\omega)$ and $I(\omega)$, over the whole frequency spectrum.

The special case $g(x) = f(x)$ is often better known as *Parseval's theorem*:

$$\int_{-\infty}^{\infty} |F(X)|^2 \mathrm{d}X = 2\pi \int_{-\infty}^{\infty} |f(x)|^2 \mathrm{d}x \,. \tag{I.90}$$

This means that the norm of a function remains unchanged by a FT except for a factor 2π [12].

I.6 Application of theorems

I.6.1 Diffraction by slits and gratings

Here a couple of freshman examples of optical diffraction (single and double slit, infinite and finite grating) will be re-examined. The emphasis will be put on the use of the convolution theorem to obtain the old results in a more simple and evident way.

The transmissivity of a single slit of width a can be described by the "mesa" or "boxcar" function

$$f(x) = \begin{cases} 1 & \text{for } -a/2 < x < a/2 \\ 0 & \text{elsewhere.} \end{cases} \tag{I.91}$$

The FT of this function is

$$F_1(X) = \int_{-a/2}^{a/2} \exp(\mathrm{i}Xx)\mathrm{d}x = \left.\frac{\exp(\mathrm{i}Xx)}{\mathrm{i}X}\right|_{-a/2}^{a/2} = \frac{2}{X} \sin\frac{Xa}{2} \,. \tag{I.92}$$

Up to constant factors the intensity of the diffraction pattern is the absolute square, namely

$$I_1(X) = |F_1(X)|^2 = \frac{4}{X^2} \sin^2\frac{Xa}{2} \,. \tag{I.93}$$

We now consider two such slits in a distance d, i.e. centred at $x = -d/2$ and $x = d/2$. Using the shifting theorem (I.52) we can state the FT of each slit separately is

[12] This factor—which is especially annoying at that point—would not appear for certain alternative definitions of the FT.

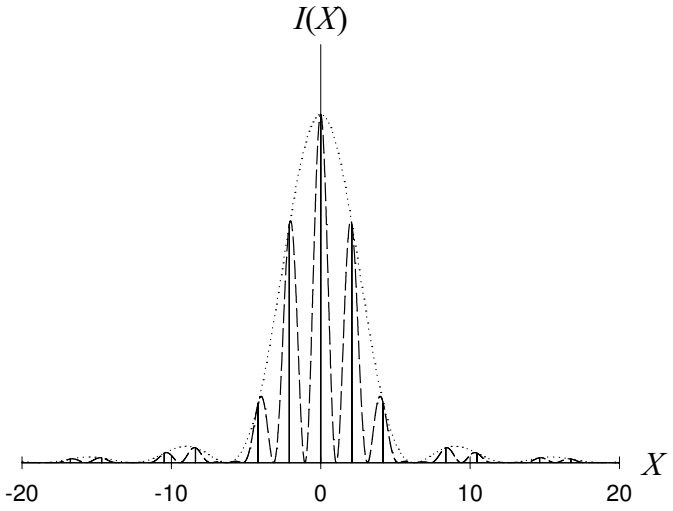

Figure I.2: Diffraction from a single slit (·····), a double slit (- - -), and an infinite array of slits (——). Slit width: $a = 1$, slit distance: $d = 3$.

$\exp(\pm \mathrm{i}Xd/2)F_1(X)$ and the sum

$$F_2(X) = 2\cos\frac{Xd}{2}\frac{2}{X}\sin\frac{Xa}{2}\,. \tag{I.94}$$

Thus the intensity is

$$I_2(X) = |F(X)|^2 = \frac{4}{X^2}\sin^2\frac{Xa}{2}\cos^2\frac{Xd}{2}\,. \tag{I.95}$$

(Fig. I.2) Alternatively, we can say that the transmissivity of a double slit is that of a single one convoluted with two delta functions in a distance d, $g(x) = \delta(x - d/2) + \delta(x + d/2)$, of which the FT is

$$G(X) = \exp(\mathrm{i}Xd/2) + \exp(-\mathrm{i}Xd/2) = 2\cos(Xd/2)\,. \tag{I.96}$$

The convolution theorem (I.61) states the the FT of the convolution is the product $F_1(X)G(X)$ which is exactly the same result as (I.94).

Analogously, one can derive the diffraction pattern of an infinite grid of slits with width a and distance d. The function to be FTed here is the convolution $f(x) \otimes g(x)$ with $f(x)$ from (I.91) and

$$g(x) = \sum_{k=-\infty}^{\infty} \delta(x + kd)\,. \tag{I.97}$$

This is just the case of a periodic function discussed in section I.1 and from (I.8) the Fourier coefficients are constant $G_K = 1/d$. The FT itself is then a sum of delta functions apart by $2\pi K/d$ with these coefficients:

$$G(X) = \sum_{K=-\infty}^{\infty} \frac{1}{d}\delta\left(X - \frac{2\pi K}{d}\right) . \tag{I.98}$$

So the diffracted intensity from the infinite grating is

$$I_3(X) = |F(X)G(X)|^2 = \sum_{K=-\infty}^{\infty} \frac{4}{K^2}\sin^2\frac{Ka}{2d}\delta^2\left(X - \frac{2\pi K}{d}\right) . \tag{I.99}$$

So the scattering is concentrated into sharp peaks (which is a consequence of the translational symmetry) but the intensity is not constant but modulated by the scattering function of a single slit.

This is the simplest one-dimensional case of decomposition of the scattered intensity into *form factor* and *structure factor*. In scattering physics one often has the situation that the sample is an arrangement of identical individual particles (atoms, molecules, colloidal particles ...) where the fictitious scattering pattern of their centres-of-mass (corresponding to $G(X)$ in the above example) is known and called the structure factor $S(\underline{Q})$. Let the density of scatterers (electrons, nuclei ...) within a single particle be $\rho(\underline{r})$. Then the squared FT of that density $P(\underline{Q}) = \left|\mathcal{F}_{\underline{Q}|\,\underline{r}}[\rho(\underline{r})]\right|^2$ is called the form factor of the particle. From the convolution theorem follows that the total scattered intensity from the arrangement of particles is $I(\underline{Q}) = P(\underline{Q})S(\underline{Q})$, the product of form- and structure factor.

As a last example we will extend the considerations to a finite grating of size l. We can do this by multiplying with a mesa function masking out the desired part from an infinite grating:

$$h(x) = \begin{cases} 1 & \text{for } -l/2 < x < l/2 \\ 0 & \text{elsewhere.} \end{cases} \tag{I.100}$$

So the total function to be transformed is $(f(x) \otimes g(x)) \cdot h(x)$ where $f(x)$ is defined by (I.91) and $g(x)$ by (I.97). In analogy to (I.92) the FT of $h(x)$ is $H(X) = (2/X)\sin(Xl/2)$. Applying both versions of the convolution theorem one obtains:

$$\begin{aligned} F_4(X) &= (F(X)\cdot G(X)) \otimes H(X) \\ &= \left(\sum_{K=-\infty}^{\infty} \frac{2}{K}\sin\frac{Ka}{2d}\delta\left(X - \frac{2\pi K}{d}\right)\right) \otimes \frac{2}{X}\sin\frac{Xl}{2} \end{aligned}$$

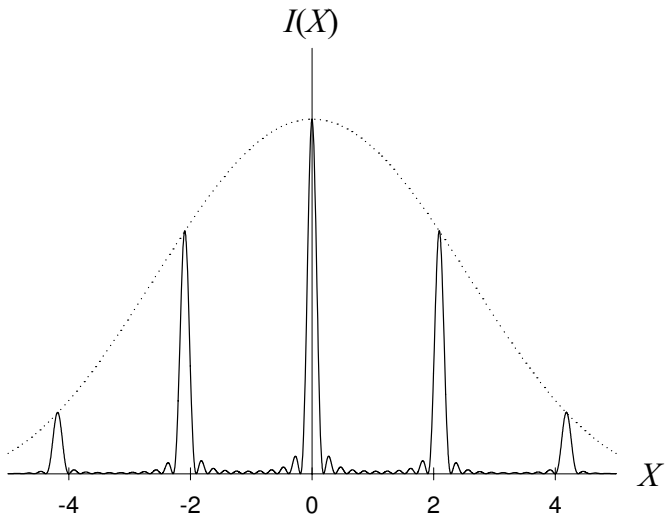

Figure I.3: Diffraction from a single slit (·····) and a finite array of slits (——). Slit width: $a = 1$, slit distance: $d = 3$, length of grating: $l = 33$ (this means 11 slits).

$$= \sum_{K=-\infty}^{\infty} \frac{2}{K} \sin\frac{Ka}{2d} \frac{2}{X - 2\pi K/d} \sin\frac{(X - 2\pi K/d)l}{2}\,. \tag{I.101}$$

It turns out that a somewhat simpler result can be obtained if we think of the finite grating generated the other way around: We multiply $g(x)$ and $h(x)$ first to obtain a finite grid of infinitely narrow slits and then convolute this with $f(x)$ representing the slit of finite width: $f(x) \otimes (g(x) \cdot h(x))$ [3]. It is clear that this function has the same values as the one representing the grating before and therefore the FT is the same:

$$\begin{aligned} F_4(X) &= F(X) \cdot (G(X) \otimes H(X)) \\ &= \frac{2}{X} \sin\frac{Xa}{2} \sum_{K=-\infty}^{\infty} \frac{2}{X - 2\pi K/d} \sin\frac{(X - 2\pi K/d)l}{2} = \end{aligned} \tag{I.102}$$

Note that the sum is now over a simpler expression. Indeed, it can be calculated in closed form now. If the grating has n slits of distance d there is some arbitrariness in the choice of l cutting out this number of slits. We assume that $l = nd$ and note that n has to be an odd number because of symmetry. Replacing l by nd one obtains:

$$\begin{aligned} &= \frac{2}{X} \sin\frac{Xa}{2} \sum_{K=-\infty}^{\infty} \frac{1}{Xnd/2 - \pi nK} \sin(Xnd/2 - \pi nK) \\ &= \frac{2}{X} \sin\frac{Xa}{2} \sum_{K=-\infty}^{\infty} \frac{1}{Xnd/2 - \pi nK} (-1)^K \sin(Xnd/2) \end{aligned}$$

$$= \frac{2}{X}\sin\frac{Xa}{2}\sin\frac{Xnd}{2}\sum_{K=-\infty}^{\infty}\frac{(-1)^K}{Xnd/2-\pi nK}$$

By applying a serial representation of the cosecant, $1/\sin x = \sum_{k=-\infty}^{\infty}(-1)^k/(x-\pi k)$ one finally gets

$$F_4(X) = \frac{2\sin(Xa/2)\sin(Xnd/2)}{nX\sin(Xd/2)} \tag{I.103}$$

and the corresponding intensity

$$I_4(X) = \frac{4\sin^2(Xa/2)\sin^2(Xnd/2)}{n^2X^2\sin^2(Xd/2)}\,. \tag{I.104}$$

It has to be conceded that the advantage of using the FT theorems to derive exact results as (I.104) is not so big if compared with a direct calculation. Nevertheless, the theorems allow a quick comprehension of how the result looks like without doing any calculation. E.g. here it is more important to see that because there is a convolution with $H(X)$ the result is that in each position where the infinite grating creates a sharp delta peak a copy of the FT of the cut-off function $h(x)$ is placed. To quickly assess such connections the researcher who works with scattering methods should always be aware of the FT theorems and their consequences.

I.6.2 AC circuits

In subsection I.2.2 we have derived the complex conductance for a single frequency. Applying the convolution theorem (I.61) on (I.31) we see that for any voltage with the Fourier spectrum $U(\omega)$ the current spectrum $I(\omega)$ is given by

$$I(\omega) = G(\omega)\cdot U(\omega)\,. \tag{I.105}$$

It is more common to formulate this with the complex *impedance* $Z(\omega) = 1/G(\omega)$ which is the analogue of the resistance for AC:

$$Z(\omega) = \frac{U(\omega)}{I(\omega)}\,. \tag{I.106}$$

Obviously the complex impedance of a resistor is $Z(\omega) = R$. For the capacitor we have the time-dependent current given by the derivative of the voltage

$$i(t) = C\frac{\mathrm{d}u}{\mathrm{d}t}\,. \tag{I.107}$$

Application of the differentiation theorem yields

$$I(\omega) = -\mathrm{i}\omega C U(\omega) \Rightarrow Z_C(\omega) = \frac{\mathrm{i}}{\omega C}\,. \tag{I.108}$$

(Note that the signs here are opposite to those found in the electronics literature because we define the FT differently.) Analogously, for the inductor we have

$$u(t) = L\frac{\mathrm{d}i}{\mathrm{d}t} \tag{I.109}$$

resulting in

$$U(\omega) = \mathrm{i}\omega L I(\omega) \Rightarrow Z_L(\omega) = -\mathrm{i}\omega L\,. \tag{I.110}$$

The attractiveness of the concept of complex impedance lies in the possibility to simply calculate the response of complex linear electronic circuits. Even a simple circuit as

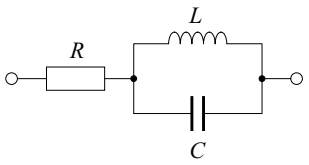

would require a system of equations and differential equations to be solved, viz

$$\begin{aligned} &i = i_1 + i_2,\ u = u_1 + u_2, \\ &u_1 = Ri,\ i_1 = C\frac{\mathrm{d}u_2}{\mathrm{d}t},\ u_2 = L\frac{\mathrm{d}i_2}{\mathrm{d}t} \end{aligned} \tag{I.111}$$

Instead of this, one can use the complex impedance in lieu of the resistance and treat the whole circuit using the rules for parallel and serial resistors:

$$Z(\omega) = R + \frac{1}{\frac{1}{Z_C} + \frac{1}{Z_L}} = R + \frac{1}{\frac{\omega C}{\mathrm{i}} - \frac{1}{\mathrm{i}\omega L}} = R + \frac{\omega L}{\omega^2 LC - 1}\mathrm{i}\,. \tag{I.112}$$

With this expression it is possible to calculate the behaviour of the circuit for any frequency ω. Especially, it can be seen that $Z(\omega)$ diverges for $\omega = 1/\sqrt{LC}$ which is the resonance frequency.

References

[1] K. B. Howell: "Principles of Fourier Analysis" (Chapman & Hall/CRC, Boca Raton, 2001).

[2] H. J. Weaver: “Theory of discrete and continuous Fourier analysis” (John Wiley & Sons, New York, 1988).

[3] J. Kauppinen, J. Partanen: “Fourier Transforms in Spectroscopy” (Wiley-VCH, Berlin, 2001).

[4] F. Oberhettinger: “Tables of Fourier Transforms and Fourier Transforms of Distributions” (Springer, Berlin, 1990).

[5] A. P. Prudnikov, Yu. A. Brychkov, O. I. Marichev: “Integrals and Series” (Gordon and Breach, New York 1986–1992).

[6] E. O. Brigham: “The fast Fourier transform and its applications” (Prentice Hall, London, 1988).

[7] O. Glatter: “The Inverse Scattering Problem in Small-Angle Scattering” in “Neutrons, X-rays and Light: Scattering Methods Applied to Soft Condensed Matter”, eds. P. Lindner, Th. Zemb (North-Holland, Amsterdam, 2002).

[8] A. N. Tikhonov, V. Y. Arsenin: “Solutions of ill-posed problems” (Halsted Press, Washington, 1977).

[9] C. W. Groetsch: “The theory of Tikhonov Regularization for Fredholm Equations of the First Kind” (Pitman, Boston, 1984).

[10] J. Skilling (ed.): “Maximum Entropy and Bayesian Methods” (Kluwer, Dordrecht, 1989).

[11] section 7.10 in J. D. Jackson: “Classical Electrodynamics” (John Wiley & Sons, New York, 1975).

[12] S. G. Samko, A. A. Kilbas, O. I. Marichev: “Fractional Integrals and Derivatives” (Gordon and Breach, Yverdon, Switzerland, 1993).

II

Basic Assumptions of Quantum Mechanics and the Born Approximation – A Brief Tutorial

Dieter Richter

II. Basic Assumptions of Quantum Mechamics and the Born Approximation – A Brief Tutorial

D. Richter

Institut für Festkörperforschung, Forschungszentrum Jülich, D-52425 Jülich, Germany

II.1.1 Introductory remarks

This manuscript constitutes (i) a short revision course on some basic principles of quantum mechanics and (ii) it outlines the quantum mechanical treatment of scattering processes. Thereby it follows to some extend the excellent book on quantum mechanics by Claude Cohen-Tannoudji, Bernard Diu and Frank Laloe [1].

Quantum mechanics plays a fundamental role in the description and understanding of nature. In fact phenomena occurring on an atomistic scale cannot be described outside the frame of quantum mechanics (Q.M.). This concerns for example the existence and the properties of atoms, the chemical bond, the propagation of an electron in a crystal. But also in the macroscopic world there are many phenomena which reveal the quantum behavior of nature. It is in this sense, that it can be said that quantum mechanics is the basis of our present understanding of all natural phenomena including those traditionally treated in chemistry, biology, etc. Even in cosmology, e.g. questions after the origin of the universe, are subject to quantum mechanical treatment.

Historically the necessity of a quantum description of nature was first discovered, when dealing with black body radiation at the end of the 19's century. There it became clear that the energy spectrum emitted by a black body could not be explained by electromagnetic theory. This prompted Planck to suggest the hypothesis of a quantization of energy (1900). For an electromagnetic wave of frequency ν the only possible energies are integral multiples of the quantum $h\nu$, where h is the new fundamental constant.

Einstein generalized this hypothesis and proposed (1905) that light consists of a beam of photons each possessing an energy $h\nu$. In this way Einstein explained in a very simple way the sofar inexplicable characteristics of the photoelectric effect.

These considerations led to the conclusion: the interaction of an electromagnetic wave with matter occurs by means of elementary indivisible processes in which the radiation appears to be composed of particles, the photons. The particle parameters (energy E and momentum $\underline{p}$ and wave parameters $\omega = 2\pi\nu$ and the wave vector $|\underline{k}| = 2\pi/\lambda$) are linked by the fundamental relations

$$E = h\nu \qquad \text{(II.1.1)}$$
$$\underline{p} = \hbar\underline{k}$$

where $\hbar = \frac{h}{2\pi}$ is defined in terms of the Planck constant $h = 6.62 \times 10^{-34}$ Js. Thus, light or electromagnetic radiation in general has also the character of particles.

The other key observation dealt with the wave character of particles: The study of atomic emission and absorption spectra uncovered a fundamental fact which classical physics was unable to explain. Such spectra are composed of narrow lines, an atom emits or absorbs only photons with well determined frequencies. This fact was interpreted assuming that the energies of an atom are quantisized and take certain discrete values E_i ($i = 1, 2 \ldots n$). The emission or absorption of a photon is then accompanied by a jump in energy of the atom from one permitted energy level E_i to another E_j. Conservation of energy implies that the photon must have a frequency ν_{ij} such that

$$h\nu_{ij} = |E_i - E_j| \qquad \text{(II.1.2)}$$

The existence of such discrete energy levels was confirmed independently by the Frank Herz experiment. Bohr interpreted these findings in terms of privileged electronic orbits and stated an empirical rule which permitted the calculation of these orbits for the hydrogen atom, but the fundamental origin of the quantization rules remained mysterious.

Finally in 1923 De Broglie stated the following hypothesis: *"Material particles just like photons can have a wave like aspect"*. With that hypothesis he derived the Bohr Sommerfeld quantization rules. Thereby the various energy levels appeared as analogous to the normal modes of a vibrating string. Electron diffraction experiments (Davisson and German, 1927) confirmed the existence of the wave like aspect of matter by showing that interference patterns could be obtained by particles such as electrons. Thus, a particle with mass having an energy E and the momentum p can be

associated with a wave of an angular frequency $\omega = 2\pi\nu$ and a wave vector k which are given by the same relations as for the photons (Eq.[II.1.1]). In other words the wavelength of a particle is

$$\lambda = \frac{2\pi}{k} = \frac{h}{|\underline{p}|} \tag{II.1.3}$$

II.1.2 Basic assumptions of quantum mechanics

(1) The classical concept of a trajectory is replaced by the notion of a time dependent wave function $\psi(\underline{r},t)$ which describes the state of a quantum mechanical system completely. E.g.

$$\psi(\underline{r},t) = \exp\left[\frac{i}{\hbar}\left(\underline{p}\cdot\underline{r} - Et\right)\right] \tag{II.1.4}$$

describes the state, where a particle with the mass m displays a momentum $\underline{p}$ and an energy $E = p^2/2m$. Comment: The wave function ψ contains all information which are possible to know about a Q.M. system.

(2) $\psi(\underline{r},t)$ is interpreted as a probability amplitude of the particle's presence. The possible positions of a particle form a continuum. Therefore the probability $dP(\underline{r},t)$ of a particle being at time t in a volume element $d^3r = dx\,dy\,dz$ situated at a point $\underline{r}$ being proportional to d^3r $|\psi(\underline{r},t)|^2$ is then interpreted as the corresponding probability density with

$$dP(\underline{r},t) = C\,|\psi(\underline{r},t)|^2\,d^3r \tag{II.1.5}$$

where C is the normalization constant.

(3) For the wave functions a superposition principle is valid. If states $\psi_1(\underline{r},t)$ and $\psi_2(\underline{r},t)$ are possible then also

$$\psi(r,t) = C_1\psi_1(\underline{r},t) + C_2\psi_2(\underline{r},t) \tag{II.1.6}$$

is a possible state.

(4) The equation describing the evolution of $\psi(\underline{r},t)$ is a differential equation called Schrödinger equation. It assumes the form

$$i\hbar \frac{\partial}{\partial t} \psi\left(\underline{r},t\right) = -\frac{\hbar^2}{2m} \Delta\psi\left(\underline{r},t\right) + V\left(\underline{r},t\right) \psi\left(\underline{r},t\right) \tag{II.1.7}$$

We note that this equation is linear and homogenous in ψ. Consequently the superposition principle which we have introduced under (3) is fulfilled. Together with the interpretation of ψ as a probability amplitude, it is the source of the wave like effect. The differential equation is of first order with respect to time. This condition is necessary, if the state of the particle at a time t_0 is to determine its subsequent state.

(5) In quantum mechanics all dynamic variables are described by linear operators. E.g. the momentum p becomes $\frac{\hbar}{i}$ grad. Considering the Hamilton function of a free particle $H = \frac{p^2}{2m}$ in quantum mechanics we arrive at $\hat{H} = -\frac{\hbar^2}{2m}(grad)^2$. Adding the potential energy the Schrödinger equation [II.1.7] can also be written as

$$\hat{H}\psi = +i\hbar\frac{\partial\psi}{\partial t} \tag{II.1.7a}$$

Remembering that the Hamilton function is giving the total energy of a system, and following Eq.[II.1.7a] we may associate with the energy E the operator $-\frac{\hbar}{i}\frac{\partial}{\partial t}$.

Note, there is an important difference between the concept of classical states and quantum states. The classical state of a particle at time t is determined by the specification of six parameters: its positions and velocities. The quantum state of a particle is determined by the values of the wave function $\psi(\underline{r},t)$ describing the quantum state at the various points in space. The classical idea of a trajectory is substituted by the idea of the propagation of the wave associated with a particle.

II.1.3 Example: free particle

We consider now a particle whose potential energy is zero or constant. The particle is thus not subjected to any force, therefore it is called free. With $V(\underline{r},t) = 0$ the Schrödinger equation [II.1.7] becomes

$$i\hbar \frac{\partial}{\partial t} \psi(\underline{r},t) = -\frac{\hbar^2}{2m} \Delta\psi(\underline{r},t) \tag{II.1.8}$$

This differential equation is obviously solved by

$$\psi(\underline{r},t) = A \exp\left[i(\underline{k}\,\underline{r} - \omega t)\right] \tag{II.1.9}$$

with $\omega = \left(\frac{\hbar^2 k^2}{2m}\right)$. Following the De Broglie relation 1.3, the energy and the momentum of the free particle are related by $E = \left(\frac{p^2}{2m}\right)$. With the probability interpretation of Eq.[II.1.5] we realize that such a wave function leads to a particle presence uniformly smeared throughout space $|\psi(r,t)|^2 = |A|^2$. The super position principle of Eq.[II.1.6] tells us that every linear combination of plane waves satisfying the proper relation between ω and k is also a solution of Eq.[II.1.8]. Such a superposition may be written as

$$\psi(r,t) = \frac{1}{(2\pi)^{3/2}} \int g(k) \exp\left[i(\underline{k}\,\underline{r} - \omega(k)t)\right] d^3k \tag{II.1.10}$$

(d^3k represents by definition the infinitesimal volume element in $\underline{k}$ space). $g(\underline{k})$ may be a complex function describing the distribution of $\underline{k}$. A wave function such as Eq.[II.1.10] is called a three dimensional wave packet. For simplicity we consider also the case of one dimensional wave packets which are obtained from the superposition of plane waves all propagating parallel to the x-axis. Then the wave function depends only on x and t.

$$\psi(x,t) = \frac{1}{\sqrt{2\pi}} \int_{-\infty}^{+\infty} g(k) \exp\left[i(kx - \omega(k)t)\right] dk \tag{II.1.11}$$

II.1.4 Heisenberg uncertainty relation

We have seen that a plane wave $\exp(i(k_0x - \omega_0t))$ corresponds to a constant probability density for the particles presence along the x-axis for all values of t. We may also say that the uncertainty Δx to find the particle along the x-axis is infinite. On the other hand only one angular frequency ω_0 and only one wave vector k_0 are involved. Taking the De Broglie relations, this means that the energy and momentum of the particle are well defined: $E = \hbar\omega_0$ and $p = \hbar k_0$. Such a plane wave can be considered as a special case of Eq.[II.1.11] with

$$g(k) = \delta(k - k_0) \tag{II.1.12}$$

the corresponding uncertainty in k, Δk is then 0.

This property may also be interpreted in the following manner. We may say that the particle at $t = 0$ $\psi(x,0) = A\exp(ikx)$ has a well determined momentum. A measurement of the momentum at this time will definitely lead to $p = \hbar k$. From this we may deduce that $\exp(ikx)$ characterizes an eigenstate of the wave function corresponding to $p = \hbar k$.

We now consider Eq.[II.1.11] at $t = 0$. $\psi(x,0)$ appears as a linear a superposition of the momentum eigenfunctions in which the coefficient of $\exp(ikx)$ is $g(k)$. We are thus lead to interpret $|g(k)|^2$ as a probability of finding $p = \hbar k$ if one measures at $t = 0$ the momentum of a particle whose state is described by $\psi(x,t)$. Keeping in mind the probability interpretation of the wave function we may just write

$$\psi(x,0) = \frac{1}{\sqrt{2\pi\hbar}} \int \overline{\psi}(p) e^{\frac{ipx}{\hbar}} dp \tag{II.1.13}$$

The wave function in real space and momentum space are related to each other by a Fourier transformation. Now taking the distribution function as a Gaussian $g(k) \approx \exp\left(-k^2 \big/ 2\Delta k^2\right)$ the wave function in real space becomes $\psi(x,0) \approx \exp\left(-x^2 \Big/ \left(2/\Delta k^2\right)\right)$. Considering the two widths in momentum and real space we are led to the famous Heisenberg uncertainty principle

$$\Delta x\,\Delta k \geq 1 \quad or \quad \Delta x\,\Delta p \geq \hbar \tag{II.1.14}$$

Obviously the product of the uncertainty in the space and the momentum coordinate is at least $\hbar$ or we may say it is impossible to define at a given time both the position of the particle and its momentum to an arbitrary degree of accuracy. When we tried to increase the precision in momentum determination, then Eq.[II.1.14] tells us that the accuracy in the position determination will decrease and finally become infinite. There is nothing like that in classical mechanics. The limitation expressed in Eq.[II.1.14] arises from the fact that h is not 0.

II.1.5 Wave functions, operators: mathematical tools

The probabilistic interpretation of the wave function $\psi(\underline{r},t)$ requires that a total probability of finding a particle somewhere in space is equal to 1. So we must have

$$\int d^3r \left|\psi\left(\underline{r},t\right)\right|^2 = \underline{1} \qquad \text{(II.1.15)}$$

where the integration extends over all space. Thus, the allowed wave functions are a set of square integrable functions. These are functions for which the integral II.1.15 converges. Mathematically this set is called L^2 and has the structure of a Hilbert space. From a physical point of view, it is clear that L^2 is too wide in scope. The wave functions have actually to possess the properties of regularity. We can only retain functions $\psi(\underline{r},t)$ which are everywhere defined, continuous and infinitely differentiable. It is also possible to confine ourselves to wave functions which are bounded. The particle can be found in a finite region of space for example the laboratory. We will not precise these requirements but we note that the functional space F, where our functions exist is a subspace of L^2. F satisfies all criteria of a vector space. For example, if $\psi_1(r)$ and $\psi_2(r,t)$ are element of F then also

$$\psi\left(\underline{r}\right) = \lambda_1 \psi_1\left(\underline{r}\right) + \lambda_2 \psi_2\left(\underline{r}\right) \qquad \text{(II.1.16)}$$

where λ_1, λ_2 are arbitrary complex numbers is an element of F (can easily be shown via the integrability of the sum).

Scalar product

We now define a scalar product on F. $\varphi(r)$ and $\psi(\underline{r})$ are associated with a complex number denoted by (ϕ,ψ) which by definition is equal to

$$(\varphi,\psi) = \int d^3r\, \varphi^*(\underline{r})\psi(\underline{r}) \tag{II.1.17}$$

The following properties follow from Eq.[II.1.17]

$$(\varphi,\psi) = (\psi,\varphi)^* \tag{II.1.18}$$
$$(\varphi, \lambda_1\psi_1 + \lambda_2\psi_2) = \lambda_1(\varphi,\psi_1) + \lambda_2(\varphi,\psi_2)$$
$$(\lambda_1\varphi_1 + \lambda_2\varphi_2,\psi) = \lambda_1^*(\varphi_1,\psi) + \lambda_2^*(\varphi_2,\psi)$$

The scalar product is linear with respect to the second function and antilinear with respect to the first one. If $(\phi,\psi) = 0$ then the two functions orthogonal.

Linear operators

As we have outlined above in quantum mechanics dynamical variables or observables are described by linear operators. Linear operators are defined as a mathematical entity which associates with every function $\psi(\underline{r}) \in F$ another function $\psi'(\underline{r}) \in F$, the correspondence being linear.

$$\psi'(\underline{r}) = \hat{A}\psi(\underline{r}) \tag{II.1.19}$$
$$\hat{A}(\lambda_1\psi_1(\underline{r}) + \lambda_2\psi_2(\underline{r})) = \lambda_1\psi_1'(\underline{r}) + \lambda_2\psi_2'(\underline{r})$$

We now give a number of examples for linear operators

(i) the parity operator Π

$$\hat{\Pi}\psi(x,y,z) = \psi(-x,-y,-z) \tag{II.1.20}$$

(ii) the space operator $\hat{X}$ (x-component), which is defined by

$$\hat{X}\psi(x,y,z) = x\psi(x,y,z) \tag{II.1.21}$$

(iii) finally an operator which differentiates with respect to x. This we call D_x (it relates to the momentum P_x by $\hat{P}x = \frac{\hbar}{i} D_x$. It is defined by

$$\hat{D}_x \psi(x,y,z) = \frac{\partial}{\partial x}\psi(x,y,z) \tag{II.1.22}$$

If $\hat{A}$ and $\hat{B}$ are linear operators then their product $\hat{A}\hat{B}$ is defined by

$$\left(\hat{A}\hat{B}\right)\psi(\underline{r}) = \hat{A}\left[\hat{B}\psi(r)\right] \tag{II.1.23}$$

This equation means that $\hat{B}$ is first acting on ψ and on the result of that the operator $\hat{A}$ is acting. In general we have $\hat{A}\hat{B} \neq \hat{B}\hat{A}$. We call the commutator of $\hat{A}$ and $\hat{B}$ the operator written $\left[\hat{A},\hat{B}\right]$. This is defined

$$\left[\hat{A},\hat{B}\right] = \hat{A}\hat{B} - \hat{B}\hat{A} \tag{II.1.24}$$

as an example we treat the commutator $\left[\hat{X},\hat{D}_x\right]$. With an arbitrary function ψ(r) we have

$$\begin{aligned}\left[\hat{X},\hat{D}_x\right]\psi(r) &= \left(x\frac{\partial}{\partial x} - \frac{\partial}{\partial x}x\right)\psi(\underline{r}) \\ &= x\frac{\partial}{\partial x}\psi(\underline{r}) - \frac{\partial}{\partial x}\left(\psi(r)\right) \\ &= x\frac{\partial}{\partial x}\psi(\underline{r}) - \psi(\underline{r}) - x\frac{\partial}{\partial x}x\psi(\underline{r}) = -\psi(\underline{r})\end{aligned} \tag{II.1.25}$$

This result is true for all functions ψ therefore we have

$$\begin{aligned}\left[\hat{X},\hat{D}_x\right] &= -1 \\ \left[\hat{X},\hat{p}\right] &= i\hbar\end{aligned} \tag{II.1.26}$$

The most important linear operator in Q.M. is the Hamilton operator $\hat{H}$ which is derived from the Hamilton function of the corresponding classical system $H = p^2/2m + V(\underline{r})$. Transcription into Q.M. leads to

$$\hat{H} = \frac{\hat{p}^2}{2m} + V(r) \tag{II.1.27}$$

For a system with energy conservation $\frac{\partial \hat{H}}{\partial t} = 0$. Then space and time variables of the Schrödinger Eq.[II.1.7] may be separated yielding a stationary Schrödinger equation of the form

$$\hat{H}\,\psi(\underline{r}) = E\psi(\underline{r}) \tag{II.1.28}$$

where E describes the possible energy states of the system

Orthonormal basis in functional space

Within the functional space F we may define an orthonormal basis $\{u_i(\underline{r})\}$. We consider a countable set of functions of F labeled by a discrete index ($i = 1, 2, \ldots n \ldots$). The set $\{u_i(\underline{r})\}$ is orthonormal if

$$(u_i, u_j) = \int d^3r\, u_i^*(\underline{r})\, u_j(\underline{r}) = \delta_{ij} \tag{II.1.29}$$

where δ_{ij} is the Kronecker symbol. δ is equal to 1 for $i = j$ and 0 otherwise. The functions u constitute a basis, if every function $\psi(\underline{r}) \in F$ can be expanded in only one way in terms of the $\{u_i(\underline{r})\}$

$$\psi(\underline{r}) = \sum_i c_i u_i(\underline{r}) \tag{II.1.30}$$

The components c_i of a wave function with respect to a basis function $u_i(\underline{r})$ is obtained by

$$c_i = (u_i, \psi) = \int d^3r\, u_i^*(\underline{r})\psi(\underline{r}) \qquad \text{(II.1.31)}$$

The component c_i of $\psi(r)$ on $u_i(r)$ is therefore equal to the scalar product of $u_i(\underline{r})$ and $\psi(\underline{r})$. Once a basis is chosen it is equivalent to specify ψ or the set of its components c_i with respect to the basis functions. The set of numbers c_i is said to represent $\psi(\underline{r})$ in the $\{u_i(\underline{r})\}$ basis.

Bra and Ket vectors

Dirac has generalized and formalized the above considerations in introducing so called ket and bra vectors. We characterize each quantum state of a particle by a state vector which belongs to an abstract space E_r called the state space of the particle. Since F is a subspace of L^2 also E_r is a subspace of a Hilbert space. We are now going to define the notation and rules for vector calculations in E_r.

Any element or vector of E_r space is called ket vector or most simply a ket. It is represented by the symbol $|\ \rangle$. Inside this symbol we place a sign which enables us to distinguish the corresponding ket from all others. For example $|\psi\rangle$. Note that now the symbol ψ is not associated any more with the space coordinate r. The letter ψ reminds us with which function the ket is associated with. $\psi(\underline{r})$ then is interpreted as a set of components of the ket vector ψ in a particular basis r.

The scalar product between two kets is formally taken over from Eq.[II.1.18] associating a complex number with a pair of kets obeying the rules establish there. We now define so called bras which are associated with each ket in an antilinear fashion

$$\lambda_1|\varphi_1\rangle + \lambda_2|\varphi_2\rangle \Rightarrow \lambda_1^*\langle\varphi_1| + \lambda_2^*\langle\varphi_2| \qquad \text{(II.1.32)}$$

With this notion we may write the scalar product as

$$(|\varphi\rangle, |\psi\rangle) = \langle\varphi|\psi\rangle \qquad \text{(II.1.33)}$$

Note that the rules II.1.18 are naturally fulfilled by these definitions. The role of linear operators may be taken over from Eqs.[II.1.19] to [II.1.23]. Eq.[II.1.19] becomes

$$|\psi'\rangle = \hat{A}|\psi\rangle \qquad \text{(II.1.34)}$$

$$\hat{A}\left(\lambda_1|\psi_1\rangle + \lambda_2|\psi_2\rangle\right) = \lambda_1 \hat{A}|\psi_1\rangle + \lambda_2 \hat{A}|\psi_2\rangle$$

with the definition of bra and ket vectors we may also define in terms of a scalar product so called matrix elements of an operator $\hat{A}$ between $|\varphi\rangle$ and $|\psi\rangle$

$$\langle\varphi|\left(A|\psi\rangle\right) \equiv \langle\varphi|A|\psi\rangle \qquad \text{(II.1.35)}$$

Eigenvalues and eigenvectors of an operator

As stated above in quantum mechanics observables correspond to linear operators. The action of such an operator on the wave function results in possible realisations of the observable. Formally it is interesting to know which wave functions or kets correspond to a specific possible realisation of an observable and what are these realizations. Mathematically this corresponds to eigenvalue problem. The possible realisations are given by the eigenvalues of an operator and the corresponding wave functions are the eigenvectors. $|\psi\rangle$ is an eigenvector or eigenket of a linear operator $\hat{A}$ if

$$\hat{A}|\psi\rangle = a|\psi\rangle \qquad \text{(II.1.36)}$$

where a is a complex number. Eq.[II.1.36] is also called the eigenvalue equation of the linear operator $\hat{A}$. In general this equation possesses a solution only if a takes certain values, called eigenvalues of $\hat{A}$. The set of the eigenvalues is called the spectrum of $\hat{A}$. Eigenvalues may be degenerate meaning that several linear independent eigenfunctions may be associated with the same eigenvalue. For the sake of simplicity, we will only consider the non-degenerate case.

Given a linear operator $\hat{A}$, how does one find all its eigenvalues and the corresponding eigenvectors? We shall consider the case, where the state space is of finite dimension N and we shall assume that the results can be generalized to an infinite dimensional state space. Let us choose a basis, e.g. $\{|u_i\rangle\}$ and let us project the vector equation [II.1.36] onto the various orthonormal basis vectors $|u_i\rangle$

$$\left\langle u_i \middle| \hat{A} \middle| \psi \right\rangle = a \left\langle u_i | \psi \right\rangle \tag{II.1.37}$$

Inserting the closure relation $\sum_j |u_j\rangle\langle u_j| = \hat{1}$, where $\hat{1}$ is the unity operator, between $\hat{A}$ and $|\psi\rangle$ we obtain

$$\sum_j \left\langle u_i \middle| \hat{A} \middle| u_j \right\rangle \left\langle u_j | \psi \right\rangle = a \left\langle u_i | \psi \right\rangle^* \tag{II.1.38}$$

With the usual notations

$$\begin{aligned} \left\langle u_i | \psi \right\rangle &= c_i \\ \left\langle u_i \middle| \hat{A} \middle| u_j \right\rangle &= A_{ij} \end{aligned} \tag{II.1.39}$$

Eq.[II.1.38] may be rewritten to

$$\sum_j \left[A_{ij} - a\delta_{ij} \right] c_j = 0 \tag{II.1.40}$$

This equation can be considered to be a system of equations, where the unknowns are the c_j, the components of the eigenvector in the chosen representation. The system is linear and homogeneous. Eq.[II.1.40] has nontrivial solutions, if and only if the determinant of the coefficients is zero. This condition is written as

$$Det\left[\underline{\underline{A}} - a\underline{\underline{I}} \right] = 0 \tag{II.1.41}$$

where $\underline{\underline{A}}$ is the N × N matrix of the elements a_{ij} and $\underline{\underline{I}}$ is the unit matrix. Solutions of Eq.[II.1.41] gives us the eigenvalues or the spectrum of $\hat{A}$. After having obtained the eigenvalues, the eigenvectors are found by inserting the respective eigenvalues into Eq.[II.1.40] and solving for c_j.

Note that observables in quantum mechanics are always associated with Hermetian linear operators $\hat{A}$. These operators have the additional property that $A^+ = A$. It can be shown that the eigenvalues of Hermetian operators are real. Furthermore, eigenvectors of Hermetian operators corresponding to

*The projector $\sum_j |u_j\rangle\langle u_j|$ provides a complete projection of ψ on the various base function $|u_j\rangle$.

different eigenvalues are orthogonal. In a space of finite dimension N a Hermetian operator always has N linearly independent eigenvectors forming a base with respect to the operator $\hat{A}$.

II.1.6 Heisenberg and Schrödinger pictures

Time evolution operator

The Schrödinger equation [II.1.7] is of first order in time. From this it follows that given the initial state $|\psi(t_0)\rangle$ the state $|\psi(t)\rangle$ at any subsequent time is uniquely determined. There is no indeterminacy in the time evolution of quantum systems. The transformation of $|\psi(t_0)\rangle$ into $|\psi(t)\rangle$ is linear. Therefore in general there exists a linear operator $\hat{U}(t,t_0)$ such that

$$|\psi(t)\rangle = \hat{U}(t,t_0)|\psi(t_0)\rangle \tag{II.1.42}$$

$\hat{U}(t,t_0)$ is also called the evolution operator of the system. Since the ket $|\psi(t_0)\rangle$ is arbitrary, it is clear from Eq.[II.1.42] that

$$\hat{U}(t_0,t_0) = 1 \tag{II.1.43}$$

$\hat{U}(t_0,t_0)$ is the unity operator. We now substitute Eq.[II.1.42] into the Schrödinger equation. With that we obtain

$$i\hbar \frac{\partial}{\partial t} \hat{U}(t,t_0)|\psi(t_0)\rangle = \hat{H}(t)\,\hat{U}(t,t_0)|\psi(t_0)\rangle \tag{II.1.44}$$

Since $|\psi\rangle$ is arbitrary we have

$$i\hbar \frac{\partial}{\partial t} \hat{U}(t,t_0) = \hat{H}(t)\,\hat{U}(t,t_0) \tag{II.1.45}$$

The first order differential equation completely defines $\hat{U}(t,t_0)$, if we take the initial condition [II.1.43] into account.

It is easily shown that U is unitary

$$\hat{U}^{+}(t,t') = \hat{U}^{-1}(t,t') = \hat{U}(t',t) \tag{II.1.46}$$

Thus, the transformation $\hat{U}$ conserves the norm of vectors, on which it acts. I.e. the norm of the state vector does not change over time.

We now consider the special case of a conservative system, where $\hat{H}$ does not depend explicitly on time. Then Eq.[II.1.45] may easily be integrated and we obtain

$$\hat{U}(t,t_0) = e^{-i\hat{H}(t-t_0)/\hbar} \tag{II.1.47}$$

The Heisenberg picture

Up to now we have been discussing in general time independent operators, which correspond to the observables of the system. For example the position, the momentum and the kinetic energy operators of a particle do not depend on time. The evolution of the system is entirely contained in that of the state vector $|\psi(t)\rangle$ and this time evolution is obtained from the Schrödinger equation. This is why this approach is called the Schrödinger picture. With the unitary transformations we have been discussing above, it is now also possible to define a unitary transformation, acting on ket and bra vectors such, that they become time independent and that all the time dependence is contained in the operators. We call this approach the Heisenberg picture. In order to distinguish both approaches, we will systematically assign an index S to the kets and operators in the Schrödinger picture, while an index H will be used for those in the Heisenberg picture.

From Eq.[II.1.42] we know that the state vector at an instant t may be expressed in terms of the state vector at an instant t_0 by the relation

$$|\psi_s(t)\rangle = \hat{U}(t,t_0)\,|\psi_s(t_0)\rangle \tag{II.1.48}$$

Since $\hat{U}$ is unitary we may perform the unitary transformation associated with the operator $U^{+}(t,t_0)$ to obtain a constant transformed vector $|\psi_H\rangle$.

$$|\psi_H\rangle = \hat{U}^+(t,t_0)|\psi_s(t)\rangle \tag{II.1.49}$$

$$= \hat{U}^+(t,t_0)\,\hat{U}(t,t_0)|\psi_S(t_0)\rangle = |\psi_S(t_0)\rangle \tag{II.1.50}$$

In the Heisenberg picture the state vector is constant and equal to $|\psi_S(t)\rangle$ at time t_0. The transform $\hat{A}_H(t)$ of an operator $\hat{A}_S$ is given by

$$\hat{A}_H(t) = \hat{U}^+(t,t_0)\;\hat{A}_S(t)\,\hat{U}(t,t_0) \tag{II.1.51}$$

$\hat{A}_H(t)$ generally depends on time even if $\hat{A}_S$ does not. There exists an interesting special case in which, if $\hat{A}_S$ is time independent, the same is true of $\hat{A}_H$. This occurs if a system is conservative and $\hat{A}_S$ commutes with $\hat{H}_S$ (or $\hat{A}_S$ is the constant of motion). Then since $\hat{U}$ is given by Eq.[II.1.47] if $\hat{A}_S$ commutes with $\hat{H}_S$ it also commutes with $\hat{U}(t,t_0)$. So that

$$\hat{A}_H(t) = \hat{U}^+(t,t_0)\;\hat{U}(t,t_0)\hat{A}_S = \hat{A}_S \tag{II.1.52}$$

The operators $\hat{A}_S$ and $\hat{A}_H$ are thus simply equal. In particular $\hat{H}_S = \hat{H}_H$ the Hamilton operator for a conservative system is identical in the Schrödinger and the Heisenberg picture. For an arbitrary operator $\hat{A}_S(t)$ the evolution of the operator $\hat{A}_H(t)$ is obtained from Eq.[II.1.51] in combination with the equation for the time dependence of the time evolution operator (Eq.[II.1.45]). Differentiating [II.1.51] and inserting [II.1.45] we obtain

$$\frac{d}{dt}\,\hat{A}_H(t) = -\frac{1}{i\hbar}\hat{U}^+(t,t_0)\;\hat{H}_S(t)\,\hat{A}_S(t)\,\hat{U}(t,t_0)$$

$$+\,\hat{U}^+(t,t_0)\,\frac{d\,\hat{A}_S(t)}{dt}\,\hat{U}(t,t_0) \tag{II.1.53}$$

$$+\,\frac{1}{i\hbar}\hat{U}^+(t,t_0)\;\hat{A}_S(t)\,\hat{H}_S(t)\,U(t,t_0)$$

If we insert in the first and last term of this expression between $\hat{A}_S$ and $\hat{H}_S$ the product $\hat{U}(t,t_0)$ $\hat{U}^+(t,t_0)$ which is equal to the identity operator, then Eq.[II.1.53] may be reduced to

$$i\hbar \frac{d}{dt} \hat{A}_H(t) = \left[\hat{A}_H(t),\, \hat{H}_H(t) \right] + i\hbar \left[\frac{d}{dt} A_S(t) \right]_H \tag{II.1.54}$$

Eq.[II.1.54] is the basic equation of motion for operators in the Heisenberg picture. For operators which in the Schrödinger picture are not explicitly depending on time, the evolution of an operator in the Heisenberg picture is just given by its commutator with the Hamilton operator. The considerations of the Heisenberg picture will become important later, when the correlation functions in terms of the van Hove picture are derived.

II.2. Scattering theory

Scattering experiments in condensed matter consist of directing a beam onto a target composed of matter and studying the resulting scattering pattern: i.e. the direction and the energy of the scattered particles at various scattering angles θ_1 and θ_2 (see Fig.2.1). From the interaction of the incoming beam – in our case neutrons – with the target detailed information about the microscopic materials properties are sought. In this chapter we first will introduce a number of definitions and then formulate the scattering problem and its general solutions in terms of stationary scattering states. Then, we will give a general calculation of the cross section. Thereafter the Born approximation will be introduced and finally the Fermi pseudo potential will be discussed.

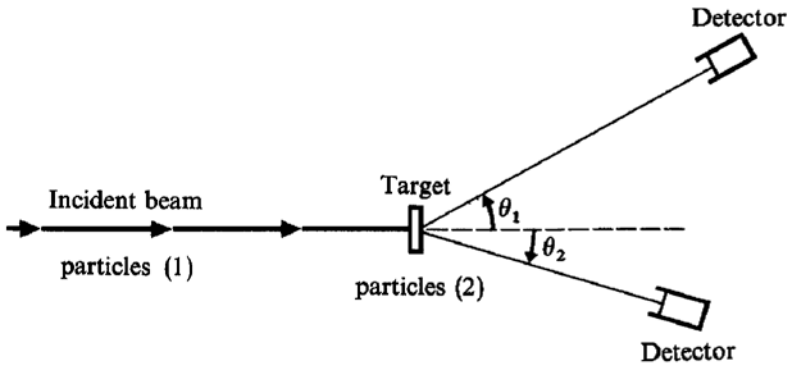

Figure 2.1: Schematic sketch of a scattering experiment.

For our treatment we make a number of assumptions, in order to simplify the problem.

(i) We shall suppose that the spin does not play a role.

(ii) We will assume that the scattering is elastic, i.e. that the final energy of the scattered particles is identical to that of the incoming particles. This assumption however can be generalized straight forwardly.

(iii) We will discuss only scattering processes on a single nucleus and thus, not discuss coherent effects which will be subject of later lectures.

(iv) We shall assume that the interactions between the incoming beam and the target can be described by a potential energy $V(\underline{r}_1 - \underline{r}_2)$ which depends only on the relative position $\underline{r} = \underline{r}_1 - \underline{r}_2$ of the particles. In that case a center of mass reference frame of the two particles may be used, which reduces the problem to the study of the scattering of the single particle by a potential $V(r)$.

Definition of the scattering cross section

Let the z direction be the direction of the incident particles (Fig.2.2).

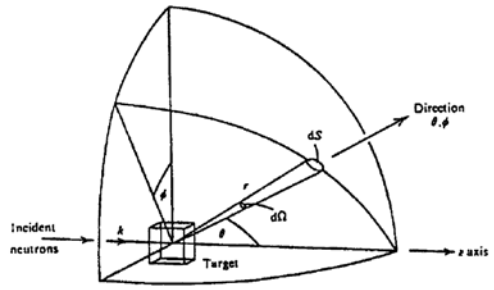

$\underline{r} = (0, 0, Z)$

Figure 2.2: Scattering geometry for an incident plane wave scattered at a target.

The potential $V(r)$ is localized around the origin of the coordinate system. We shall designate by F_i the flux of the particles in the incident beam, i.e. the number of particles per unit time, which traverse the unit surface perpendicular to the z direction.

We place a detector far from the region under the influence of the potential (or the target). In the direction fixed by the polar angles θ and φ with an opening facing the target and spanning a solid angle $d\Omega$. In such an arrangement we can count the number dn of particles scattered per unit time into the solid angle $d\Omega$ around the direction (θ,φ). dn is obviously proportional to $d\Omega$ and to the incident flux F_i. We define $d\sigma(\theta,\varphi)$ to be the coefficient of proportionality between dn and $F_i\, d\Omega$

$$dn = F_i d\sigma(\theta,\varphi) d\Omega \tag{II.2.1}$$

The dimensions of dn and F_i are respectively t^{-1} and $(\ell^2 t)^{-1}$, where t is the time and ℓ is a length defining the cross section of the incident beam. $d\sigma(\theta,\varphi)$ therefore has the dimension of a surface. It is called the differential scattering cross section in the direction (θ,φ). Cross sections are commonly measured in barns.

$$1\ barn = 10^{-24} cm^2 \tag{II.2.2}$$

The definition II.2.1 may be interpreted in the following way. The number of particles per unit time which reach the detector is equal to the number of particles which would cross a surface $\sigma(\theta,\varphi)\, d\Omega$

placed perpendicular to the z direction in the incident beam. Similarly the total scattering cross section σ is defined by the formula

$$\sigma = \int d\sigma(\theta,\varphi)\, d\Omega \tag{II.2.3}$$

II.2.1 Formulation of the scattering problem; stationary scattering states

In order to describe in quantum mechanical terms the scattering of a given incident particle by the potential $V(r)$ it is necessary to study the time evolution of a wave packet representing the state of the incoming particle. Each of such wave packages at large negative times were $V(r)$ is not yet active, may be described as a superposition of stationary states (see Eq.[II.1.11]), which we are going to treat here. Thus, we have to study the eigenvalue equation for the Hamiltonian

$$H = H_0 + V(\underline{r}) \text{ with } H_0 = \frac{p^2}{2\mu} \tag{II.2.4}$$

Here p describes the momentum and μ the reduced mass of the incoming particle. Schrödingers equation describing the evolution of the particle in the potential $V(\underline{r})$ is satisfied by solutions associated with a well defined energy E (stationary states).

$$\Psi(\underline{r},t) = \varphi(\underline{r})\ e^{-iEt/\hbar} \tag{II.2.5}$$

where $\varphi(r)$ is the solution of the eigenvalue equation

$$\left[-\frac{\hbar^2\Delta}{2\mu} + V(\underline{r})\right]\varphi(\underline{r}) = E\varphi(\underline{r}) \tag{II.2.6}$$

In the following we assume that the potential $V(r)$ decreases faster than $1/r$ as r approaches infinity. We shall be concerned with solutions with Eq.[II.2.6] associated with a positive energy E equal to the kinetic energy of the incident particle before it reaches the zone of influence of the potential. Defining

$$E = \frac{\hbar^2 k^2}{2\mu} \tag{II.2.7}$$

$$V(\underline{r}) = \frac{\hbar^2}{2\mu} U(\underline{r})$$

allows us to rewrite Eq.[II.2.6]

$$\left[\Delta + k^2 - U(\underline{r})\right] \varphi(\underline{r}) = 0 \qquad \text{(II.2.8)}$$

For each value of k Eq.[II.2.8] can be satisfied by an infinite number of solutions (the positive eigenvalues of the Hamiltonian H are infinitely degenerate). Among these large number of possible solutions we have to choose that, which satisfies the physical problem. We will now specify the conditions that must be imposed on the solutions of Eq.[II.2.8] if they are to be used in the description of the scattering process. We shall call the eigenstates of the Hamiltonian which satisfy these conditions stationary scattering states and we shall designate by $\psi_k(r)$ the associated wave functions.

For large negative values of t the incident particle is free and its state must be presented in form of plane wave e^{ikz}, where k is the constant which appears in Eq.[II.2.8]. In the region of the potential the evolution of the incoming wave is complicated. However, for large positive values of t, when the scattered particle has left the region of influence of the potential, once again we have to have a simple form. Now, the wave will be splitted into a transmitted wave which continues to propagate along the z direction and the scattered wave. The wavefunction $\psi_k(r)$ will be obtained from a superposition of the plane wave e^{ikz} and a scattered wave.

The structure of the scattered wave obviously depends on the potential. However, its asymptotic form is simple. By analogy with wave optics, the scattered wave must present the following characteristics at large r

(i) In a given direction (θ,φ) its radial dependence is of the form e^{ikr}/r. The outgoing wave has the same energy as the incident wave. The factor $1/r$ ensures that Eq.[II.2.8] is satisfied. (In optics the factor $1/r$ insures that the total flux of energy passing through a sphere of radius r is independent of r for large r. In quantum mechanics it is the probability flux passing through the sphere that does not depend on r.)

(ii) Since the scattering is generally not isotropic the amplitude of the outgoing wave depends on the direction θ,φ which is considered. The asymptotic form of ψ_k thus becomes

$$\Psi_k(r) \underset{r\to\infty}{\sim} e^{ikz} + f_k(\theta,\varphi)\frac{e^{ikr}}{r} \tag{II.2.9}$$

The function $f_k(\theta,\varphi)$ is called the scattering amplitude. It is the only function which depends on the potential $V(r)$.

Calculation of the cross section in terms of probability currents

We want to calculate the contributions of the incident wave and the scattered wave to the probability current in a stationary scattering state. The expression for the current $J(r)$ associated with a wave function $\varphi(r)$ is

$$J(r) = \frac{1}{\mu}\,\mathrm{R_e}\left[\varphi^*(r)\frac{\hbar}{i}\nabla\varphi(r)\right] \tag{II.2.10}$$

The incident current J_i is obtained from 2.10 by replacing $\varphi(k)$ by the plane wave e^{ikz}. J_i is therefore directed belong the positive z direction. Its expectation value is

$$|J_i| = \frac{\hbar k}{\mu} \tag{II.2.11.}$$

Since the scattered wave is expressed in spherical coordinates we will calculate the components of the scattered current J_d along the local axis defined by this coordinate system. We recall that the corresponding components of the operator ∇ are

$$(\nabla)_r = \frac{\partial}{\partial r} \tag{II.2.12}$$

$$(\nabla)_\theta = \frac{1}{r}\frac{\partial}{\partial\theta}$$

$$(\nabla)_\varphi = \frac{1}{r\sin\theta}\frac{\partial}{\partial\varphi}$$

If we replace $\varphi(r)$ in Eq.[II.2.10] by the function $f_k(\theta,\varphi)e^{ikr}/r$ we easily obtain the scattered current in the asymptotic region

$$\begin{aligned}
\left(J_d\right)_r &= \frac{\hbar k}{\mu}\frac{1}{r^2}\left|f_k(\theta,\varphi)\right|^2 \\
\left(J_d\right)_\theta &= \frac{\hbar}{\mu}\frac{1}{r^3}\ \mathrm{Re}\left[\frac{1}{i}f_k^*(\theta,\varphi)\frac{\partial}{\partial\theta}f_k(\theta,\varphi)\right] \\
\left(J_d\right)_\varphi &= \frac{\hbar}{\mu}\frac{1}{r^3\sin\theta}\ \mathrm{Re}\left[\frac{1}{i}f_k^*(\theta,\varphi)\frac{\partial}{\partial\varphi}f_k(\theta,\varphi)\right]
\end{aligned} \tag{II.2.13}$$

Since r is large $(J_d)_\theta$ and $(J_d)_\varphi$ are negligible compared to $(J_d)_r$ i.e. the scattered current is practically radial.

In order to go to the flux, we note that sending a great number of particles on a target the same experiment is repeated a large number of times. Therefore flux and current are proportional. Similarly, the number dn of particles hitting a detector at θ,φ per unit time is proportional to the flux of the vector J_d across the detector surface ds of the opening. The proportionality constants are the same in both cases. Thus, we have

$$\begin{aligned}
dn = C\,J_d\,dS &= C\left(J_d\right)_r\,r^2\,d\Omega \\
&= C\frac{\hbar k}{\mu}\left(f_k(\theta,\varphi)\right)^2\,d\Omega
\end{aligned} \tag{II.2.14}$$

We see that dn is independent of r for sufficiently large r. If we substitute Eq[II.2.11] and Eq.[II.2.14] into Eq.[II.2.1] we obtain

$$d\sigma(\theta,\varphi) = \left|f_k(\theta,\varphi)\right|^2 \tag{II.2.15}$$

The differential cross section is simply the square of the scattering amplitude.

II.2.2 Calculation of the cross section

We now address the more formal solution of the scattering Eq.[II.2.6]. In order to do so, we introduce the integral scattering equation, whose solutions are precisely the stationary scattering state wave functions. We go back to the eigenvalue equation [2.6] and put it in a different form.

$$\left(\Delta + k^2\right) \varphi\left(\underline{r}\right) = U\left(\underline{r}\right) \varphi\left(\underline{r}\right) \tag{II.2.16}$$

For the moment let us assume that there exist a function $G(\underline{r})$ such that

$$\left(\Delta + k^2\right) G\left(\underline{r}\right) = \delta\left(\underline{r}\right) \tag{II.2.17}$$

$G(\underline{r})$ is called the Green function of the operator $\Delta + k^2$. Then any function $\varphi(\underline{r})$ which satisfies

$$\varphi\left(\underline{r}\right) = \varphi_0\left(\underline{r}\right) + \int d^3r' \, G\left(\underline{r} - \underline{r}'\right) U\left(\underline{r}'\right) \varphi\left(\underline{r}'\right) \tag{II.2.18}$$

where $\varphi_0(r)$ is a solution of the homogenous equation

$$\left(\Delta + k^2\right) \varphi_0\left(\underline{r}\right) = 0 \tag{II.2.19}$$

is a solution of the differential equation [II.2.16]

In order to show this, we apply the operator $\Delta + k^2$ to both sides of Eq.[II.2.18]. Taking II.2.19 into account. This gives

$$\left(\Delta + k^2\right) \varphi\left(\underline{r}\right) = \left(\Delta + k^2\right) \int d^3r' \, G\left(\underline{r} - \underline{r}'\right) U\left(\underline{r}'\right) \varphi\left(r'\right) \tag{II.2.20}$$

Assuming that we can move the operator inside the integral - it will only act on the variable r and following II.2.17 we get

$$\left(\Delta + k^2\right) \varphi\left(\underline{r}\right) = \int d^3r' \, \delta\left(\underline{r} - \underline{r}'\right) U\left(\underline{r}'\right) \varphi\left(\underline{r}'\right) = U\left(\underline{r}\right) \varphi\left(\underline{r}\right) \tag{II.2.21}$$

Inversely, it can also be shown that any solution of Eq.[II.2.16] satisfies Eq.[II.2.18]. In practical terms it is often easier to use the integral equation. Its principal advantage derives from the fact that by choosing $\varphi_0(\underline{r})$ and $G(\underline{r})$ correctly one can incorporate into the equation the desired asymptotic behavior. Thus, the integral equation called the integral scattering equation becomes the equivalent of the differential equation [II.2.16] together with the asymptotic conditions.

Now we have first have to construct the Green function defined in Eq.[II.2.17]. We show, that the functions

$$G_{\pm}(\underline{r}) = -\frac{1}{4\pi}\,\frac{e^{\pm ikr}}{r} \tag{II.2.22}$$

precisely fulfill the conditions of Eq.[II.2.16]. We may write

$$\Delta G_{\pm}(\underline{r}) = e^{\pm ikr}\,\Delta\left(\frac{-1}{4\pi r}\right) - \frac{1}{4\pi r}\,\Delta\left(e^{\pm ikr}\right) + 2\left(\nabla\left(-\frac{1}{4\pi r}\right)\right)\left(\nabla e^{\pm ikr}\right) \tag{II.2.23}$$

A simple calculation gives

$$\Delta G_{\pm}(\underline{r}) = -k^2\; G_{\pm}(\underline{r}) + \delta(\underline{r}) \tag{II.2.24}$$

which is what we wanted to prove. G_+ and G_- are called respectively outgoing and incoming Green functions. The actual form of the desired asymptotic behavior (Eq.[II.2.9]) suggest the choice of the incident plane wave e^{ikz} for $\varphi_0(\underline{r})$ and the choice of the outgoing Green function $G_+(\underline{r})$ for $G(\underline{r})$. We will now show that the integral scattering equation may be written as

$$\psi_k(\underline{r}) = e^{ikz} + \int d^3r'\, G_+(\underline{r} - \underline{r}')\, U(\underline{r}')\, \psi_k(\underline{r}') \tag{II.2.25}$$

To do so, we place ourselves at a point M (position $\underline{r}$) very far from the various points (position $\underline{r}'$) of the target, with a linear dimension of the order L^* (Fig.2.3).

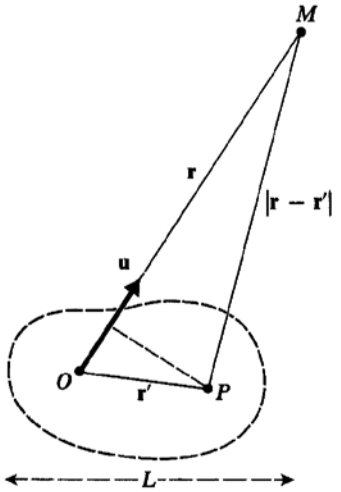

Figure 2.3: Approximate calculation of the distance $|r - r'|$ between a point M very far from O and a point P situated in the zone of influence of the potential (the dimensions of this zone of influence are of the order of L).

Since the angle between MO and MP is very small the length MP (that is $|\underline{r} - \underline{r}'|$) is equal within a good approximation to the projection of MP on MO.

$$\left|\underline{r} - \underline{r}'\right| \approx r - \underline{u}\,\underline{r}' \tag{II.2.26}$$

where $\underline{u}$ is the unit vector in the $\underline{r}$ direction. Thus, for large r

$$G_+\left(\underline{r} - \underline{r}'\right) = -\frac{1}{4\pi}\frac{e^{ik|\underline{r}-\underline{r}'|}}{\left|\underline{r} - \underline{r}'\right|} \sim -\frac{1}{4\pi}\frac{e^{ikr}}{r}\,e^{-ik\underline{u}\,\underline{r}'} \tag{II.2.27}$$

substituting back this expression into Eq.[II.2.25] we obtain the asymptotic behavior of $\psi_k(\underline{r})$.

$$\psi_k\left(\underline{r}\right)_{r\to\infty} \sim e^{ikz} - \frac{1}{4\pi}\frac{e^{ikr}}{r}\int d^3r'\, e^{ik\underline{u}\,\underline{r}'}\,U\left(\underline{r}'\right)\psi_k\left(\underline{r}'\right) \tag{II.2.28}$$

which is indeed of the form II.2.9. Setting

$$f_k\left(\theta,\varphi\right) = -\frac{1}{4\pi}\int d^3r'\, e^{ik\underline{u}\,\underline{r}'}\,U\left(\underline{r}'\right)\psi_k\left(\underline{r}'\right) \tag{II.2.29}$$

we arrive at an expression which is identical to II.2.9. At the end of this paragraph we introduce a number of further definitions. We define the incident wave factor k_i as a vector of modulus k, directed along the z direction of the beam such that

$$e^{ikz} = e^{i\underline{k}_i \underline{r}} \tag{II.2.30}$$

In the same way the vector k_d which has the same value as the incident wave vector but whose direction is fixed by the angles θ and φ is called the scattered wave vector in the direction (θ,φ)

$$\underline{k}_f = k\underline{u} \tag{II.2.31}$$

Finally, the scattering wave vector in the direction (θ,φ) is a difference between k_f and k_i (Fig.2.4)

$$\underline{Q} = \underline{k}_f - \underline{k}_i \tag{II.2.32}$$

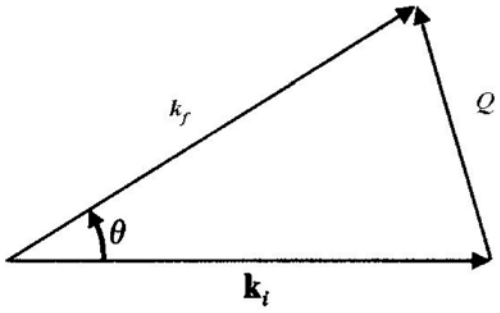

Figure 2.4: Scattering triangle with the incident wave vector $\underline{k}_i$ the scattered wave vector $\underline{k}_f$ and the transferred wave vector $\underline{Q}$.

II.2.3 The Born approximation

We now are trying to solve the scattering Eq.[II.2.18] by iteration.

$$\psi_k(\underline{r}') = e^{i\underline{k}_i\underline{r}'} + \int d^3\underline{r}''\, G_+(\underline{r}' - \underline{r}'')\, U(\underline{r}'')\, \psi_k(\underline{r}'') \tag{II.2.33}$$

We insert this equation into Eq.[II.2.25] yielding

$$\begin{aligned}\psi_k(\underline{r}) = {} & e^{i\underline{k}_i\underline{r}} + \int d^3r'\, G_+(\underline{r} - \underline{r}')\, U(\underline{r}')\, e^{i\underline{k}_i\underline{r}'} \\ & + \int d^3r' \int d^3r''\, G_+(\underline{r} - \underline{r}')\, U(\underline{r}')\, G_+(\underline{r}' - \underline{r}'')\, U(\underline{r}'')\, \psi_k(\underline{r}'')\end{aligned} \tag{II.2.34}$$

There the first two terms on the right hand side are known. Only the third contains the unknown function $\psi_k(\underline{r})$. The procedure may be repeated in the next step yielding

$$\begin{aligned}\psi_k(r) = {} & e^{ik_i r} + \int d^3r'\, G_+(\underline{r} - \underline{r}')\, U(\underline{r}')\, e^{i\underline{k}_i\underline{r}} \\ & + \int d^3r' \int d^3r''\, G_+(\underline{r} - \underline{r}')\, U(\underline{r}')\, G_+(\underline{r}' - \underline{r}'')\, U(\underline{r}'')\, e^{i\underline{k}_i\underline{r}''} \\ & + \int d^3r' \int d^3r'' \int d^3r'''\, G_+(\underline{r} - \underline{r}')\, U(\underline{r}')\, G_+(\underline{r}' - \underline{r}'')\, U(\underline{r}'') \\ & \times G_+(\underline{r}'' - \underline{r}''')\, U(\underline{r}''')\, \psi_k(\underline{r}''')\end{aligned} \tag{II.2.35}$$

where now the first three terms are known. The unknown function $\psi_k(r)$ has been pushed back to the fourth term. In this way we may construct step by step what is called the Born approximation of the stationary scattering wave function. We note that each term of this expansion brings one higher power of the potential than the preceding one. Thus, if the potential is weak, each successive term is smaller than the preceding one. If one pushes the expansion far enough, then one can neglect the last term on the right hand side and thus obtains $\psi_k(\underline{r})$ entirely in terms of known quantities.

If we now substitute this expansion of $\psi_k(\underline{r})$ into the expression for the scattering amplitude (II.2.29) then we obtain the Born approximation of the scattering amplitude. In particular if we limit ourselves to the first order in the potential all what we need to do is to replace $\psi_k(\underline{r}')$ by $e^{i\underline{k}\underline{r}'}$ on the right hand side of Eq.[II.2.29]. This is called the first Born approximation.

$$f_k^{(B)}(\theta,\varphi) = -\frac{1}{4\pi}\int d^3r'\, e^{-ik\underline{u}\,\underline{r}'}\, U(\underline{r}')\, e^{i\underline{k}_i\underline{r}'}$$

$$= -\frac{1}{4\pi}\int d^3r'\, e^{-i(\underline{k}_f-\underline{k}_i)\underline{r}'}\, U(\underline{r}') \qquad \text{(II.2.36)}$$

$$= -\frac{1}{4\pi}\int d^3r'\, e^{-i\underline{Q}\underline{r}'}\, U(\underline{r}')$$

where $\underline{Q}$ is the scattering vector defined in Eq.[II.2.32]. The scattering cross section in the first Born approximation is thus very simply related to the Fourier transformation of the potential. For the cross section this implies (Eq.[II.2.7], [II.2.15] and [II.2.36])

$$d\sigma_k^{(B)}(\theta,\varphi) = \frac{\mu^2}{4\pi^2\hbar^4}\left|\int d^3r\; e^{-\underline{Q}\underline{r}}V(\underline{r})\right|^2 \qquad \text{(II.2.37)}$$

Let us try to give a very simple physical interpretation of Eq.[II.2.34]. We draw a formal analogy between quantum mechanics and wave optics. Let us consider the target area to be a scattering medium whose density is proportional to $U(\underline{r})$. The function $G_+(\underline{r}-\underline{r}')$ represents the amplitude at the point $\underline{r}$ of a wave radiated by a point source situated at $\underline{r}'$. Consequently the first two terms in Eq.[II.2.34] describes the total wave at a point r as a result of the superposition of the incident wave $e^{i\underline{k}_i\underline{r}}$ and an infinite number of waves coming from secondary sources induced in the scattering medium by the incident wave. The amplitude of each of these sources is indeed proportional to the incident wave and the density of the scattering material ($U(\underline{r}')$) evaluated at the corresponding point r'. This interpretation is symbolized by Fig.2.5 recalling Huygen's principle in wave optics. Formula 2.34 includes a third term. We can interpret in an analogous fashion also the successive terms of the Born expansion. Since the scattering medium extends over a certain area, a given secondary source is excited not only by the incident waves but also by scattered waves coming from other secondary sources inducing multiple scattering.

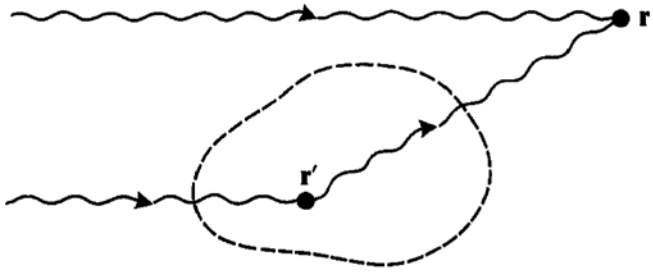

Figure 2.5: Schematic representation of the Born approximation: we only consider the incident wave and the waves scattered by one interaction with the potential.

Fig.2.6 represents symbolically the third term of the Born expansion. If the scattering medium has a very low density, we can neglect the influence of the secondary sources on each other.

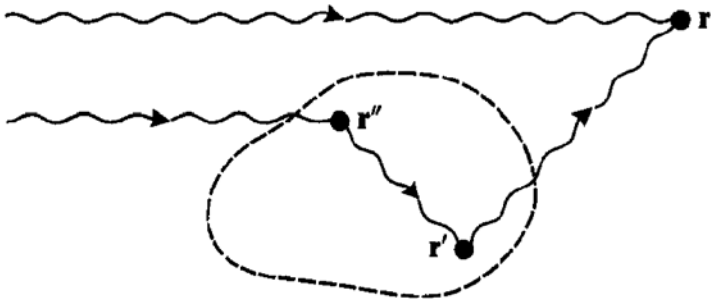

Figure 2.6: Schematic representation of the second-order term in the Born expansion: here we consider waves which are scattered twice by the potential.

Comment: The first Born approximation is valid for weak potentials ($\sigma/a^2\pi << 1$), where a is the size of the scattering object. For neutron scattering on a single nucleus this estimation gives about 10^{-7} and the Born approximation is well fulfilled. We note one important exception. The dynamic scattering theory which considers the scattering problem close to a Bragg reflection in a crystal. Then multiple beam interferences are important and the Born approximation ceases to apply. For most practical purposes however in neutron scattering the Born approximation is valid.

II.2.4 The Fermi pseudo potential

The interaction of the neutron with a nucleon occurs under the strong interaction on a length scale of $1.5 \cdot 10^{-15}$m. For that process, the Born criterion is not fulfilled and for the scattering process on a single nucleus the Born series would have to be summed up. Fortunately, this is a problem of nuclear physics and for the purposes of neutron scattering a phenomenological approach suffices. Considering that the wavelengths of thermal neutrons are in the order of 10^{-10}m, we realize that they are much larger than the dimension of a nucleus of about 10^{-15}m. Therefore, for any scattering event the scattering cannot dependent on the shape of the object and must be isotropic (we may perform a separation into partial waves and consider only the isotropic *S*-wave scattering formally). Such scattering processes may be described by one parameter the scattering length $b = b_1 + i \cdot b_2$. Thereby b_1 describes scattering, while b_2 is the absorption part. For thermal neutrons the scattering potential of a single nucleus becomes (Fermi pseudo potential).

$$V(\underline{r}) = \frac{2\pi \ \hbar^2}{m_n} \ b\delta \ (\underline{r} - \underline{R}) \tag{II.2.38}$$

The scattering lengths b have been measured as a function of neutron energy. For thermal and lower energies the real parts of these scattering lengths are constant and depend in an non-systematic way on the number of nucleons (see Fig.2.7).

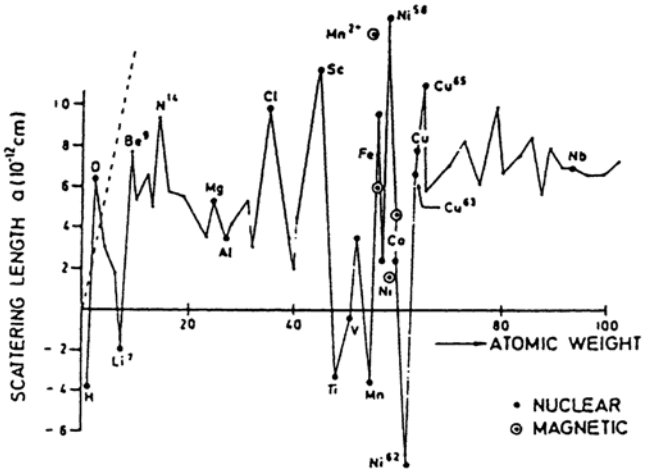

Figure 2.7: Scattering length of nuclei for thermal neutrons as a function of atomic weight.

We realize, that there are positive as well as negative scattering lengths. Following a convention most of the scattering lengths are positive. In this case, we have potential scattering with a phase shift of 180° between the incoming and scattered wave. Negative values result from resonance scattering where the neutrons penetrate the nuclei and create a compound nucleus. Then the emitted neutrons do not undergo a phase shift. We also realize strong differences in the scattering lengths for some isotopes. In particular important is the difference in scattering length between hydrogen and deuterium (b_h = -0.374, b_d = +0.667). This significant difference in scattering length is the basis of all contrast variation experiments in soft condensed matter research as well as in biology (see later lectures). We also note, that the scattering lengths may depend on the relative orientation of the neutron spin with respect to the spin of the scattering nucleus. Again a very prominent example is the hydrogen. There the scattering length for the triplet state - neutron and hydrogen spins are parallel - amounts to $b_{triplet} = 1.04 \cdot 10^{-12}$cm while the scattering length for the singlet situation - neutron and hydrogen spins are antiparallel - is $b_{singlet} = -0.474 \cdot 10^{-12}$cm.

References:

[1] Quantum Mechanics, Eds. Claude Cohen Tannoudji, Bernhard Diu and Frank Laloe, Wiley, New York (1977)

III

Symmetry in Crystals

Gernot Heger

III. Symmetry in Crystals

G. Heger

III.1 Introduction

The term “crystal” comes from the Greek κρυσταλλοσ, which was first used as description of ice and later on - more general - of transparent minerals with regular morphology (regular crystal faces and edges).

Fig. 1. Example: rock crystal – quartz (SiO_2), mineral from the Gotthard-Massif.

Matter is usually classified into three states: gaseous – liquid – solid. Crystals are representatives of the solid state. **Crystalline solids are thermodynamically stable** in contrast to glasses and are **characterised by a regular three-dimensional periodic arrangement of atoms (ions, molecules) in space**.

III.2 Crystal lattices

The three-dimensional periodicity of crystals can be represented by the so-called crystal lattice. The repeat unit in form of a parallelepiped - known as the **unit cell** – is defined by 3 non-linear basis vectors $\underline{a}$, $\underline{b}$, and $\underline{c}$, whose directions form the reference axes X, Y, and Z of the corresponding right-handed crystallographic coordination system. The 6 lattice parameters are given as the lengths of the basis vectors $a = |\underline{a}|$, $b = |\underline{b}|$, $c = |\underline{c}|$ and the angles between the basis vectors: angle $(\underline{a},\underline{b}) = \gamma$, angle $(\underline{b},\underline{c}) = \alpha$, angle $(\underline{c},\underline{a}) = \beta$. The faces of the unit cell are named as face $(\underline{a},\underline{b})$ = C**,** face $(\underline{b},\underline{c})$ = A**,** face $(\underline{c},\underline{a})$ = B.

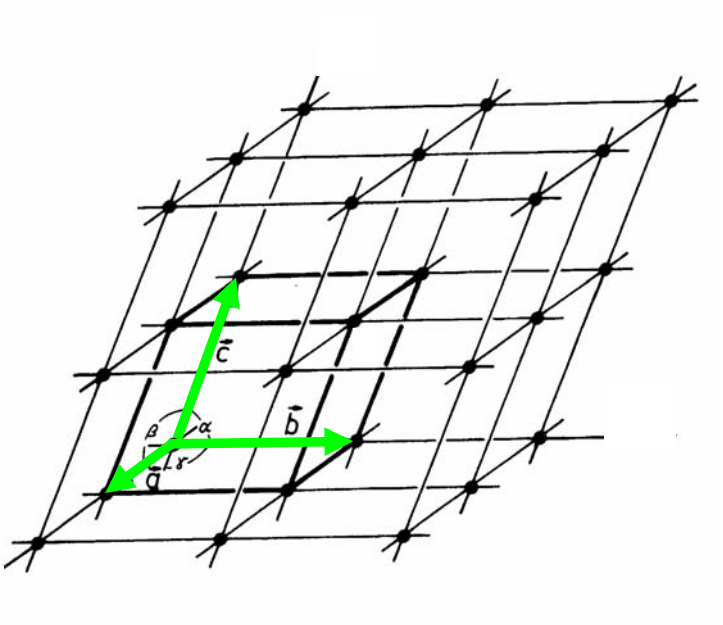

Fig. 2. Notation for a unit cell and a point lattice.

If the vertices of all repeat units (unit cells) are replaced by points, there results the crystal lattice in the form of a **point lattice**. Each lattice point is given by a vector $\underline{\tau} = u\underline{a} + v\underline{b} + w\underline{c}$, with u, v, w being integers. As a symmetry operation of parallel displacement, $\underline{\tau}$ - also known as **translation vector** – maps the atomic arrangement of the crystal (crystal structure) onto itself.

A **lattice point** is named "uvw", according to the coefficients (integers) of the translation vector $\underline{\tau} = u\underline{a} + v\underline{b} + w\underline{c}$ from the origin to the lattice point. A **lattice direction** - given by the symbol [uvw] - is defined by the orientation of the corresponding translation vector.

A plane passing through three lattice points is known as a **lattice plane**. Since all lattice points are equivalent (by translation symmetry) there will be infinitely many parallel planes passing through all the other points of the lattice. Such a set of equally spaced planes is known as a **set of lattice planes**. If the first plane from the origin of a set of lattice planes makes intercepts a/h, b/k, c/l on the X, Y, Z axes respectively, where h, k, l are integers, then the **Miller indices** of this set of lattice planes are (hkl), the three factors h, k, l being enclosed in round brackets. The equation of lattice planes can be written in intercept form as

$$(hx/a) + (ky/b) + (lz/c) = n, \qquad (1)$$

where n is an integer. If n = 0 the lattice plane passes through the origin; if n = 1 the plane makes intercepts a/h, b/k, c/l on the X, Y, Z axes respectively; if n = 2 the intercepts are 2a/h, 2b/k, 2c/l; and so on.

The line of intersection of any two non-parallel lattice planes is a row of lattice points common to both planes. This lattice point row defines a lattice direction [uvw] which is known as **zone axis**. All lattice planes intersecting in a common lattice point row are said to lie in a **zone**. The condition for lattice planes to be parallel to a lattice vector $\underline{\tau} = u\underline{a} + v\underline{b} + w\underline{c}$ is the **zone equation**

$$uh + vk + wl = 0 \qquad (2)$$

The zone axis symbol [uvw] for the zone containing the two planes $(h_1k_1l_1)$ and $(h_2k_2l_2)$ is obtained in solving the simultaneous equations $uh_1 + vk_1 + wl_1 = 0$ and $uh_2 + vk_2 + wl_2 = 0$,

$$[uvw] = [k_1l_2\text{-}k_2l_1,\ l_1h_2\text{-}l_2h_1,\ h_1k_2\text{-}h_2k_1]. \qquad (3)$$

III.3 Crystallographic coordinate systems

The description of a crystal structure consists first of the choice of a unit cell as smallest repeat unit of the crystal with its basis vectors. In this way a crystal-specific coordinate system is defined which is used to localize all the atoms in the unit cell. Whereas in physics and chemistry usually cartesian coordinate systems are used, in crystallography quite different systems are applied. The crystallographic coordinate systems are based on the symmetry of the crystals. In three dimensions there exists 7 different crystal systems and hence 7 crystallographic coordinate systems:

name of system	minimum symmetry	conventional unit cell
triclinic	1 or $\bar{1}$	$a \neq b \neq c$; $\alpha \neq \beta \neq \gamma$
monoclinic	one diad – 2 or m ($\parallel$ Y)	$a \neq b \neq c$; $\alpha=\gamma=90°$, $\beta>90°$
orthorhombic	three mutually perpendicular diads – 2 or m ($\parallel$ X, Y and Z)	$a \neq b \neq c$; $\alpha=\beta=\gamma=90°$
tetragonal	one tetrad – 4 or $\bar{4}$ ($\parallel$ Z)	$a = b \neq c$; $\alpha=\beta=\gamma=90°$
trigonal (hexagonal cell)	one triad – 3 or $\bar{3}$ ($\parallel$ Z)	$a = b \neq c$; $\alpha=\beta=90°$, $\gamma=120°$
hexagonal	one hexad – 6 or $\bar{6}$ ($\parallel$ Z)	$a = b \neq c$; $\alpha=\beta=90°$, $\gamma=120°$
cubic	four triads – 3 or $\bar{3}$ ($\parallel$ space diagonals of cube)	$a = b = c$; $\alpha=\beta=\gamma=90°$

The choice of the origin of the coordinate system is free in principle, but for convenience it is usually chosen in a centre of symmetry (inversion centre), if present, otherwise in a point of high site symmetry of the space group.

In order to complete the symmetry conventions of the coordinate systems it is necessary to add to the 7 so-called primitive unit cells of the crystal systems (primitive lattice types with only one lattice point per unit cell) 7 centred unit cells with two, three or four lattice points per unit cell (centred lattice types). These centred unit cells are consequently two, three or four times larger than the smallest repeat units of the crystals. The resulting 14 **Bravais lattice types** with their centring conditions are collected in Fig. 3.

A set of lattice planes (hkl) is separated by a characteristic interplanar spacing d(hkl). According to the different crystallographic coordinate systems these d(hkl) values are calculated in a specific manner:

For the cubic lattice (a = b = c, $\alpha = \beta = \gamma = 90°$), ex. NaCl

$$d(hkl) = a \cdot \left(h^2 + k^2 + l^2\right)^{-\frac{1}{2}}$$

For the hexagonal lattice (a = b, c, $\alpha = \beta = 90°$, $\gamma = 120°$), ex. Graphite

$$d(hkl) = \left(\frac{4}{3}\frac{h^2 + k^2 + hk}{a^2} + \frac{l^2}{c^2}\right)^{-\frac{1}{2}}$$

For the tetragonal lattice (a = b, c, $\alpha = \beta = \gamma = 90°$)

$$d(hkl) = \left(\frac{h^2 + k^2}{a^2} + \frac{l^2}{c^2}\right)^{-\frac{1}{2}}$$

For the orthorhombic lattice (a, b, c, $\alpha = \beta = \gamma = 90°$)

$$d(hkl) = \left(\frac{h^2}{a^2} + \frac{k^2}{b^2} + \frac{l^2}{c^2}\right)^{-\frac{1}{2}}$$

For the monoclinic lattice (a, b, c, $\alpha = \gamma = 90°$, $\beta > 90°$)

$$d(hkl) = \left(\frac{h^2}{a^2\sin^2\beta} + \frac{k^2}{b^2} + \frac{l^2}{c^2\sin^2\beta} - \frac{2hl\cos\beta}{ac\sin^2\beta}\right)^{-\frac{1}{2}}$$

For the triclinic lattice (a, b, c, α, β, γ), the most general case,

$$d(hkl) = \left(1 - \cos^2\alpha - \cos^2\beta - \cos^2\gamma + 2\cos\alpha\cos\alpha\cos\gamma\right)^{\frac{1}{2}}$$
$$\left(\frac{h^2}{a^2}\sin^2\alpha + \frac{k^2}{b^2}\sin^2\beta + \frac{l^2}{c^2}\sin^2\gamma \right.$$
$$\left. + \frac{2kl}{bc}\left(\cos\beta\cos\beta c - \cos\alpha\right) + \frac{2lh}{ca}\left(\cos\gamma\cos\gamma c - \cos\beta\right) + \frac{2hk}{ab}\left(\cos\alpha\cos\alpha c - \cos\gamma\right)\right)^{-\frac{1}{2}} \qquad (4)$$

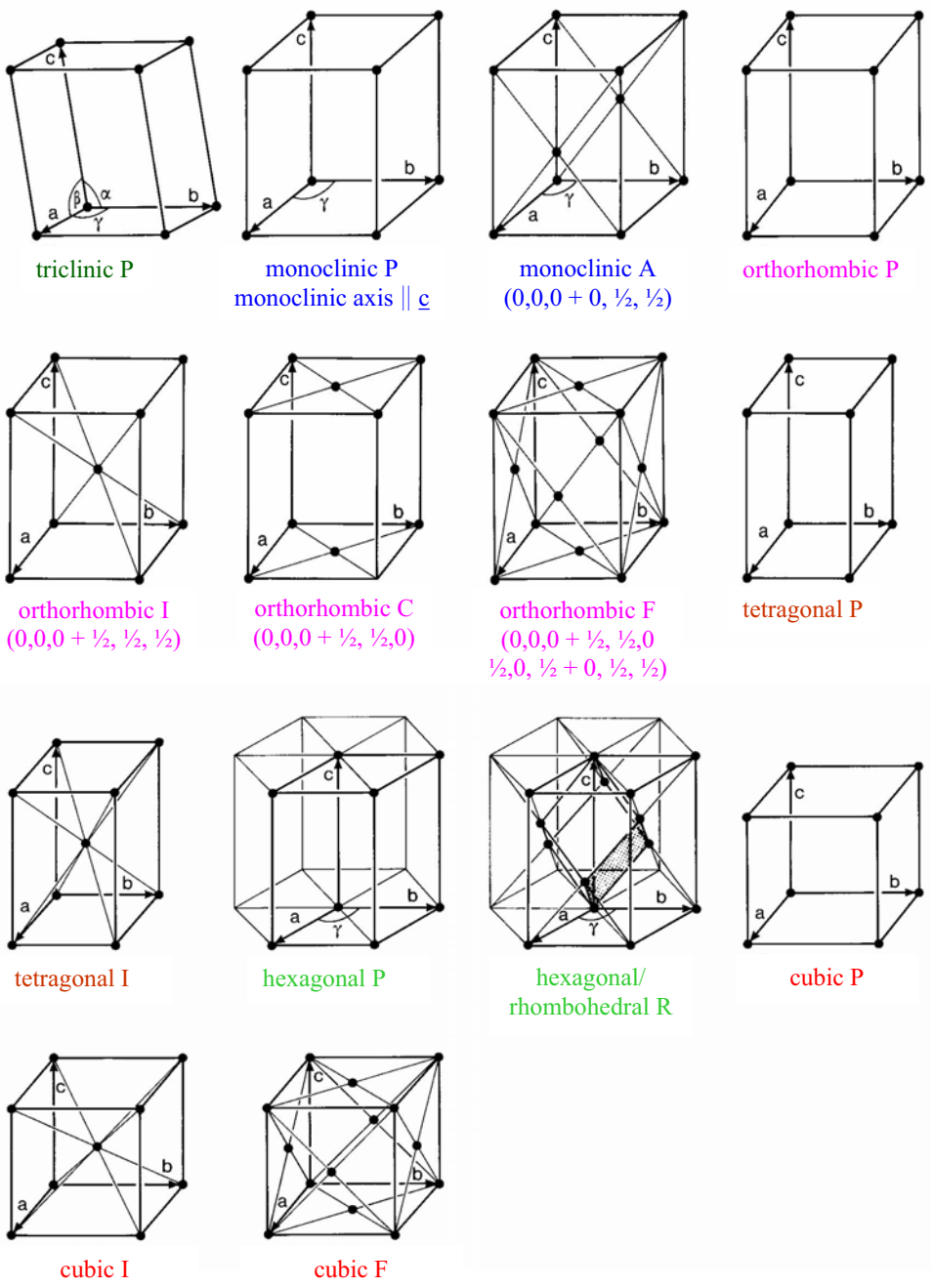

Fig. 3. The 14 Bravais lattices consisting of the 7 primitive lattices **P** for the 7 crystal systems with only one lattice point per unit cell + the 7 centred (multiple) lattices **A**, **B**, **C**, **I**, **R** and **F** with 2, 3 and 4 lattice points per unit cell

III.4 Crystallographic symmetry operations and symmetry elements

The **symmetry operations** of a crystal are isometric transformations or motions, i.e. mappings which preserve distances and, hence, also angles and volumes. An object and its transformed object superpose in a perfect manner, they are indistinguishable.

The simplest crystallographic symmetry operation is the **translation**, which is a parallel displacement of the crystal by a translation vector $\underline{\tau}$ (see chapt. III.2). There is no fixed point, the entire lattice is shifted and therefore, theoretically, the crystal lattice is considered to be infinite.

Crystallographic **rotations** n around an axis by an angle $\varphi = 360°/n$ (n-fold rotations) and **rotoinversions** (combination of rotations and inversions) $\bar{n}$ are called point symmetry operations because they leave at least one point of space invariant (at least one fixed point). An important fact of crystallographic symmetry is the restriction of the rotation angles by the three-dimensional crystal lattice to $\varphi = 360°$ (n = 1), 180° (n = 2), 120° (n = 3), 90° (n = 4), 60° (n = 6). Only for these crystallographic rotations the space can be covered completely without gaps and overlaps. The rotoinversion $\bar{n} = \bar{1}$ is an **inversion** in a point, $\bar{n} = \bar{2} \equiv m$ (mirror) describes a **reflection** across a plane.

The combination of n-fold rotations with $m/n \cdot \underline{\tau}$ translation components ($m < n$) $\parallel$ to the rotation axis leads to the so-called **screw rotations** n_m, e.g. 2_1, 3_2, 4_2, 6_5. These symmetry operations have no fixed points.

The combination of a reflection through a plane (glide plane) with translation components (glide vectors) of $\underline{a}/2$, $\underline{b}/2$, $\underline{c}/2$, $(\underline{a}+\underline{b})/2$, … $\parallel$ to this plane are known as **glide reflections** a, b, c, n, …, d. Again no fixed points are compatible with these symmetry operations.

In addition to the symmetry operations which represent isometric motions of an object, symmetry can also be described in (static) geometrical terms by **symmetry elements**. They form the geometrical locus, oriented in space, on which a symmetry operation is performed (line for a rotation, plane for a reflection, point for an inversion) together with a description of this operation. Symmetry elements are mirror planes, glide planes, rotation axes, screw axes and inversion centres. The geometrical descriptions of the crystallographic symmetry operations are illustrated in Figs. 4-6.

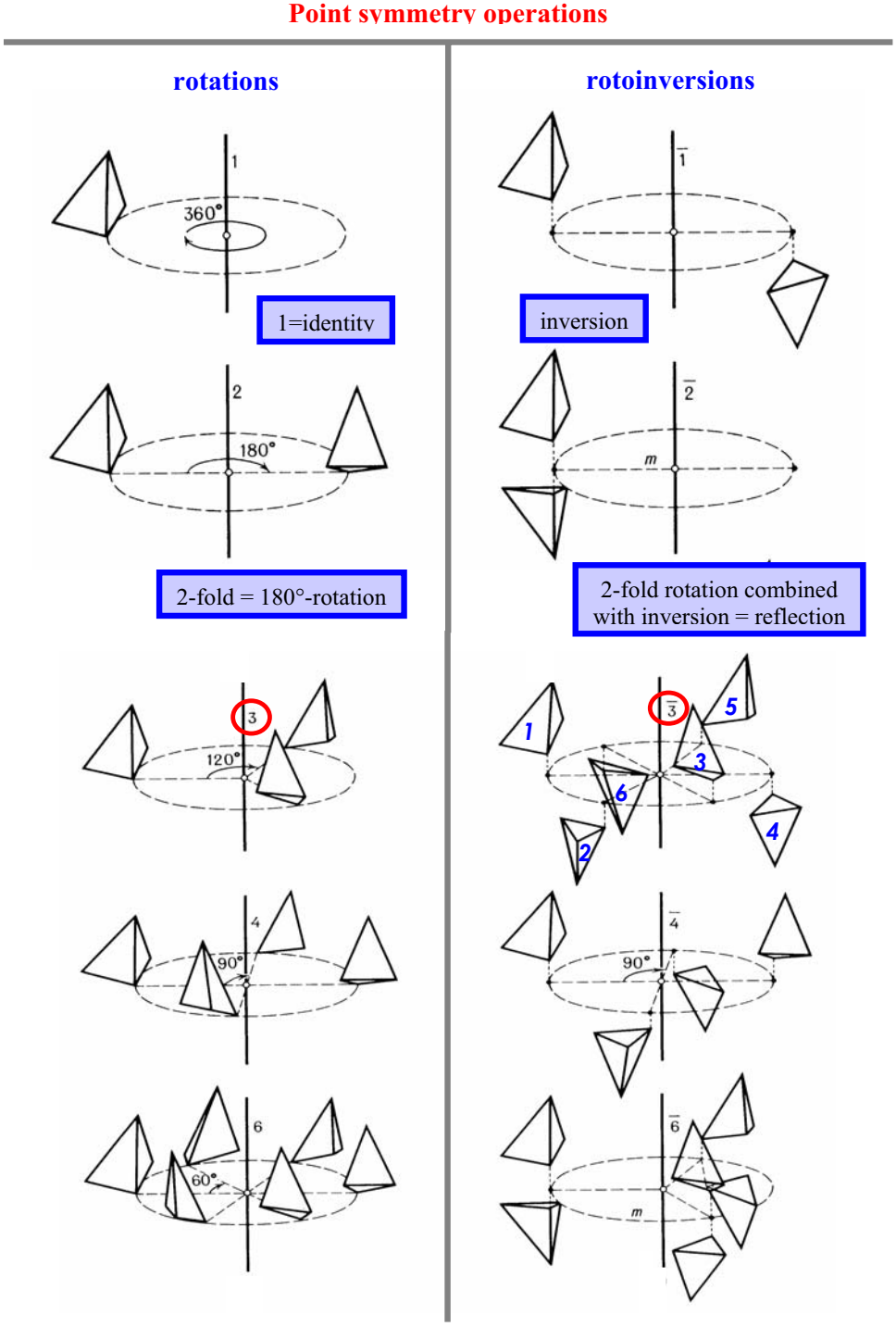

Fig. 4. Rotations: n=1 (identity), n=2 (rotation angle 180°), n=3 (120°), n=4 (90°), n=6 (60°)
Rotoinversions: $\bar{1}$ (inversion), $\bar{2} \equiv$ m (reflection), $\bar{3} = 3 + \bar{1}$, $\bar{4}$, $\bar{6}$

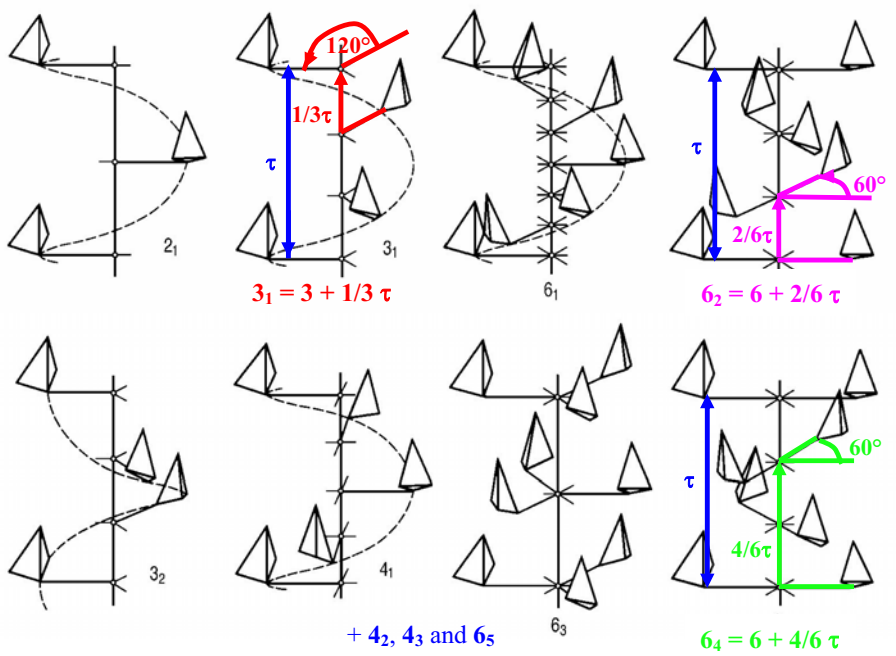

Fig. 5. Screw rotations n_m: combination of rotations n and translation components m/n·τ ∥ to the rotation axis

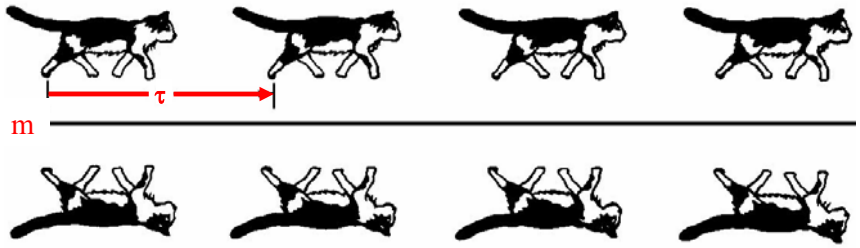

reflection: mirror plane m ⊥ image plane

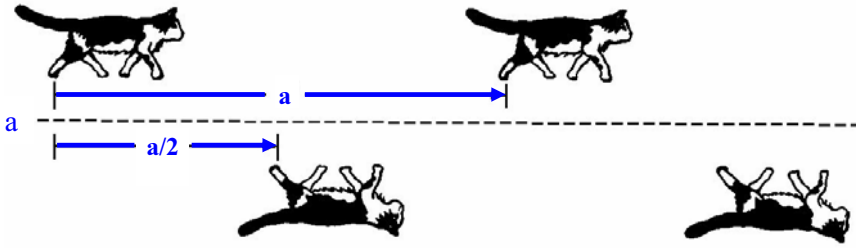

glide reflection: glide plane a ⊥ with glide vector **a**/2

Fig. 6. Examples of reflections and glide reflections

A symmetry operation transforms a point X with coordinates x, y, z (according to a position vector $\underline{X} = x\underline{a} + y\underline{b} + z\underline{c}$) into a symmetrically equivalent point X' with coordinates x', y', z' mathematically by the linear equations

$$\begin{aligned} x' &= W_{11}x + W_{12}y + W_{13}z + w_1 \\ y' &= W_{21}x + W_{22}y + W_{23}z + w_2 \\ z' &= W_{31}x + W_{32}y + W_{33}z + w_3 \end{aligned} \qquad (5)$$

or, in matrix notation:

$$\begin{pmatrix} x' \\ y' \\ z' \end{pmatrix} = \begin{pmatrix} W_{11} & W_{12} & W_{13} \\ W_{21} & W_{22} & W_{23} \\ W_{31} & W_{32} & W_{33} \end{pmatrix} \circ \begin{pmatrix} x \\ y \\ z \end{pmatrix} + \begin{pmatrix} w_1 \\ w_2 \\ w_3 \end{pmatrix}; \quad \underline{X}' = \mathbf{W} \circ \underline{X} + \mathbf{w} = (\mathbf{W}, \mathbf{w}) \circ \underline{X}. \qquad (6)$$

The (3×3) matrix **W** is the rotation part and the (3×1) column matrix **w** the translation part of the symmetry operation. The two parts **W** and **w** can be assembled into an augmented (4×4) matrix $\boldsymbol{W}$ according to

$$\begin{pmatrix} x' \\ y' \\ z' \\ 1 \end{pmatrix} = \begin{pmatrix} W_{11} & W_{12} & W_{13} & w_1 \\ W_{21} & W_{22} & W_{23} & w_2 \\ W_{31} & W_{32} & W_{33} & w_3 \\ 0 & 0 & 0 & 1 \end{pmatrix} \circ \begin{pmatrix} x \\ y \\ z \\ 1 \end{pmatrix} = \boldsymbol{W} \circ \boldsymbol{X} \qquad (7)$$

Since every symmetry transformation is a "rigid-body" motion, the determinant of all matrices **W** and $\boldsymbol{W}$ is $\det \mathbf{W} = \det \boldsymbol{W} = \pm 1$ (+ 1: preservation of handedness; - 1:change of handedness of object).

The sequence of two symmetry operations (successive application) is given by the product of their matrices $\boldsymbol{W_1}$ and $\boldsymbol{W_2}$:

$$\boldsymbol{W_3} = \boldsymbol{W_1} \circ \boldsymbol{W_2}\,, \qquad \text{whereby } \boldsymbol{W_3} \text{ is again a symmetry operation.} \qquad (8)$$

III.5 Crystallographic point groups and space groups

The symmetry of a crystal and its crystal structure can be described by mathematical group theory. The symmetry operations are the group elements of a crystallographic group G and the combination of group elements is the successive execution of symmetry operations. All possible combinations of crystallographic point symmetry operations in three-dimensional space lead to exactly 32 crystallographic point groups (≡ crystal classes) which all are of finite order (the maximum order is 48 for the cubic crystal class $m\bar{3}m$). For the different crystal

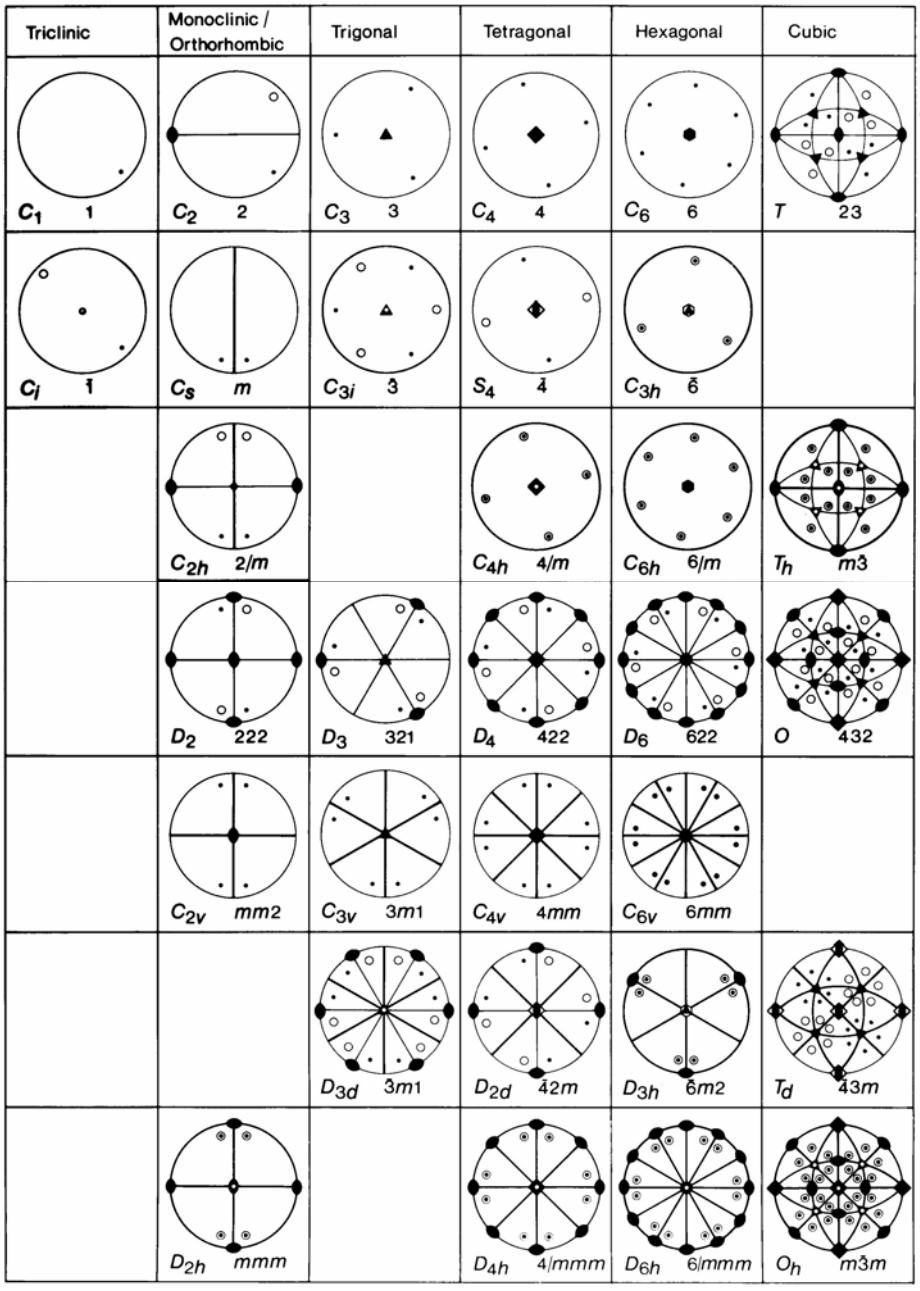

Fig. 7. The 32 crystallographic point groups (≡ crystal classes) in three-dimensional space represented by their stereographic projections. The group symbols are given according to Schoenflies (bottom left) and to Hermann-Mauguin (bottom right).

systems they are represented by stereographic projections in Fig. 7. There are two types of group symbols in use: for each crystal class the corresponding Schoenflies symbols are given at the bottom left and the Hermann-Mauguin (international) symbols at the bottom right. A maximum of 3 independent main symmetry directions ("Blickrichtungen") is sufficient to describe the complete symmetry of a crystal. These Blickrichtungen are specifically defined for the 7 crystal systems (Hermann-Mauguin symbols). As an example the Blickrichtungen of the cubic system are shown in Fig. 8.

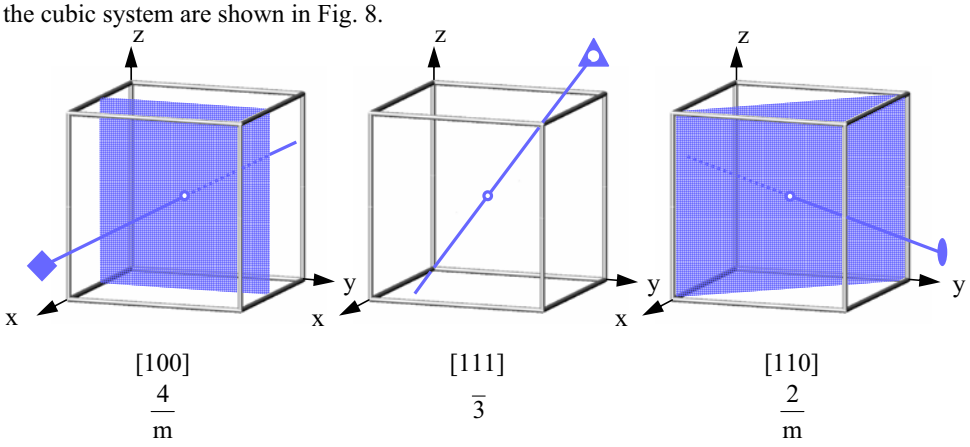

Fig. 8. Symmetry directions ("Blickrichtungen") of the cubic lattice (a=b=c, α=β=γ=90°)
Along [100]: 4/m, along [111]: $\bar{3}$, along [110]: 2/m.

The point group symmetries determine the anisotropic (macroscopic) physical properties of crystals, i. e. mechanical, electrical, optical and thermal properties. By diffraction methods normally only the 11 centrosymmetric Laue classes can be determined:

crystal system	Laue class
triclinic	1
monoclinic	1 2/m 1 = 2/m
orthorhombic	2/m 2/m 2/m = 2/m m m
tetragonal	4/m 4/m 2/m 2/m = 4/m m m
trigonal	3 $\bar{3}$ 2/m = $\bar{3}$ m
hexagonal	6/m 6/m 2/m 2/m = 6/m m m
cubic	2/m $\bar{3}$ = m $\bar{3}$ 4/m $\bar{3}$ 2/m = m $\bar{3}$ m

In three dimensions all possible combinations of the point symmetries of the 32 crystallographic point groups with the lattice translations of the 14 Bravais lattices lead to exactly 230 space groups, all of infinite order. As already mentioned, there result new symmetry operations: screw rotations and glide reflections. The conventional graphical symbols for the symmetry elements according to the International Tables for Crystallography Vol. A (ITA, 2002 [1]) are shown in Fig. 9.

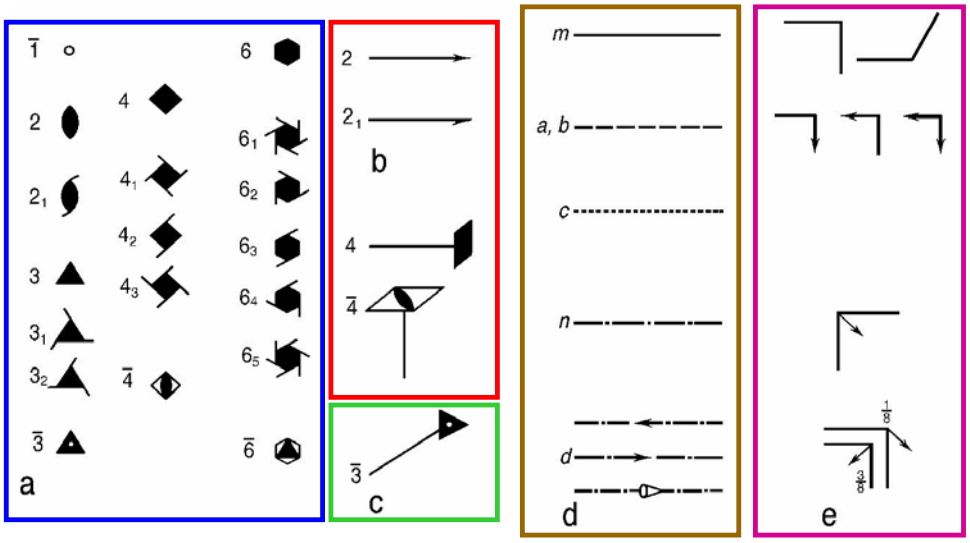

Fig. 9. Conventional graphical symbols for symmetry elements:
- symmetry axes (a) perpendicular, (b) parallel, and (c) inclined to the image plane
- symmetry planes (d) perpendicular and (e) parallel to the image plane

In the International Tables for Crystallography Vol. A [1] all space groups are described in detail with their Hermann-Mauguin symbols and corresponding crystal classes, the relative locations and orientations of the symmetry elements with respect to a chosen origin and the crystal-specific basis vectors, a listing of the general and all special positions (with their symmetrically equivalent points) and the related reflection conditions.

III.6 Example of the crystal structure description of $YBa_2Cu_3O_{7-\delta}$ using the ITA

The crystal structure determination with atomic resolution is achieved by diffraction experiments with X-rays, electron or neutron radiation. As an example, the results of a structure analysis by neutron diffraction on a single crystal of the ceramic high-T_C superconductor $YBa_2Cu_3O_{7-\delta}$ with T_C = 92 K are presented. The atomic arrangement of the orthorhombic structure, space group Pmmm, and the temperature dependent electrical resistivity is shown in Fig. 10.

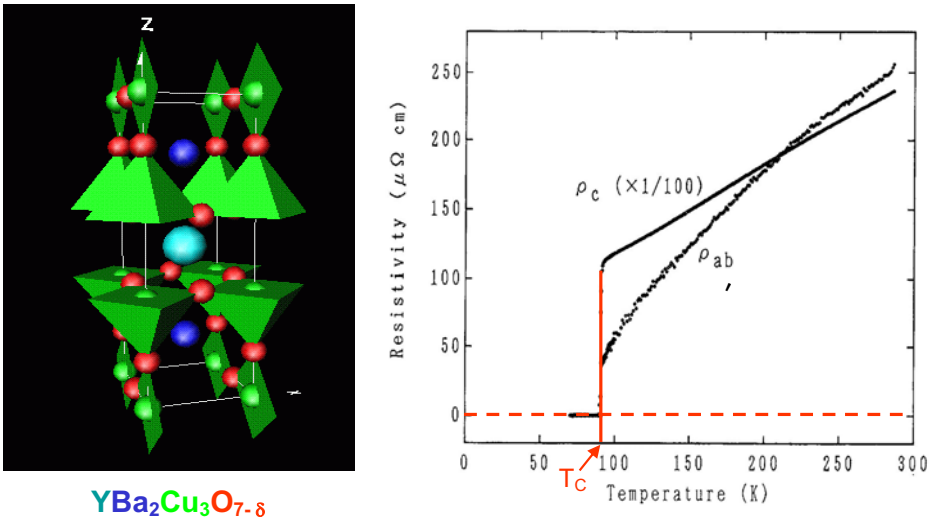

Fig. 10. Crystal structure (unit cell) of $YBa_2Cu_3O_{7-\delta}$ with the CuO_x-polyhedra (left) and the electrical resistivity as a function of temperature ∥ and ⊥ to the [001] direction.

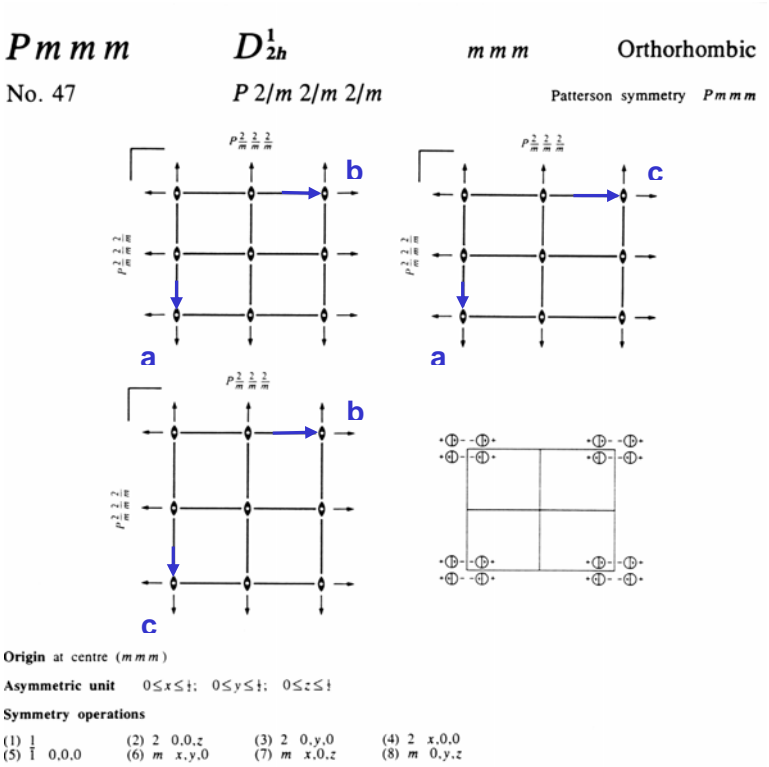

Fig. 11. Description of the orthorhombic space group Pmmm in ITA (2002).

Information from of ITA on the relative locations and orientations of the symmetry elements (symmetry operations 1, 2_z, 2_y, 2_x, $\bar{1}$, m_z, m_y, m_x) of the orthorhombic space group Pmmm together with the choice of the origin (in an inversion centre) is shown in Fig. 11. The general position (site symmetry 1) of multiplicity 8 and all special positions with their site symmetries are listed in Fig. 12. There are no special reflection conditions for this space group.

CONTINUED $YBa_2Cu_3O_{7-\delta}$ No. 47 *Pmmm*

Generators selected (1); $t(1,0,0)$; $t(0,1,0)$; $t(0,0,1)$; (2); (3); (5)

Positions

Multiplicity, Wyckoff letter, Site symmetry			Coordinates				Reflection conditions
8	α	1	(1) x,y,z	(2) $\bar{x},\bar{y},z$	(3) $\bar{x},y,\bar{z}$	(4) $x,\bar{y},\bar{z}$	General: no conditions
			(5) $\bar{x},\bar{y},\bar{z}$	(6) $x,y,\bar{z}$	(7) $x,\bar{y},z$	(8) $\bar{x},y,z$	
4	z	$..m$	$x,y,\frac{1}{4}$	$\bar{x},\bar{y},\frac{1}{4}$	$\bar{x},y,\frac{1}{4}$	$x,\bar{y},\frac{1}{4}$	Special: no extra conditions
4	y	$..m$	$x,y,0$	$\bar{x},\bar{y},0$	$\bar{x},y,0$	$x,\bar{y},0$	
4	x	$.m.$	$x,\frac{1}{4},z$	$\bar{x},\frac{1}{4},z$	$\bar{x},\frac{1}{4},\bar{z}$	$x,\frac{1}{4},\bar{z}$	
4	w	$.m.$	$x,0,z$	$\bar{x},0,z$	$\bar{x},0,\bar{z}$	$x,0,\bar{z}$	
4	v	$m..$	$\frac{1}{4},y,z$	$\frac{1}{4},\bar{y},z$	$\frac{1}{4},y,\bar{z}$	$\frac{1}{4},\bar{y},\bar{z}$	
4	u	$m..$	$0,y,z$	$0,\bar{y},z$	$0,y,\bar{z}$	$0,\bar{y},\bar{z}$	
2	t	$mm2$	$\frac{1}{4},\frac{1}{4},z$	$\frac{1}{4},\frac{1}{4},\bar{z}$			
2	s	$mm2$	$\frac{1}{4},0,z$	$\frac{1}{4},0,\bar{z}$			
2	r	$mm2$	$0,\frac{1}{4},z$	$0,\frac{1}{4},\bar{z}$			
2	q	$mm2$	$0,0,z$	$0,0,\bar{z}$			
2	p	$m2m$	$\frac{1}{4},y,\frac{1}{4}$	$\frac{1}{4},\bar{y},\frac{1}{4}$			
2	o	$m2m$	$\frac{1}{4},y,0$	$\frac{1}{4},\bar{y},0$			
2	n	$m2m$	$0,y,\frac{1}{4}$	$0,\bar{y},\frac{1}{4}$			
2	m	$m2m$	$0,y,0$	$0,\bar{y},0$			
2	l	$2mm$	$x,\frac{1}{4},\frac{1}{4}$	$\bar{x},\frac{1}{4},\frac{1}{4}$			
2	k	$2mm$	$x,\frac{1}{4},0$	$\bar{x},\frac{1}{4},0$			
2	j	$2mm$	$x,0,\frac{1}{4}$	$\bar{x},0,\frac{1}{4}$			
2	i	$2mm$	$x,0,0$	$\bar{x},0,0$			
1	h	mmm	$\frac{1}{4},\frac{1}{4},\frac{1}{4}$				
1	g	mmm	$0,\frac{1}{4},\frac{1}{4}$				
1	f	mmm	$\frac{1}{4},\frac{1}{4},0$				
1	e	mmm	$0,\frac{1}{4},0$				
1	d	mmm	$\frac{1}{4},0,\frac{1}{4}$				
1	c	mmm	$0,0,\frac{1}{4}$				
1	b	mmm	$\frac{1}{4},0,0$				
1	a	mmm	$0,0,0$				

Fig. 12. General and special positions (coordinates of all symmetrically equivalent positions) of space group Pmmm with their site symmetries and multiplicities as well as reflection conditions. The special positions of the $YBa_2Cu_3O_{7-\delta}$ structure are indicated by frames.

The atomic parameters of the structure refinement of $YBa_2Cu_3O_{6..96}$ at room temperature [2] are given in the following Table:

Atomic positions of $YBa_2Cu_3O_{6.96}$ orthorhombic, space group type P *2/m 2/m 2/m* a = 3.8658 Å, b = 3.846 Å, c = 11.680 Å (at room temperature)					
atom/ion	**multiplicity**	**site symmetry**	**x**	**y**	**z**
$Cu1/Cu^{2+}$	1	*2/m 2/m 2/m*	0	0	0
$Cu2/Cu^{2+}$	2	*m m 2*	0	0	0.35513(4)
Y/Y^{3+}	1	*2/m 2/m 2/m*	½	½	½
Ba/Ba^{2+}	2	*m m 2*	½	½	0.18420(6)
$O1/O^{2-}$	2	*m m 2*	0	0	0.15863(5)
$O2/O^{2-}$	2	*m m 2*	0	½	0.37831(2)
$O3/O^{2-}$	2	*m m 2*	½	0	0.37631(2)
$O4/O^{2-}$	1	*2/m 2/m 2/m*	0	½	0

References

[1] International Tables for Crystallography Vol. A, Space-group Symmetry, edited by Th. Hahn, Dordrecht: Kluwer Academic Publishers (5. Edition, 2002).

[2] P. Schweiss, W. Reichardt, M. Braden, G. Collin, G. Heger, H. Claus, A. Erb, Phys. Rev. **B49**, 1387 – 1396 (1994).

1

Neutron Sources

Alexander Ioffe

1. Neutron Sources

Alexander Ioffe

1.1 Introduction

Neutron scattering is a very important tool for studies of fundamental properties of condensed matter as well as material research. It has a special stand among other kinds of radiation as light, X-rays or synchrotron radiation, electrons or ions because of electrical neutrality of neutrons, its large magnetic moment and low kinetic energy. Due to these unique properties of neutrons they became irreplaceable for the investigations of static and dynamic properties of condensed matter, magnetic properties and living biological objects.

The performance of neutron scattering instruments, i.e. the precision of carried out experiments, is primarily determined by the recorded intensity of the scattered beam. The latter is proportional to the unit scattering power of a sample (the scattering cross-section), to its volume and to the incident neutron flux. A general tendency in modern science is to investigate smaller samples (such as nanostructures, biological objects, etc.) and weaker effects, so that the flux at the neutron scattering instrument becomes an ultimate parameter that defines the quality of the experiment.

Usually, under the neutron source one understands a nuclear installation emitting neutrons. However, from the point of view of neutron scattering the neutron source should be considered more generally, including also a spectrum transformer, tailoring the neutron spectrum according to the parameters of the neutron scattering instruments and the neutron transport system that delivers neutrons to the instrument sites. In this lecture we will discuss all these three components in more details.

1.2 Nuclear reactions

In nature neutrons are strongly bound in the atomic nuclei. Therefore, despite the fact that neutrons constitute about a half of each atom so that nature for a half is comprised of neutrons, it is rather difficult to set them free. Therefore, the only way to free neutrons from the nuclear confinement is to break a nucleus apart by means of a nuclear reaction. Further we will consider two types of such reactions – fission and spallation nuclear reactions – that are used in modern continuous and pulsed neutron sources, respectively.

1.2.1 Nuclear fission reaction

Namely by this way, bombarding the beryllium nuclei with of α-particles obtained from decay of natural polonium, Chadwick has produced the first free neutrons in 1932. However, the neutron flux available from such sources was far away from being useful for the condensed matter investigation. The

breakthrough happened in the 40^{ies}, when nuclear reactors using the nuclear fission reactions have been constructed. Although these reactors have been primarily developed for purposes of the nuclear weapon industry, a by-product of their operation - an enormous for that time neutron flux, about 10^7 neutrons per square centimetre per second (n/cm^2 s) at the CP-1 reactor in USA - was immediately used for first neutron scattering experiments. Developments in technology of fission reactors during the next 30 years resulted in a tremendous, by 8 orders of magnitude increase of the neutron flux of nuclear research reactors that approached 10^{15} n/cm^2 s for the high-flux reactor of the Institut-Laue-Langevin (Grenoble, France) in 1972.

These reactors are using the fission of the uranium isotope ^{235}U. Following the capture of a slow neutron, this nucleus is deformed and is split into two fragments, simultaneously releasing 2 or 3 (on average 2.5) "prompt" neutrons with energies $E_T \approx 1.29$ MeV (Fig. 1):

$$^{235}\text{U} + \text{neutron} \rightarrow \text{fission fragments} + 2.52\ \text{neutrons} + 180\ \text{MeV}. \qquad (1)$$

Each of these practically instantly (within 10 ns) emitted neutrons can cause the fission of another 2-3 nuclei, so that each of them will also emit 2 to 3 neutrons, and so on (see Fig. Chain). This process is called the chain reaction, where the amount of fissile material needed to sustain the chain reaction is called critical mass. If the mass of fissile material is more than critical, the number of neutrons will increase exponentially and the reaction will become uncontrollable very quickly, leading to a huge energy release. If the mass of fissile material is less than critical, it will be impossible to sustain a chain reaction: the number of neutrons will decrease over time.

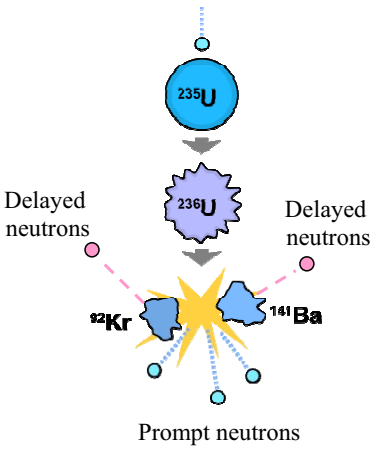

Fig. 1. Schematic representation of the fission process of U235.

However, the fission fragments are also rich in neutrons and emit neutrons (as a part of their radioactive decay), which can also contribute to the fission of any U-235 nucleus they strike. These so-called "delayed" neutrons are extremely important because they are emitted with the average time delay of the order of seconds and thanks to them the chain reaction can be controlled. Practically one runs a reactor sub-critically as far as only prompt neutrons are concerned, i.e. neutron multiplication is suppressed, so that the chain reaction vanishes. The delayed neutrons come a moment later but just in time to sustain the chain reaction when it is going to die out, thus allowing to reach criticality. More precisely, the neutrons in the reactor are moderated to decrease their energy and to increase their absorption by control roads that are made of a neutron absorbing material (usually containing boron). When inserted in the reactor core, these roads will reduce the number of slow neutrons to the amount just as necessary for the self–sustaining chain reaction and may be adjusted, so that the reaction remains critical only with the inclusion of the delayed neutrons. Thus, a simple and reliable mechanical control system can be used for the control of the chain reaction in the nuclear reactor. Another inherent safety factor is the so-called negative coefficient of reactivity. A mass of a fissile material that is exactly critical at room temperature becomes sub-critical if it is warmed. Intrinsically, fission becomes less probable as the fuel temperature increases due to more intense fission, and the chain reaction dies out.

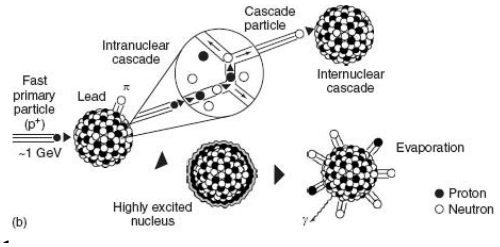

Fig. 2. Schematic representation of the spallation process.

1.2.2 Spallation reaction

The fission is not the only nuclear reaction allowing us to obtain free neutrons. Another kind of nuclear reactions that can be used for neutron production is the spallation reaction (Fig. 2.), where extremely high energy particles (e.g. protons) hit the target made of a neutron-rich material, "breaking" a heavy nucleus into highly excited fragments. In contrast to the fission reaction, the de Broglie wavelength

$$\lambda = \sqrt{h^2/2mE} \tag{2}$$

of the bombarding particles is shorter than the size of the nuclei, and collisions can take place with individual nuclides in the nucleus rather than with the nucleus as a whole. Indeed, a large amount of energy is transferred to the nuclides, which in turn can hit other nuclides in the same nucleus. As the result of this so-called intranuclear cascade, energy is more or less evenly distributed over the nucleus, bringing it to a highly excited state, so that the excited nucleus will "evaporate" neutrons and a smaller amount of protons. However, some energetic particles can escape from the nucleus and either hit another one (internuclear cascade) or just escape from the target. The energy of these neutrons is extended up to the energy of the incident particles (i.e. up to 1 GeV).

The spallation process is very short and ends within less than 10^{-15} s after the nucleus is hit. Thus, the time distribution of the spallation neutrons is entirely determined by the time distribution of the driving particle pulse, generally provided by a linear accelerator. This pulse that can be made either rather long, about 5 ms (called the long pulse spallation source (LPSS)), or rather short, about 10 μs (called the short pulse spallation source (SPSS)), by compressing charged particles in a compressor ring.

The most intense up-to-day spallation neutron source ISIS at Chilton (Great Britain) provides instantaneous thermal neutron fluxes over 10^{16} n/cm^2 s with short pulse lengths of ~50 μs. Next generation of pulsed neutron sources – SNS in USA and JHP in Japan - with fluxes more than 10^{17} n/cm^2 s are currently under construction. The European project of 5MW spallation source ESS with flux more than 10^{17} n/cm^{2}s is expected to take off within the next years.

Comparing possible nuclear reactions that can be used for neutron production (see Table 1), one should pay attention not only to their efficiency. The heat deposition that accompanies the neutron production results in the cooling problem, which is the real limiting factor for all kinds of neutron sources. From this point of view, fusion is the most attractive process, although it is still a technique of a far future.

Table 1. Neutron yields and deposited heat for selected neutron-producing reactions.

Reaction	Energy/event	Yield (neutron/event)	Deposited heat (MeV/neutron)
(T,d) fusion		~1 neutron/fusion	3
^{235}U fission		~1 neutron/fission	200
Pb spallation	1 GeV	~20 neutron/proton	23
^{238}U spallation	1 GeV	~40 neutron/proton	50

1.3 Neutron spectrum and spectrum transformation

To be useful for condensed matter investigations neutrons wavelength λ should be about few Angstroms, that corresponds to the meV energy range. However, the energy spectrum of neutrons produced by fission or spallation nuclear reactions is in the range of 1 MeV, i.e. the spectrum transformation aiming an energy shift of several orders of magnitude is required. Let us express the neutron energy in the terms of the mean temperature T of the neutron ensemble as $E=kT$, where k *is* the conversion coefficient k = 11600 K/eV (the Boltzmann constant): then one can say that required energy shift can be achieved by cooling the neutrons down to a much lower temperature. For this purpose neutrons should be brought into the thermal equilibrium with a cold body (moderator): such thermalization process is accomplished by the moderation of neutrons via their multiple inelastic collisions with the light atoms of the moderator.

Depending on the type of neutron source the moderator should provide either the highest possible flux in the largest possible volume for continuous neutron sources or in the shortest possible time for pulsed neutron sources. This can be achieved by using water or heavy water moderators. Neutrons are slowing down and achieving thermal equilibrium with the moderator within 10^{-6} s. The neutron energy spectrum is given by the Maxwellian distribution

$$\Phi(E) = \frac{2\sqrt{E}}{\sqrt{\pi k^3 T^3}} \exp\left\{-\frac{E}{kT}\right\} \tag{3}$$

where T is the moderator temperature. Practically, moderators are big (light or heavy) water volumes (also serving as a biological shielding) surrounding the reactor core or the spallation target and are generally kept at the room temperature of $T \approx 300$ K. Because of this reason the corresponding neutrons are called thermal neutrons, with a maximum peak flux around $\lambda \approx 1$ Å.

Tables 2 and 3 contains some neutron properties and useful relations between different parameters of neutrons.

Table 2. Neutron properties

Mass	$m = 1.675 \cdot 10^{-27}$ kg
Electrical charge	$q = 0$
Magnetic dipole moment	$\mu_n = -1.913\ \mu_B$ (μ_B – nuclear magneton)
Life time	$t_{1/2} = 820$ s

Table 3. Useful relations.

$\lambda(\text{Å}) = \frac{h}{mv} = \frac{3956}{v(m/s)} = \frac{0.286}{\sqrt{E(eV)}}$	$v(m/s) = \frac{h}{m\lambda} = \frac{3956}{\lambda(\text{Å})}$

1.4 Nuclear reactor and spallation source

Now we can consider the construction of a neutron source. In all cases its heart is a core where the nuclear fission reaction takes plays. In the case of the nuclear reactor a set of uranium ^{238}U fuel elements (or a complex single fuel element) is enriched by the isotope ^{235}U. One distinguishes between high-enriched (~95%) and low-enriched (~20%) uranium: because the amount of fission material necessary to support the chain reaction is predetermined (the critical mass), the enrichment of

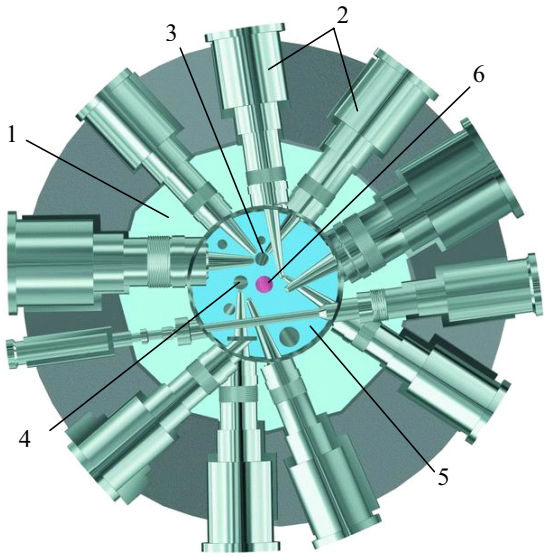

Fig. 3. Horizontal section through the reactor pool of the FRM-2 reactor in Garching, Germany. The reactor tank with internal diameter approx. 5m is filled with light water (1). In the centre of the arrangement the reactor core is situated. The experimental installations as horizontal beam tubes (2), a cold (3) and a hot (4) neutron source are arranged in the heavy water tank (5) around the fuel element (6).

the used uranium fuel actually defines the volume of the core and the neutron flux density. Compact cores made of high-enriched uranium at the reactors of the Institut-Laue-Langevin (Grenoble, France) and the Maier-Leibnitz Neutron Source (FRM-2) (Garching, Germany) provide the highest flux density and therefore, the highest neutron source luminosity achievable up to this day.

The reactor core is surrounded by (heavy) water (T=300 K) that plays the role of the moderator of high-energy fission neutrons (Fig. 3). Obviously, the full thermalization of these neutrons requires some time necessary for a few collisions with hydrogen (or deuterium) atoms, so that the density of thermal neutrons increases with the distance r from the core. On the other hand, the neutron absorption is inverse proportional to the neutron velocity, so that the flux of already thermalized neutrons decreases with r. As the result of these two competing processes, the thermal neutron flux density achieves its maximum at a certain distance of r = 10-15 cm from the core. Obviously, to extract thermal neutrons from the reactor, the entrance of a neutron beam tube should be placed exactly in this position. Aiming the decrease in undesirable background of fast (i.e. still not thermalized) neutrons and γ-rays from the core, one should avoid the direct view of the core through the neutron beam tube. All together, it leads to the conclusion that the optimal arrangement of beam tubes is tangential to the reactor core (see Fig. 3).

In case of the spallation source, the role of the reactor core plays a target made of heavy metal as Bi, Pb or Hg. The proton beam is obtained from negatively charged hydrogen ions produced by powerful ion sources (Fig. 4). These ions are accelerated in a linear accelerator (linac) by a number of

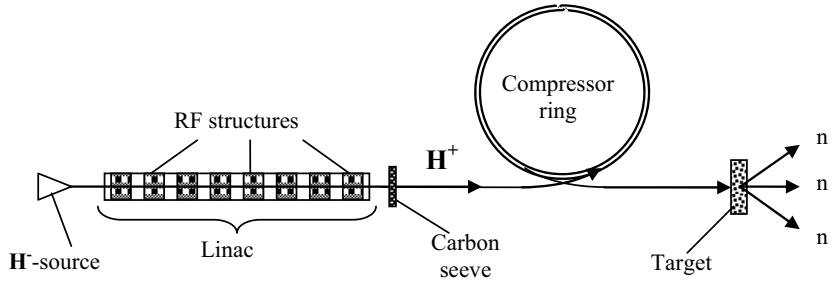

Fig. 4. Layout of the neutron spallation source

subsequent radio-frequency cavities with strong electro-magnetic fields, thus achieving kinetic energies in the GeV range (i.e. about 90% of the speed of light). When these hydrogen ions leave the linac, they are stripped off all their electrons by passing through a thin carbon sieve, so that the negative hydrogen ions become protons. Now, depending on the design of the spallation source, LPSS or SPSS (see Chapter 2) the protons are either sent to the target directly or through a compressor ring, respectively. The latter collects the protons from a large number of successive bunches from the linac into a single very high-intensity proton pulse. It is achieved by an assembly of magnets that send each accelerated proton bunch into a circular orbit of such a large diameter (~50–100 m), so that the

travelling time is equal to the time interval between the bunches. Indeed, the next bunch of protons arrives exactly when the previous has made a full turn and both of them are sent around again. When about 1000 bunches are piled up by such a procedure, sufficient intensity is accumulated and the full proton pulse with a pulse length of about 1 μs is sent to the target. The target is normally a liquid metal (mercury or a lead–bismuth eutectic mixture), placed in special materials to consume the beam power of a few megawatts. The proton pulse repetition rate on the target should be about 10–100 Hz to achieve an optimal use of neutrons in time-of-flight scattering experiments.

Thus, there are two kinds of neutron sources and certainly the question arises, which of them is better answering future trends. These trends, as discussed in the Ch.1 require a significant increase in the luminosity of neutron sources in order to improve the counting statistics of neutron scattering experiments. However, the evolution of nuclear reactors that was very impressive some decades ago, shows no progress since 1972, when the high-flux reactor at the ILL, Grenoble became operative. The reason for this is clearly the technical difficulty of removing the heat from the reactor core.

Let us make some rough estimations. As it was mentioned in Table 1, the deposited heat amounts to 200 Mev/fission with the yield of 1 neutron from 2.5 to be extracted for neutron scattering experiments. Using the relation 1 eV = $1.6 \cdot 10^{-19}$ J, we obtain the source strength (i.e. the number of neutrons emitted per second) $Q = 3 \cdot 10^{16}$ n/s per MW of the reactor power to be removed. However, this is a kind of a "point neutron source" that immersed into the moderator to slow neutrons down till thermal energies (see Ch. 2). Indeed, all neutrons emitted by the point source will be spread over the moderator surface of about 2000 cm^2 (r =10-15 cm), so that the thermal neutron flux will amount to 0.0005 of Q, i.e. about $1.5 \cdot 10^{13}$ n/s·cm^2 per MW of reactor power. Thus, for the 57 MW reactor at the ILL, one may expect the thermal flux of $1 \cdot 10^{15}$ n/s·cm^2 to be compared with the actual value of $2 \cdot 10^{15}$ n/s·cm^2 .

Thus, a further increase in the thermal neutron flux from nuclear reactors will require a significant increase in their power. However, such an increase will also require a very sophisticated reactor cooling and result in even stronger radiation damage of the reactor vessel components (beam tube noses, cold source, etc.). Experience gained at the ILL reactor shows that their service time is seven years. Already now new reactors are being designed in a way allowing for a regular exchange of the beam tube noses. Tenfold increase of the reactor power will result in a rather unpractical service time of these elements. Another problem is the worldwide concern about a potential risk associated with nuclear fission installations. On the other hand, pulsed sources are inherently safer because of the absence of any critical configuration that is potentially explosive. The deposited heat is 10 times less with the simultaneous significantly large neutron output (see Table 1) allows for a high peak flux about 50 times higher than the one for the ILL reactor (Table 2). Losses in the average thermal neutron flux will be compensated by the opportunities offered for neutron scattering instrumentation by the

time-structured neutron beams, when the instrument performance depends on the peak flux in the pulse rather than on the time-averaged flux.

Therefore, it is not surprising that all new sources under construction, SNS in USA and JHP in Japan as well as planned new European neutron source ESS, are spallation neutron sources. However, SNS and JHP are 1–2 MW spallation sources designed to create rather short neutron pulses of about 100 μs and further increase in their power level is rather problematic due to possible target problems. In contrast to this, ESS is planned as 5MW spallation source because it will create neutron pulses of a few milliseconds duration. It was demonstrated that such long pulse provides significant advantages for certain categories of neutron scattering instruments. Although target problems for LPSS also become increasingly severe with the increase of power, nevertheless it seems realistic to approach the ultimate limit of 20MW (i.e. 20 mA proton current at 1 GeV).

1.5 Cold, thermal and hot neutrons

As it was shown in the previous Chapter, the energies of neutrons produced by neutron sources cover many orders of magnitude. Depending on their energy E, neutrons are classified by commonly used names (see Table 2). Neutrons with $E < 1$ keV are called slow neutrons; in turn they are classified in 6 groups, but the most relevant for purposes of neutron scattering are hot, thermal and cold neutrons –energy ranges corresponding to these groups that are presented in Table 3. The maximum of the spectrum of thermal neutrons is defined by room temperature of the water moderator and is about $\lambda \approx 1$ Å (see Ch. 3). As one can see from Fig. 5, most of the neutrons are concentrated around this wavelength in the range of (0.8÷2) Å. These neutron wavelengths perfectly match the interatomic distances in solids and therefore, are extensively used for the studies of structure and dynamics of crystalline.

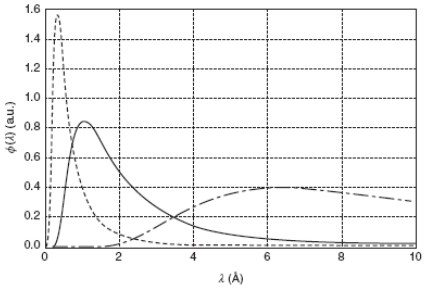

Fig. 5. Neutrons wavelength distribution from cold (dot dashed line, T=50 K), thermal (solid line, T=300K) and hot (dashed line, T=1000 K) moderators.

However, it also means that the amount of hot or cold neutrons in the thermal neutron spectrum is very small, so that any scattering experiment which requires hot or cold neutrons will

suffer from enormous flux losses. To enhance the hot or cold neutron flux one has to transform the thermal neutron spectrum shifting it towards high or low energies: in other words by heating or cooling the thermal neutron spectrum.

To achieve a significant gain factor by such spectrum transformations, the moderator temperature should be as high as 2000K and as low as 20K, respectively. Obviously, it is unrealistic to heat or to cool the whole water in the reactor vessel - tens of cubic meters – to such temperatures. The trick that is used to solve this problem is to insert other small local moderators inside the water and to set their temperatures accordingly. These devices are called hot and cold sources.

The hot source is usually made of a graphite block heated up to T=2400 K, when the cold sources is usually a vessel filled with liquid H_2 or D_2 or their mixture cooled down to 20 K. Hot and cold neutron spectra are shown in Fig. 5. Each of them allows for a significant, up to 20 times gain in the corresponding neutron flux. By choosing the adequate neutron spectrum scattering experiments can be optimally tailored to particular experimental requirements.

Finally, in Table 2 we present the basic properties of the neutron, as well as some useful relations.

1.6 Neutron beam transport

However, it is not enough to produce neutrons in the moderator – they still have to be transported to a neutron scattering instrument. As it was already mentioned in Ch. 4, neutrons are extracted from the moderator by neutron beam tubes, inserted in a heavy biological shielding surrounding the reactor tank and necessary because neutrons are isotropically emitted from the moderator.

The angular acceptance of a neutron beam tube is defined by its diameter (~10 cm) and length (~5m). Thus, the beam divergence of a beam tube is about ~1°, so that the neutron flux available at its output is drastically reduced by about six orders of magnitude, in comparison to the core flux.

This situation can be significantly improved by using neutron optical devices called neutron guides. The principle of their operational is rather similar to the one of light guides, where the light propagating in an optically dense media (i.e. with the refraction index n >1) is totally reflected from the glass air-interface due to the effect of total external reflection (the refraction index of air is equal to unity). In contrast to light, the refraction index of glass for neutrons is n <1, so that the effect of the total external reflection will take place on the air-glass interface. However, in case of neutrons this phenomenon takes place only for incident angles, i.e. less than the critical angle θ_c which is given by

$$\theta_c = \lambda\sqrt{\frac{2\rho b_c}{\pi}},$$

1 – 10

where ρ and b_c are the density and the coherent scattering length of the wall material, respectively. To increase θ_c the Ni coating with the critical angle $0.1° \cdot \lambda$ is used. Moreover, the wall of the neutron guide can be coated with so-called supermirrors, with the critical angle up to three times as much as the nickel's one. Indeed, the neutron guide is made as a hollow glass tube, Ni or supermirror coated from the inside (Fig. 5). Because the intensity at the neutron guide output is proportional to θ_c^2, they provide an order of magnitude flux increase as compared to a beam tube.

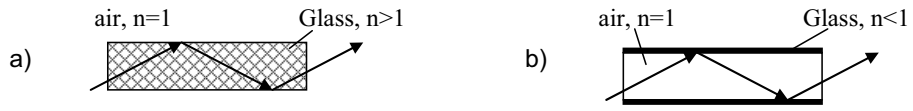

Fig. 5. To principle of the operation of light guides (a) and neutron guides (b)

Moreover, neutron guides can be bent or shaped. Bent neutron guides allow to avoid direct sight-of-view of the reactor core, drastically reducing γ- and neutron background at the instrument position. The parabolic or elliptic shaping of neutron guides opens exciting possibilities for the concentrating (focusing) of neutrons on a sample, thus providing additional increase in intensity at the position of neutron scattering instruments.

References:

1. G.R. Bauer (1993) Neutron sources. In: A.Furrer (ed.) *Neutron Scattering*, pp. 331–357. PSI-Proceedings No. 93-01, ISSN 1019-6447, Paul Scherrer Institute, Villigen.
2. J.M. Carpenter and W.B. Yelon (1986) Neutron sources. In: K. Sköld and D.L. Price (eds.) *Methods of Experimental Physics*, vol. 23A, pp. 99–196. London: Academic Press.
3. K. Clausen (2001) *Neutron sources*. Office for Official Publications of the European Communities, Luxembourg, ISBN 92-894-0037-4.

2

A neutron primer: Elastic scattering and the properties of the neutron

Thomas Brückel

2. A neutron primer: Elastic scattering and the properties of the neutron

Thomas Brückel, IFF, FZ-Jülich

2.1 Introduction

After we have learnt how neutrons are produced in neutron sources, we will explain in this chapter, how neutrons can be used to study the atomic structure and dynamics of condensed matter systems. We will give a basic introduction into scattering methods in general and then introduce the special properties of the neutrons, which make them an invaluable probe for condensed matter research. Neutrons tell us, where the atoms are, how the atoms move and how the atomic magnetic moments are arranged.

Our present understanding of the properties and phenomena of condensed matter science is based on atomic theories. The first question we pose when studying any condensed matter system is the question concerning the internal structure: what are the relevant building blocks (atoms, molecules, colloidal particles, ...) and how are they arranged? The second question concerns the microscopic dynamics: how do these building blocks move and what are their internal degrees of freedom? For magnetic systems, in addition we need to know the arrangement of the microscopic magnetic moments due to spin and orbital angular momentum and their excitation spectra. In principle, the macroscopic response and transport properties, such as specific heat, thermal conductivity, elasticity, viscosity, susceptibility, magnetization etc., which are the quantities of interest for applications, result from the microscopic structure and dynamics. To determine these macroscopic properties from the microscopic information provided by experiment represents a huge challenge to condensed matter theory as we are dealing with an extreme many body problem with typically 10^{23} particles involved. It is a true masterly achievement of mankind that for many solid state systems, such microscopic theories could be developed, based on quantum mechanics and statistical physics.

For the development of modern condensed matter research, the availability of probes to study the structure and dynamics on a microscopic level is therefore essential. Modern scattering techniques can provide all the required information. Radiation, which has a rather weak interaction with the sample under investigation provides a non-invasive, non-destructive probe for the microscopic structure and dynamics. This has been shown for the first time by W. Friedrich, P. Knipping and M. von Laue in 1912, when interference of x-ray radiation scattered from a single crystal was observed. Max von Laue received the Nobel prize for the interpretation of these observations. One cannot overestimate this discovery: it was the first definite proof that atoms are the elementary building blocks of condensed matter and that they are arranged in a periodic manner within a crystal. The overwhelming part of our present-day knowledge of the atomic structure of condensed matter is based on x-ray structure investigations. Of course the method has developed rapidly since 1912. With the advent of modern synchrotron x-ray sources, the source brilliance has since then increased by 18 orders of magnitude. Currently X-ray Free Electron Lasers, e. g. the XFEL project (http://xfel.desy.de/), are proposed which will increase this brilliance by another 10 orders of magnitude. Nowadays the structure of highly complex biological macromolecules can be determined with atomic resolution such as the crystal structure of the ribosome. Extremely weak phenomena such as magnetic x-ray scattering can be exploited successfully at modern synchrotron radiation sources. Besides x-ray scattering, light scattering is an important tool in soft condensed matter re-

search, where one is interested in the dynamics on larger lengths scales, such as of colloidal particles in solution. Finally, intense neutron beams have properties, which make them an excellent probe for condensed matter investigations. Neutron scattering is a unique tool to solve magnetic structures and determine magnetic excitations and fluctuations. In soft matter and life science, neutrons excel due to the possibility to apply contrast variation techniques by selective deuteration of molecules or molecular subunits. Neutrons give access to practically all lengths scales relevant in condensed matter investigations from the sub-atomic level of some pm up to about 1000 nm and are particularly well suited for the investigations of the movement of atoms and molecules. As with x-rays, the experimental techniques are in rapid evolution, mainly due to the advent of new neutron optical devices, but also of new sources. The new spallation sources such as the American Spallation Neutron Source SNS (http://www.sns.gov/) or the proposed European Spallation Source ESS (http://neutron.neutron-eu.net/n_ess) will increase the capabilities of neutron investigations in condensed matter science drastically in the years to come.

This lecture is organised as follows: First we give a very basis introduction into elementary scattering theory for elastic scattering, which is generally valid for any probe. Then a more rigorous derivation in the framework of the Born series follows. We will introduce the concepts of coherence and pair correlation functions. Then we will discuss, which probes are most relevant for condensed matter investigations and present in some detail the interaction of neutrons with matter leading to the absorption and scattering cross-sections. More details can be found in [1 - 4].

We will frequently make use of the particle-wave dualism of quantum mechanics, which tells us that the radiation used in the scattering process can be described in a wave picture, whenever we are interested in interference phenomena, and in a particle picture, when the interaction with matter is relevant, e. g. for the detection process.

2.2 Elementary scattering theory: Elastic scattering

Throughout this lecture we assume that the atoms within our sample are rigidly fixed on equilibrium positions in space. Therefore we only look at those processes, in which the recoil is being transferred to the sample as a whole so that the energy change for the radiation is negligible and the scattering process appears to be elastic. In subsequent lectures, this restriction will be dropped and so-called inelastic scattering processes will be discussed due to excitations or internal fluctuations in the sample, which give rise to an energy change of the radiation during the scattering process.

A sketch of the scattering experiment is shown in Figure 1.

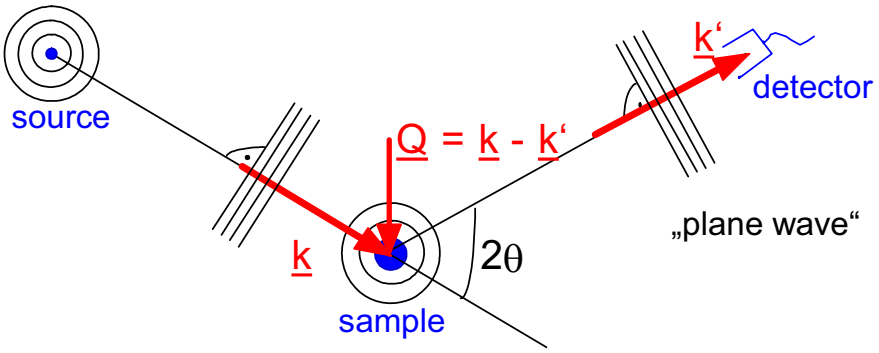

Fig. 1: *A sketch of the scattering process in the Fraunhofer approximation in which it is assumed that plane waves are incident on sample and detector due to the fact that the distances source-sample and sample-detector, respectively, are significantly larger than the size of the sample.*

Here we assume the so-called *Fraunhofer approximation*, where the size of the sample has to be much smaller than the distance between sample and source and the distance between sample and detector, respectively. This assumption holds in all cases discussed in this lecture. In addition we assume that the source emits radiation of one given energy, i. e. so-called *monochromatic* radiation. Then the wave field incident on the sample can be considered as a plane wave, which is completely described by a wave vector $\underline{k}$. The same holds for the wave incident on the detector, which can be described by a vector $\underline{k}'$. In the case of elastic scattering (diffraction) we have

$$k = |\underline{k}| = |\underline{k}'| = k' = \frac{2\pi}{\lambda} \tag{1}$$

Let us define the so-called *scattering vector* by

$$\underline{Q} = \underline{k} - \underline{k}' \tag{2}$$

$\hbar\underline{Q}$ represents the momentum transfer during scattering, since according to de Broglie, the momentum of the particle corresponding to the wave with wave vector $\underline{k}$ is given by $\underline{p}=\hbar\underline{k}$. The magnitude of the scattering vector can be calculated from wavelength λ and scattering angle 2θ as follows

$$Q = |\underline{Q}| = \sqrt{k^2 + k'^2 - 2kk'\cos 2\theta} \Rightarrow Q = \frac{4\pi}{\lambda}\sin\theta \tag{3}$$

A scattering experiment comprises the measurement of the intensity distribution as a function of the scattering vector. The scattered intensity is proportional to the so-called *cross section*, where the proportionality factors arise from the detailed geometry of the experiment. For a definition of the scattering cross section, we refer to Figure 2.

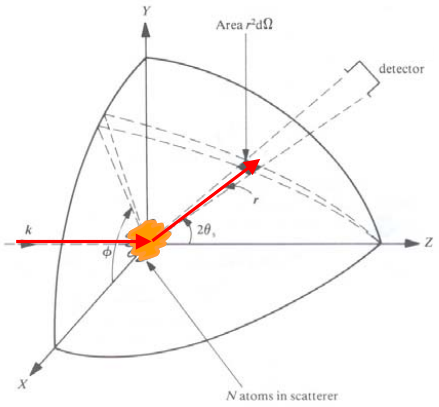

Fig. 2: *Geometry used for the definition of the scattering cross section.*

If n' particles are scattered per second into the solid angle dΩ seen by the detector under the scattering angle 2θ and into the energy interval between E' and E' + dE', then we can define the so-called *double differential cross section* by:

$$\frac{d^2\sigma}{d\Omega dE'} = \frac{n'}{j d\Omega dE'} \tag{4}$$

Here j refers to the incident beam flux in terms of particles per area and time. If we are not interested in the change of the energy of our radiation during the scattering process, or if our detector is not able to resolve this energy change, then we will describe the angular dependence by the so-called *differential cross section:*

$$\frac{d\sigma}{d\Omega} = \int_0^\infty \frac{d^2\sigma}{d\Omega dE'} dE' \tag{5}$$

Finally the so-called *total scattering cross section* gives us a measure for the total scattering probability independent of changes in energy and scattering angle:

$$\sigma = \int_0^{4\pi} \frac{d\sigma}{d\Omega} d\Omega \tag{6}$$

Therefore our task is to determine the arrangement of the atoms in the sample from the knowledge of the scattering cross section $d\sigma/d\Omega$. The relationship between scattered intensity and the structure of the sample is particularly simple in the so-called *Born approximation*, which is often also referred to as *kinematic scattering approximation*. In this case, refraction of the beam entering and leaving the sample, multiple scattering events and the extinction of the primary beam due to scattering within the sample are being neglected. Following Figure 3, the phase difference between a wave scattered at the origin of the coordinate system and at position $\underline{r}$ is given by

$$\Delta\Phi = 2\pi \cdot \frac{\left(\overline{AB} - \overline{CD}\right)}{\lambda} = \underline{k}' \cdot \underline{r} - \underline{k} \cdot \underline{r} = \underline{Q} \cdot \underline{r} \tag{7}$$

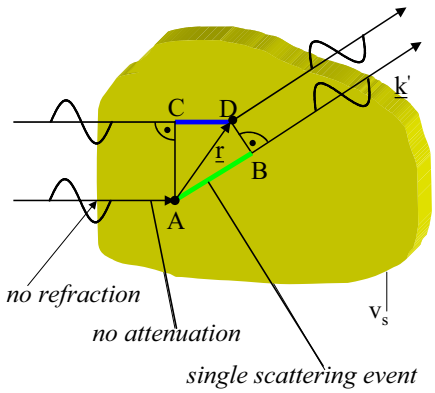

Fig. 3: *A sketch illustrating the phase difference between a beam scattered at the origin of the coordinate system and a beam scattered at the position* $\underline{r}$.

The scattered amplitude at the position $\underline{r}$ is proportional to the scattering power density, or simply scattering density $\rho_s(\underline{r})$. ρ_s depends on the type of radiation used and its interaction with the sample. In fact, ρ_s is directly proportional to the interaction potential, as will be shown in the next chapter. Assuming a laterally coherent beam, the total scattering amplitude is given by a coherent superposition of the scattering from all points within the sample, i. e. by the integral

$$A = A_0 \cdot \int_{V_S} \rho_S(\underline{r}) \cdot e^{i\underline{Q}\cdot\underline{r}} d^3r \qquad (8)$$

Here A_0 denotes the amplitude of the incident wave field. (8) demonstrates that the scattered amplitude is connected with the scattering power density $\rho_s(\underline{r})$ by a simple Fourier transform. A knowledge of the scattering amplitude for all scattering vectors $\underline{Q}$ allows us to determine via a Fourier transform the scattering power density uniquely. This is the complete information on the sample, which can be obtained by the scattering experiment. Unfortunately nature is not so simple. On one hand, there is the more technical problem that one is unable to determine the scattering cross section for all values of momentum transfer $\hbar\underline{Q}$. The more fundamental problem, however, is given by the fact that normally the amplitude of the scattered wave is not measurable. Instead only the scattered intensity

$$I \sim |A|^2 \qquad (9)$$

can be determined. Therefore the phase information is lost and the simple reconstruction of the scattering density via a Fourier transform is no longer possible. This is the so-called *phase problem* of scattering. There are ways to overcome the phase problem, i.e. by the use of reference waves. Then the scattering density becomes directly accessible. The question, which information we can obtain from a scattering experiment despite the phase problem will be addressed below.

Which wavelength do we have to choose to obtain the required real space resolution? For information on a length scale L, a phase difference of about $Q \cdot L \approx 2\pi$ has to be achieved. Otherwise according to (7) $\underline{k}'$ and $\underline{k}$ will not differ significantly. According to (3) $Q \approx 2\pi/\lambda$ for typical scattering angles ($2\theta \sim 60°$). Combining these two estimates, we end up with the requirement that the wavelength λ has to be in the order of the real space length scale L under investigation. To give an example: with the wavelength in the order of 0.1 nm, atomic resolution can be achieved in a scattering experiment.

2.3 Fundamental scattering theory: The Born series

In this chapter, we will give a simple formulation of scattering theory. Our purpose is to derive (8) from fundamental principles. The conditions under which (8) holds and the limitations of kinematical scattering theory will thus become clearer. The derivation will be done for particle beams – in particular neutrons - for which the Schrödinger equation holds. Beginners can skip this chapter and continue with 2.4.

In quantum mechanics, neutrons are described as particle wave fields through the Schrödinger equation:

$$H\Psi = \left(-\frac{\hbar^2}{2m_n}\Delta + V \right)\Psi = i\hbar\frac{\partial}{\partial t}\Psi \tag{10}$$

ψ is the probability density amplitude, V the interaction potential. In the case of purely elastic scattering E = E', the time dependence can be described by the factor $\exp\left(-i\frac{E}{\hbar}t\right)$. Assuming this time dependence, a wave equation for the spatial part of the probability density amplitude ψ can be derived from (10):

$$\Delta\Psi + k^2\left(\underline{r}\right)\Psi = 0 \tag{11}$$

In (11) we have introduced a spatially varying wave vector with the magnitude square:

$$k^2\left(\underline{r}\right) = \frac{2m_n}{\hbar^2}\left(E - V\left(\underline{r}\right)\right) \tag{12}$$

Solutions of (10) in empty space can be guessed immediately. They are given by plane waves $\Psi = \Psi_0 \exp\left[i\left(\underline{k}\cdot\underline{r} - \frac{E}{\hbar}t\right)\right]$ with $k^2 = \frac{2m_n}{\hbar^2}E$. The relations between magnitude of the wave vector, wave length and energy of the neutron E can be written in practical units:

$$\begin{aligned} k\left[\text{Å}^{-1}\right] &\approx 0.695\sqrt{E\left[meV\right]} \\ \lambda\left[\text{Å}\right] &\approx 9.045/\sqrt{E\left[meV\right]} \\ E\left[meV\right] &\approx 81.8/\lambda^2\left[\text{Å}\right] \end{aligned} \tag{13}$$

To give an example, neutrons of wavelength λ = 2.4 Å = 0.24 nm have an energy of 14.2 meV with a magnitude of the neutron wave vector of k = 2.6 Å^{-1}.

To obtain solutions of the wave equation (11) in matter, we reformulate the differential equation by explicitly separating the interaction term:

$$\left(\Delta + k^2\right)\Psi = \frac{2m_n}{\hbar^2}V\cdot\Psi =: \chi \tag{14}$$

Here $\underline{k}$ denotes the wave vector for propagation in empty space. The advantage of this formulation is that the solutions of the left hand side are already known. They are the plane waves in empty space. Equation (14) is a linear partial differential equation, i. e. the superposition principle holds: the general solution can be obtained as a linear combination of a complete set of solution functions. The coefficients in the series are determined by the boundary conditions. To solve (14) one can apply a method developed for inhomogeneous linear differential equations. For the moment, we assume that the right hand side is fixed (given as χ). We define a *Greens-function* by:

$$\left(\Delta + k^2\right)G\left(\underline{r},\underline{r}'\right) = \delta\left(\underline{r} - \underline{r}'\right) \tag{15}$$

A solution of (15) is given by:

$$G(\underline{r},\underline{r}') = \frac{e^{ik|\underline{r}-\underline{r}'|}}{4\pi|\underline{r}-\underline{r}'|} \tag{16}$$

The meaning of (16) is immediately clear: the scattering from a point-like scatterer (δ-potential) gives a emitted spherical wave.

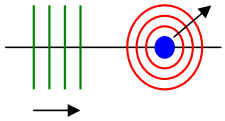

Using the "Greens-function" G(r,r'), a formal solution of the wave equation (14) can be given:

$$\Psi = \Psi^o + \int G(\underline{r},\underline{r}')\,\chi(\underline{r}')\,d^3r' \tag{17}$$

Here, we have taken the initial conditions of a incident plane wave ψ^0 into account. That (17) is indeed a solution of (14) can be easily verified by substituting (17) into (14). If we finally substitute the definition of χ, one obtains:

$$\Psi(\underline{r}) = \psi^\circ(\underline{r}) + \frac{2m_n}{\hbar^2}\int G(\underline{r},\underline{r}')V(\underline{r}')\Psi(\underline{r}')\,d^3r' \tag{18}$$

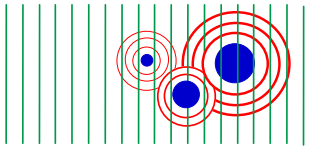

(18) has a simple interpretation: the incident plane wave $\psi^0(\underline{r})$ is superimposed by spherical waves emitted from scattering at positions r'. The intensity of these spherical waves is proportional to the interaction potential V(r') and the amplitude of the wave field at the position r'. To obtain the total scattering amplitude, we have to integrate over the entire sample volume.

However, we still have not solved (14): our solution ψ appears again in the integral in (18). In other words, we have transformed differential equation (14) into an integral equation. The advantage is that for such an integral equation, a solution can be found by iteration. In the zeroth approximation, we neglect the interaction V completely. This gives $\psi = \psi^0$. The next higher approximation for a weak interaction potential is obtained by substituting this solution in the right hand side of (18). The first non-trivial approximation can thus be obtained:

$$\Psi^1(\underline{r}) = e^{i\underline{k}\cdot\underline{r}} + \frac{2m_n}{\hbar^2}\int \frac{\exp(ik|\underline{r}-\underline{r}'|)}{4\pi|\underline{r}-\underline{r}'|} V(\underline{r}')\,e^{i\underline{k}\underline{r}'}\,d^3r' \tag{19}$$

(19) is nothing else but a mathematical formulation of the well-known *Huygens principle* for wave propagation.

The approximation (19) assumes that the incident plane wave is only scattered once from the potential V(r'). For a stronger potential and larger sample, multiple scattering processes can occur. Again, this can be deduced from the integral equation (18) by further iteration. For simplification we introduce a new version of equation (18) by writing the integral over the "Greens function" as operator **G**:

$$\psi = \psi^o + \mathbf{G}V\psi \tag{20}$$

The so-called *first Born approximation*, which gives the *kinematical scattering theory* is obtained by substituting the wave function ψ on the right hand side by ψ^0:

$$\psi^1 = \psi^o + \mathbf{G}V\psi^o \qquad (21)$$

This first approximation can be represented by a simple diagram as a sum of an incident plane wave and a wave scattered once from the potential V.

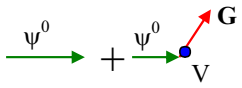

The second approximation is obtained by substituting the solution of the first approximation (21) on the right hand side of equation (20):

$$\psi^2 = \psi^o + \mathbf{G}V\psi^1 = \psi^o + \mathbf{G}V\psi^o + \mathbf{G}V\mathbf{G}V\psi^o \qquad (22)$$

Or in a diagrammatic form:

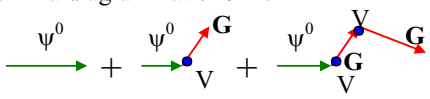

I. e. in the second approximation, processes are being taken into account, in which the neutron is scattered twice by the interaction potential V. In a similar manner, all higher order approximations can be calculated. This gives the so-called *Born series*. For a weak potential and small samples, this series converges rather fast. Often, the first approximation, the kinematic scattering theory, holds very well. This is especially the case for neutron scattering, where the scattering potential is rather weak, as compared to x-ray- or electron- scattering. Due to the strong Coulomb interaction potential, the probability for multiple scattering processes of electrons in solids is extremely high, making the interpretation of electron diffraction experiments very difficult. But even for neutrons, the kinematic scattering theory can break down, for example in the case of Bragg scattering from large ideally perfect single crystals, where the Born series does not converge rapidly. The wave equation has to be solved exactly under the boundary conditions given by the crystal geometry. For simple geometries, analytical solutions can be obtained. This is then called the *dynamical scattering theory*. Since for neutrons, the kinematical theory holds in most cases, or multiple scattering events can be corrected for easily, we will no longer discuss dynamical theory in what follows and refer to [3, 5].

Let us return to the first Born approximation (19). According to Fraunhofer, we assume in a further approximation that the size of the sample is significantly smaller than the distance sample-detector. The geometry to calculate the far field limit of (19) is given in Figure 4.

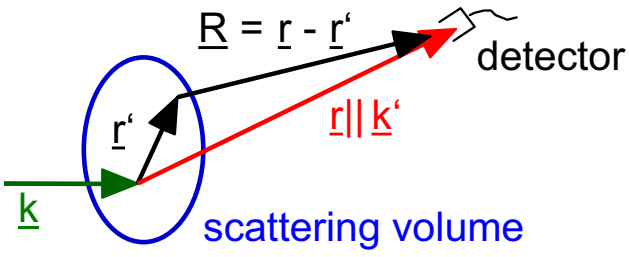

Fig. 4: *Scattering geometry for the calculation of the far field limit at the detector. In the Fraunhofer approximation, we assume that* $|\underline{R}| >> |\underline{r}'|$.

Under the assumption $|\underline{R}| >> |\underline{r}'|$, we can deduce from Figure 4 the following approximation for the emitted spherical wave:

$$\frac{\exp\left(ik\left|\underline{r}-\underline{r}'\right|\right)}{\left|\underline{r}-\underline{r}'\right|}\approx\frac{\exp\left(ik\left(R-\underline{r}'\cdot\hat{\underline{R}}\right)\right)}{R}\approx\frac{\exp(ikR)}{R}\cdot e^{-i\underline{k}'\cdot\underline{r}'} \tag{23}$$

The probability density amplitude for the scattered wave field in the limit of large distances from the sample is thus given by:

$$\Rightarrow\psi^1\left(\underline{R}\right)=e^{i\underline{k}\cdot\underline{R}}+\frac{2m_n}{\hbar^2}\frac{e^{ikR}}{4\pi R}\int V\left(\underline{r}'\right)e^{i\underline{Q}\cdot\underline{r}'}d^3r' \tag{24}$$

This is just the sum of an incident plane wave and a spherical wave emitted from the sample as a whole. The amplitude of the scattered wave is given according to (24):

$$\mathrm{A}\left(\underline{\mathrm{Q}}\right)=\frac{\mathrm{m_n}}{2\pi\hbar^2}\int\mathrm{V}\left(\underline{\mathrm{r}}\right)\mathrm{e}^{\mathrm{i}\underline{\mathrm{Q}}\cdot\underline{\mathrm{r}}}\mathrm{d}^3\mathrm{r}\sim\mathrm{F}\left[\mathrm{V}\left(\underline{\mathrm{r}}\right)\right] \tag{25}$$

The integral in the above equation is nothing but the transition matrix element of the interaction potential V between the initial and final plane wave states, therefore:

$$\frac{\mathrm{d}\sigma}{\mathrm{d}\Omega}=\left(\frac{\mathrm{m_n}}{2\pi\hbar^2}\right)^2\left|\left\langle\underline{\mathrm{k}}'\middle|\mathrm{V}\middle|\underline{\mathrm{k}}\right\rangle\right|^2 \tag{26}$$

This formula corresponds to *Fermis Golden Rule* from time-dependent perturbation theory, where the transition probability per time interval from state r to states r' is given by:

$$\mathrm{W_{r'r}}=\frac{2\pi}{\hbar}\left|\left\langle\mathrm{r}'\middle|\mathrm{V}\middle|\mathrm{r}\right\rangle\right|^2\cdot\rho\left(\mathrm{E_{r'}}\right) \tag{27}$$

Here, $\rho\left(E_{r'}\right)$ denotes the density of states for the final states.

We now allow for inelastic processes, where the sample undergoes a charge of its state from α to α' (α denotes a set of quantum numbers characterizing an eigenstate of the sample). In this case, due to the different length of the wavevectors for incoming and outgoing waves, we have to introduce factors k' and k, which arise from the density of states factor in (27). Since the scattering event must fulfil energy and momentum conservation, we arrive at the double differential cross section:

$$\frac{\mathrm{d}^2\sigma}{\mathrm{d}\Omega\mathrm{d}\omega}=\frac{\mathrm{k}'}{\mathrm{k}}\left(\frac{\mathrm{m_n}}{2\pi\hbar^2}\right)^2\sum_\alpha\mathrm{p}_\alpha\sum_{\alpha'}\left|\left\langle\underline{\mathrm{k}}',\alpha'\middle|\mathrm{V}\middle|\underline{\mathrm{k}},\alpha\right\rangle\right|^2\cdot\delta\left(\hbar\omega+\mathrm{E}_\alpha-\mathrm{E}_{\alpha'}\right) \tag{28}$$

The summation over α is carried out over all possible initial states α of the systems, weighted with their thermodynamic occupation probability p_α. The sum over α' is the sum over all final states allowed by energy conservation, which is guaranteed through the δ-function. $\hbar\omega$ denotes the energy transfer of the neutron to the system. This double differential cross section will be discussed in the following lectures on inelastic scattering.

2.4 Coherence

In the above derivation, we assumed plane waves as initial and final states. For a real scattering experiment, this is an unphysical assumption. In the incident beam, a wave packet is produced by collimation and monochromatisation. This wave packet can be described as a superposition of plane waves. As a consequence, the diffraction pattern will be a superposition of patterns for different incident wavevectors $\underline{k}$ and the question arises, which information is lost due to these non-ideal conditions. This *instrumental resolution* is intimately connected with the *coherence* of the beam. Coherence is needed, so that the interference pattern is not significantly destroyed. Coherence requires a phase relationship between the different components of the beam. Two types of coherence can be distinguished.

• *Temporal or longitudinal coherence* due to a wavelength spread.
A measure for the longitudinal coherence is given by the length, on which two components of the beam with largest wavelength difference (λ and $\lambda + \Delta\lambda$) become fully out of phase. According to the following figure, this is the case for $l_{\parallel} = n \cdot \lambda = \left(n - \frac{1}{2}\right)(\lambda + \Delta\lambda)$.

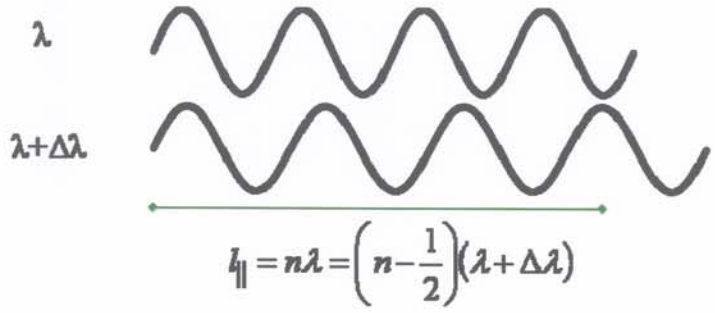

Fig. 5: *A sketch illustrating the longitudinal coherence due to a wavelength spread.*

From this, we obtain the *longitudinal coherence length* $l_{\parallel}$ as

$$l_{\parallel} = \frac{\lambda^2}{2\Delta\lambda} \tag{29}$$

• *Transversal coherence* due to source extension
Due to the extension of the source (transverse beam size), the phase relation is destroyed for large source size or large divergence. According to the following figure, a first minimum occurs for $\frac{\lambda}{2} = d \cdot \sin\theta \approx d \cdot \theta$.

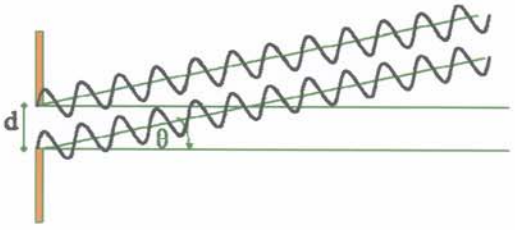

Fig. 6: *A sketch illustrating the transverse coherence due to source extension.*

From this, we obtain the *transversal coherence length* $l_{\perp}$ as

$$l_{\perp} = \frac{\lambda}{2\Delta\theta} \tag{30}$$

where $\Delta\theta$ is the divergence of the beam. Note that $l_{\perp}$ can be different along different spatial directions: in many instruments, the vertical and horizontal collimations are different.

Together, the longitudinal and the two transversal coherence lengths define a *coherence volume*. This is a measure for a volume within the sample, in which the amplitudes of all scattered waves superimpose to produce an interference pattern. Normally, the coherence

volume is significantly smaller than the sample size, typically a few 100 Å for neutron scattering, up to µm for synchrotron radiation. Scattering between different coherence volumes within the sample is no longer coherent, i. e. instead of the amplitudes, the intensities of the contributions to the scattering pattern have to be added. This limits the spatial resolution of a scattering experiment to the extension of the coherence volume.

2.5 Pair correlation functions

After having clarified the conditions under which we can expect a coherent scattering process, let us now come back to the question, which information is accessible from the intensity distribution of a scattering experiment. From (9) we see that the phase information is lost during the measurement of the intensity. For this reason the Fourier transform of the scattering power density is not directly accessible in most scattering experiments (note however that phase information can be obtained in certain cases).

Substituting (8) into (9), we obtain for the magnitude square of the scattering amplitude, a quantity directly accessible in a scattering experiment:

$$I \sim \left| A\left(\underline{Q}\right)\right|^2 \sim \int d^3r'\, \rho_s\left(\underline{r}'\right) e^{i\underline{Q}\cdot\underline{r}'} \int d^3r\, \rho_s^*\left(\underline{r}\right) e^{-i\underline{Q}\cdot\underline{r}} = \iint d^3r'\, d^3r\, \rho_s\left(\underline{r}'\right) \rho_s^*\left(\underline{r}\right) e^{i\underline{Q}\cdot\left(\underline{r}'-\underline{r}\right)}$$

$$= \iint d^3R\, d^3r\, \rho_s\left(\underline{R}+\underline{r}\right) \rho_s^*\left(\underline{r}\right) e^{i\underline{Q}\cdot\underline{R}} \qquad (31)$$

This shows that the scattered intensity is proportional to the Fourier transform of a function P(R):

$$I\left(\underline{Q}\right) \sim \int d^3R\, P\left(\underline{R}\right) e^{i\underline{Q}\cdot\underline{R}} \qquad (32)$$

This function denotes the so-called *Patterson function* in crystallography or more general the *static pair correlation function:*

$$P\left(\underline{R}\right) = \int d^3r\, \rho_s^*\left(\underline{r}\right) \rho_s\left(\underline{r}+\underline{R}\right) \qquad (33)$$

P(R) correlates the value of the scattering density at position r with the value at the position r + R, integrated over the entire sample volume. If, averaged over the sample, no correlation exists between the values of the scattering power densities at position r and r+R, then the Patterson function P(R) vanishes. If, however, a periodic arrangement of a pair of atoms exists in the sample with a difference vector R between the positions, then the Patterson function will have an extremum for this vector R. Thus the Patterson function reproduces all the vectors connecting one atom with another atom in a periodic arrangement.

Quite generally, in a scattering experiment, pair correlation functions are being determined. In a coherent inelastic scattering experiment, we measure the *scattering law S(Q,ω)*, which is the Fourier transform with respect to space and time of the spatial and temporal pair correlation function:

$$\frac{d^2\sigma}{d\omega d\Omega} \sim S\left(\underline{Q},\omega\right) = \frac{1}{2\pi\hbar} \int_{-\infty}^{+\infty} dt\, e^{-i\omega t} \int d^3r\, e^{i\underline{Q}\cdot\underline{r}} G\left(\underline{r},t\right) \qquad (34)$$

While the proportionality factor between the double differential cross section and the scattering law depends on the type of radiation and its specific interaction potential with the system studied, the spatial and temporal pair correlation function is only a property of the system studied and independent of our probe:

$$G\left(\underline{r},t\right) = \frac{1}{N} \sum_{ij} \int d^3r' \left\langle \delta\left(\underline{r}'-\underline{r}_j\left(0\right)\right) \cdot \delta\left(\underline{r}'+\underline{r}-\underline{r}_i\left(t\right)\right)\right\rangle = \frac{1}{N} \int d^3r' \left\langle \rho\left(\underline{r}',0\right) \rho\left(\underline{r}'+\underline{r},t\right)\right\rangle \qquad (35)$$

Here, the pair correlation function is once expressed as a correlation between the position of N point-like particles (expressed by the delta function) and once by the correlation between

the densities at different positions in the sample for different times. In a magnetic system, we scatter from the atomic magnetic moments, which are vector quantities. Therefore, the scattering law becomes a tensor - the Fourier transform of the spin pair correlations (α, ß denote the Cartesian coordinates x, y, z; $\underline{R}_0$ and $\underline{R}_l$ are the spatial coordinates of a reference spin 0 and a spin l in the system)

$$\mathbf{S}^{\alpha\beta}(\underline{Q},\omega) = \frac{1}{2\pi}\sum_l \int dt\, e^{i\left[\underline{Q}(\underline{R}_l - \underline{R}_0) - \omega t\right]} \left\langle S_0^{\alpha}(0) S_l^{\beta}(t) \right\rangle \tag{36}$$

2.6 Form-factor

So far we have not specified the nature of our sample. Now we assume an assembly on N scatterers of finite size, see Figure 7.

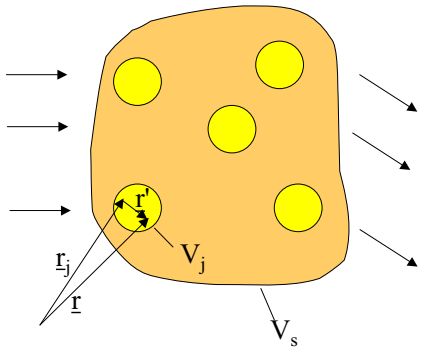

Fig. 7: *Sketch showing the assembly of N scatterers of finite size and defining the quantities needed for the introduction of the form factor.*

These could be atoms in a solid, or colloidal particles in a homogeneous solution. In what follows, we will separate the interference effects from the scattering within one such a particle from the interference effects arising from scattering from different particles. With the decomposition of the vector $\underline{r}$ into the centre-of-gravity-vector $\underline{r}_j$ and a vector $\underline{r}'$ within the particle, the scattering amplitude can be written as (all particles are assumed to be identical):

$$A \propto \int_{V_S} d^3r\, \rho_S(\underline{r}) e^{i\underline{Q}\cdot\underline{r}} = \sum_{j=1}^{N} \int_{V_j} d^3r\, \rho_S(\underline{r}) e^{i\underline{Q}\cdot\underline{r}} = \sum_{j=1}^{N} e^{i\underline{Q}\cdot\underline{r}_j} \int_{V_j^0} d^3r'\, \rho_S(\underline{r}') e^{i\underline{Q}\cdot\underline{r}'} \tag{37}$$

The *form-factor* is defined as the normalised amplitude of scattering from within one particle:

$$f(\underline{Q}) \equiv \frac{\int_{V_j^0} d^3r'\, \rho_s(\underline{r}')\, e^{i\underline{Q}\cdot\underline{r}'}}{\int_{V_j^0} d^3r'\, \rho_s(\underline{r}')} \tag{38}$$

For a homogeneous sphere

$$\rho_S(\underline{r}) = \begin{cases} 0 & |\underline{r}| > R \\ 1 & |\underline{r}| \le R \end{cases} \tag{39}$$

the form-factor can be calculated by using spherical co-ordinates:

$$\Rightarrow f(Q) = 3 \cdot \frac{\sin QR - QR \cdot \cos QR}{(QR)^3} \tag{40}$$

The function (40) is plotted in Figure 8. In forward direction, there is no phase difference between waves scattered from different volume elements within the sample (note: we assume the Fraunhofer approximation and work in a far field limit). The form-factor takes its maximum value of one. For finite scattering angles 2θ, the form-factor drops due to destructive interference from various parts within one particle and finally for large values of the momentum transfer shows damped oscillations around 0 as a function of QR.

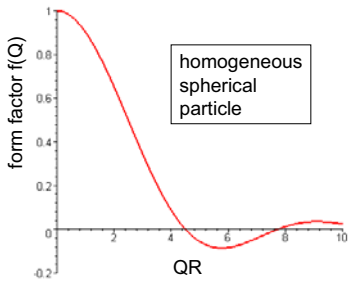

Fig. 8: *Form-factor for a homogeneous sphere according to (40).*

2.7 Scattering from a periodic lattice in three dimensions

As an example for the application of (8) and (9), we will now discuss the scattering from a three dimensional lattice of point-like scatterers. As we will see later, this situation corresponds to the scattering of thermal neutrons from a single crystal. More precisely, we will restrict ourselves to the case of a Bravais lattice with one atom at the origin of the unit cell. To each atom we attribute a scattering power α. The single crystal is finite with N, M and P periods along the basis vectors $\underline{a}$, $\underline{b}$ and $\underline{c}$. The scattering density, which we have to use in (8) is a sum over δ-functions for all scattering centres:

$$\rho_s(\underline{r}) = \sum_{n=0}^{N-1}\sum_{m=0}^{M-1}\sum_{p=0}^{P-1} \alpha \cdot \delta\left(\underline{r} - \left(n\cdot\underline{a} + m\cdot\underline{b} + p\cdot\underline{c}\right)\right) \tag{41}$$

The scattering amplitude is calculated as a Fourier transform:

$$A(\underline{Q}) \sim \alpha \sum_{n=0}^{N-1} e^{in\underline{Q}\cdot\underline{a}} \sum_{m=0}^{M-1} e^{im\underline{Q}\cdot\underline{b}} \sum_{p=0}^{P-1} e^{ip\underline{Q}\cdot\underline{c}} \tag{42}$$

Summing up the geometrical series, we obtain for the scattered intensity:

$$I(\underline{Q}) \sim \left|A(\underline{Q})\right|^2 = |\alpha|^2 \cdot \frac{\sin^2\frac{1}{2}N\underline{Q}\cdot\underline{a}}{\sin^2\frac{1}{2}\underline{Q}\cdot\underline{a}} \cdot \frac{\sin^2\frac{1}{2}M\underline{Q}\cdot\underline{b}}{\sin^2\frac{1}{2}\underline{Q}\cdot\underline{b}} \cdot \frac{\sin^2\frac{1}{2}P\underline{Q}\cdot\underline{c}}{\sin^2\frac{1}{2}\underline{Q}\cdot\underline{c}} \tag{43}$$

The dependence on the scattering vector $\underline{Q}$ is given by the so-called *Laue function*, which factorizes according to the three directions in space. One factor along one lattice direction $\underline{a}$ is plotted in Figure 9.

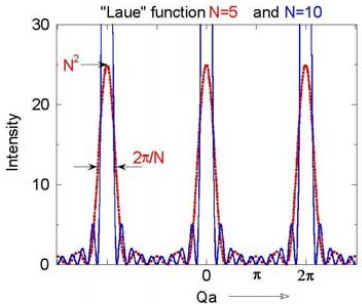

Fig. 9: *Laue function along the lattice direction a for a lattice with five and ten periods, respectively.*

The main maxima occur at the positions $Q = n \cdot 2\pi/a$. The maximum intensity scales with the square of the number of periods N^2, the half width is given approximately by $\Delta Q = 2\pi/(N \cdot a)$. The more periods contribute to coherent scattering, the sharper and higher are the main peaks. Between the main peaks, there are N-2 site maxima. With increasing number of periods N, their intensity becomes rapidly negligible compared to the intensity of the main peaks. The main peaks are of course the well known *Bragg reflections*, which we obtain when scattering from a crystal lattice. From the position of these Bragg peaks in momentum space, the metric of the unit cell can be deduced (lattice constants a, b, c and unit cell angles α, β, γ). The width of the Bragg peaks is determined by the size of the coherently scattering volume (parameters N, M, and P) - and some other factors for real experiments (resolution, mosaic distribution, internal strains, ...).

2.8 Probes for scattering experiments in condensed matter science

In this chapter, we will discuss which type of radiation is suitable for condensed matter investigations. For neutron beams, we will then discuss the relevant interaction processes with matter in detail.

A list of requirements for the type of radiation used in condensed matter investigations looks as follows:

(1) The achievable spatial resolution should be in the order of the inter-particle distances, which implies (see section 2.2) that the wavelength λ is in the order of the inter-particle distance L.
(2) If we want to study volume effects, the scattering has to originate from the bulk of the sample, which implies that the radiation should be at most weakly absorbed within matter.
(3) For a simple interpretation of the scattering data within the Born approximation (see chapter 2), multiple scattering effects should be negligible, i. e. the interaction of the radiation with matter should be weak.
(4) For the sake of simplicity, the probe should have no inner degrees of freedom, which could be excited during the scattering process (i. e. avoid beams of molecules, which have internal vibrational or rotational degrees of freedom).
(5) To study magnetic systems, we need a probe which interacts with the atomic magnetic moments in the sample.

(6) If, in addition to structural studies, we want to investigate elementary excitations, we would like the energy of the probe to be in the order of the excitation energies, so that the energy change during the scattering process is easily measurable.

This list of requirements leads us to some standard probes in condensed matter research. First of all, electromagnetic radiation governed by the Maxwell equations can be used. Depending on the resolution requirements, we will use x-rays with wavelength λ about 0.1 nm to achieve atomic resolution or visible light (λ ~ 350 - 700 nm) to investigate e. g. colloidal particles in solution. Besides electromagnetic radiation, particle waves can be used. It turns out that thermal neutrons with a wavelength λ ~ 0.1 nm are particularly well adapted to the above list of requirements. The neutron beams are governed by the Schrödinger equation of quantum mechanics. An alternative is to use electrons, which for energies of around 100 keV have wavelengths in the order of 0.005 nm. As relativistic particles, they are governed by the Dirac equation of quantum mechanics. The big drawback of electrons as a condensed matter probe is the strong Coulomb interaction with the electrons in the sample. Therefore neither absorption, nor multiple scattering effects can be neglected. However the abundance of free electrons and the relative ease to produce optical elements makes them very suitable for imaging purposes (electron microscopy). Electrons, but also atomic beams are very powerful tools for surface science: due to their strong interaction with matter, both types of radiation are very surface sensitive. Low Energy Electron Diffraction LEED and Reflection High Energy Electron Diffraction RHEED are both used for in-situ studies of the crystalline structure during thin film growth, e.g. with Molecular Beam Epitaxy MBE. In what follows we will concentrate on neutron scattering as one of the probes, which is best suited for bulk studies on an atomic scale. We will introduce the properties of the neutron, discuss the absorption of neutrons with matter and derive the scattering cross sections for the main interaction processes with matter.

2.9 Properties of the neutron

We mentioned in the introduction that neutron beams provide a particularly useful probe for condensed matter investigations. The neutron is an elementary particle, a nucleon, consisting of three valance quarks, which are hold together by gluons. It thus has an internal structure, which, however, is irrelevant for condensed matter physics, since the energy scales involved in internal excitations are much too high. Keeping in mind the difference in lengths scales (diameter of an atom: about 0.1 nm = 10^{-10} m; diameter of a neutron: about 1 fm = 10^{-15} m), we can safely consider the neutron as a point-like particle without internal structure for our purposes. Due to the weak interaction, the neutron is not a stable particle. A free neutron undergoes a β-decay after an average lifetime of about 15 minutes:

$$n \xrightarrow{15\,\mathrm{min}} p + e^- + \bar{\nu} \tag{44}$$

This leaves ample time for scattering investigations. In contrast to the massless photon, the neutron has a mass m of about one atomic mass unit ~ $1.675 \cdot 10^{-27}$ kg. The finite neutron mass is comparable to the mass of a nucleus and thus an appreciable amount of energy can be transferred during the scattering process. The neutron is a chargeless particle and thus does not show the strong Coulomb interaction with matter. This results in large penetration depths. Finally, the neutron has a nuclear spin 1/2 giving rise to a magnetic dipolar moment of

$$\mu_n = \gamma \mu_N; \quad \gamma = 1.91; \quad \mu_N = 5.05 \cdot 10^{-27} J/T \tag{45}$$

Due to this magnetic moment, the neutron can interact with the magnetic field of unpaired electrons in a sample leading to *magnetic scattering*. Thus magnetic structures and excitations can be studied by neutron scattering.

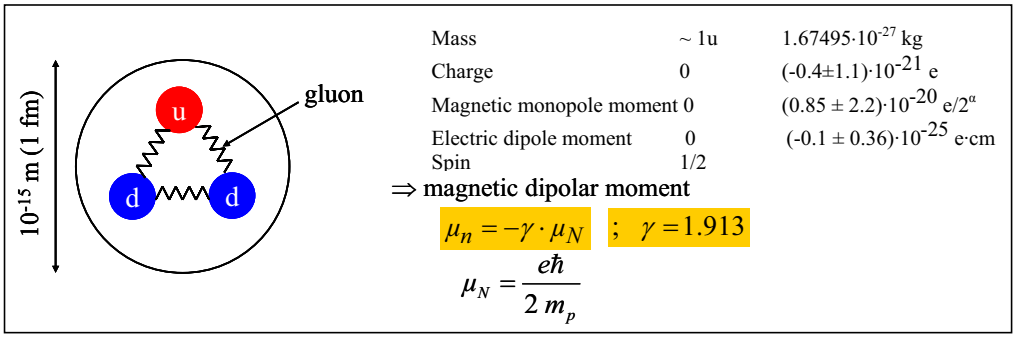

Fig. 10: *Schematics of the neutron being composed of three quarks and gluons and the main quantities characterising the neutron as a particle.*

To calculate the interference effects during the scattering process, a neutron has to be described as a matter wave with momentum

$$\underline{p} = m \cdot \underline{v} = \hbar \underline{k};\ p = h/\lambda \tag{46}$$

and energy

$$E = \frac{1}{2} m v^2 = \frac{\hbar^2 k^2}{2m} = \frac{h^2}{2m\lambda^2} \equiv k_B T_{eq} \tag{47}$$

where $\underline{v}$ is the velocity of the neutron and T_{eq} defines the temperature equivalent of the kinetic energy of the neutron. In practical units:

$$\lambda[nm] = \frac{400}{v[m/s]}$$
$$E[meV] = \frac{0.818}{\lambda^2[nm]} \tag{48}$$

Let us consider the example of so-called *thermal neutrons* from a moderator at ambient temperature corresponding to a temperature equivalent of $T_{eq} \sim 300$ K. According to (47), their wavelength is 0.18 nm, matching perfectly the distance between atoms. The energy of thermal neutrons is around 25 meV, which matches well the energy of elementary excitations, such as spin waves (magnons) or lattice vibrations (phonons). Together with the usually large penetration depths (charge = 0) and the magnetic interaction, these properties make neutrons so extremely useful for condensed matter investigations.

In our simple scattering theory of chapter 2.3, we saw that the relevant quantity is the interaction potential $V(\underline{r})$ of the probe with the system from which the probe is scattered. This potential enters in the cross-section in kinematical theory derived either from Born approximation or from Fermi's golden rule. This is why - in what follows - we will look in more detail at the interaction of neutrons with matter. In fact for neutrons there exist two dominant interactions: the interaction of the neutron with nuclei and its interaction with the magnetic field in the sample. The nuclear interaction results from the so-called strong interaction of particle physics, which is also responsible for the binding of neutrons and protons in the atomic nuclei. The interaction with the magnetic field is nothing but the magnetic dipole interaction of the neutron due to its dipolar moment with the magnetic field of unpaired electrons. There are other interactions, which are significantly weaker. One is the interaction of the neutron with the electric fields in the sample due to the neutrons magnetic dipole moment. This is a purely relativistic effect. Another is the magnetic dipole interaction of the neutron with the magnetic field produced by the nuclei. Since such interactions are several orders of magnitude weaker

than the nuclear and magnetic interaction, they can usually be neglected and we will not discuss them further in this lecture.

2.10 Nuclear interaction: Scattering and absorption

To evaluate the cross section (26) for nuclear scattering, we have to specify the interaction potential with the nucleus. To derive this interaction potential is one of the fundamental problems of nuclear physics. Fermi has proposed a phenomenological potential based on the argument that the wavelength of thermal neutrons is much larger than the nuclear radius. This means that the nuclei are point-like scatterers and leads to isotropic, Q-independent, (so-called s-wave) scattering. We will therefore use the so-called *Fermi-pseudo-potential:*

$$V(\underline{r}) = \frac{2\pi\hbar^2}{m} b\delta(\underline{r} - \underline{R}) \tag{49}$$

to evaluate the cross section (26).

Note, that despite the fact that the strong interaction of high energy physics is responsible for the scattering of the neutron with the nucleus, the scattering probability is small due to the small nuclear radius. Therefore, we can apply the first Born approximation. The quantity b introduced in (49) is a phenomenological quantity describing the strength of the interaction potential and is referred to as the *scattering length*. Tabulated values of b can be found in [6]. The total cross section of a given nucleus is $\sigma = 4\pi|b|^2$, corresponding to the surface area of a sphere with radius b. Since the interaction potential obviously depends on the details of the nuclear structure, b is different for different isotopes of the given element and also for different nuclear spin states. This fact gives rise to the appearance of so-called *coherent* and *incoherent scattering*, see 2.12. Figure 11 shows the variation of the scattering amplitude as a function of atomic weight throughout the periodic table.

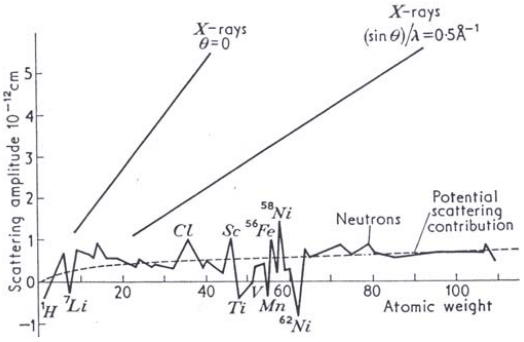

Fig. 11: *Scattering length as a function of atomic weight throughout the periodic table.*

The scattering length is mostly positive but can also adopt negative values. Since -1 = exp(iπ) this negative sign corresponds to a phase shift of π (or 180°) during the scattering process. The scattering length roughly follows the dashed line labelled *potential scattering* contribution, despite the fact that there are rather large fluctuations around this line. In the simplest one dimensional model, we can describe the nucleus as a rectangular potential well, see Figure 12.

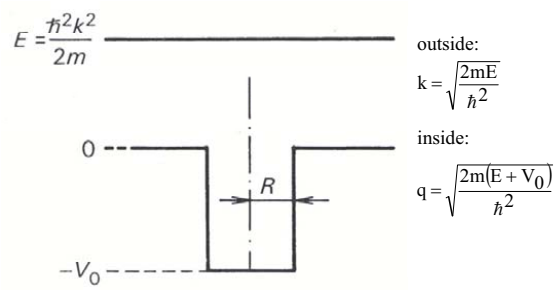

Fig. 12: *The nucleus described as a potential well of radius R and depth -V_0, while the neutron has the kinetic energy* $E = \frac{\hbar^2 k^2}{2m}$.

The wave function of the neutron being scattered from such a potential well can be written as:

$$\Psi(\underline{r}) \sim e^{i\underline{kr}} + \frac{f}{r} e^{ikr} \tag{50}$$

where the first term describes the incident plane wave and the second term describes a spherical wave emitted from the nucleus. f describes the scattering amplitude. In the limit of a hard sphere, the wave function on the surface of the nucleus has to vanish since the neutron cannot penetrate inside the nucleus. Mathematically this is described by the condition $\psi(R) = 0$ or $-f = R$. The scattering length is just defined as b: = -f, so that its value is positive for most nuclei. Therefore for purely potential scattering, where the nucleus is assumed to be a hard sphere, b attains the value of the nuclear radius b = R, which is plotted in Figure 12 as a dashed line: the *potential scattering* contribution. The marked deviations from this overall behaviour are due to so-called *resonance scattering*. In a simplified picture, such resonances occur, when the neutron energy is such that absorption of the neutron in the nucleus produces a bound excited state. This can lead to a resonant absorption process, but it can also lead to resonance scattering, a typical second order perturbation process: In the initial state, the nucleus is in its ground state and the interaction with the neutron can be described as a virtual transition into an excited state of the compound nucleus and a virtual re-emission of the neutron, where the nucleus decays back from the excited compound system into its ground state. This process

$n + K \rightarrow C^* \rightarrow K + n$

has a cross-section given by the famous *Breit-Wigner-formula*.

$$\sigma_R = 4\pi \left| R + \frac{const}{E - E_R + \frac{1}{2} i\Gamma} \right|^2 \tag{51}$$

Here R is the radius of the nucleus, E the neutron energy, E_R the resonance energy and Γ a damping term connected with the life-time of the excited state. As one can see, this formula describes a very strong energy dependence with a pronounced maxima, when the neutron energy equals the resonance energy. Moreover, the resonance amplitude has an imaginary part, which describes the *resonance absorption*. In the resonant absorption process, the neutron is captured by the nucleus, leading to a compound nucleus in an excited state, containing one more neutron then the original nucleus. In a subsequent nuclear reaction, the compound nucleus gets rid of its excess energy. Examples for such absorption reactions will be given in the subsequent section. Finally the Breit-Wigner-formula gives an indication that the scattering length can be negative whenever the resonant term is negative (i. e. $E < E_R$), and its magnitude is larger than the contribution from potential scattering.

2.11 Neutron absorption

As explained above, neutron absorption can occur during nuclear reactions. Far away from the resonance, the absorption cross section is given by

$$\sigma_a \sim \lambda \sim \frac{1}{v} \tag{52}$$

This proportionality to the wavelength λ or the inverse velocity is a result of the density of states appearing in Fermi's golden rule. One can argue that wavelength and neutron velocity v are inversely proportional and thus, for longer wavelength i. e. smaller velocity, the neutron remains correspondingly longer close to the nucleus, which leads to a higher absorption cross-section. Table 1 gives examples for neutron absorption processes connected with nuclear reactions.

Examples:		
σ_a (25 meV) [barn]		
5333	$n + {}^{3}He \rightarrow {}^{4}He^{*} \rightarrow p + {}^{3}T$	neutron detection
940	$n + {}^{6}Li \rightarrow {}^{7}Li^{*} \rightarrow {}^{3}T + {}^{4}He$	
3837	$n + {}^{10}B \rightarrow {}^{11}B^{*} \rightarrow {}^{4}He + {}^{7}Li + \gamma$	
681	$n + {}^{235}U \rightarrow$ fission	

Table 1 *Examples for neutron absorption processes due to nuclear reactions. The absorption cross-section is given for neutrons of energy 25 meV in barn = 10^{-28} m^2 = 100 fm^2.*

As an example, there is a high probability of neutrons to be absorbed by ^{3}He nuclei, because the ^{4}He or α-particle is very stable, since it corresponds to a closed nuclear shell. However, during the absorption of the neutron, the ^{4}He nucleus is produced in an excited state. It gets rid of its surplus energy by decay into a proton and a triton. The latter is nothing but a form of hydrogen containing one proton and two neutrons. Since these two particles have very high energies due to the nuclear reaction of about 0.5 meV, charged particles are created during this decay, which can be used for neutron detection in a proportional counter. In a similar manner, the reaction with ^{6}Li, ^{10}B or ^{235}U can be used to build neutron detectors. It should be mentioned, however, that the neutron absorption in ^{3}He is very strongly dependent on the relative orientation of their nuclear spins. While for antiparallel spin direction, the absorption cross-section is 6000 barn, it reduces to 2 barn for parallel spin direction. This effect can be used to build efficient neutron polarisation filters. By optical pumping with laser light, the nuclear moment of the ^{3}He nuclei can be aligned along one direction (so-called hyperpolarised ^{3}He gas). If an unpolarised neutron beam passes a filter cell filled with hyperpolarised ^{3}He, the neutrons with spin moment antiparallel to the nuclear moment of the ^{3}He have a high probability to be absorbed, while neutrons with the other spin direction have a high probability to be transmitted. For an appropriate thickness of the filter cell, a very high neutron beam polarisation can be achieved in this manner.

Another class of absorption processes are so-called *(n, γ)-resonances*. Examples are given in Table 2. In these processes, a nucleus is produced, which contains one additional neutron and this compound nucleus decays into the ground state by emission of γ-radiation. Prominent (n,γ)-resonances occur for Cadmium or Gadolinium where, depending on the isotope, the absorption cross-section can be very high, see Table 2. These metals are often used as neutron absorbers in shieldings or diaphragms, which define the size of the neutron beam. One should, however, be aware that in these reactions, γ-radiation of very high energy is being released, which requires additional lead shielding for radiation protection.

	nucleide	σ_γ[barn]	$E_{resonance}$[meV]
(n, γ)-resonances:	^{113}Cd	20600	178
	^{151}Eu	9200	321
	^{155}Gd	60900	26.8
	^{157}Gd	254000	31.4

Table 2 *Example for (n, γ)-resonances with the cross-section in barn and the resonance energy in meV.*

As described by the Breit-Wigner-Formula, these resonance absorption cross-sections have a very strong energy dependence. The simple proportionality to the wavelength given in equation (52) no longer holds close to the resonance energies. As an example, we show the energy dependence of the absorption cross-section for Cadmium in Figure 13. Such data can be found in the compilation [7].

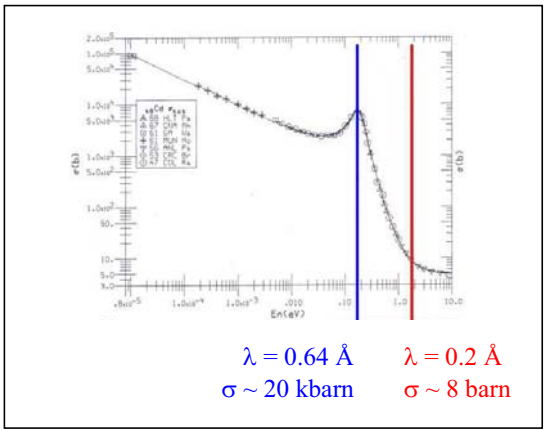

Fig. 13: *Absorption cross-section of the element Cadmium as a function of energy in a double logarithmic representation.*

Figure 13 shows that for lower energies, i. e. long wavelengths, the proportionality of the absorption cross-section to the wavelength holds to very good approximation. However, there is a strong resonance for a wavelength of 0.64 Å, where the cross-section attains a maximum of about 20 kbarn. Above this energy, i. e. for shorter wavelengths, the absorption cross-section drops drastically. At a wavelength of 0.2 Å, it attains a value of only 8 barn. This shows that in the thermal energy range, Cadmium can be used as an efficient neutron absorber. However, one has to be careful and not use it for the same purpose in case of hot neutrons, where Cadmium becomes virtually transparent. There are many more resonances for higher neutron energies, which are not relevant for neutron scattering, where only hot, thermal and cold neutrons are being used.

A similar strong energy dependence occurs for the element Gadolinium. Usually, neutron scatterers try to avoid samples containing Gadolinium since it is the most absorbing element,

especially the isotope ^{157}Gd. However, the resonances lay right in the thermal neutron energy range. If the scattering experiment is performed with hot neutrons, the absorption cross-section of Gadolinium becomes much smaller and scattering experiments become feasible.

2.12 Coherent and incoherent scattering

As mentioned above, the nuclear interaction potential depends on the details of the nuclear structure and thus, the scattering length b is different for different isotopes of a given element and also for different nuclear spin states. In this section, we will discuss the effects of these special properties of the interaction of neutrons and nuclei for the scattering from condensed matter.

Let us assume an arrangement of atoms with scattering lengths b_i on fixed positions $\underline{R}_i$. For this case, the scattering potential writes:

$$V(\underline{r}) = \frac{2\pi\hbar^2}{m_n} \sum_i b_i \delta(\underline{r} - \underline{R}_i) \tag{53}$$

The scattering amplitude is obtained from a Fourier transform:

$$A(\underline{Q}) = \sum_i b_i e^{i\underline{Q}\cdot\underline{R}_i} \tag{54}$$

When we calculate the scattering cross section, we have to take into account that the different isotopes are distributed randomly over all sites. Also the nuclear spin orientation is random, except for very low temperatures in external magnetic fields. Therefore, we have to average over the random distribution of the scattering length in the sample:

$$\frac{d\sigma}{d\Omega}(\underline{Q}) \sim \left|A(\underline{Q})\right|^2 = \left\langle \sum_i b_i \; e^{i\underline{Q}\cdot\underline{R}_i} \cdot \sum_j b_j^* e^{-i\underline{Q}\underline{R}_j} \right\rangle \tag{55}$$

In calculating the expectation value of the product of the two scattering lengths at sites i and j, we have to take into account that according to the above assumption, the distribution of the scattering length on the different sites is completely uncorrelated. This implies that for $i \neq j$, the expectation value of the product equals to the product of the expectation values. Only for $i = j$ a correlation occurs, which gives an additional term describing the mean quadratic deviation from the average:

$$\left\langle b_i b_j \right\rangle = \begin{cases} \langle b\rangle\langle b\rangle = \langle b\rangle^2 & i \neq j \\ \left\langle b^2 \right\rangle = \langle b\rangle^2 + \left\langle \left(b - \langle b\rangle\right)^2 \right\rangle & i = j \end{cases}$$

The line for $i = j$ results from the identity:

$$\left\langle \left(b - \langle b\rangle\right)^2 \right\rangle = \left\langle b^2 - 2b\langle b\rangle + \langle b\rangle^2 \right\rangle = \left\langle b^2 \right\rangle - \langle b\rangle^2 \tag{56}$$

Therefore, we can write the cross section in the following form:

$$\begin{aligned} \frac{d\sigma}{d\Omega}(\underline{Q}) &= \langle b\rangle^2 \left| \sum_i e^{i\underline{Q}\cdot\underline{R}_i} \right|^2 \quad \text{"}coherent\text{"} \\ &+ N\left\langle \left(b - \langle b\rangle\right)^2 \right\rangle \quad \text{"}incoherent\text{"} \end{aligned} \tag{57}$$

The scattering cross section is as a sum of two terms. Only the first term contains the phase factors $e^{i\underline{Q}\cdot\underline{R}}$, which result from the coherent superposition of the scattering from pairs of scatterers. This term takes into account interference effects and is therefore named *coherent scattering*. Only the scattering length averaged over the isotope- and nuclear spin- distribution

enters this term. The second term in (57) does not contain any phase information and is proportional to the number N of atoms (and not to N^2!). This term is not due to the interference of scattering from different atoms. As we can see from (56) (line i = j), this term corresponds to the scattering from single atoms, which subsequently superimpose in an incoherent manner (adding intensities, not amplitudes!). This is the reason for the intensity being proportional to the number N of atoms. Therefore the second term is called *incoherent scattering*. Coherent and incoherent scattering are illustrated in Figure 14.

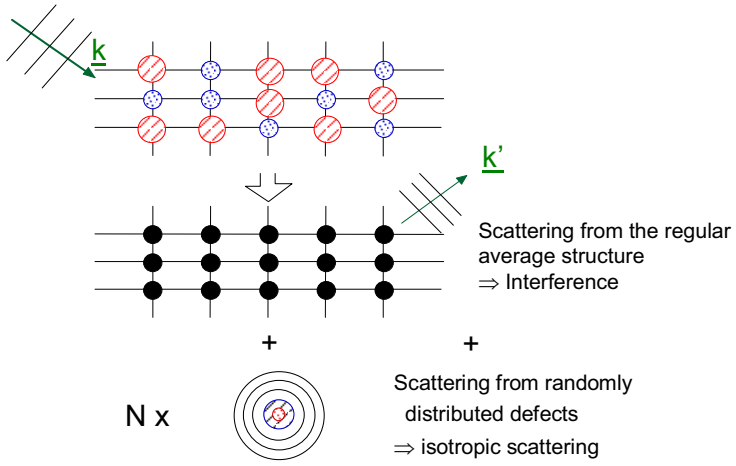

Fig. 14: *Two-dimensional schematic illustration of the scattering process from a lattice of N atoms of a given chemical species, for which two isotopes (small dotted circles and large hatched circles) exist. The area of the circle represents the scattering cross section of the single isotope. The incident wave (top part of the figure for a special arrangement of the isotopes) is scattered coherently only from the average structure. This gives rise to Bragg peaks in certain directions. In the coherent scattering only the average scattering length is visible. Besides these interference phenomena, an isotropic background is observed, which is proportional to the number N of atoms and to the mean quadratic deviation from the average scattering length. This incoherent part of the scattering is represented by the lower part of the figure.*

The most prominent example for *isotope incoherence* is elementary nickel. The scattering lengths of the nickel isotopes are listed together with their natural abundance in Table 3 [6]. The differences in the scattering lengths for the various nickel isotopes are enormous. Some isotopes even have negative scattering lengths. This is due to resonant bound states, as compared to the usual potential scattering.

Isotope	Natural Abundance	Nuclear Spin	Scattering Length [fm]
^{58}Ni	68.27 %	0	14.4(1)
^{60}Ni	26.10 %	0	2.8(1)
^{61}Ni	1.13 %	$^{3}/_{2}$	7.60(6)
^{62}Ni	3.59 %	0	-8.7(2)
^{64}Ni	0.91 %	0	-0.37(7)
Ni			10.3(1)

Table 3 *The scattering lengths of the nickel isotopes and the resulting scattering length of natural $_{28}$Ni [6].*

Neglecting the less abundant isotopes ^{61}Ni and ^{64}Ni, the average scattering length is calculated as:

$$\langle b \rangle \approx [0.68 \cdot 14.4 + 0.26 \cdot 2.8 + 0.04 \cdot (-8.7)] fm \approx 10.2\, fm \tag{58}$$

which gives the total coherent cross section of:

$$\Rightarrow \sigma_{coherent} = 4\pi \langle b \rangle^2 \approx 13.1\, barn\ (exact: 13.3(3) barn) \tag{59}$$

The incoherent scattering cross section per nickel atoms is calculated from the mean quadratic deviation:

$$\sigma_{incoherent}^{Isotope} = 4\pi \left[0.68 \cdot (14.4 - 10.2)^2 + 0.26 \cdot (2.8 - 10.2)^2 + 0.04 \cdot (-8.7 - 10.2)^2 \right] fm^2 \tag{60}$$
$$\approx 5.1 barn\ (exact: 5.2(4) barn)$$

Values in parentheses are the exact values taking into account the isotopes ^{61}Ni and ^{64}Ni and the nuclear spin incoherent scattering (see below). From (59) and (60), we learn that the incoherent scattering cross section in nickel amounts to more than one third of the coherent scattering cross section.

The most prominent example for *nuclear spin incoherent scattering* is elementary hydrogen. The nucleus of the hydrogen atom, the proton, has the nuclear spin I = ½. The total nuclear spin of the system H + n can therefore adopt two values: J = 0 and J = 1. Each state has its own scattering length: b_- for the singlet state (J = 0) and b_+ for the triplet state (J = 1) - compare Table 4.

Total Spin	**Scattering Length**	**Abundance**
J = 0	b_- = - 47.5 fm	$\frac{1}{4}$
J = 1	b_+ = 10.85 fm	$\frac{3}{4}$
<b> = - 3.739(1) fm		

Table 4 *Scattering lengths for hydrogen [6].*

As in the case of isotope incoherence, the average scattering length can be calculated:

$$\langle b \rangle = \left[\frac{1}{4}(-47.5) + \frac{3}{4} \cdot (10.85) \right] fm = -3.74\, fm \tag{61}$$

This corresponds to a coherent scattering cross section of about ≈ 1.76 barn [6]:

$$\Rightarrow \sigma_{coherent} = 4\pi \langle b \rangle^2 = 1.7568(10)\, barn \tag{62}$$

The nuclear spin incoherent part is again given by the mean quadratic deviation from the average:

$$\sigma_{incoherent}^{nuclear\ spin} = 4\pi\left[\frac{1}{4}(-47.5+3.74)^2 + \frac{3}{4}(10.85+3.74)^2\right] fm^2 = 80.2\ barn$$

(*exact:* 80.26(6) *barn*) (63)

Comparing (62) and (63), it is immediately clear that hydrogen scatters mainly incoherently. As a result, we observe a large background for all samples containing hydrogen. We note immediately that we should avoid all hydrogen containing glue for fixing our samples to a sample stick. Finally, we note that deuterium with nuclear spin I = 1 has a much more favourable ratio between coherent and incoherent scattering:

$$\sigma_{coh.}^{D} = 5.592(7) barn; \quad \sigma_{inc.}^{D} = 2.05(3) barn \tag{64}$$

The coherent scattering lengths of hydrogen (-3.74 fm) and deuterium (6.67 fm) are significantly different. This can be used for contrast variation by isotope substitution in all samples containing hydrogen, i. e. in biological samples or soft condensed matter samples, see corresponding chapters.

A further important element, which shows strong nuclear incoherent scattering, is vanadium. Natural vanadium consists to 99,75 % of the isotope ^{51}V with nuclear spin 7/2. By chance, the ratio between the scattering lengths b_+ and b_- of this isotope are approximately equal to the reciprocal ratio of the abundances. Therefore, the coherent scattering cross section is very small and the incoherent cross section dominates [6]:

$$\sigma_{coh}^{V} = 0.01838(12)\ barn; \quad \sigma_{incoh}^{V} = 5.08(6)\ barn \tag{65}$$

For this reason, Bragg scattering of vanadium is difficult to observe above the large incoherent background. However, since incoherent scattering is isotropic, the scattering from vanadium can be used to calibrate multi-detector arrangements.

Here, we will not discuss scattering lengths for further elements and refer to the values tabulated in [6].

2.13 Magnetic neutron scattering

So far, we have only discussed the scattering of neutrons by the atomic nuclei. Apart from nuclear scattering, the next important process is the scattering of neutrons by the magnetic moments of unpaired electrons. This so-called magnetic neutron scattering comes about by the magnetic dipole-dipole interaction between the magnetic dipole moment of the neutron and the magnetic field of the unpaired electrons, which has spin and orbital angular momentum contributions. This magnetic neutron scattering allows us to study the magnetic properties of a sample on an atomic level, i. e. with atomic spatial- and atomic energy- resolution. In what follows, we will give an introduction into the formalism of magnetic neutron scattering, restricting ourselves to the case of elastic magnetic scattering. Inelastic magnetic scattering will we discussed in subsequent lectures.

To derive the magnetic scattering cross section of thermal neutrons, we consider the situation shown in Figure 15: a neutron with the nuclear moment μ_n is at position $\underline{R}$ with respect to an electron with spin $\underline{S}$, moving with a velocity $\underline{v}_e$.

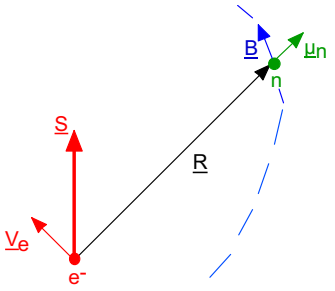

Fig. 15: *Geometry for the derivation of the interaction between neutron and electron.*

Due to its magnetic dipole moment, the neutron interacts with the magnetic field of the electron according to:

$$\mathbf{V}_m = -\underline{\mu}_n \cdot \underline{B} \tag{66}$$

Here, the magnetic moment of the neutron is given by:

$$\underline{\mu}_n = -\gamma_n \mu_N \cdot \underline{\sigma} \tag{67}$$

$\underline{\sigma}$ denotes the spin operator, μ_N the nuclear magneton and γ_N = -1.913 the gyromagnetic factor of the neutron. The magnetic field $\underline{B}$ of an electron is due to a spin- and orbital- part $\underline{B} = \underline{B}_S + \underline{B}_L$. The dipole field of the spin moment is given by:

$$\underline{B}_S = \underline{\nabla} \times \left(\frac{\underline{\mu}_e \times \underline{R}}{R^3} \right) \quad ; \quad \underline{\mu}_e = -2\mu_B \cdot \underline{S} \tag{68}$$

The field due to the movement of the electron is given according to Biot-Savart:

$$\underline{B}_L = \frac{-e}{c} \frac{\underline{v}_e \times \underline{R}}{R^3} \tag{69}$$

The magnetic scattering cross section for a process, where the neutron changes its wave vector from $\underline{k}$ to $\underline{k}'$ and the projection of its spin moment to a quantisation axis z from σ_z to σ_z' can be expressed within the first Born approximation:

$$\frac{d\sigma}{d\Omega} = \left(\frac{m_n}{2\pi\hbar^2} \right)^2 \left| \langle \underline{k}' \sigma_z' | \mathbf{V}_m | \underline{k} \sigma_z \rangle \right|^2 \tag{70}$$

As mentioned, we only consider the single differential cross section for elastic scattering. Introducing the interaction potential from (66) to (69) in (70) we obtain after some algebra [1, 4]:

$$\frac{d\sigma}{d\Omega} = (\gamma_n r_0)^2 \left| -\frac{1}{2\mu_B} \left\langle \sigma_z' \left| \underline{\sigma} \cdot \underline{M}_\perp(\underline{Q}) \right| \sigma_z \right\rangle \right|^2 \tag{71}$$

The pre-factor $\gamma_n r_0$ has the value $\gamma_n r_0 = 0.539 \cdot 10^{-12}$ cm = 5.39 fm. Here, $\underline{M}_\perp(\underline{Q})$ denotes the component of the Fourier transform of the sample magnetisation, which is perpendicular to the scattering vector $\underline{Q}$ (see Figure 16):

$$\underline{M}_\perp(\underline{Q}) = \hat{\underline{Q}} \times \underline{M}(\underline{Q}) \times \hat{\underline{Q}} \tag{72}$$

$$\underline{M}(\underline{Q}) = \int \underline{M}(\underline{r}) e^{i\underline{Q}\underline{r}} d^3 r \tag{73}$$

The total magnetisation is given as a sum of the spin- and orbital-angular- momentum part according to:

$$\begin{aligned} \underline{M}(\underline{r}) &= \underline{M}_S(\underline{r}) + \underline{M}_L(\underline{r}) \\ \underline{M}_S(\underline{r}) &= -2\mu_B \cdot \underline{S}(\underline{r}) = -2\mu_B \sum_i \delta(\underline{r} - \underline{r}_i) \underline{S}_i \end{aligned} \tag{74}$$

(71) tells us that with magnetic neutron scattering, we are able to determine the magnetisation $\underline{M}(\underline{r})$ in microscopic atomic spatial co-ordinates $\underline{r}$. This gives a lot more information than a simple macroscopic measurement, where we obtain the ensemble average of the magnetisation over the entire sample. We also see from (71) that the orientation of the nuclear spin momentum of the neutron (represented by σ_z) plays an important role in magnetic scattering. This is not surprising, since magnetism is a vector property of the sample and obviously there should be an interaction with the vector property of the neutron, its nuclear magnetic moment. Therefore, the analysis of the change of the direction of the neutron nuclear moment in the scattering process should give us valuable additional information as compared to a determination of the change of energy and momentum direction of the neutron alone. These so-called polarisation analysis experiments are discussed in the following lecture. Finally, to obtain an idea of the size of magnetic scattering relative to nuclear scattering, we can replace the matrix element in (71) for a spin ½ particle by the value 1 μ_B. This gives us an "equivalent" scattering length for magnetic scattering of 2.696 fm for a spin ½ particle. This value corresponds quite well to the scattering length of cobalt, which means that magnetic scattering is comparable in magnitude to nuclear scattering.
In contrast to nuclear scattering, we obtain for magnetic scattering a directional term: neutrons only "see" the component of the magnetisation perpendicular to the scattering vector (see Figure 16).

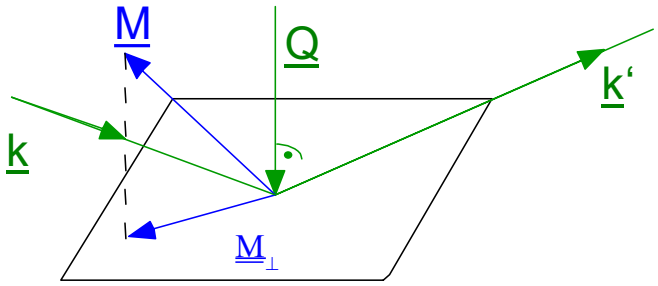

Fig. 16: *For magnetic neutron scattering, only the component $\underline{M}_\perp$ of the magnetisation perpendicular to the scattering vector $\underline{Q}$ is of relevance.*

A second speciality of magnetic scattering as compared to nuclear scattering is the existence of the *magnetic form factor*. How the form factor comes about is most easily understood in the simple case of pure spin scattering, i. e. for atoms with spherical symmetric (L = 0) ground state, such as Mn^{2+} or Fe^{3+}. Moreover, the derivation is simplified for ionic crystals, where the electrons are located around an atom. We denote the spin operators of the electrons of atom i with $\underline{s}_{ik}$. The spatial co-ordinates of the electron number k in atom i are $\underline{r}_{ik} = \underline{R}_i + \underline{t}_{ik}$, where $\underline{R}_i$ denotes the position vector to the nucleus of atom i. Now we proceed to separate the intra-atomic quantities. We can write the operator for the magnetisation density as:

$$\underline{M}_S(\underline{r}) = -2\mu_B \sum_{ik} \delta(\underline{r} - \underline{r}_{ik}) \cdot \underline{s}_{ik} \tag{75}$$

The Fourier transform of this magnetisation density is calculated to:

$$\underline{M}(\underline{Q}) = \int \underline{M}_S(\underline{r}) e^{i\underline{Q}\cdot\underline{r}} d^3r = \sum_{ik} e^{i\underline{Q}\cdot\underline{r}_{ik}} \underline{s}_{ik} = \sum_i e^{i\underline{Q}\cdot\underline{R}_i} \sum_k e^{i\underline{Q}\cdot\underline{t}_{ik}} \cdot \underline{s}_{ik} \tag{76}$$

To calculate the scattering cross section, we now have to determine the expectation value of this operator for the quantum mechanical state of the sample averaged over the thermodynamic ensemble. This leads to

$$\underline{M}\left(\underline{Q}\right) = -2\mu_B \cdot f_m\left(\underline{Q}\right) \cdot \sum_i e^{i\underline{Q}\cdot\underline{R}_i} \cdot \underline{S}_i \tag{77}$$

The single differential cross section for elastic scattering is thus given by:

$$\frac{d\sigma}{d\Omega} = \left(\gamma_n r_0\right)^2 \left| f_m\left(\underline{Q}\right) \sum_i S_{i\perp} e^{i\underline{Q}\underline{R}_i} \right|^2 \tag{78}$$

Here, $f_m(Q)$ denotes the form factor, which is connected with the spin density of the atom via a Fourier transform:

$$f_m\left(\underline{Q}\right) = \int_{Atom} \rho_s\left(\underline{r}\right) e^{i\underline{Q}\cdot\underline{r}} d^3r \tag{79}$$

With the form (78), we have expressed the cross section in simple atomic quantities, such as the expectation values of the spin moment $\underline{S}_i$ at the various atoms. The distribution of the spin density within an atom is reflected in the magnetic form factor (79).

For ions with spin and orbital angular momentum, the cross section takes a significantly more complicated form [4]. Under the assumption that spin- and orbital- angular momentum of each atom couple to the total angular momentum $\underline{J}_i$ (L/S-coupling) and for rather small momentum transfers (the reciprocal magnitude of the scattering vector has to be small compared to the size of the electron orbits), we can give a simple expression for this cross section in the so-called *dipole approximation*:

$$\frac{d\sigma}{d\Omega} = \left(\gamma_n r_o\right)^2 \cdot \left| \frac{g_J}{2} f_m\left(Q\right) \sum_i J_{i\perp} e^{i\underline{Q}\cdot\underline{R}_i} \right|^2 \tag{80}$$

Here the magnetic form factor writes:

$$f_m\left(Q\right) = \left\langle j_o\left(Q\right)\right\rangle + C_2 \left\langle j_2\left(Q\right)\right\rangle \tag{81}$$

g_J denotes the Lande g-factor, $C_2 = \frac{2}{g_J}$ -1 and

$$\left\langle j_l\left(Q\right)\right\rangle = 4\pi \int_0^\infty j_l\left(Qr\right) R^2\left(r\right) r^2 dr \tag{82}$$

are the spherical transforms of the radial density distributions R(r) with the spherical Bessel functions $j_l(Qr)$. For isolated atoms, the radial part R(r) has been determined by Hartree-Fock-calculations and the functions $\left\langle j_0(Q)\right\rangle$ and $\left\langle j_2(Q)\right\rangle$ in (82) have been tabulated [8].

Since the distribution of the magnetic field for spin and orbital angular momentum is completely different, different Q-dependencies of the corresponding form factors result. Moreover, because only the outer electrons in open shells contribute to magnetic scattering, the magnetic form factor also differs from the x-ray form factor introduced above, see Figure 17.

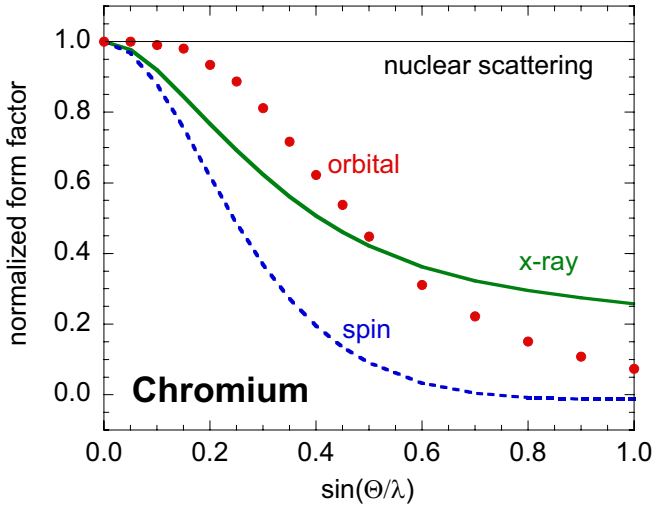

Fig. 17: *Form-factor of Cr [9, 10]. Due to the different distribution of the magnetic field for S and L, a more rapid decrease of the scattering amplitude as a function of momentum transfer results for the spin momentum. For the x-ray form factor, the inner electrons play an important role, too. Therefore, the x-ray form factor drops slower as compared to the magnetic form factor. On the Å length scale of the thermal neutron wavelength, the nucleus is point-like. Therefore, nuclear scattering is independent of the momentum transfer. Finally, we want to mention that the magnetic form factor can in general be anisotropic, if the magnetisation density distribution is anisotropic.*

2.14 Comparison of probes

In this lecture, we have so far introduced the elementary formalism to describe the scattering process and discussed the interaction of neutrons with matter. We now want to ask the questions, for which problems in condensed matter research, neutrons can be utilised successfully also in comparison to other probes, such as x-ray scattering or electron microscopy and electron scattering. To answer these questions, we have to look at the ranges of energies, wavelength or scattering vector, which can be covered by various probes as well as the different contrast mechanisms.

Figure 18 shows a double logarithmic plot of the dispersion relation "wavelength versus energy" for the three probes neutrons, electrons and photons. The plot demonstrates, how thermal neutrons of energy 25 meV are ideally suited to determine interatomic distances in the order of 0.1 nm, while the energy of x-rays or electrons for this wavelength is much higher. However with modern techniques at a synchrotron radiation source, energy resolutions in the meV-region become accessible even for photons of around 10 keV corresponding to a relative energy resolution $\Delta E/E \approx 10^{-7}$! The graph also shows that colloids with a typical size of 100 nm are well suited for the investigation with light of energy around 2 eV. These length scales can, however, also be reached with thermal neutron scattering in the small angle region. While Figure 18 thus demonstrates for which energy-wave-length combination a certain probe is particularly useful, modern experimental techniques extend the range of application by several orders of magnitude.

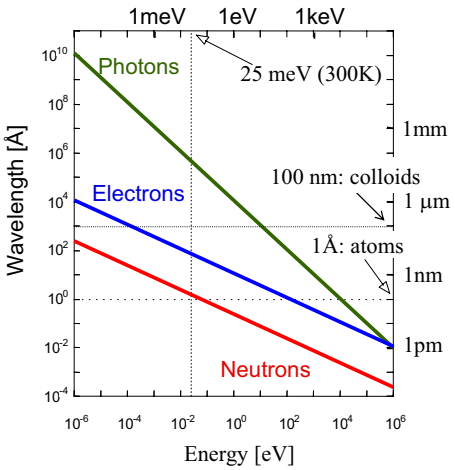

Fig. 18: *Comparison of the three probes - neutrons, electrons and photons - in a double logarithmic energy-wavelength diagram.*

It is therefore useful to compare the scattering cross sections as it is done in Figure 19 for x-rays and neutrons. Note that the x-ray scattering cross sections are in general a factor of 10 larger as compared to the neutron scattering cross sections. This means that the signal for x-ray scattering is stronger for the same incident flux and sample size, but that caution has to be applied that the conditions for kinematical scattering are fulfilled. For x-rays, the cross section depends on the number of electrons and thus varies in a monotonic fashion throughout the periodic table. Clearly it will be difficult to determine hydrogen positions with x-rays in the presence of heavy elements such as metal ions. Moreover, there is a very weak contrast between neighbouring elements as can be seen from the transition metals Mn, Fe and Ni in Figure 19. However, this contrast can be enhanced by anomalous scattering, if the photon energy is tuned close to the absorption edge of an element. Moreover, anomalous scattering is sensitive to the anisotropy of the local environment of an atom. For neutrons the cross section depends on the details of the nuclear structure and thus varies in a non-systematic fashion throughout the periodic table. As an example, there is a very high contrast between Mn and Fe. With neutrons, the hydrogen atom is clearly visible even in the presence of such heavy elements as Uranium. Moreover there is a strong contrast between the two Hydrogen isotopes H and D. This fact can be exploited for soft condensed matter investigations by selectively deuterating certain molecules or functional groups and thus varying the contrast within the sample.

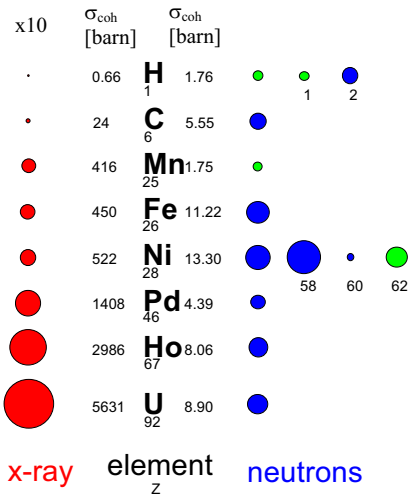

Fig. 19: *Comparison of the coherent scattering cross-sections for x-rays and neutrons for a selection of elements. The area of the coloured circles represent the scattering cross section, where in the case of x-rays a scale factor 10 has to be applied. For neutrons, the dark and light grey circles distinguish the cases where the scattering occurs with or without a phase shift of π.*

Finally, both neutrons and x-rays allow the investigation of magnetism on an atomic scale. Magnetic neutron scattering is comparable in strength to nuclear scattering, while non-resonant magnetic x-ray scattering is smaller than charge scattering by several orders of magnitude. Despite the small cross sections, non-resonant magnetic x-ray Bragg scattering from good quality single crystals yields good intensities with the brilliant beams at modern synchrotron radiation sources. While neutrons are scattered from the magnetic induction within the sample, x-rays are scattered differently from spin and orbital momentum and thus allow one to measure both form factors separately. Inelastic magnetic scattering e.g. from magnons or so called quasielastic magnetic scattering from fluctuations in disordered magnetic systems is a clear domain of neutron scattering and cannot be done with x-rays up to now. Finally, resonance exchange scattering XRES allows one not only to get enhanced intensities, but also to study magnetism with element- and band sensitivity [11].

With appropriate scattering methods, employing neutrons, x-rays or light, processes in condensed matter on very different time and space scales can be investigated. Which scattering method is appropriate for which region within the "scattering vector Q - energy E plane" is plotted schematically in Figure 20. A scattering vector Q corresponds to a certain length scale, an energy to a certain frequency, so that the characteristic lengths and times scales for the various methods can be directly determined from the Figure. Examples for applications and information on instrumentation will follow in subsequent lectures.

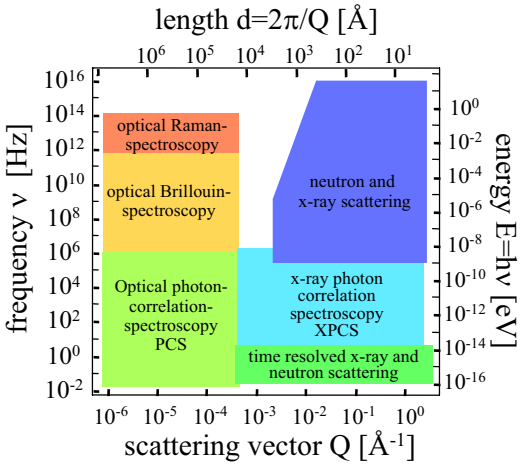

Fig. 20: *Regions in frequency ν and scattering vector Q or energy E and length d plane, which can be covered by various scattering methods.*

References

[1] G. L. Squires "Introduction to the Theory of Thermal Neutron Scattering" Dover 1997

[2] K. Sköld, D. Price (Eds.) "Methods of Experimental Physics" Neutron Scattering Part A-C Academic Press 1987

[3] J. M. Cowley "Diffraction Physics" North Holland, Amsterdam 1995

[4] S. W. Lovesey "Theory of neutron scattering from condensed matter" Clarendon Press, Oxford, 1987

[5] B. W. Batterman, H. Cole "Dynamical Diffraction of X-Rays by Perfect Crystals" Rev. Mod. Phys. 36 (1964), 681 - 717.

[6] A. Dianoux, G. Lander (Eds.) "Neutron Data Booklet", Institute Laue-Langevin (2002) - see also [8] -

[7] D. E. Garber, R. R. Kinsey "Neutron Cross-Section II" BNL-Report (1976)

[8] E. Price (Ed.) "International Tables for Crystallography, Volume C" International Union of Crystallography (2004) - see also [6] -

[9] J. Strempfer et al. Eur. Phys. J B **14** (2000), 63 - 72

[10] J. Strempfer et al. Physica B **267 - 268** (1999), 56 - 59

[11] Th. Brückel "Scattering Techniques II: Magnetic X-Ray Scattering" Schriften des Forschungszentrum Jülich, Materie und Material **26** (2006), B5.1 - B5.34

3

Polarized neutron scattering

Werner Schweika

3. Polarized neutron scattering

Werner Schweika

The neutron's magnetic moment is an ideal probe to study magnetic structures and excitations in condensed matter physics. Many physical properties of a system can be inferred from the energy and momentum transfer in the scattering process. Specific magnetic properties and correlations may be identifiable that way or by parametric studies with temperature or magnetic field variation. However, it might be intuitively clear that polarization analysis gives valuable additional information on vector properties involving spin and orbital momentum. Neutron scattering is a low flux technique which is particularly true when polarization of neutrons is involved. This is not a concern for structure determination from measured Bragg scattering but for scattering due to magnetic fluctuations, spin-correlations in the disordered paramagnetic phase or spin excitations, where scattering is typically weak. However, the benefit of such effort of polarization analysis is not only the separation of scattering, it may also reveal new unique and most detailed information on correlations involving magnetic fluctuations. The lecture will give an introduction to neutron polarization analysis including most recent advances, and will discuss as an example for applications the spin correlations in highly frustrated spin systems, the scattering from a complex chiral structure, and an application to the local structure in soft matter materials.

3.1 Neutron spins in magnetic fields

3.1.1 Precession of neutron spins

Neutrons are fermions with spin 1/2 and have a magnetic moment $\boldsymbol{\mu} = -1.91\mu_N$ in terms of the nuclear Bohr magneton μ_N. The characteristic motion of the neutron magnetic moment in a magnetic field is Larmor precession, which for simplicity can be considered in a classical treatment[1]. In fact, even the quantum mechanical treatment, which introduces Pauli spin matrices $\hat{\boldsymbol{\sigma}}$ into the Schrödinger equation, is effectively a classical treatment considering the origin of these matrices. They result from the problem of mapping three

dimensions onto two by introducing a complex component and were treated by Cayley and Klein (1897) [2] describing the classical problem of a spinning top.

Classical mechanics shows that a torque exerted on a magnetic moment $\boldsymbol{\mu}$ by a magnetic field $\mathbf{H}$ inclined at an angle θ relative to the magnetic moment causes the magnetic moment of the neutron to precess about the direction of the field with the *Larmor* frequency ω_L. The precession frequency is independent of the angle of inclination θ. Different to the motion of a spinning top in a gravity field the neutron's motion shows no nutation, its angular momentum $\mathbf{L} = \hbar\mathbf{S}$ and its energy is a constant of motion. $S = \frac{1}{2}$ denotes the spin quantum number of the neutron and $\hbar$ is Planck's constant divided by 2π. The ratio of angular momentum $\mathbf{L}$ and magnetic moment $\boldsymbol{\mu}$ defines the *gyromagnetic ratio* γ, $\boldsymbol{\mu} = \gamma\mathbf{L}$. An applied magnetic field will tend to align this magnetic moment and exerts a torque. No force is exerted by a homogeneous field, therefore, the resulting equation of motion

$$\dot{\mathbf{L}} = -\gamma\,\mathbf{L} \times \mathbf{H} \tag{1}$$

simply describes a precession of the magnetic moment around the magnetic field, see Fig.1, in which L_z and hence the polarization along the field axis is a constant of motion.

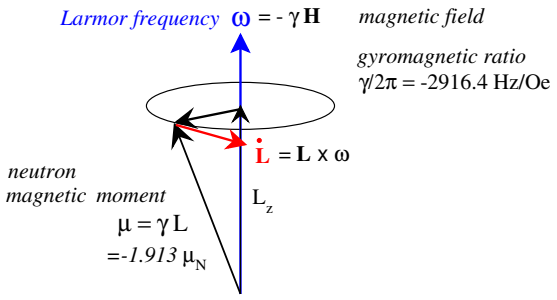

Figure 1: Larmor precession: the motion of the neutron in a constant magnetic field.

3.1.2 Motion in time dependent fields

Thermal neutrons move with a speed of thousands of meters per second. When passing through magnetic fields, the neutrons experience time-depedent changes in the field. Replacing $\mathbf{H}$ by $\mathbf{H}(t)$, the differential equation Eq. (1) can be used to calculate numerically

the effect of all relevant field variations in an experimental set-up. Besides the precession in constant fields, in practice however, it is usually possible to work at least within two simple limiting cases of either **(i) slow adiabatic field variation**, in which the non-precessing spin component parallel to the field smoothly follows the field direction, or of **(ii) sudden field reversal**, in which the non-precessing spin component has no time to reorient itself, when traversing abruptly from a parallel to anti-parallel field or vice versa. Slow field variation means that the field **H** changes or rotates in the coordinate system of the neutron with a frequency that is small compared to the Larmor frequency.

3.1.3 Polarized neutron beams

Polarization of a neutron beam is defined by the average over the neutron spin operators **S**

$$\mathbf{P} = \langle 2\mathbf{S} \rangle \tag{2}$$

Polarization will be measured with respect to a magnetic field defining a quantization axis and any device for polarization analysis will take the projection of the spins in up- and down state state, $n_\uparrow$ and $n_\downarrow$ respectively,

$$\mathrm{P} = \frac{n_\uparrow - n_\downarrow}{n_\uparrow + n_\downarrow}, \tag{3}$$

Typical neutron beams have a cross-section of a few cm^2. In order to preserve the beam polarization **P** one could try to avoid and screen any disturbing magnetic fields, however, it is more convenient to use magnetic fields to guide the polarization **P**, fields which may show even smooth field variations. When working with a precessing polarization **P**, however, there are more stringent requirements for field homogeneity in direction and magnitude to keep the neutron spins in phase.

3.2 Experimental set-up for neutron polarization analysis

3.2.1 The DNS instrument

The diffuse neutron scattering spectrometer DNS (now being transferred from Jülich to the new research reactor at Munich FRM2 in Munich) is equipped with polarization analysis and is particularly devoted to elastic and inelastic diffuse scattering that may

arise from spin correlations and magnetic disorder and ordering in materials. A layout of the instrument is shown in Fig. 2. DNS is a time-of-flight instrument[3] with a multi-detector system similar to the D7 instrument at the ILL[4]. The monochromatic incident beam is polarised with a focusing supermirror bender, xyz-field coils allow to change the polarization at the sample, and the polarisation analysis is performed with supermirror analysers in focusing arrangement in front of each detector.

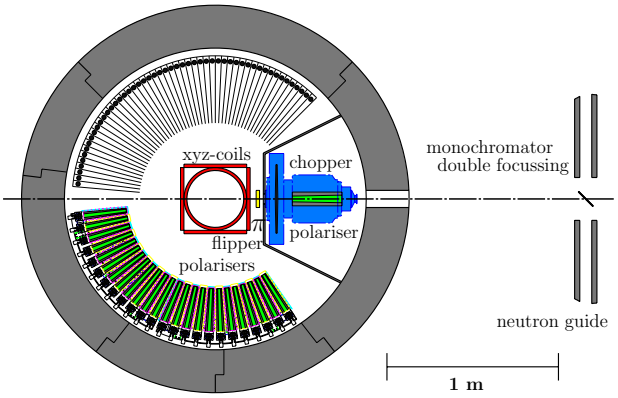

Figure 2: Scheme of the DNS instrument.

3.2.2 Polarization analyzers

The most common methods to polarize neutrons are (i) using the total reflection from magnetic multi-layers, (ii) using Bragg reflection of polarizing single crystals (typically Heusler crystals) and (iii) polarized He-3 filters, in which for anti-parallel spins the (n,^{3}He)-compound has a large absorption cross-section while all neutrons with parallel spins may pass the filter cell. The first two methods use an interference effect of nuclear and magnetic scattering amplitudes having the same absolute value.

The polarization analysis at the DNS is performed with supermirrors using total reflection. The angle of total reflection for a single ferromagnetic (FM) layer is given by

$$\Theta_c^{\pm} = \lambda\sqrt{n(b-p)/\pi}. \tag{4}$$

Here n denotes the particle density and b and p the nuclear and magnetic scattering lengths, respectively. However, the critical angle can be further increased by artificial multi-layers (supermirrors) of alternating FM and non-magnetic layers of varying thickness [5]. The alternating layers of the DNS polarizers consist of the materials $Fe_{50}Co_{48}V_2$ / TiN_x, with critical angles up to $\Theta_c = 0.3^o \times \lambda/\text{Å}$. The degree of polarization that can be achieved is rather high, typically 98%.

Both the polarizer in the initial flight-path and the polarization analyzers in front of the detectors are made out of supermirrors being curved to avoid any direct flight path without reflection, and in addition the curvature is such that neutrons are focussed on the sample. The common polarization axis of initial and final polarizers is vertical.

3.2.3 Guide-fields

A magnetic *guide field* is used to maintain the direction of the spin and the polarization of the neutron beam. The guide field preserves the quantization axis to which the neutron moments have align either parallel or anti-parallel. Guide fields are typically weak so that the sample magnetization is not significantly influenced, but sufficiently stronger than for instance the magnetic field of the earth or any other stray magnetic fields from the surrounding. In the DNS instrument the polarizers and polarization analyzers are kept in a permanent vertical field that is not screened. This vertical stray-field is used as a guide field throughout the instrument. At the sample position its strength is still about 5 Gauss.

3.2.4 π and $\pi/2$-Flipper

The purpose of a π-flipper is to reverse the polarization and to detect whether the sample causes spin-flip scattering.

When applying a magnetic field perpendicular to the polarized neutron beam, the polarization immediately starts its Larmor precession. A flipper that reverses the neutron polarization with respect to the guide field has to induce a well-defined field pulse that the polarization precesses by an angle π. Therefore, one can use the homogenous field of a long rectangular coil, see Fig.3.2.4. Neutrons see a sudden field change when they enter

and exit the coil, in between they precess around the flipping field, whose magnitude is tuned with respect to the time of flight that the neutrons spent inside the coil.

In the DNS set-up the initial polarization is along the vertical guide field. In a combination of two perpendicular coils, one is used to compensate the guide field and the second is used for flipping. (To give an example for typical flipping fields, a π-flip is achieved by 17 Gauss for neutrons with a wave length of $\lambda = 4$Å and a flight path of 1 cm through the coil.)

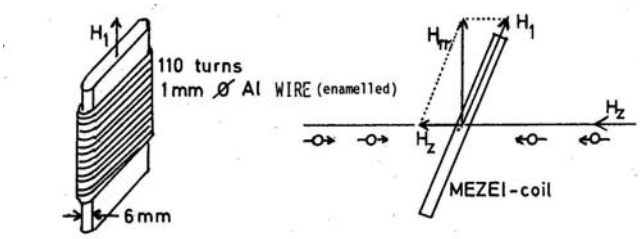

Figure 3: Principle of a neutron π-spin flipper. The neutrons perform half of a Larmor-precession inside a long rectangular coil. The field $\underline{H}_\pi$ is perpendicular to spin orientation and to the travel direction of the neutron and has to be adjusted to the speed of the neutrons. Here the flipper is tilted to compensate the guide field inside the flipper coil (Fig. from [1]).

A $\boldsymbol{\pi}$ **/2-flip** of the polarization can also be performed with the same flipper coils and will initiate Larmor precessions along the further flight path. A precessing polarization is used for instance in high resolution Neutron Spin Echo spectroscopy (see D.6 Monkenbusch). On the DNS instrument, a precessing neutron polarization technique is used for spherical polariation analysis. Scattering of complex magnetic structures, for example may cause a rotation of 90^o and may put the polarization back into a non-precessing mode that can be analyzed.

3.2.5 xyz-coils

In order to set the polarization into any desired direction at the sample position, there is (in the simplest version) a set-up of three orthogonal pairs so-called xyz-coils. Fig.3.2.5 illustrates the field setting along x-direction. One can see that the z-coil has been used

to compensate the guide field at the sample position, and that the x-coils produce a field of a few Gauss. The field is sufficiently strong that the neutron polarization can follow adiabatically the smooth variation of the field, finally turning back into the z-direction of the guide field around the xyz-coils.

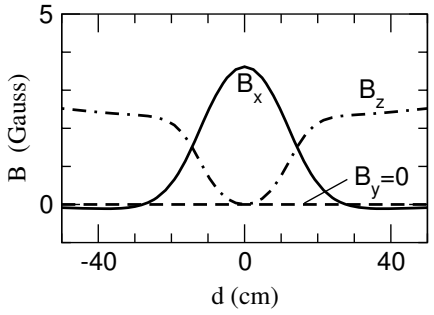

Figure 4: Magnetic field setting by the xyz-coils for an adiabatic nutation of the polarization in x-direction at the sample.

When after a $\pi/2$ flip the polarization is precessing perpendicular to the guide field, the same field conditions that nutate the polarization as shown in Fig.3.2.5 will also turn now adiabatically the precession plane. For an applied field in x-direction the polarization precesses in the yz-plane, and its precession angle at the sample is determined by the total field integral along its flight path and can be tuned in phase by the applied field.

3.3 Scattering and polarization

3.3.1 Interaction of neutrons with matter

The interaction of neutrons with matter and neutron scattering amplitudes have been introduced before (D.1 Brückel). We briefly recall basics results and discuss effects of scattering events on the polarization (see also textbooks [6, 7]). The total scattering amplitude consists of two parts, a nuclear and magnetic term, that are often comparable in magnitude

$$F_Q = N_{\mathbf{Q}} + \hat{\boldsymbol{\sigma}} \cdot \mathbf{M}_{\mathbf{Q}}^{\perp}. \tag{5}$$

The **nuclear interaction** can be described by a point-like Fermi potential, which is

isotope-specific. The interaction is spin-dependent if the scattering nuclei have a non-zero spin $\mathbf{I}$. Since nuclear spins are usually randomly oriented, this leads to spin-incoherent scattering. In contrast to coherent nuclear scattering, spin-incoherent scattering effects the neutron polarization. As shown in detail in the Appendix, the component of $\mathbf{I}$ parallel to $\mathbf{P}$, say $I_z \parallel P_z$, does not affect $\mathbf{P}$, but the two perpendicular components I_x and I_y change P_z to $-P_z$ upon scattering. Therefore, two thirds of the spin-incoherent scattering is spin-flip scattering, and the final polarisation $\mathbf{P'} = -\frac{1}{3}\mathbf{P}$, has changed in sign, is reduced magnitude, but shows no inclination towards $\mathbf{P}$.

Therefore, we can distinguish three contributions of the nuclear scattering

$$\sigma^N_{\mathbf{Q}} = |N_{\mathbf{Q}}|^2, \text{ with } N_{\mathbf{Q}} = \sum_j b_j e^{i\mathbf{Q}\cdot\mathbf{R}_j} \tag{6}$$
$$\sigma^N_{\mathbf{Q}} = \sigma^N_{\mathbf{Q},coh} + \sigma^N_{isotop-inc} + \sigma^N_{spin-inc}.$$

The coherent part of the nuclear scattering can be separated from the spin-incoherent scattering by measuring spin-flip and non-spin-flip scattering.

The **magnetic interaction** arises from the scattering potential $-\mu \cdot \mathbf{H}$ describing the dipole-dipole interaction between the magnetic moment of the neutron μ and a magnetic field $\mathbf{H}$ that is due to the spins $\mathbf{s}_j$ of the unpaired electrons j and their orbital momentum $\mathbf{p}_j = -i\nabla_j$. The Fourier transform of the interacting magnetic moments is given by

$$\mathbf{M}_{\mathbf{Q}} = r \int d\tau \psi^*_b(\tau) \sum_j e^{i\mathbf{Q}\cdot\mathbf{R}_j} (\mathbf{s}_j - i(\mathbf{Q} \times \mathbf{p}_j)) \psi^*_a(\tau) \tag{7}$$

where $r = |\gamma| e^2/mc^2$ is the magnetic scattering length of an electron and e^2/mc^2 is the classical electron radius. As illustrated in Fig. 5 the component of a magnetic dipole field parallel to the scattering vector $\mathbf{Q}$ cancels out. Therefore, in contrast to the spin-incoherent scattering, magnetic scattering is anisotropic with respect to $\mathbf{Q}$ and only $\mathbf{M}^{\perp}_{\mathbf{Q}}$, the component perpendicular to $\mathbf{Q}$ can be observed. The transition matrix elements for magnetic interaction also show the same dependence for the neutron spin operators when applied to components of $\mathbf{M}^{\perp}_{\mathbf{Q}}$ (see Appendix), which is illustrated in Fig. 6. These selection rules including the $\mathbf{Q}$-dependence provide another simple rule: If $\mathbf{P} \parallel \mathbf{Q}$, all magnetic scattering will be spin-flip.

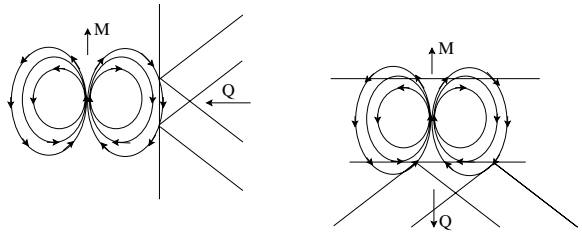

Figure 5: Illustration why only $\mathbf{M}_{\mathbf{Q}}^{\perp}$ is measured. Magnetic field amplitudes of the dipole field show for a) $\mathbf{M} \perp \mathbf{Q}$ constructive interference; and for b) $\mathbf{M} \parallel \mathbf{Q}$ destructive interference.

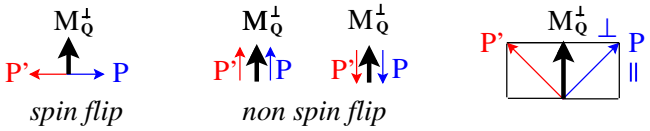

Figure 6: Polarization $\mathbf{P}$ perpendicular to $\mathbf{M}_{\mathbf{Q}}^{\perp}$ reverses sign but not the component parallel to $\mathbf{M}_{\mathbf{Q}}^{\perp}$.

3.3.2 Scattering cross-section for polarized neutrons

A theoretical description of neutron scattering including magnetic interactions has been derived by Blume [8] and Maleyev [9]. The scattering process can be completely described by two master equations, (i) for the scattering cross-section σ and (ii) for $\mathbf{P}'\sigma$, where $\mathbf{P}'$ denotes the final polarization.

$$\begin{aligned} \sigma_{\mathbf{Q}} &= \sigma^{N}_{\mathbf{Q},coh} + \sigma^{N}_{isotop-inc} + \sigma^{N}_{spin-inc} \\ &\quad + |\mathbf{M}_{\mathbf{Q}}^{\perp}|^2 + \mathbf{P}(N_{-\mathbf{Q}}\mathbf{M}_{\mathbf{Q}}^{\perp} + \mathbf{M}_{-\mathbf{Q}}^{\perp}N_{\mathbf{Q}}) + i\mathbf{P}(\mathbf{M}_{-\mathbf{Q}}^{\perp} \times \mathbf{M}_{\mathbf{Q}}^{\perp}) \end{aligned} \tag{8}$$

$$\begin{aligned} \mathbf{P}'\sigma_{\mathbf{Q}} &= \mathbf{P}\sigma^{N}_{\mathbf{Q},coh} + \mathbf{P}\sigma^{N}_{isotop-inc} - \frac{1}{3}\mathbf{P}\sigma^{N}_{spin-inc} \\ &\quad + \mathbf{M}_{\mathbf{Q}}^{\perp}(\mathbf{P}\mathbf{M}_{-\mathbf{Q}}^{\perp}) + \mathbf{M}_{-\mathbf{Q}}^{\perp}(\mathbf{P}\mathbf{M}_{\mathbf{Q}}^{\perp}) - \mathbf{P}\mathbf{M}_{\mathbf{Q}}^{\perp}\mathbf{M}_{-\mathbf{Q}}^{\perp} \\ &\quad + \mathbf{M}_{\mathbf{Q}}^{\perp}N_{-\mathbf{Q}} + \mathbf{M}_{-\mathbf{Q}}^{\perp}N_{\mathbf{Q}} + i\mathbf{M}_{\mathbf{Q}}^{\perp} \times \mathbf{M}_{-\mathbf{Q}}^{\perp} + i(\mathbf{M}_{\mathbf{Q}}^{\perp}N_{-\mathbf{Q}} - \mathbf{M}_{-\mathbf{Q}}^{\perp}N_{\mathbf{Q}}) \times \mathbf{P} \end{aligned} \tag{9}$$

The first equation shows that for unpolarized neutrons, $\mathbf{P}$=0, one can measure the square of $N_{\mathbf{Q}}$ and the square of $\mathbf{M}_{\mathbf{Q}}^{\perp}$ but some of the scattering terms are not detectable. These terms are related to *nuclear-magnetic interference* and the cross-products of $\mathbf{M}_{\mathbf{Q}}^{\perp}$ to *chiral*

correlations $\langle \mathbf{s}_i \times \mathbf{s}_j \rangle$ that can be found in many more complex magnetic materials; as follows from the second equation, due to such terms, polarization can be created in a scattering process.

For $\mathbf{P} = 0$, the scattering contribution due to the interference term of nuclear and magnetic scattering amplitudes as well as the chiral term vanish. On the other hand, polarization may be created by Bragg scattering with nuclear-magnetic interference. For example, for $\mathbf{P} = 0$ and vanishing chiral terms, one obtains

$\sigma_{\mathbf{Q}} = |N_{\mathbf{Q}}|^2 + |\mathbf{M}^{\perp}_{\mathbf{Q}}|^2$ and $\mathbf{P}'\sigma_{\mathbf{Q}} = \mathbf{M}^{\perp}_{\mathbf{Q}} N_{-\mathbf{Q}} + \mathbf{M}^{\perp}_{-\mathbf{Q}} N_{\mathbf{Q}}$, yielding a polarization

$\mathbf{P}' = \frac{\mathbf{P}'\sigma_{\mathbf{Q}}}{\sigma_{\mathbf{Q}}} = \frac{\mathbf{M}^{\perp}_{\mathbf{Q}} N_{-\mathbf{Q}} + \mathbf{M}^{\perp}_{-\mathbf{Q}} N_{\mathbf{Q}}}{|N_{\mathbf{Q}}|^2 + |\mathbf{M}^{\perp}_{\mathbf{Q}}|^2} = 1$, if $N_{\mathbf{Q}} = \mathbf{M}^{\perp}_{\mathbf{Q}}$.

Polarization creation is also possible from scattering of chiral structures, with $\mathbf{P}' = \frac{i\mathbf{M}^{\perp}_{\mathbf{Q}} \times \mathbf{M}^{\perp}_{-\mathbf{Q}}}{\mathbf{M}^{\perp}_{\mathbf{Q}} \cdot \mathbf{M}^{\perp}_{-\mathbf{Q}}}$, and it can be seen also that scattering is sensitive to the sign of the chirality, for instance the helicity of a magnetic spiral.

In general, polarization analysis demands to measure an arbitrary rotation and a change in magnitude of the polarization in a scattering process. The relationship between initial and final polarization vectors, $\mathbf{P}$ and $\mathbf{P}'$ can be conveniently described by a tensor equation

$$P'_i = P_{ij} P_j + P''_i, \tag{10}$$

defining a 3×3 polarization matrix P_{ij} that rotates the initial polarization $\mathbf{P}$, while $\mathbf{P}''$ is the polarization that is created by the scattering process. The polarization matrix P_{ij} and $\mathbf{P}''$ can be determined experimentally.

3.3.3 Spin-flip and non-spinflip scattering

One interesting application of polarized neutron scattering is the separation of coherent and spin-incoherent scattering. Typical soft matter samples contain hydrogen which causes a huge spin-incoherent background in the wide-angle scattering that contains information about local correlations. Here, a precise determination of coherent scattering, ideally combined with the method of contrast variation, can be achieved by measuring spin-flip and non-spin-flip scattering. Fig.3.3.3 shows the separated coherent scattering of a polymer glass. Such results can be compared to those obtained in molecular dynamics simulations of theoretical polymer models [10]. A recent application to water also showed

that the simplest type of polarization analyis provides a new, unprecedented quality of data and a better insight into local correlations in water [11].

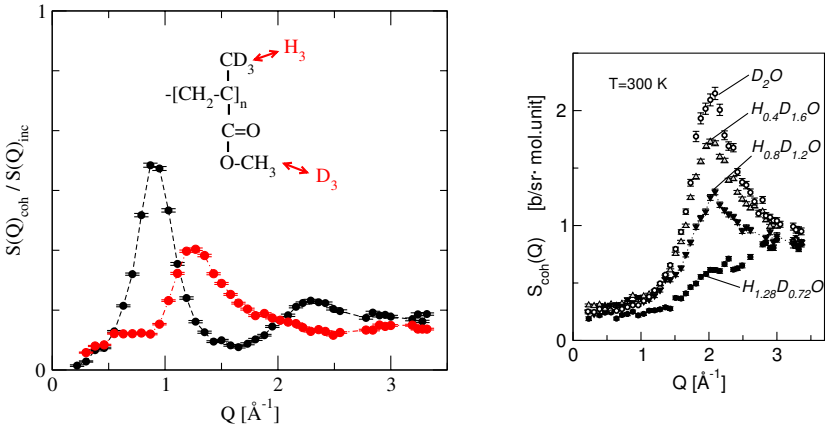

Figure 7: Neutron polarisation analysis separates coherent scattering from spin-incoherent scattering which is typically a disturbing large background in materials that contain hydrogen. The examples show results for the coherent scattering of (left) a polymer glasses [10] and (right) water [11]. Both experiments also show the effect of H/D contrast.

3.3.4 xyz-polarization analysis

In order to separate magnetic scattering, one needs a polarization analysis with directional dependence. The standard technique has been developed by Moon, Riste and Koehler in a seminal paper[12], and is usually called longitudinal polarization analysis (LPA). In LPA the change of polarization is measured with respect to an applied field, and allows one to determine the trace of the (3×3) polarization matrix. This method cannot identify all magnetic scattering contributions; scattering with chirality and magnetic-nuclear interference may change the direction of the polarization and appear as an apparent depolarization. However, paramagnetic scattering and scattering from collinear magnetic structures can be separated from nuclear scattering by measuring both with polarization parallel and perpendicular to **Q**. The difference retains only magnetic scattering contributions [13]. This principle is also used in the method of **x**yz-polarization analysis [14], where the polarization is set into three orthogonal directions. This requires an ad-

ditional measurement, however, it also applies for larger area- or multi-detectors, when $\mathbf{P} \parallel \mathbf{Q}$ cannot be achieved simultaneously. A measurement with $\mathbf{P}$ along z-direction is perpendicular to the scattering plane and thus to $\mathbf{Q}$; measurements with $\mathbf{P}$ along the x- and y-direction in the scattering plane comprise the sum of the intensities with initial polarization parallel and perpendicular to $\mathbf{Q}$. Hence, the paramagnetic scattering or the scattering of anti-ferromagnetic powder samples is given by [14]:

$$\frac{d\sigma}{d\Omega}_{pm} = 2\left(\frac{d\sigma}{d\Omega}^{SF}_{\mathrm{x}} + \frac{d\sigma}{d\Omega}^{SF}_{\mathrm{y}} - 2\frac{d\sigma}{d\Omega}^{SF}_{\mathrm{z}}\right) = -2\left(\frac{d\sigma}{d\Omega}^{NSF}_{\mathrm{x}} + \frac{d\sigma}{d\Omega}^{NSF}_{\mathrm{y}} - 2\frac{d\sigma}{d\Omega}^{NSF}_{\mathrm{z}}\right) , \qquad (11)$$

Any nuclear scattering will be eliminated by these differences. An application of xyz-polariation analysis to magnetic spin-fluctuations in a geometrically frustrated lattice is given below.

A highly frustrated spin system: the kagome anti-ferromagnet

The topology of many crystal structures has an important influence on the collective behavior of interacting magnetic moments. In lattices with triangular networks, the anti-ferromagnetic (AF) coupling between all spins can not be satisfied simultaneously owing to geometrical frustration that strongly reduces the ordering temperature and disturbs the settling of the system into a long range ordered state. A typical signature of geometrical frustration is the appearance of non-collinear and chiral spin configurations. In addition, ordering is particularly difficult in lower dimensions. According to the Mermin-Wagner theorem, the Heisenberg AF does not order in 2D lattices at any finite temperature.

We shall discuss such an example of high spin frustration and show recent results on low-temperature spin correlations in a new oxide material, the compound $Y_{0.5}Ca_{0.5}BaCo_4O_7$, that exhibits a layering of Co-atoms in a kagomé lattice, see Fig. 8. The ground state of kagomé AF exhibits an infinite degeneracy, with a competition between two different chiral structural motifs, depicted in Fig. 9. Diffuse neutron scattering experiments with xyz-polarization analysis performed on the DNS instrument achieved a separation of magnetic scattering from nuclear coherent spin-incoherent background.

The temperature dependence of the magnetic scattering, see Fig. 8, does not show long range order at low T, although according to susceptibility measurements, the Curie-Weiss temperature (the mean-field estimate of the ordering temperature) is about 2000

K. Furthermore, the asymmetric shape of the diffuse peak is characteristic for 2-D spin correlations.

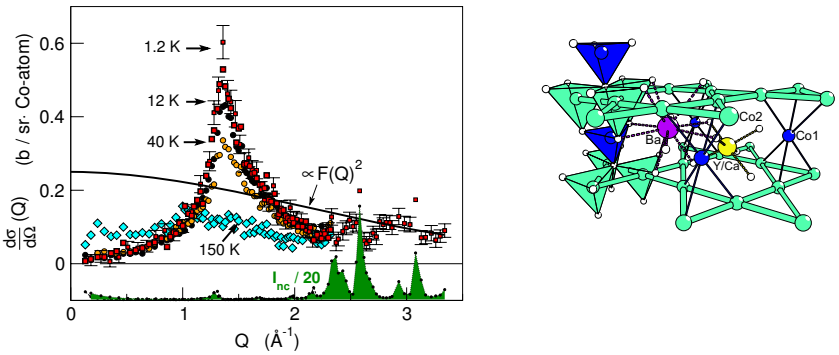

Figure 8: *(left)* Temperature dependence of the diffuse magnetic scattering; data are calibrated by the spin-incoherent scattering of Co (0.382 b/sr); the separated nuclear coherent scattering, I_{nc}, has been rescaled and shifted (bottom part). *(right)* The $Y_{0.5}Ca_{0.5}BaCo_4O_7$ crystal structure. Thicker bonds between the Co2 atoms highlight the kagomé layers.

The magnetic scattering can be described in terms of the Fourier transform of the spin pair-correlations [16]

$$\frac{d\sigma}{d\Omega}_{mag}(Q) \;=\; \frac{2}{3}\, r_0^2\, F_Q^2 \sum_r \langle \underline{S}_0 \cdot \underline{S}_r \rangle \frac{\sin Qr}{Qr}, \tag{12}$$

where Q is the modulus of the scattering vector, $r_0 = -0.54 \times 10^{-12}$cm the magnetic scattering length, S the spin quantum number of the scattering ion, and F_Q the magnetic scattering form-factor of a single Co^{2+} ion. By this quantitative description it is possible to determine the average Co spin moment. The most plausible explanation is a Co high spin state 3/2 in the kagomé layers and a low spin S=0 state in the intermediate layers, which explains the 2-D character by a decoupling of the kagomé layers. The low-T data has been normalized to $S(Q) = \sum_r \langle \hat{S}_0 \cdot \hat{S}_r \rangle \sin Qr/(Qr)$, where $\hat{S}$ are unit length spins, see Fig. 9. Spin correlations $\langle \hat{S}_0 \cdot \hat{S}_r \rangle$ based on the two competing chiral structures have been modeled with a suitable asymptotic spatial decay function ($\propto r^{-\eta}$, η 0.6) and reveal a clear preference for the $\sqrt{3} \times \sqrt{3}$ structure. One can also obtain the spin correlations by Fourier analysis, using a linear least squares refinement, see Fig. 9. Compared to the model of the $\sqrt{3} \times \sqrt{3}$ structure, a peak (at $\mathbf{q}_{\sqrt{3}}$) is missing in the data, indicating an

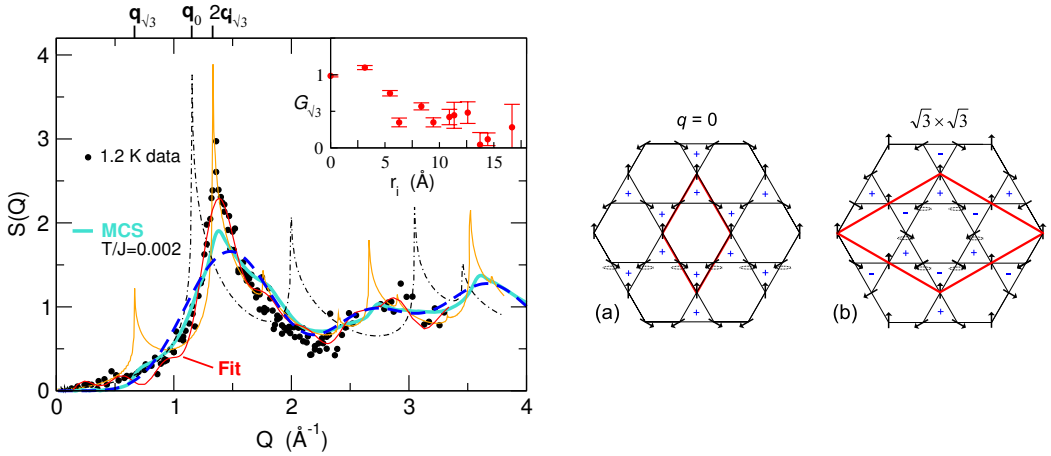

Figure 9: Modeling of 1.2 K scattering data. (i) power law decay of spin correlations (thin lines, dashed dotted and solid) in the q_0 and $\sqrt{3} \times \sqrt{3}$ structures respectively; (ii) Fourier analysis (Fit), yielding $G_{\sqrt{3}}$ (inset) spin correlations normalized to those of the $\sqrt{3} \times \sqrt{3}$ structure with ideal staggered chirality; (iii) Monte Carlo simulation (MCS) data (thick line) for a classical Heisenberg AF at $T/J = 0.002$ [17]; (iv) hexagon spin mode (dashed line) see also Fig. 10.

incompletely ordered ground state of the system in agreement with earlier Monte Carlo simulations [17].

The $\sqrt{3} \times \sqrt{3}$ structure is entropically favored, because of local degeneracies of the spin alignments on hexagon. Spins on hexagons gather in a collective local rotations, a characteristic feature of the disorder at low T, on one side. On the other side, this dynamic correlation is a robust feature driving the structural formation, a reason why the selectionof the $\sqrt{3} \times \sqrt{3}$ structure has been called an *order by disorder phenomenon*. The hexagon mode can still be seen in the quasi-elastic paramagnetic scattering at intermediate temperatures, see Fig. 10,

3.3.5 Spherical polarization analysis

Spherical polarization analysis is a recent development, which allows to determine complex magnetic structures that cannot be uniquely identified by other standard techniques. The method has been successfully applied to anti-ferromagnets with propagation vector $\mathbf{q} = 0$,

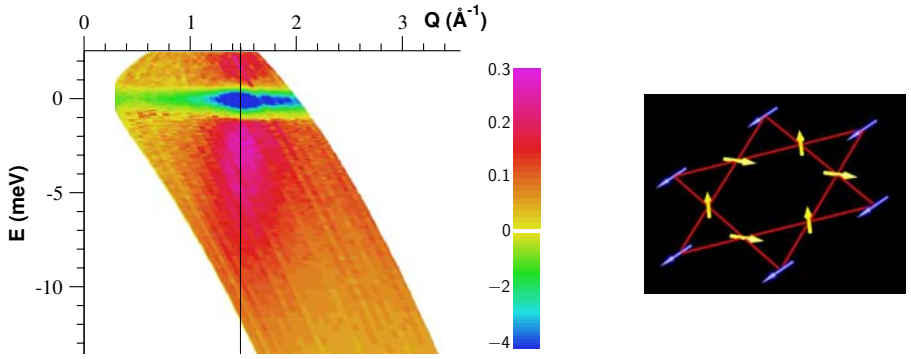

Figure 10: Quasi-elastic broadening due to thermal spin fluctuations. The difference of S(Q,ω) measured at 150 K and 40 K in time-of-flight mode reveals a loss of elastic intensity (blue) and a relaxation response (red) with a Q-dependence consistent with hexagon spin modes (right).

where the magnetic and nuclear structure has the same unit cell size and structure factors are in phase quadrature, to spiral structures, systems with magnetic domains, and to systems in which ferro-electricity couples to magnetism, etc. All these examples cause a change of polarization in the scattering process, such that the final polarization will be tilted from the initial polarization. Using standard LPA and applying a magnetic field, the final polarization starts to precess and only the projection to the field is measured. The transverse precessing components have been (falsely) believed to depolarize rapidly and to be lost. Therefore, one has built zero-field chambers, using superconducting Meissner screens, best known is the device CryoPAD developed at the ILL. Clearly zero-field avoids any precession of the polarization, and the polarization of the scattered intensity can be realigned by a flipper-coil parallel to the external field guiding the polarization to the analyzer.

Of course, it is also possible to work with precessing polarization and this is used in diverse neutron instruments. Very recently, spherical polarization analysis has been developed with a new precession technique on the DNS instrument [20, 21]. Therefore, one starts with a precessing initial polarization analyzing only the non-precessing final polarization. A simulation is shown in Fig. 3.3.5 and an experimental verification can be seen in Fig. 12.

One of the early successful examples of spherical polarization analysis solving a com-

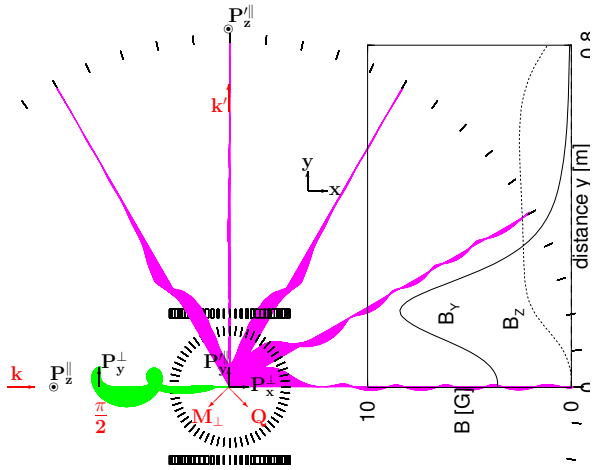

Figure 11: Simulation of precessing neutron polarisation analysis for typical parameters of the DNS instrument. Neutrons with wave-vector $\underline{k}$ are polarized in P_z undergo a $\pi/2$-flip into P_y, then precess to the sample into P_x in a field turning the normal vector of the precessing plane from z to y. Scattering is simulated for five different scattering angles, and in each case the final polarization turns up adiabatically from P_y to P_z. The inset shows the field variation for 90^o scattering.

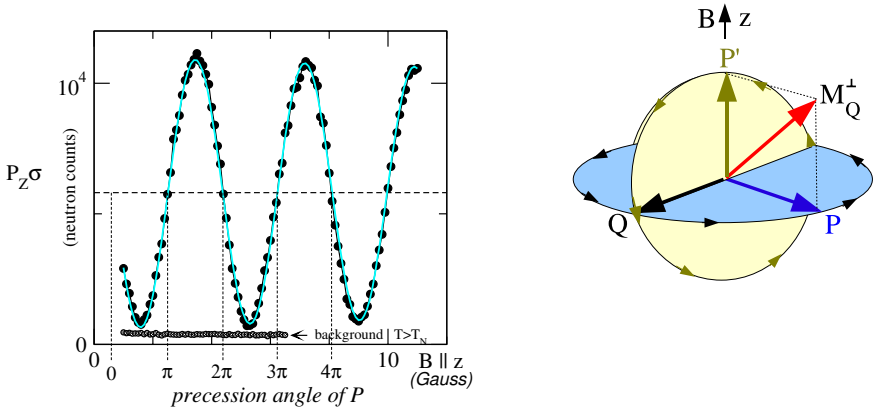

Figure 12: $\mathbf{P}'\sigma$ versus a precessing initial polarization $\mathbf{P}$ for magnetic Bragg scattering of MnF_2, with moments inclined by 45°. (The precision in phase is 0.5 degrees keeping up to 98% of the polarization).

plex antiferromagnetic structure is the study of $U_{14}Au_{51}$ (with zero-field polarimetry on CryoPAD-2)[22]. It is a magnetic structure with zero propagation vector, for which nuclear and magnetic Bragg peaks coincide. We repeated the experiment on DNS with the new precession technique. Fig. 13 illustrates the identification of nuclear and magnetic scattering for the (201) Bragg peak. The crystal is oriented vertically with its b-axis parallel to z. The spins are ordered within the a-b plane with a hexagonal star-like structure. The nuclear scattering is confirmed by a measurement above the Neel temperature at 30K and remains independent of the polarisation. Maxima are found for a rotation of the polarisation from the z to the y direction. For an initial polarisation along x (which is set parallel to the scattering vector) only spin-flip scattering is observed for the magnetic scattering, as it must be. For all cases, when taking nuclear scattering into account, an effective depolarisation is observed. These results are in excellent agreement with the results obtained with CryoPAD [22].

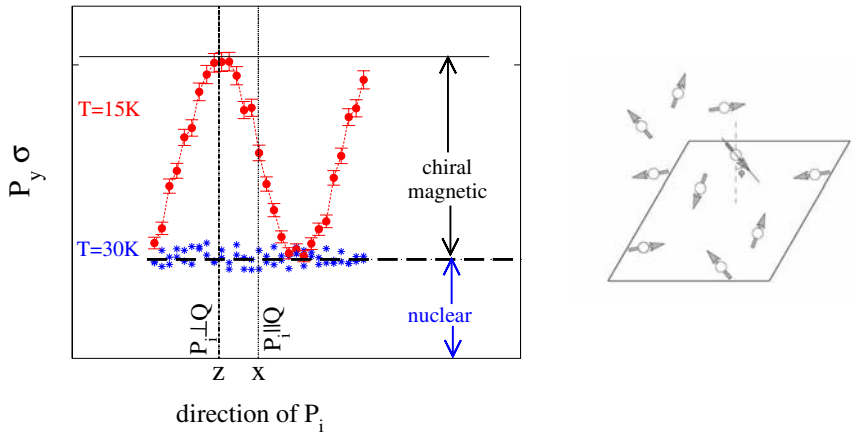

Figure 13: Spherical polarisation analysis on the (201) Bragg peak of $U_{14}Au_{51}$. Initially the polarisation precesses perpendicular to the applied field in y-direction. At 30 K there is only a nuclear Bragg component which continues to precess after the scattering event. At lower temperatures, T=15 K, there is an additional magnetic contribution for which the neutron polarisation changes from $P_i \parallel$z to $P_f \parallel$y.

3.4 Final remarks

In this lecture we have considered only a few applications of polarized neutron scattering. Interested readers are referred to the literature [23, 24] and references therein. Plakhty has given a recent review on chiral scattering[25] which exhibit critical exponents that belong to new universality classes. Such experiments demand single crystalline samples with a preference for one of the usually two occuring domains with left and right handed screws.

Considering instrumentation for polarization analysis, such as the DNS instrument or the similar instrument D7 (ILL), there has been an enormous gain in efficiency compared to the original set-up of Moon, Riste and Koehler. There are new developments in progress, for instance the so-called Pastis set-up at the ILL Grenoble, a He-3 filter cell best suited for polarization analysis of thermal neutrons, which are needed to investigate higher energy excitations. The He-3 polarizer which will also cover more efficiently a larger solid angle for detection. However,, requirements for field homogeneity are very challenging.

The new precessing technique for spherical neutron polarization analysis has the great advantage compared to zero-field methods, that it is not necessary anymore to align the final polarization with respect to the guide field. Apart from avoiding complicated cryogenic sample enviroments and zero-field restrictions, the more important progress is that $\mathbf{P}'$ can be simultaneously measured independent of momentum and energy transfer, and the realization of spherical polarization analysis on a multi-detector and time-of-flight instrument. Hence, this method will have a great future potential for the diffuse scattering involving magnetic fluctuations and may reveal new insights in correlations between magnetic fluctuations and structural or lattice fluctuations, for example, in high T_c superconductors and in the recently discovered multi-ferroica. Complex and chiral spin ordering is characteristic for these materials where electric fields couple to magnetic properties. Strongly coupled magnetic moments that do not settle into stable ordering because of geometrical frustration or because of low dimensionality of space can be influenced and determined by rather subtle higher order interaction terms. Hence unexpected and promising rich and interesting complex phenomena may emerge. Magnetic fluctuations are considered to be of fundamental importance for the mechanism of unconventional superconductivity. For example, alternatively to the common picture of collinear stripes with sinusoidal AF

spin correlations fluctuations from a spiral spin phase ground state have been proposed recently [26] explaining the inelastic magnetic response; in order to test such a interesting hypothesis, tools of neutron polarization analysis will be required.

Appendix

Nuclear scattering

The interaction of thermal and cold neutrons with the nuclei of of scattering system is given by the sum of Fermi potentials $V(r) = \frac{2\pi\hbar^2}{m_N} b\delta(r)$, where b is a scalar complex parameter called scattering length. Tabulated values comprise average scattering lengths for each element, with further distinction of scattering lengths of isotopes[27]. The interaction potential depends also on the spin of the scattering compound of nucleus and neutron. Therefore, if the nucleus has a non-zero spin, one can distinguish further the scattering lengths b_+ and b_- for parallel and anti-parallel spin alignment. If the nucleus has zero spin, there is of course no spin-dependent interaction potential.

In general, we can decompose the nuclear scattering into two parts, the average coherent nuclear scattering and the spin-dependent and spin-incoherent scattering. The reason why the latter part is incoherent, except for some unusual cases, is because the orientation of nuclear spins is given by a random distribution.

Therefore, in general, the scattering length needs to be replaced by the scattering length operator $\mathbf{b} = A + B\,\boldsymbol{\sigma}\cdot\mathbf{I}$ with $A = \frac{(I+1)\,b_+ + I\,b_-}{2I+1}$ and $B = \frac{b_+ - b_-}{2I+1}$ where $\mathbf{I}$ denotes the nuclear spin operator. One may calculate the transition probability from the initial spin state $|S\rangle$ to the final spin state $\langle S'|$, which yields the scattering amplitude $\mathrm{A}_{\mathbf{Q}}$, assuming an arbitrary orientation of the neutron spin, say along z-direction,

$$\mathrm{A}_{\mathbf{Q}} = \langle S'_{(z)}|A + B\boldsymbol{\sigma}\cdot\mathbf{I}|S_{(z)}\rangle = \begin{cases} A + B\mathrm{I_z} & \left\{ \begin{array}{l} + \rightarrow + \\ - \rightarrow - \end{array} \right\} NSF \\ B(\mathrm{I_x} + \mathrm{iI_y}) & \left\{ \begin{array}{l} + \rightarrow - \\ - \rightarrow + \end{array} \right\} SF \end{cases} \tag{13}$$

Thermal averaging yields, for random orientation of nuclear spins $\langle \mathrm{I_x}\rangle = \langle \mathrm{I_y}\rangle = \langle \mathrm{I_z}\rangle = 0$, so that the (coherent) scattering amplitude is given only by the non-spin flip matrix

element equal to $A \equiv b_{coh} = \bar{b}$ and the coherent nuclear scattering is proportional to the square of $\bar{b}^2$

$$\frac{d\sigma}{d\Omega}^{(NSF)}_{coherent} = \bar{b}^2 \sum_{\mathbf{r},\mathbf{r}'} \mathrm{e}^{\mathrm{i}\mathbf{Q}\cdot(\mathbf{r}'-\mathbf{r})}. \tag{14}$$

The coherent nuclear scattering does not change the polarization of the neutrons.

We have used that the neutron spin operator σ can be described by the Pauli-spin matrices $\underline{\underline{\sigma}}_\alpha$

$$\underline{\underline{\sigma}}_{\mathrm{x}} = \begin{pmatrix} 0 & 1 \\ 1 & 0 \end{pmatrix}, \underline{\underline{\sigma}}_{\mathrm{y}} = \begin{pmatrix} 0 & -\mathrm{i} \\ \mathrm{i} & 0 \end{pmatrix}, \underline{\underline{\sigma}}_{\mathrm{z}} = \begin{pmatrix} 1 & 0 \\ 0 & -1 \end{pmatrix} \tag{15}$$

When applied to spin-up and down states $|+\rangle = \begin{pmatrix} 1 \\ 0 \end{pmatrix}$ and $|-\rangle = \begin{pmatrix} 0 \\ 1 \end{pmatrix}$ respectively, one obtains the following relations:

$$\begin{aligned} \underline{\underline{\sigma}}_{\mathrm{x}}|+\rangle &= \ |-\rangle \quad , \quad \underline{\underline{\sigma}}_{\mathrm{x}}|-\rangle = \ \ |+\rangle \\ \underline{\underline{\sigma}}_{\mathrm{y}}|+\rangle &= \mathrm{i}\,|-\rangle \quad , \quad \underline{\underline{\sigma}}_{\mathrm{y}}|-\rangle = -\mathrm{i}\,|+\rangle \\ \underline{\underline{\sigma}}_{\mathrm{z}}|+\rangle &= \ |+\rangle \quad , \quad \underline{\underline{\sigma}}_{\mathrm{z}}|-\rangle = \ -|-\rangle\,. \end{aligned} \tag{16}$$

The incoherent scattering intensity is determined only by the thermal average of the squares of the matrix elements. With $\langle \mathrm{I}_{\mathrm{x}}^2 \rangle = \langle \mathrm{I}_{\mathrm{y}}^2 \rangle = \langle \mathrm{I}_{\mathrm{z}}^2 \rangle = \frac{1}{3}\mathrm{I}\langle|\mathrm{I}+1\rangle$ and Eq. (13), the spin-incoherent scattering (per atom)

$$\frac{d\sigma}{d\Omega}^{(\substack{+\to+\\-\to-},NSF)}_{spin-incoherent} = (\bar{b^2} - \bar{b}^2)^{NSF} = \frac{1}{3}\langle B^2 \mathrm{I}(\mathrm{I}+1)\rangle \tag{17}$$

$$\frac{d\sigma}{d\Omega}^{(\substack{+\to-\\-\to+},SF)}_{spin-incoherent} = (\bar{b^2} - \bar{b}^2)^{SF} = \frac{2}{3}\langle B^2 \mathrm{I}(\mathrm{I}+1)\rangle \tag{18}$$

The result is that 1/3 of the spin-incoherent part of the nuclear scattering is non-spin flip scattering and 2/3 of it is spin-flip scattering, and it is independent of the (direction) of an external field $\mathbf{H}$.

Magnetic scattering

For pure magnetic scattering we consider the interaction of the neutron magnetic moment $\boldsymbol{\mu_N}$ with the magnetic field of the electrons $\mathbf{B} = \mathbf{B}_{spin} + \mathbf{B}_{orbital}$ due to spin and orbital

momentum. The magnetic interaction potential $V_m = -\mu_n \cdot \mathbf{B}$ defines the magnetic scattering amplitude

$$A_{\mathbf{Q}} = \langle S'_{\rm z}| \frac{-\gamma_n r_o}{2\mu_B} \boldsymbol{\sigma} \cdot \mathbf{M}^{\perp}_{\mathbf{Q}}) |S_{\rm z}\rangle = \frac{-\gamma_n r_o}{2\mu_B} \sum_{\alpha} \langle S'_{\rm z}|\underline{\sigma}_{\alpha}|S_{\rm z}\rangle \, M_{\alpha,\mathbf{Q}} \, . \tag{19}$$

Here $\gamma_n = -1.913$ denotes the magnetic dipole moment of the neutron expressed in nuclear magnetons $\mu_N = 5.051 \cdot 10^{-27} J/T$, and $r_0 = e^2/(m_e c^2)$ is the classical electron radius. Inserting the relations of Eq.(16) into Eq. (19) we obtain the matrix elements (scattering amplitudes) for spin-flip and non-spin flip scattering:

$$A_{\mathbf{Q}} = \frac{-\gamma_n r_o}{2\mu_B} \times \left\{ \begin{array}{c} \mathbf{M}^{\perp}_{z,\mathbf{Q}} \\ -\mathbf{M}^{\perp}_{z,\mathbf{Q}} \\ (\mathbf{M}^{\perp}_{x,\mathbf{Q}} - i\mathbf{M}^{\perp}_{y,\mathbf{Q}}) \\ (\mathbf{M}^{\perp}_{x,\mathbf{Q}} + i\mathbf{M}^{\perp}_{y,\mathbf{Q}}) \end{array} \right. \quad \text{for} \left\{ \begin{array}{ll} + \rightarrow + & \text{(NSF)} \\ - \rightarrow - & \text{(NSF)} \\ + \rightarrow - & \text{(SF)} \\ - \rightarrow + & \text{(SF)} \end{array} \right. \tag{20}$$

Different to the coherent nuclear scattering now we can also observe "spin-flip" processes that reverse the neutron spin direction. Recall that $\mathbf{M}^{\perp}_{\mathbf{Q}}$ is the perpendicular component of $\mathbf{M}_{\mathbf{Q}}$ with respect to the scattering vector $\mathbf{Q}$, and the neutron polarization has been chosen parallel to an external field $\mathbf{H}_z$. We obtain two rules for the magnetic scattering:

The "spin-flip" processes are observed for the component $\mathbf{M}^{\perp}_{\mathbf{Q}}$ *that is perpendicular to the neutron polarization. The "non-spin flip" processes are observed for the component of* $\mathbf{M}^{\perp}_{\mathbf{Q}}$ *that is parallel to the neutron polarization.*

References

[1] O. Schärpf, in *Neutron Spin Echo* Lecture Notes in Physics **128**, Ed. F. Mezei, Springer (1980) 27-52.

[2] F. Klein, *The mathematical theory of the top*, Princeton 1897; see also H. Goldstein, *Klassische Mechanik*, Akademische Verlagsges. Frankfurt am Main (1974).

[3] W. Schweika and P. Böni, Physica B **297**, 155 (2001).

[4] O. Schärpf, Physica B **182** (1992) 376.

[5] O. Schärpf, J. Physics E: Sci. Instrum. **8** (1975) 268; F. Mezei, Commun. Phys. **1** (1976) 81; P. Böni, J. Neutron Research **5** (1996) 63.

[6] G.L. Squires, *Introduction to the theory of thermal neutron scattering*, Cambridge University Press, Cambridge (1978).

[7] S.W. Lovesey, *Theory of neutron scattering from condensed matter*, Volume 2: Polarization and magnetic scattering, Clarendon Press, Oxford (1987).

[8] M. Blume, Phys. Rev. **130** (1963) 1670; Phys. Rev. **133** (1964) A1366.

[9] S.V. Maleyev, Zh. Eksperim. i Teor. Fiz. **33** (1958) 129 [English Translation: Soviet Phys.-JETP **34** (1958) 89]; S.V. Maleev, Zh. Eksperim. i Teor. Fiz. **40** (1961) 1224 [English Translation: Soviet Phys.-JETP **13** (1961) 860].

[10] A. C. Genix *et. al.* Macromolecules **39** (2006) 3947.

[11] L. Temleitner, L. Pusztai, and W. Schweika, J. Phys. Cond. Mat., accepted (2007).

[12] R.M. Moon, T. Riste, W.C. Koehler, Phys. Rev. **181** (1969) 920.

[13] G. Shirane, Y.J. Uemura, J.P.Wicksted, Y. Endoh, Y. Ishikawa, Phys. Rev. B **31** (1985) 1227.

[14] Th. Brückel, *Dissertation* Tübingen (1988); O. Schärpf, H. Capellmann, Phys. Stat. Sol. (a) **135** (1993) 359.

[15] W. Schweika, M. Valldor, P. Lemmens, Phys. Rev. Lett. **98**, 067201 (2007).

[16] Eq.12 holds in the limit $|J| \gg T$.

[17] J. N. Reimers and A. J. Berlinsky, Phys. Rev. B **48** (1993) 9539.

[18] F. Tasset, Physica B **156-157** (1989) 627; F. Tasset, Physica B **241-243** (1998) 177.

[19] P. J. Brown, J. B. Forsyth, and F. Tasset, Proc. Roy. Soc. London A 442 (1993) 147; P.J. Brown, *Polarimatric Neutron Scattering*, in lecture notes on *Polarized Neutron Scattering* (Eds. Th. Brückel and W. Schweika), Schriften des Forschungszentrums Jülich, Series Matter and Materials Vol.12, Forschungszentrums Jülich (2002).

[20] W. Schweika, Physica B **335** (1-4), (2003) 157-163.

[21] W. Schweika, S. Easton, and K.-U. Neumann, Neutron News **16** (2005) 14.

[22] P. J. Brown, J. Crangle, K.-U. Neumann, J. G. Smith, and K. R. A. Ziebeck, J. Phys.: Cond. Mat. **9** (1997) 4729.

[23] J. R. Stewart, K. H. Andersen, R. Cywinski, and A. P. Murani, J. Appl. Phys. **87** (2000) 5425.

[24] B. Roessli, P. Böni, cond-mat/0012180.

[25] V. P. Plakhty *et al.*, Physica B **385-386** (2006) 441-451.

[26] P.-A. Lindgard, Phys. Rev. Lett. **95** (2005) 217001.

[27] V. F. Sears, Neutron News **3** (1992).

4

Correlation Functions Measured by Scattering Experiments

Reiner Zorn and Dieter Richter

4. Correlation Functions Measured By Scattering Experiments

Reiner Zorn, Dieter Richter

In this lecture static and dynamic correlation functions will be introduced. We will start by introducing probability densities, relate those to the scattering cross section and define the pair correlation function. Two examples will be given, one from the physics of liquids and one from polymer physics. The concept of dynamic correlation functions will be explained firstly by the example of correlation spectroscopy. Then the Van Hove correlation function will be introduced which is the basis for the calculation of the double differential scattering cross section. Finally, the concept will be applied to the example of an ideal gas.

4.1 Probability Densities

We start by considering a homogeneous monatomic liquid with N atoms in a volume V. We denote the probability to find a certain atom in a volume element d^3r at $\underline{r}$ by $P(\underline{r})\mathrm{d}^3r$. Because of the homogeneity $P(\underline{r})$ is constant and evidently

$$P(\underline{r}) = \frac{1}{V}\,. \tag{4.1}$$

Then the number density of atoms at $\underline{r}$ is

$$\rho(\underline{r}) = NP(\underline{r}) = \frac{N}{V} \equiv \rho_0\,. \tag{4.2}$$

We call the probability density to find a certain atom at $\underline{r}_1$ and another at $\underline{r}_2$ $P(\underline{r}_1, \underline{r}_2)$. This function fulfills the basic relations

$$P(\underline{r}_1, \underline{r}_2) = P(\underline{r}_2, \underline{r}_1) \text{ and} \tag{4.3}$$

$$\int_V \mathrm{d}^3r_2 P(\underline{r}_1, \underline{r}_2) = P(\underline{r}_1)\,. \tag{4.4}$$

If there is no interaction between the atoms $P(\underline{r}_1, \underline{r}_2)$ factorizes into

$$P(\underline{r}_1, \underline{r}_2) = P(\underline{r}_1)P(\underline{r}_2)\,. \tag{4.5}$$

In real liquids however usually an interaction exists which depends (only) on the distance of the atoms $\underline{r}_{12} = \underline{r}_2 - \underline{r}_1$. We express the deviation from (4.5) by a pair correlation function defined by

$$g(\underline{r}_{12}) \equiv \frac{P(\underline{r}_1, \underline{r}_2)}{P(\underline{r}_1)P(\underline{r}_2)} \,. \tag{4.6}$$

With the pair distribution function $n(\underline{r}_1, \underline{r}_2) = N(N-1)P(\underline{r}_1, \underline{r}_2)$ which expresses the probability density for any pair of atoms to occupy positions $\underline{r}_1$ and $\underline{r}_2$ we obtain

$$g(\underline{r}_{12}) = \frac{n(\underline{r}_1, \underline{r}_2)}{{\rho_0}^2} \tag{4.7}$$

because in the limit of large N we have $N(N-1) \approx N^2$.

The qualitative features of the pair correlation function are shown in figure 4.1. For $r \to 0$ one finds $g(r) = 0$ because two atoms cannot be at the same position. Usually, this is also true for distances $r < r_0$ because the atoms cannot penetrate each other and have a "hard core" radius r_0. For $r \to \infty$ the limit is $g(r) = 1$ because the interactions decay with distance and the $P(\underline{r}_1, \underline{r}_2)$ reverts to its default value 4.5. At intermediate distances $g(r)$ shows a peak because the probability density which is lacking at $r < r_0$ must be compensated. Its location is usually close to the minimum of the interatomic potential, i.e. close to the average next neighbour distance r_{nn}.

Using the pair correlation function one can formulate the differential neutron cross section for a monatomic liquid[1]

$$\left(\frac{\mathrm{d}\sigma}{\mathrm{d}\Omega}\right)_{\mathrm{coh}} = |\overline{b}|^2 \left\langle \sum_{i,j=1}^{N} \exp\left(\mathrm{i}\underline{Q} \cdot \left(\underline{r}_i - \underline{r}_j\right)\right) \right\rangle \,. \tag{4.8}$$

Here $(\mathrm{d}\sigma/\mathrm{d}\Omega)_{\mathrm{coh}}$ denotes the angle dependent coherent scattering cross section and $\overline{b}$ is the average scattering length of the liquid atoms. $\underline{Q}$ is the scattering vector, i.e. the difference between incoming and scattered wave vector of the radiation, $\underline{Q} = \underline{k} - \underline{k}'$. The average in the expression can be evaluated using the pair correlation function (4.7):

$$\left(\frac{\mathrm{d}\sigma}{\mathrm{d}\Omega}\right)_{\mathrm{coh}} = |\overline{b}|^2 \left(1 + \left\langle \sum_{i \neq j}^{N} \exp\left(\mathrm{i}\underline{Q} \cdot \left(\underline{r}_i - \underline{r}_j\right)\right) \right\rangle\right)$$

[1] Exactly speaking, this expression is valid only for mon*isotopic* liquids. Otherwise, there would be an additional incoherent term like the one discussed for the dynamic correlation function in section 4.3. Nevertheless, this term is just a constant and therefore only visible as a flat background in the experiment. The Q dependent (coherent) part of the cross section is still correctly represented by (4.8).

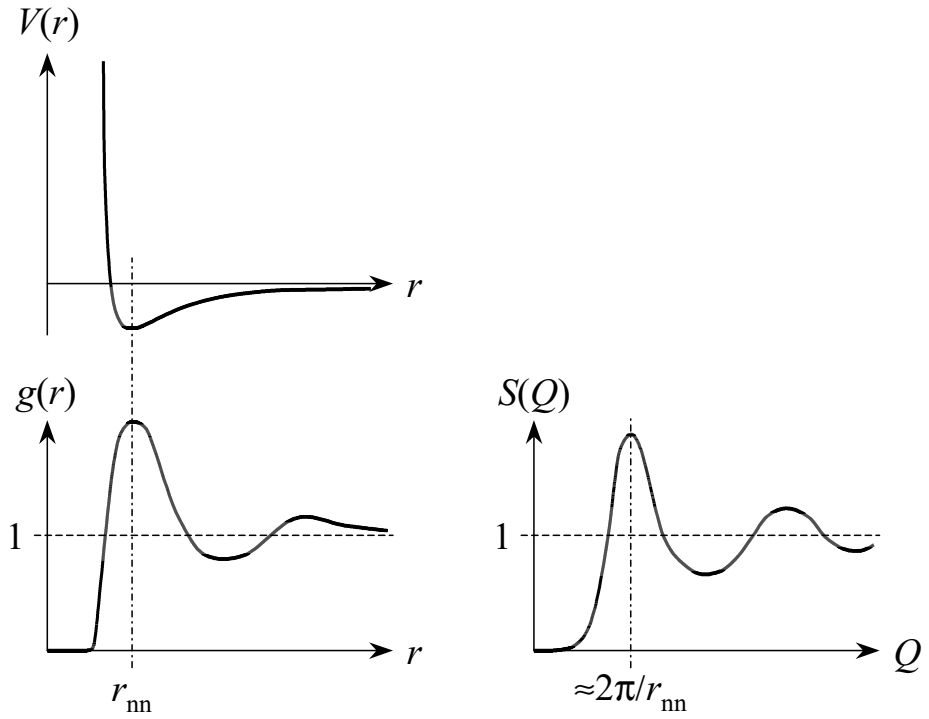

Figure 4.1: Schematic representation of interaction potential $V(r)$, pair correlation function $g(r)$, and scattering function $S(Q)$.

$$\begin{aligned} &= |\bar{b}|^2 \left(N + \int_V \mathrm{d}^3 r_1 \int_V \mathrm{d}^3 r_2 n(\underline{r}_1, \underline{r}_2) \exp\left(\mathrm{i}\underline{Q} \cdot (\underline{r}_1 - \underline{r}_2) \right) \right) \\ &= |\bar{b}|^2 \left(N + {\rho_0}^2 V \int_V \mathrm{d}^3 r_{12} g(\underline{r}_{12}) \exp\left(\mathrm{i}\underline{Q} \cdot \underline{r}_{12} \right) \right) \\ &= |\bar{b}|^2 N \left(1 + \rho_0 \int_V \mathrm{d}^3 r_{12} g(\underline{r}_{12}) \exp\left(\mathrm{i}\underline{Q} \cdot \underline{r}_{12} \right) \right) . \end{aligned} \tag{4.9}$$

This equation states that the scattering cross section can be represented as the Fourier transform of the pair correlation function. Assuming isotropy (as is found in the homogeneous liquid discussed here) one can replace $g(\underline{r}_{12})$ by the radial correlation function $g(r)$:

$$\left(\frac{\mathrm{d}\sigma}{\mathrm{d}\Omega} \right)_{\mathrm{coh}} = |\bar{b}|^2 N \left(1 + 4\pi\rho_0 \int_0^\infty r^2 \mathrm{d}^3 r g(r) \frac{\sin Qr}{Qr} \right) \tag{4.10}$$

Equation (4.10) follows from (4.9) by radial averaging of $\exp\left(\mathrm{i}\underline{Q} \cdot \underline{r}_{12} \right)$ (i.e. an average over all possible orientations of $\underline{r}_{12}$).

The term in big parentheses of equations (4.9) and (4.10)

$$S(\underline{Q}) \equiv 1 + \rho_0 \int_V \mathrm{d}^3 r_{12} g(\underline{r}_{12}) \exp\left(\mathrm{i}\underline{Q} \cdot \underline{r}_{12}\right) \tag{4.11}$$

is usually called structure factor or scattering law[2]. $S(Q)$ is solely determined by the properties of the sample and does not depend on the radiation used in examining the sample.

For $Q \to \infty$, $\exp\left(\mathrm{i}\underline{Q} \cdot \underline{r}_{12}\right)$ becomes a rapidly oscillating function and the integral vanishes. Then one has

$$\lim_{Q\to\infty} S(Q) = 1\,. \tag{4.12}$$

For $Q \to 0$, $S(Q)$ measures only the overall density fluctuation, i.e. the fluctuation of the particle number:

$$\lim_{Q\to 0} S(Q) = \frac{V^2\langle\delta\rho^2\rangle}{N} = \frac{\langle N^2\rangle - \langle N\rangle^2}{\langle N\rangle} = \rho_0 k_\mathrm{B} T \kappa_T\,. \tag{4.13}$$

Here, k_B denotes the Boltzmann factor, T the temperature and κ_T the isothermal compressibility. At intermediate Q, the structure factor of liquids shows a diminishing series of broad peaks, remainders of the Bragg peaks of a crystalline structure. The first peak occurs at a scattering vector roughly corresponding to the next neighbour distance by $Q_\mathrm{max} = 2\pi/r_\mathrm{nn}$.

[2] The usual definition of the structure factor found in the literature is

$$S'(\underline{Q}) \equiv 1 + \rho_0 \int_V \mathrm{d}^3 r_{12}\,(g(\underline{r}_{12}) - 1) \exp\left(\mathrm{i}\underline{Q} \cdot \underline{r}_{12}\right)$$

subtracting the long distance limit 1 from $g(r)$. Because the Fourier transform of the constant 1 is the delta function the two definitions differ only by a delta function, $S(Q) = S'(Q) + \rho_0\delta(Q)$. This means that apart from the unobservable scattering at zero angle ($Q = 0$) both are the same.

The reason for this alternative definition is to avoid the singularity. Another way to accomplish this is to use the density fluctuation $\delta\rho(\underline{r}) = \rho(\underline{r}) - \rho_0$ from the start (equation (4.2)). From this approach it becomes clear that the structure factor at $Q \neq 0$ depends only on the fluctuation of the density but not on its absolute level.

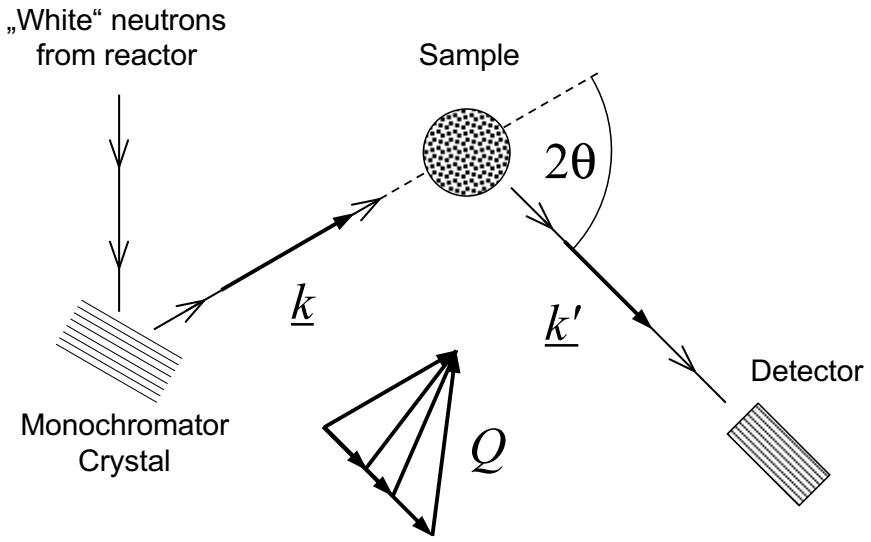

Figure 4.2: Schematic set-up of a diffraction experiment. The inset shows the relation between incident and final wave vectors k, k' and the scattering vector Q.

4.2 Experimental Examples: Static Scattering

4.2.1 Placzek corrections

Figure 4.2 shows the schematics of a scattering experiment for the determination of $S(Q)$. By using a monochromator the incident neutron energy or the wave vector k is fixed. After scattering the intensity is recorded as a function of the scattering angle 2θ without energy discrimination. This means that the diffraction setup fixes only the direction of $\underline{k}_\mathrm{f}$ but not its magnitude. Therefore, for a given angle different scattering vectors Q are mixed as figure 4.3 shows.

Strictly speaking, this invalidates the relation $(\mathrm{d}\sigma/\mathrm{d}\Omega)_\mathrm{coh} = |\overline{b}|^2 N S(Q)$ between (angle) differential cross section and structure factor.

Nevertheless, for high incident energies it is an excellent approximation as long as the energy transfer due to inelastic scattering is small compared to the incident energy E. This condition is always fulfilled for x-ray scattering because the incident energy lies in the keV range there and the inelasticity of scattering is limited mainly to thermal energies $k_\mathrm{B}T$ which are of the order of meV.

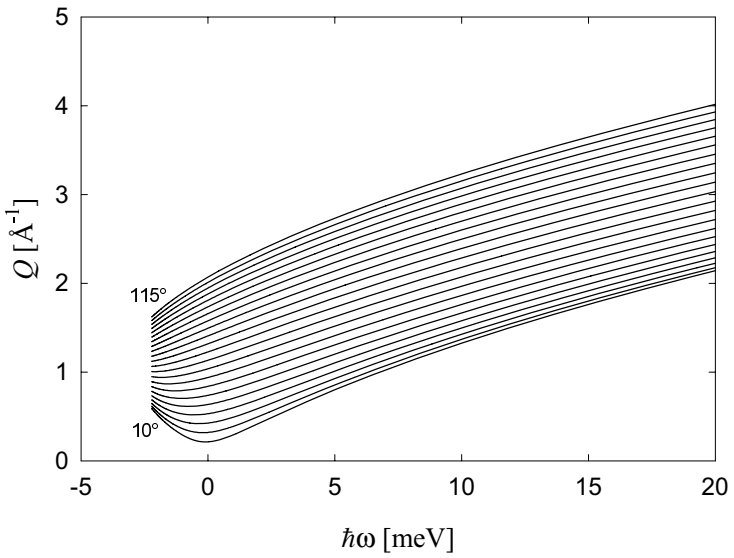

Figure 4.3: Scattering vectors Q accessed by a diffraction experiment with the detector at scattering angles $2\theta = 10 \ldots 115°$ vs. the energy transfer $\hbar\omega$ (incident wavelength $\lambda_\mathrm{i} = 5.1$ Å).

For neutrons on the other hand, incident energies are just in the latter range. Fortunately, the errors which occur due to neglect of inelasticity are still not too large. Therefore, it is possible to derive a correction formula by expanding the true differential cross section under constant angle into a series in the ratio of the mass of the scattering nucleus and the neutron mass $m_\mathrm{n}/m_\mathrm{sc}$. In this way one obtains to first order[3]:

$$\left(\frac{\mathrm{d}\sigma}{\mathrm{d}\Omega}\right)_{2\theta} = |\bar{b}|^2 N \left(S(Q) + f_\mathrm{P}(Q)\right) \text{ with } f_\mathrm{P}(Q) = \frac{m_\mathrm{n}}{m_\mathrm{sc}} \left(\frac{k_\mathrm{B}T}{E} - \left(\frac{Q}{k}\right)^2\right) . \qquad (4.14)$$

Here, E is the incident energy and $k = \sqrt{2m_\mathrm{n}E}/\hbar$ the respective wave vector.

[3] This formula is actually the specification of Placzek's original result [6] to the case of a detector which is equally sensitive for all neutron energies ("black" detector). As pointed out in [7] the correction depends strongly on the energy dependence of the sensitivity. Therefore, except for low Q values, formula (4.14) is not the one which is used in practical applications.

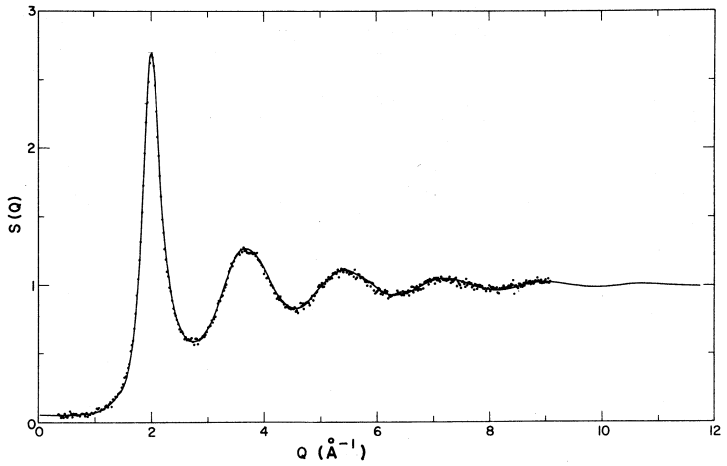

Figure 4.4: Structure factor $S(Q)$ of liquid ^{36}Ar at 85 K. The points are from a neutron scattering experiment, the curve is generated by a molecular dynamics calculation using a Lennard-Jones potential [7].

4.2.2 Experiments on Liquid Argon

As an example of the structure factor $S(Q)$ of a monatomic liquid we consider the neutron scattering results of Yarnell et al. [7] from liquid Argon. The result of the experiment is shown in figure 4.4. The wavelength of the incident neutrons was $\lambda = 0.978$ Å. Under this condition the Placzek corrections vary between 0.0012 near $Q = 0$ and -0.0426 at $Q = 9.08\,\text{Å}^{-1}$. The pair correlation function $g(r)$ was obtained by numerical inverse Fourier transform of $S(Q) - 1$ and is shown in figure 4.5. The oscillations at small r are a consequence of cut-off effects on the Fourier transform. They occur below the atomic diameter r_0 and therefore do not impede the interpretation. The determination of $g(r)$ is important for the calculation of equilibrium properties of the liquid and allows scrutinization of theoretical models for the interatomic forces.

Two methods of theory based calculation of $g(r)$ have to be emphasized: (1) In Monte Carlo (MC) calculations a large number of possible atomic configurations is created. Their probability is determined by the Boltzmann factor on the basis of interatomic potentials. Finally, the ensemble average is calculated. (2) In Molecular Dynamics (MD) calculations one starts from an initial configuration and solves (numerically) the equations

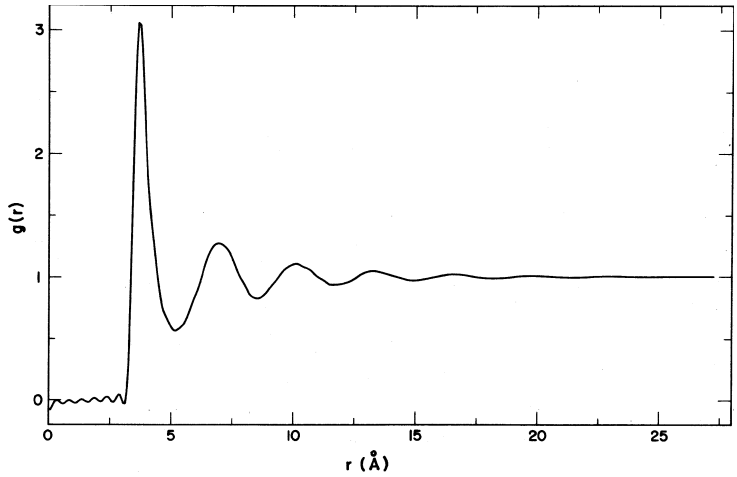

Figure 4.5: The pair correlation function $g(r)$ of liquid Argon calculated by inverse Fourier transform from the data in figure 4.4 [7].

of motions using the interatomic forces. These calculations yield the time average[4]. The solid curve in figure 4.5 shows the result of an MD calculation with a Lennard-Jones-Potential ($V(r) \propto (\sigma/r)^{12} - (\sigma/r)^6$)—the agreement is excellent.

Unfortunately, the pair correlation function is comparatively insensitive to details of the pair potential. To obtain exact information on $V(r)$ it is necessary to do extremely accurate measurements with errors in the per mille range.

4.2.3 Scattering from a Polymer Chain

We consider a polymer, i.e. a long chain molecule consisting of equal building blocks, the monomers. In the melt the spatial arrangement of the monomers is simply given by a random walk[5]. The mean squared distance between monomers i and j for such a coiled chain is proportional to the difference of indices

$$\langle {r_{ij}}^2 \rangle = \ell^2 |i - j| \tag{4.15}$$

[4] The ergodic hypothesis ensures that the results of both methods are the same.

[5] This is a result by no means trivial. It was actually confirmed for the first time by the neutron scattering results shown here.

where r_{ij} denotes the monomer distance and ℓ is the characteristic monomer length. This is the same expression as for a random walk but with the time t replaced by $|i-j|$. Because for not too small distances r_{ij} is the sum of many random variables the central limit theorem is applicable and the final distribution of the distance is a Gaussian:

$$g(r_{ij}) = \left(\frac{3}{2\pi\langle {r_{ij}}^2\rangle}\right)^{3/2} \exp\left(-\frac{3{r_{ij}}^2}{2\langle {r_{ij}}^2\rangle}\right) . \tag{4.16}$$

Application of equation (4.8) (radially averaged as (4.10)) yields the so-called form factor[6] of the monomer

$$P(Q) = \frac{1}{\mathcal{N}^2}\sum_{i,j=1}^{\mathcal{N}} 4\pi \int {r_{ij}}^2 \mathrm{d}^3 r_{ij} \frac{\sin Qr_{ij}}{Qr_{ij}} g(r_{ij}) = \sum_{i,j=1}^{\mathcal{N}} \exp\left(-\frac{Q^2}{6}|i-j|\ell^2\right) \tag{4.17}$$

where $\mathcal{N}$ is now the number of monomers. Analogous to the preceding derivation of (4.9) we take the diagonal part out of the sum and convert the double sum into a single sum over all differences $k \equiv |i-j|$:

$$P(Q) = \frac{1}{\mathcal{N}}\left(1 + 2\sum_{k=1}^{\mathcal{N}}\left(1-\frac{k}{\mathcal{N}}\right)\exp\left(-\frac{Q^2}{6}k\ell^2\right)\right) . \tag{4.18}$$

Here it is taken account that in contrast to (4.9) not all pairs are equally probable but an index distance k occurs $2(\mathcal{N}-k)$ times in the chain. Converting this sum into an integral one obtains

$$P(Q) = \frac{2}{z^2}\left(\mathrm{e}^{-z} - 1 + z\right) \equiv D(z) \text{ with } z = \frac{Q^2 N\ell^2}{6} . \tag{4.19}$$

The expression $D(z)$ is usually called the Debye function. It describes the scattering of a single polymer coil in the melt which is labeled e.g. by isotopic contrast. Figure 4.6 shows the scattering cross section of protonated polystyrene in a deuterated polystyrene matrix. The solid curve represents a fit with equation (4.19). At large scattering vectors the leading asymptotic term of $D(z)$ is $2/z$ and $P(Q)$ becomes proportional $1/Q^2$—characteristic for a Gaussian random walk. In a so-called Kratky plot ($Q^2 \cdot \mathrm{d}\sigma/\mathrm{d}\Omega$ vs. Q) one expects a plateau at high scattering vector Q. Figure 4.7 shows this plateau for polystyrene. At very large Q values deviations occur again which signalize the breakdown of Gauss statistics for small distances.

[6] Here the monomers are simply considered as "big atoms" neglecting their inner structure. One has to keep in mind that the thus obtained results only represent the actual scattering law for small scattering vector when $2\pi/Q$ is larger than the size of a monomer.

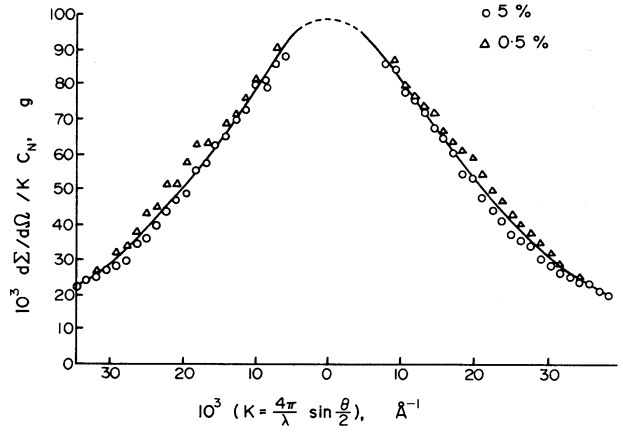

Figure 4.6: Partial differential cross section for protonated polystyrene in a deuterated polystyrene matrix [8]. The concentration of the protonated component is 5% (o) and 0.5% (Δ) respectively. The curve is a fit with the Debye function.

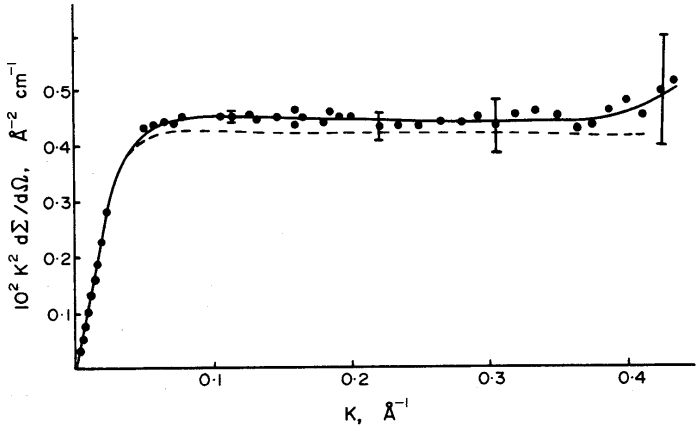

Figure 4.7: Kratky plot of the data from figure 4.6.

4.3 Dynamical Correlation Function

4.3.1 Correlation Spectroscopy

We consider an observable A of a system which fluctuates randomly because of the thermal motion of the system. A could be e.g. the pressure on the wall exerted by a gas in a cylinder or the particle density in a liquid. Figure 4.8 shows exemplarily the time-dependent value of a quantity A fluctuating around its average value $\langle A \rangle$.

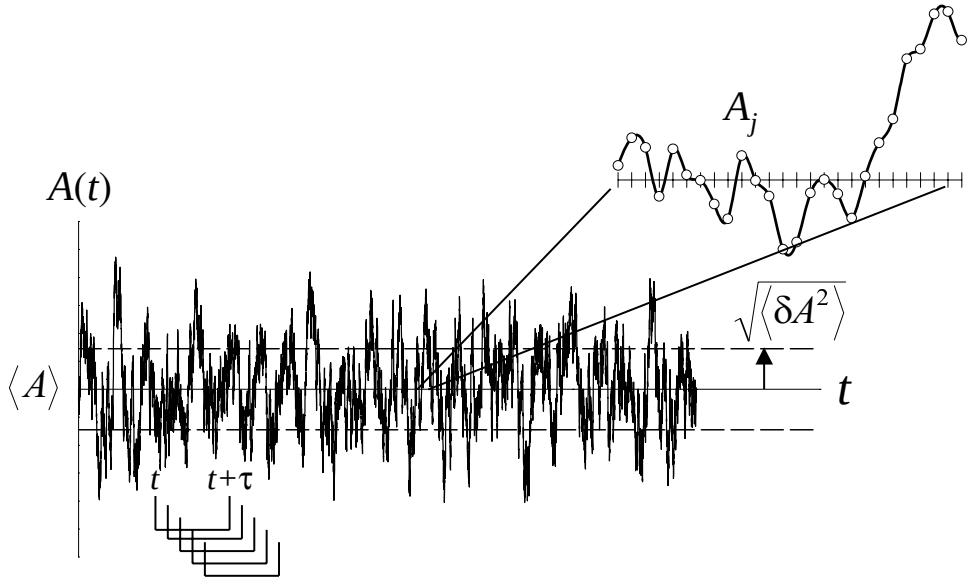

Figure 4.8: Fluctuating observable $A(t)$ of an ensemble of molecules as a function of time. The time axis is subdivided into discrete intervals of length Δt.

If one takes a time average over a long time interval as compared with the fluctuation periods one obtains a stationary result which is independent of the start of the time interval

$$\lim_{T\to\infty} \frac{1}{T} \int_{t_0}^{t_0+T} \mathrm{d}t A(t) = \text{const.} \equiv \langle A \rangle \tag{4.20}$$

but in general $A(t+\tau) \neq A(t)$. If τ is very small compared to typical times of the system $A(t+\tau)$ approaches the value of $A(t)$ which means that the both are correlated in time. As a measure of this correlation the autocorrelation function is introduced:

$$\langle A(0)A(\tau)\rangle = \lim_{T\to\infty} \frac{1}{T} \int_{t_0}^{t_0+T} \mathrm{d}t A(t)A(t+\tau)\,. \tag{4.21}$$

This function correlates the observable A with itself in a certain time displacement τ and then averages over all starting times.

In a real experiment (figure 4.8) this can be done by sampling values A_i at equidistant times $t_i = i\delta t$. Let j denote the index of the starting time ($t = j\delta t$), n the distance counted in time intervals ($\tau = n\delta t$), and N the number of intervals to be averaged ($T = N\delta t$).

Then equation (4.21) can be converted into a sum:

$$\langle A(0)A(\tau)\rangle = \lim_{N\to\infty} \frac{1}{N} \sum_{j=1}^{N} A_j A_{j+n} \,. \tag{4.22}$$

In optical correlation spectroscopy sums like (4.22) are calculated from the photodetector signal by special purpose computers. In this case A is the number of photons detected per time interval, i.e. the light intensity.

It is easy to see that the autocorrelation function has the following properties

$$\langle A(0)A(\tau)\rangle \;\leq\; \langle A(0)A(0)\rangle \equiv \langle A^2\rangle \tag{4.23}$$

$$\lim_{\tau\to\infty} \langle A(0)A(\tau)\rangle \;=\; \langle A\rangle^2 \,. \tag{4.24}$$

Figure 4.9 shows a simulation of data of a light scattering experiment. Such data could arise e.g. from scattering of polystyrene spheres in an aqueous dispersion.

The correlation function usually decays following a simple exponential law:

$$\langle A(0)A(\tau)\rangle = \langle A\rangle^2 + \left(\langle A^2\rangle - \langle A\rangle^2\right) \exp\left(-\tau/\tau_r\right) \tag{4.25}$$

where τ_r is the correlation time of the system. In general, also more complicated decays, e.g. involving multiple characteristic times, are possible. But the decay always takes places between the limits given by (4.23) and (4.24).

Alternatively, one can consider the fluctuations $\delta A(t) = A(t) - \langle A\rangle$, i.e. the deviations of the observable from its average. For its autocorrelation function follows:

$$\begin{aligned} \langle \delta A(0)\delta A(t)\rangle \;&=\; \langle A(0)A(\tau)\rangle - \langle A\rangle^2 \\ &=\; \langle \delta A^2\rangle \exp\left(-\tau/\tau_r\right) \,. \end{aligned} \tag{4.26}$$

The general result is that the fluctuation autocorrelation function decays starting from the variance of the observable, $\langle \delta A^2\rangle = \langle A^2\rangle - \langle A\rangle^2$ to zero.

The time-dependent autocorrelation function describes the temporal fluctuation behaviour of the system. In the case presented here of a polymer colloid the characteristic time is directly connected to the diffusion constant: ${\tau_r}^{-1} = DQ^2$.

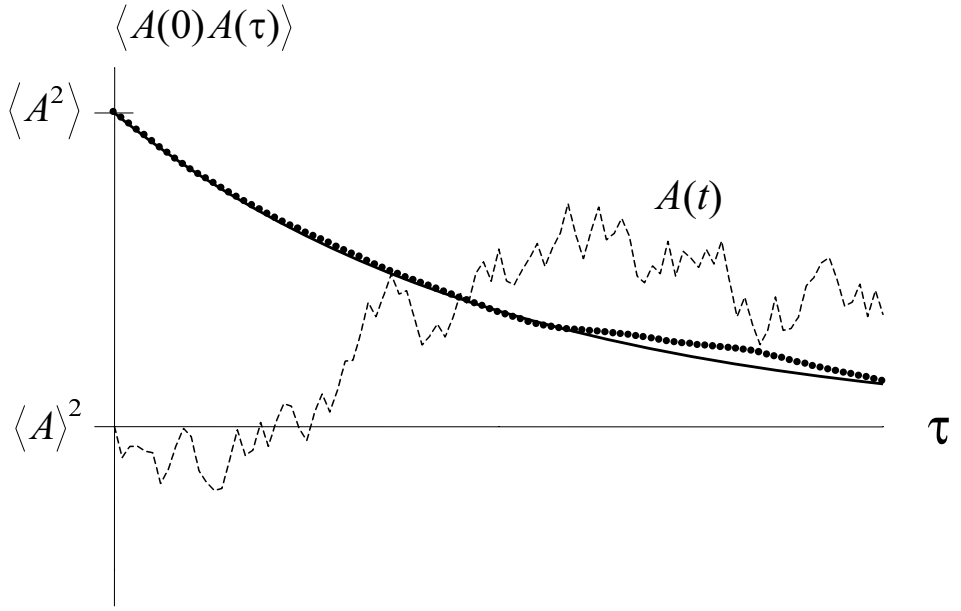

Figure 4.9: Simulated result of a dynamic light scattering experiment. The circular dots show the output of the correlator electronics. The continuous curve is the expected exponential decay (4.25). The dashed line shows the underlying fluctuating intensity.

4.3.2 The Van Hove Correlation Function

In order to consider inelastic scattering the differential cross section $\mathrm{d}\sigma/\mathrm{d}\Omega$ is generalized with respect to its dependence on the energy transfer $\hbar\omega$. This leads to the double differential cross section in quantum mechanical notation:

$$\frac{\partial^2\sigma}{\partial\Omega\partial\omega} = \frac{k'}{k}\sum_{\lambda,\sigma} P_\lambda P_\sigma \sum_{\lambda',\sigma'} \left| \sum_i \langle\lambda',\sigma'|b_i \exp(\mathrm{i}\underline{Q}\cdot\underline{\mathbf{r}}_i)|\lambda,\sigma\rangle \right|^2 \delta\left(\hbar\omega + E_\lambda - E_{\lambda'}\right) . \qquad (4.27)$$

Here, λ and σ describe the relevant space and spin quantum number respectively in the initial state of the scattering system and λ' and σ' those in the final state. P_λ and P_σ are the respective probabilities for the initial states λ and σ. The inner sum refers to all particles with scattering lengths b_i and single-particle coordinate operators $\underline{\mathbf{r}}_i$. k and k' are the wave vectors of the incident and scattered neutrons. The delta function expresses energy conservation: the energy transfer of the neutron $\hbar\omega$ is exactly compensated by the energy change of the quantum state of the scattering system $E_{\lambda'} - E_\lambda$. In the following we will neglect the spin coordinates for the sake of simplicity. We also do not consider

magnetic neutron scattering which would give rise to an additional term in the matrix element.

The route from expression (4.27) to the Van Hove correlation function starts with an integral representation of the delta function:

$$\delta\left(\hbar\omega + E_\lambda - E_{\lambda'}\right) = \frac{1}{2\pi\hbar}\int_{-\infty}^{\infty} \mathrm{d}t \exp\left(-\mathrm{i}\left(\omega + \frac{E_\lambda - E_{\lambda'}}{\hbar}\right)t\right) \tag{4.28}$$

which results from the fact that the delta function is the Fourier transform of a constant one. With this expression the matrix element in equation (4.27) can be written as a Fourier transform in time:

$$\begin{aligned}
& \left|\sum_i \langle\lambda'|b_i \exp(\mathrm{i}\underline{Q}\cdot\underline{\mathbf{r}}_i)|\lambda\rangle\right|^2 \delta\left(\hbar\omega + E_\lambda - E_{\lambda'}\right) \\
= \; & \frac{1}{2\pi\hbar}\int_{-\infty}^{\infty} \mathrm{d}t \exp(-\mathrm{i}\omega t) \exp\left(-\mathrm{i}\frac{E_\lambda}{\hbar}t\right) \exp\left(-\mathrm{i}\frac{E_{\lambda'}}{\hbar}t\right) \\
& \qquad \sum_i b_i \langle\lambda'|\exp(\mathrm{i}\underline{Q}\cdot\underline{\mathbf{r}}_i)|\lambda\rangle \sum_j b_j^* \langle\lambda|\exp(-\mathrm{i}\underline{Q}\cdot\underline{\mathbf{r}}_j)|\lambda'\rangle \\
= \; & \frac{1}{2\pi\hbar}\int_{-\infty}^{\infty} \mathrm{d}t \exp(-\mathrm{i}\omega t) \sum_{i,j} b_i b_j^* \langle\lambda|\exp(-\mathrm{i}\underline{Q}\cdot\underline{\mathbf{r}}_j)|\lambda'\rangle \\
& \qquad \langle\lambda'|\exp(\mathrm{i}E_{\lambda'}t/\hbar)\exp(\mathrm{i}\underline{Q}\cdot\underline{\mathbf{r}}_i)\exp(-\mathrm{i}E_\lambda t/\hbar)|\lambda\rangle
\end{aligned} \tag{4.29}$$

If $\mathbf{H}$ is the Hamiltonian of the scattering system, the fact that $|\lambda\rangle$ are energy eigenstates is expressed by

$$\mathbf{H}|\lambda\rangle = E_\lambda|\lambda\rangle\,. \tag{4.30}$$

Iterating this equation n times yields:

$$\mathbf{H}^n|\lambda\rangle = {E_\lambda}^n|\lambda\rangle\,. \tag{4.31}$$

By expanding the exponential into a power series one finally obtains from this relation

$$\exp(\mathrm{i}\mathbf{H}t/\hbar)|\lambda\rangle = \exp(\mathrm{i}E_\lambda t/\hbar)|\lambda\rangle\,. \tag{4.32}$$

With this result and the analogous one for λ' it is possible to replace the eigenvalues E_λ in (4.29) by the Hamiltonian $\mathbf{H}$:

$$\ldots\langle\lambda'|\exp(\mathrm{i}\mathbf{H}t/\hbar)\exp(\mathrm{i}\underline{Q}\cdot\underline{\mathbf{r}}_i)\exp(-\mathrm{i}\mathbf{H}t/\hbar)|\lambda\rangle\,. \tag{4.33}$$

In the picture of time dependent Heisenberg operators the application of the operator $\exp(\mathrm{i}\mathbf{H}t/\hbar)$ and its conjugate just means a propagation by time t:

$$\exp\left(\mathrm{i}\underline{Q}\cdot\underline{\mathbf{r}}_i(t)\right) = \exp(\mathrm{i}\mathbf{H}t/\hbar)\exp(\mathrm{i}\underline{Q}\cdot\underline{\mathbf{r}}_i(0))\exp(-\mathrm{i}\mathbf{H}t/\hbar) \tag{4.34}$$

where we can arbitrarily set $\underline{\mathbf{r}}_i = \underline{\mathbf{r}}_i(0)$ because of translation of time invariance. Using this result the final expression for the double differential cross section is obtained:

$$\begin{aligned}\frac{\partial^2\sigma}{\partial\Omega\partial\omega} &= \frac{k'}{k}\frac{1}{2\pi\hbar}\int_{-\infty}^{\infty}\mathrm{d}t\exp(-\mathrm{i}\omega t) \\ &\quad \sum_\lambda P_\lambda \sum_{i,j} b_i b_j^* \left\langle \lambda \left| \exp(-\mathrm{i}\underline{Q}\cdot\underline{\mathbf{r}}_j(0))\exp(\mathrm{i}\underline{Q}\cdot\underline{\mathbf{r}}_i(t)) \right| \lambda \right\rangle . \end{aligned} \tag{4.35}$$

(Here, the sum over λ' vanishes because of the completeness relation $\sum_{\lambda'}|\lambda'\rangle\langle\lambda'| = 1$.) This equation averages over the scattering length distribution (which may depend on the spin orientation distribution with respect to the incident neutron's spin). This produces coherent and incoherent scattering as explained in lecture 1. In addition the initial states of the scattering system are averaged weighted with the probability of their occurrence P_λ. The latter is given by the Boltzmann distribution

$$P_\lambda = \frac{1}{Z}\exp\left(-E_\lambda/k_\mathrm{B}T\right) \text{ with } Z = \sum_\lambda \exp\left(-E_\lambda/k_\mathrm{B}T\right) . \tag{4.36}$$

We now denote this thermal average by angular brackets $\langle\ldots\rangle$ while that over the scattering lengths be written as an overline $\overline{\ldots}$. Keeping in mind that for equal indices $b_i b_i^* = |b_i|^2$ has to be averaged while for unequal indices the scattering lengths itself will be averaged we end up with the usual separation into incoherent and coherent part:

$$\begin{aligned}\frac{\partial^2\sigma}{\partial\Omega\partial\omega} &= \sum_\lambda P_\lambda \\ &\quad \frac{k'}{k}\frac{\overline{|b|^2}-|\bar{b}|^2}{2\pi\hbar}\int_{-\infty}^{\infty}\mathrm{d}t\exp(-\mathrm{i}\omega t)\sum_i \left\langle \lambda \left| \exp(-\mathrm{i}\underline{Q}\cdot\underline{\mathbf{r}}_i(0))\exp(\mathrm{i}\underline{Q}\cdot\underline{\mathbf{r}}_i(t)) \right| \lambda \right\rangle \\ &\quad + \frac{k'}{k}\frac{|\bar{b}|^2}{2\pi\hbar}\int_{-\infty}^{\infty}\mathrm{d}t\exp(-\mathrm{i}\omega t)\sum_{i,j} \left\langle \lambda \left| \exp(-\mathrm{i}\underline{Q}\cdot\underline{\mathbf{r}}_i(0))\exp(\mathrm{i}\underline{Q}\cdot\underline{\mathbf{r}}_j(t)) \right| \lambda \right\rangle . \end{aligned} \tag{4.37}$$

The first term is the incoherent scattering. It involves the coordinate vector operators of the *same* atom at different times. The second, the coherent term correlates also *different* atoms at different times. The material dependent parts are now defined as the scattering functions

$$S_\mathrm{inc}(Q,\omega) \equiv \frac{1}{2\pi\hbar N}\int_{-\infty}^{\infty}\mathrm{d}t\exp(-\mathrm{i}\omega t)\sum_i \langle\exp(-\mathrm{i}\underline{Q}\cdot\underline{\mathbf{r}}_i(0))\exp(\mathrm{i}\underline{Q}\cdot\underline{\mathbf{r}}_i(t))\rangle \tag{4.38}$$

$$S_\mathrm{coh}(Q,\omega) \equiv \frac{1}{2\pi\hbar N}\int_{-\infty}^{\infty}\mathrm{d}t\exp(-\mathrm{i}\omega t)\sum_{i,j} \langle\exp(-\mathrm{i}\underline{Q}\cdot\underline{\mathbf{r}}_i(0))\exp(\mathrm{i}\underline{Q}\cdot\underline{\mathbf{r}}_j(t))\rangle . \tag{4.39}$$

In terms of the scattering functions the double differential cross section can be written as

$$\frac{\partial^2\sigma}{\partial\Omega\partial\omega} = \frac{k'}{k}N\left(\left(\overline{|b|^2}-|\bar{b}|^2\right)S_\mathrm{inc}(\underline{Q},\omega) + |\bar{b}|^2 S_\mathrm{coh}(\underline{Q},\omega)\right) . \tag{4.40}$$

In addition it is often useful to define the intermediate scattering function which denotes the time dependent parts of definitions (4.38) and (4.39) before Fourier transform:

$$S_{\mathrm{inc}}(\underline{Q},t) \equiv \frac{1}{N}\sum_i \langle \exp(-\mathrm{i}\underline{Q}\cdot\underline{\mathbf{r}}_i(0))\exp(\mathrm{i}\underline{Q}\cdot\underline{\mathbf{r}}_i(t))\rangle \tag{4.41}$$

$$S_{\mathrm{coh}}(\underline{Q},t) \equiv \frac{1}{N}\sum_{i,j} \langle \exp(-\mathrm{i}\underline{Q}\cdot\underline{\mathbf{r}}_i(0))\exp(\mathrm{i}\underline{Q}\cdot\underline{\mathbf{r}}_j(t))\rangle\,. \tag{4.42}$$

If one compares this result with the definition of the structure factor (4.8–4.11) one recognizes that $S_{\mathrm{coh}}(Q,\omega)$ is in an analogous way the Fourier transform in space and time of a dynamical pair correlation function $G(\underline{r},t)$:

$$G(\underline{r},t) = \left(\frac{1}{2\pi}\right)^3 \int \mathrm{d}^3Q \exp\left(-\mathrm{i}\underline{Q}\cdot\underline{r}\right) \frac{1}{N}\sum_{i,j}\left\langle \exp\left(-\mathrm{i}\underline{Q}\cdot\underline{\mathbf{r}}_i(0)\right)\exp\left(\mathrm{i}\underline{Q}\cdot\underline{\mathbf{r}}_j(t)\right)\right\rangle\,. \tag{4.43}$$

The derivation of the relation between the coherent dynamical structure factor $S_{\mathrm{coh}}(Q,\omega)$ and the generalized pair correlation function requires a strict quantum mechanical calculation. This problem results from the fact that the coordinate vector operators commute only at identical times. Therefore, in all algebraic manipulations the order of $\underline{\mathbf{r}}_i(0)$ and $\underline{\mathbf{r}}_i(t)$ must not be interchanged.

To begin, one writes the operator $\exp\left(-\mathrm{i}\underline{Q}\cdot\underline{\mathbf{r}}_i(0)\right)$ as the Fourier transform of the delta function:

$$\exp\left(-\mathrm{i}\underline{Q}\cdot\underline{\mathbf{r}}_i(0)\right) = \int \mathrm{d}^3r' \delta\left(\underline{r}' - \underline{\mathbf{r}}_i(0)\right)\exp(-\mathrm{i}\underline{Q}\cdot\underline{r}')\,. \tag{4.44}$$

Using this expression equation (4.43) can be rewritten as

$$\begin{aligned} G(\underline{r},t) &= \left(\frac{1}{2\pi}\right)^3 \frac{1}{N}\sum_{i,j}\Bigg\langle \int \mathrm{d}^3r' \delta\left(\underline{r}' - \underline{\mathbf{r}}_i(0)\right) \\ &\qquad \underbrace{\int \mathrm{d}^3Q \exp\left(-\mathrm{i}\underline{Q}\cdot\underline{r} - \mathrm{i}\underline{Q}\cdot\underline{r}' + \mathrm{i}\underline{Q}\cdot\underline{\mathbf{r}}_j(t)\right)}_{=(2\pi)^3\delta\left(\underline{r}+\underline{r}'-\underline{\mathbf{r}}_j(t)\right)}\Bigg\rangle \\ &= \frac{1}{N}\sum_{i,j}\int \mathrm{d}^3r' \left\langle \delta\left(\underline{r}-\underline{r}'+\underline{\mathbf{r}}_i(0)\right)\delta\left(\underline{r}'-\underline{\mathbf{r}}_j(t)\right)\right\rangle \end{aligned} \tag{4.45}$$

without changing the order of the operators at different times.

Now the particle density operator is introduced as a sum over delta functions at the particle position operators:

$$\boldsymbol{\rho}(\underline{r},t) \equiv \sum_i \delta\left(\underline{r} - \underline{\mathbf{r}}_i(t)\right)\,. \tag{4.46}$$

With this definition the pair correlation function can be written as time-dependent density-density correlation function:

$$G(\underline{r},t) = \frac{1}{N}\int \mathrm{d}^3r' \left\langle \boldsymbol{\rho}(\underline{r}'-\underline{r},0)\boldsymbol{\rho}(\underline{r}',t)\right\rangle \ . \tag{4.47}$$

With this form of the dynamic pair correlation function the dynamical structure factor can be—analogously to equation (4.11)—written as the double Fourier transform of the correlator of the particle density:

$$S_{\mathrm{coh}}(\underline{Q},\omega) = \int_{-\infty}^{\infty} \mathrm{d}t \exp(-\mathrm{i}\omega t)\int \mathrm{d}^3r \int \mathrm{d}^3r' \exp\left(\mathrm{i}\underline{Q}\cdot\underline{r}\right)\left\langle \boldsymbol{\rho}(\underline{r}'-\underline{r},0)\boldsymbol{\rho}(\underline{r}',t)\right\rangle \ . \tag{4.48}$$

We now define the density operator in reciprocal space as the Fourier transform of (4.46):

$$\boldsymbol{\rho}_{\underline{Q}}(t) \equiv \sum_i \exp\left(\mathrm{i}\underline{Q}\cdot\underline{\mathbf{r}}_i(t)\right) \tag{4.49}$$

and obtain for the dynamic structure factor

$$S_{\mathrm{coh}}(\underline{Q},\omega) = \frac{1}{2\pi\hbar N}\int_{-\infty}^{\infty} \mathrm{d}t \exp(-\mathrm{i}\omega t)\left\langle \boldsymbol{\rho}_{\underline{Q}}(0)\boldsymbol{\rho}_{-\underline{Q}}(t)\right\rangle \ . \tag{4.50}$$

Correspondingly, the intermediate scattering function is

$$S_{\mathrm{coh}}(\underline{Q},t) = \frac{1}{N}\left\langle \boldsymbol{\rho}_{\underline{Q}}(0)\boldsymbol{\rho}_{-\underline{Q}}(t)\right\rangle \tag{4.51}$$

which after insertion of (4.49) turns out to be equivalent to (4.42).

Analogously, one can define a self correlation function by setting $i = j$ in the preceding equations leading to

$$G_{\mathrm{s}}(\underline{r},t) = \frac{1}{N}\sum_i \int \mathrm{d}^3r' \left\langle \delta\left(\underline{r}-\underline{r}'+\underline{\mathbf{r}}_i(0)\right)\delta\left(\underline{r}'-\underline{\mathbf{r}}_i(t)\right)\right\rangle \tag{4.52}$$

as the equivalent of (4.45).

The pair correlation function has some general properties:

1. For spatially homogeneous systems the integrand in (4.47) is independent of $\underline{r}'$ which can be arbitrarily set to the origin $\underline{0}$:

$$G(\underline{r},t) = \frac{V}{N}\left\langle \boldsymbol{\rho}(-\underline{r},0)\boldsymbol{\rho}(\underline{0},t)\right\rangle = \frac{1}{\rho_0}\left\langle \boldsymbol{\rho}(\underline{0},0)\boldsymbol{\rho}(\underline{r},t)\right\rangle \ . \tag{4.53}$$

2. The pair correlation function has the following asymptotic behaviour: For fixed distance and $t \to \infty$ or fixed time and $r \to \infty$ the averages in equation (4.47) can be executed separately and in consequence

$$G(\underline{r}, t) \to \frac{1}{N} \int \mathrm{d}^3 r' \, \langle \boldsymbol{\rho}(\underline{r}' - \underline{r}, 0) \rangle \, \langle \boldsymbol{\rho}(\underline{r}', t) \rangle = \rho_0 \, . \tag{4.54}$$

3. For $t = 0$ the operators commute and the convolution integral of equation (4.47) can be carried out:

$$G(\underline{r}, 0) = \frac{1}{N} \sum_{i,j} \left\langle \delta \left(\underline{r} + \underline{\mathbf{r}}_i(0) - \underline{\mathbf{r}}_j(0) \right) \right\rangle \, . \tag{4.55}$$

For indistinguishable particles the relation to the static pair correlation function as defined in (4.6) can be drawn. Because of the identity of the particles we can set $i = 1$ in (4.55) and drop the average over i:

$$G(\underline{r}, 0) = \sum_{j} \left\langle \delta \left(\underline{r} + \underline{\mathbf{r}}_1(0) - \underline{\mathbf{r}}_j(0) \right) \right\rangle = \delta(\underline{r}) + \sum_{j \neq 1} \left\langle \delta \left(\underline{r} + \underline{\mathbf{r}}_1(0) - \underline{\mathbf{r}}_j(0) \right) \right\rangle \, . \tag{4.56}$$

We now consider the average number of particles $\delta N(\underline{r})$ in a volume δV at a vector distance $\underline{r}$ from a given particle at $\underline{r}_1$. It is obviously given by the integral over the second term in the preceding expression which for small δV can be written as

$$\delta N(\underline{r}) = \delta V \sum_{j \neq 1} \left\langle \delta \left(\underline{r} + \underline{\mathbf{r}}_1(0) - \underline{\mathbf{r}}_j(0) \right) \right\rangle \, . \tag{4.57}$$

Using the definition (4.6) and the expression for the number density in homogeneous fluids (4.2) one can relate $\delta N(\underline{r})$ also to the static pair correlation function:

$$\delta N(\underline{r}) = \rho_0 g(\underline{r}) \delta V \, . \tag{4.58}$$

Finally, by comparison of the last three equations we get a relation between the dynamic correlation function at time zero and its static counterpart:

$$G(\underline{r}, 0) = \delta(\underline{r}) + \rho_0 g(\underline{r}) \, . \tag{4.59}$$

This equation expresses the fact that the diffraction experiment ($g(r)$) gives an average snapshot picture ($G(r, 0)$) of the sample.

In the classical approximation the operators commute always, especially also at different times. Then the integrals of equations (4.45) and (4.52) can be carried out and yield

$$G^{\mathrm{cl}}(\underline{r}, t) = \frac{1}{N} \sum_{i,j} \delta(\underline{r} - \underline{r}_j(t) + \underline{r}_i(0)) \text{ and} \tag{4.60}$$

$$G_{\mathrm{s}}^{\mathrm{cl}}(\underline{r}, t) = \frac{1}{N} \sum_{i} \delta(\underline{r} - \underline{r}_i(t) + \underline{r}_i(0)) \, , \tag{4.61}$$

respectively. The former equation expresses the probability to find *any* particle at a time t in a distance $\underline{r}$ from another at time 0. The latter equation denotes this probability for the *same* particle. It therefore depends only on the particle's displacement during a time interval $\Delta\underline{r}_i(t) = \underline{r}_i(t) - \underline{r}_i(0)$ leading to a simple expression for the intermediate incoherent scattering function:

$$S_{\mathrm{inc}}^{\mathrm{cl}}(\underline{Q}, t) = \frac{1}{N} \sum_i \left\langle \exp\left(-\mathrm{i}\underline{Q} \cdot \Delta\underline{r}_i(t)\right)\right\rangle . \tag{4.62}$$

In certain cases this expression can be further simplified using the "Gaussian approximation"[7]:

$$S_{\mathrm{inc}}^{\mathrm{Gauss}}(Q, t) = \exp\left(-\frac{1}{6}Q^2\langle\Delta r^2(t)\rangle\right) . \tag{4.63}$$

Here $\langle\Delta r^2(t)\rangle$ is the average mean squared displacement which often follows simple laws, e.g. $\langle\Delta r^2(t)\rangle = 6Dt$ for simple diffusion. Because one of the prerequisites of the Gaussian approximation is that all particles move statistically in the same way (dynamic homogeneity) the particle average and the index i vanish. An analogous expression can be derived for the coherent scattering.

In order to decide whether the classical approximation can be used the following rule has to be taken into account: Quantum effects play a rôle if the distance of two particles is of the order of the DeBroglie wavelength $\lambda_{\mathrm{B}} = \hbar/\sqrt{2m_{\mathrm{sc}}k_{\mathrm{B}}T}$ or if the times considered are smaller than $\hbar/k_{\mathrm{B}}T$.

Figure 4.10 schematically shows on the left side the behaviour of the correlation functions $G(r, t)$ and $G_{\mathrm{s}}(r, t)$ for a simple liquid (in classical approximation). On the right side the corresponding intermediate scattering functions $S_{\mathrm{coh}}(Q, t)$ and $S_{\mathrm{inc}}(Q, t)$ are displayed:

- For $t = 0$ the self correlation function is given by a delta function at $r = 0$. The pair correlation function follows the static correlation function $g(r)$. The intermediate scattering functions are constant one for the incoherent and the static structure factor for the coherent.

- For intermediate times the self correlation function broadens to a bell-shaped function while the pair correlation function loses its structure. The intermediate scat-

[7] For solids the long-time limit of this equation is called the Lamb-Mößbauer factor. Its coherent counterpart is the Debye-Waller factor.

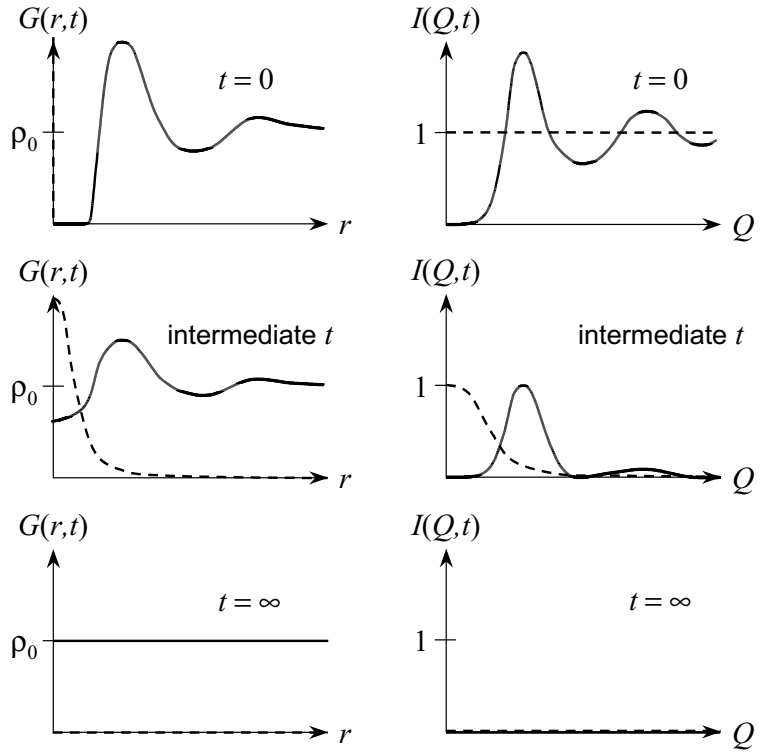

Figure 4.10: Schematic Comparison of the correlation functions $G(r,t)$, $G_s(r,t)$ and the intermediate scattering functions $S_{coh}(Q,t)$, $S_{inc}(Q,t)$ for a simple liquid at different times. The solid lines denote the coherent case, the dashed lines the self/incoherent.

tering functions decay with respect to the $t = 0$ value. The decay is faster for higher Q and (in the coherent case) less pronounced at the structure factor maximum.

- The long time limit of the pair correlation function is the average density ρ_0 while the self correlation simply vanishes (in a liquid). In consequence both the coherent and the incoherent intermediate scattering function decay to zero for long times and any Q.

4.4 Scattering from an Ideal Gas

We consider a gas of N atoms in a volume V neglecting the spin coordinates σ and assume that all scattering lengths are identical $b_i = 1$. The wave function of a free atom confined

to a volume V is simply a plane wave with wave vector $\underline{\kappa}$:

$$\Psi_{\underline{\kappa}}(\underline{r}) = \langle \underline{r}|\underline{\kappa}\rangle = \frac{1}{\sqrt{V}} \exp(\mathrm{i}\underline{\kappa}\cdot\underline{r})\,. \tag{4.64}$$

Using this expression, the matrix element in the double differential cross section (4.27) can immediately be calculated:

$$\langle \underline{\kappa}'|\exp \mathrm{i}\underline{Q}\cdot\underline{\mathbf{r}}|\underline{\kappa}\rangle = \frac{1}{V}\int_V \mathrm{d}^3 r \exp(\mathrm{i}(\underline{Q}+\underline{\kappa}-\underline{\kappa}')\cdot\underline{r}) = \delta(\underline{Q}+\underline{\kappa}-\underline{\kappa}')\,. \tag{4.65}$$

The resulting delta function expresses the momentum conservation. Only if momentum is conserved the matrix element is 1—otherwise zero.

In the second step we have to consider energy conservation. The energy of the atom with wave vector κ is

$$E_\kappa = \frac{\hbar^2}{2m_{\mathrm{sc}}}\kappa^2 \tag{4.66}$$

where m_{sc} is the mass of the scattering atom. For the evaluation of the delta function in (4.27) we need the energy difference between the states κ and κ'. Because of the delta function factor (4.65) only such states with $\underline{\kappa}' = \underline{\kappa} - \underline{Q}$ have to be considered and for those the energy difference is:

$$E_\kappa - E_{\kappa'} = -\frac{\hbar}{2m_{\mathrm{sc}}}\left(Q^2 + 2\underline{Q}\cdot\underline{\kappa}\right)\,. \tag{4.67}$$

With this result one can calculate the scattering function:

$$S(Q,\omega) = \sum_{\underline{\kappa}} P_{\underline{\kappa}}\,\delta\left(\hbar\omega - \frac{\hbar}{2m_{\mathrm{sc}}}\left(Q^2 + 2\underline{Q}\cdot\underline{\kappa}\right)\right)\,. \tag{4.68}$$

In the limit of a large volume V, $\underline{\kappa}$ becomes a continuous variable. In addition only the component of $\underline{\kappa}$ parallel to Q is relevant. Therefore, (4.68) can be written as a one-dimensional integral:

$$S(Q,\omega) = \int_{-\infty}^{\infty} \mathrm{d}\kappa P_\kappa\,\delta\left(\hbar\omega - \frac{\hbar}{2m_{\mathrm{sc}}}\left(Q^2 + 2Q\kappa\right)\right)\,. \tag{4.69}$$

The probability of a momentum state κ follows from the Boltzmann distribution:

$$P_\kappa = \frac{1}{Z}\exp\left(-\frac{\hbar^2\kappa^2}{2m_{\mathrm{sc}}k_{\mathrm{B}}T}\right) \tag{4.70}$$

with the state sum being

$$Z = \int_{-\infty}^{\infty}\mathrm{d}\kappa \exp\left(-\frac{\hbar^2\kappa^2}{2m_{\mathrm{sc}}k_{\mathrm{B}}T}\right) = \frac{\sqrt{2\pi m_{\mathrm{sc}}k_{\mathrm{B}}T}}{\hbar}\,. \tag{4.71}$$

Insertion of this result into (4.69) yields:

$$S(Q,\omega) = \frac{\hbar}{\sqrt{2\pi m_{\rm sc} k_{\rm B} T}} \int_{-\infty}^{\infty} {\rm d}\kappa \exp\left(-\frac{\hbar^2\kappa^2}{2m_{\rm sc}k_{\rm B}T}\right) \delta\left(\hbar\omega - \frac{\hbar}{2m_{\rm sc}}\left(Q^2 + 2Q\kappa\right)\right) . \quad (4.72)$$

Substitution of $w \equiv \hbar\omega - \frac{\hbar}{2m_{\rm sc}}\left(Q^2 + 2Q\kappa\right)$ into this integral allows the evaluation of the delta function:

$$\begin{aligned} S(Q,\omega) &= \frac{\hbar}{\sqrt{2\pi m_{\rm sc} k_{\rm B} T}} \\ &\qquad \int_{-\infty}^{\infty} {\rm d}w \frac{m_{\rm sc}}{\hbar^2 Q} \exp\left(-\frac{\hbar^2}{2m_{\rm sc}k_{\rm B}T}\left(\frac{m_{\rm sc}}{\hbar^2 Q}(\hbar\omega - w) - \frac{Q}{2}\right)^2\right) \delta(w) \\ &= \sqrt{\frac{1}{4\pi E_{\rm r} k_{\rm B} T}} \exp\left(-\frac{(\hbar\omega - E_{\rm r})^2}{4E_{\rm r}k_{\rm B}T}\right) \end{aligned} \quad (4.73)$$

with $E_{\rm r} = \hbar^2 Q^2/2m_{\rm sc}$ being the recoil energy experienced by the atom during the scattering event. Thus, the dynamical structure factor of an ideal gas is a Gaussian centred around the recoil energy for a given Q. The width of the Gaussian $\sqrt{2E_{\rm r}k_{\rm B}T} = \sqrt{k_{\rm B}T/m_{\rm sc}}\hbar Q$ increases with temperature and scattering vector Q.

Double inverse Fourier transform with respect to ω and Q gives the correlation function $G(r,t)$:

$$\begin{aligned} S(Q,t) &= \hbar \int_{-\infty}^{\infty} {\rm d}\omega \exp({\rm i}\omega t) \sqrt{\frac{1}{4\pi E_{\rm r} k_{\rm B} T}} \exp\left(-\frac{(\hbar\omega - E_{\rm r})^2}{4E_{\rm r}k_{\rm B}T}\right) \\ &= \exp\left(-\frac{Q^2}{2m_{\rm sc}}\left(k_{\rm B}Tt^2 - {\rm i}\hbar t\right)\right) , \end{aligned} \quad (4.74)$$

$$\begin{aligned} G(r,t) &= \left(\frac{1}{2\pi}\right)^3 \int {\rm d}^3 Q \exp(-{\rm i}\underline{Q}\cdot\underline{r}) \exp\left(-\frac{Q^2}{2m_{\rm sc}}\left(k_{\rm B}Tt^2 - {\rm i}\hbar t\right)\right) \\ &= \left(\frac{m_{\rm sc}}{2\pi k_{\rm B}Tt(t - {\rm i}\hbar/k_{\rm B}T)}\right)^{3/2} \exp\left(-\frac{m_{\rm sc}r^2}{2k_{\rm B}Tt(t - {\rm i}\hbar/k_{\rm B}T)}\right) . \end{aligned} \quad (4.75)$$

Because of the quantum mechanical nature of the underlying dynamics both $S(Q,t)$ and $G(r,t)$ have an imaginary part.

The same result can be obtained via the Van Hove correlation function. For this route we start with equation (4.39) for which we have to calculate $\exp({\rm i}\underline{Q}\cdot\underline{\mathbf{r}}(t))$ for a free atom. This can be done using the equation of motion

$${\rm i}\hbar\frac{\rm d}{{\rm d}t}\exp({\rm i}\underline{Q}\cdot\underline{\mathbf{r}}(t)) = \left[\exp({\rm i}\underline{Q}\cdot\underline{\mathbf{r}}(t)), \mathbf{H}\right] \quad (4.76)$$

where

$$\mathbf{H} = \frac{1}{2m_{\rm sc}}\mathbf{p}^2 \quad (4.77)$$

is the Hamiltonian of a free atom and $\mathbf{p}$ the momentum operator. In the following the time dependent operator $\exp(\mathrm{i}\underline{Q}\cdot\underline{\mathbf{r}}(t))$ shall be calculated. This is done using the equation of motion

$$\mathrm{i}\hbar\frac{\mathrm{d}}{\mathrm{d}t}\exp(\mathrm{i}\underline{Q}\cdot\underline{\mathbf{r}}(t)) = \left[\exp(\mathrm{i}\underline{Q}\cdot\underline{\mathbf{r}}(t)), \mathbf{H}\right] . \tag{4.78}$$

Here, the bracket on the right hand side is the commutator. In analogy to equation (4.34)

$$\frac{1}{2m_{\mathrm{sc}}}\left[\exp(\mathrm{i}\underline{Q}\cdot\underline{\mathbf{r}}(t)), \mathbf{p}^2\right] = \frac{1}{2m_{\mathrm{sc}}}\exp(\mathrm{i}t\mathbf{H})\left[\exp(\mathrm{i}\underline{Q}\cdot\underline{\mathbf{r}}(t)), \mathbf{p}^2\right]\exp(-\mathrm{i}t\mathbf{H}) \tag{4.79}$$

holds. The commutator at equal times on the right hand side of the last equation can easily be calculated. For this purpose one uses the coordinate representation $\underline{\mathbf{p}} = -\mathrm{i}\hbar\underline{\nabla}$. By calculation of the derivatives

$$\left[\exp(\mathrm{i}\underline{Q}\cdot\underline{\mathbf{r}}(t)), \mathbf{p}^2\right] = -\hbar\exp(\mathrm{i}\underline{Q}\cdot\underline{\mathbf{r}}(0))\left(\hbar Q^2 + 2\underline{Q}\cdot\underline{\mathbf{p}}\right) \tag{4.80}$$

follows. Since $\underline{\mathbf{p}}$ commutes with the Hamiltonian in the equation of motion the Hamiltonian can be applied directly on $\underline{\mathbf{r}}(0)$:

$$\mathrm{i}\hbar\frac{\mathrm{d}}{\mathrm{d}t}\exp(\mathrm{i}\underline{Q}\cdot\underline{\mathbf{r}}(t)) = -\frac{\hbar}{2m_{\mathrm{sc}}}\exp(\mathrm{i}\underline{Q}\cdot\underline{\mathbf{r}}(0))\left(\hbar Q^2 + 2\underline{Q}\cdot\underline{\mathbf{p}}\right) \tag{4.81}$$

This differential equation can be solved immediately and one obtains for the time dependent operator:

$$\exp(\mathrm{i}\underline{Q}\cdot\underline{\mathbf{r}}(t)) = \exp(\mathrm{i}\underline{Q}\cdot\underline{\mathbf{r}}(0))\exp\left(\frac{\mathrm{i}t}{2m_{\mathrm{sc}}}\left(\hbar Q^2 + 2\underline{Q}\cdot\underline{\mathbf{p}}\right)\right) . \tag{4.82}$$

With this result the correlator in the scattering function (4.39) can be calculated:

$$\left\langle\exp(-\mathrm{i}\underline{Q}\cdot\underline{\mathbf{r}}(0))\exp(\mathrm{i}\underline{Q}\cdot\underline{\mathbf{r}}(t))\right\rangle = \exp\left(\frac{\mathrm{i}\hbar Q^2}{2m_{\mathrm{sc}}}\right)\left\langle\exp\left(\frac{\mathrm{i}\hbar\underline{Q}\cdot\underline{\mathbf{p}}}{2m_{\mathrm{sc}}}\right)\right\rangle . \tag{4.83}$$

As in equation (4.72) the average is taken by using the Boltzmann factor yielding

$$\left\langle\exp\left(\frac{\mathrm{i}\hbar\underline{Q}\cdot\underline{\mathbf{p}}}{2m_{\mathrm{sc}}}\right)\right\rangle = \exp\left(-\frac{t^2Q^2k_{\mathrm{B}}T}{2m_{\mathrm{sc}}}\right) . \tag{4.84}$$

Insertion into (4.83) gives

$$\left\langle\exp(-\mathrm{i}\underline{Q}\cdot\underline{\mathbf{r}}(0))\exp(\mathrm{i}\underline{Q}\cdot\underline{\mathbf{r}}(t))\right\rangle = \exp\left(-\frac{Q^2}{2m_{\mathrm{sc}}}\left(t^2k_{\mathrm{B}}T - \mathrm{i}\hbar t\right)\right) . \tag{4.85}$$

identical to equation (4.74). Thus using the Van Hove correlation function we obtain the same result as was originally derived directly from the definition of the scattering function.

With this example we can also demonstrate that neglecting the operator character of the position vectors leads to a wrong result. If we write the scattering function using the classical expression (4.60)

$$S^{\mathrm{cl}}(Q,\omega) = \frac{1}{2\pi\hbar}\int_{-\infty}^{\infty} \mathrm{d}t \exp(-\mathrm{i}\omega t)\left\langle \exp\left(-\mathrm{i}\underline{Q}\cdot(\underline{r}(t)-\underline{r}(0))\right)\right\rangle \tag{4.86}$$

is obtained. For a free atom we have $\underline{r}(t) = \underline{r}(0) + t\underline{p}/m_{\mathrm{sc}}$. Inserting this expression into (4.86) and averaging leads to:

$$S^{\mathrm{cl}}(Q,\omega) = \sqrt{\frac{1}{4\pi E_{\mathrm{r}} k_{\mathrm{B}} T}}\exp\left(-\frac{\omega^2 m_{\mathrm{sc}}}{2k_{\mathrm{B}}TQ^2}\right). \tag{4.87}$$

Comparison with (4.73) shows that this result is wrong by neglecting the recoil energy term. Instead of being centred at E_{r} the expression (4.87) is symmetric with respect to $\omega = 0$.

References

[1] G. E. Bacon: "Neutron Diffraction" (Clarendon Press, Oxford, 1975).

[2] G. E. Bacon (ed.): "Fifty Years Of Neutron Diffraction: The Advent Of Neutron Scattering" (Adam Hilger, Bristol, 1986).

[3] S. W. Lovesey: "Theory of Neutron Scattering from Condensed Matter" (Clarendon Press, Oxford, 1984).

[4] G. L. Squires: "Introduction to the theory of thermal neutron scattering" (Cambridge University Press, Cambridge, 1978).

[5] M. Bée: "Quasielastic neutron scattering" (Adam Hilger, Bristol, 1988).

[6] G. Placzek, *Phys. Rev.* **86** 377 (1952).

[7] J. L. Yarnell, M. J. Katz, R. G. Wenzel, S. H. Koenig, *Phys. Rev. A* **7** 2130 (1973).

[8] G. D. Wignall, D. G. H. Ballard, J. Schelten, *Eur. Polym. J.* **10** 861 (1973).

5

Continuum Description: Grazing Incidence Neutron Scattering

Oliver H. Seeck and Emmanuel Kentzinger

5. Continuum description: Grazing Incidence Neutron Scattering

O.H. Seeck and E. Kentzinger
IFF-Streumethoden, FZ Jülich

5.1 Introduction

When studying solids or soft matter the explicit molecular structure is not always of particular importance. Quite often the properties investigated are long ranged and not directly connected with the atoms or their positions. One example is a material with a continuous ferromagnetic phase transition: Far below a well defined temperature (the critical temperature called Curie temperature) the material is in a complete ferromagnetic state. Far above no ferromagnetic behavior can be detected. Close to the critical temperature magnetic fluctuations appear. The typical width of the magnetic areas is in the range of several nanometers up to macroscopic distances depending on the temperature (see Fig. 5.1a). The width is basically independent of the lattice spacing or the particular kind of atoms. Therefore, the knowledge of the detailed molecular structure is not necessary to explain the physical properties of ferromagnets.

Other examples are surfaces or layer systems. The properties of the samples such as film thicknesses or in-plane correlation lengths are usually also long ranged compared to the atomic distances and the information about the exact atomic positions is not relevant (see Fig. 5.1b).

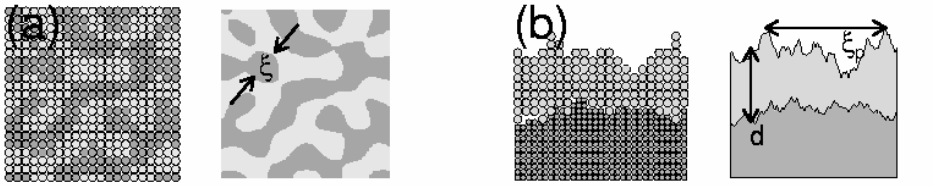

Figure 5.1: *Sketch of systems with relevant mesoscopic or macroscopic properties. (a) Ferromagnet close to the Curie temperature. Ordered regions with a correlation length* ξ *exist. (b) Monolayer system. The layer thickness* d *and the in-plane correlation length of the rough surface* ξ_p *are much larger than the atomic spacing. The left picture of each example shows the real atomic structure the right part the approximation as a continuous system.*

A straightforward method to investigate mesoscopic length scales without taking into account the exact molecular structure of the samples is the small angle scattering. 'Small angle' in this case means that the mean value of the wave vector transfer $|\underline{Q}|$ of the scattered beam is much smaller than the typical reciprocal spacing of the atoms in the sample (e.g., the reciprocal lattice vector $|\underline{a}^*|$ for a crystal with cubic symmetry). In this case the effects of the atomic structure on the scattered signal are negligible. This is schematically explained in Figure 5.2.

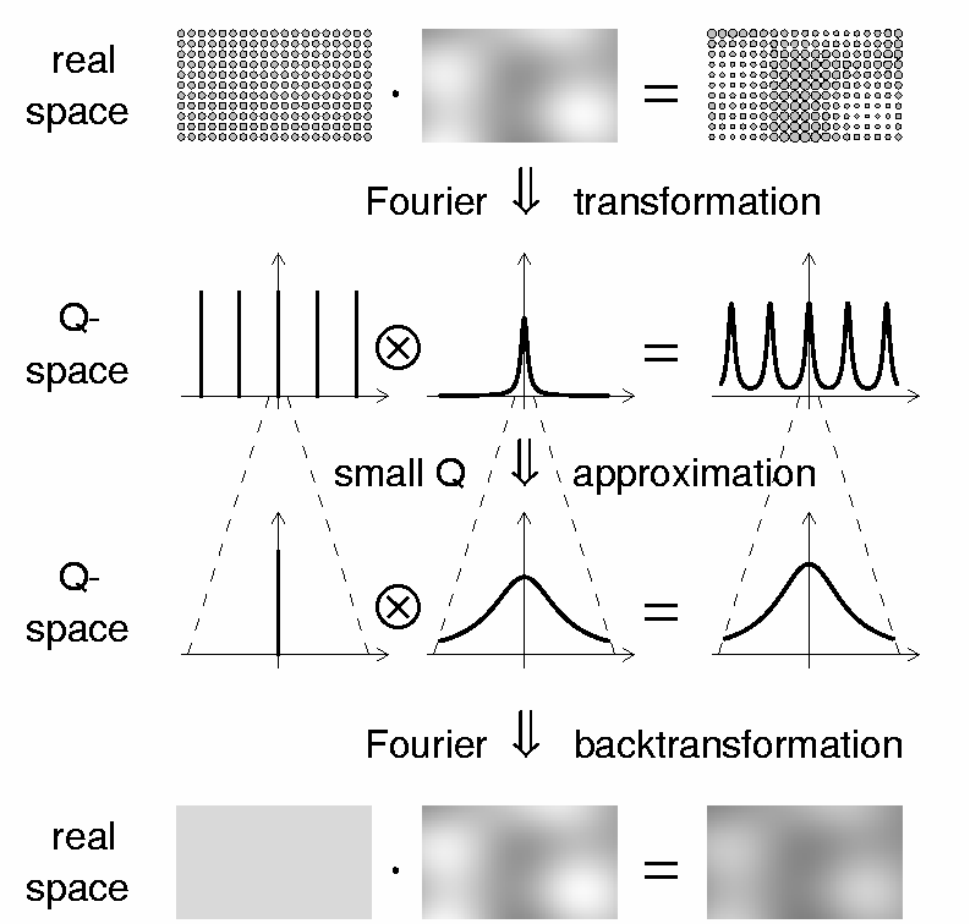

Figure 5.2: *Principles of small angle scattering. The method is not sensitive to the exact atomic structure but only to mesoscopic or macroscopic length scales. Therefore, samples can be treated as continuous systems. The operator* $\otimes$ *denotes the convolution of two functions. A more detailed explanation is given in the text.*

Starting point is the exact atomic structure of the sample. In this section a crystal with some density modulations is chosen (Fig. 5.2 top row). The potential $V(\underline{r})$ of such a system can be written as a product of the undisturbed infinite crystal lattice potential $V_{\text{latt}}(\underline{r})$ and the modulation $V_{\text{mod}}(\underline{r})$. As it was shown in previous sections in Born approximation the scattered intensity

$$I(\underline{Q}) \sim |A(\underline{Q})|^2 \sim \left| \int V(\underline{r}) \exp(i\underline{Q} \cdot \underline{r}) \mathrm{d}^3 r \right|^2 = \left| \int V_{\text{latt}}(\underline{r}) V_{\text{mod}}(\underline{r}) \exp(i\underline{Q} \cdot \underline{r}) d^3 r \right|^2 = |\mathbf{F}\{V_{\text{latt}}(\underline{r}) V_{\text{mod}}(\underline{r})\}(\underline{Q})|^2 \tag{5.1}$$

of the sample can be calculated by performing a Fourier transformation $\mathbf{F}\{V(\underline{r})\}$ of $V(\underline{r})$. The convolution theorem for Fourier transformations can be used to modify equation (5.1). This theorem states that the convolution $\otimes$ of two Fourier transformed functions $f_i = \mathbf{F}\{g_i\}$ gives the same result as the Fourier transformation of the product of both functions g_i. Thus,

$$\mathbf{F}\{g_1 \cdot g_2\} = \mathbf{F}\{g_1\} \otimes \mathbf{F}\{g_2\} = f_1 \otimes f_2 = \int f_1(\underline{q}) f_2(\underline{q} - \underline{Q}) \mathrm{d}^3 q \tag{5.2}$$

where the integral is the definition of the convolution.

It is also known from previous sections that for an infinite periodic crystal the lattice potential $V_{\text{latt}}(\underline{r})$ can be written as a sum of delta-functions weighted with the scattering length and located at the position of the atoms. The Fourier transformation of $V_{\text{latt}}(\underline{r})$ also yields delta-functions: the Bragg peaks at the reciprocal lattice positions. In contrast, the Fourier transformation of $V_{\text{mod}}(\underline{r})$ is usually a 'smooth' function which is strongly decreasing for large $|\underline{Q}|$. The result of the convolution is depicted in the second row of Figure 5.2.

By doing a small angle scattering experiment only wave vector transfers $\underline{Q}$ with a mean value close to 0 are considered. All other values are omitted. The result of the magnification around $\underline{Q}=0$ is shown in the third row of Figure 5.2. In good approximation it is identical to a convolution of just a **single** delta-function at $\underline{r}=0$ with the Fourier transformation of $V_{\text{mod}}(\underline{r})$. In real space (Fourier backtransformation) a single delta peak corresponds to an infinite sample with homogeneous potential which turns out to be the averaged value of $V_{\text{latt}}(\underline{r})$. The fourth row of Figure 5.2 proofs that no information about the atomic structure is necessary to explain a small angle scattering pattern.

To study the morphology of surfaces or interfaces of thin layer systems such as polymer films on silicon substrates or magnetic multilayer systems some specific kinds of small angle neutron (or x-ray) scattering experiments can be performed. Especially for buried interfaces these surface sensitive methods are the only way to investigate the film properties without destroying the sample. Therefore, they are very frequently applied and have an enormous impact on solid states and soft condensed matter physics in general.

The so-called **specular reflectivity** is a scan with a wave vector transfer $\underline{Q}$ perpendicular to the sample surface which is defined as the z-direction in this section. Because of the missing Q_x- and Q_y-component the reflectivity is only sensitive to the thickness, the potential and the roughness of each film. In-plane properties of the interfaces such as lateral correlation lengths are accessible with different kinds of **diffuse scattering experiments** where at least one of the components Q_x or Q_y is not vanishing.

In the following, the specular reflectivity and the diffuse scattering are explained in more detail. The usual experimental setup will be shown and the basic theory of specular and diffuse scattering will be presented with some examples. Then, polarized neutron specular reflectivity and diffuse scattering for the study of magnetism will be introduced.

5.2 Experimental Principals of Surface Sensitive Neutron Scattering

A sketch of a typical neutron surface scattering experiment is displayed in Figure 5.3, a more detailed description is given in other sections. The direction of the primary beam is defined by some slits. Before the primary beam hits the sample the flux is usually monitored. The incident angle θ which is determined with respect to the sample surface is set by rotating the sample in the beam. The scattered beam is detected at an angle θ' (also with respect to the surface) which is determined by θ and the scattering angle $\phi=\theta'+\theta$. In the literature ϕ is sometimes called 2θ (which is actually inaccurate because ϕ is not necessarily equal to $2\cdot\theta$).

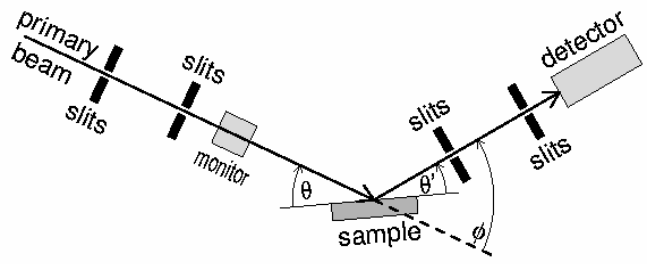

Figure 5.3: *Sketch of a typical surface sensitive neutron scattering experiment. The incident angle is denoted by* θ, *the outgoing angle with respect to the surface by* θ'. *The scattering angle is called* ϕ.

For specular reflectivity measurements the condition θ=θ' holds which is usually not true for diffuse scattering experiments. The mean value of the wave vector transfer is given by

$$|\underline{Q}| = \frac{4\pi}{\lambda}\sin\left(\frac{\phi}{2}\right) \tag{5.3}$$

with the de Broglie wavelength of the neutrons $\lambda = h/(2mE)^{1/2}$. As it was mentioned before for a small angle scattering experiment $|\underline{Q}|$ has to be much smaller than the typical reciprocal distance of the atoms in the sample. Therefore, ϕ also has to be small. Depending on the chosen wavelength the angle ϕ is almost never larger than a few degrees. For a surface sensitive experiment, which is performed in reflection and not in transmission (see Fig. 5.4), this means that θ and θ' are also small and positive.

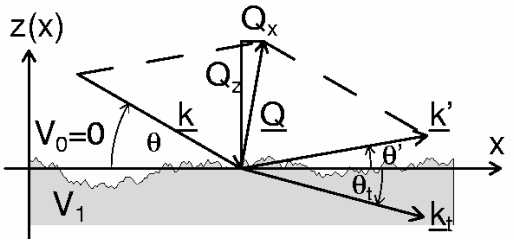

Fig. 5.4: *Sketch of the wave vectors for a surface sensitive experiment. The parameters of the transmitted beam are labeled with the index* t. *The potential of air is denoted by* V_0 *that one of the substrate with* V_1.

From simple geometrical considerations the components of the wave vector transfer can be deduced. They are defined by

$$Q_x = \frac{2\pi}{\lambda}(\cos\theta' - \cos\theta) \qquad Q_y = 0 \qquad Q_z = \frac{2\pi}{\lambda}(\sin\theta' + \sin\theta) \tag{5.4}$$

and can be used to estimate the accessible Q-range of surface sensitive experiments. At a typical wavelength of the neutrons of about 0.2nm=2Å and angles not larger than 1.0 degree Q_z would always be less than 0.1Å^{-1}. $|Q_x|$ would even be restricted to $5\cdot10^{-4}\text{Å}^{-1}$. For comparison: A simple cubic crystal with 3Å lattice spacing has a smallest reciprocal lattice vector of 2.1Å^{-1}.

5.3 Specular Neutron Reflectivity in Born Approximation

For specular reflectivity measurements the exit angle θ' is always identical to the incident angle θ. Therefore, the Q_x-component is equal to zero and the reflectivity data does not contain any particular information about the in-plane structure of the sample. In first order Born approximation [1] the scattered intensity is given by

$$I(Q_z) \sim \frac{1}{Q_z^4}\left|\int \frac{\mathrm{d}V(z)}{\mathrm{d}z}\exp(-iQ_z z)\mathrm{d}z\right|^2 \tag{5.5}$$

which means, that the specular reflectivity is basically determined by the Fourier transformation of the gradient of the potential profile perpendicular to the sample surface. The averaged (continuous) potential of a particular material with N components is defined by

$$V = \frac{2\pi\hbar^2}{m_n}\sum_{j=1}^{N} b_j \rho_j \tag{5.6}$$

where the b_j are the scattering lengths and the ρ_j are the particle number densities of the components. A one-component sample with a perfectly smooth and flat surface which is oriented in the (x,y)-plane would yield a step function for the z-dependent potential:

$$V(z) = \frac{2\pi\hbar^2 b\rho}{m_n}\left(\frac{1}{2} - \frac{1}{2}\Theta(z)\right) = \begin{cases} 0 & : \; z > 0 \\ 2\pi\hbar^2 b\rho / m_n & : \; z \le 0 \end{cases} \tag{5.7}$$

The derivative of $V(z)$ is a delta-function $dV(z)/dz \sim \delta(z)$. With Eq. (5.5) one gets $I(Q_z) \sim Q_z^{-4}$ because the Fourier transformation of a delta-function at $z=0$ is identical to 1.

However, a perfectly smooth and flat surface does not exist. Instead surface roughness or density gradients have to be taken into account [2,3]. As shown in Fig. 5.5 roughness means that the z-position of the surface is locally different from the mean position at $z=0$. Averaging the density in the (x,y)-plane at each z-coordinate gives a smooth profile $V(z)$ perpendicular to the surface. The exact shape of the profile depends on the actual physical and chemical properties close to the surface. For simple rough surfaces in good approximation an error-function

$$V(z) = \frac{V}{2} - \frac{V}{2}\mathrm{erf}\left(\frac{z}{\sqrt{2}\sigma}\right) \qquad \text{with} \qquad \mathrm{erf}(z) = \frac{2}{\sqrt{\pi}}\int_0^z \exp(-t^2)\mathrm{d}t \tag{5.8}$$

is sufficient to model the profile. The parameter σ is called rms-roughness and is a measure for the root mean square width of $V(z)$ given by the gaussian probability function

$$\frac{\mathrm{d}V(z)}{\mathrm{d}z} \sim P(z) = \frac{1}{\sqrt{2\pi}\sigma}\exp\left(-\frac{z^2}{2\sigma^2}\right). \tag{5.9}$$

Figure 5.5 also shows that the profile does not contain any information about the lateral structure of the rough surface. Therefore, the reflectivity is insensitive to different in-plane length scales ξ_p. It even cannot be used to distinguish between a rough interface and a density gradient caused by e.g., interdiffusion. It will be explained later that this can only be done by using diffuse scattering experiments.

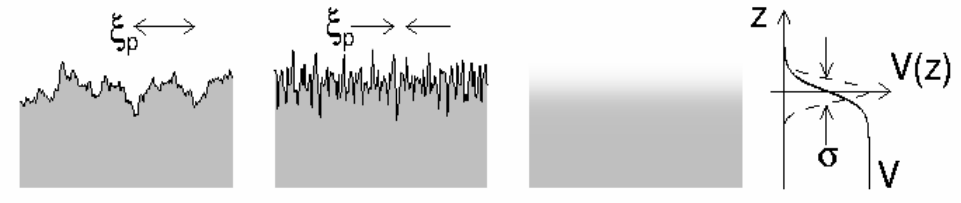

Figure 5.5: *Three different surfaces with the same rms-roughness σ determined by the root mean square width of the probability function (dashed line) of the profile* V(z) *(solid line). The in-plane structure is determined by the lateral correlation length* ξ_p *which is large for the very left example quite small for the rough surface shown in the center and not defined for the density gradient example (right).*

The reflectivity of a rough surface with an error function profile can easily be calculated. The derivative of $V(z)$ is determined by the probability function P(z) [see Eq. (5.9)]. With Eq. (5.5) this yields $I(Q_z) \sim Q_z^{-4}\exp(-Q_z^2\sigma^2)$. Compared with the perfectly smooth surface the reflected intensity is damped by a Debye-Waller factor: The rougher the surfaces the less intensity is reflected at large Q_z (see Figure 5.6 left).

Reflectivity scans are not only extremely sensitive to surfaces roughnesses but also to film thicknesses of layer systems. If a thin film with thickness d and an averaged potential V_1 is deposited on a substrate with potential V_2 the density profile $V(z)$ is given by

$$V(z) = \begin{cases} 0 & : \quad z > d \\ 2\pi\hbar^2 b_1\rho_1 / m_n = V_1 & : \quad d \geq z > 0 \\ 2\pi\hbar^2 b_2\rho_2 / m_n = V_2 & : \quad 0 \geq z \end{cases} \tag{5.10}$$

if the interfacial rms-roughnesses σ_1 and σ_2 are neglected. The derivative yields two delta-functions: $dV(z)/dz \sim (b_2\rho_2 - b_1\rho_1)\delta(z) + b_1\rho_1\delta(z-d)$. Using Eq. (5.5), the specularily reflected intensity of a perfectly smooth monolayer system is given by

$$I(Q_z) \sim \frac{1}{Q_z^4}\left[\left(b_2\rho_2 - b_1\rho_1\right)^2 + \left(b_1\rho_1\right)^2 + 2\left(b_2\rho_2 - b_1\rho_1\right)\left(b_1\rho_1\right)\cos\left(Q_z d\right)\right]. \tag{5.11}$$

This means that films cause oscillations in the reflectivity. The period is determined by the film thickness the strength (usually called 'contrast') by the difference of the potentials V_1 and V_2 (see Fig. 5.6 right).

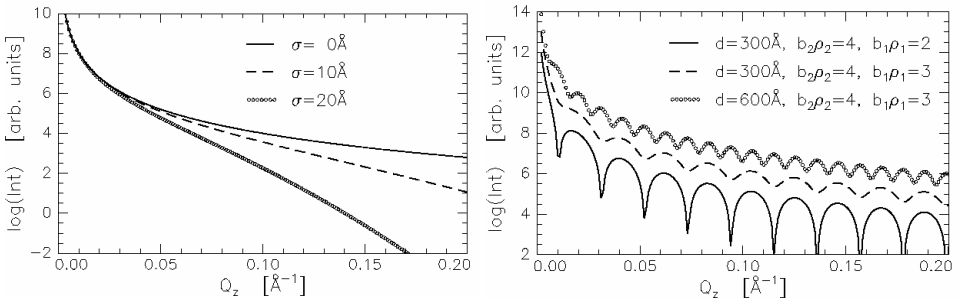

Figure 5.6: *The left graph displays the effect of the surface roughness on the specularily reflected intensity: the rougher the surface the less intensity is reflected at large* Q_z. *The right figure shows reflectivities of perfectly smooth monolayer systems. The curves are shifted in intensity for clarity. The thicker the film the smaller the distance of the so-called Kiessig fringes. The less the contrast (given by* $[b_2\rho_2\text{-}b_1\rho_1]$*) the less pronounced the oscillations are.*

In this way every additional layer appears as an oscillation in the reflectivity curve. Interface roughnesses can also quite easily be included in the theory and yield a typical damping of each oscillation. Multilayer systems with different parameters for each layer generally show very complicate reflectivities. They are usually difficult to analyze especially because of the so-called 'phase problem' which prevents an unambiguous solution of Eq. (5.5). The „phase problem" appears when performing the mean square of the complex

function $\mathbf{F}\{\mathrm{d}V(z)/\mathrm{d}z\}$ to calculate the reflected intensity [see Eq. (5.5)]. The loss of the phase information may end up in identical reflectivities even though the potential profiles are different. E.g., using Eq. (5.11) it can easily be shown, that a monolayer system with $b_2\rho_2=4$ and $b_1\rho_1=3$ exactly results in the same reflectivity as $b_2\rho_2=4$ and $b_1\rho_1=1$, if the film thicknesses are identical.

5.4 Diffuse Neutron Scattering in Born Approximation

Performing a surface scattering experiment it turns out that some intensity is also scattered in directions with $\theta\neq\theta'$. In this case the wave vector transfer $\underline{Q}$ has a component in Q_x-direction (see Fig. 5.4). This off-specular signal is called diffuse scattering and is caused by lateral structures (in-plane, in the (x,y)-plane) of the sample [4]. If the samples are perfectly smooth or if there is no lateral structure (see Fig. 5.5 right) no diffuse scattering is expected.

In general, for rough layer systems the diffuse scattering is sensitive to the correlation function $C_{jk}(\underline{R})$ between two interfaces j and k where $\underline{R}$ is an in-plane vector (x,y). The correlation function is defined by

$$C_{jk}(\underline{R}) = \int z_j(\underline{r}) z_k(\underline{r}+\underline{R})\mathrm{d}^2 r \tag{5.12}$$

with the local deviation $z_j(\underline{r})$ from the averaged position of the interface j. The correlation function between two different interfaces is usually called 'cross-correlation'. If $j=k$ holds $C_{jk}(\underline{R})=C_{jj}(\underline{R})$ is called 'auto-correlation'. Qualitatively, $C_{jk}(\underline{R})$ is large if two areas of the interfaces j and k, which are $\underline{R}$ apart from each other, 'look similar'. E.g., if the two interfaces contain a periodic structure with the same periodic distance D the correlation function exhibits maxima at D,$2D$,$3D$ ... . For an auto-correlation function of a single rough surfaces one gets a monotone decreasing function: For very small distances the parts of the surface look similar, the larger the distance the more different they become. The width of the curve is connected to the lateral correlation length ξ_p of the interface (see e.g., Fig 5.5) [5].

The diffuse scattering can be used to investigate periodic in-plane structures, in-plane correlation lengths of a single rough interface and correlations between two different interfaces. Figure 5.7 depicts some examples. The complete mathematical formalism to deduce the diffusely scattered intensity is quite complicate [6]. Therefore, the full theory is

omitted in this section. Instead, the diffuse scattering is explained using a simple monolayer system.

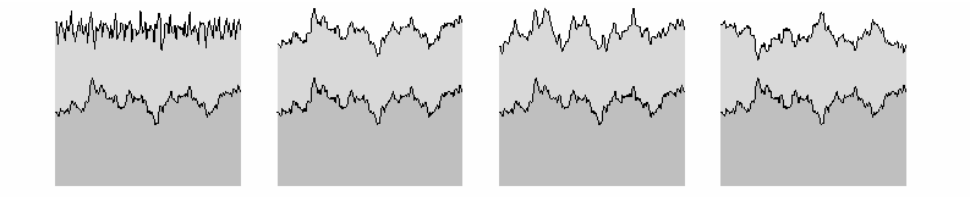

a) **b)** **c)** **d)**

Figure 5.7: *Some examples of monolayer systems with rough surfaces. a) Both interfaces are not correlated at all. b) Perfect cross-correlation between the lower and the upper interface. c) A cross-correlation is visible but it is not perfect: The interfaces do not exactly look the same. d) Perfectly anti-correlated interfaces.*

In Born Approximation the diffusely scattered intensity of a monolayer system with the interfaces j=1,2 and the film thickness d can be calculated by

$$I_{\text{diff}}(Q_x,Q_z) \sim \frac{1}{Q_z^2}\Big[\left(b_2\rho_2 - b_1\rho_1\right)^2 \exp\left(-Q_z^2\sigma_2^2\right)S_{22}(Q_x) + \left(b_1\rho_1\right)^2 \exp\left(-Q_z^2\sigma_1^2\right)S_{11}(Q_x) + 2\left(b_2\rho_2 - b_1\rho_1\right)\left(b_1\rho_1\right)\exp\left(-Q_z^2\left[\sigma_2^2+\sigma_1^2\right]/2\right)S_{12}(Q_x)\cos(Q_z d)\Big] \tag{5.13}$$

The rms-roughnesses are given by $\sigma_{1,2}$ and the so-called structure factor by

$$S_{jk}(Q_x) = \int\left(\exp\left[Q_z^2 C_{jk}(x)\right]-1\right)\exp\left(-iQ_x x\right)\mathrm{d}x\,. \tag{5.14}$$

Eq. (5.13) obviously looks similar to Eq. (5.11) which describes the specular reflectivity. The exponential Debye-Waller functions would also appear in Eq. (5.11) if roughness is taken into account, the only difference are the additional structure factors $S_{jk}(Q_x)$ which modify the scattering due to the in-plane structure of the interfaces.

Some examples of diffuse scattering experiments are depicted in Fig. 5.8. They show that the in-plane correlation length ξ_p of a rough surface (see Fig 5.5) is directly connected with the width of the diffuse scattering in Q_x-direction. Furthermore, a Q_z-scan at fixed Q_x contains the information about cross-correlations of two interfaces. If cross-correlations are present with $S_{jk}\neq 0$ for $j\neq k$ the last term of Eq. (5.13) leads to characteristic oscillations of the

diffuse scattering which are in-phase with the specular reflectivity in the case of correlated interfaces and out-of-phase in the case of anti-correlation.

Equation (5.13) also shows that the diffuse scattering can be detected in the whole Q-space even at Q_x=0 which is actually the position of the specularily reflected signal. This means that reflectivity measurements (Q_z-scans at Q_x=0) **always** contain both the specular reflectivity and the diffuse scattering at Q_x=0. To extract the specular reflectivity from the reflectivity measurement the diffuse scattering has to be subtracted. This is usually done by performing a Q_z-scan with a small offset ΔQ_x so that the specular condition is not exactly matched. This so-called longitudinal diffuse scan is subtracted from the measured reflectivity to get the true specular reflectivity.

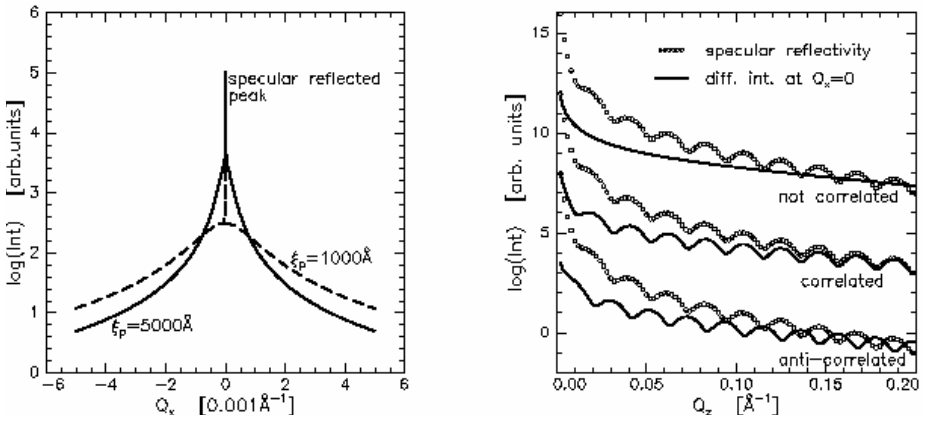

Figure 5.8: *Examples of diffuse scattering experiments. Left:* Q_x*-scan at fixed* Q_z *from a single rough surface. The solid curve corresponds to a sample with an in-plane correlation length of* ξ_p*=5000Å the dashed line to* ξ_p*=1000Å. The peaks at the condition* Q_x*=0 (where* $\theta=\theta'$*) are* ***not*** *diffuse scattering but caused by the specular reflectivity. Right: Specular reflectivity (symbols) and diffuse scattering* Q_z*-scans at* Q_x*=0 (solid lines) of a monolayer system with* d*=300Å,* $b_2\rho_2$*=4,* σ_2*=5Å,* $b_1\rho_1$*=3 and* σ_1*=5Å. The diffuse scans show the effect of cross-correlations. The* ***measured*** *reflectivity is determined by the sum of the specular and the diffuse scan.*

Unfortunately, the intensity of the diffuse scattering is usually orders of magnitude smaller than the specularily reflected signal. To get good statistics and reliable data a very high primary flux is necessary. This can easily be achieved with synchrotron radiation x-ray sources but is hardly possibly for neutron sources (see section 5.6). Therefore, it is extremely difficult to extract quantitative information from the neutron diffuse scattering data.

5.5 The Regime of the Total External Reflection: Exact Solution of the Wave Equation

It is obvious that the Born approximation [Eqs. (5.5) and (5.13)] fails for $Q_z \to 0$ because the intensity would become infinite at $Q_z=0$. The reason is that multiple scattering processes are neglected within the Born approximation. For surface sensitive experiments multiple scattering processes become essential at very small angles [7]. An exact description of the scattered intensity can be deduced for a perfectly smooth surface from quantum theory.

Starting point is the Schrödinger equation

$$\left[-\frac{\hbar^2}{2m_n}\Delta + V(\underline{r})\right]\Psi(\underline{r}) = E\Psi(\underline{r}) \tag{5.15}$$

for the wave function of the neutrons $\Psi(\underline{r})$. The energy of the neutrons is given by $E = \hbar^2 k^2 / (2m_n)$ with the mean value $k=2\pi/\lambda$ of the wave vector $\underline{k}$ (the incident and the outgoing beam have identical k because elastic scattering is assumed). For a homogeneous sample the potential is determined by Eq. (5.6), thus

$$\left[\Delta + \left(k^2 - 4\pi \sum_j b_j \rho_j\right)\right]\Psi(\underline{r}) = \left[\Delta + k^2\left(1 - \frac{\lambda^2}{\pi}\sum_j b_j \rho_j\right)\right]\Psi(\underline{r}) = \left[\Delta + k_t^2\right]\Psi(\underline{r}) = 0 \tag{5.16}$$

with the wave vector k_t inside the medium (see Fig. 5.4). From Eq. (5.16) it is justified to introduce the refraction index $n_t=k_t/k$ of the material. In very good approximation one yields

$$n_t = 1 - \frac{\lambda^2}{2\pi}\sum_j b_j \rho_j = 1 - \delta_t \tag{5.17}$$

for the refraction index which is a number close to 1 for neutrons of approximate 1Å wavelength (the correction δ_t is called **dispersion** and is on the order of $10^{-5}...10^{-6}$)

By introducing the refraction index the basic principles of optics can be applied for all further considerations. First of all it is remarkable that for many materials n_t is smaller than 1 (because b_j is usually and ρ_j always positive, thus δ_t is usually positive). This means that the transmitted beam is refracted towards the sample surface ($\theta_t<\theta$, see Fig. 5.4). For values of θ below the so-called **critical angle** θ_c the incoming beam cannot penetrate the sample surface

but is completely reflected. The critical angle can be estimated by $\theta_c \approx (2\delta_t)^{1/2}$ and is on the order of some 0.1 degree depending on the density, the scattering lengths of the atoms and the wavelength of the neutrons. For θ values beyond θ_c the beam can penetrate the sample and is only partly reflected. At the sample surface the reflection and transmission coefficients r_f and t_f are obtained by the Fresnel formulars

$$r_f = \frac{k_z - k_{t,z}}{k_z + k_{t,z}} \qquad \text{And} \qquad t_f = \frac{2k_z}{k_z + k_{t,z}} \tag{5.18}$$

with $k_z = k\sin\theta$ and $k_{t,z} = k_t \sin\theta_t = k(n_t^2 - \cos^2\theta)^{1/2}$ (see Fig. 5.4). The specular reflected intensity $I = |r_f|^2$ is determined by the absolute square of the reflection coefficient. It shows the typical plateau below the critical angle, the regime of the total external reflection, and the rapidly decreasing intensity beyond θ_c. With appropriate approximations one gets $I \approx \delta_t^2/(4\sin^4\theta) \sim Q_z^{-4}$ for incident angles θ larger than $3\delta_t$ which is the confirmation of the Born approximation (see Fig. 5.9).

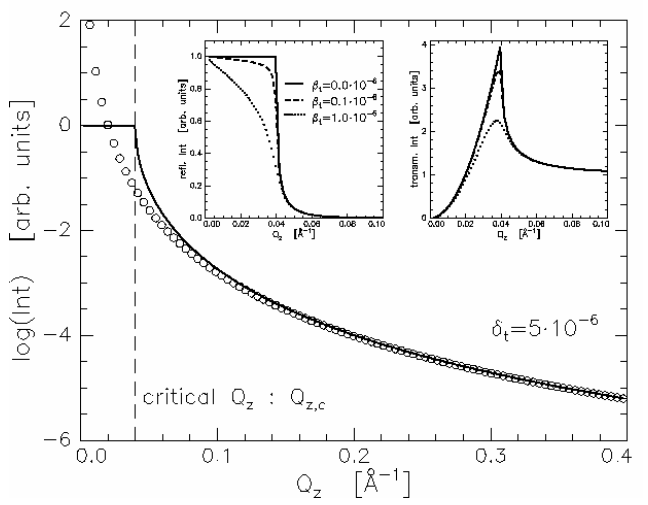

Figure 5.9: *Effect of the total external reflection. The large figure shows a reflectivity of a smooth surface in Born approximation (symbols) and the exact Fresnel form (solid line). The dashed line marks the critical* Q_z. *The left inset displays absorption effects in the reflectivity on a linear scale. The same is depicted for the transmitted intensity in the right inset.*

Not addressed yet in this section is the **absorption** β_t of the neutrons inside the sample. For most materials such as silicon the absorption is negligible but this is not the case for e.g. cadmium or indium. Most straightforward, it can be introduced by including an imaginary part to the refraction index

$$n_t = 1 - \delta_t + i\beta_t . \tag{5.19}$$

The effect of the absorption is shown in Fig. 5.9. It basically smoothes the sharp features of the intensity close the critical angle and also restricts the penetration depth of the neutrons to finite values.

The diffuse scattering is also modified in the regime of the total external reflection [8,9]. In good approximation one gets

$$I_{\text{diff}}(Q_x, Q_z) \sim \left|t_f(\theta)\right|^2 Q_z^{-2} \exp\left(-Q_z^2\sigma_1^2\right) S_{11}(Q_x) \left|t_f(\theta')\right|^2 \tag{5.20}$$

for a single rough surface. For layer systems this expression becomes much more complicate. Eq. (5.20) shows, that the transmission functions of the incoming and the outgoing beam have to be taken into account. The transmission function t_f exhibits a maximum at the critical angle (or the critical Q_z, respectively, see Fig. 5.9) because for incident angles $\theta = \theta_c$ an evanescent wave appears which runs parallel to the surface ($\theta' = 0$) [10]. Therefore, the diffuse scattering also has maxima called Yoneda wings at the positions $\theta=\theta_c$ and $\theta'=\theta_c$ (see Fig. 5.10).

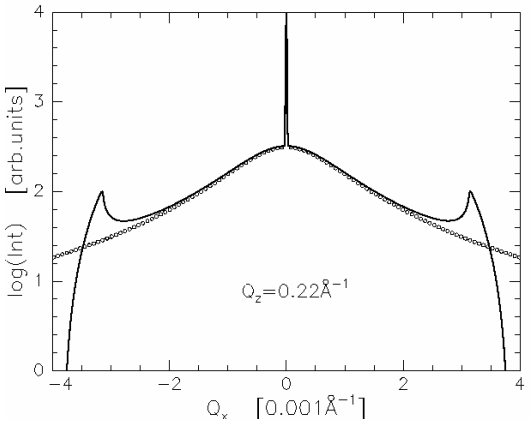

Figure 5.10: *Diffuse scattering scan at fixed* Q_z. *The symbols correspond to the Born approximation (dashed line in Fig. 5.8). The solid line displays the better approximation including the scattering effects due to the total external reflection at* $\theta=\theta_c$ *and* $\theta'=\theta_c$. *They are visible as the Yoneda-maxima at* $|Q_x|\approx 0.0032\text{Å}^{-1}$.
The peak at the center is the specular reflected intensity ($\theta=\theta'$).

In summary, the optical properties of the sample affect the scattering only if the incident or the exit angle is comparable or smaller than the critical angle which is usually smaller than 0.4°. The full dynamical theory can only be deduced for the specular reflectivity. For the diffuse scattering no exact solution exists right now.

5.6 An Important Application of Neutron Reflectometry

For many standard scattering experiments on layer systems x-rays are much more suitable than neutrons because of the higher flux, the better collimation and the less divergence. In numbers: A standard synchrotron radiation source has a primary beam intensity of about 10^{10} counts/sec at a typical spot size of $(0.2\times1)\text{mm}^2$. The beam divergence which determines the $\underline{Q}$-space resolution is less than 1/100 of a degree. For a modern neutron source one gets less than 10^7 counts/sec in an area of $(0.5\times20)\text{mm}^2$ with a divergence of larger than 0.02°.

However, for some topics of research neutron scattering is superior. One example is the investigation of materials which mainly contain hydrogen, carbon, nitrogen or oxygen such as organic molecules. In this case the electron density [which for x-rays replaces the potential $V(\underline{r})$] is very low and the x-ray contrast becomes very small. In contrast, for neutron $V(\underline{r})$ strongly depends on the isotope of the elements. Therefore, by using deuterated or hydrogenated organic materials the scattering contrast can easily be tuned without changing the chemical properties of the samples. Figure 5.11 shows an example of a polymer bilayer.

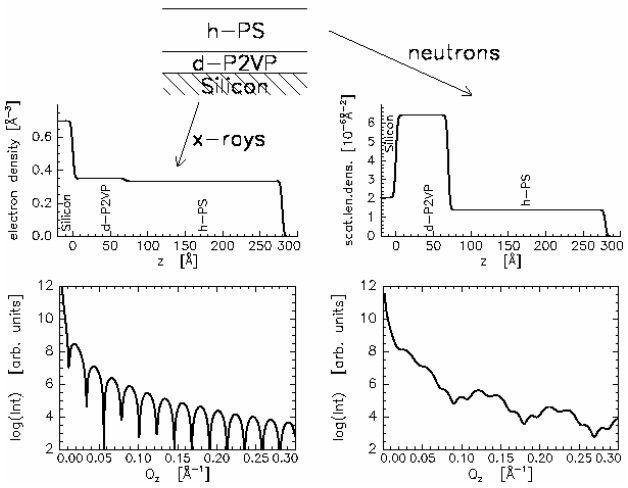

Figure 5.11: *Comparison of an x-ray (left column) and a neutron (right column) reflectivity of a polymer bilayer (210Å polystyrene [PS] on 70Å deuterated polyvinylpyrridine [d-P2VP] on a silicon substrate). The x-ray contrast between the two polymers given by the electron density is only about 5%.*

It can clearly be seen that the x-ray reflectivity only exhibits one significant oscillation period which is due to the whole film thickness. The x-ray contrast at the polymer interface is too small to modulate the intensity. Advanced analyzing methods have to be used to extract

the information of the polymer-polymer interface [11]. This is different for neutrons: By deuterating the bottom polymer the contrast is enhanced dramatically. The reflectivity shows separate oscillations: a long period due to the thin d-P2VP film and a short period which is caused by the h-PS film. The analysis is straightforward and usually very reliable.

5.7 Polarized Neutron Methods – Introduction.

The physical properties of magnetic multilayers and nanostructures, such as electron correlations, spin transport and molecular magnetism, do not depend only of the molecular structure of the layers but also on their nuclear and magnetic structure at the mesoscopic level [13]. In the following, we will concentrate on the investigation of the magnetisation density profiles and their in-plane fluctuations in multilayers using specular reflectivity and off-specular scattering of polarized neutrons.

The most popular laboratory techniques for the investigation of magnetism in multilayers, such as magnetic force microscopy (MFM) or Kerr microscopy, are surface or near surface techniques and can sometimes be disturbing. For example, the interaction of the MFM tip with the sample can disturb its magnetic field distribution inside it when it is made of a material of low magnetic coercivity. The magnetic and the nuclear interaction of neutrons with matter are very weak, making it a fully non-disturbing probe.

At and below the critical angle of total reflection θ_c, the neutron wave is evanescent and has a small penetration depth, usually of the order of 100 to 200 Å at θ_c. As the angle of incidence of the neutron increases from zero, the penetration increases. Just above θ_c, the penetration depth shows a sharp increase and then further increases as θ increases. This dependency of the neutron penetration depth as a function of the angle of incidence makes therefore reflectometry and scattering under grazing incidence close to the critical angle of total reflection a unique probe to investigate in a depth-resolved way the nuclear and magnetisation profiles in thin films. We will exemplify this aspect in the example given later in this manuscript.

An important quantity to consider for the interpretation of specular reflectivity and off-specular scattering data is the projection l_* of the coherence length of the neutron beam on the sample surface and its value with respect to the value of the lateral magnetic or nuclear correlation length. Within the coherence length, neutron waves can interfere, outside interference is not possible. If a sample is flat and homogeneous within l_*, no lateral

momentum $\boldsymbol{\kappa} = Q_x \mathbf{e}_x + Q_y \mathbf{e}_y$ can be transferred, and intensity is seen only in the specular direction. The measured specular reflectivity is the incoherent sum of the different reflectivities from all the illuminated coherence volumes of the sample. If the sample is not translational invariant in-plane on the length scale of l_*, lateral momentum transfer can occur and some intensity can be detected off-specular, i.e. at $\boldsymbol{\kappa} \neq 0$. The measured scattering cross section is then an average over the different scattering cross sections from the different coherence volumes of the sample. Usually, when spanning a whole range of θ and θ' values, off-specular signal (θ ≠ θ') coexists with specular reflectivity (θ = θ'). Specular reflectivity originates from the laterally averaged neutron-matter interaction potential and diffuse scattering from the fluctuations around this value.

In appropriate approximation the value of the lateral coherence length is given by the resolution of the in-plane component of the momentum transfer ($l_* \sim \delta Q_*$) and therefore depends of the wavelength resolution and on the collimation of the neutron beam. It typically ranges from a μm to several mm. It can therefore be greatly extended, leading to a high probability for coherent multiple scattering of the neutrons. In that case, the Born approximation fails to describe properly the measured diffuse scattering. The Distorted Wave Born Approximation (DWBA), already introduced in section 5.5, works usually quite well to reproduce the measured data.

5.9 Specular reflectivity of polarized neutron

We stay in the homogeneous and flat approximation, where the neutron-matter interaction potential is only depth depending. In the case of magnetic multilayers, the neutron-matter interaction in layer l can be separated into two parts, i.e. $\hat{V}_l = V_l^N \hat{1} + \hat{V}_l^M$ where V_l^N is the neutron-nuclei interaction and $\hat{V}_l^M = -\mu_n \hat{\boldsymbol{\sigma}} \cdot \mathbf{B}_l$ is the magnetic dipole interaction operator between the neutron magnetic moment operator $\mu_n \hat{\boldsymbol{\sigma}}$ and the magnetic field $\mathbf{B}_l$. $\hat{\boldsymbol{\sigma}}$ is the vector of Pauli matrices, i.e. $\hat{\boldsymbol{\sigma}} = (\sigma_\perp, \sigma_z, \sigma_{//})$ with

$$\sigma_\perp = \begin{pmatrix} 0 & 1 \\ 1 & 0 \end{pmatrix} \quad \sigma_z = \begin{pmatrix} 0 & -i \\ i & 0 \end{pmatrix} \quad \sigma_{//} = \begin{pmatrix} 1 & 0 \\ 0 & -1 \end{pmatrix}. \qquad (5.21)$$

The magnetic interaction operator in the magnetic layer l can be decomposed into terms:

$$\hat{V}_l^M = -\mu_n \hat{\boldsymbol{\sigma}} \cdot [\mathbf{B}_0 + \mu_0 (1 - D)\mathbf{M}] \qquad (5.22)$$

where $\mathbf{B}_0$ is the applied field, **M** is the magnetisation inside the layer, D is the demagnetising factor. In the case of an infinite magnetic thin film, $(1-D)\mathbf{M}$ in Equ. (5.22) is equal to the in-plane component of the magnetisation [14]. It is only possible to measure the in-plane component of magnetisation.

The total interaction potential operator can be rewritten as

$$\hat{V}_l = \frac{2\pi\hbar^2}{m}\left(\rho_l^N \hat{1} + \rho_l^M \hat{\boldsymbol{\sigma}}\cdot\mathbf{b}_l\right) \qquad (5.23)$$

where ρ_l^N and ρ_l^M are respectively the nuclear and magnetic scattering length densities. $\mathbf{b}_l$ is the unit vector oriented along $\mathbf{B}_l$. It provides a quantization axis for the neutron spin. The eigenvectors $|+\rangle$ and $|-\rangle$ of the operator $\hat{\boldsymbol{\sigma}}\cdot\mathbf{b}_l$ with eigenvalues +1 and -1 respectively define states of the neutron with "up" and "down" spin projections along the quantization axis. The neutron state $|\Psi(\mathbf{r})\rangle$, solution of the Schrödinger equation in coordinates and spin space for the potential operator $\hat{V}_l$, is a linear combination of those two eigenvectors:

$$|\Psi(\mathbf{r})\rangle = \Psi^+(\mathbf{r})|+\rangle + \Psi^-(\mathbf{r})|-\rangle = \begin{pmatrix}\Psi^+(\mathbf{r})\\ \Psi^-(\mathbf{r})\end{pmatrix}. \qquad (5.24)$$

Before describing the interaction of the neutron dipole moment with the multilayer, we have to define one single quantization axis that will be fixed during the consideration of the whole interaction process. Usually the quantization axis is taken along the guiding magnetic field outside the sample and it is called the // axis. The states $|+\rangle$ and $|-\rangle$ representing spin up and spin down neutrons respectively are then the eigenvectors of the operator $\hat{\boldsymbol{\sigma}}\cdot\mathbf{b}_0 = \hat{\sigma}_{//}$ where $\mathbf{b}_0$ is the unit vector directed along the magnetic field outside the sample $\mathbf{B}_0$. The unit matrix $\hat{1}$ in (5.22) is the matrix that leaves those states unchanged.

Before the interaction with the sample and its surrounding magnetic field, the neutron can be considered as a plane wave with wave vector $\mathbf{k}_0$ and energy $\hbar^2 k_0^2/(2m)$. The interaction potential has no dependency along the lateral coordinate $\boldsymbol{\rho}$ of the sample and the neutron wave vector in layer l can be written as $|\Psi_l(\mathbf{r})\rangle = e^{i\boldsymbol{\kappa}\cdot\boldsymbol{\rho}}|\Psi_l(z)\rangle$ where $\boldsymbol{\kappa}$ is the in-plane conserving component of the wave vector $\mathbf{k}_l = k_{z,l}.\mathbf{e}_z + \boldsymbol{\kappa}.\mathbf{e}_{\boldsymbol{\rho}}$. The three dimensional Schrödinger equation can therefore be reduced to a set of one dimensional equations:

$$\begin{aligned}\Psi''_{l,+}(z)+\left[k_{z,l}^2-4\pi\left(\rho_l^N+\rho_l^M b_{l,//}\right)\right]\Psi_{l,+}(z)-4\pi\rho_l^M b_{l,\perp}\Psi_{l,-}(z)=0\\ \Psi''_{l,-}(z)+\left[k_{z,l}^2-4\pi\left(\rho_l^N+\rho_l^M b_{l,//}\right)\right]\Psi_{l,-}(z)-4\pi\rho_l^M b_{l,\perp}\Psi_{l,+}(z)=0\end{aligned} \qquad (5.25)$$

The solutions of these coupled linear differential equations are of the form

$$\left|\Psi_l(z)\right\rangle=\left(e^{i\hat{k}_{z,l}(z-z_{l-1})}\hat{t}_l+e^{-i\hat{k}_{z,l}(z-z_{l-1})}\hat{r}_l\right)\left|\Psi_l(0)\right\rangle \qquad (5.26)$$

where

$$\hat{k}_{z,l}=\sqrt{k_{z,0}^2-4\pi\left(\rho_l^N+\rho_l^M\hat{\boldsymbol{\sigma}}\cdot\mathbf{b}_l\right)} \qquad (5.27)$$

is the component perpendicular to the sample surface of the incoming wave vector. Note that $\hat{k}_{z,l}$ is an operator in spin space, and has two different eigenvalues along the quantization axis: $k_{z,l}^{\pm}=\sqrt{k_{z,0}^2-4\pi\left(\rho_l^N\pm\rho_l^M\right)}$ where $k_{z,o}=(2\pi\sin\theta)/\lambda$ is the perpendicular component of the incoming wave vector in vacuum. $\hat{t}_l$ and $\hat{r}_l$ are the reflection and transmission operators in layer l. They are also operators in spin space, with two different eigenvalues.

The operators of reflection and transmission amplitude in each layer can be deduced recursively by considering the continuities of the wave function and its first derivative at the interfaces between two layers. If N is the number of layers in the system, the number of interfaces is N+1 and the continuity relations lead to 2(N+1) equations. Considering the vacuum on top of the system and the substrate, 2(N+2) reflection and transmission amplitudes operators have to be found. Two other conditions are added by considering that the transmission amplitude in the vacuum is equal to the unit matrix ($\hat{t}_0=\hat{1}$) and that the substrate, as a semi-infinite medium, has no reflection amplitude ($\hat{r}_{N+1}=\hat{0}$). The resolution of this system of equations is not complicated but lengthy. Its solution can be found in [15].

Four types of reflectivities follow, by projecting the reflection amplitude in vacuum on the bra and kets representing up and down neutrons. The measured reflectivity is then the modulus squared of the obtained number:

$$R^{\pm\pm}=\left|\left\langle\pm\left|\hat{r}_0\right|\pm\right\rangle\right|^2. \qquad (5.28)$$

The above equations have a clear physical meaning. From (5.25), it is clear that only the nuclear scattering length and the component of the in-plane magnetisation parallel to the external field ($B_{l,//}$) lead to non-spin-flip (NSF) reflectivities. The component of the in-plane magnetic induction perpendicular to the external field ($B_{l,\perp}$) lead to spin-flip (SF) reflectivities. By measuring both the SF and NSF reflectivities and comparing their relative

intensities it is therefore possible to get vector information on the magnetisations inside each layer.

Depending of the neutron spin orientation $\hat{k}_{k,l}$ has two different projections along the quantization axis. The transmitted part of the wave amplitude in layer l (first part of equ.5.26) will therefore be evanescent below two different values of $k_{z,0}$, leading to two different critical angles of total reflection θ_c^+ and θ_c^- in the R^{++} and the R^{--} channels respectively.

The principle of a polarized neutron reflectivity measurement is depicted in fig. 5.12. A beam prepared with all neutrons having spin up or spin down projection along the quantization axis defined by the external field $\mathbf{B}_0$ impinge on the sample surface with wave vector **k** under a glancing angle θ. After reflection ($\theta = \theta'$) some neutrons have changed their spin projection and some have not. Each neutron is then spin analyzed and detected. In such an experiment four different reflectivities channels can therefore be recorded: R^{++}, R^{+-}, R^{-+} and R^{--}. A practical realization of such an experiment can be found on the web site given in reference [16].

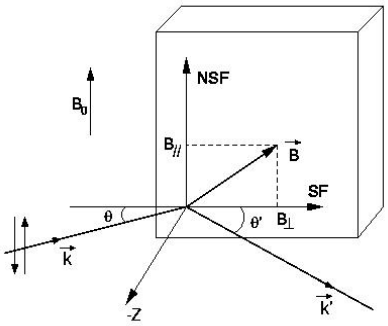

Fig 5.12: *Principle of a neutron specular reflectivity ($\theta = \theta'$) and off-specular scattering ($\theta \neq \theta'$) experiment.*

5.10 Example: Layer-by-layer magnetometry in a remanent polarizing supermirror

Polarizing supermirrors are commonly used for the polarization of cold neutron beams. They consist of a series of alternating ferromagnetic and non-magnetic layers with a gradient in the layer thickness.

The presented sample contains 100 $Fe_{50}Co_{48}V_2$ layers separated by 100 TiN_x layers. $Fe_{50}Co_{48}V_2$ has been chosen for its large total scattering length density for up neutrons $\rho^+ = \rho^N + \rho^M$, leading to a large critical angle of total reflection and a strong contrast with TiN_x, whereas it does not reflect the down neutrons: $\rho^- = \rho^N - \rho^M < 0$. The content of

nitrogen in TiN_x has been tuned such that the contrast between its scattering length density (ρ_{TiN_x}) and the scattering length density for down neutrons of $Fe_{50}Co_{48}V_2$ vanishes. ($\rho_{TiN_x} - \rho_- = 0$), leading to a strongly reduced reflectivity for down neutrons.

In order to further increase the range of angles for which the reflectivity for up neutrons stays close to 1, a gradient in the FeCoV/TiN bi-layer thicknesses has been introduced from the bottom to the top of the stack. It leads to a broadened multilayer Bragg peak spreading from the critical angle of total reflection for up neutrons to an angle defined by the bottom-most and thinnest bilayer. This arrangement permits to reflect an increased amount of neutrons coming from a non-collimated source of neutrons.

In remanent polarizing supermirrors, an uniaxial anisotropy allows to keep a remanent magnetisation after the magnetizing field is switched-off or even slightly reversed, putting the quantization axis of the neutrons anti-parallel to the magnetisations. In this state, the supermirror reflects neutrons with the spin opposite to the guiding field (i.e. spin down neutrons). This feature can be used to build an instrument providing both spin directions without the use of a spin flipper [17]. Those three different properties are schematized in fig. 5.13.

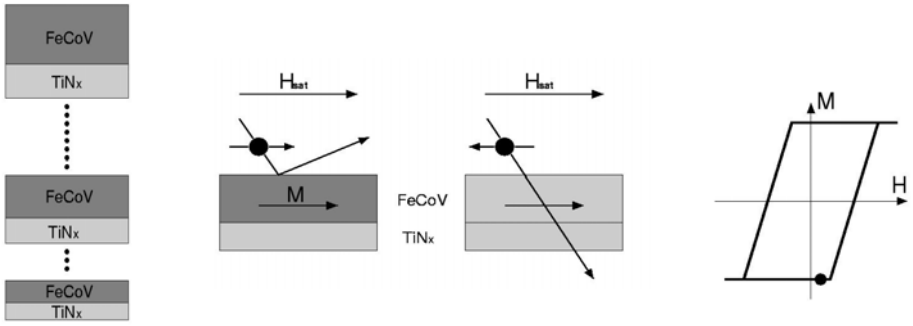

Fig. 5.13: *The three characteristics of a remanent (right) polarizing (center) supermirror (left picture)*

The remagnetization process of this system has been studied by reflectivity of polarized neutrons with polarization analysis. The measurements performed at several fields along the remagnetization curve are depicted in fig. 5.14. In (a) the measurements have been performed in the remanent state (no magnetisation has started to flip or to rotate); in (d) the measurements have been performed in the saturated state.

At saturation, all the layer magnetisations are aligned along the field: we observe a good reflectivity for up neutrons up to 20 mrad (the critical angle of total reflection for up neutrons of FeCoV is 8 mrad). The reflectivity for down neutrons is low. The measured spin flip reflectivities do not come from spin-flip processes happening in the sample. They are due to inefficiencies of the spin polarizing and analyzing devices. At remanence all the layer magnetisations are aligned against the field: the reflectivities in the R^{++} and the R^{--} channels are interchanged with respect to the saturation case.

One might expect that the remagnetization process proceed via a single flip of all the layers at the same coercive field or a simultaneous rotation of all the layers at the same range of fields. The specular reflectivity measurements shown in (b) and (c) along the remagnetization curve teach us that this is actually not the case. At $\mu_0 H$ = 3.8 and 5.6 mT, angular regions of strong R^{++} and strong R^{--} coexist. As the field is increased, the higher angular part of the strong R^{--} reflectivity gets strongly reduced, while it is replaced by strong R^{++} reflectivity. This shows that the thinnest FeCoV layers, contributing to the reflection at higher angles, have lower magnetic coercivity than the thicker ones, contributing to the reflection at lower angles. From the fits to the data using the formalism exposed in § 5.9, it was deduced that, out of the 100 FeCoV magnetisations, 48 of them have flipped along the field at 3.8 mT and 94 at 5.6 mT.

Another interesting point to notice is that, during the remagnetization process, no additional SF reflectivity has been observed, i.e. that the layer magnetisations never have any in-plane component perpendicular to the field. It means that the remagnetization process happen via sudden flips of the magnetisations from opposite to along the field, not via rotation.

This study is a good example of the power of polarized neutron reflectometry for depth-resolved investigations of the magnetisation configurations in a multilayer system.

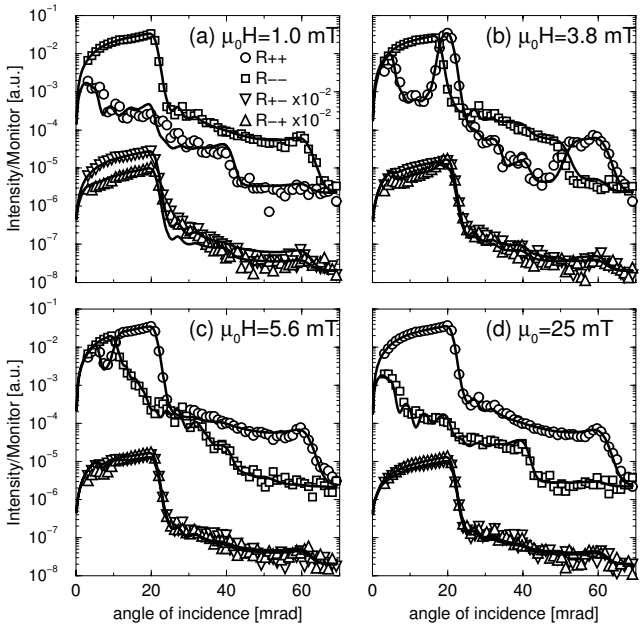

Fig. 5.14: *Polarized neutron reflectivity of a function of the angle of incidence θ on a remanent polarizing supermirror measured at four fields along the remagnetisation curve. The intensities have been plotted on a logarithmic scale. The measurements were performed at a neutron wavelength λ = 4.52 Å. The lines are fits to the data.*

5.11 Off-specular scattering of polarized neutrons

If, on a length scale smaller than the projection of the coherence length of the neutron beam on the sample surface, in-plane fluctuations of the magnetisation are present, then some intensity can be collected off-specular ($\theta \neq \theta'$ in fig. 5.12).

The theoretical description of off-specular scattering of polarized neutrons with polarization analysis lies out of the scope of this school. A description within the DWBA can be found in references [18] and [19]. Let's mention however that its scattering cross section looks like the one in Equ. 5.29, and that birefringence effects due to the different spin projections on the quantization axis have also to be taken into account.

In Fig. 5.15 (a) we show the off-specular scattering measured together the specular reflectivity on the supermirror of the preceding section at $\mu_0 H$ = 3.8 mT. Along the main diagonal we recognize the specular reflectivity depicted in Fig. 5.14 (b). Off-diagonal, the diffuse scattering is very spin-polarized. The NSF off-specular signals result essentially from the scattering by interfacial roughness whose profile replicates itself from interface to interface. The SF diffuse scattering originates from in-plane magnetic fluctuations perpendicular to the applied field inside the layers that have not yet flipped along the field.

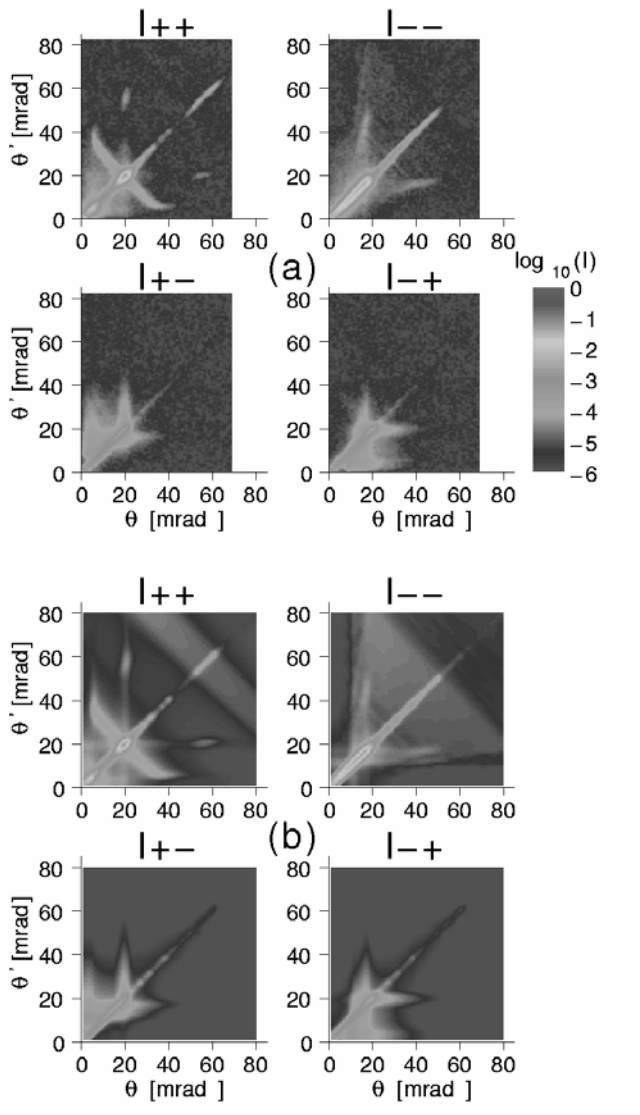

Fig. 5.15: *(a): Reflectivity and off-specular scattering of polarized neutrons with polarization analysis (all four channels I++, I--, I+- and I-+) from a remanent polarizing supermirror in a partially remagnetized state. θ is the angle of incidence with respect to the sample surface, θ' the outgoing angle. Along the main diagonal of each figure (θ = θ'), specular reflectivity is measured, giving access to laterally averaged information. Off-diagonal (θ ≠ θ'), off-specular scattering gives access to structural and magnetic correlations on length scales smaller than the in-plane projection of the coherence length of the neutron beam. (b): Simulation of the measured intensities within the DWBA.*

Those affirmations are confirmed by the simulations of the measured data within the DWBA shown in Fig. 5.15 (b)

Measuring off-specular scattering angular resolved leads therefore, in the same way as neutron specular reflectivity for the in-plane net magnetisations, to depth-resolved information on the in-plane magnetisation fluctuations.

References

[1] J. Als-Nielsen, *Topics in Current Physics. Structure and Dynamics of Surfaces* (Springer, Berlin, 1986).

[2] P. Beckmann, A. Spizzichino, *The Scattering of Electromagnetic Waves From Rough Surfaces* (Pergamon, New York, 1963).

[3] L. Névot, P. Croce, Revue de Physique appliqué **15**, 761 (1980).

[4] S.K. Sinha, E.B. Sirota, S. Garoff. H.B. Stanley, Phys. Rev. B **38**, 2297 (1988).

[5] A.L. Barabási, H.E. Stanley, *Fractal Concepts in Surface Growth* (Cambridge University Press, Cambridge, 1995).

[6] V. Holý, J. Kubena, I. Ohlídal, K. Lischka, W. Plotz, Phys. Rev. B **47**, 15896 (1993).

[7] J. Lekner, *Theory of Reflection* (Martinus Nijhoff, Dordrecht, Boston, 1987).

[8] S. Dietrich, A. Haase, Phys. Rep. **260**, 1 (1995).

[9] V. Holý, U. Pietsch, T. Baumbach, *X-Ray Scattering from Thin Films (High Resolution X-Ray Scattering from Crystalline Thin Films)* (Springer Tracts in Modern Physics, Vol. 149, Berlin, 1998).

[10] H. Dosch, *Critical Phenomena at Surfaces and Interfaces (Evanescent X-Ray and Neutron Scattering)* (Springer Tracts in Modern Physics, Vol. 126, Berlin, 1992).

[11] O.H. Seeck, I.D. Kaendler, M. Tolan, K. Shin, M.H. Rafailovich, J. Sokolov, R. Kolb, Appl. Phys. Lett. **76**, 2713 (2000).

[12] C.F. Majkrzak, J.F. Ankner, N.F. Berk, D. Gibbs, *Neutron and X-Ray Diffraction Studies of Magnetic Multilayers* (in: *Magnetic Multilayers*, World Scientific, Singapore, 1994).

[13] S. Blügel, T. Brückel, C.M. Schneider (Eds.), *Magnetism goes Nano*, Lecture Manuscripts of the 36th Spring School of the IFF, Forschungszentrum Jülich, Series "Matter and Materials" **26** (2005)

[14] C. Fermon, F. Ott and A. Menelle, "Neutron Reflectometry" in J. Daillant and A.

Gibaud (Eds), *X-ray and Neutron Reflectivity: Principles and Applications*, Springer (1999)

[15] E. Kentzinger, U. Rücker and B. Toperverg, Physica B **335**, 82 (2003)

[16] http://www.fz-juelich.de/iff/wns_hadas

[17] P. Böni, D. Clemens, M. Senthil Kumar, S. Tixier, Physica B **241-243**, 1060 (1998)

[18] B. Toperverg, Physica B **297**, 160 (2001)

[19] B. Toperverg, „Polarized Neutron Reflection ad Off-Specular Scattering“ in T. Brückel and W. Schweika (Eds.), *Polarized Neutron Scattering*, Forschungszentrum Jülich, Series “Matter and Materials”, **12** (2002)

7

Diffractometer

Gernot Heger

7. Diffractometer

G. Heger

7.1 Introduction

For pure elastic scattering the scattering function $S(\underline{Q},\omega)$ is reduced to the special case without energy transfer ($E_0 = E_1$ and $\hbar\varpi = E_0 - E_1 = 0$) and equal length of the wave vectors of the incident and scattered beams ($|\underline{k_0}| = |\underline{k_1}|$). $S(\underline{Q},\omega = 0)$ and hence the scattering intensity is only depending on the scattering vector $\underline{Q} = \underline{k_0} - \underline{k_1}$. The coherent elastic neutron scattering (≡ neutron diffraction) yields information on the positions (distribution) of the atomic nuclei and the arrangement of the localised magnetic spins in crystalline solids, the pair correlation function of liquids and glasses, and the conformation of polymer chains.

Depending on the scientific problem to be investigated adequate diffraction methods may be quite different. For fluids and glasses diffraction data of high statistical relevance over a very large $|\underline{Q}|$ range are required. The direction of the scattering vector $\underline{Q}$ is not defined for these non-crystalline states and a good resolution $|\underline{\Delta Q}|/|\underline{Q}|$ is of no importance. Besides of the pure elastic scattering also inelastic contributions are involved.

Completely different are the needs for a diffraction study of crystalline solids. The diffraction at the crystal lattice gives rise to pure elastic scattering localised at the nodes of the so-called reciprocal lattice. The scattering vectors $\underline{Q}$ for the different “Bragg-reflections” are well defined. For the separation of reflections with similar $\underline{Q}$ values a good resolution $\underline{\Delta Q}/\underline{Q}$ is very important. A measured data-set of Bragg-intensities (integrated intensities of Bragg-reflections) as complete as possible over a large $|\underline{Q}|$ range is required. An experimental stability and accuracy leading to a precision of the intensity data of about 2% is desired and may be achieved.

Diffraction measurements on polycrystalline samples depend only on the length of the scattering vector $|\underline{Q}|$. Very small line widths (according to an excellent resolution $|\underline{\Delta Q}|/|\underline{Q}|$) combined with well defined reflection profiles are prerequisites for a quantitative line-profile analysis. The complete powder diagrams resulting from overlapping reflections are described and analysed by means of the Rietveld method.

For all diffraction methods firstly the energy of the incident neutron beam (expressed in another way as its wavelength or velocity) must be specified. In the case of angular dispersive diffraction, the 2-axes diffractometer (see Fig. 1) is equipped with a crystal monochromator to

select a special wavelengths band ($\lambda \pm \Delta\lambda/\lambda$) out of the "white" beam according to the Bragg condition for its scattering plane (*hkl)*

$$2d_{hkl} \cdot \sin\theta_{hkl} = \lambda, \qquad (1)$$

with the interplanar spacing d_{hkl} and the monochromator scattering angle $2\theta_{hkl} = 2\theta_M$. The width of the wavelengths band $\Delta\lambda/\lambda$, which is important for the Q-resolution, depends on the divergences of the beam before and after the monochromator (collimations α_1 and α_2), on the mosaic spread of the monochromator crystal ΔM, and on the monochromator angle $2\theta_M$. In order to increase the intensity of the monochromatic beam at the sample position the monochromator crystal is often bent in vertical direction perpendicular to the diffraction plane of the experiment. In this way the vertical beam divergence is increased leading to a loss of resolution in the reciprocal space. The diffracted intensity from the sample is measured as a function of the scattering angle 2θ and the sample orientation (especially in case of a single crystal):

for a single crystal $\rightarrow$ $I(\underline{Q})$, and for a polycrystalline sample $\rightarrow$ $I(|\underline{Q}|)$.

2θ is defined by the collimators α_2 and α_3. As there is no analysis of the energy of the

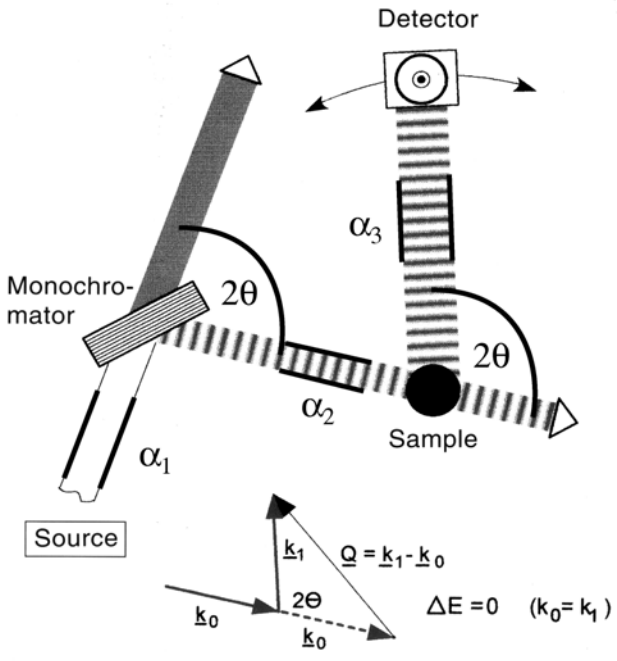

Fig. 1. Schematic representation of a 2-axes diffractometer.

scattered beam behind the sample, the energy resolution ΔE/E of a 2-axes diffractometer is not well defined (typically of the order of some %). In addition to the dominant elastic scattering also quasi-elastic and some inelastic scattering contributions are to be taken into account. The name 2-axes-diffractometer results from its two axes of rotation, the monochromator axis defining $2\theta_M$ and the sample axis (2θ).

In the case of energy dispersive diffraction, the time-of-flight diffractometer uses the complete energy spectrum of a pulsed neutron beam and the wavelengths of the scattered neutrons are determined by velocity analysis. The measurement of the neutron intensity as a function of velocity at fixed scattering angle 2θ has to be calibrated according to the energy spectrum of the neutron beam. Assuming no energy transfer at the sample the time-of-flight diffraction yields again I(Q) (and for a polycrystalline sample I(|Q|).

7.2 Reciprocal lattice and Ewald construction

Bragg scattering (diffraction) means coherent elastic scattering of a wave by a crystal. The experimental information consists of the scattering function S(Q,ω = 0) with no change of energy or wavelength of the diffracted beam. For an ideal crystal and an infinite lattice with the basis vectors $\underline{a}_1$, $\underline{a}_2$, $\underline{a}_3$, there is only diffraction intensity I(H) at the vectors

$$\underline{H} = h\underline{a}_1^* + k\underline{a}_2^* + l\underline{a}_3^* \qquad (2)$$

of the reciprocal lattice. *h,k,l* are the integer Miller indices and $\underline{a}_1^*$, $\underline{a}_2^*$, $\underline{a}_3^*$, the basis vectors of the reciprocal lattice, satisfying the two conditions

$$\underline{a}_1^* \cdot \underline{a}_1 = \underline{a}_2^* \cdot \underline{a}_2 = \underline{a}_3^* \cdot \underline{a}_3 = 1 \text{ and } \underline{a}_1^* \cdot \underline{a}_2 = \underline{a}_1^* \cdot \underline{a}_3 = \underline{a}_2^* \cdot \underline{a}_1 = \ldots = 0,$$

or in terms of the Kronecker symbol with i, j and k = 1, 2, 3

$$\delta_{ij} = 0 \text{ for } i \neq j \text{ and } \delta_{ij} = 1 \text{ for } i = j \text{ with } \delta_{ij} = \underline{a}_i^* \cdot \underline{a}_j^*. \qquad (3)$$

The basis vectors of the reciprocal lattice can be calculated from those of the unit cell in real space

$$\underline{a}_i^* = (\underline{a}_j \times \underline{a}_k)/V_c, \qquad (4)$$

where × means the cross product, and $V_c = \underline{a}_1 \cdot (\underline{a}_2 \times \underline{a}_3)$ is the volume of the unit cell.

Here is a compilation of some properties of the reciprocal lattice:

- The reciprocal lattice vectors are perpendicular to those in real space: $\underline{a}_i^* \perp \underline{a}_j$ and $\underline{a}_k$ ($i \neq j,k$)
- The lengths of the reciprocal lattice vectors are $|\underline{a}_i^*| = 1/V_c \cdot |\underline{a}_j| \cdot |\underline{a}_k| \cdot \sin\angle(\underline{a}_j, \underline{a}_k)$.
- Each point *hkl* in the reciprocal lattice refers to a set of planes (*hkl*) in real space.

• The direction of the reciprocal lattice vector $\underline{H}$ is normal to the (*hkl*) planes and its length is reciprocal to the interplanar spacing d_{hkl}: $|\underline{H}| = 1/d_{hkl}$.

• Duality principle: The reciprocal lattice of the reciprocal lattice is the direct lattice.

From the positions of the nodes of the reciprocal lattice obtained by diffraction experiments one can determine directly the parameters of the unit cell of a crystal.

Although somewhat abstract, the concept of the reciprocal space provides a practical tool to express geometrically the condition for Bragg scattering in the so-called Ewald construction. In this way the different diffraction methods can be discussed.

We consider the reciprocal lattice of a crystal and choose its origin 000. In Fig. 2 the wave vector $\underline{k}_0$ (defined in the crystallographers' convention with $|\underline{k}_0| = 1/\lambda$) of the incident beam is marked with its end at 000 and its origin P. We now draw a sphere of radius $|\underline{k}_0| = 1/\lambda$ around P passing through 000. Now, if any point *hkl* of the reciprocal lattice lies on the surface of this Ewald sphere, then the diffraction condition for the (*hkl*) lattice planes is fulfilled: The wave vector of the diffracted beam $\underline{k}$ (with its origin also at P) for the set of planes (*hkl*), is of the same length as $\underline{k}_0$ ($|\underline{k}| = |\underline{k}_0|$) and the resulting vector diagram satisfies $\underline{k} = \underline{k}_0 + \underline{H}$. Introducing the scattering angle 2θ (and hence the Bragg angle θ_{hkl}),we can deduce immediately from $2|\underline{k}|\cdot\sin\theta = |\underline{H}|$ the Bragg equation:

$$2d_{hkl}\cdot\sin\theta_{hkl} = \lambda. \qquad (5)$$

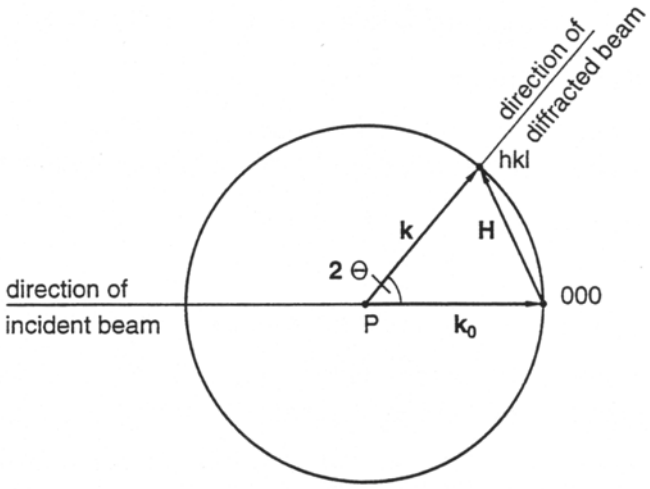

Fig. 2. Ewald construction in reciprocal space, showing the diffraction condition for the *hkl* reflection.

In the case of single crystal diffraction a rotation of the crystal and therefore also of the corresponding reciprocal lattice (which is rigidly attached to the crystal) is often used to set the diffraction conditions for the measurement of intensities I($\underline{H}$).

If $|\underline{H}| > 2/\lambda$ (then $d_{hkl} < \lambda/2$) the reflection *hkl* cannot be observed. This condition defines the so called limiting sphere, with center at 000 and radius $2/\lambda$: only the points of the reciprocal lattice inside the limiting sphere can be rotated into diffraction positions. Vice versa if $\lambda > 2d_{max}$, where d_{max} is the largest interplanar spacing of the unit cell, then the diameter of the Ewald sphere is smaller then $|\underline{H}|_{min}$. Under these conditions no node of the reciprocal lattice can intercept the Ewald sphere. That is the reason why diffraction of visible light (wavelength $\cong$ 5000 Å) can never be obtained from crystals. λ_{min} determines the amount of information available from a diffraction experiment. In ideal conditions λ_{min} should be short enough to measure all points of the reciprocal lattice with significant diffraction intensities.

For a real crystal of limited perfection and size the infinitely sharp diffraction peaks (delta functions) are to be replaced by broadened line shapes. One reason can be the local variation of the orientation of the crystal lattice (mosaic spread) implying some angular splitting of the vector $\underline{H}$. A spread of interplanar spacings $\Delta d/d$, which may be caused by some inhomogeneities in the chemical composition of the sample, gives rise to a variation of its magnitude $|\underline{H}|$. The ideal diffraction geometry on the other hand is also to be modified. In a real experiment the primary beam has a finite divergence and wavelength spread. The detector aperture is also finite. A gain of intensity, which can be accomplished by increasing the angular divergence and wavelengths bandwidth, has to be paid for by some worsening of the resolution function and hence by a limitation of the ability to separate different Bragg reflections.

All of these influences can be studied by the Ewald construction. The influence of a horizontal beam divergence on the experimental conditions for a measurement of Bragg-intensities of a single crystal is illustrated in Fig. 3 where strictly monochromatised radiation (only one wavelength λ with $\Delta\lambda/\lambda = 0$) is assumed. A so-called ω-scan, where the crystal is rotated around the sample axis perpendicular to the diffraction plane, may be used for a reliable collection of integrated intensities in adapting the detector aperture $\Delta 2\theta$ as a function of the scattering angle 2θ. It is obvious that larger $\Delta 2\theta$-values will give rise to a higher background and may lead to difficulties for the separation of neighboured reflections with similar $\underline{H}$-vectors in the reciprocal lattice. It is shown by this example that a larger beam divergence with an increase in intensity can restrict the resolution conditions.

Bragg-intensities of single crystals are recorded in general by $\omega/n \cdot 2\theta$-scans ($0 \leq n \leq 1$) with a coupled rotation of the sample and the detector. The mainly used bisectic special case consists of $\omega = \theta$. The horizontal and vertical detector aperture must be chosen in a way to avoid systematic errors from cutting some intensity of a reflection. The pure ω-scan (rocking-scan) records an intensity distribution of reflection almost perpendicular to the scattering vector $\underline{Q} = 2\pi\underline{H}$ – i.e. almost corresponding to a transversal scan. The $\omega/2\theta$-scan represents a longitudinal scan in reciprocal space recording reflection profiles along $\underline{H}$.

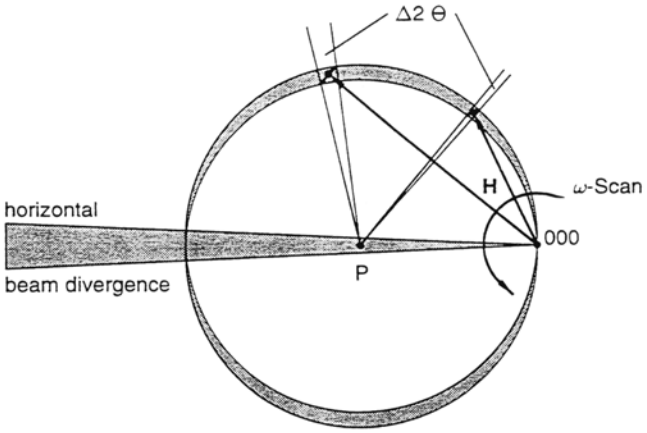

Fig. 3. Ewald-construction: Influence of the horizontal beam divergence on the experimental conditions for the measurement of Bragg-intensities

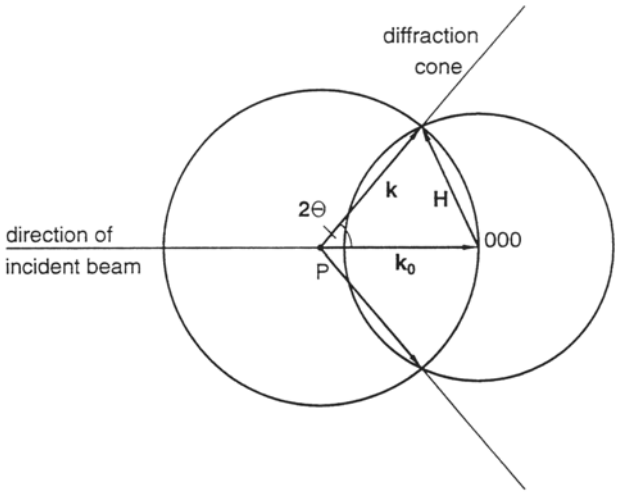

Fig. 4. Ewald-construction in case of powder diffraction

Powder diffraction also may be discussed on the basis of the Ewald-construction. An ideal polycrystalline sample is characterised by a very large number of arbitrary oriented small crystallites. Therefore, for a powder only $|\underline{H}|$ is defined without preferred orientation. In Fig. 4 the corresponding sphere with radius $|\underline{H}| = 1/d_{hkl}$ is drawn around the origin of the reciprocal lattice at 000. For each Bragg-reflection the circle of intersection with the Ewald-sphere yields a diffraction cone. All reflections with equal interplanar spacing are perfectly superposed and cannot be separated.

7. 3 Powder diffractometer

There are two principally different powder diffraction techniques: the angular-dispersive ADP-method and the energy-dispersive EDP-method, better known as time-of-flight method in the case of neutron diffraction. In the ADP measurement the sample is irradiated by a monochromatic beam (λ = const.). To each d_{hkl} belongs a Bragg-angle θ_{hkl}.Most of the neutron powder diffractometers at steady-state reactor sources work according to the ADP method (e. g. the D2B-instrument at the HFR/ILL in Grenoble). The angular resolution of a powder diffraction diagram depends on the beam divergences before and behind the

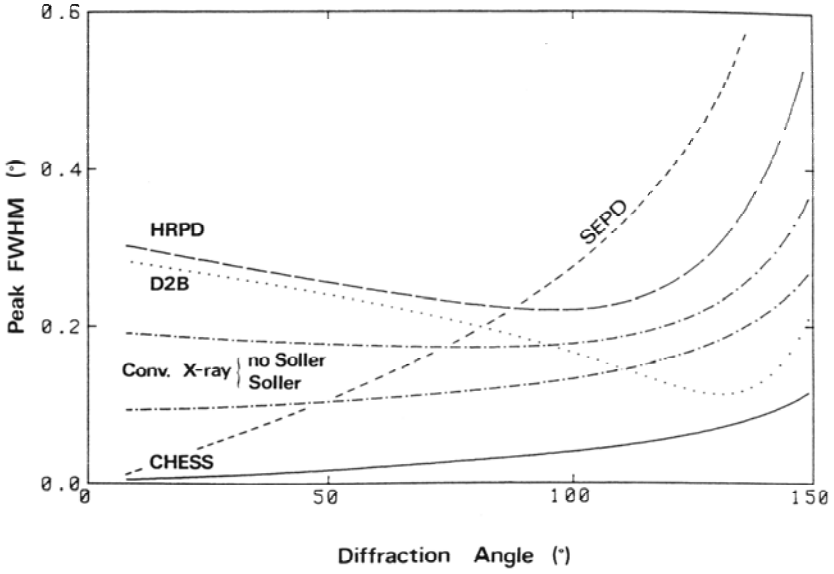

Fig. 5. Comparison of the half-widths of powder lines for selected neutron powder diffractometers: D2B at the HFR/ILL in Grenoble(F), HRPD at NBSR in Lucas Heights (USA), SEPD at ANL in Argonne (USA) – the time-of-flight data of this instrument with $\Delta d/d \approx 1.5 \cdot 10\text{-}3$ are converted in 2θ-values – and X-ray powder diffractometers: conventional and synchrotron facilities (CHESS, USA) [1]

monochromator, on the mosaic spread of the monochromator crystal, and on the monochromator's scattering angle $2\theta_M$. In Fig. 5 for several X-ray- and neutron powder diffractometers the half-width of powder lines (Bragg-reflections) $\Delta 2\theta$ is given as a function of the scattering angle 2θ. A large $2\theta_M$-value can be favourable to realise smaller line widths $\Delta 2\theta$ at higher diffraction angles as can be seen for the D2B-instrument ($2\theta_M = 135°$).

The plan of the E9 instrument at the HMI-reactor BER II in Berlin is shown in Fig. 6. The typical technical data of this new powder diffractometer are:

- collimations $\alpha_1 = 10'$, $\alpha_2 = 20'$, $\alpha_3 = 10'$
- germanium and graphite monochromators with mosaic-spreads $\Delta M(Ge) \approx 20'$ and $\Delta M(PG) \approx 30'$
- monochromator's scattering angle $40° \leq 2\theta_M \leq 140°$
- 64 high pressure gas detectors (^3He, 8 bar) arranged with an angular interval of $\Delta 2\theta = 2.5°$

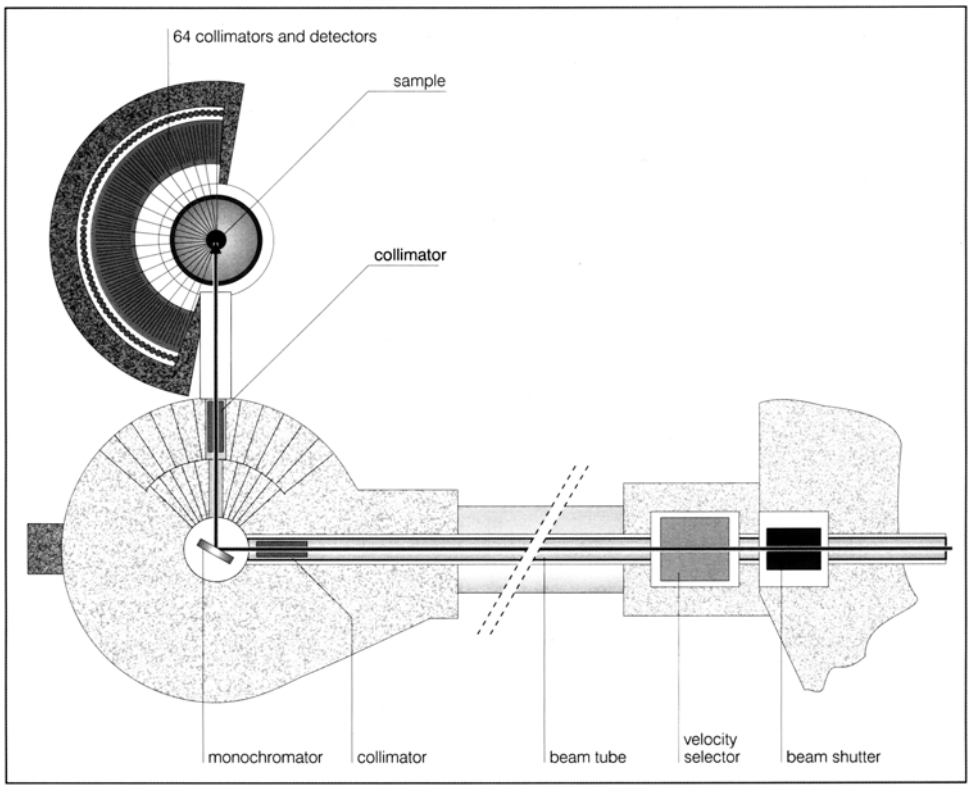

Fig. 6. Plan of the **E9** powder diffractometer at BER II/HMI in Berlin.

For a ADP-powder diffractometer the measuring time can be reduced substantially by the simultaneous use of many single detectors or of linear multidetector systems.

As an example for a 2-axes diffractometer specially designed for the investigation of amorphous systems and liquids the 7C2-instrument installed at the hot neutron source of the ORPHEE-reactor in Saclay (F) is shown in Fig. 7. Combined with an exchange of monochromator crystals there are three different standard wavelengths available: λ(Ge(111)) = 1.1 Å, λ(Cu(111)) = 0.7 Å, λ(Ge(311)) = 0.57 Å. The linear multidetector allows a continuous intensity measurement over a range in scattering angle of 128°. The angular resolution of this instrument is limited as there is no collimation in between the sample position and the detector. But the $|\underline{Q}|$-range is very large. For the shortest wavelength λ(Ge(311)) = 0.57 Å the accessible values extend up to $|\underline{Q}|_{max} = 2\pi|\underline{H}|_{max} = 20$ Å^{-1}.

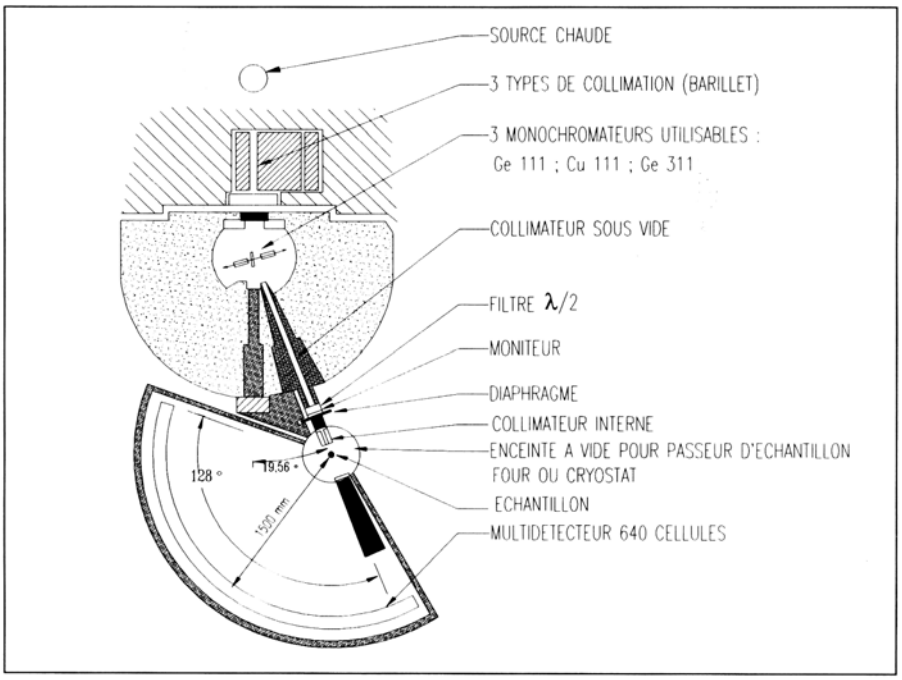

Fig. 7. Plan of the 2-axes diffractometer **7C2** at the hot source of the ORPHEE-reactor in Saclay (F)

To speed-up the measuring time and to improve the data statistics, i. e. for time resolved experiments, the future of neutron diffraction instrumentation lies in the use of large multidetector systems. The powder diffractometer D20 at the ILL in Grenoble is know equipped with a large 1600 element microstrip detector (Fig. 8).

Fig. 8. Large 1600 element microstrip detector of the powder diffractometer **D20** at the ILL Grenoble (F)

In the case of the EDP method a polychromatic white beam is used with the scattering angle being fixed (2θ = const.). The d_{hkl}-values result from the time-of-flight measurement of the neutron velocities – converted to wavelengths - for the *hkl* reflections. This technique is specially suitable for pulsed neutron sources. Moreover, it offers some advantages for complex sample environments, such as extreme temperatures, magnetic fields, external pressures, etc. due to its fixed scattering geometry. The resolution of the time-of-flight analysis Δt/t depends on the wavelength-dependant pulse structure of the moderator, on the length of the flight path, and on the scattering angle 2θ (a back-scattering geometry is recommended). As there are normally relatively short wavelengths in the beam, too, also higher indexed reflections with shorter d_{hkl}-values may be reached. Some typical technical data of the HRPD installed at the spallation source ISIS/RAL in England are shown in Fig. 9. A special feature of this instrument consists in the very long flight path of about 100 m.

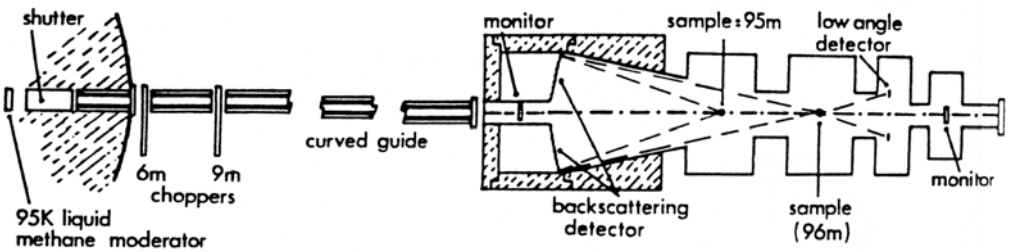

Fig. 9. **HRDP** (high-resolution powder diffractometer) at the spallation source ISIS/RAL, England. A resolution of $\Delta d/d \approx 4 \cdot 10^{-4}$ is achieved with a sample position at 95 m.

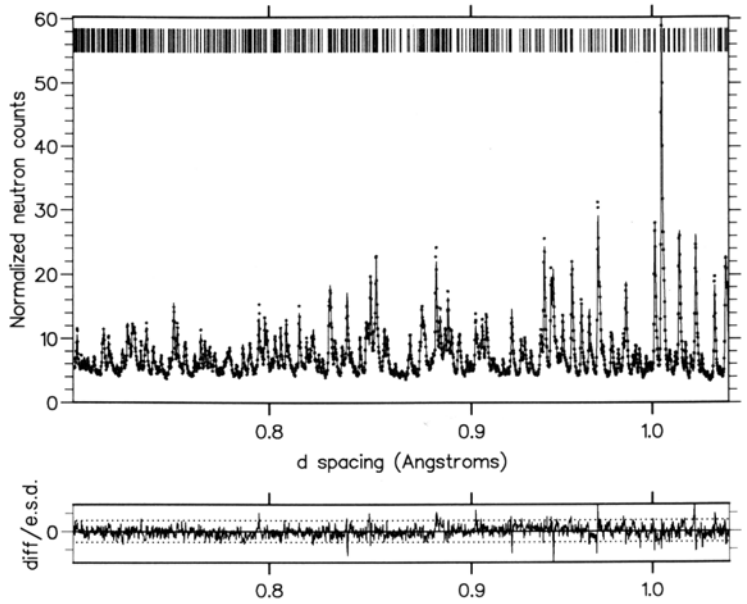

Fig. 10. Powder diffractogram of benzene: (a) section from 0.72 Å ≤ d ≤ 1.03 Å

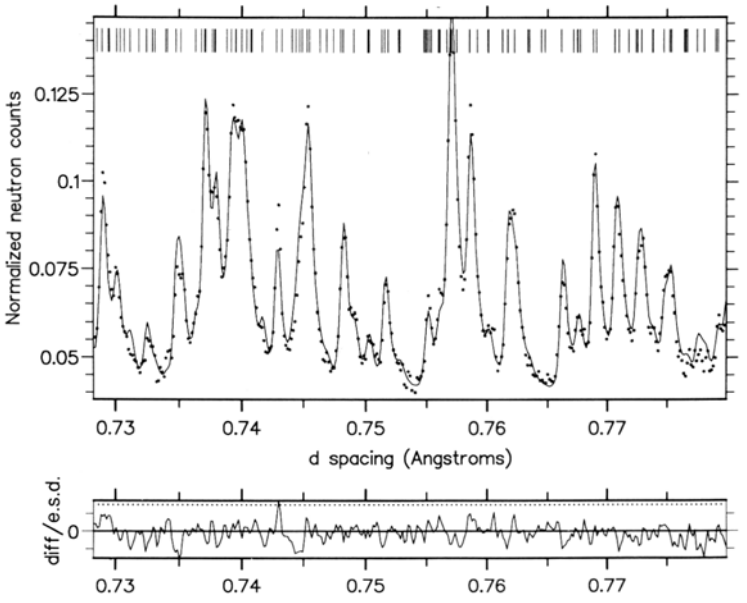

Fig. 10. Powder diffractogram of benzene: (b) enlarged section from 0.73 Å ≤ d ≤ 0.78 Å

The calculated d_{hkl}-values are indicated by the small lines at the top of the upper graph. The quality of the refinement can be judged from the difference in between experimental data and profile calculation in the lower graph.

The excellent resolution of this time-of-flight diffractometer is demonstrated by sections of the powder diffractogram of benzene shown in Fig. 10. The complete rage of $0.5 \leq d \leq 2.0$ Å was analysed by means of the Rietveld profile method in order to refine the crystal structure of this molecular compound [2] (space group Pbca; lattice parameters: a = 7.3551 Å, b = 9.3712 Å, c = 6.6994 Å).

7.4 Single crystal diffractometer

For neutron diffraction studies on single crystals actually there are in use the Laue-method with 2-dim. positional sensitive detectors (e.g. LADI-instrument with an image-plate detector at HFR/ILL in Grenoble (F)) and 2-axes diffractometers with single detectors. New developments with 2-dim. detection systems become more and more important.

To fulfil the diffraction condition for all vectors $\underline{H}$ of the reciprocal lattice (within $2\sin\theta/\lambda < |\underline{H}|_{max}$) single crystal diffractometers are equipped with a special goniometer consisting of three independant rotations. The eularian cradle in Fig. 10 has in addition to the ω-axis ($\perp$ to the diffraction plane) two further rotation axes χ and φ, which are perpendicular to each other. The χ-axis is also perpendicular to the ω-axis. Together with the rotation axis of the detector 2θ ($\parallel$ to the ω-axis) this mechanical unit is called 4-circle goniometer (leading to the name 4-circle diffractometer for this type of single crystal diffractometers). The measurement of integrated intensities $I(\underline{H})$ of individual Bragg-reflections is performed according to the $\omega/n{\cdot}2\theta$-scan techniques described in chapter 7.2. For a computer-controlled automatic data collection a detailed knowledge of the crystal lattice is needed. Therefore, a single crystal diffraction experiment starts by a systematic search of reflections in varying χ and φ, with the restriction $\omega = \theta$ (bisected condition). From the accurate angular positions of typically 20 indexed reflections the lattice constants and the orientation matrix are determined.

As an example for a single crystal neutron diffractometer the P110/5C2-instrument installed at the hot neutron source of the ORPHEE-reactor in Saclay (F) is shown in Fig. 11. The monochromatic neutron flux at the sample position is increased by a monochromator system with vertical focussing. The use of small wavelengths allows the measurement of Bragg-intensities up to large $|\underline{H}|$-values ($|\underline{H}|_{max} = 2\sin\theta_{max}/\lambda = 2.8$ Å^{-1}).

Attention: The lengths of both the vector $\underline{H}$ of the reciprocal lattice used in crystallography and the scattering vector $\underline{Q}$ of solid state physics are expressed in Å^{-1}. But there is a factor of 2π which means that $|\underline{H}| = 2.8$ Å^{-1} corresponds to $|\underline{Q}| = 17.6$ Å^{-1}.

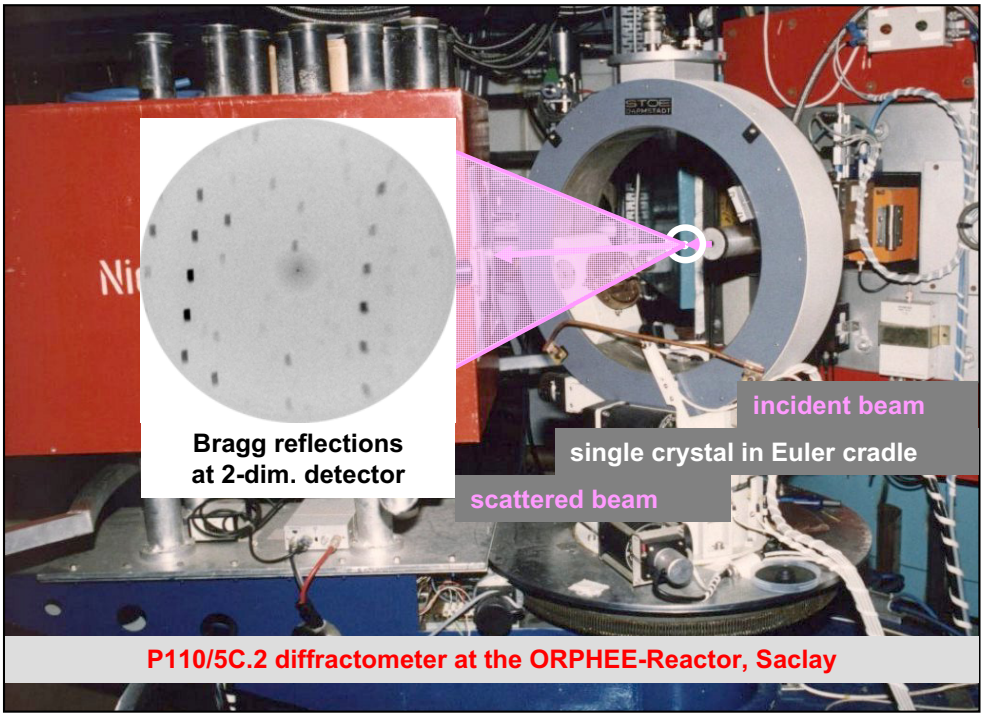

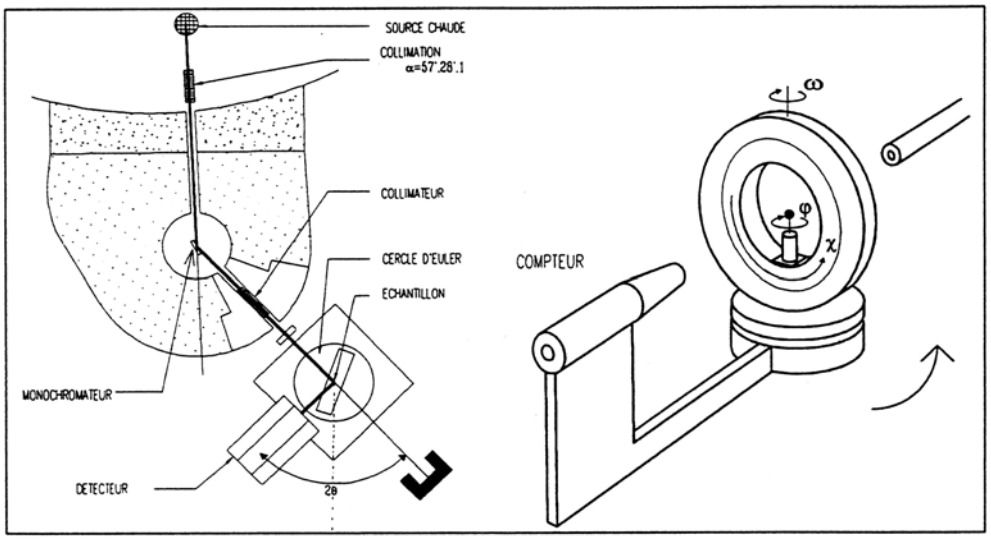

Fig. 11. Single crystal diffractometer **P110/5C2** at the hot neutron source of the ORPHEE-reactor in Saclay (F)

The influence of the primary collimation α_1 on the half-width of Bragg-reflections of a perfect Ge crystal is shown in Fig. 12. The resolution curves for two different wavelengths λ(Cu(420)) = 0.525 Å and λ(Cu(220)) = 0.831 Å are plotted as a function of sin θ/λ.

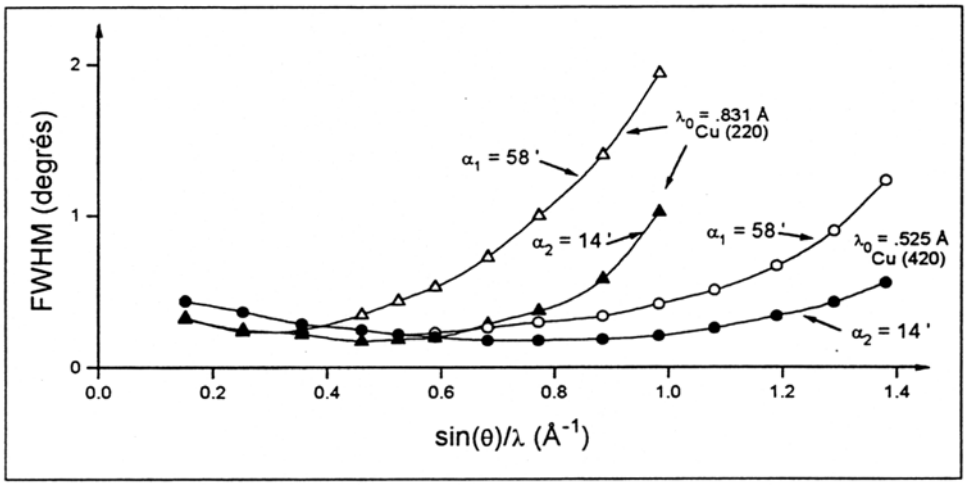

Fig. 12. Resolution curves of the single crystal diffractometer **P110/5C2** at the hot neutron source of the ORPHEE-reactor in Saclay (F)

References

[1] R. J. Hill, The Riedveld Method, ed. R. A. Young, Chap. 5, Oxford University Press (1993)

[2] W. I. F. David and J. D. Jorgensen, The Riedveld Method, ed. R. A. Young, Chap. 11, Oxford University Press (1993)

8

Small-Angle Scattering

Henrich Frielinghaus

8. Small Angle Scattering

Henrich Frielinghaus

8.1. Introduction

Small angle scattering is used in conventional solid state physics and, nowadays, strongly in the field of soft matter research. This field embraces polymer melts, solutions, and rubbers, but also complex fluids such as microemulsions, colloidal dispersions, and micellar solutions. The similarity to biological systems brings biologists and physicists together at a small angle scattering machine. The measured magnitude of such a small angle scattering experiment is the intensity as a function of the momentum transfer Q:

$$Q = \frac{4\pi}{\lambda} \sin\Theta \tag{8.1}$$

with the scattering angle 2Θ and the wavelength λ of the neutrons. The momentum transfer $\vec{Q}$ is the difference of the momenta of the incoming and scattered neutrons. In an elastic scattering experiment the absolute momentum does not change, i.e. $\left|\vec{k}_i\right| = \left|\vec{k}_f\right| = 2\pi/\lambda$, since the observed objects are large and, therefore, move only slowly. The length scale of the observed objects is given by the momentum transfer *Q*, which is in the range of 0.3 to 10^{-4}Å^{-1} due to the wavelength λ = 5 to 20Å and the small angles. Thus, the considered length scales in real space $\ell = 2\pi / \lambda$ are of the order 10 to 10^5Å (or 1nm to 10μm). The different instruments are optimized for different length scales; the technical realizations will be presented in this lecture. While the geometrical realizations of each instrument are discussed first, some components are discusses in the last sections in general. The discussed instruments are optimized for continuous radiations sources as the FRM-2. Spallation sources generate neutron pulses of different periodicity. Then, a whole spectrum of wavelengths is treated simultaneously, and the instruments need much quicker detectors for instance.

8.2. Absolute Intensity at Sample and Detector

The discussed conditions of a scattering experiment are depicted in Fig. 8.1 for a real space and a reciprocal space interpretation. In a realistic experiment the incoming and final neutrons have some uncertainty in direction (divergence) and wavelength. This detail is an issue of the resolution of the experiment, and will also be discussed below. The illuminated area of the sample is indicated by F.

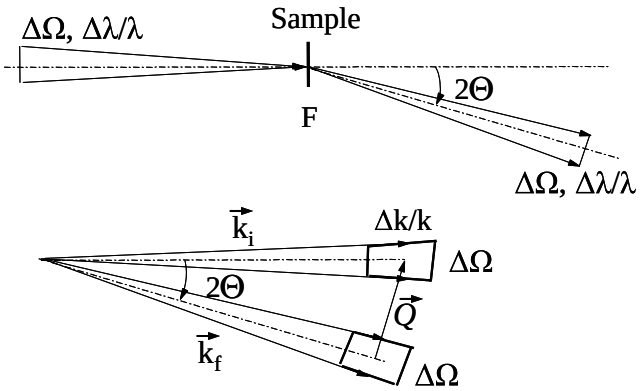

Figure 8.1: The changes of momentum due to the scattering process in a real space and a reciprocal space interpretation. The realistic experiment gives rise to uncertainties of the direction and wavelength, which will also be discussed in the context of the instrument resolution.

The intensity obtained by a reactor is characterized by the equilibrium of the neutrons with the moderator and/or the cold source. Thus, the neutrons are characterized by a certain temperature T or a typical wave vector $k_T = \sqrt{2m_n k_B T}/\hbar$ with m_n being the neutron mass, and k_B and $\hbar$ being the Boltzmann and Planck constants. The luminosity of the source is given by

$$L = \frac{\Phi}{2\pi}\left(\frac{k}{k_T}\right)^4 e^{-(k/k_T)^2}\frac{\Delta k}{k} \tag{8.2}$$

in units $cm^{-2}s^{-1}steradian^{-1}$. It is determined by the total thermal flux of the neutrons Φ and the selected wavelength band Δk due to the monochromator, which can be freely adjusted to any wave vector k. The intensity at the sample is then given by:

$$\Delta I_0 = L \cdot F \cdot \Delta\Omega \tag{8.3}$$

This intensity is also called *primary intensity*, and is proportional to the irradiated area F and the divergence $\Delta\Omega$ due to an adjustable collimation. The interplay of intensity and resolution is discussed below.

For the scattered neutrons the first Born approximation is assumed to be valid. This means that each incoming neutron is scattered at most once. Practically, this means that only 10% of the neutrons are scattered coherently. Another large fraction (up to 40%) is scattered incoherently, and the remaining neutrons pass the sample unscattered. Within this approximation the scattered intensity can be related to the macroscopic cross section, according to:

$$\Delta I_D(\vec{Q}) = \Delta I_0 \cdot D \cdot T \cdot \frac{d\Sigma}{d\Omega}(\vec{Q}) \cdot \Delta\Omega_D \qquad (8.4)$$

The scattered intensity ΔI_D is detected at the detector in an element with the solid angle $\Delta\Omega_D$. The scattering vector $\vec{Q}$ is determined by the scattering angle 2Θ and a polar angle. For isotropic samples the intensity is independent of the polar angle. The sample thickness *D* and the transmission *T*, which is the ratio of the transmitted non-scattered and the primary intensities, determine the scattered intensity as well. The macroscopic cross section $d\Sigma/d\Omega$ is the experimental result given in absolute units [cm^{-1}]. It is free from most instrumental details, and, therefore, can be compared with other experiments or theoretical descriptions. Only resolution aspects remain inherent, which have to be treated separately as discussed below.

Since the primary intensity is too high to be measured by the detector directly, a secondary standard is usually used to measure the incident intensity indirectly. An incoherent scatterer (water or plexiglass) with a known macroscopic cross section delivers a constant intensity on the detector. The intensities of the sample and the standard are compared relatively, and the primary intensity cancels out. In this relative measurement the detector efficiency, which we did not treat explicitly here, is also removed from the final result.

8.3. Small Angle Scattering with Neutrons

The method of small angle neutron scattering (SANS) is frequently used for structural investigations in the nanometer scale. There are three different SANS techniques: The pin-hole SANS covers the conventional range of 1 to 100nm. This range is extended by the focusing SANS with either mirrors or lenses up to 1000nm. The double crystal (Bonse Hart) diffractometer reaches length scales in the µm range. While the pin-hole SANS is refurbished with an option of lenses at the JCNS in Garching, the conventional focusing mirror SANS runs in Garching as well. The double crystal diffractometer is not currently installed at the FRM-2, but such instruments exist at several institutions.

8.3.1. Pin-Hole SANS

After thermalization in the cold source at ca. 30K (see §8.2) the neutrons are guided through neutron guides to the instrument. A scheme of a pin-hole SANS is shown in Fig. 8.2. The monochromator is a mechanical velocity selector with tilted lamellae on a rotating cylinder (see §8.4.2). Typically, neutrons are prepared with a wavelength λ of 5 to 20Å and a relative distribution $\Delta\lambda_{FWHM}/\lambda$ (full width at half maximum) of 10 to 20%. One far aperture and the

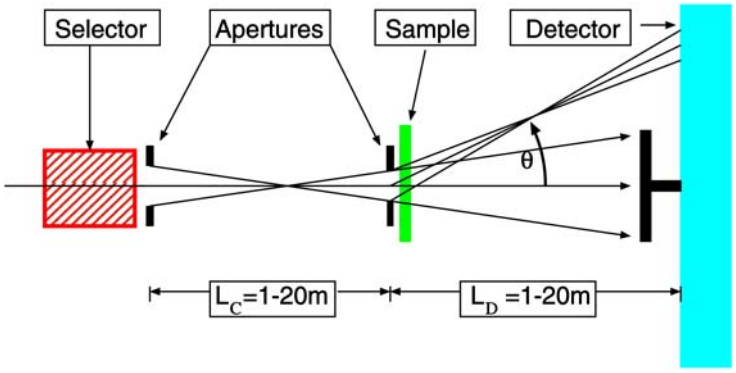

Figure 8.2: Scheme of a pin-hole SANS: The neutrons pass a velocity selector; the divergence is determined by two apertures in the collimation; then the neutrons hit the sample. The non-scattered neutrons are absorbed by the beam-stop. The scattered neutrons are collected by the position sensitive area detector.

sample aperture determine the divergence of the beam. The absorbing material contains usually boron (or even pure ^{11}B) in the form of boron carbide; but cadmium is another option. Then the beam hits the sample. The non-scattered neutrons are absorbed at the beam-stop in front of the detector. A small monitor in the beam-stop allows to determine the transmitted intensity. The scattered neutrons are collected by the position sensitive area detector. From the position the angle Θ and the scattering vector Q are obtained, to which the measured intensity is assigned.

The for the specific sample needed range of scattering vectors Q is set by different detector distances L_D between 1.3 and 20m, while the neutron wavelength (typically 7Å) is changed in extreme cases only. The typical Q-range is thus 0.3 to 10^{-3}Å^{-1}. The collimation length L_C is usually set symmetrically, which means $L_C = L_D$. The varying distance between the monochromator and the entrance aperture is bridged by 1m segments of neutron guides. So the collimation length L_C can only be varied in 1m steps. The shorter collimation distances L_C for larger scattering angles Q have the advantage, that the relaxed divergence conditions lead to higher intensities and thus to shorter measurement times. The intensity at the sample position as a function of the collimation length L_C is shown in Fig. 8.3.

From the variation of eq. 8.1 the principal equation of the resolution correction can be obtained:

$$\left(\frac{\Delta Q}{Q}\right)^2 = \left(\frac{\Delta\Theta}{\Theta}\right)^2 + \left(\frac{\Delta\lambda}{\lambda}\right)^2 \qquad (8.5)$$

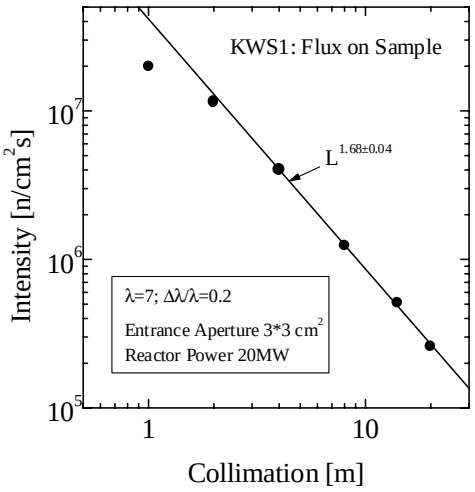

Figure 8.3: The intensity at the sample position for different collimation distances L_C. This dependence was measured at the instrument KWS-1 at the Jülich reactor FRJ-2. Higher intensities are expected for Garching. The saturation at small collimation lengths is due to the total angle of reflection of the Ni neutron guides.

The uncertainty of the scattering vector ΔQ is of interest for either deconvoluting the measured spectrum to an ideal spectrum, or for convoluting a theoretical function, which is fitted to the measured intensity. On the right hand side of eq. 8.5 the two independent contributions are listed: $\Delta\Theta$ is the collection of all angular uncertainties, which are due to the two collimation apertures and the finite size of the detector elements. $\Delta\lambda$ arises from the wavelength distribution of the selector.

As a first approach [4], all angular contributions can be assumed to be independent. This means that three terms arise from the entrance aperture with the diameter d_E, the sample aperture with the diameter d_S and the detector elements with the diameter d_D:

$$\sigma_Q^2 = \frac{2}{12} k^2 \left(\left(\frac{d_E}{L_C} \right)^2 + \left(\frac{d_S}{L_C} + \frac{d_S}{L_D} \right)^2 + \left(\frac{d_D}{L_D} \right)^2 + \Theta^2 \left(\frac{\Delta\lambda}{\lambda} \right)^2 \right) \qquad (8.6)$$

The left hand side of eq. 8.6 is solved for the variance σ_Q of the scattering angle, while the Δ-values represent full width at half maximum values. The additional factor 2 in eq. 8.6 with respect to reference [4] was added due to the 2-dimensional distribution of the intensity (at the detector). A more detailed study [5] includes the dependence of the angular uncertainty from the entrance and sample apertures. The final result reads:

$$\sigma_Q^2 = \frac{1}{8\ln 2} k^2 \left((\Delta\beta)^2 + \left(\frac{d_D}{L_D}\right)^2 + \Theta^2 \left(\frac{\Delta\lambda}{\lambda}\right)^2 \right) \tag{8.7}$$

with:
$$\Delta\beta = \begin{cases} \dfrac{d_E}{L_C} - \dfrac{1}{4}\dfrac{d_S^2}{d_E}\dfrac{(L_C + L_D)^2}{L_C L_D^2} & \text{for } \dfrac{d_E}{L_C + L_D} \geq \dfrac{d_S}{L_D} \\ \left(\dfrac{d_S}{L_C} + \dfrac{d_S}{L_D}\right) - \dfrac{1}{4}\dfrac{d_E^2}{d_S}\dfrac{L_D}{L_C(L_C + L_D)} & \text{for } \dfrac{d_E}{L_C + L_D} < \dfrac{d_S}{L_D} \end{cases} \tag{8.8}$$

The first case of eq. 8.8 is the more common case, which means that the collimation aperture covers a larger angle than the sample aperture regarded back from the detector. The two prefactors of eqs. 8.6 and 8.7 are virtually identical.

As already mentioned, the instrument is usually set up symmetrically. Then, the optimized condition of the instrument – resolution-wise and intensity-wise – is obtained by:

$$L_C = L_D \qquad \text{and} \qquad d_E = d_D = 2\,d_S \tag{8.9}$$

Arguing on the basis of eq. 8.6, all independent contributions should be equal. The refined analysis with eq. 8.7 leads to the same result, since Δβ is minimal then. Since the detector technique is highly developed, the single detector element d_D is rather small, and generally can be neglected in the resolution consideration. The optimized intensity at the sample position is given by eq. 8.3, and reads:

$$\Delta I_0 = L_{\text{luminosity}} \cdot \frac{d_E^2}{L_C^2} \cdot \frac{d_S^2}{L_D^2} \cdot L_D^2 \quad \propto \quad L_{\text{luminosity}} \cdot \left(\frac{\Delta Q}{k}\right)^4 \cdot L_D^2 \tag{8.10}$$

The second part of this equation is just given without a precise prefactor, since the general dependence is more important: The intensity decreases with the power of 4 with a higher resolution, but longer instruments can compensate partially for this intensity loss. This is the reason, why typical SANS instruments are 40m long.

The quality of a SANS instrument can be judged by the primary neutron beam on the detector (with an attenuated direct beam). On the one hand the width of the beam can be compared with the theoretically expected width (eqs. 8.6 and 8.7), since the measured curve coincides with the resolution function at Q = 0. On the other hand the background intensity near the primary beam tells about the minimum detectable signal of a weakly scattering sample. An example measurement has been depicted in Fig. 8.4. The full width at half maximum is $\Gamma_{½}$, and the background is typically read off at $2\Gamma_{½}$. For good SANS instruments this background is in the range of 10^{-5} to 10^{-6}, and the beam stop can be made as small as possible.

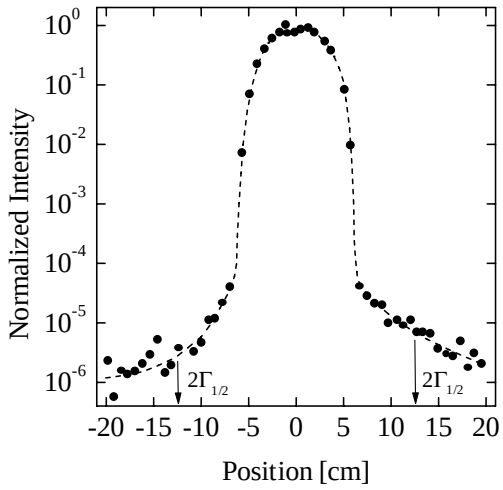

Figure 8.4: Semi-logarithmic intensity scan of the primary beam. This curve coincides with the resolution function at a scattering angle zero. The residual intensity next to the primary beam tells about the minimum signal detectable from a scattering sample. This background is typically read off at twice the full width at half maximum $\Gamma_{½}$.

8.3.2 Pin-hole SANS with focusing lenses

As we have seen with eqs. 8.6 and 8.7 and Fig. 8.4 the collimation aperture is imaged by the pin-hole SANS on the detector, and the sharpness of this image is connected with the resolution of the instrument. A simple improvement of the simple pin-hole SANS can be reached by placing a set of MgF_2 lenses right in front of the sample. This allows to open the sample aperture virtually infinitely while the imaged collimation aperture on the detector remains the same (or is even slightly improved). Regarding the sample intensity one obtains:

$$\Delta I_0 = L_{\text{luminosity}} \cdot \frac{d_E^2}{L_C^2} \cdot \frac{d_S^2}{L_D^2} \cdot L_D^2 \quad \propto \quad L_{\text{luminosity}} \cdot \left(\frac{\Delta Q}{k}\right)^2 \cdot \gamma_C^2 \cdot L_D^2 \qquad (8.11)$$

The collimation aperture is connected with the resolution, while the maximum sample aperture is limited by the transported divergence of the neutron guide, i.e. the total angle of reflection γ_C. There are two possible applications of the neutron lenses: (i) The resolution is kept constant, and the intensity is increased due to the smaller exponent 2 (instead of 4); (ii) the intensity is kept at a reasonable level, and the resolution is increased by choosing a smaller collimation aperture.

Some extremely well suited lenses are depicted in Fig. 8.5. These lenses are manufactured from MgF_2 and have a diameter of 5.2 cm. Due to the negative refractive index for neutrons

Figure 8.5: Aspherical MgF_2 lenses as focusing neutron device. The lenses are concave since the refractive index is smaller than unity for the neutrons. The lenses have a parabolic shape in order to reduce the spherical aberrations.

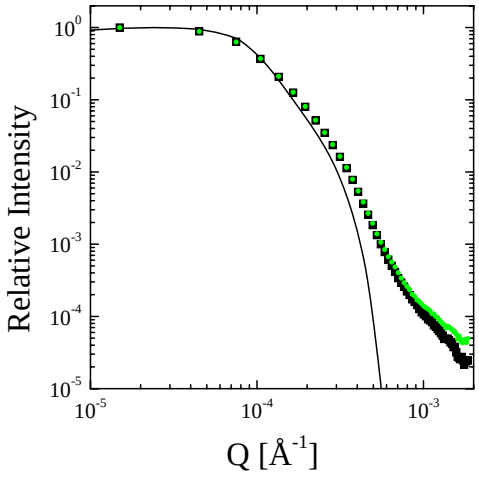

Figure 8.6: The primary beam of a pin-hole SANS instrument with 7 neutron lenses. The instrument setup was L_C = 10m, L_D = 10m, d_E = 5mm, d_S = 5cm, d_D = 0.5mm, λ=19Å. The black squares were measured, while the solid line was computer simulated. The difference is due to scattering windows material. The small greed dots are the scattering signal of a sample.

the lenses are concave. Furthermore we chose a parabolic shape in order to reduce the spherical aberrations. Seven of these lenses have been successfully tested in a conventional pin-hole SANS machine. Since the maximum collimation and detector distances were 10m, we had to chose a neutron wavelength of λ = 19Å to reach a focus of 5m. A high resolution detector with a spatial resolution of d_D = 0.5mm was used. The measured primary beam, as

depicted in Fig. 8.6, agrees well with the computer simulations. Only some scattering of window material shows an additional signal at higher Q. A sample measured with these conditions shows considerable scattering at the higher Q, but a detailed analysis shows, that considerable differences are detectable down to $Q = 10^{-4}$Å^{-1}. In this way the neutron lenses proved to be successful in the high resolution application. The simpler high intensity application was not tested so far since the desired 28 lenses have not been manufactured so far, but a 10 times higher intensity is expected if the lenses are cooled down to 100 to 150K to reduce the thermal diffuse scattering.

The Q-resolution of a lens based SANS instrument can be found in reference [6]. The general problem is the chromatic aberration which is proportional to the selected wavelength band $\Delta\lambda$. This additional term slightly reduces the quality of this solution; and this problem is overcome with focusing mirrors.

8.3.3. Focusing SANS

Historically, the concepts of a focusing SANS instrument were developed for a mirror based solution. However, these concepts do not differ from the lens based instrument, as we will see. A scheme of this instrument is given in Fig. 8.7. The monochromatized neutrons enter the instrument through an aperture of $d_E \approx 2$mm. The focusing mirror is installed at a rather flat angle close to the total angle of reflection. To cover the full divergence of the neutron guide, the mirror has a quite large area (length up to 1.2m). The sample is placed directly behind the mirror, and the detector collects the scattered neutrons. The instrument is symmetric, i.e $L_C = L_D = 11$m, and the focus of the mirror is exactly in the middle $f = 5.5$m. The position sensitive detector has a spatial resolution of $d_D = 0.5$mm. With a typical wavelength of 15Å the instrument covers the typical Q-range between 10^{-3} and 10^{-4}Å^{-1}, which is also typical for light scattering.

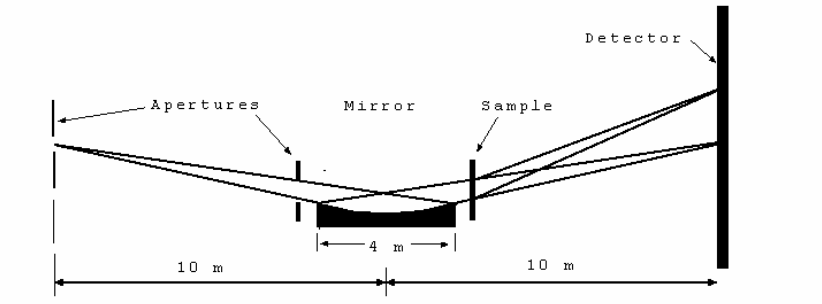

Figure 8.7: Scheme of the focusing SANS instrument KWS-3.

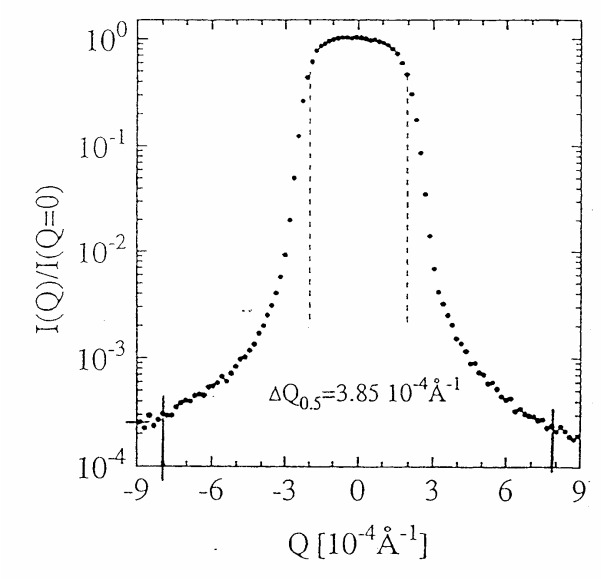

Figure 8.8: Footprint of the primary beam of the focusing SANS. The width of this curve $\Delta Q_{0.5}$ is the resolution at zero scattering angle. The residual intensity at $2\Delta Q_{0.5}$ is much higher than for the conventional SANS instrument.

The intensity at the sample position is given by the same concepts as for neutron lenses:

$$\Delta I_0 = L_{\text{luminosity}} \cdot \frac{d_E^2}{L_C^2} \cdot \frac{d_S^2}{L_D^2} \cdot L_D^2 \quad \propto \quad L_{\text{luminosity}} \cdot \left(\frac{\Delta Q}{k}\right)^2 \cdot \gamma_C^2 \cdot L_D^2 \tag{8.12}$$

The break even point for the focusing SANS instrument in comparison to the pin-hole setup appears for Q in the 10^{-3}Å^{-1} region. The focusing SANS concept has been known for a long time, but only recent developments of high quality mirrors made this instrument possible. An example of a primary beam measurement is shown in Fig. 8.8. The mirrors originate to a development of X-ray satellites, and were successfully transferred for the purposes of neutron scattering.

8.3.4. Double Crystal Diffractometer

This double crystal diffractometer (DCD), or this Bonse-Hart diffractometer has the highest resolution in comparison with the other SANS instruments. A scheme of this instrument is given in Fig. 8.9. The essential parts are two perfect silicon single crystals mounted on an optical bench. The reflectivity $R(y)$ of a perfect crystal is described by the Darwin curve:

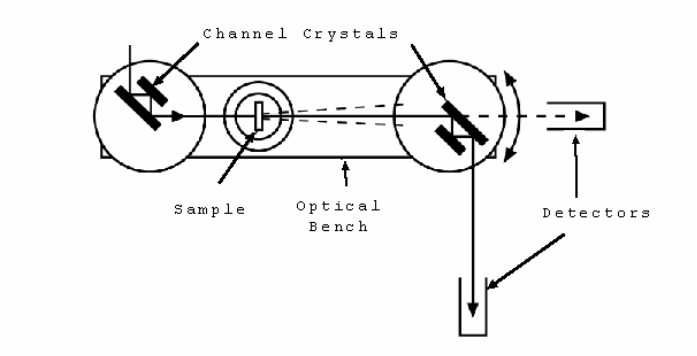

Figure 8.9: Schematic design of a double crystal diffractometer

$$R(y)=\begin{cases}1 & |y|\le 1\\ 1-(1-y^{-2})^{0.5} & |y|>1\end{cases} \tag{8.13}$$

The ideal Darwin curve is depicted in Fig. 8.10. The Bragg angle is called Θ, and the parameter y is the deviation of the scattering angle $\Delta\Theta$ normalized with respect to the Darwin width $\Delta\Theta_C$, i.e. $y = \Delta\Theta / \Delta\Theta_C$. So for smaller deviating angles than the Darwin width all neutrons are reflected.

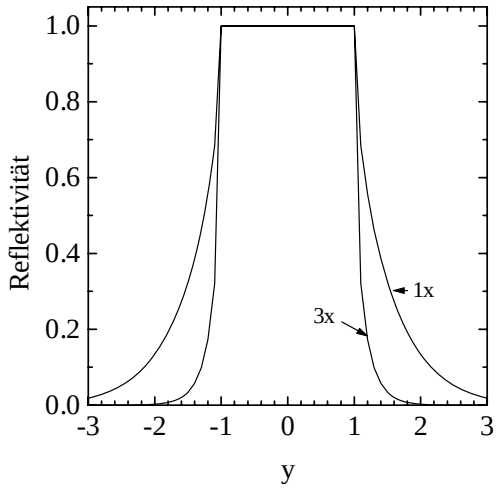

Figure 8.10: Ideal Darwin curve of a single crystal (indicated by 1x). After three reflections the Darwin curve is much sharper (indicated by 3x, i.e. the third power of the original curve).

The analyzing crystal is rotated with respect to the first one by an angle δ. The resulting intensity as a function of δ arises from the convolution of two Darwin curves as given by eq. 8.13 and Fig. 8.10. This convolution is depicted in Fig. 8.11. At an angle δ = 0 the lattice planes of both crystals are oriented parallel, the two Darwin curves overlap totally, and the maximum intensity is obtained. With a finite rotation δ the two Darwin curves overlap only partially, and the reflected intensity is reduced. The width of this convolution function Δδ is characteristic for the minimum scattering angle $Q_{\min}$, and is given by the Darwin width $\Delta\delta \approx \Delta\Theta_C$, which in turn is given by:

$$\Delta\Theta_C = \frac{b_C\, e^{-W} |F|\, N\, \lambda^2}{4\pi \cdot \sin(2\Theta)} \tag{8.14}$$

For the (331) lattice planes of a Silicon single crystal and neutrons with a wavelength of λ = 1.8Å the Bragg angle of diffraction is about 45° and the half width of the resolution curve is $\Delta\Theta_C$ = 3.2μrad, which corresponds to an angle of slightly more than half a second of arc or a scattering vector of $Q = 1.12 \cdot 10^{-5}$Å^{-1} (the missing symbols are the scattering length b_C of silicon, the Debye-Waller factor exp(-*W*), the structure factor *F*, and the atom number density *N*). So this diffractometer opens access to smallest scattering angles, which demands protections against mechanical vibrations, fluctuations of temperature, and much patience from experimentalist.

The strength of this instrument is its very high resolution, which is even better than of light and its relatively simple and cheap design in comparison with most other neutron scattering instruments. This instrument can also be successfully operated at smaller research reactors. Disadvantages are (i) the slit geometry, which needs a special deconvolution formula for isotropic samples, (ii) the sequential scanning of different *Q*-vectors, which is time consuming, and (iii) a rather low intensity, which needs good background conditions. Improvements are possible by a special design of the crystals: The relatively high background near the primary beam can be strongly suppressed by a 'channel cut' in the crystals, which separates the crystal volumes of each reflection, and interference of guided waves within the crystal are reduced. A nearly ideal triple reflection is obtained as indicated by Figs. 8.9 and 8.10. The resulting resolution function is depicted in Fig. 8.11 with highly suppressed tails. Experimentally, this change from single-single to triple-triple reflections was verified as shown in Fig. 8.12. The multiple reflections clearly lead to a sharper resolution and a strongly suppressed background next to the primary beam. The background level of 10^{-4} is sufficient for many samples since the observed objects are large anyways, and thus scatter strongly.

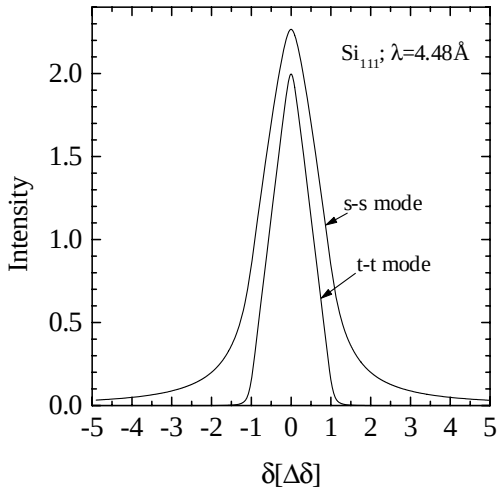

Figure 8.11: Theoretical resolution curves of a double crystal diffractometer as obtained from the self-convolution of a Darwin curve (Fig. 8.10). The two different curves represent the modes of a single-single (s-s) and a triple-triple (t-t) reflection. Clearly, the resolution is improved, and the background suppressed. The angle δ is given in relative units of the Darwin width Δδ.

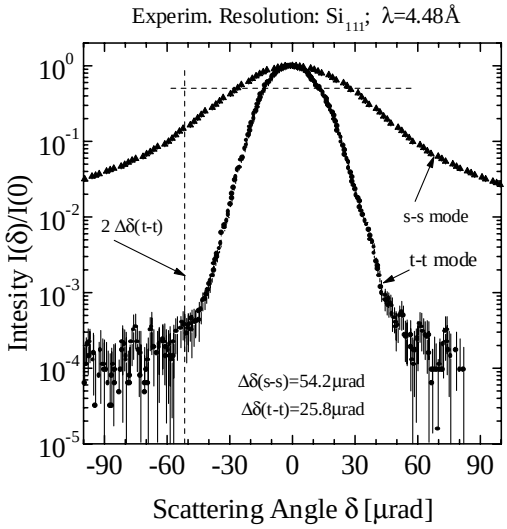

Figure 8.12: An experimental resolution of a double crystal diffractometer for the two modes of a single-single and triple-triple reflection. The 'channel cut' in the crystal was necessary to obtain a much more ideal result, since guided waves within the crystal are suppressed.

8.4. Important Elements of Small Angle Scattering

Important elements of a small angle neutron scattering diffractometer are: (i) the neutron guides transport the neutrons from the cold source to the instrument, and are used to bridge distances within the collimation; (ii) the velocity selector selects mechanically the wavelength of the neutrons (or crystals are used for the DCD); (iii) the position sensitive detector allows for the allocation of intensities to scattering angles in one snapshot.

8.4.1. Neutron Guide

Neutron guides transport neutrons over long distances without large losses. As we have already seen in the discussion of intensities of focusing SANS instruments (eqs. 8.11 and 8.12) an essential parameter is the maximum divergence, which is transported by the neutron guide. It is tightly connected with the angle of total reflection, which reads:

$$\gamma_C = \lambda\ (\rho / \pi)^{0.5} \tag{8.15}$$

The coherent scattering length density is given by $\rho = b_C \cdot N$. Already natural nickel is a good choice for the coating to reach large angles of total reflection. An even better choice is the isotope nickel 58 because of the large coherent scattering length. The total angle of reflection is $\gamma_C = 6' \cdot \lambda[\text{Å}]$ and $\gamma_C = 7.1' \cdot \lambda[\text{Å}]$ for natural and pure nickel. Some 40 years ago neutron guides were invented at the research reactor in Munich. Neutron guides made neutron scattering instruments more popular since many more instruments can be placed around the reactor. The intensity is still high far away from the reactor core.

An advanced technique to transport neutrons with an even higher critical angle is connected to the super mirrors. Alternating layers of two different metals with sufficiently different scattering length densities and a continuous range of layer thicknesses leads to Bragg scattering over a larger continuous range of angles. The total angle of reflection can be increased my more than a factor of two with respect to ^{58}Ni (this is called the m-factor). The disadvantage is a slightly reduced reflectivity close to the smallest angles, which means considerable neutron losses over longer distances (and this radiation has to be absorbed).

Another application of the super mirrors is a curved neutron guide. The curvature can be made rather large when the m-factor is large. The bender guides can have one or many channels. Super mirrors in a constant magnetic field can also serve as polarizer either in reflection or in transmission.

8.4.2. Velocity Selector

A rotor of a velocity selector is depicted in Fig. 8.13. In the vacuum housing the rotor can rotate with a speed of up to 30,000 rpm. The selector lets neutrons with the right speed pass through the rotating lamellae. The wavelength distribution of the monochromatized neutrons is shown in Fig. 8.14. The wavelength is inversely proportional to the rotation speed. The slower and faster neutrons are absorbed in the lamellae, which contain either lithium or boron.

Figure 8.13: The rotor of the velocity selector of KWS-3 built at the FZ-Jülich.

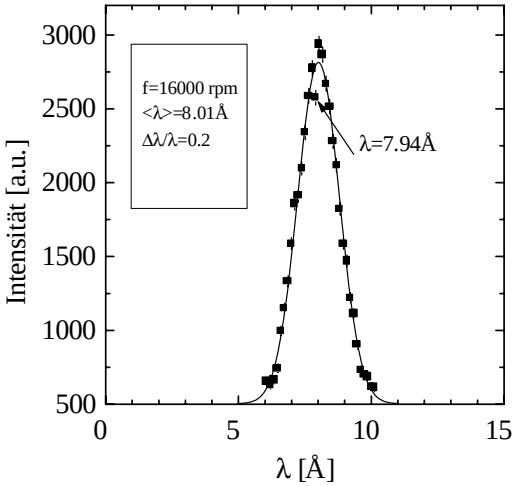

Figure 8.14: Time-of-flight spectrum of a velocity selector. By measuring the flight time with a triggered chopper, the velocity and the wavelength are determined. Due to the Bragg scattering of the bismuth filter the wavelength can be calibrated by the small dip at 7.94Å.

8.4.3. Position Sensitive Detectors

Position sensitive detectors can collect much information by one snapshot, which reduces the measurement times dramatically (compared to the DCD for instance). The spatial resolution of pin-hole SANS detector is typically 0.5 to 1cm, and the focusing (lens and mirror) SANS needs a spatial resolution of 0.5 to 1mm. The number of channels ranges from 64x64 over 128x128 to 256x256. Usually the spatial resolution is much better than required by the experimental resolution (as given by eqs. 8.6 and 8.7). There are gas- and scintillation-detectors available which all base on a nucleus reaction with the neutron.

8.4.3.1. Gas Detector

^{3}He gas detectors are frequently used for neutron scattering experiments. The neutron is absorbed by the helium atom and decays according to

$$^3\text{He} + \text{n} \rightarrow {}^3\text{H} + {}^1\text{H} + 0.77\text{MeV} \qquad (8.16)$$

in two ionic particles with kinetic energies of 0.573Mev and 0.191Mev for the proton and the ^{3}H (tritium), respectively. As shown in Figure 8.15, this 'primary ionization' generates free electrons. The free electrons are accelerated by the electric field and produce further charges by the 'secondary ionization' process. The acceleration of the electrons dominates due to their smaller mass, and finally a full avalanche of electrons generates a measurable current at the anode for the detector electronics.

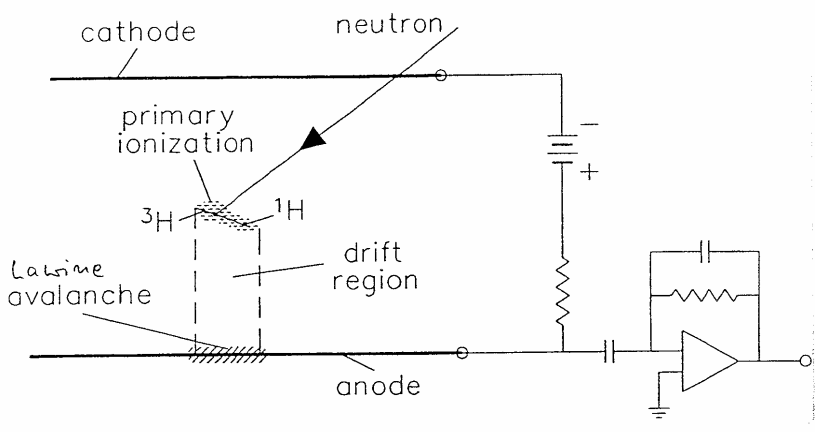

Figure 8.15: Circuit of the ^{3}He gas detector and the movement of charges inside

In a one-dimensional position sensitive detector tube the electric pulses are measured at both ends of the tube. The ratio of these pulses is related to the exact position of the original detection. In a two-dimensional detector there are two meander-wires with perpendicular orientation. By coincidental measurements of the pulses, even the position of the detected neutron on the area can be determined.

Gas detectors have a low sensitivity to γ-radiation which is good in the presence of neighboring instruments. Not all detectors have an efficiency close to 100%. A single gas detector is slower compared to scintillation detectors, but a large number of one-dimensional parallel ^{3}He tubes can process high count rates if the intensity is evenly distributed.

8.4.3.2. Scintillation Detector

The scintillation detectors use a solid state material for the primary detection. The underlying radioactive reaction is:

$$^{6}\text{Li} + \text{n} \rightarrow {}^{4}\text{He} + {}^{3}\text{H} + 4.79\text{MeV} \qquad (8.17)$$

A lithium glass with 6.6% ^{6}Li is mixed with cerium (Ce). Again, by the nuclear reaction two ionic nuclei are formed, which interact with the cerium and produce per neutron about 4000 photons of 400nm wavelength. In the disperser the photons form a light cone with an opening angle of about 90° as depicted in Fig. 8.16. The air gap between the scintillatior and the disperser (total reflection) and the thickness of the disperser are rendered in a way, that the light cone covers two photo multipliers (per dimension). The single multiplier has a diameter of 8cm, and the array of 8x8 photomultipliers covers an area of ca. 60x60 cm^{2}.

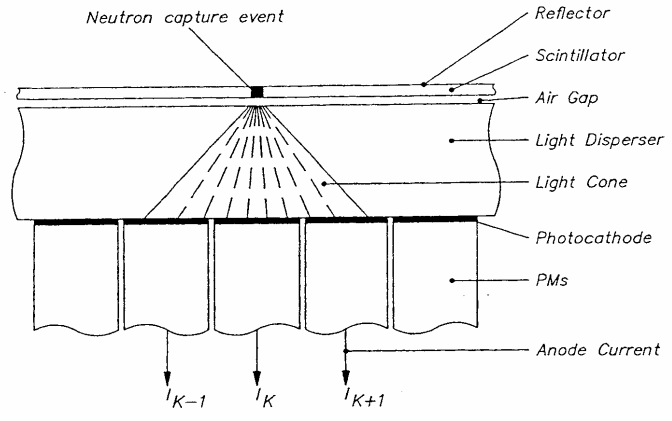

Figure 8.16: Geometry of a ^{6}Li scintillation detector with its detection light cone

Due to a subtle computer algorithm the position of the detected neutron can be specified within 0.5cm. First, the photo multiplier with the mayor intensity determined. In a second step, by the distribution of light on the neighbored photomultipliers the position of the original process can be calculated within a precision of 0.5cm.

An important advantage of this detector is the large atomic density of the absorbing material and its consequently large detection probability. A 1mm thick scintillation material has a detection probability of 93% for 7Å neutrons. Such a detector (Anger camera) was developed at the Forschungszentrum Jülich and is used for our KWS-1 and KWS-2 small angle instruments.

Acknowledgement:

This lecture bases on material of D. Schwahn, who generously supported this lesson.

References:

Books:

[1] J.S. Higgins und H.C. Benoit, *Polymers and neutron scattering*. Clarendon Press, Oxford (1994)

[2] C.G: Windsor, *Pulsed Neutron Scattering*. Taylor & Francis, London(1981)

[3] P. Convert and J.B. Forsyth (eds.), *Position-Sensitive Detection of Thermal Neutrons*. Academic Press, London (1983)

Articles:

[4] W. Schmatz, T. Springer, T. Schelten and K. Ibel, *J. Appl. Cryst.* **7**, 96 (1974)

[5] J. Skov Pedersen, D. Posselt, K. Mortensen, *J. Appl. Cryst.* **23**, 321 (1990)

[6] D.F.R. Mildner, *J. Appl. Cryst.* **38**, 488 (2005)

[7] D. Schwahn, A. Miksovsky, H. Rauch, E. Seidl and G. Zugarek, *Nucl. Instrum. Methods* **A239**, 229 (1985)

[8] B. Alefeld, H.J. Fabian, D. Schwahn and T. Springer, *Physica* **B156&157**, 602 (1989)

[9] D.Schwahn, G.Meier and T.Springer, *J. Appl. Cryst.* **24**, 568 (1991)

[10] M. Heiderich, R. Reinartz, R. Kurz and J. Schelten, *Nucl. Instrum. Methods* **A305**, 423 (1991)

9

Inelastic Crystal Spectrometers

Joachim Wuttke

9. Inelastic Crystal Spectrometers

Joachim Wuttke

Here and in the following chapter, we will consider *inelastic* scattering. While elastic scattering experiments yield information about *structure* or *texture* of a sample, inelastic scattering is used to investigate its *dynamics*. More specifically, one studies atomic and molecular motion, as well as magnetic and crystal field excitations.

In inelastic scattering, scattering intensity is measured as function of energy. As in other areas of physics, a data set of the form intensity-versus-energy is called a *spectrum*. An instrument that resolves inelastic scattering is therefore called a *spectrometer*.

In this chapter, we will get acquainted with two important neutron spectrometers: the triple-axis-spectrometer, and the backscattering spectrometer. Both of them use Bragg reflection from crystals for selecting (and thereby measuring) neutron energies. This method is essentially based on the neutron's wave nature. In contrast, the time-of-flight method presented in the next chapter treats the neutron as a classical particle.

9.1 Inelastic Scattering, Triple-Axis Spectrometer

Figure 9.1 shows the basic design of an inelastic neutron spectrometer. A *monochromator* (also called *primary spectrometer*) selects neutrons of a certain energy E_i. The neutron flux that reaches the sample is measured by a *monitor* (a neutron counter with high transmission). In the *secondary spectrometer*, scattered neutrons are registered as function of scattering angle 2θ and energy E_f.

To see how different methods of energy selection are related to each other, we use the first de Broglie equation,

$$\mathbf{p} = \hbar\mathbf{k}\,, \tag{9.1}$$

and insert it in the kinetic energy

$$E = \frac{m}{2}v^2 = \frac{p^2}{2m} \tag{9.2}$$

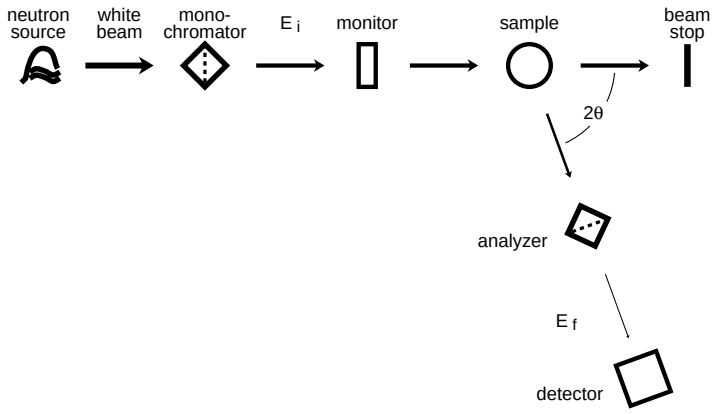

Figure 9.1: Basic design of an inelastic neutron spectrometer.

to obtain the *dispersion relation* of the free neutron:

$$E = \frac{\hbar^2}{2m}k^2 = \frac{\hbar^2 c^2}{2mc^2}k^2 = 2.07\text{meV}\,\text{Å}^2\,k^2 \tag{9.3}$$

(note in passing the expansion by c^2 which is a useful trick once one has memorised some basic constants in *atomic units*: $\hbar c = 1973\text{eVÅ}$ and $m_n c^2 = 940$ MeV). In time-of-flight methods, neutron energies are selected and measured via the velocity v. In crystal spectrometers, energies are selected according to the wavelength $\lambda = 2\pi/k$, using Bragg reflection from crystals:

$$n\lambda = 2d_{hkl}\sin\Theta \tag{9.4}$$

where d_{hkl} is the interplanar distance of lattice planes with Miller indices h, k, l, and Θ is the glancing angle of reflection from these planes. The integer n indicates that along with a fundamental wavelength λ_1, integer fractions $\lambda_n = \lambda_1/n$ are transmitted as well. To suppress these unwanted higher orders, experimental setups include either a mechanical neutron velocity selector, or a beryllium filter. Table 9.1 lists some frequently used monochromator materials. Figure 9.2 shows a monochromator used at FRM-II.

The triple-axis-spectrometer (TAS) owes its name to its main degrees of freedom. Neutron paths are always horizontal; the three axes are vertical. Figures 9.3 and 9.4 show two typical instruments. The first axis goes through the monochromator crystal. Incident

material	structure	$[hkl]$	d_{hkl}	used e. g. at
Si	diamond	111	3.14 Å	backscattering: SPHERES
C	graphite	002		thermal TAS: PUMA
Cu		002		thermal TAS: PUMA

Table 9.1: Frequently used monochromator materials.

Figure 9.2: Pyrolythic graphite PG(002) monochromator of PUMA, the Göttingen-München thermal triple-axis-spectrometer at FRM-II.

energies are selected by orienting the monochromator towards the appropriate Bragg angle Θ_i. Simultaneously, the entire downstream instrument is moved on air cushions so that the incident beam is deflected by the appropriate angle $2\Theta_i$. The second axis goes through the sample. The downstream part of the instrument is positioned so that scattering is observed under the chosen scattering angle 2θ. The sample orientation needs also to be controlled. The third axis goes through the analyzer crystal. The crystal is oriented at angle Θ_f, according to the chosen final energy. The neutron detector is positioned at angle $2\Theta_f$. Obviously, routine measurements require computer control to coordinate the movements of crystals and axes.

For a quantitative description of inelastic scattering, some formalism must be agreed upon. The second de Broglie equation relates the kinetic energy to a frequency or angular

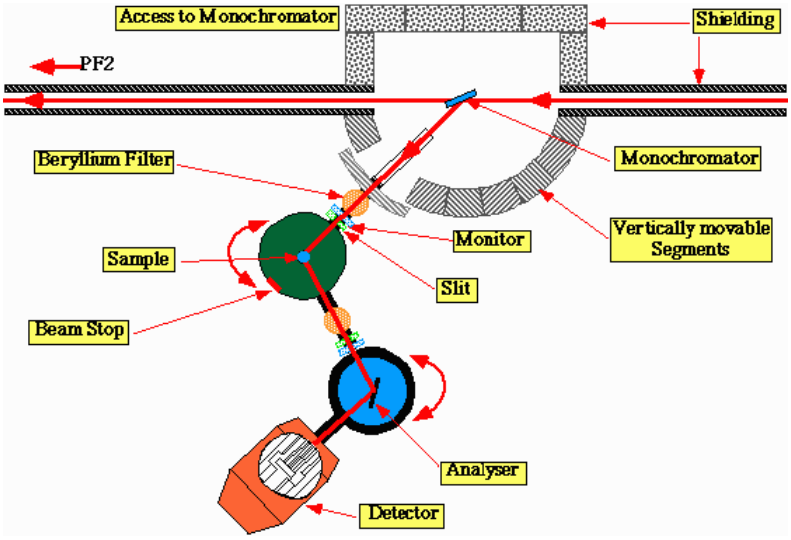

Figure 9.3: *Layout of the triple-axis spectrometer IN12. The instrument is located on a cold neutron guide at the ILL; it is jointly operated by JCNS and by the French CEA.*

frequency: $E = 2\pi\hbar\nu = \hbar\omega$. However, it is convention in neutron scattering to reserve the expression $\hbar\omega$ for the *energy loss* of the neutron in the scattering process,

$$\hbar\omega = E_\mathrm{i} - E_\mathrm{f}\,. \tag{9.5}$$

Theoretical formulæ, for instance the relation between double differential cross section and scattering law,

$$\frac{\partial^2\sigma}{\partial\Omega\partial\omega} = \frac{\sigma}{4\pi}\frac{k_\mathrm{f}}{k_\mathrm{i}}S(\mathbf{Q},\omega)\,, \tag{9.6}$$

are almost always written in terms of ω. However, actual numeric values are rarely given in s^{-1}: most often, energy transfers are expressed in meV or THz. It is not unusual that an axis is labelled ω, though values are reported in energy or frequency units.[1]

[1] Even worse things happen in biophysics where energy transfers are sometimes expressed as *wave numbers*. This comes from *light scattering* where the dispersion relation, in contrast to (9.3), is linear so that energy differences are proportional to wave number differences. In order to be understood by biologists for whom inelastic neutron scattering is quite exotic, a neutron scattering event is described by the wave number change a photon would experience if it underwent the same energy change as the neutron.

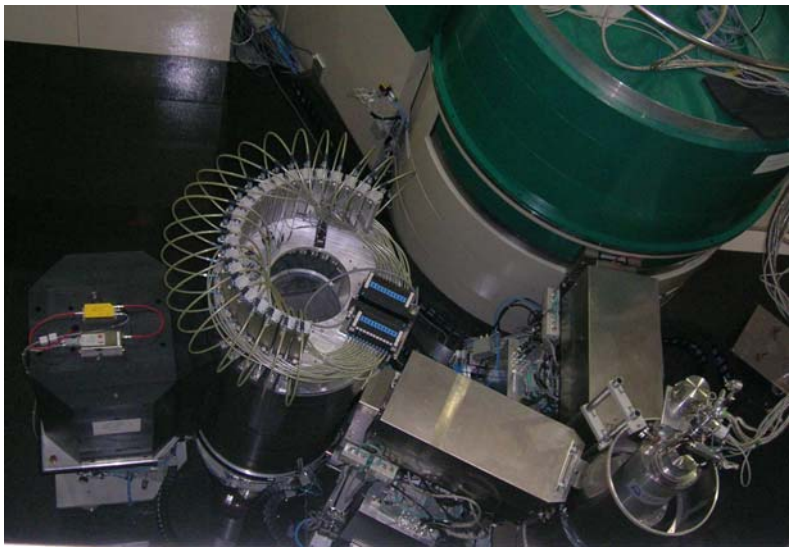

Figure 9.4: View from the gallery onto the triple-axis spectrometer TRISP, located in the FRM-II reactor building, build and operated by the Max-Planck-Gesellschaft. The beam path before and after the sample is protected by a mu-metal housing because the instrument has a spin-echo option that greatly enhances its energy resolution.

The letter $\mathbf{Q}$ is commonly used to designate the wave number change of the scattered neutron,

$$\mathbf{Q} = \mathbf{k}_\mathrm{i} - \mathbf{k}_\mathrm{f} \,. \tag{9.7}$$

Correspondingly, $\hbar\mathbf{Q}$ is the momentum transfer in the scattering event.

From conservation laws it is clear that an energy or momentum loss of the scattered neutron is accompanied by an opposite gain of the sample. In the literature as well as in the practice at neutron scattering institutes, there is no general agreement over the *sign* of the energy and momentum transfer. The conventions (9.5), (9.7) are, however, highly recommendable because they emphasize the physics of the sample over the physics of the spectrometer: *positive* values of ω and Q mean that the *sample* has *gained* energy and momentum.

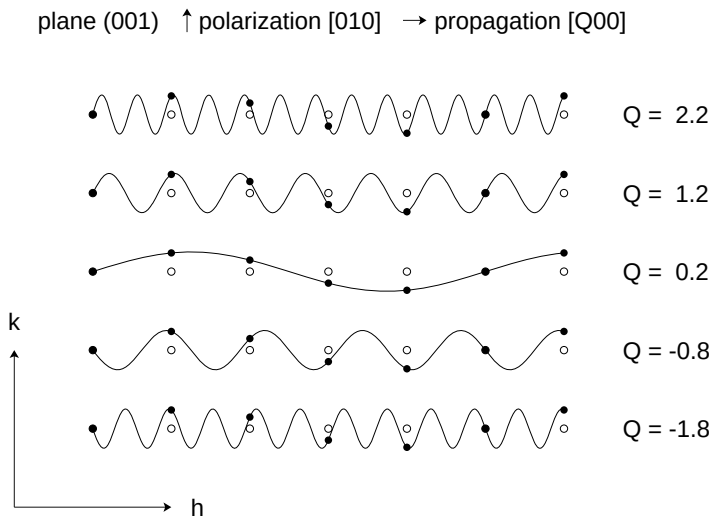

Figure 9.5: *A square lattice, representing the (001) plane of a cubic lattice. Open circles: equilibrium positions of the atoms. Solid circles: momentary positions when atoms take part in a transverse lattice oscillation. The lines show that the same oscillation can be described by different sine functions. Their wave numbers Q agree up to an arbitrary integer. More generally, the propagation vector $\mathbf{Q}$ can be written as $\mathbf{G} + \mathbf{q}$ where $\mathbf{G}$ is a reciprocal lattice vector, and $\mathbf{q}$ is located in the first Brillouin zone. In this example $q = [0.2, 0, 0]$.*

9.2 Phonon Scattering

Let us start with a mechanical picture of neutron scattering. Suppose neutrons are scattered by particles of mass M. These particles are allowed to have arbitrary thermal velocity distributions. Since the sample as a whole is at rest, we just require $\langle v \rangle = 0$. In a scattering event, a sample particle takes up a momentum $\mathbf{P} = \hbar\mathbf{Q}$. A short calculation shows that this momentum transfer is accompanied on average by an energy transfer of $P^2/(2M)$. This, however, is not compatible with the existence and dominance of *elastic* neutron scattering which by definition has *zero* energy transfer.

The only escape is to let M become macroscopically large. In this limit, the recoil of the scattered neutron is taken up not by individual scattering centers, but by the entire sample. This leads to a new reading of the Bragg condition for elastic scattering: a crystal lattice can take up a momentum $\hbar\mathbf{Q}$ iff $\mathbf{Q}$ coincides with a reciprocal lattice vector $\mathbf{G}_{hkl}$.

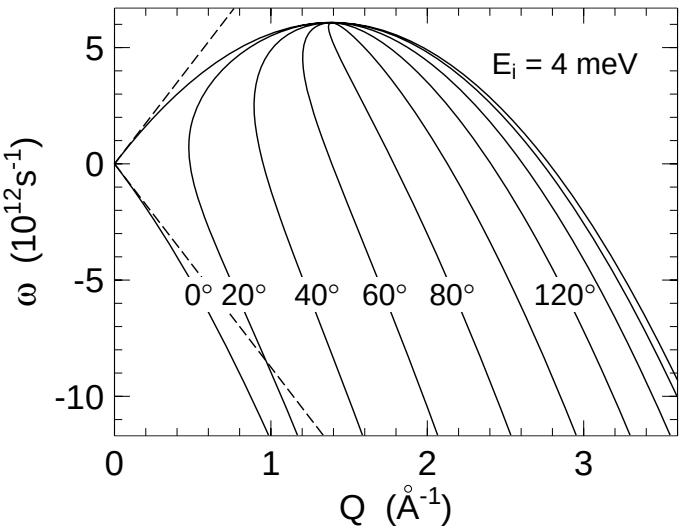

Figure 9.6: ω–Q–range accessible for inelastic scattering for a given incident neutron energy of 4 meV. Solid lines correspond to fixed scattering angles 2θ from $0°$ to $180°$. The initial slope of the $0°$ lines, indicated by the dashed lines, is given by the incident neutron velocity v_i, in this example 875 m/s.

Inelastic scattering happens if some excess momentum $\hbar\mathbf{q}$ with $\mathbf{q} = \mathbf{G}_{hkl} - \mathbf{Q}$ is taken up by emitting or absorbing a phonon with wave vector $\mathbf{q}$. This exchange of momentum is accompanied by an exchange of energy $\hbar\omega_\mathbf{q}$ where $\omega_\mathbf{q}$ is the phonon's angular frequency, as given by its dispersion relation.

An alternative explanation of inelastic scattering is the Doppler shift a wave experiences when reflected by a moving wall. In order to apply this picture to neutron scattering by phonons, the moving wall must be replaced by a stack of oscillating lattice planes. Significant scattering intensity is observed iff the spatial periodicity of the excursions agrees with the scattering vector $\mathbf{Q}$. The real-space representation of a phonon in Figure 9.5 shows that this periodicity is only determined up to a shift by $\mathbf{G}_{hkl}$; again, it is found that the condition for inelastic scattering depends only on the excess wave number $\mathbf{q} = \mathbf{G}_{hkl} - \mathbf{Q}$ which may always be chosen within the first Brillouin zone.

Equivalently, we may say that phonon dispersions are invariant under translation by reciprocal lattice vectors, $\omega_\mathbf{q} = \omega_{\mathbf{q}+\mathbf{G}}$. This allows us to choose freely the Brillouin zone

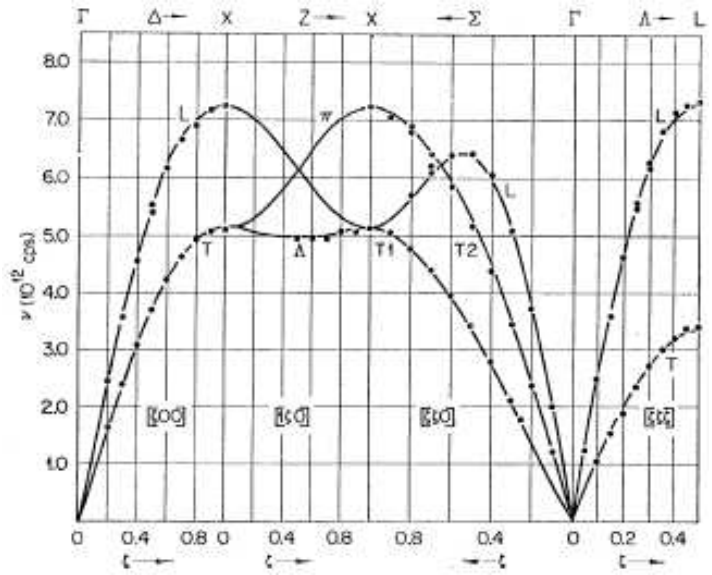

Figure 9.7: Phonon dispersion curves for copper at 49 K in the main symmetry directions. Lines are fits with a force model that takes into account up to sixth nearest neighbours [1]. As usual, wave numbers are expressed in relative units. Copper crystallises in a fcc lattice with $a = 3.61$ Å. The vertical axis shows frequency, not angular frequency.

in wich phonons can be measured best. This is hardly ever the first Brillouin zone. To understand why, consider Figure 9.6. The lines show which combinations of Q and ω can be accessed by inelastic neutron scattering. Different lines correspond to different scattering angles. In practice, scattering angles near 0° are contaminated by the unscattered part of the incident beam; in general, they are blocked by a beamstop. For obvious geometrical reasons, scattering angles close to 180° are also inaccessible. Therefore, on any real spectrometer the accessible Q–ω–range is even more restricted than the figure shows.

Figure 9.6 has been produced for one particular incident energy E_i. The lines, however, are scale invariant. Changing E_i changes the numbers on the two axes, but not the shape of the lines. Unless we go to very high neutron energies, high frequencies at low wave numbers remain inaccessible. Unfortunately, this is just the region we would need for scattering from first Brillouin zone phonons. To see this, compare Figure 9.6 *quantitatively*

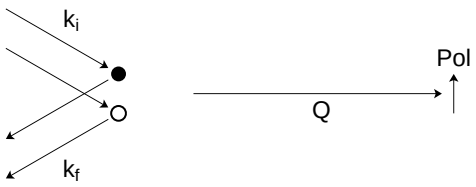

Figure 9.8: Atomic displacement perpendicular to **Q** *does not change the path length of scattered neutrons. Therefore, it does not change the interference pattern of the scattered neutron waves. In consequence, phonons with transverse polarisation cannot be observed in the first Brillouin zone.*

with a typical phonon dispersion curve, as shown in Figure 9.7. The initial slope of the acustic phonons is the macroscopic *sound velocity*. Compare this with the initial slope of the 0°-curve in Fig. 9.6 which is given by the incident neutron velocity: in order to measure phonons in the first Brillouin zone, neutrons must be considerably faster than the sound in the sample. This requires very high incident energies. Choosing such energies would deteriorate the energy resolution to inacceptable widths.[2]

Figure 9.8 explains a second reason why we must move freely through different Brillouin zones in order to measure full phonon dispersions: phonons are not observable if their polarisation vector is perpendicular to the scattering vector **Q**. This is in particular the case for transverse phonons in the first Brillouin zone. More generally, the scattering intensity is proportional to the scalar product of **Q** and the phonon's polarisation vector. Therefore, in order to measure a specific phonon branch, one chooses the Brillouin zone so that **Q** is about perpendicular to the polarisation. This is explained by some examples in Figure 9.9

In order to measure one particular phonon dispersion branch, one chooses a sequence of **Q** vectors, ranging from the center to the surface of a Brillouin zone. For each **Q**, one measures scattering intensity as function of ω (constant **Q** scan). Figure 9.10 shows results of such scans. The scattering intensity is peaked where ω agrees with a phonon frequency

[2]When studying sound in disordered materials one has actually no choice but to measure in the first Brillouin zone — there are no other zones. Such experiments cannot be done on triple-axis spectrometers; they require a very sophisticated small-angle, high-E_i, high-resolution setup at a time-of-flight spectrometer.

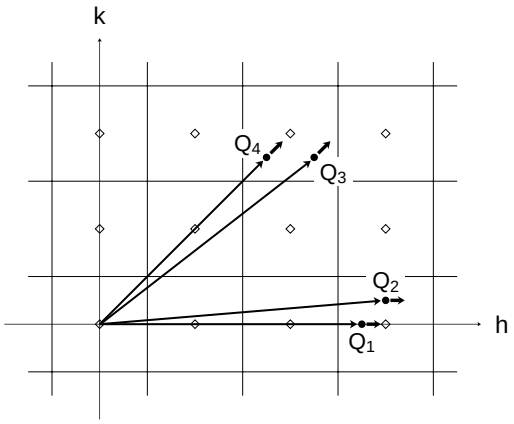

Figure 9.9: A 001 plane in the reciprocal space of a cubic lattice. Examples show how $\mathbf{Q}$ *is chosen in order to measure specific phonon spectra:* $\mathbf{Q}_1$ *is used to measure a longitudinal phonon with propagation vector* $[-\frac{1}{2},0,0]$*,* $L_{-\frac{1}{2},0,0}$ *for short.* $\mathbf{Q}_2$ *sees a transverse phonon with propagation vector* $[0,\frac{1}{2},0]$ *and polarisation* $[100]$*, abbreviated* $T[100]_{0,\frac{1}{2},0}$*.* $\mathbf{Q}_3$ *and* $\mathbf{Q}_4$ *are used to measure* $T[110]_{-\frac{1}{2},\frac{1}{2},0}$ *and* $L_{-\frac{1}{2},-\frac{1}{2},0}$*, respectively.*

$\omega_{\mathbf{q}}$. The peaks have finite widths because of (1) the finite lifetime of the phonon, and (2) the finite resolution of the spectrometer.

9.3 Resolution of Crystal Spectrometers

So far, we have considered *ideal* monochromators which select exactly one well defined wave vector $\mathbf{k}_\mathrm{i}$ out of the incident spectrum, and transform it into an equally well defined $\mathbf{k}_\mathrm{f}$. A spectrometer based on such monochromators would have perfect resolution, but zero count rates. We better accept finite wave vector distributions.

The resolution of a crystal spectrometer may be limited by any of the following causes: (1) absorption in the monochromator crystal, (2) imperfections of the monochromator crystal, (3) especially *mosaicity* (non-parallelity) of the Bragg planes, (4) finite apertures for incoming and outgoing beam.

Cause (1) is physically unavoidable. Its effect can be described by a finite width $\delta\mathbf{G}$ of the Bragg vector $\mathbf{G}_{hkl}$. Cause (4) is also unavoidable if nonzero intensities shall be obtained.

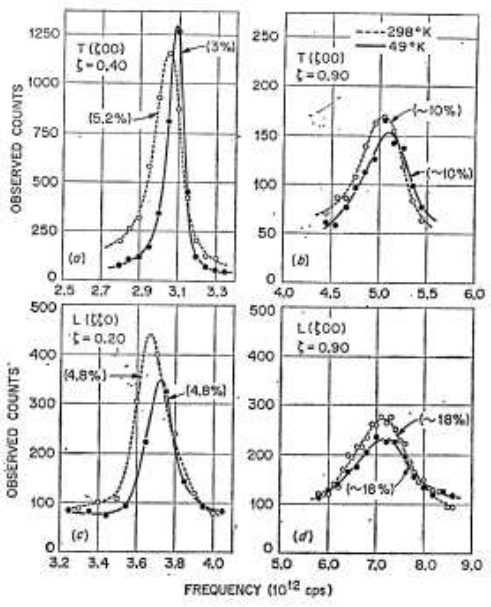

Figure 9.10: *Some of the constant-***Q***-scans that led to the dispersion curve shown in Fig. 9.7. Open circles have been measured at 298 K, filled circles at 49 K. Percentages in parentheses indicate relative line widths. Line widths are in part due to finite instrumental resolution [1].*

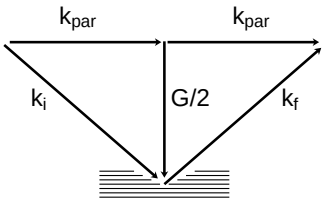

Figure 9.11: *Bragg scattering by a perfect crystal: the vector components of* $\mathbf{k}_\mathrm{i}$ *and* $-\mathbf{k}_\mathrm{f}$ *that are perpendicular to a lattice plane* $[hkl]$ *must equal half a reciprocal lattice vetor* $\mathbf{G}_{hkl}$*; the parallel components of* $\mathbf{k}_\mathrm{i}$ *and* $\mathbf{k}_\mathrm{f}$ *must be equal.*

The combined impact of (1) and (4) on the wave number $k = k_\mathrm{i} = k_\mathrm{f}$ can be estimated by differentiating the Bragg equation. A particularly simple starting point is the form

$$k = \frac{G}{2\sin\Theta} \tag{9.8}$$

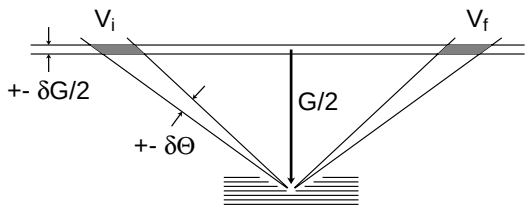

Figure 9.12: *In a real monochromator, incident neutrons are accepted from a finite angular range* $\pm\delta\Theta$. *Neutron absorption and certain crystal imperfections lead to a finite width* δG *of the reciprocal lattice vector. As a result, Bragg scattering is possible for neutrons from a finite phase-space volume* V_i. *This volume is symmetrically mapped onto an outgoing phase-space volume* V_f.

which leads to

$$\frac{\delta k}{k} = \frac{\delta G}{G} + \cot\Theta\,\delta\Theta\,. \tag{9.9}$$

Usually, the first summand can be neglected against the second. Except for extreme angles, the resolution is then essentially given by the aperture $\delta\Theta$.

To visualise these and other resolution effects, Figure 9.11 gives a geometric interpretation of the Bragg equation (9.8). Figure 9.12 shows that a Bragg reflection in the presence of (1) and (4) maps a $\mathbf{k}_\mathrm{i}$-volume to a $\mathbf{k}_\mathrm{f}$-volume without changing its shape.

This symmetry can be broken by using mosaic crystals. Figure 9.13 explains how such crystals act as *phase-space transformers*. For a given incident aperture they accept a relatively wide range of incident wavelengths. In the outgoing beam this phase-space volume is transformed to one with wider angular spread, but narrower wavenumber distribution. This transform »from white to wide« is employed in many spectrometers to improve the resolution-intensity balance.

Of course wave vector distributions are not produced by rectangular cut-off functions. Insofar the shaded areas in Figs. 9.12–9.13 are inappropriate representations; actually the intensity fall off smoothly at the edges of these areas. This is even more the case when the $\mathbf{k}_\mathrm{f}$ distribution of the monochromator and the $\mathbf{k}_\mathrm{i}$ distribution of the analyser are convoluted to yield the distribution that describes how accurately the wave vector $\mathbf{Q}$ of the scattering event in the sample is resolved by the instrument. Consequently,

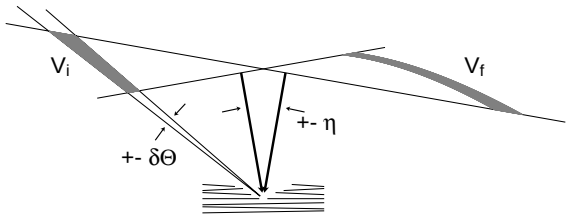

Figure 9.13: *A crystal with mosaic spread η turns a »white« incoming phase-space volume V_i into a volume V_f with a comparatively »wide« angular distribution, and a comparatively narrow wavelength distribution.*

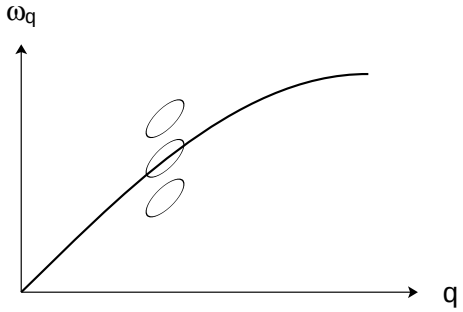

Figure 9.14: *Constant* **Q** *scan with resolution ellipsoids optimally oriented with respect to an acoustic phonon branch.*

this distribution is well approximated as an ellipsoid. Depending on the setup of the entire triple-axis spectrometer, different orientations of this ellipsoid can be achieved. Furthermore, Bragg zones and **q** vectors can be chosen so that the long axis of the ellipsoid is approximately parallel to the dispersion curve (Figure 9.14).

9.4 Backscattering

In backscattering ($2\Theta \simeq 180°$), the $\cot\Theta$ in (9.9) goes to zero. In this case, the wavelength spread of the Bragg reflected beam depends mainly on $\delta G/G$, besides a $(\delta\Theta)^2$ term. In a backscattering spectrometer, both monochromator and analyser are operated under backscattering conditions. Relative energy resolutions between 10^{-3} and 10^{-4} are routinely obtained. The Jülich backscattering spectrometer SPHERES uses 2.08 meV neutrons from the Si(111) reflection, and achieves a resolution (full width at half maxi-

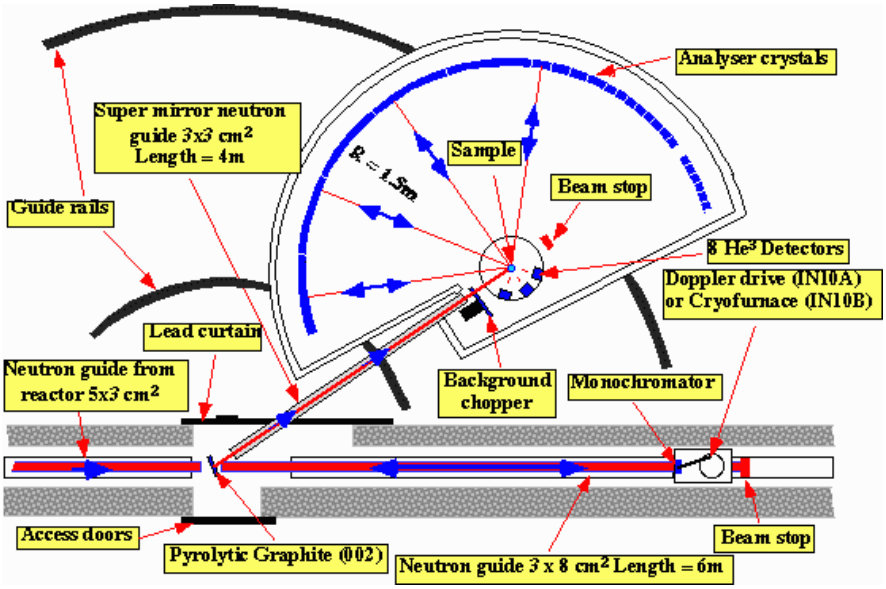

Figure 9.15: *Layout of the backscattering spectrometer IN10 at the ILL.*

mum) of 0.65 μeV. With such a resolution one can study processes that are considerably slower than phonons: side group rotations, including tunneling phenomena at low temperatures; jump diffusion; relaxation in viscous liquids; chain motion in polymers; dynamics of membranes and proteins.

While the basic operation principle is the same as for a triple-axis spectrometer, the design of a backscattering spectrometer is quite different. Figure 9.15 shows the classical layout of a first-generation instrument. Besides the three axis (monochromator, sample, analyser) there are two more elements in the beam path. They are required to cope with the very special $2\Theta = 180°$ geometry. Obviously, the sample cannot be placed in the incoming beam. Therefore, (1) a *deflector* is needed to redirect the backscattered beam into the secondary spectrometer which is placed in a separate housing outside the primary beam casemate.

Furthermore, neutrons that are backscattered from an analyser have to traverse the sample a second time before they reach the detector. This geometry exposes the detector to neutrons that are scattered directly from the sample into the detector, without being energy analysed. These uninformative neutrons have to been discounted. Therefore, every

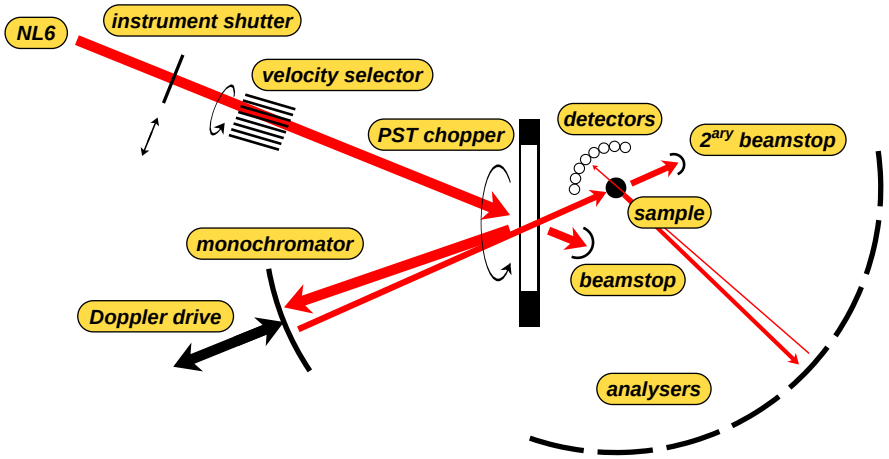

Figure 9.16: *Layout of the Jülich backscattering spectrometer SPHERES at FRM-II. The central component is the phase-space transforming chopper. Half of its circumference is covered with deflecting graphite crystals.*

backscattering instrument needs (2) a *chopper* to pulse the incoming beam. Analysed and unanalysed neutrons are then distinguished by their different time of flight.

A third fundamental difference between triple-axis and backscattering spectroscopy concerns the way energies are scanned. In triple-axis spectroscopy this is done by varying Bragg reflection angles in monochromator or/and analyser. In backscattering, this is no option, as even a few degrees deviation from $2\Theta = 180°$ would ruin the energy resolution. Instead, two other methods are used to vary $\hbar\omega = E_\mathrm{i} - E_\mathrm{f}$: (a) Varying the lattice constant of the monochromator by cooling/heating. Used on two instruments at the ILL: IN13, and as an option at IN10. (b) Doppler shift of E_i by periodic motion of the monochromator. Used on all other backscattering spectrometers.

Fourthly, keeping the Bragg angles fixed facilitates simultaneous measurements at different scattering angles: backscattering spectrometers are always built as multi-detector instruments.

However, using several detectors is only a weak antidote against the notoriously low count rates of backscattering instruments. At the first-generation instruments BSS (Jülich) and IN10 (ILL), the neutron flux at the sample was/is only (1 to 2)$\cdot 10^4$ n/cm^2/s. In the

second-generation instrument IN16 (ILL), the intensity was increased by focussing optics, taking advantage of phase-space transformation by a deflector with high mosaicity. In the third-generation instruments HFBS (NIST, USA) and SPHERES (Jülich at FRM-II), the intensity is further increased by integrating deflector and chopper into *one* component, the *phase-space transform chopper* (Figure 9.16). This chopper carries mosaic crystals on half of its circumference. Thereby, it both pulses the primary beam and deflects it towards the monochromator. The fast motion of the deflector crystals (ideally 300 m/s) improves the efficiency of the phase-space transform.

References

[1] R. M. Nicklow, G. Gilat, H. G. Smith, L. J. Raubenheimer, and M. K. Wilkinson: Phonon Frequencies in Copper at 49 and 298°K. Phys. Rev. 164, 922–928 (1967).

Exercises and Problems

1. Express an energy transfer of 1 meV in THz and in cm^{-1} (light scattering wave number).

2. In triple-axis-spectrometers, polycrystalline beryllium, cooled to the temperature of liquid nitrogen, is placed before sample and monitor to suppress higher order Bragg reflections from the monochromator. How does that work? Name at least two properties that make beryllium the optimum material for this purpose.

3. Which degrees of freedom are varied in a constant-**Q**-scan?

4. Explain how a Z-shaped double monochromator facilitates scans with variable $\mathbf{k}_\mathrm{i}$.

5. Derive without explicit calculation of $Q(\omega)$ how the axis in Fig. 9.6 must be rescaled so that the lines remain unchanged when the incident neutron energy is changed.

6. Use the law of cosines

$$Q^2 = k_\mathrm{i}^2 + k_\mathrm{f}^2 - 2k_\mathrm{i}k_\mathrm{f}\cos 2\theta \tag{9.10}$$

to find an analytic expression for Q as function of ω, E_i, and 2θ. Verify that the slopes $\mathrm{d}\omega/\mathrm{d}Q$ at $2\theta = 0$ and $\omega \to 0$, as shown by the dashed lines in Fig. 9.6, are indeed equal to $\pm v_\mathrm{i}$.

7. Why does the resolution deteriorate if high incident energies are chosen? Does this hold for any type of spectrometer?

8. Determine the speed of sound in copper from Fig. 9.7, and check against a handbook value.

9. Name the two main reasons why phonons have finite lifetimes.

10. Reconsider the derivation of the Bragg equation for a crystal with finite penetration depth. Assume that every lattice plane absorbs a given fraction of a traversing neutron beam.

11. The phase-space transform »from white to wide« is quite useful. Yet it is a compromise. A transform »from white and wide to monochromatic and narrow« would be much more useful. Any idea, how such a transform could be achieved, or why it has proved so difficult?

10

Time-of-flight spectrometers including NSE

Michael Monkenbusch

10. Time-of-flight spectrometers including NSE

Michael Monkenbusch

10.1 Introduction

The information that may be extracted from a neutron scattering experiment can be expressed in terms of the *scattering function* $S(\underline{Q},\omega)$. All properties accessible by these kinds of scattering experiments are contained in $S(\underline{Q},\omega)$. The resulting intensity represents the double differential cross section:

$$\frac{d^2\sigma}{d\Omega dE'} = N\,\frac{k'}{k}b^2 S(\underline{Q},\omega) \tag{10.1}$$

where k', k is the modulus of wavevectors the scattered and incoming neutrons respectively. N denotes the number of atoms in the sample and b is the *scattering length.* [1]. The energy transfer during scattering is $\hbar\omega = (E - E')$, thereby E , E' denotes the energies of the incoming and scattered neutrons respectively. The variables of the scattering function depend on $\underline{k}$, $\underline{k'}$; $\underline{Q} = \underline{k} - \underline{k'}$ is the momentum transfer and

$$\hbar\omega = (\hbar^2/2m_n)(k^2 - k'^2) \tag{10.2}$$

the energy transfer that occured during the scattering process. Since the modulus of the wavevector $\underline{k}$ of the neutron is related as well to the neutron velocity, $\underline{v}$ (momentum) as to the wavelength (1/wavenumber):

$$\underline{v}m_n = \hbar\underline{k} \tag{10.3}$$

$$\frac{2\pi}{\lambda} = k \tag{10.4}$$

it is possible to determine the energy transfer (10.2) as well –by employing the wave proerties of the neutron– by analysis of the wavelength λ' as –by using the particle character– by measurement of the velocity v' of the scattered neutrons. The first method is applied in crystal-spectrometers like the classical **triple-axis-spectrometer** or the **backscattering-(π)-spectrometer**. The second method leads to the spectrometer types that are the topic of this chapter, namely different variants of **time-of-flight (TOF)-spectrometers**. Also the **neutron spin-echo spectrometer, NSE** employs –somewhat

[1] For compounds containing different types of atoms (elements or isotopes) the corresponding expression consists of the sum of partial structure factors multiplied by the corresponding scattering lengths $b_i b_j$ in bilinear combination. For the discussion of instruments the simple version is sufficient.

less obvious– the velocity **change** of the neutrons to infer the energy transfer. The generic geometry of a scattering experiment in reciprocal (i.e. velocity, momentum or wavevector) space is illustrated in Fig. 10.1. The scattering triangle consisting of the incoming

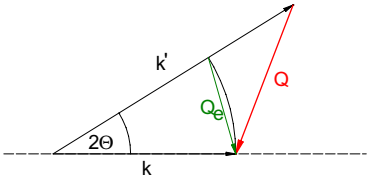

Figure 10.1: Scattering triangle.

wavevector $\underline{k}$, the wavevector of the scattered neutrons $\underline{k'}$ and the resulting momentum transfer ($\div\hbar$), $\underline{Q}$, the figure shows the general situation of inelastic scattering (here: energy gain of the neutron). 2Θ is the scattering angle, $\underline{Q}_e$ indicates the momentum transfer for elastic scattering (i.e. **without** energy transfer).

A nuclear research reactor as neutron source basically yields a thermal (Maxwellian) spectrum of neutron velocities, the temperature of the moderator (D_2O-cooling water apporx. 60^0C) determines the temperature of the neutron cloud. Many facilities contain additional small moderators of different temperature that supply single beam tubes with neutrons of a different spectral distribution (different temperature). In particular the so called "cold sources" have to be mentioned, which typically consist of a volume filled with liquid liquid H_2 or D_2 corresponding to a temperature of 20 K. On the other hand some ractors are also equipped with a "hot source", e.g. an vacuum isolated block of graphite that is heated by the nuclear radiation inside the moderator tank. The following table enables a quick survey over the average values of the corresponding neutron spectra.

$T_{\text{Moderator}}/K$	$\sqrt{\overline{v^2}}$/m/s	λ/nm	$\hbar\omega$/eV	$\nu = \omega/2\pi/\text{s}^{-1}$
2000	7060	0.056	170×10^{-3}	42×10^{12}
330	2870	0.14	28×10^{-3}	6.87×10^{12}
20	706	0.56	1.7×10^{-3}	0.42×10^{12}

For specific experiments of course also neutrons of deviating velocities within a band around the average are employed. However, with increasing deviation from the optimum wavelength the flux drops strongly. Typical neutron velocities are in the order of 1000 m/s the corresponding time-of-flight per meter is 1 ms/m, i.e. such neutrons need a couple of milliseconds for their journey through a spectrometer.

The energy resolution –respectively resolution in ω– of time-of-flight (TOF) instruments depends strongly on the used wavelength ($\Delta\omega \propto 1/\lambda^3$). But also the different techniques used to detect differences in neutron energy determine the available resolution. TOF instruments perform the energy transfer measurement by neutron velocity measurements.

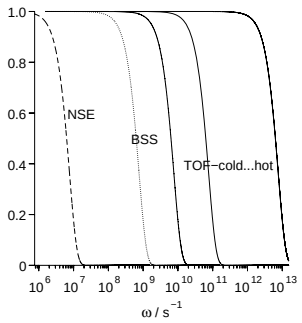

Figure 10.2: Range of resolution widths.

The range spanned by combining different wavelengths and experimental methods spans about $7 \cdots 8$ decades in energy resolution, as illustrated in figure 10.2.

10.2 The classic time-of-flight spectrometer

Basically there are two types of classic time-of-flight (TOF) spectrometer types, which use at least TOF-techniques either to analyze the velocity distribution after the sacttering process or tag the incoming velocity by the time.

10.2.1 Normal Geometry TOF-spectrometer

Figure 10.3 illustrates the generic setup of a classical time-of-flight (TOF) instrument.

From the thermal spectrum of the neutron beam entering from the left a monochromator (of any type) filters a limited wavelength band $\lambda \pm \Delta\lambda$, thereby typically a bandwidth of $\Delta\lambda/\lambda \approx 10^{-2}$ is achieved. The thus monochromatized beam enters a so-called chopper which opens the beam path periodically for a short moment. Typical frequencies are between 20 and 400 Hz, the ratio of time-open:time-closed is around 1:100. The resulting pulse widths are of the order of several (tens) of microseconds. After an – as short as – possible flight path the neutron bunches hit the sample and are scattered according to the double differential cross section of the sample material, thereby some neutrons exchange kinetic energy with excitations in the sample, i.e. change their velocities. After scattering into different directions the neutrons transverse the flight space between sample and the detectors. The path length between sample and detector is usually kept the same for all detectors placed at the periphery of the flight space. The detectors most often consists of ^{3}He ($\simeq$10 bar) filled counting tubes of $30 \cdots 40$ cm length. Up to 1000 (and more) tubes are used in some installations to cover as much solid angle as possible.

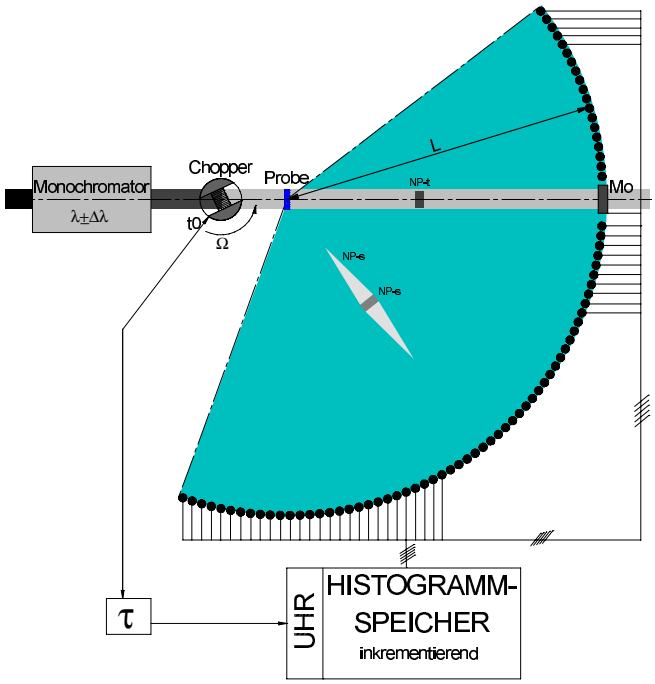

Figure 10.3: Generic setup of a classical TOF instrument.

The elastically scattered neutrons (like those from the direct beam) reach the detectors after the time $t_{CP} + t_0 = d_{\text{chopper-sample}}/v_0 + L/v_0$, those scattered inelastically arrive earlier (energy gain of the neutron) or later (energy loss of the neutron). Each pulse from a counting tube causes via the associated electronics an increment of one cell in the histogrammic memory. The address of this cell is derived from the time difference between chopper opening and arrival time of the neutron (pulse), i.e. TOF, and the detector number ($\rightarrow$ scattering angle). Thus the distribution of flight times evolves as a histogram of $512 \cdots 2048$ channels with a width of around 10μs each. For each detector (resp. group of detectors) such an histogramm vs. time is obtained. A monitor (Mo) in the direct beam serves to normalize the histograms to the incoming neutron flux. [2]

The neutron path-time diagram that corresponds to the scattering situation in this type of TOF instruments is show in figure 10.4.

[2] A "monitor" is a detection device (counting "tube") that covers the beam cross section and has a high transmission for neutrons ($> 90\%$) and low detection probability ($10^{-3} \cdots 10^{-7}$). In the figure only one monitor behind the sample is shown for clarity. Generally another monitor (more important) is located between chopper and sample, it measures the incoming flux without the influence of the sample transmission.

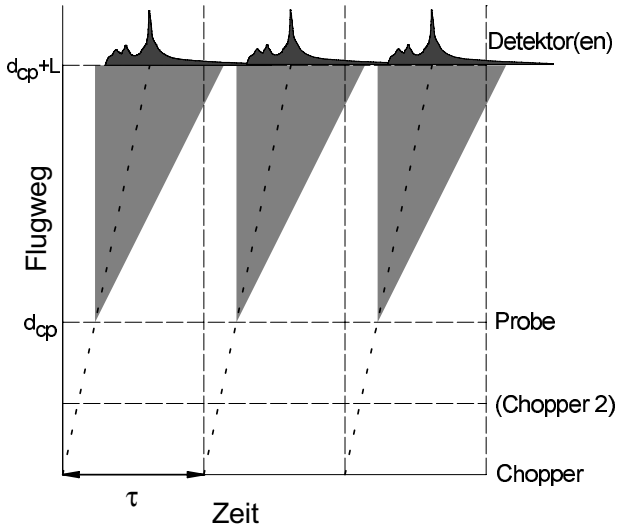

Figure 10.4: Path-time diagram of neutrons in a normal geometry TOF instrument..

10.2.2 Inverted Geometry TOF-spectrometer

In the spectrometer type described above the sample was "illuminated" by pulses of neutrons with a single defined wavelength (velocity) which have been prepared by a chopper-monochromator combination. The analysis of the velocities of the scattered neutrons was effected by TOF-measurement.

It is also possible to **invert** this sequence, the incoming velocity (i.e. wavelength, energy, k) is determined by the TOF between chopper (pulsed source) and sample. Then –to obtain a defined energy and momentum transfer– only scattered neutrons of a given final wavelength that may pass an analyzer are detected. Neutrons emerging the pulsed source fly according to their individual velocity in direction of the sample, the associated pathes are indicated by the grey triangle. The intensity within the range of this triangle is of course not uniform but depends on the spectral properties of the source. [3] Neutrons that have been elastically scattered by the sample (path 2) pass the analyzer/filter M/F and lead to the elastic line in the TOF-histogram. Neutrons that loose energy (path 1) are faster before the sample scattering and arrive earlier at the detector than the elastically scattered ones. Analogously path 3 represents neutrons that gained energy during scattering. Compared to a "normal" TOF instrument the energy gain and energy loss sides of the histogram are reversed. Therefore also high energy excitations that are thermally not occupied may be measured. Figure 10.5 shows a corresponding setup.

The pulse at the chopper contains neutrons from a broad velocity distribution (Maxwellian

[3] In particular overlap of the triangles ("frame overlap") may happen, which may be suppressed by filters tayloring the incoming spectrum.

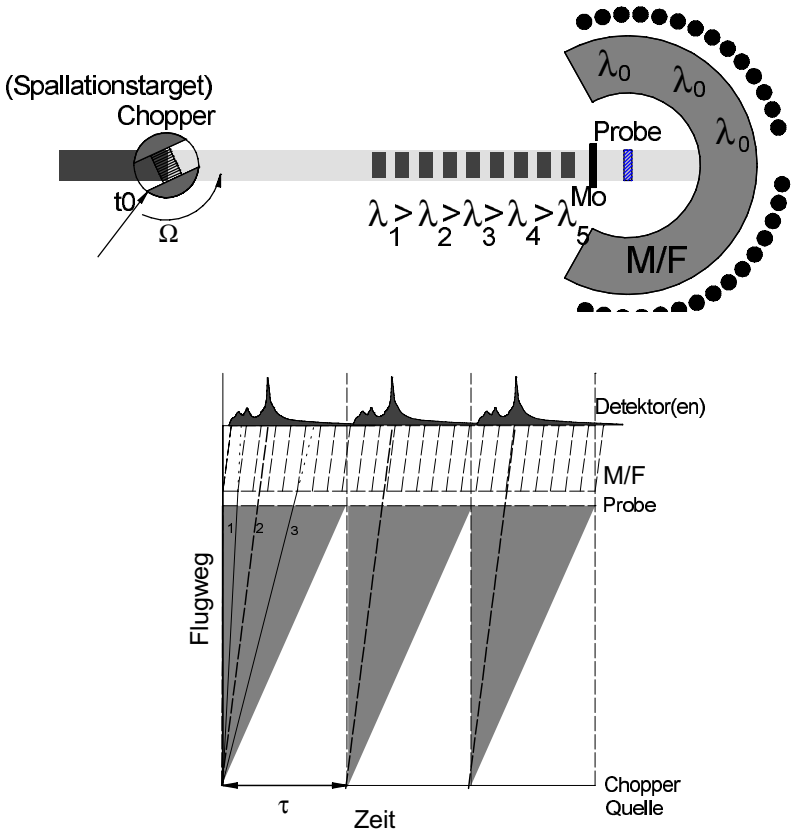

Figure 10.5: Setup and path-time diagram of a TOF spectrometer with inverted geometry.

spectrum at moderator temperature). During the path from chopper (pulsed source) to sample this pulse separates into different wavelengths λ, resp. different incident energies, that arrive at different times at the sample. Since a wavelength selection (to λ_0) is performed between sample and detectors, all detected neutrons have the same velocity and the distance sample-detector adds a constant offset to the TOF. To be able to correct the TOF-histograms with respect to the spectral distribution of the incoming pulse, it is important to detected the incoming neutron flux by a monitor (Mo) located close to the sample position accumulated in a separate TOF-histogram. This type of TOF-spectrometer is preferentially used at pulsed sources, ideally it may be possible to omit the first chopper by taking the pulse as generated by the pulsed source (spallation target). [4] All neutrons from the pulse (flying into the right direction) are utilized. This method has a few specific advantages and disadvantages, advantages are:

- The pulse contains neutrons with high incident energy that may perform energy loss scattering, the resolution at high energy loss is relatively good, especially if the pulsed source supplies very short pulses at high neutron energies.

The utilization of the full spectrum has however also disadvantages:

1. The full "white" pulse enters the shielded sample detector space. Any parasitic scattering and any imperfection of the analyzing filters or failure to absorb neutrons of "unused" final wavelength or direction leads to increased background. In addition the background depends on the sample which makes correcting subtractions difficult.

2. Samples are hit by a higher integral flux and therfore become more radioactive.

In general also "normal" TOF instruments perform better on a pulsed source in comparison with a reactor (if the average fluxes are equal) since by synchronizing source and chopper only a small part of the generated neutrons (with the desired wavelength) are not used. The distance source-chopper may serve at the same time as TOF-monochromator. In total the efficiency is comparable with the inverted type because in both cases on one side of the sample the spectrum is restricted by filters/monochromators and on the other side the full spectrum is utilized and sorted according to the TOF. Energy transfer analysis without filter on any side is impossible.

Analysis by filters

The analyzer that is indicated by the grey segement labelled M/F in fig. 10.5 may either consist of an array of crystals reflecting scattered neutrons of the selected wavelength

[4] To suppress background or to prevent "frame overlap" it may be nevertheless advisable to use an additional chopper.

λ_0 onto the assocaiated detectors or of a filter. Especially in the early days of neutron scattering filters made from polycrystalline blocks of Be , BeO etc. were used. These filters are transparent only for neutrons with energies below the "Bragg-edge", i.e. for wavelengths larger than twice the largest lattice spacing. All faster neutrons will be reflected by some crytallite in the block. By integrated absorbing plates the thus reflected neutrons are removed. For the filter to be sufficiently transparent below the Bragg-edge the used material may only have a very low absorption cross section. In addition the thermal diffuse scattering by fluctuating lattice deformations (phonons) has to be suppressed by cooling (liquid nitrogen). Below the Bragg-edge these filters transmit all neutrons from nearly zero energy to the edge energy of a few meV. For the spectroscopy of high energy excitation this is accceptable since the energy transfer is then determined by the incident energy of a few 100 meV. High resolution quasielastic scattering has to be done with other instruments. By employing the difference between data obtained with two different filters (e.g. Be and BeO) the effective window of final energies may be narrowed, however two measurements are needed and the final signal is obtained from a small difference of two larger counting signals with the corresponding statistical errors. Modern versions of inverted TOF spectrometers also have narrower filters for analysis. In particular with the introduction of the new high intensity spallation sources spectrometers of the inverted TOF geometry with Bragg scattering crystals in (near) backscattering geometry were build. Short pulses in combination with a long flight path ($\simeq 100\,\mathrm{m}$) allow to get a resolution in the range of μeV for the incoming neutrons, the scattered neutrons are then analyzed by (perfect) crystals in backscattering geometry.

10.2.3 Transforms

Since the physics of the systems under investigation is usually expressed in terms of $S(Q,\omega)$, transformation of the raw data $I(2\Theta,t)$ into the (Q,ω)-space are needed. The following is formulated for the normal TOF geometry, however, the expressions for the inverted geometry are analogous. With $t = L/v'$ and $t_0 = L/v$ inserted in Eqn. 10.2 yields

$$\omega(t) = \frac{m_n}{2\hbar} L^2 \frac{t^2 - t_0^2}{t^2 t_0^2} \tag{10.5}$$

and

$$Q = \frac{m_n}{\hbar} L \sqrt{\frac{t^2 + t_0^2 - 2cos(2\Theta) t_0 t}{t_0^2 t^2}} \tag{10.6}$$

The nonlinear mapping from channels to energy given by Eqn. 10.5 also causes a strongly varying energy-width of TOF-channels, K.

$$I(2\Theta, K) \propto \int_{(K-1)\Delta\tau}^{K\Delta\tau} \frac{k'}{k} 4\pi b^2 S(\underline{Q}, \omega(t)) \frac{d\omega}{dt} dt \tag{10.7}$$

or somewhat simpler (but **not** applicable if $\delta(\hbar\omega)$-contributions or quasi- or inelastic components with intrinsic width comparable or smaller than a time channel):

$$I(2\Theta, K) \propto \frac{k'}{k} 4\pi b^2 S(\underline{Q}, \omega(K\Delta\tau)) \frac{d\omega}{dt} \Delta\tau \tag{10.8}$$

with

$$\frac{k'}{k} = \frac{t_0}{t} \tag{10.9}$$

and

$$\frac{d\omega(t)}{dt} = \frac{m_n}{\hbar} L^2 \frac{1}{t^3} \tag{10.10}$$

the result

$$I(2\Theta, K) \propto S(\underline{Q}, \omega(K\Delta\tau)) \ \frac{1}{t^4} \tag{10.11}$$

is obtained, all constant factors are omitted and lumped into a still undetermined proportionality factor [5]. Note the factor t^{-4} between S and I which causes a significant intensity enhancement for the early arriving time channels, however, intimately connected with a corresponding loss of energy resolution.

Finally the true TOF raw data are only obtained if the resolution of the instrument is accounted for. The simplest basic assumption is a constant broadening on the time-of-flight scale. Thus

$$I_{raw}(2\Theta, K) \simeq \sum_{K'} R(K - K') I(2\Theta, K') \tag{10.12}$$

where $R(K)$ is the normalized TOF "spectrum" of an elastic resolution sample (e.g. Vanadium).

Remark: application of a coordinate transform (here $(Q, \omega) \rightarrow (2\Theta, K)$ resp. $(Q, \omega) \leftarrow (2\Theta, K)$) requires –besides the observation of the (nonlinear) coordinate dependence– the application of a Jacobian determinant as factor to preserve "volume". For the time-frequency part this is also done here (t^{-4}-factor). The transform $2\Theta \rightarrow Q$, however is performed without Jacobian due to an asymmetry in definitions of $S(Q, \omega)$, namely $d\sigma(2\Theta)/d\Omega = S(Q(2\Theta))$!

10.3 Neutron Spin-Echo Spectrometers

10.3.1 The Resolution versus Intensity Trap

In order to improve the resolution of the above TOF spectrometers e.g. by a factor 0.1 this factor has to be applied as well to the monochromatization as to the pulse length (chopper opening time). This would on the one hand increase the resolution accordingly by a factor

[5] For practical purposes the proportionality factor is determined by an absolute calibration using a standard sample, e.g. vanadium which is a purely incoherent elastic scatterer.

of about 10 but at the same time the intensity is reduced by $0.1_{monoch.} \times 0.1_{chopper} = 10^{-2}$. Still other necessary measures to preserve the increased resolution as the reduction of sample size (definition of flight path) are not contained in this reduction factor. In general an improvement of the spectral resolution requires the narrowing of the filter transmission functions **before** and **after** the sample scattering by the desired improvement factor. This implies an intensity reduction by the square of the resolution improvement factor. However, the problem of vanishing intensity if one would try to further increase the resolution by narrowing velocity/wavelength bands can be overcome using a technique that is able to detect the tiny velocity differences due to scattering of neutrons within a broad velocity distribution.

10.3.2 The Spin-echo Knack

The attempt to increase the resolution of the TOF instruments far beyond the $\Delta E/E \approx 1\%$ of the present realizations would lead to an unacceptable loss of intensity (as expressed in terms of detector count rate). However, this situation would immeadiately improve, if it would be possible to equip each neutron with an individual stop watch which could be read in a way that the run time difference between test tracks before and after the sample is obtained at detection. If this stop watch has a sufficient time resolution it would be possible to observe very small velocity changes even if a beam with a wide range of initial neutron velocities is used. This would allow to escape the intensity trap.

With some restrictions (with important consequences for the application) it is indeed possible to use the neutron spin directions as kind of individual stop watch pointers. The clockwork of this watch is then effected by the precession of the neutron spins in an external magnetic field. [6] The restrictions affecting application are caused by the fact that the "spin-stop watch" can only be read up to an unknown integer number of complete precession turns. The reading is performed by the cosine type transmission function of an analyzer and yields only ensemble averages and not individual rotation angles. The intensity at the detector is modulated accordingly.

In addition the scattering function $S(Q,\omega)$ as a rule is not such that there is only one defined velocity change induced but Δv is distributed according to $S(Q,\omega \approx k\Delta v)$. The detector signal is then proportional to the integral of precession-angle-cosine modulated intensity contributions with weight according to the Δv from $S(Q,\omega)$. Therefore the signal of the NSE spectrometer –as explained in this chapter– is completely different from the TOF histogramms of classical TOF-spectrometers. Instead it is proportional to the

[6] It is somewhat involved to extract this analogy starting from a quantum mechanical view with spin eigenstates and eigenvalues. Implicitly we are talking about the behaviour of the ensemble average of the spin vectors which obeys the "classical" Bloch equation concerning its precession in the magnetic field. As long as the kinetic energy of the neutrons is much bigger than the magnetic level splitting the classical picture is completely sufficient and much easier to visualize to understand the NSE spectrometer than a quantum mechanical treatment.

cosine-Fourier transform of $S(Q,\omega)$, i.e. the intermediate scattering function $S(Q,t)$. A detailed derivation and discussion is given below. But first of all a concrete setup of an NSE spectrometer is presented.

10.4 Setup and function

The upper part of figure 10.6 shows the directions of the spin expectation value during the passage of a neutron through the spectrometer.

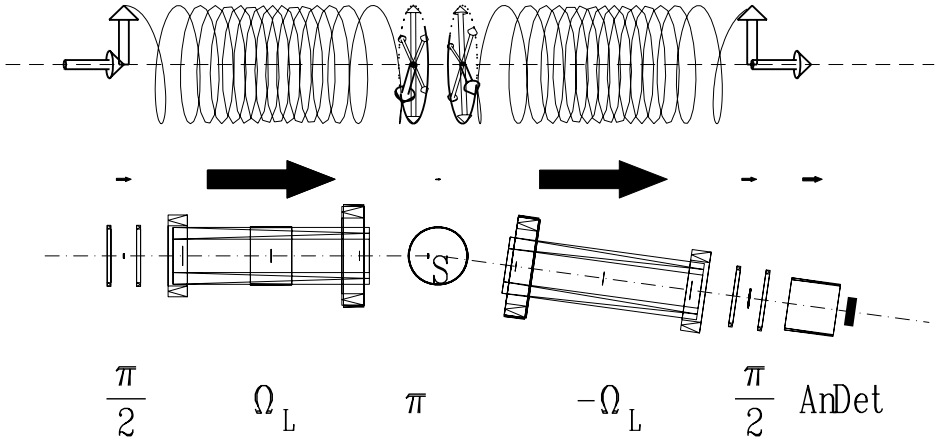

Figure 10.6: Spin roatations and setup of a generic NSE-spectrometer. Upper part: Spin rotrtation, middle part: magnitude of the magnetic field, lower part: schematic setup of the Jülich NSE-spectrometer.

Longitudinally polarized neutrons [7] (i.e. spin expectation value parallel to the beam direction) enter the spectrometer from the left. In the first so-called $\pi/2$-flipper the spin is rotated such that on exit it is orthogonal to the longitudinal magnetic field of the precession path. That defines the start of the "spin stop watch", immediately after the flipper a precession of the spins around the axial magnetic field begins. The precession frequency increases during the approach of the center of the main precession solenoid, where it reaches its maximum of up to a few MHz. The accumulation of precession angle

[7] The polarized neutron beam is obtained by reflection by a magnetic multilayer mirror. The layer stack consists of alternating nonmagnetic (e.g. Fe, Si or Ti) and magnetic (Fe or Co) layers. The effective index of refraction of the magnetic layers depends on the relative orientation of magnetization and spins of the neutrons such that there is a modulation of index of refraction for neutrons in one spin state only. Those neutrons are reflected, the others are transmitted. For layer distances of $5 \cdots 10$nm reflection angles of a few degrees result for wavelengths around 10Å. Both the reflected and the transmitted beam are polarized (with opposite spin directions).

continues –with decreasing frequency– until the neutrons reach the π-flipper close to the sample (S). The total precession angle at that point is:

$$\Psi \;=\; \frac{\gamma}{v}\int_l |B|dl \;=\; n2\pi + \alpha \tag{10.13}$$

where $\gamma = 2\pi \times 2913.06598 \times 10^4 \mathrm{s}^{-1}/\mathrm{Tesla}$ is the gyromagnetic ratio of the neutrons ($\rightarrow$ rad/sec !) and $|B|$ is the modulus of the magnetic induction along the path l.

The "stop watch" does not proceed uniformly but with a position dependend frequency that is proportional to the local magnetic field along the neutron path, see fig. 10.6. This may also be considered as a field dependend distance streching, which releases e.g. the mechanical positioning accuracy requirements for the flippers since they are located in low field regions. The total number of precessions a neutron spin undergoes on passage through one arm of the spectrometer lies between 10 and some 10^4.

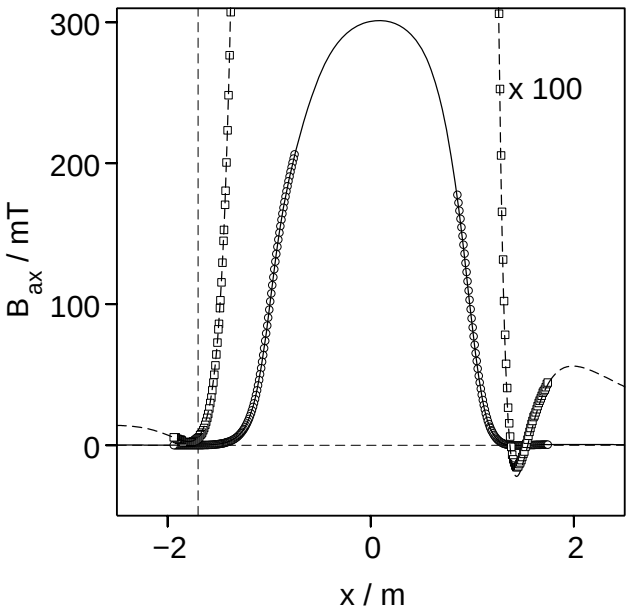

Figure 10.7: Field along the axis of a main precession coil.

Close to the sample (ideal: at the sample position) the so-called π-flipper is located, it rotates the spins by 180^0 around a vertical axis, thereby the total precession angle is transformed to $\Psi_1 = n2\pi+\alpha \rightarrow n2\pi-\alpha$. The parameters n and α are –according to eqn. 10.13 – extremely dependend on velocity and therefore very different for different neutrons in a

beam with finite width of the wavelength distribution. As a consequence the spin vectors at the sample position (π-flipper) are evenly distributed on a disc orthogonal to the field direction. If no velocity change occurs during scattering at the sample (elastic scattering) each neutron enters the secondary arm of the spectrometer with unchanged velocity. The precession field and path length of the secondary arm exactly match the corresponding elements of the primary arm before the sample (π-flipper). Accordingly the precession accumulated in the secondary arm is $\Psi_2 = n2\pi + \alpha$ and the total precession angle at the second $\pi/2$-flippers is $\Psi_1 + \Psi_2 = (n+n)2\pi - \alpha + \alpha = 2n2\pi$. I.e. all spins –irrespective of their initial velocity– reassemble at the same vertical position they had at the start point, the rotation imposed by the second π-flipper converts this back to the initial logitudinal polarization that is fully restored. The flippers limit the the two race tracks and realize "start", "time reversal" and "stop" of the "spin stop watches". The second $\pi/2$-flipper is the last element used to manipulate the spins it converts the average precession angle to a longitudinal polarisation component. Since the field after the second $\pi/2$-flipper is again longitudinal, further precessions do not influence the analyzed longitudinal polarization component (the stop watch is stopped!). The analyzer consists –like the polarizer– of mgnetic multilayer mirrors which only reflect neutrons of one longitudinal spin state into the detector. After ensemble averaging this means that the count rate at the detector is proportional to $(1 \pm \cos(\overline{\Psi}))/2$, [8] where $\overline{\Psi}$ is the expectation value of the angle between spin and axial direction.

10.5 The detector signal

As mentioned above the detector signal results from the cosine-of-net-precession-angle shaped transmission function of the analyzer in combination of the distribution of net precession angles due to the distribution of velocity changes during scattering. The velocity distribution is proportional to the spectral part of $S(Q,\omega)$. The intensity on the detector is proportional to the cos-modulated distribution. In the following this is derived in terms of mathematical expressions. First the field integrals along the primary and secondary pathes of precession are defined:

$$J_1 = \int_{l((\pi/2)_1)}^{l(\pi)} |B| dl \tag{10.14}$$

$$J_2 = \int_{l(\pi)}^{l((\pi/2)_2)} |B| dl \tag{10.15}$$

[8] The sign in front of the cosine depends on the technical realization of polarizer and analyzer (both reflecting, transmitting, one reflecting one transmitting) and on the orientation of flippers. It may be selected by choosing the signs of the flipper currents.

for a symmetric setup $J_1 = J_2$; $l(\pi, (\pi/2)_{1,2})$ denotes the positions of the corresponding flippers. The precession angle accumulated on a path is

$$\Psi_i \;=\; \frac{\gamma J_i}{v} \tag{10.16}$$

where v is the neutron velocity (typically several 100 m/s). Because the π-flipper inverts the sign of Ψ_1 (i.e. of the part $\Psi_1 \mathrm{mod}\, 2\pi$), a total precession angle of

$$\Psi_{1,2} \;=\; -\frac{\gamma J_1}{v} \;+\; \frac{\gamma J_2}{v+\Delta v} \;+\; 4n\pi \tag{10.17}$$

results, where Δv is the velocity change of the neutron during scattering and n is an integer. The transmission function of an (assumed ideal) analyzer is

$$T_a \;=\; \frac{1}{2}\left[1 + \cos(-\frac{\gamma J_1}{v} \;+\; \frac{\gamma J_2}{v+\Delta v})\right] \tag{10.18}$$

From that the detector intensity

$$I \;=\; \eta S(Q) \iint \frac{1}{2}\left[1 \pm \cos(-\frac{\gamma J_1}{v} \;+\; \frac{\gamma J_2}{v+\Delta v})\right] w_\omega(\Delta v) w_\lambda(v)\; d\Delta v\; dv \tag{10.19}$$

results, where η is an irrelevant calibration factor and w_ω resp. w_λ are normalized distribution functions. w_ω represents the spectrum of the sample as found in the scattering function and w_λ takes account for the fact that the NSE spectrometers usually are operated with a broad incoming wavelength distribution ($\Delta\lambda_{FWHM}/\lambda = 10 \cdots 20\%$). Observing the linear dependences of k, λ and v and series expansion of the squares in Eqn. 11.2 and insertion into Eqn. 10.19 leads to:

$$I = \eta \iint \frac{1}{2}\left[1 \pm \cos(-\frac{\gamma J_1}{(h/m_n)\lambda^{-1}} + \frac{\gamma J_2}{(h/m_n)\lambda^{-1} + \lambda\omega/2\pi})\right] S(Q,\omega) w_\lambda(\lambda)\; d\omega\; d\lambda \tag{10.20}$$

.

10.5.1 Symmetric case

At the point of symmetry $J_1 = J_2 = J$ it is possible to collect the λ-dependend terms in Eqn. 10.20 and to write them as series expansion for small ω:

$$-\frac{1}{\lambda^{-1}} + \frac{1}{\lambda^{-1} + \lambda(m_n/h)\omega/2\pi} \approx -\lambda^3 \frac{m_n \omega}{h 2\pi} \tag{10.21}$$

To see the salient features of the spectrometer signal more clearly the finite wavelength distribution is temporarily ignored

$$I \;=\; \eta \frac{1}{2}\left[S(Q) + \int \cos(\underbrace{\gamma J \frac{m_n^2}{h^2 2\pi}\lambda^3}_{t} \;\omega) S(Q,\omega) d\omega\right] \tag{10.22}$$

The underbraced product has the unit "time", the integral in Eqn. 10.22 represents the cos-Fourier transform of $S(Q,\omega)$ with respect to ω, the resulting function is called **intermediate scattering function,** $S(Q,t)$ [9] From Eqn. 10.22 it is further reckognizable that the time parameter $t = \gamma J(m_n^2)/(h^2 2\pi)\lambda^3$ depends on the third power of the wavelength λ (i.e. long wavelength $\rightarrow$ very long Fourier times). In addition $t \propto J$, i.e. mainly proportional to the current throught the main precession solenoids. This current usually is the parameter used to stepwise scan the Fourier time during an experiment to get a table of $S(Q,t)$ vs. t.

10.5.2 Elastic scattering of a finite width wavelength distribution

For a transmitted beam or elastically scattered neutrons from a reference sample $\omega = 0$ holds, i.e $S(Q,\omega) = \delta(\omega)$. With that Eqn. 10.20 becomes

$$I = \frac{1}{2}\int \left[1 \pm \cos(\lambda \underbrace{\gamma(m_n/h)\{J_2 - J_1\}}) \right] w_\lambda(\lambda) d\lambda \qquad (10.23)$$

For this case the intensity is proportional to the Fourier transform of the wavelength distribution, thereby the underbraced part is the external control parameter. It contains the difference between the field integrals along the primary and secondary pathes $J_2 - J_1$. This difference is easily controllable by sending a current through an auxiliary coil of a few windings around one of the precession solenoids. For a Gaussian wavelength distribution the envelope of the Fourier transform is again a Gaussian the width of which is inversely proportional to the width of the wavelength distribution. Since w_λ is centered at a finite nominal wavelength λ_0 the envelope is multiplied by a cosine with a period $\propto 1/\lambda_0$. This function follows immediately from Eqn. 10.23 if $w_\lambda = \delta(\lambda)$ is assumed. Figure 10.8 displays the results of a extensive measurement using the attenuated direct beam with a central wavelength of $\lambda_0 = 0.7$nm and $\Delta\lambda_{FWHM}/\lambda_0 = 0.1$ compared to a calculation (fit) assuming a Gaussian wavelength distribution.

At the echo point (=perfect symmetry) at a phase coil current close to 1.5 A the count rate has a minimum. Ideally the rate there should be zero, but because all elements that contribute to the polarization manipulation and analysis are imperfect a residual intensity is left that has to be determined by calibration measurements. From the function intensity vs. phase current it is possible to determine the wavelength distribution.

[9] Strictly this is only true for a $S(Q,\omega)$ that is symmetric with respect to ω. For any practical problems however this is well fulfilled since the minute energy transfers corresponding to the NSE time scale are very small compared to $k_B T$.

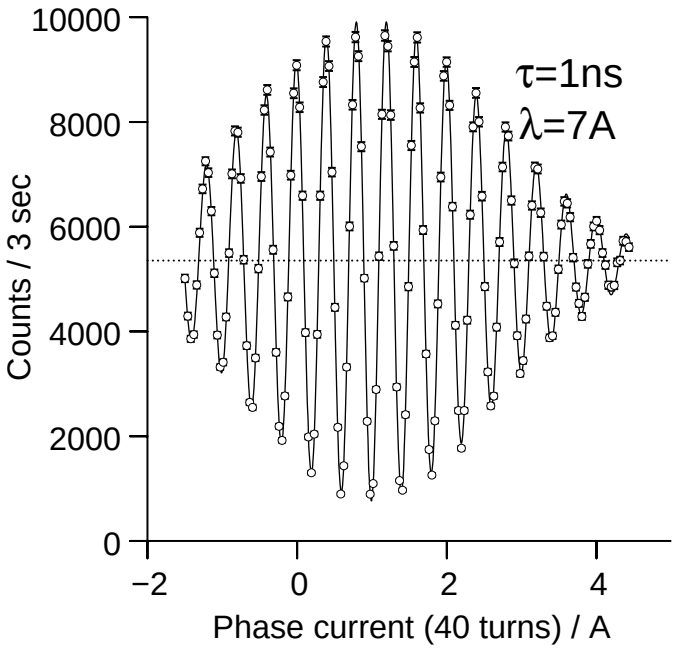

Figure 10.8: Echoform: count rate as function of the magnetic symmetry ($\propto$ phase coil current).

10.6 Experimental procedures and evaluation

In principle the information on $S(Q,t)$ according to Eqn. 10.22 is contained in the ratio of the intensities at the symmetry point and the average intensity $(\eta/2)\ S(Q)$. However there are practical reasons that prevent the reliable setting of the symmetry point alone. The location of the symmetry point (i.e. phase zero current in the phase coil) is extremely sensitive to tiny variations of the magnetic environment caused e.g. by displacement of larger iron parts at neighbouring instruments, movement of the crane and/or thermal displacements of coils ... . Therefore the position of the symmetry point has to be measured as well as the intensitiy each time. In fig. 10.9 the minimum of single countings is indicated, intensity must be determined for 3 points $P_1 \cdots P_3$ separated by a symmetry change corresponding to a quarter precession each. From these 3 values it is possible to extract the average intensity $I(Q,0)$, the echo amplitude $I(Q,t)$ and the exact symmetry point location. This also holds if any disturbance shifted the location as indicated by the three hollow circles in the figure.

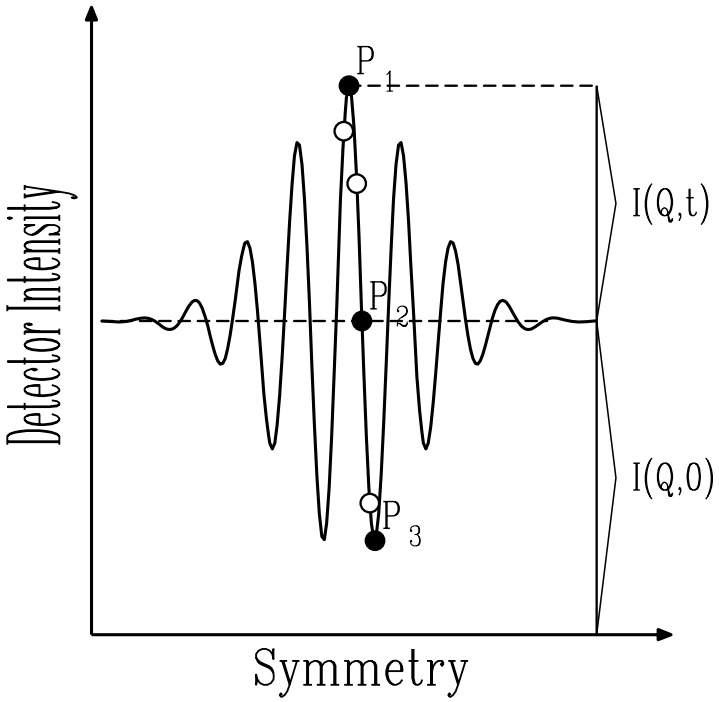

Figure 10.9: Schematic echo form, idealized.

For an ideal spectrometer $I(Q,t)/I(Q,0) = S(Q,t)/S(Q)$ would be the desired value of the normalized intermediate scattering function. In reality resolution effects and polarization losses reduce the value of $I(Q,t)/I(Q,0)$ compared to $S(Q,t)/S(Q)$.

10.7 Field integral homogeneity and resolution

Besides the decay of $S(Q,t)$ as a consequence of the dynamical processes in the sample the measured echo amplitude suffers a further reduction due to resolution effects (different from the above mentioned depolarization effects) that must be accounted for in the data evaluation. These effects result from residual differences of the path integral over the magnetic field along various paths connecting the beam apertures. They are quantified by a measurement with a purely elastic scattering reference sample. Resolution correction may then be performed by division of the echo-amplitudes by those of the reference sample.

10.8 Practical aspects, peculiarities

From the above description it follows that the NSE spectrometer measures the Fourier transform $S(Q,t)$ of the spectral part of $S(Q,\omega)$ directly. As a consequence the average count rate at the detector corresponds to half of all neutrons scattered from the sample into the soild angle of the detector (Fourier**integral**). Therefore weak spectral features are buried under the noise due to counting statistics. However the method is perfectly adapted to relaxations that are performed by most of the scattering structure since the realxation functions are measured in the time domain directly and resolution correction consists of a division instead a deconvolution in the frequency space. One very important field for NSE investigations are "soft matter" problems. These comprise polymer melts and solutions and other complex fluids. The NSE methods opens a dynamics window in the SANS regime. Since in that regime the dynamics is determined by the balance between elastic (entropic) forces and friction and in comparison inertial forces are negligible the observed fluctuations are pure relaxations and well suited for investigation by NSE. In addition SANS scattering is coherent and usually intense compared to scattering at large angles.

The spin incoherent scattering is caused by the dependence of the scattering length on the relative orientation of nuclear and neutron spins. The fluctuating part of the scattering length due to random spin orientation contains no interference of scattering from different nuclei, i.e. the scattering intensity distributes evenly over 4π solid angle and is "diluted" accordingly. The intensity is very small compared to typcial SANS intensities. The dynamics of the incoherent scattering reflects the one-particle motion (self correlation). For the NSE method it is important to note that the spin-dependend scattering flips 2/3 of the neutron spins. This means that a considerable loss of polarization is encountered, only 1/3 of the neutrons contribute to the echo signal the rest is background. This 1/3 stems form the spin flipped neutrons, i.e. the echo amplitude is also inverted (negative). If coherent and incoherent scattering contributions are present this may lead to peculiar effects since the amplitudes may cancel each other depending on their –potentially different– dynamics.

10.9 Scattering cross section and time-of-flight spectra for some basic systems

In this chapter the scattering from a number of very basic physical systems is presented and the corresponding features of the neutron time-of-flight spectra are discussed. It should help the reader to gain a feeling of what kind of effects determine the shape of TOF

spectra in different energy and resolution regime and for samples in various states of aggregation. The expressions of scattering functions mainly follows the textbooks of Marshall & Lovesey [Marshall and Lovesey(1971)] and Doi & Edwards [Doi and Edwards(1994)], which are recommended as reference books for the field of neutron scattering respectively polymer dynamics.
We start from the high energy side where scattering results in broad spectral distributions.

10.9.1 Ideal monoatomic Gas

As a starting point for the discussion of general features of TOF spectra we consider the simple gas model as alredy presented in chapter 5 first. We deal with scattering centers (atoms) with totally uncorrelated mutual distances. Therefore on average all interference terms from the superposition of partial waves cancel and –as for incoherent scattering– the observed cross section represents the (Maxwellian) velocity distribution. Figure 10.10 shows spectra which may be obtained with a hot source or an "eV" spectrometer at a pulsed source, they are dominated by the recoil shifted velocity(momentum) distribution. Please note that in the following figures the intensity data are plotted versus the neutron wavelength which is synonym, respecttively direct proportional to the time-of-flight!

The gas scattering obtained with thermal incident energy is shown in figure 10.11 which also reveals the fact that only a part of the $[Q, \omega]$-space is kinematically accessible.

The scattering function for a gas is given by:

$$S(Q,\omega) \;=\; \sqrt{\frac{\beta M}{2\pi\hbar^2 Q^2}}\;\exp\left[-\frac{\beta M}{2\hbar^2 Q^2}(\hbar\omega - \frac{\hbar^2 Q^2}{2M})^2\right] \tag{10.24}$$

where M is the particle mass, $\beta = (k_B T)^{-1}$ and $\hbar^2 Q^2/(2M)$ is the recoil energy. At high Q, i.e. at high incident neutron velocity a significant shift of the center of neutron velocity is encountered which depends on the mass of the scattering particle. The width of the neutron spectrum reflects the momentum distribution (here Maxwellian velocity distribution) of the ensemble of scatterers of this mass. Note that $S(Q, \omega)$ in this regime is assymetric with respect to ω.

10.9.2 Ensemble of Harmonic Oscillators

An interesting insight into the interrelation of recoil and incorporation of the scatterers in a condensed matter system is obtained by consideration of a particle in a harmonic potential (i.e. Einsteins model of a solid), which is the next example to be discussed.

For an ensemble of particles in identical spatially uncorrelated isotropic harmonic poten-

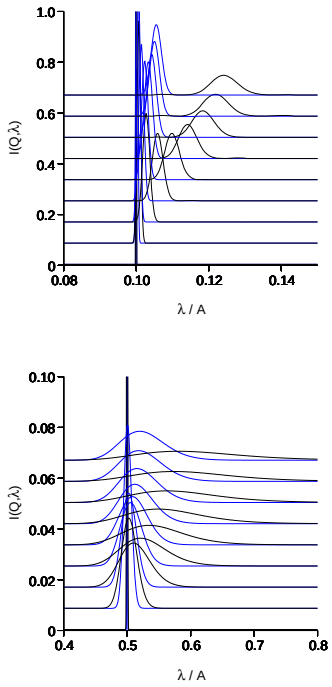

Figure 10.10: Computed time-of-flight spectra from monoatomic gases with atomic weight 1 (wide recoil peaks) and 4 (narrow recoil peaks) at $T = 300K$. The incident neutron wavelength is $\lambda_0 = 0.1$Å (left) and $\lambda_0 = 0.5$Å (right) the scattered wavelength λ is proportional to the time of flight. The series of curves correspond to equidistant scattering angles between 1^0 and 161^0. Observe the mass dependent loss of average energy of the neutron due to the recoil effect, visisble at larger scattering angle.

tials the scattering function is [Marshall and Lovesey(1971)]:

$$S(Q,\omega) = \exp\left[-\frac{\hbar Q^2}{2M\omega_{osz}}\coth(\hbar\omega_{osz}\beta/2)+\hbar\omega\beta/2\right]\times \sum_{n=-\infty}^{\infty}\delta(\hbar\omega-n\hbar\omega_{osz})I_n(\frac{\hbar Q^2}{2M\omega_{osz}\sinh(\hbar\omega_{osz}\beta/2)}) \qquad (10.25)$$

the corresponding spectrum is shown in figs. 10.12, 10.13, 10.14, where the δ-function has been replaced by a narrow Gaussian. As is seen from the figures the oscillator frequency may easily be inferred by the spacing between the excitation lines. Their positions do not depend on Q, but their intensities that reflect the form factor due to the oscillator eigenfunctions weighted by their thermal occupation do so. The varying spacing of lines in the TOF-diagrams $I(\lambda,\theta)$ results from the nonlinear tranformation from experimental TOF representation to $S(Q,\omega)$.

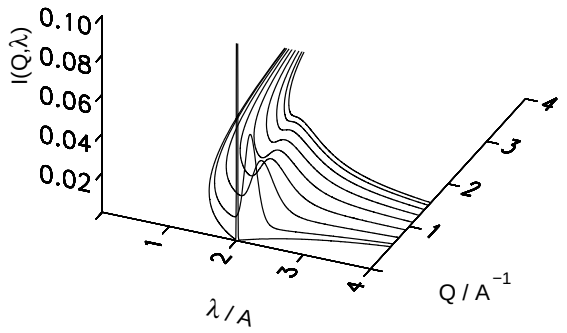

Figure 10.11: Gas ($m = 4$) scattering displayed as intensity vs Q and λ for an equidistant series of scattering angles. The incident wavelength is $\lambda_0 = 2$Å. As is visible only a part of the $[Q, \omega = \hbar/(8\pi^3 m_n)(\lambda^{-2} - \lambda_0^{-2})]$ space is kinematically accessible.

As a dense line spacing of the oscillator illustrates that at low resolution ,i.e. high enough incident neutron energy, the intensity distribution is such that the oscillator scattering approaches that of a gas of free particles (short time behaviour), see fig. 10.15. This is another way to state that for high energy neutrons and at short times the particle in a (shallow) potential looks very similar to a free particle.

However, why don't we see more effects from recoil? In particular in high resolution spectroscopy this would even at low Q lead to significant energy shifts. A closer look to the oscillator spectra reveals the answer. There is always a line at $\omega = 0$ separated by the oscillators excitation energy from the closest inelastic lines. Only the envelope over the line intensities displays the trace of the recoil. The physical explanation is that observation for longer times (ω small) reveals that the particle is bound and attached to the (immovable, "infinitely" heavy) background (e.g. a macroscopic crystal) and therefore the recoil energy becomes infinitely small. If the neutron transfers more energy and exites higher oscillator states the effect more and more resembles a kick to the confined particle that leaves a localized oscillating distribution within the potential. For the short effective interaction time of the neutron this more and more resembles the collision with a free particle, as the illustration of fig. 10.15 corroborates.

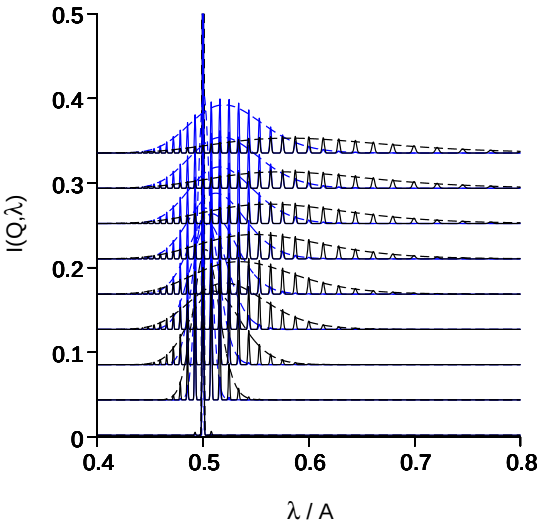

Figure 10.12: Computed time-of-flight spectra from particles of mass 1 (black) and 4 (blue) in a harmonic potential (such that $\hbar\omega_{osz} = 10\,\text{meV}$) at $T = 300K$. The incident neutron wavelength $\lambda_0 = 0.5\text{Å}$ (right) the scattered wavelength λ is proportional to the time of fligth. The dashed lines correspond to the gas scattering shown in fig. 10.10.

Phonon density of states

Whereas the "Einstein solid" gave some insights and may be the right model for localized optical modes, e.g. realized by hydrogen in metals, the dominant atomic motions in a normal solid can be described as sound-like phonons.

The simplest model of the phonon density of states of a solid is the Debye spectrum which assumes sound waves with linear dispersion up to a cut-off frequency ω_D. Then the density of states is

$$Z(\omega) = \frac{3\omega^2}{\omega_D^3} \tag{10.26}$$

The Bose factor that describes the temperature dependent occupation of phonon states is

$$n(\omega) = \frac{1}{e^{\hbar\omega\beta} - 1} \tag{10.27}$$

and with

$$\gamma(t) = \int_{-\infty}^{\infty} \frac{Z(\omega)}{\omega}\, n(\omega) \exp(-i\omega t)\, d\omega \tag{10.28}$$

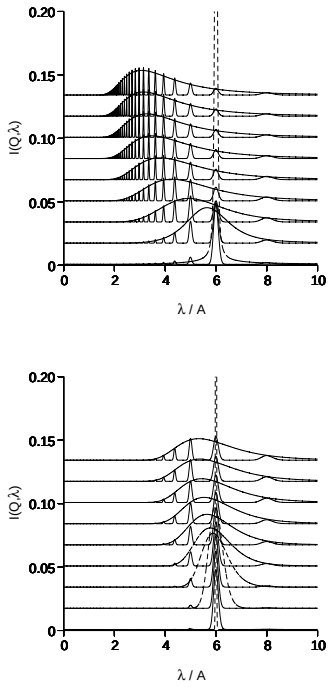

Figure 10.13: Comparison of time-of-time of flight spectra computed for a gas (m=4) and an ensemble of oscillators (m=4) at $T = 300K$ and $T = 30K$ for an incident wavelength of $\lambda = 6$Å. The series of curves correspond to equidistant scattering angles between 1^0 and 161^0.

the Debye-Waller factor is

$$\exp(-2W(q)) \quad \text{with} \quad 2W(q) = \frac{\hbar q^2}{2M}\gamma(0) \tag{10.29}$$

with that the phonon scattering (in incoherent approximation, e.g. by decorating protons) is

$$\frac{d^2\sigma}{d\Omega dE'} = Nb^2\frac{k'}{k}\frac{1}{2\pi\hbar}\int_{-\infty}^{\infty} exp[-i\omega t - 2W(q) + \frac{\hbar q^2}{2M}\gamma(t)]dt \tag{10.30}$$

this may be expanded by using the series expansion of $exp[\frac{\hbar q^2}{2M}\gamma(t)]$ as series of 0-, 1- and multiple phonon scattering contributions.

$$\frac{d^2\sigma}{d\Omega dE'} \simeq Nb^2\frac{k'}{k}\, e^{-2W(q)}\, \left[\delta(\hbar\omega) + \frac{\hbar^2 q^2}{2M}\frac{Z(\omega)}{\omega}\{1 + n(\omega)\} + \cdots\right] \tag{10.31}$$

Equation 10.31 shows a way how the density of states $Z(\omega)$ may be derived from the results of a TOF-experiments on a solid.

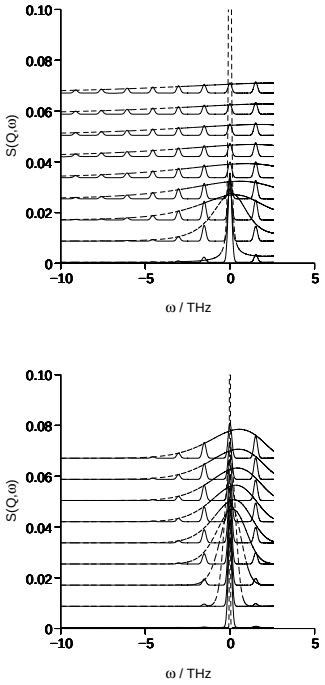

Figure 10.14: Comparison of scattering function corresponding to figure 10.13.

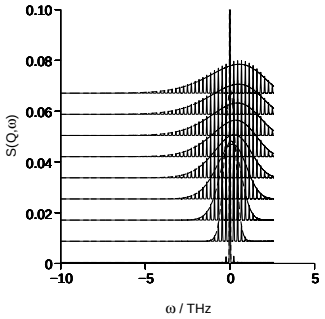

Figure 10.15: Comparison of scattering functions of a gas compared to an oscillator with narrow spacing at $T = 30K$.

Note

Strictly speaking the above expression is only valid for a simple monoatomic solid in incoherent approximation. I.e. either composed of incoherent scatterers (like Vanadium) or measured in powder average

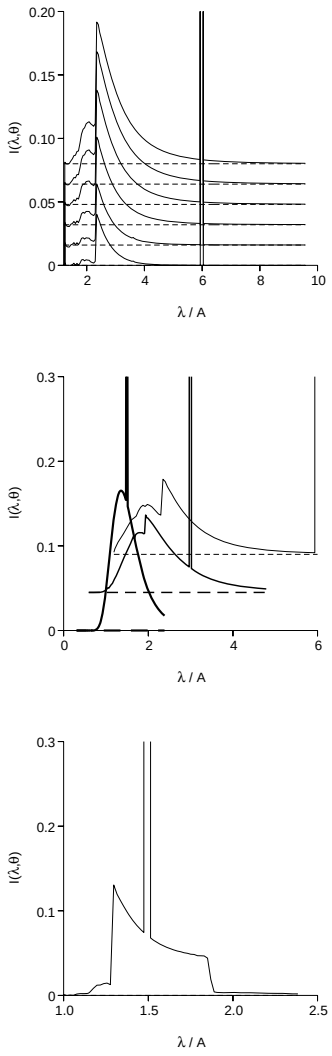

Figure 10.16: Multiphonon spectra of a Debye solid with a Debye temperature of 150. The effective mass was taken as 1 amu. Upper left: TOF spectra computed for an incident wavelength of 6 Å for scattering angles $10^0 \cdots 150^0$ at $T = 100\,\mathrm{K}$. Upper right: TOF spectra at 90^0 scattering angle and $T = 300\,\mathrm{K}$ for incoming wavelengths $\lambda = 1.5$, 3, 6 Å. Note the approach to the free gas scattering with increasing incident energy. Lower curve: situation that allows to estimate the one phonon spectrum $Z(\omega)$ at the low scattering angle of 15^0 even with $\lambda = 1.5$ Å $T = 300\,\mathrm{K}$.

at large Q such that coherent effects are averaged out. For more complex structures a amplitude and scattering length weighted density of states is obtained rather than the plain $Z(\omega)$. The exact treatment

becomes more involved.

As far as the single phonon scattering dominates $Z(\omega)$ directly follows from Eq. 10.31 by separating the elastic scattering ($\delta(\hbar\omega)$) and multiplication of the rest with $\omega/(1+n(\omega))$. However, care must be taken to avoid the effects of multiphonon scattering. As the occurence of multiple excitation with the simple oscillator also here the nonlinearity in the exponential functions of displacement $\times$ Q lead to multiphonon contributions. The effect is large at high Q and T as can be read from fig. 10.16. Similar to the ensemble of decoupled oscillators also the Debey solid approaches the response of a gas of "free" particles if the energy/momentum transfer is large. I.e. to plan an experiment to extract $Z(\omega)$ from TOF-data one should select low Q values and low T, which unfortunately contradicts the quest for high intensity of the desired signal.

10.10 Measured Spectra

In fig. 10.17 several spectra as they are accumulated in the histograammatic memory are displayed. The time-of-flight scale of the horizontal axis refers to the distance L between sample and detectors. This time-of-flight is directly proportional to the wavelength λ' of the scattered neutrons as is indicated by the diagonal representing this linear relation using the right hand vertical scale. This diagonal straight line intersects the level $\lambda_0 = 6$Å at the location of the "elastic channel" where neutrons are collected that did not change their velocity during scattering. Since in liquid water which was the sample all moelcules may diffuse without restriction only a so called **quasielastic** line is observed which corresponds to a Lorentzian with a width proportional to Q^2. The maximum of intensity is nevertheless at the elastic channel ($\rightarrow$ quasielastic).

The difference between a solid with atoms/molecules fixed at lattice sites and a liquid is illustrated by the right part of the figure. Imidazole in the solid state exhibits an intense line at the elastic channel with a width corresponding to the instrumental resolution, the small inelastic intensity around the elastic line can be associated with a Debye solid like density of states, which at larger energy transfer, however, displays different structures according to the phonon dispersion of the imidazole crystal. Also multiphonon contribute there.

In contrast molten imidazole (especially for the relatively large scattering angle displayed here $\rightarrow$ large Q) shows only a broad quasielastic intensity distribution. At shorter times-of-fligth corresponding to larger energy transfers (gains) structures in the spectra are visible that stem from molecular and lattice virbrations. Note the second left scale in combination with the dashed line that illustrates the strongly nonlinear relation between energy and time-of-flight. For energy gains $\Delta E \gg k_B T$ the scattering energy dies out due to the exponential Boltzmann factor. At ambient temperature $k_B T$ is equivalent to 25meV. Well above that energy gain the unavoidable virtually constant background due

to “frame overlap” may be determined.

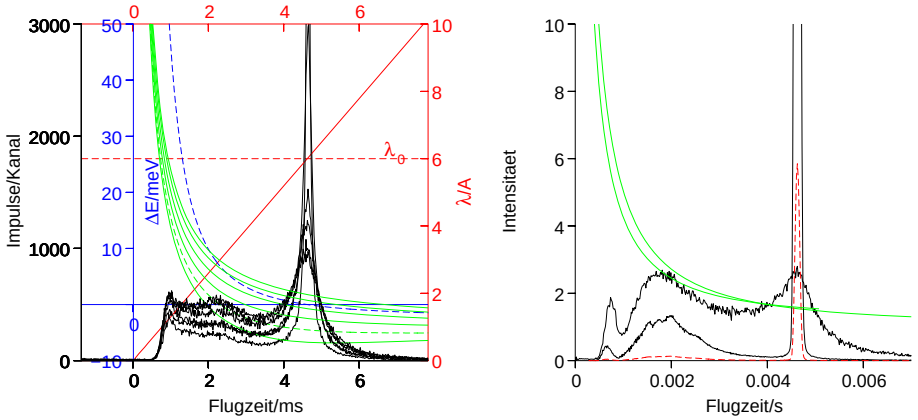

Figure 10.17: Left: TOF-spectra from liquid water at ambient temperature for different scattering angles between 30^0 and 140^0. Parameters: $\lambda_0 = 0.6$nm, $\Delta\tau = 18\mu$s, $L = 3.05$m, $N = 512$. Right: TOF-spectrum from imidazole (C_4H_4NH) as crystalline solid at 300K (the dashed lines displays the same data scaled by $\times 0.1$) and as melt at 403K at a scattering angle of 95^0.

That corresponds to the situation of the scattering triangle as depicted in fig. 10.1. $\underline{Q}$ (depending on energy transfer) for elastic and inelastic scattering have to be assigned to the different time channels of the histogram from one specific detector. That applies as well for the modulus Q as for the direction of $\underline{Q}$. The sequence of curves in the left figure 10.17 shows the values of Q as function of scattering angle (different curves) and time channel. The property that the values become very similar for large energy gains –also expressed by the similar intensity distribution of that part of the spectra for different angles– follows from the fact that the main contribution to Q at high energy gain stems from the length difference of k and k' (see fig. 10.1). The variation of $|\underline{Q}|$ may be compensated within certain limits by combining the data from different detectors (angles), however that does not apply for the direction change of $\underline{Q}$. Therfore TOF-instruments –in contrast to triple-axis spectrometers– are better suited for isotropic samples (liquids, powders, amorhpous substances) than for single crystals or other highly oriented samples.

Conversion to $S(Q,\omega)$

Application of the transforms Eqns. 10.5 and 10.11 allows for a display of the spectra in terms of $S(2\Theta,\omega)$. Figure 10.18 shows a corresponding $S(2\Theta,\omega)$ derived from the water data (medium angle data in fig. 10.17).

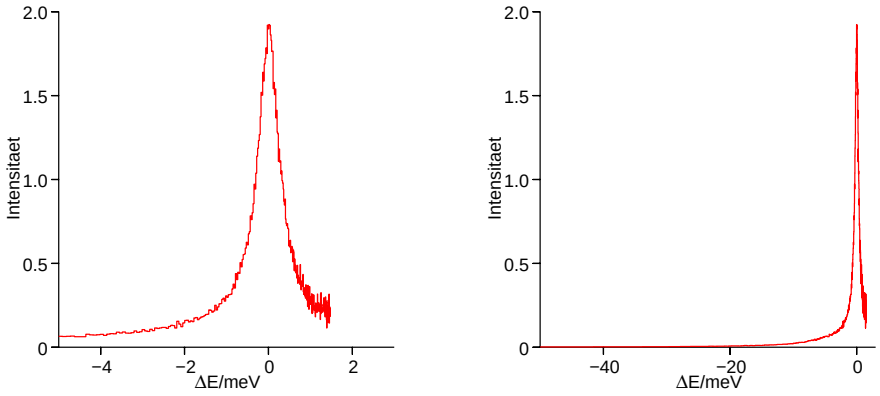

Figure 10.18: TOF spectrum from liquid water (see fig. 10.17) converted to $S(2\Theta, \omega)$ displayed over two different energy ranges.

The diffusion is easily reckognizable but the structur due to (internal) vibrations is lost in this type of representation. As soon as a model for $S(Q, \omega)$ is available, it is in most cases more advantageous to apply the inverse transform to that model to compute $I(2\Theta, K)$ and to compare this result with the raw TOF data. This procedures also allows for a simpler more direct application of resolution corrections.

NSE Experiment Data

The single chain structure factor of a linear polymer in the melt in terms of the standard NSE data representation as $S(Q,t)/S(Q)$ for a series of different Q-values is shown in figure 10.19. The sample was a melt of polyethylethylene with 10% protonated chains in 90% deuterated chains of the same chemical architecture.
Flexible linear polymer chains in solution follow a different universal behaviour due to the long range hydrodynamic coupling between different segments of the same chain. The corresponding model is called ZIMM model, within the so-called preavaeraging approximation it has the same structure as that of the Rouse model (see [Doi and Edwards(1994)]). Please refer to chapter 13 for further details. In the universal regime the decay rate is $\propto Q^3$ instead of Q^4 as in the Rouse model. Except "trivial" temperature factors, the only parameter that determines the decay rates is the solvent viscosity. Figure 10.20 shows results from a measurement of a linear polymer solution the fitted viscosity coincides within 10% with the known solvent viscosity.

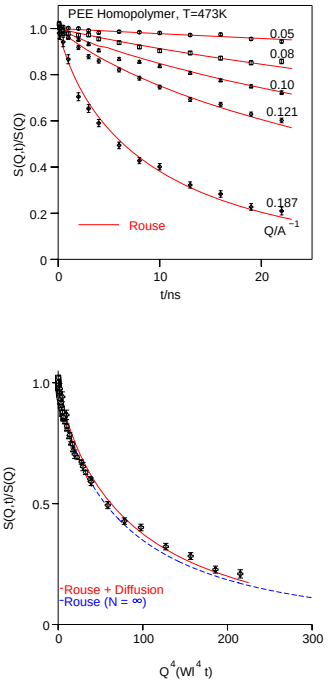

Figure 10.19: Single chain scattering from a a PEE-polymer melt in standard representation for NSE data as $S(Q,t)/S(Q)$ (right). On the left a scaling plot of the same data is shown. Curves correspond to a (one parameter) fit to the Rouse model. They show nearly pure Rouse scaling (i.e. rate $\propto Q^4$) following the master function given in chapter 13 with marginal distortion due to the centre-of-mass motion.

10.11 Resolution and Intensity

10.11.1 TOF

For TOF-spectrometers –unlike for triple-axis instruments– for many applications mainly/only the energy resolution is important since the scattering intensity has to be collected and accumulated in a large solid angle anyway to yield a sufficient number of counts. The energy resolution is determined by the accuracy of the TOF-measurement and by the width of the incoming (or analyzed) wavelength band. The latter is given by the beam divergence in combination with the mosaik width of the crystals (see also chapter on triple-axis spectrometres). The TOF-uncertainity is given by the chopper pulse length and the accuracy of the flight path. The flight path cannot be defined with arbitrary accuracy, since finite sample size of cm and a detection position uncertainity of some

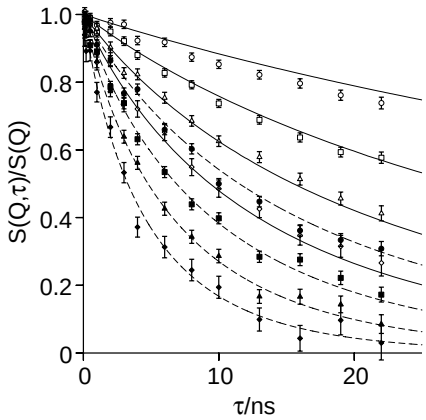

Figure 10.20: $S(Q,t)/S(Q)$ of a 2.5 % polymer solution with a fit to the Zimm model that theoretically describes $S(Q,t)$ for a dilute polymer solution. The data have been measured using the area detector at only two angluar positions of the secondary spectrometer arm within 8 h time. The hollow symbols habe been obtained at an arm setting of $\bar{Q} = 0.05\text{Å}^{-1}$ and correspond to $Q/\text{Å}^{-1} = 0.038, 0.05, 0.061, 0.072$. The filled symbols were measured at $\bar{Q} = 0.08\text{Å}^{-1}$ and correspond to $Q/\text{Å}^{-1} = 0.067, 0.08, 0.09, 0.102$.

mm in the detectors. [10] If all timing uncertainities are lumped into Δt, a classical TOF instruments has the following resolution:

$$\Delta\omega \;=\; \sqrt{(\frac{\partial\omega}{\partial t}\Delta t)^2 + (\frac{\partial\omega}{\partial\lambda}\Delta\lambda)^2} \tag{10.32}$$

From Eqns. 10.2 - 10.5 follows:

$$\Delta\omega \;=\; \sqrt{(\frac{m_n L}{\hbar t^3}\Delta t)^2 + (\frac{4\pi^2\hbar}{m_n\lambda^3}\Delta\lambda)^2} \tag{10.33}$$

Because $\lambda' \propto 1/v' \propto t$ and close to the elastic line ($\lambda' \approx \lambda$) it follows that $\Delta\omega \propto 1/\lambda^3$, i.e. the most efficient measure to increase the "elastic" resolution is the use of a long neutron wavelength/ For a matched setup the relative timing uncertainity $\Delta t/t_0$ and the relative wavelength width $\Delta\lambda/\lambda$ should be about equal. Eqn.10.33 shows in addition that the timing uncertainity term $\propto \Delta t$ dominates the resolution width for short time t, i.e. large energy gain of the neutron. If path uncertainities ΔL are treated separately, Δt represents only the chopper opening and Eqn. 10.33 reads:

$$\Delta\omega \;=\; \sqrt{(\frac{m_n L}{\hbar t^2}\Delta L)^2 + (\frac{m_n L}{\hbar t^3}\Delta t)^2 + (\frac{4\pi^2\hbar}{m_n\lambda^3}\Delta\lambda)^2} \tag{10.34}$$

[10] For sample in form of thin plates the path uncertainity due to scattering position in the sample may be reduced for (only) one scattering angle (region) to the plate thickness.

For the inverted spectrometer the expressions stay the same expect for the exchange of λ and λ'.

10.11.2 NSE

For NSE spectrometers the high energy resolution is not realized directly but comes as large (Fourier)time, t, in the intermediate scattering function $S(Q,t)$. Again the relative Q-resolution is less important for many applications. However, the range of interest often is located at small Q where the large structures of typical "soft"-matter samples contribute to the scattering intensity. This implies that the covered solid angle is more limited than for the TOF instruments described above. The resolution in terms of maximum Fouriertime is either limited by the product $t = \lambda^3 \int |B| dl$ or by the field integral inhomogeniety within the paths in the neutron beam. The first limitation is given by the spectrum of the neutron source and the technical ability to increase the magnetic field. The second limitation depends on the ability to maintain equal field integrals by sufficiently accurate coils and correction elements. Currently the latter factor is the limiting one. High resolution NSE requires relative field integral of less than $10^{-5} \cdots 10^{-6}$. The effect of loss of resolution due to inhomgenieties is a strong reduction of the echo amplitude even for a perfectly elastic reference scatterer. An echo reduction by a factor of $\simeq 2$ marks the approximate resolution limit.

10.11.3 Intensity Issues

The available neutron sources are rather weak compared to sources of electromagnetic radiation (laser, synchrotron), they emit neutrons in form of a thermalized gas with a broad distribution of velocities and into all directions. Preparation of collimated and monochromatic beams is only possible by selection, i.e. removing all unwanted neutrons. The resulting beams –even at high flux reactors– contain only relatively few neutrons. [11] For this reason the available neutrons have to be utilized as efficient as possible. Even if an increase in resolution may be achieved by stricter wavevector $\underline{k}$ selection (velocity, direction) and by reduction of the chopper pulse length, it is often not advisable to enhance all elements of the resolution up to the technological limits because this goes along with a drastic loss of intensity (detector count rate). Design of (neutron)-spectrometers means the search for the best compromise between resolution and intensity. The optimum depends on the nature of the problem, i.e. the features and structures expected in $S(Q,\omega)$. TOF-spectrometer as described in this chapter are preferentially used to investigate isotropic to weakly anisotropic samples with only weak structures in $S(Q)$.

[11] The typical neutron flux in front of the chopper of a classical TOF instrument is in the order of $10^7 \mathrm{n/cm^2 s}$, after chopping only $10^5 \mathrm{n/cm^2 s}$ hit the sample and are available for scattering. In comparison a beam of a small 1 mW HeNe laser is strictly collimated and monochromatic and represents an integral flux of 3×10^{15}Photonen/s with a cross section of maybe $1mm^2$, i.e. $3 \times 10^{17} \mathrm{photons/cm^2 s}$.

This enables the utilization of a large solid angle for detection which compensates for the losses caused by energy analysis. In the schematics of the spectrometers this is already indicated by the large number of detectors. Modern TOF instruments contain more than 1000 single counting tubes covering a detecting area of $30 \times 1\text{cm}^2$ each. The total area coverd by 1000 detectors is about 3m^2, for a fligth path of 3 m this corresponds to a solid angle of 0.333 or 1000 degrees squared. Thereby an intensity gain of a factor 500 is obtained compared to a triple axis spectrometer with a detecting area of 2 degrees squared, the loss caused by the fact that the chopper opens only for about 1% of the time is more than compensated. In addition the TOF instrument has a multiplex advantage: all energy transfers are detected simultaneously and not sequentially as in the case of a triple-axis spectrometer. However it is seldom useful to sum the data of ALL detectors into one spectrum but different scattering angle regions have to be evaluated separately. Still they are measured all at the same time! Generally the TOF instruments is more efficient than a triple-axis spectrometer for isotroic samples. As soon as single crystals or very anisotropic samples with a strong dependence of the spectra on $\underline{Q}$ are to be investigated the conventional triple-axis spectrometers are better suited.

Since many NSE problems –as the NSE tecniques– do not allow to increase the solid angle to very large values, the intensity loss of high energy resolution must be recovered by other means. As it is explained above the NSE method decouples the incident beam enregy width from the energy transfer detection limit, it is possible to operate NSE spectrometers with 10% to 20% incident wavelength width. Thereby intense incoming beams may be employed. The reduction in Q-resolution associated with the wavelength width is often tolerable as in the typical SANS experiments. Even then the data collection efficiency of an NSE instrument can be boosted by empoying an area detector to cover an angular range of several degrees in horizontal and vertical direction.

Both TOF and NSE methods have resolutions that depend on λ^3 and therfore it is tempting to use this factor to increase resolution. But in the regime of long wavelength all available sources (even the cold sources) suffer from a λ^{-5} dependence of intensity, which sets a practial limit of $\lambda = 15 \cdots 20\,\text{Å}$ for virtually all applications.

Bibliography

[Marshall and Lovesey(1971)] W. Marshall and S. W. Lovesey, *Theory of Thermal Neutron Scattering* (Oxford University Press, London, 1971).

[Doi and Edwards(1994)] M. Doi and S. Edwards, *The Theory of Polymer Dynamics*, vol. 73 of *International Series of Monographs on Physics* (Oxford University Press, Oxford, 1994).

Contents

11

Structure determination

Gernot Heger

11. Structure determination

G. Heger

11.1 Introduction

The analysis of crystal structure and magnetic ordering is usually based on diffraction phenomena caused by the interaction of matter with X-rays, neutrons, or electrons. Even though electron microscopy can achieve atomic resolution, more detailed information on the 3dim. atomic arrangement of crystals with its symmetry and chemical bonding as well as magnetic structures and spin densities requires diffraction methods. The basic theory of diffraction is the same for all types of radiation. Complementary information is achieved due to the different character of X-rays, neutrons and electrons, and hence their different interactions with matter and further practical aspects.

Considering only X-rays and thermal neutrons one finds that their wavelengths are similar (0.5 Å < λ < 2.4 Å). While the electromagnetic X-ray radiation yields the total electron density distribution, the nuclear scattering of neutrons probes the density distribution of the nuclei and the magnetic neutron scattering the spin density of unpaired electrons.

X-ray diffraction using conventional laboratory equipment and/or synchrotron installations is the most important method for structure analyses. The purpose of this paper is to discuss special cases, for which, in addition to this indispensable part, neutrons are required to solve structural problems. Even though the huge intensity of modern synchrotron sources allows in principle the study of magnetic X-ray scattering the investigation of magnetic structures is still one of the most important applications of neutron diffraction.

11.2 Structure factor and Bragg intensities

The characteristic feature of the crystalline state consists of its periodic ordering, which may be represented by a (translational) lattice. In the 3dim. case three basis vectors $\underline{a}$, $\underline{b}$, and $\underline{c}$ define a parallelepiped, called unit cell. The general lattice vector

$$\underline{\tau} = u\underline{a} + v\underline{b} + w\underline{c} \qquad (1)$$

results from a linear combination of the basis vectors with coefficients u, v, and w being positive or negative integers (incl. 0). According to their point-symmetry properties seven crystal systems are distinguished:

Triclinic, *Monoclinic*, *Orthorhombic*, *Tetragonal*, *Trigonal*, *Hexagonal*, and *Cubic*.

Besides of the related seven primitive lattices, with only one lattice point per unit cell, multiple lattices with centred unit cells are possible. In this way a total of 14 Bravais lattices is defined.

The position of atom j in the unit cell is given by the vector

$$\underline{r}_j = x_j\underline{a} + y_j\underline{b} + z_j\underline{c}. \quad (2)$$

The coefficients x_j, y_j, and z_j are called atomic coordinates ($0 \le x_j < 1$; $0 \le y_j < 1$; $0 \le z_j < 1$).

Lattice planes (that means a set of parallel planes containing lattice points) defined by three integers (*hkl*) called Miller indices have the characteristic interplanar spacing d_{hkl}.

For scattering studies of crystals the concept of the reciprocal lattice with the basis vectors $\underline{a}^*$, $\underline{b}^*$, and $\underline{c}^*$ was developed. The lattice vector of the reciprocal lattice is defined in crystallography by

$$\underline{H} = h\underline{a}^* + k\underline{b}^* + l\underline{c}^*. \quad (3)$$

In solid state physics instead of $\underline{H} = 1/d_{hkl}$ there is normally used the scattering vector

$$\underline{Q} = 2\pi\underline{H}. \quad (4)$$

11.2.1 Nuclear scattering

In kinematical approximation, assuming that the magnitude of the incident wave amplitude is the same at all points in the specimen (this implies a small sample size, weak scattering intensities, no multiple diffraction and neglecting of absorption), the diffracted intensity is proportional to the square of the amplitude of the scattered wave for each individual reflection; it can be regarded as a weight ascribed to the reciprocal lattice nodes

$$I(\underline{H}) \sim |F(\underline{H})|^2. \quad (5)$$

The structure factor $F(\underline{H})$, in terms of the Fourier transform, contains the complete information on the distribution of the scatterer density in the unit cell, including the atomic coordinates x_j, y_j, and z_j,

$$F(\underline{H}) = \sum_j b_j \exp[2\pi i(\underline{H}\cdot\underline{r}_j)]\cdot T_j(\underline{H}) = |F(\underline{H})|\cdot\exp[i\varphi(\underline{H})]. \quad (6)$$

In the case of nuclear scattering of neutrons the structure factor has the dimension of a length, as has the scattering length $b_j(\underline{H}) = b_j$ = const. of nucleus j. $T_j(\underline{H})$ is the Debye-Waller factor which takes into account dynamical and static displacements of the nucleus j from its average position $\underline{r}_j$ (see Eq. 2) in the unit cell. With the fractional coordinates x_j, y_j and z_j the scalar product in the exponential function can be written as

$$\underline{H}\cdot\underline{r}_j = hx_j + ky_j + lz_j. \quad (7)$$

Important: The measured Bragg intensities $I(\underline{H})$ from diffraction experiments yield only the modulus of the structure factors, $|F(\underline{H})| \propto \sqrt{I(\underline{H})}$, and not their phases $\varphi(\underline{H})$ (see Eq. 5), which would be required for the inverse Fourier transform of the data (Fourier synthesis) to give directly the arrangement of the atoms in the unit cell. The lack of the phase information is known as the phase problem of crystallography.

In a diffraction experiment normally only relative Bragg intensities are measured. A SCALE factor is assumed to be rigorously the same for all reflections of one data set. For merely nuclear neutron scattering and single crystals the integrated relative intensities are given by

$$I(\underline{H}) = \text{SCALE} \cdot L \cdot A \cdot |F(\underline{H})|^2. \quad (8)$$

The Lorentz factor L is instrument specific. The absorption correction A depends on the geometry and linear absorption coefficient of the sample.

The geometrical diffraction conditions and hence the reciprocal lattice yield the periodicity of a crystal. Information on the crystal system, the Bravais lattice type and the basis vectors $\underline{a}$, $\underline{b}$, $\underline{c}$ of the unit cell (lattice constants a, b, c, α, β, γ) may be directly deduced from the reciprocal lattice. The $|F(\underline{H})|^2$ values associated as weights to the nodes of the reciprocal lattice give the diffraction symbol and hence valuable information on the space-group symmetry. Here systematic absences (zero structure factors) can be related to the choice of a non-primitive Bravais lattice, or to the presence of non-symmorphic symmetry operations (symmetry operations with translation components).

11.2. 2 Magnetic scattering

The dipolar interaction between the neutron magnetic moments and the magnetic moments of atoms/ions (and nuclei) $\underline{m}_j$ leads to the magnetic neutron scattering in addition to the nuclear contribution. In the case of an ordering of the magnetic moments over the whole crystal (periodic magnetic structure) the magnetic structure factor is given by

$$F_M(\underline{H}) = \sum_j b_{Mj}(\underline{H}) \cdot \exp[2\pi i(\underline{H} \cdot \underline{r}_j)] \cdot T_j(\underline{H}) \quad (9)$$

with the magnetic scattering amplitude

$$b_{Mj}(\underline{H}) = (e^2\gamma/2m_ec^2) \cdot f_{Mj}(\underline{H}) \cdot \sigma \cdot \underline{m}_{\perp j}(\underline{H}). \quad (10)$$

$\frac{1}{2}\sigma$ is the neutron spin operator and $\underline{m}_{\perp j}(\underline{H})$ the projection of the magnetic moment $\underline{m}_j$ onto the scattering plane (*hkl*). The magnetic form factor $f_{Mj}(\underline{H})$ is the Fourier transform of the normalised magnetisation density $M_j(\underline{r})$ of the atom or ion j

$$f_{Mj}(\underline{H}) = \int_V M_j(\underline{r})\cdot\exp[2\pi i(\underline{H}\cdot\underline{r})]\cdot d\underline{r} \qquad (11)$$

with $f_M(0) = \int_V M_j(\underline{r})\cdot d\underline{r} = 1.$

This is a function of the reciprocal lattice vector $\underline{H}$, whereas the atomic scattering factor f_j of X-ray diffraction

$$f_j(|\underline{H}|) = \int_V \rho_j(r)\cdot\exp[2\pi i(\underline{H}\cdot\underline{r})]\cdot d\underline{r}, \qquad (12)$$

for a spherical electron density $\rho_j(r)$, depends only on the length of $\underline{H}$.

The intensity of magnetic and nuclear neutron scattering is of the same order of magnitude. For unpolarised neutrons the Bragg intensity of nuclear and magnetic neutron diffraction is simply an incoherent superposition

$$I(\underline{H}) = I_N(\underline{H}) + I_M(\underline{H}) \sim |F_N(\underline{H})|^2 + |F_M(\underline{H})|^2. \qquad (13)$$

For polarised neutrons on the other hand the coherent superposition gives

$$[|F(\underline{H})|^2]^{\pm} = |F_N(\underline{H}) \pm F_M(\underline{H})|^2 \qquad (14)$$

with the interference terms $\pm\ 2\cdot |F_N(\underline{H})\cdot F_M(\underline{H})|$ according to the two possible directions of polarisation (+ and -). In measuring the flipping ratio at superimposed Bragg reflections, that means the ratio of the intensities for the two polarisations up and down, even small magnetic structure factors can be determined quite accurately.

The analysis of a magnetic structure starts with the determination of its periodicity with respect to that of the crystal structure. The identification of magnetic reflections is usually accomplished by a careful comparison of powder diagrams recorded below and above the magnetic phase transition temperatures. A more detailed study of the scattering vectors, e.g. for incommensurate structures, may require also single-crystal experiments. The nuclear structure factors $F_N(\underline{H})$ can be calculated from the known crystal structure. In this way the SCALE factor of the data set can be obtained and the absolute values of the magnitudes of the magnetic structure factors $|F_M(\underline{H})|$ can be determined. The individual orientations of the magnetic moments $\underline{m}_j$ with respect to the basis vectors of the crystal lattice and their magnitudes are then to be calculated.

11.3 Contrast variation

Neutron diffraction can be used for an experimental distinction of atoms/ions with almost equal X-ray scattering amplitudes. In the case of mixed systems it is furthermore possible to determine a fractional site occupation. Another application of neutron diffraction is the

determination of accurate atomic parameters (positional and thermal parameters, site occupations) of lighter elements in the presence of heavy ones.

The contrast in conventional X-ray diffraction is directly related to the ratio of the number of electrons Z_j of the different atoms or ions j involved. The atomic scattering factor f_j in the structure-factor formula, which represents the Fourier transform of the atomic electron density distribution, is proportional to Z_j ($f_j = Z_j$ for $\sin\theta/\lambda = 0$). Standard X-ray techniques can hardly differentiate between atoms/ions of a similar number of electrons, and only an average structure - including a total occupation probability of mixed occupied sites - may be obtained in such cases.

For neutrons the atomic scattering factor f_j is replaced by the nuclear scattering length (or coherent scattering amplitude) b_j, which is of the same order of magnitude for all nuclei but varies from nucleus to nucleus in a non-systematic way. b_j values, which can be either positive or negative, depend on the isotopes and nuclear spin states of the element j. A nucleus of an isotope with spin I may have two different neutron scattering lengths: one for the combined spin state J = I + ½ and one with J = I - ½. An important and fundamental example is provided by the simplest of all nuclei, the proton with spin I = ½. The two spin states, J = 1 (triplet) and J = 0 (singlet), with statistical weights ¾ and ¼ respectively, have the scattering lengths for a *free* proton:

$b^s_H = -23.7$ fm, $b^t_H = +5.38$ fm, $b_{freeH} = \frac{1}{4}b^s_H + \frac{3}{4}b^t_H = -1.89$ fm (with 10^{-15} m = 1 fm).

The value for the *bound* proton in a crystal structure, which is to be used in the structure factor calculations, amounts to $b_H = 2 \cdot b_{freeH} = -3.741$ fm.

The natural isotope mixture and a statistical spin-state distribution lead to the commonly used general formula $b_j = \alpha \cdot b_{j\alpha} + ß \cdot b_{j\beta} + \gamma \cdot b_{j\gamma} + ...$ with the sum of the different isotope fractions $\alpha + ß + \gamma + ... = 1$ ($b_{j\alpha}$, $b_{j\beta}$, $b_{j\gamma}$ being the individual scattering lengths of the different isotopes of the element j). The natural nickel isotopes, for instance, have extremely different coherent scattering amplitudes:

$b(^{58}Ni) = +14.4$ fm, $b(^{60}Ni) = +3.0$ fm, $b(^{61}Ni) = +7.6$ fm, $b(^{62}Ni) = -8.7$ fm, $b(^{64}Ni) = -0.37$ fm

resulting in an overall scattering length $b_{Ni} = +10.34$ fm.

Neutron experiments frequently make use of compounds containing single isotope elements, like fully deuterated samples. Incoherent scattering due to a statistical distribution of isotopes and nuclear spin states is not discussed here. It may influence the effective absorption and the background conditions of neutron diffraction studies.

11.3.1 Example of contrast variation:

Crystal structure and magnetic ordering of $(Mn_{1-x}Cr_x)_{1+\delta}Sb$

A special possibility of contrast variation, the combination of X-ray and neutron diffraction information, is demonstrated for the example of the intermetallic compounds $(Mn_{1-x}Cr_x)_{1+\delta}Sb$, with $0 \leq x \leq 1$ [1]. This mixed system is of special interest due to its magnetic properties: competing magnetic interactions with isotropic ferromagnetic behaviour for $Mn_{1+\delta}Sb$ and an uniaxial antiferromagnetic structure for $Cr_{1+\delta}Sb$. It crystallises in the hexagonal NiAs-type structure (space group: $P6_3/mmc$) with some additional partial occupation (≤ 0.14) of the interstitial site 2(d) (see Fig. 1):

2(a) - 0,0,0; 0,0,1/2 and 2(d) - 2/3,1/3,1/4; 1/3,2/3,3/4.

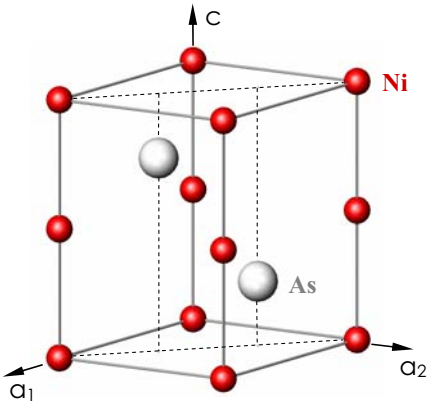

Fig. 1a. NiAs structure

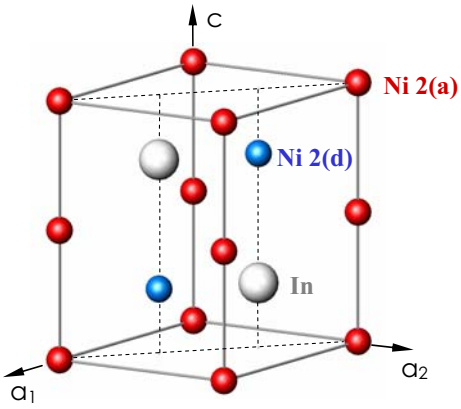

Fig. 1b. Ni_2In structure (filled NiAs-type)

Conventional X-ray diffraction cannot differentiate between chromium (Z_{Cr}= 24) and manganese (Z_{Mn}= 25) on these sites but yields important information on their overall occupation probabilities M = (Mn,Cr): M_aM_dSb, where M_a stands for the occupation probability of site 2(a) and M_d for that of site 2(d). The Sb position is assumed to be fully occupied, thus serving as an internal standard.

The corresponding nuclear scattering lengths of neutron diffraction are extremely different with a negative sign for manganese: b_{Cr} = +3.52 fm and b_{Mn} = -3.73 fm.

Remember: A positive value of b_j means that there is a phase shift of 180° between the incident and scattered neutron waves as a consequence of predominant potential scattering. The few negative b_j values - no phase change - result from resonant scattering.

The knowledge of the overall occupation probabilities M_a and M_d - from conventional X-ray studies - allows the evaluation of the Cr : Mn ratios of the different sites 2(a) and 2(d) from the corresponding effective scattering lengths determined by neutron diffraction. In the structure analyses based on the neutron data $b_{eff} = b_{Mn} \cdot PP$ is obtained individually for the two sites

($PP_a = a$ and $PP_d = d$ stands for refined pseudo-occupation probabilities). According to

$$b_{eff}(2a) = a[(1-y) \cdot b_{Mn} + y \cdot b_{Cr}] \quad \text{and} \quad b_{eff}(2d) = d[(1-z) \cdot b_{Mn} + z \cdot b_{Cr}]$$

we can calculate

$$y = [b_{eff}(2a)/a - b_{Mn}] / [b_{Cr} - b_{Mn}] \quad \text{and} \quad z = [b_{eff}(2d)/d - b_{Mn}] / [b_{Cr} - b_{Mn}].$$

The detailed site occupations lead to the general formula

$$(Mn_{1-y}Cr_y)_a(Mn_{1-z}Cr_z)_dSb$$

site 2(a) site 2(d)

corresponding to a chemical composition of $Mn_{[(1-y)a + (1-z)d]}Cr_{[ya +zd]}Sb$. It is evident, that the individual (Cr,Mn) distribution on the two crystallographically different sites 2(a) and 2(d) is not accessible merely by a chemical analysis. For most of the samples studied, the site 2(a) was found to be fully occupied: $a \approx 1.0$. But the formula $(Mn_{1-x}Cr_x)_{1+\delta}Sb$ used normally is only correct for the special case of equal Cr : Mn ratios on both sites:

$$x = y = z \quad \text{and} \quad 1+\delta = a+d.$$

The detailed information on the (Cr,Mn) distribution is needed to explain the magnetic properties of these intermetallic compounds, for which only the spins localised on the 2(a) sites are involved in the magnetic ordering leading to a complex magnetic phase diagram of the MnSb – CrSb system (see Fig. 3). An overall Cr : Mn ratio from chemical analysis is not sufficient. The ferromagnetic $Mn_{1+\delta}Sb$ changes its axis of easy magnetisation from parallel to the hexagonal c-axis at high temperatures to $\perp$c at low temperatures. The magnetic spins of the uniaxial antiferromagnetic $Cr_{1+\delta}Sb$ are oriented parallel (or antiparallel) to c. For mixed crystals $(Mn_{1-x}Cr_x)_{1+\delta}Sb$ in between the pure end members there exist various ferro- and antiferromagnetic states with inclined spin orientations, with non-colinear magnetic arrangements, and regions with co-existing magnetic ordering. Several magnetic structures of the intermetallic MnSb – CrSb system are shown in Fig. 2.

In general, a mixed occupation of one crystallographic site with three kinds of scatterers - e.g. Mn, Cr, and "vacancies" - requires at least two independent and sufficiently different experimental data to determine the fractional occupancies.

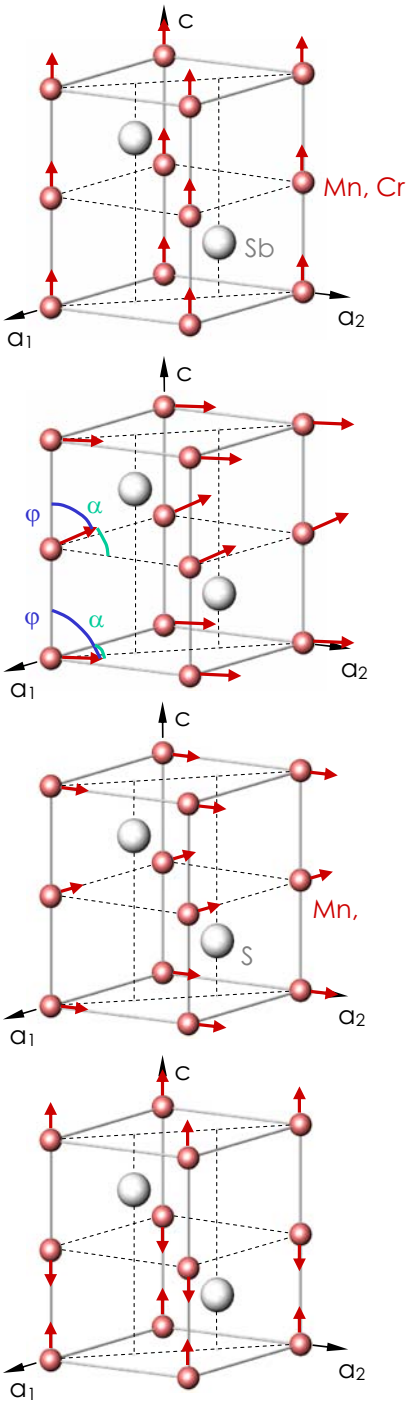

Ferromagnetism:
spin orientation ||**c**

Canted magnetic structure
(weak ferromagnet):
the spins are turned out of [001]
by an angle φ and || within (001) planes
with an antiphase rotation around **c**

Canted magnetic structure:
canting angle α = 60°
all spins lie in (001) planes

Antiferromagnetism:
spin orientation ||**c**

Fig. 2. Various types of magnetic structures in the intermetallic system $(Mn_{1-x}Cr_x)Sb$ (NiAs structure type)

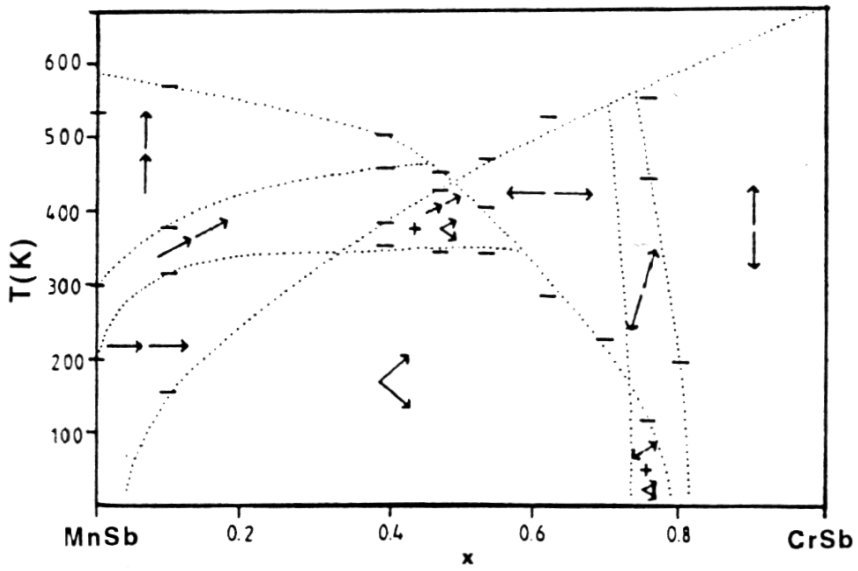

Fig. 3. Magnetic phase diagram of the intermetallic system MnSb – CrSb. The vectors indicate the spin orientations in the different magnetic structures.

11.4 The hydrogen problem in structure analysis

The determination of the structure parameters of hydrogen atoms is a special problem involving different aspects of X-ray and neutron diffraction. It is obvious that H/D atoms with Z = 1 give only a small contribution to the electron density and, therefore, they are hardly visible in X-ray structure analyses. This holds especially when heavy atoms are present. But there is a more general problem: the single electron of H/D is engaged in the chemical bonding and is not localised at the proton/deuteron position. This position, however, is of importance when hydrogen bonds - eventually related to the lattice dynamics or structural phase transitions - are discussed.

X-ray studies of electron densities of simple molecular crystals, for which theoretical calculations for isolated molecules are possible, are of special interest in order to compare experimental and theoretical results for a better understanding of chemical bonding in crystalline solids. Molecular crystals consist normally of light atoms often including hydrogen. A combination with neutron diffraction experiments is important to determine the structure parameters of the H/D atoms properly. More generally, the structure analysis by neutron diffraction yields separately and independently from the X-ray data the structure parameters of all atoms including the mean square displacements due to static and dynamic (even anharmonic) effects. This complete information can be used in a so-called X-N

synthesis to obtain experimental electron deformation densities from the measured X-ray Bragg intensities.

11.4.1 Example of the determination of H/D positions:

Study of hydrogen bonds in $Na_2S{\cdot}9D_2O$

One of the most important fields of application of neutron diffraction is the determination of H/D sites and of their Debye-Waller factors. As an example for a study of a variety of hydrogen bonds, where the structure model was established by conventional X-ray analysis and neutron diffraction served especially to localise the hydrogen atoms, the case of fully deuterated $Na_2S{\cdot}9D_2O$ was chosen [2]. Its crystal structure (non-centrosymmetric space group: $P4_122$ or $P4_322$) is dominated by discrete $[Na(D_2O)_5]$ and $[Na(D_2O)_4]$ spiral chains of $Na(D_2O)_6$ octahedra (see Fig. 4). There are five different water molecules (see Fig. 5) with O-D distances between 0.949 Å and 0.983 Å, and D-O-D angles from 104.6° to 107.5°. These water molecules are furthermore involved in six different O-D...S bridges to the S^{2-} ions. Details of the various O-D...O/S hydrogen bonds (given in Table I) were combined with results from Raman spectroscopy from which the uncoupled O-D(H) stretching frequencies could be reasonably well assigned to the nine different O-D(H) groups of the crystal structure.

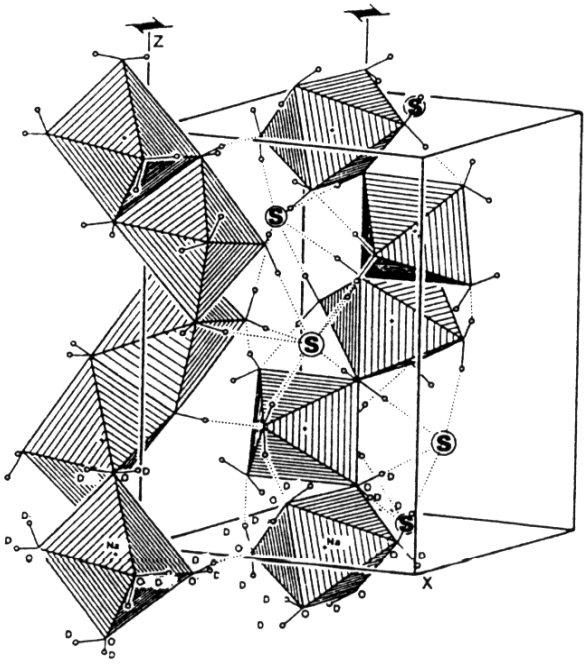

Fig. 4. $Na_2S{\cdot}9D_2O$: A partial view of the crystal structure

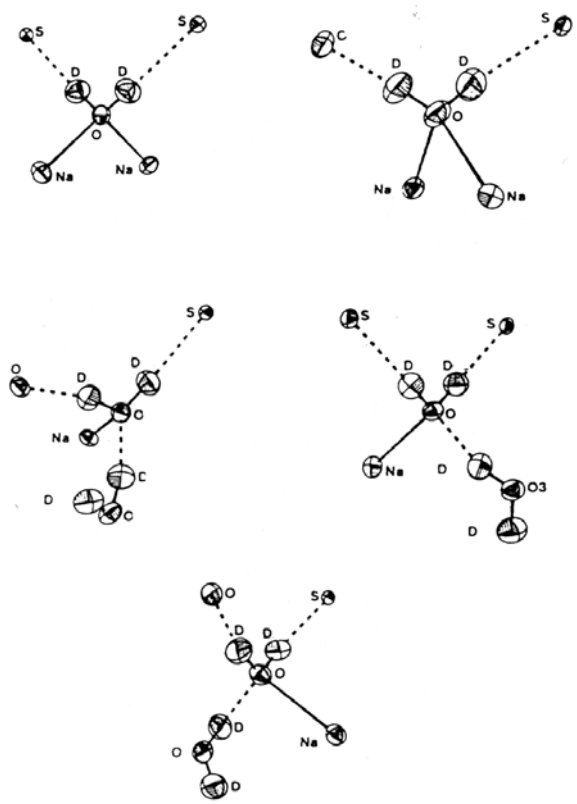

Fig. 5. Coordination of the D_2O molecules in $Na_2S \cdot 9D_2O$.

A	B	C	A-B	B-C	A-C	∠BAC	∠ABC	∠BAB'	∠CAC'	L	A-L	∠LAL'
O(1)	-D(1)...S		0.961(7)	2.359(5)	3.319(5)	1.4(4)	178.0(6)	106.3(7)	103.4(2)	Na(1)	2.411(4)	116.1(2)
	-D(1')...S		0.961(7)	2.359(5)	3.319(5)	1.4(4)	178.0(6)			Na(1')	2.411(4)	
O(2)	-D(21)...O(5)		0.964(7)	1.793(7)	2.752(7)	4.9(4)	172.4(6)	106.1(7)	111.5(2)	Na(2)	2.588(5)	97.6(2)
	-D(22)...S		0.962(7)	2.550(6)	3.506(5)	5.2(4)	172.8(6)			Na(2')	2.380(5)	
O(3)	-D(31)...S		0.977(7)	2.311(5)	3.284(5)	4.7(4)	173.3(5)	107.5(7)	116.9(2)	Na(1)	2.397(5)	104.8(2)
	-D(32)...O(4)		0.953(7)	1.797(7)	2.730(7)	9.6(4)	165.3(6)			O(5)	2.768(7)	
O(4)	-D(41)...S		0.983(7)	2.294(5)	3.274(4)	3.4(4)	175.1(5)	104.6(6)	104.1(2)	Na(2)	2.418(5)	105.5(2)
	-D(42)...S'		0.973(7)	2.359(5)	3.333(5)	0.3(4)	179.6(5)			O(3)	2.730(7)	
O(5)	-D(51)...O(3)		0.949(7)	1.838(7)	2.768(7)	9.2(4)	166.1(6)	105.5(6)	103.4(2)	Na(1)	2.485(5)	101.7(2)
	-D(52)...S		0.967(7)	2.441(5)	3.401(5)	5.7(4)	172.1(5)			O(2)	2.752(7)	
mean values			0.965					106.0	107.9	<Na-O>	2.447	
mean values O-D...O			0.955	1.809	2.750		167.9					
mean values O-D...S			0.970	2.386	3.353		175.2					

Table I. Interatomic distances (Å) and angles (°) for the hydrogen bonds and the ligands to the water molecules in $Na_2S \cdot 9D_2O$.

Remember: The scattering lengths of the proton and the deuteron are b_H = -3.74 fm and b_D = +6.67 fm, respectively. Their magnitudes are comparable to the average of all b_j magnitudes and, therefore, H/D can be considered as "normal" atoms for neutron diffraction. The different signs of b_H and b_D may be of interest in Fourier maps for contrast reasons. Experimental conditions like background and effective absorption are strongly affected by the huge and exceptional incoherent neutron scattering cross-section of hydrogen ($\sigma_{inc}(H)$ = 79.7 barns as compared to $\sigma_{inc}(D)$ = 2.0 barns).Very often deuterated compounds are preferred in order to profit from the larger b_D value, but mainly to reduce the background from incoherent scattering. This volume-dependent background may become crucial for neutron powder diffraction experiments, for which normally sample volumes of more than 1 cm^3 are required.

11.4.2 Example of a study of H/D ordering:

Ferroelectric phase transition in KH_2PO_4 (KDP)

The hydrogen problem is of special importance for structural phase transitions driven by proton ordering. As a well known example the ferroelectric transition in KH_2PO_4 (KDP) is presented. A characteristic feature of its crystal structure consists of the PO_4 groups linked by strong hydrogen bonds (see Fig. 6). At room temperature KDP crystallises in a tetragonal phase (space group: I $\bar{4}$2d), where the protons in the O···H···O bonds are dynamically disordered according to a double-well potential. At T_C = 122 K, KDP transforms to a

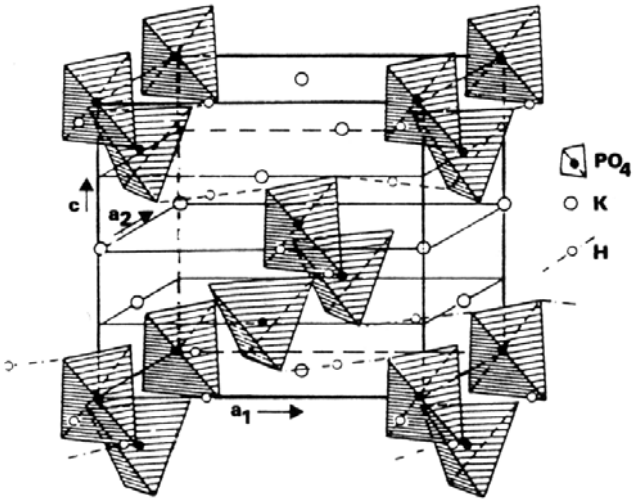

Fig. 6. Crystal structure of KH_2PO_4.

ferroelectric phase of orthorhombic symmetry (space group: Fdd2) in which the protons order in short asymmetric O-H...O bonds [3]. The contour plots of the proton distribution at different temperatures are shown in Fig. 7.

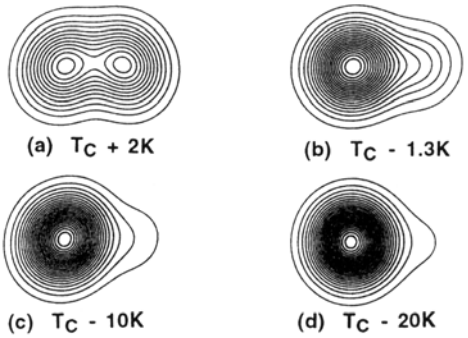

Fig. 7. Contour plots of the refined proton distributions in KH_2PO_4 at:
(a) T_C + 2 K, (b) T_C – 1.3 K, (c) T_C – 10 K, (d) T_C - 20 K.

11.5 Molecular disorder

Disordered structures and pseudosymmetries related to dynamical reorientation and/or structural phase transitions are of great current interest. In principal, the dynamical disorder of molecules is due to the fact that the intermolecular bonds are very much stronger than the external ones between the molecular groups and the surrounding crystalline frame. It is obvious that the chemical bonding scheme predicts the symmetry of a crystal structure, and not the other way around. We can state, however, that in the case of an incompatible point-group symmetry of a molecule with respect to its site symmetry in the crystal structure, molecular disorder is the necessary consequence. In order to modellize the atomic density distributions correctly in a way to obtain physically meaningful potentials, very accurate Bragg intensities over a large $\sin\theta/\lambda$ range are required. X-ray experiments are generally more restricted than neutron studies because of the $\sin\theta/\lambda$ dependence of the atomic scattering factor f_j.

11.5.1 Example of molecular disorder:

Almost free rotation of NH_3 groups in the crystal structure of $Ni(NH_3)_6I_2$

As an example, related to the H/D problem, the dynamical disorder of the NH_3 group in the cubic high temperature phase of the metal hexamine halide $Ni(NH_3)_6I_2$ (space group: Fm3m) is presented. The corresponding crystal structure is shown in Fig. 8. With the NH_3 tetrahedra

(3m symmetry) on crystallographic sites of 4mm symmetry it is obvious that they must be orientationally disordered. At 19.7 K, $Ni(NH_3)_6I_2$ undergoes a first order phase transition to a probably ordered rhombohedral low temperature modification [4].

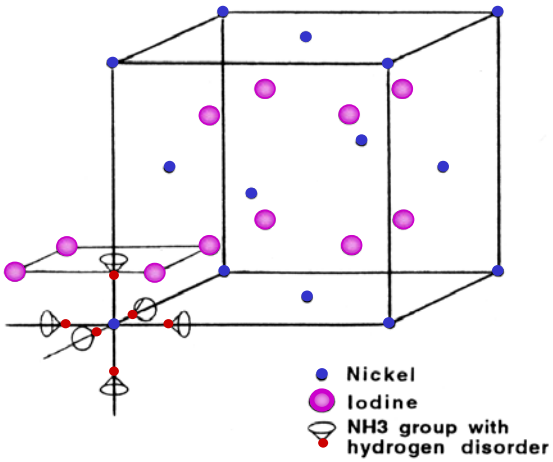

Fig. 8. High temperature structure of $Ni(NH_3)_6I_2$ The hexamine coordination is shown only for the Ni atom at the origin.

Single crystal neutron diffraction experiments of $Ni(NH_3)_6I_2$ have been performed at 295 K and 35 K [5] in order to study the proton density distribution. In Fig. 9 there is shown a Fourier density map of a [110] section with the negative proton density of the NH_3 group represented by broken lines.

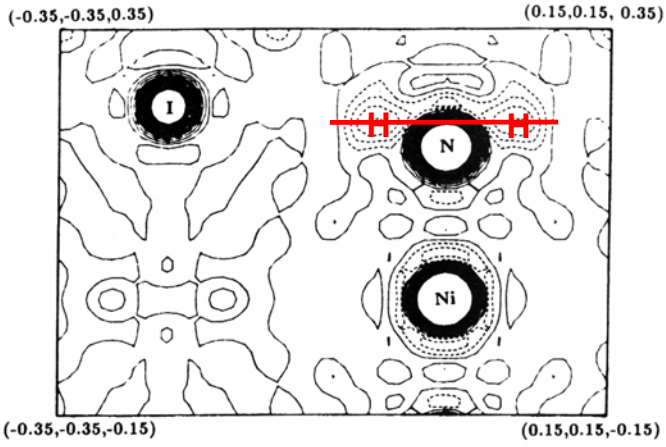

Fig. 9. Fourier map ([110] section) of the nuclear density of $Ni(NH_3)_6I_2$. The negative proton contributions of the ammine group are represented by broken lines, its orientation perpendicular to the four-fold axis is indicated by a horizontal beam.

The H-density of a [001] section perpendicular to the four-fold axes (corrected for contributions of the neighboured nitrogen) reveals the 4mm symmetry (Fig. 10). Its four maxima are directed towards the adjacent iodines according to the influence of N-H···I hydrogen bonding. This proton density can be explained as a consequence of a coupled rotational-translational motion of the ammine group. The experimental results obtained at 295 K and 35 K are perfectly reproduced by corresponding model calculations (see Fig. 11).

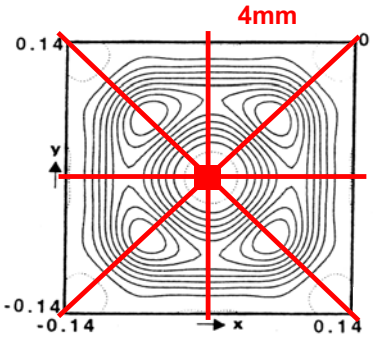

Fig. 10. Proton density of $Ni(NH_3)_6I_2$ at 295 K, [001] section for z = 0.23. The four maxima are directed towards adjacent iodines (N–H···I hydrogen bondings)

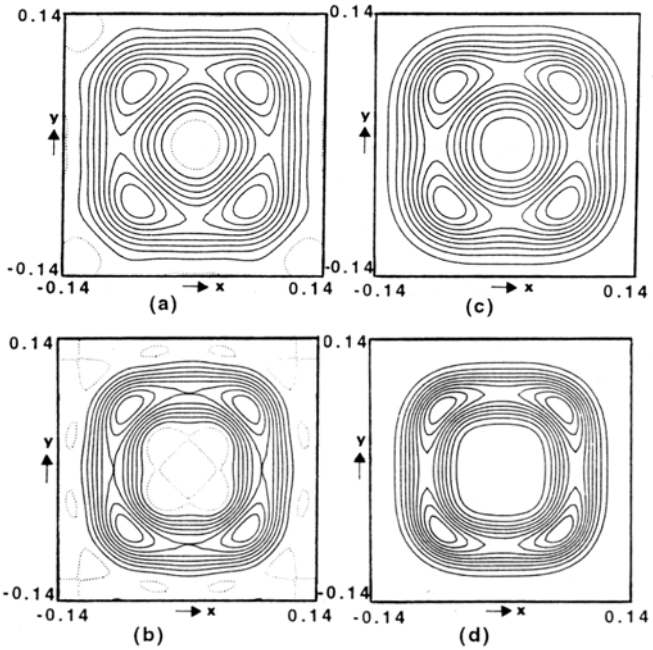

Fig. 11. $Ni(NH_3)_6I_2$: Proton density in a [001] section at z = 0.23;
(a) and (b) experimental results at 295 K and 35 K,
(c) and (d) calculated densities at 295 K and 35 K.

11.6 Spin densities in magnetic molecular compounds

Molecular magnetic compounds are of great actual interest due to both, applicational perspectives and fundamental research. The spin density distribution is an essential information for the understanding of the magnetic properties of these materials; it yields the localisation of the magnetic electrons and give rise to the microscopic magnetic interactions. Polarised neutron diffraction on single crystals is presently the most powerful tool for determining the spin densities in molecular compounds [6]. Results obtained from a data treatment by the maximum-entropy reconstruction method are presented in Fig. 12 for the purely organic ferromagnet, β-4,4,5,5-tetramethyl-2-*p*-(nitro-phenyl)-3-oxido-4,5-dihydro-imidazolium 1-oxyl (*p*NPNN) [7].

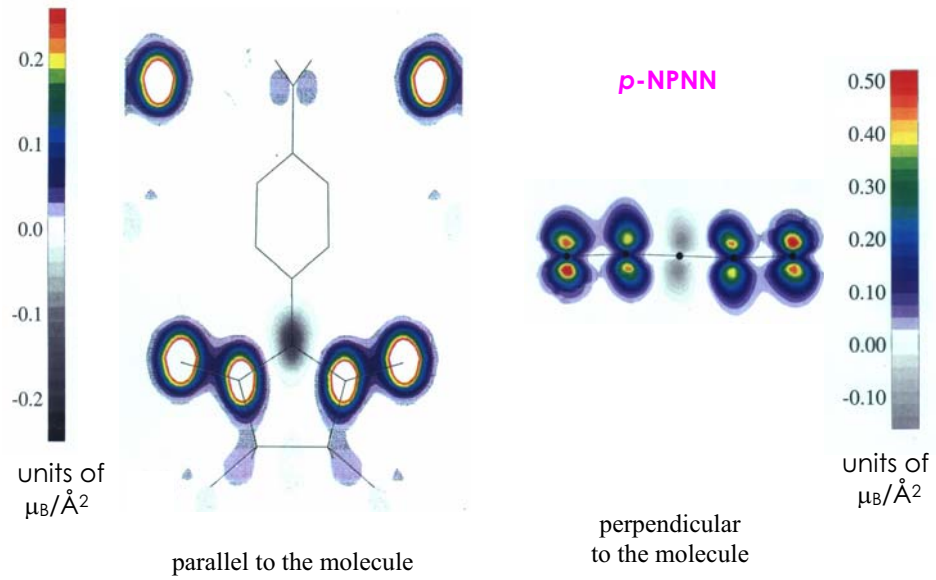

Fig. 12. Spin density distribution of *p*-NPNN
(magnetization density reconstructed by MAXENT)

References

1. W. Reimers, E. Hellner, W. Treutmann, and G. Heger,
   J. Phys. C: Solid State Phys. **15**, 3597 (1982).
2. A. Preisinger, K. Mereiter, O. Baumgartner, G. Heger, W. Mikenda, and H. Steidl,
   Inorg. Chem. Acta **57**, 237 (1982).
3. R. J. Nelmes, W. F. Kuhs, C. J. Howard, J. E. Tibballs, and T. W. Ryan,
   J. Phys. C: Solid State Phys. **18**, L711 (1985).
4. J. Eckert and W. Press, J. Chem. Phys. **73**, 451 (1980).
5. P. Schiebel, A. Hoser, W. Prandl, G. Heger, and P. Schweiss,
   J. Phys. I France **3**, 987 (1993).
6. J. Schweizer, Physica B **234-236**, 772 (1997).
7. P. Schleger, A. Puig-Molina, E. Ressouche, O. Rutty and J. Schweizer,
   Acta Cryst. **A53**, 426 (1997).

Textbooks

8. G. E. Bacon, Neutron Diffraction, Clarendon Press, Oxford (1975).
9. HERCULES: Neutron and Synchrotron Radiation for Condensed Matter Studies,
   Vol. I and II (edited by J. Baruchel, J. L. Hodeau, M. S. Lehmann, J. R. Regnard and
   C. Schlenker), Les Editions de Physique, Les Ulis & Springer-Verlag, Berlin (1993-1994).
10. L. Dobrzynski and K. Blinowski, Neutrons and Solid State Physics,
    Ellis Horwood Series in Physics and its Applications, New York (1994)

12

Inelastic neutron scattering: phonons and magnons

Markus Braden

12. Inelastic neutron scattering : phonons and magnons

Markus Braden
II. Physikalisches Institut, Universität zu Köln,
Zülpicher Str. 77, D-50937 Köln
braden@ph2.uni-koeln.de

12.1 Interaction and scattering law

12.1.1 Basic concepts of scattering experiments

Scattering experiments are performed with almost all types of radiation on various systems (solids, liquids, gases, atoms, nuclei, ...). The radiation with well defined initial properties (wavevector $\underline{k}$; energy E) hits the sample, gets scattered and may be detected again with well defined final properties (wavevector $\underline{k'}$; energy E') in the angular segment $r^2 d\Omega$, the schematic picture of the scattering arrangement is drawn in figure 1. Aim of any scattering experiment is to obtain information on the states of the sample by use of the knowledge of the interaction between the radiation (for example neutrons) and the particles forming the sample. In this chapter we deal with the inelastic neutron scattering in solids which is till today the most efficient way to study dispersion relations of lattice vibrations and magnetic excitations. We give examples of simple phonon and magnon dispersions studied in the early days of neutron scattering as well as results of recent research on complex materials.

The initial and final states of the neutron may be denoted by σ_i and σ', those of the sample by λ_i and λ'. σ_i is characterized by the wavevector $\underline{k}$ and the energy $E = \frac{\hbar^2}{2m}k^2$, σ' respectively. The momentum transferred to the sample crystal, $\underline{Q}$, and the energy transfer, $E = \hbar\omega$, have to fulfill the conservation laws, $\underline{Q} = \underline{k} - \underline{k'}$ and $\omega = \hbar(\frac{1}{2m})^2(k^2 - k'^2)$. The probability to observe a scattered neutron in the angular segment $d\Omega$ and in the energy interval dE' is described by the partial differential cross section which may be obtained within the Born-approximation. This is a perturbation theory of first order, i.e. one considers the interaction between radiation and sample crystal to be small.

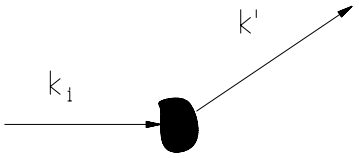

Figure1 Schematical drawing of a general scattering experiment.

$$\frac{d^2\sigma}{d\Omega dE'} = (k'/k)(m/2\pi)^2 \sum_{\lambda_i,\sigma_i} P_{\lambda_i} P_{\sigma_i} \sum_{\lambda',\sigma'} \qquad (12.1)$$
$$| < \sigma'\lambda' | \int d^3r \; exp(i\underline{k'} \cdot \underline{r}) \hat{V}(r) exp(i\underline{k} \cdot \underline{r}) | \sigma_i \lambda_i > |^2$$
$$* \delta(\omega + E' - E)$$

The cross section in equation (12.1) is given by the sum of the transition matrix elements between initial states $\sigma_i\lambda_i$ and the final states $\sigma'\lambda'$ weighted by the probabilities of the initial states. In order to calculate the cross section and the observable intensity distribution, one needs the interaction potential $\hat{V}(\underline{r})$ and detailed knowledge of the states in the sample λ_i. In the inverse way one may use a measured intensity distribution in order to characterize the sample states, for example the phonons. This is the usual way to interpret any scattering experiment. The sample states may be characterized by specific parameters, for example the frequencies and the polarization patterns in case of phonons, which with the aid of equation (12.1) will be deduced from the experimental intensity distribution.

12.1.2 Nuclear interaction – phonons

The nuclear interaction between the neutron and the core of the atoms is characterized by an extension of 10^{-5}Å, which is small in comparison to the wavelength of thermal neutrons. Therefore, the scattering is isotrope and may be described by only one parameter, the scattering length. The interaction with the entire crystal is given by the sum over the atoms :

$$\hat{V}(\underline{r}) = \frac{2\pi}{m} \sum_j b_j \delta(\underline{r} - \underline{R}_j) \qquad (12.2),$$

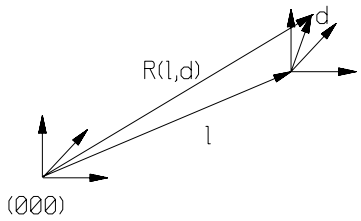

Figure 2 Schematic drawing of the vectors determining the position of an atom in the crystal lattice.

where b_j and $\underline{R}_j$ are the scattering length and the position of the j-th atom. The mixing of different isotopes at the same atom site in the crystallographic lattice yields a further complication, since different isotopes have different scattering lengths. This means that the interaction potential (12.2) does not show the full translation symmetry of the crystal lattice. The local variation of the scattering length splits the differential cross section into two contributions :

$$\frac{d^2\sigma}{d\Omega dE'} = (\frac{d^2\sigma}{d\Omega dE'})_{coh.} + (\frac{d^2\sigma}{d\Omega dE'})_{incoh.} \qquad (12.3).$$

The coherent contribution is determined by the mean scattering length, whereas the incoherent contribution is given by the root mean square deviation to the averaged scattering length.

In order to calculate the differential cross section in (12.1) it is necessary to know the states in the sample or at least to parameterize them. The sum over the states λ_i in (12.1) may be transformed to the correlation function, in which one has to introduce the parameterized Eigen-states of the system. In order to achieve this transformation in case of the phonons we consider the vibrations of a crystal in harmonic approximation.

– *Description of lattice dynamics in harmonic approximation* – A crystal consists of N unit cells with n atoms within each of them, the equilibrium position of any atom is given by the position of the unit cell to which it belongs, $\underline{l}$, and by the position of the atomic site in the unit cell, $\underline{d}$. At a certain time the atom may be displaced from its equilibrium position by $\underline{u}(\underline{l},\underline{d})$. The instantaneous position is hence given by $\underline{R}_{\underline{l},\underline{d}} = \underline{l}+\underline{d}+\underline{u}(\underline{l},\underline{d})$ (see figure 2).

For simplification we consider first a lattice with only one atom in the unit cell, $\underline{d} = \underline{0}$; $\underline{l}$ describes then the equilibrium position of the atom. The interaction potential between

two atoms $\underline{l}$ and $\underline{l}'$, $\Phi(\underline{l},\underline{l}')$, may be expanded at the equilibrium position in terms of $\underline{u}(\underline{l})$=$\underline{u}(\underline{l}')$=0. The constant term does not give any contribution to the equations of movement, it is relevant only for the total energy of the crystal structure. Since at the equilibrium position the atom should not experience any forces, terms of first order are not allowed. In harmonic approximation one assumes the expansion till the second order to be sufficient. This assumption is essential for the following analysis, because the presence of third order terms already prohibits one to solve the equations of movement in the general case. In most solids, anharmonic contributions to the potential are, however, small justifying the assumption. If the anharmonic effects have to be taken into consideration (for example close to the melting of the crystal lattice), perturbation theory is the usual technique.

Using the definition :

$$D_{\alpha,\beta}(\underline{l},\underline{l}') = \frac{d^2\Phi(\underline{l},\underline{l}')}{du_\alpha(\underline{l})du_\beta(\underline{l}')} \qquad (12.4)$$

one obtains the equations of movement ($\alpha,\beta = x,y,z$) to :

$$M\ddot{u}_\alpha(\underline{l}) = -\sum_{\beta,\underline{l}'} D_{\alpha,\beta}(\underline{l},\underline{l}')u_\beta(\underline{l}') \qquad (12.5).$$

The displacement of the atom $\underline{l}'$ in β-direction yields a force on the atom $\underline{l}$ in α-direction of strength $D_{\alpha,\beta}(\underline{l},\underline{l}')u_\beta(\underline{l}')$, $D_{\alpha,\beta}(\underline{l},\underline{l}')$ are therefore called the force-constants. The real problem in treating lattice dynamics consists in the large number of these equations, there are 3N equations to be solved with N being of the order of 10^{23}. In order to avoid this complexity one makes the Ansatz of plane waves : the movements of all atoms are given by the displacement in one unit cell at time zero propagating in time and space as a plane wave :

$$u_\alpha(\underline{l}) = e_\alpha M^{-1/2} \cdot exp(i\underline{q}\underline{l} - \omega_0 t) \qquad (12.6).$$

Figure 3 shows the displacement pattern of a plane wave characterized by the wave vector $\underline{q}$, reflecting the propagation of the wave (planes perpendicular to $\underline{q}$ are always identically displaced), the vibration frequency ω_0 of each atom and the direction of the oscillation given by the polarization vector $\underline{e} = (e_x, e_y, e_z)$. In the single atom lattice there are only acoustic modes, they are called longitudinal (LA) if $\underline{q}$ is parallel to $\underline{e}$ and

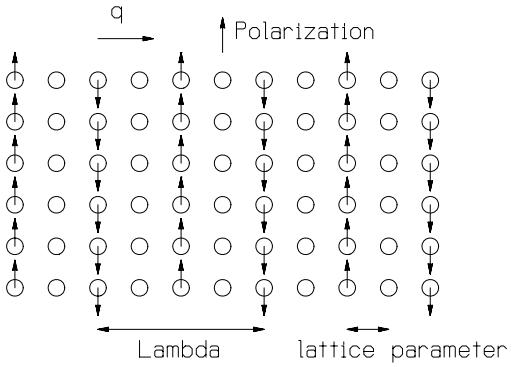

Figure 3 Scheme of the displacements in a transversal plane wave.

transversal (TA) for $\underline{q}$ perpendicular to $\underline{e}$.

The plane wave Ansatz (12.6) for the equations of movement yields a system of three equations for each $\underline{q}$-value :

$$\omega_0^2 e_\alpha = 1/M \sum_{\underline{l},\beta} D_{\alpha,\beta}(\underline{l},0) exp(-i\underline{q}\underline{l}) e_\beta \qquad (12.7).$$

Here we use that the force constants depend only on the distance in real space $(\underline{l}-\underline{l'})$ and not on the particular values of $\underline{l}$ and $\underline{l'}$. With (12.7) one obtains an easily solvable system; the original complexity of the problem is transferred to the number of these 3-dimensional problems. For a complete solution of the crystal dynamics one would need to solve the problem (12.7) for each of the N$\sim 10^{23}$ allowed $\underline{q}$-values. In reality, however, one has to analyze only a few different $\underline{q}$-values. In general it is sufficient to study only $\underline{q}$-values within the first Brillouin-zone.

We may define the dynamical matrix as

$$\bar{D}_{\alpha,\beta}(\underline{q}) = 1/M \sum_{\underline{l},\beta} D_{\alpha,\beta}(\underline{l},0) exp(-i\underline{q}\underline{l}) \qquad (12.8),$$

which allows to rewrite the equations (12.7) in matrix form :

$$\omega_0^2 \underline{e} = \bar{D} \cdot \underline{e} \qquad (12.9).$$

The system (12.9) is just a three-dimensional Eigen-value problem.

For fixed $\underline{q}$ one has to determine the three Eigen-vectors $\underline{e}_j$, j=1,2,3, together with the three corresponding Eigen-values, $\omega_j(\underline{q})$. This may be achieved with the standard numerical techniques. The dependence of the Eigen-frequencies on the wave-vector, $\omega_j(\underline{q})$ with $j = 1, 2, 3$, is called the dispersion relation.

The extension to a system with n Atoms in the primitive cell can be easily done, one gets for each $\underline{q}$ an Eigen-value problem in $3n$ dimensions. The Eigen-vectors have the dimension $3n$ and the dynamical matrix is $3n * 3n$ dimensional. For each $\underline{q}$ one finds hence $3n$ Eigen-modes, therefore the complete phonon dispersion consists of $3n$ branches, three of which have zero frequency for $q \to 0$. The latter branches are called acoustic since they are associated with the propagation of sound. The upper part of Figure 4 shows the typical presentation phonon frequency, ω, against wave-vector $\underline{q}$ for the phonon dispersion of elementary aluminum, whereas the lower part shows the result of a recent study on the phonon dispersion in $CuGeO_3$. In the latter material, there are 10 atoms in the primitive unit cell yielding a phonon dispersion with 30 branches. In order render the presentation clearer, one has to separate the phonon modes according to their symmetry following group theory. The symbols denote the frequencies determined by inelastic neutron scattering and the line give the calculation with a shell model [7].

The plane waves including Eigen-frequencies and Eigen-vectors for each of the allowed $\underline{q}$-values form a complete set of functions for the displacements of the N times n atoms in the crystal. Any distortion can be represented as a linear combination of these plane waves. Obviously it is rather favorable to use this set for calculating the differential apply quantum mechanics to the lattice vibrations, the corresponding quasi-particle is called a phonon. A one-phonon process is shown in the schematic figure 5. The momentum transfer $\underline{Q} = \underline{k} - \underline{k'}$ consists of the sum of a reciprocal lattice vector $\underline{\tau}$ and the wave-vector $\underline{q}$, which lies within the first Brillouin-zone. Only $\underline{q}$ determines the wave vector of the contributing phonons, however $\underline{Q}$ determines the differential cross section, i.e. the intensity.

The exact scattering may be deduced from the correlation function. In the following we only want to discuss the meaning of the different terms in the cross section :

$$(\frac{d^2\sigma}{d\Omega dE'})^{\pm} = (k'/k)\frac{(2\pi)^3}{2v_0}\sum_{\underline{\tau}}\sum_{j,\underline{q}} \qquad |G_j(\underline{q},\underline{Q})|^2 \qquad (12.10.a)$$

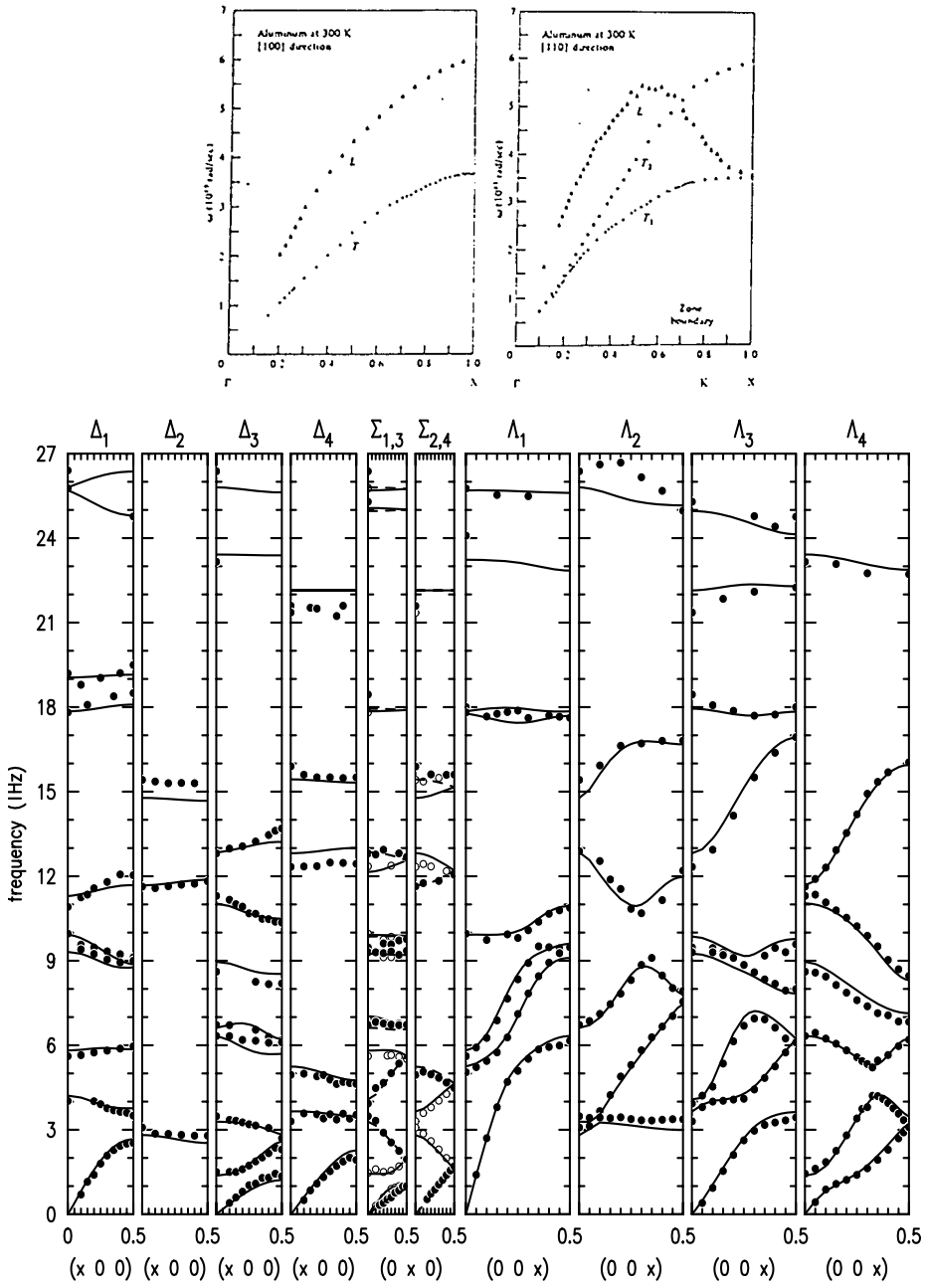

Figure 4 Upper part :Phonon dispersion of Al along the [100] and [011]-directions (from reference [1]); lower part : Phonon dispersion of $CuGeO_3$, a material with 10 atoms in the primitive unit cell and accordingly 30 phonon branches, which are separated following the group theory analysis [7].

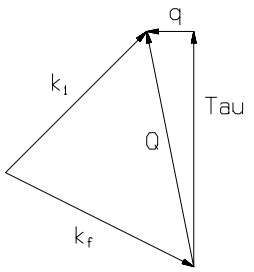

Figure 5 Scattering triangle corresponding to the observation of a phonon mode with wave vector $\underline{q}$ at the reciprocal lattice vector $\underline{\tau}$.

$$\cdot\frac{1}{\omega_j(\underline{q})} \qquad (12.10.b)$$

$$\cdot(n(\omega_j(\underline{q})) + 1/2 \pm 1/2) \qquad (12.10.c)$$

$$\cdot\delta(\omega \mp \omega_j(\underline{q})) \cdot \delta(\underline{Q} \mp \underline{q} - \underline{\tau}) \qquad (12.10.d),$$

with v_0 the volume of the reciprocal unit cell. Equation (12.10) describing the intensity of a one-phonon measurement at specific $\underline{Q}$ closely resembles the elastic structure factor of the Bragg reflection intensity, a part of expression (12.10) is called dynamic structure factor. The intensity is given by the sum over all reciprocal lattice and all wave vectors; however only the combination $\underline{q}+\underline{\tau} = \underline{Q}$ may contribute due to the δ-function in (12.10.d). The second δ-function in (12.10.d) reflects the law of energy conservation, however, one has to take into account that the scattering processes may lead to a creation as well as to an annihilation of a single phonon, corresponding to the upper and the lower signs respectively. There are two more general factors determining the intensity of the phonon observation by neutron scattering. The term (12.10b) indicates, independently of all other terms, that the intensity is inversely proportional to the frequency of the mode. High energy modes are always more difficult to observe than the low-lying ones. Since neutron experiments suffer from the low flux of the existing sources, this effect frequently prohibits the study of the high-energy part of the phonon dispersion. The term (12.10.b) results from the quantum mechanics of a single harmonic oscillator : the square of the amplitude is proportional to $\frac{1}{\omega_j(\underline{q})}$.

The term (12.10.c) results from the Bose-statistics of the phonon mode with frequency $\omega_j(q)$, the occupation number is given by the Bose-function:

$$n(\omega_j(\underline{q})) = \frac{1}{exp(\frac{\hbar\omega_j(q)}{kT}) - 1} \qquad (12.11).$$

$n(\omega_j(\underline{q}))$ tends for $T \to 0$ towards zero, the phonons are frozen. For $T \to \infty$, $n(\omega_j(\underline{q}))$ approaches $(\frac{\hbar\omega_j(q)}{kT})$, i.e. the classical relation. The term (12.10.c) indicates that the Bose-function is increased by +1 only in case of phonon creation. At low temperature where $n(\omega_j(\underline{q}))$ is close to zero, the phonon may be observed only in the creation mode, the cross section for the annihilation process vanishes since the phonon states are no longer occupied. At finite temperature the Bose-statistics further simplifies the observation of phonons with low frequencies.

The complex term in (12.10.a) is called the dynamical structure factor:

$$G_j(\underline{q}, \underline{Q}) = \sum_d \frac{b_d}{\sqrt{m_d}} \cdot exp(-W_d(\underline{Q}) + i\underline{Q}\underline{d}_d) \cdot (\underline{Q} \cdot \underline{e}_d^j(\underline{q})) \qquad (12.12),$$

where the sum extends over the atoms, numbered by d, in the primitive cell. The atoms possess the mass m_d scattering length b_d and a three-dimensional polarization vector $\underline{e}_d^j(q)$, the equilibrium position in the unit cell is given by $\underline{d}_d$. Without the last part equation (12.12) corresponds to the elastic structure factor, in particular one finds the same Debye-Waller-factor $exp(-W_d(\underline{Q}))$. The whole term in the exponential function determines whether the interference between atoms is constructive or destructive. In the dynamical structure-factor equation, there is in addition to the elastic one the polarization term (last parenthesis); for instance only those atoms may contribute whose polarization vector, $\underline{e}_d^j(\underline{q})$, possesses a component parallel to $\underline{Q}$. Since $\underline{Q}$ enters this term directly, the structure factor increases with $|Q|$; the intensity is proportional to Q^2. The interference and the polarization term in (12.12) cannot be separated in general, therefore one has to calculate the structure factors precisely.

In addition to the interpretation of the frequency data the prediction of the scattered intensity is an important result of model calculations. Only with the help of these predictions a neutron scattering experiment aiming at the lattice dynamics of a complex material can be performed in an efficient manner.

Some easy examples may illustrate the significance of the terms in (12.12). Let us

consider a longitudinal acoustic mode polarized in the [100]-direction; for this mode all $\underline{e}_d$ are parallel to [100]. The polarization term becomes maximum for $\underline{Q}$=(h+ξ 0 0) and can be extracted from the sum. The remaining interference sum corresponds for small ξ to the elastic structure-factor of (h00), The dynamic structure becomes hence strong for strong Bragg-reflections. In general, acoustic phonons have to be measured close to the strong Bragg-reflections. Since for optical modes the atoms may be displaced in opposite directions, the polarization term can change sign yielding a rather distinct sum of the interference term. In a simple two-atomic structure the optical mode has only a weak dynamical structure factor close to the strong Bragg-reflections (this argument is, however, no longer valid in case of negative scattering lengths).

Why does inelastic neutron scattering play such a dominant role in the study of lattice dynamics? The central advantage certainly concerns the similar masses of the atoms and of the neutron. This yields the possibility of elastic as well as that of inelastic scattering and renders the wave-vectors of thermal neutrons comparable to the wave-vectors of the phonons. Inelastic neutron scattering allows to determine the phonon dispersion over the whole Brillouin zone, whereas optical techniques (Raman and Infra-Red-scattering) yield only the analysis of modes at the zone center.

Recently, there are serious efforts to perform lattice dynamical studies using synchrotron radiation. In case of thermal neutrons the energies amount to 1–100 meV and correspond to the typical phonon energies. For comparison, CuK$_\alpha$-radiation has an energy of $8 \cdot 10^6$meV. In order to determine phonon frequencies, one needs a relative energy resolution of $10^{-6} - 10^{-7}$, which may be achieved only by extreme experimental effort. The concomitant loss of intensity permits these measurements only at powerful synchrotron sources, and even then the measurements remain slow. We have seen that the one-phonon process yields an intensity proportional to Q^2, this may be used in case of neutron scattering due to the nuclear interaction. In case of the x-rays the large $\underline{Q}$-range is not favorable, because the form-factor strongly reduces the interaction. In the closer future one may not expect, that inelastic x-ray scattering will supply results comparable to neutron studies concerning their efficiency. The x-ray measurements, however, may become valuable in cases where the neutron scattering is hampered either by sample size or by absorption.

12.1.3 Magnetic interaction – magnetic excitations

The neutron has a spin 1/2 which implies a coupling to the magnetic fields. The interaction operator is given by :

$$-\gamma_n \mu_N \hat{\sigma} \cdot \underline{H} \qquad (12.13);$$

here γ_n=1.913 is the magnetic moment of the neutron, expressed in μ_N, the nuclear magneton, $\hat{\sigma}$ the Pauli-spin operator and $\underline{H}$ the magnetic field induced by the electrons in the sample. $\underline{H}$ may arise from the velocity of the electrons as well as from their magnetic moment. In the following we limit the discussion to the latter contribution.

Furthermore we assume, that the orbital moment has vanished. This assumption is justified in case of quenching by crystal fields or for a half-filled shell (Mn^{2+}, Fe^{3+}, Gd^{3+}).

The Fourier-component of the interaction potential is :

$$\hat{V}(\underline{Q}) = \frac{2\pi}{m} \frac{\gamma_n e^2}{M_e c^2} \hat{\sigma} \hat{D}_\perp(\underline{Q}) \qquad (12.14)$$

with

$$\hat{D}_\perp(\underline{Q}) = \sum_{\underline{l},d} (1/2) \gamma_d F_d(Q) \hat{\sigma} \hat{S}_\perp(\underline{l},d) exp(i\underline{Q} \cdot \underline{R}_{\underline{l}d}) \qquad (12.15),$$

here γ_d is the gyro-magnetic factor, $F_d(\underline{Q})$ the form-factor of the atom d and $S_\perp(\underline{l},d) = \underline{Q} \times (\hat{S}_{\underline{l}d} \times \underline{Q})$ with $\hat{S}(\underline{l}d)$ being the spin-operator of the atom.

There are two important differences between the magnetic and the nuclear interaction of the neutron with the atom. Due to the spatial extension of the electron cloud, which causes the magnetic moment, the interaction is non-local. Described by the form-factor, $F(Q)$, the interaction gradually decreases towards large $\underline{Q}$. The detailed dependence of $F(Q)$ is determined by the single ion. Rare earths show, due to the strong localization of the 4f-electrons, a less pronounced decrease when compared to the transition metal ions with more delocalized electrons. In the latter case the decrease may be quite strong limiting any measurement to the first Brillouin-zones. The Q-dependence of the magnetic signal due to the form-factor may be used to separate magnetic and nuclear contributions. Furthermore, the magnetic interaction is mediated by vector-operators. Only those magnetic moments may contribute to the interaction, which have a component perpendicular to $\underline{Q}$. This yields the possibility to determine not only the size but also the direction of magnetic moments.

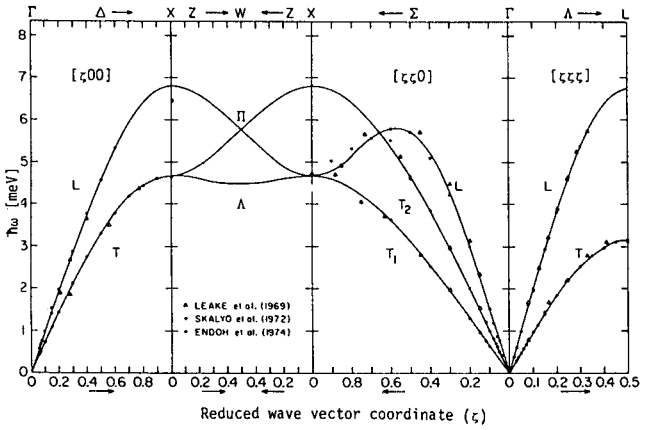

Figure 6 Phonon dispersion of Ne along the three main symmetry directions (from Ref. [2]).

12.2 Analysis of lattice vibrations

12.2.1 Lattice dynamics in simple structures

For a simple crystal lattice one may determine the polarization patterns without detailed model calculations. The lattice dynamics of such a system may then be studied experimentally without particular effort.

In figure 6 we show the phonon dispersion of Ne in the three main symmetry directions, which according the common use are labeled Δ, Σ and Λ. Ne crystallizes in a fcc-lattice with only one atom in the primitive cell, therefore one expects only three acoustic branches per $\underline{q}$-value. One observes the three distinct branches only in the [xx0]-direction, whereas there are only single transverse branches along [x00] and [xxx]. In the [x00]-direction these acoustic polarization patterns may be easily understood. In the longitudinal mode atoms are vibrating in [100]-direction, i.e. parallel to the wave vector. The two transverse modes are characterized by displacements in [010] or in [001]-directions, i.e. perpendicular to the wave-vector. Since [100] represents a four-fold axis in the fcc lattice, the latter two modes cannot be distinguished; they are degenerate. The same situation is found along the [111]-direction which is a three-fold axis of the lattice. This behavior is a simple example of the general relation between crystal symmetry and the phonon dispersion. The crystal symmetry yields constraints for the phonon modes which may be necessarily degenerate at certain points or - like in the Ne-structure - along a direction. In the case of more

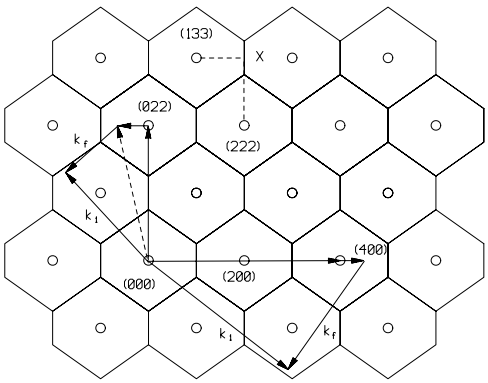

Figure 7 The plane in reciprocal space spanned by the (100) and (011) vectors for a fcc-lattice; the scattering triangle indicates the observation of Δ-modes.

complex structures it is essential to profit from symmetry analysis. The [110]-direction represents only a two-fold axis since [1-10] and [001] are not identical, as consequence the corresponding transverse acoustic branches are not equivalent.

In addition, figure 6 shows that at X=(100)=(011) Δ and Σ-branches are coinciding, which may be explained due to the shape of the Brillouin-zone. Figure 7 presents the plane of the reciprocal space spanned by (100) and (011); one recognizes that starting at the zone-center, Γ, in the figure (133), in the [100]-direction one will reach the zone-boundary at (233)$\equiv$(100)=X. Similar, one will reach this point when starting at the neighboring point (222) in [011]-direction. However, in this path one finds the border of the Brillouin-zone earlier and continues the last part on the zone boundary. (100) and (011) are equivalent points in reciprocal space; they are connected by a reciprocal lattice vector, (-1 1 1). For the phonon branches we conclude that Δ- and Σ-branches have to coincide. The symmetry further determines which branches coincide : for example the longitudinal Σ-branch with the transversal Δ-branch. Again, similar considerations in more complex systems may decisively contribute to the identification of the branches.

Figure 7 further shows how to measure the Δ-branches. One may observe the longitudinal branch in the (400)-zone passing to (4+x 0 0) (the (400)-zone has to be preferred to (200) due to the larger value of Q^2), whereas one may determine the transverse frequencies in the (022)-zone at (x 2 2).

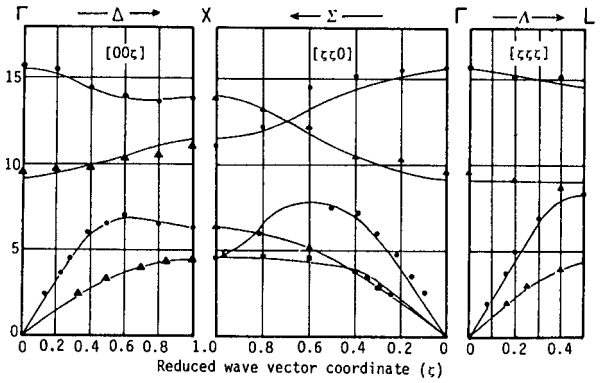

Figure 8 Dispersion curves and crystal structure of FeO (from reference [2]).

– *NaCl-structure* – The NaCl-structure represents one of the most simple possible crystal structures with two atoms per primitive cell. It consists of two fcc-lattices shifted against each other by (0.5 0.5 0.5). The entire crystal structure possesses fcc-symmetry too. Figure 8 shows the dispersion curves of FeO.

The six branches expected for the two-atomic structure are observed only in [xx0]-direction. Like in case of the fcc Ne-lattice, the transverse Δ- and Λ-branches are doubly degenerate. Also in other aspects, there is some resemblance with the Ne-phonon dispersion; in both cases LA-Δ and TA-Σ branches coincide at the zone boundary.

A more detailed discussion is needed in order to understand the optical modes at Γ. The polarization pattern of an optical mode corresponds to an anti-phase axial movement of the ion pairs connected in [100], [010] or [001] direction. The three vibrations polarized in the crystal directions should, however, be degenerate due to the cubic symmetry; one might expect only one optical frequency. The optical vibration in the ionic lattice possesses a polar character, i.e. there is a local polarization due to the opposite shifts of cations and anions. For large wave-length, i.e. close to the zone-center, the local polarization adds to a macroscopic polarization only in case of the longitudinal mode. This macroscopic polarization requires an additional energy, the longitudinal optic (LO) mode is always higher in frequency than the trnaversal optic (TO) mode (note, that these modes are only defined as the limit for $\underline{q}$ tending to zero. The splitting between LO and TO-mode frequencies is called Lydane-Sachs-Teller (LST) splitting and is related by the LST-

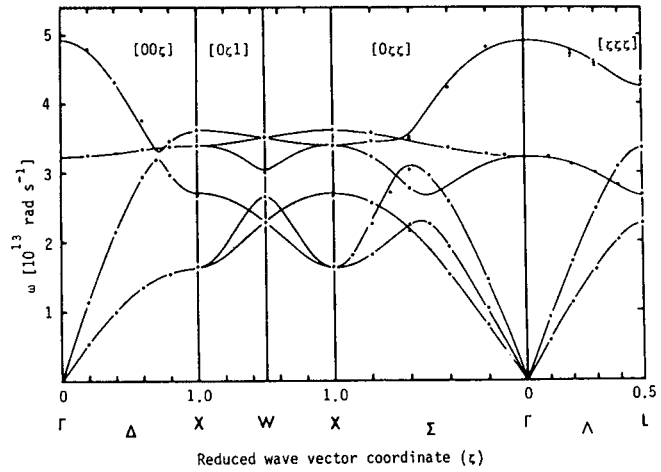

Figure 9 Phonon dispersion of NaCl (from reference [2]).

relation to the dielectrical constant. Polar mode frequencies may be easily determined by Infra-Red techniques. Inelastic neutron scattering on this topic is frequently difficult, due to the unfavorable form of the resolution ellipsoid. In metallic materials electric fields are screened due to the free charge carriers at least for macroscopic distances. As a consequence, the LST-splitting disappears. The phonon dispersion may then give information on the efficiency of the metallic screening.

Figure 9 shows the phonon dispersion in NaCl, which is isostructural to FeO. Compared to the latter one recognizes the perturbation of the curves arising mainly from the lower optical frequencies. Within the Brillouin-zone it is no longer possible to separate optical and acoustic modes, the branches tend to cross each other but there is always a small gap between branches of the same symmetry. This represents a general property : branches of the same symmetry may not cross. By mixing the polarization patterns it is always possible to yield a gap reducing the total energy of the system. Whether this gap is small or large depends on the similarity between the polarization patterns of the two branches. Similar branches may induce larger gaps, they are called to strongly interact.

12.2.2 Model calculations

The examples discussed above are characterized through their simplicity, which permits to analyze the polarization patterns without detailed calculations. In actual topics

one has to deal with systems of more than 10 atoms per primitive cell, see lower part of figure 4, one may identify then the character of the phonon modes only with the aid by predictions of model calculations.

As discussed above the lattice dynamics is described by the $3n$-dimensional Eigen-value problem with the dynamical matrix :

$$\omega^2 \underline{e} = \tilde{D}\underline{e} \qquad (12.16)$$

$$D_{\alpha,\beta}(d,d') = \frac{1}{(m_d m_{d'})^{1/2}} \sum_{\underline{l'}} \Phi_{\alpha,\beta}(\underline{0}d, \underline{l'}d') exp(i\underline{q}\underline{l'}) \qquad (12.17).$$

$\Phi_{\alpha,\beta}(0d, l'd')$ denote the force constants between the atoms d and d' in by $\underline{l}$ shifted cells. The determination of the force constants represents the real problem in lattice dynamics, in particular the question which constants are relevant.

Already by symmetry, the nine parameters per atom-pair are significantly reduced. Furthermore, one may reduce the analysis to the closer neighbors, as far as no long range force is involved. The next step consists in the development of potentials, from which one may obtain the force constants for many pairs inducing only a few free parameters.

Frequently it is sufficient to consider axial-symmetric potentials with $V(\underline{l}d, \underline{l'}d') = V(r)$, i.e. the potential depends only on the distance between the two atoms. Such a potential yields only two force constants, a radial and a transversal one :

$$\Phi_R(\underline{l}d, \underline{l'}d') = \frac{\partial^2 V}{\partial r^2}|_{r=r_o} \qquad (12.18),$$

$$\Phi_T(\underline{l}d, \underline{l'}d') = 1/r \frac{\partial V}{\partial r}|_{r=r_o} \qquad (12.19).$$

In the most simple model one may only introduce these radial and transverse force constants for the close neighbors (Born-von-Kàrmàn Model). However, extending more and more shells will rapidly increase the number of parameters. In particular the lattice dynamics of ionic compounds with the long range Coulomb-interaction, can only be poorly described by such a model.

Even when parameterizing the Coulomb-potential $V(r) \propto \frac{Z_d Z_{d'} e^2}{r}$ by the charges, $Z_d, Z_{d'}$, in order to deduce the respective force constants, the problem of the long range

persists. It is not possible to cut the sum at a certain distance, since the sums do not converge. The satisfying solution of this problem consists in the Ewald-method [1].

The Coulomb-potentials in an ionic crystal yields an attractive potential, which has to be compensated by a repulsive one. If the electron clouds of two ions of opposite charge start to overlap upon decrease of their distance, this repulsive potential will increase rapidly. One may describe this interaction by a Born-Mayer-potential $V(r) = B{\cdot}exp(-r/r_o)$, inducing only two parameters for one type of ionic pair, B and r_0. Amongst the various extensions of this type of model, called "rigid ion", we mention only the shell model, where the polarizability of the ions is described by a separation between an electron cloud (the shell) and the cores. There are many different ways to couple the cores and the clouds by force constants.

In order to prepare an inelastic neutron scattering study on the lattice dynamics of a complex material, even a simple and un-adapted model may be helpful, as long as the crystal structure and, therefore, the symmetry is correctly entered. By symmetry, degenerations are fixed for certain points or even for lines in reciprocal space, and frequently the structure factors follow some inelastic extinction rules. In principle these predictions may also be found by a careful analysis through group theory; however, the use of a simple model which does not need to describe the frequencies well is much less time demanding. Some of these aspects have already been illustrated for the example of the NaCl structure. Concerning the dynamic structure factors one may add, that one will observe the optical modes close to Γ best at the odd reciprocal lattice vectors (for example (333)) independently of the forces involved.

12.2.3 Structural phase transitions and soft mode behavior

Structural phase transitions form still a topic of actual interest, where information about the underlying microscopic mechanism may frequently be achieved only by inelastic neutron scattering.

In figure 10 one finds the representation of a fictive structural phase transition in a two-dimensional crystal structure with two atoms in the primitive cell. In the high-symmetry high-temperature phase the black ion in the middle occupies a site with inversion symmetry. This symmetry is broken at the phase transition due to the displacement of the black ion. The right part of figure 10 shows the corresponding dispersion curve, here the polarization pattern of the Γ-mode corresponds to the static distortion below the transition

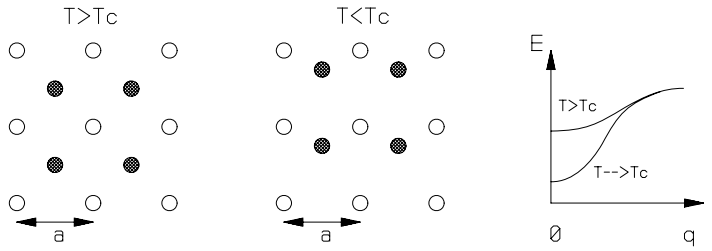

Figure 10 Schematic picture of a displacive phase transition occuring at the zone center and the corresponding dispersion curve.

temperature, T_c. The phonon frequency of this mode softens upon approaching the phase transition and is, therefore, called a "soft-mode". The structural instability, however, can be also seen in the dispersion quite above T_c : the frequency of the relevant mode at Γ is lower than those of modes with $\underline{q}$-values in the Brillouin-zone.

In addition to the phonon softening one expects a broadening of the line width in frequency; finally the width of the phonon mode may surpass its frequency. Such over-damped modes may no longer be described in the harmonic approximation.

The best-studied example for a zone-center phase transition may be found in the ferroelectric transition in perovskites, for example $PbTiO_3$ see figure 11. In the low-temperature phase the anions are deplaced against the cations, Pb, Ti, the corresponding phonon frequency vanishes almost completely. This polarization pattern has a strong polar character and is connected to the dielectric constant through the LST-relation. The softening of the TO mode induces a divergence in the dielectric constant, which explains the interest of the phenomena for technical applications.

A structural phase transition may also lead to an enlargement of the unit cell. Here, the equivalent atoms in neighboring cells are not displaced identically; a schematic picture is given in figure 12, where neighboring black ions are shifting in opposite direction. The phonon mode associated with such a displacement pattern necessarily has a finite wave-vector, since the translation symmetry is broken. In case of figure 12, $\underline{q}$ is situated on the zone boundary. But like for the zone-center transition, one may find a softening for the zone-boundary mode too. The best-known example for such a transition can again be found amongst the perovskites ABO_3. The perovskite structure consists of BO_6 octahedra

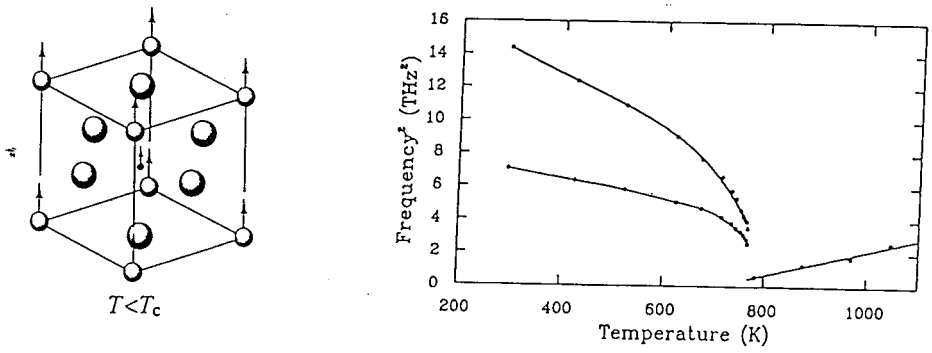

Figure 11 Structure and displacement pattern of the ferroelectric transition in the perovskite $PbTiO_3$ (left) small black dots in the center designate Ti the small and the large open spheres Pb and O respectively; square of the corresponding phonon frequency as function of temperature from reference [3] (right).

with partially covalent and quite hard bonds; the octahedra are connected only through their corners. Therefore, all these systems are more or less unstable against a rotation of the octahedra around an arbitrary axis. Only the strength of this instability and therefore the question whether a transition occurs or not, depends on the composition. For example the octahedron in $SrTiO_3$ below 105 K is rotated around a [100]-direction. The coupling of rotations around different directions leads to a variety of distinct low-temperature symmetries.

Recently the rotation phase transitions in the perovskites have regained interest, since they seem to be closely connected in the manganates to the electronic properties in particular their colossal-magneto-resistivity. Also the high-T_c-cuprates show similar transitions.

12.2.4 Electron phonon interaction

The study of the electron-phonon interaction represents an important field in lattice dynamics, which is analyzed almost exclusively by inelastic neutron scattering since the largest effects are expected in the Brillouin-zone.

The screening of the inter-atomic potentials through free charge carriers is determined by the topology of the Fermi-surface. In particular there are singularities in the electronic

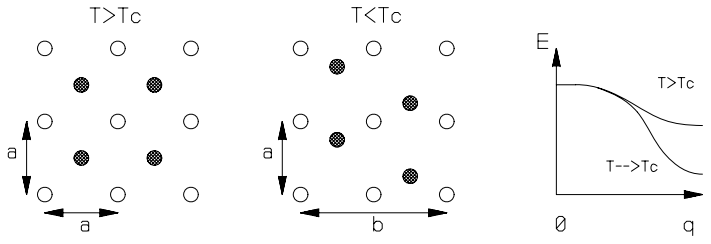

Figure 12 Schematic picture of a displacive phase transition corresponding to a zone-boundary mode.

susceptibility when parts of the Fermi-surface are parallel and may, hence, be connected by a single nesting vector. The susceptibility at this vector will be essentially increased and may renormalize the phonon frequency of a mode just at this wave vector. In most cases this type of electron-phonon coupling leads to a reduction of the phonon frequency, which shows up as a dip in the dispersion curve, called a Kohn-anomaly. In particular the conventional superconductors, for example TaC in Figure 13, exhibit such effects. The phonon dispersion of TaC shows pronounced dips, which are not observed in the phonon dispersion of normal metals. The study and interpretation of similar anomalies in the high-T_c-cuprates is subject of present research. However, in this case the analysis gets rather complicated due to the large number of atoms in these systems.

12.3 Magnetic excitations

12.3.1 Spin waves in a ferromagnet

Like the crystal structure, magnetic order may be perturbed at finite temperature with the perturbation propagating through the crystal. In full analogy with the phonons, the quantisized excitations are called magnons.

The ground state of a ferromagnet results from the interaction between spins of neighboring atoms, which favors a parallel alignment. The energy of a neighboring pair, $\underline{S}_i, \underline{S}_j$, depending on the relative orientation of the spins is described within the Heisenberg-model by $e = -J\underline{S}_i \cdot \underline{S}_j$, where J is the Heisenberg exchange constant. For a chain of coupled spins the energy of the magnetic interaction amounts to :

$$U = -2J \sum_{p=1}^{N} S_p \cdot S_{p+1} \qquad (12.20).$$

In the ground state all spins are parallel and $U_0 = -2NJS^2$, this corresponds to figure

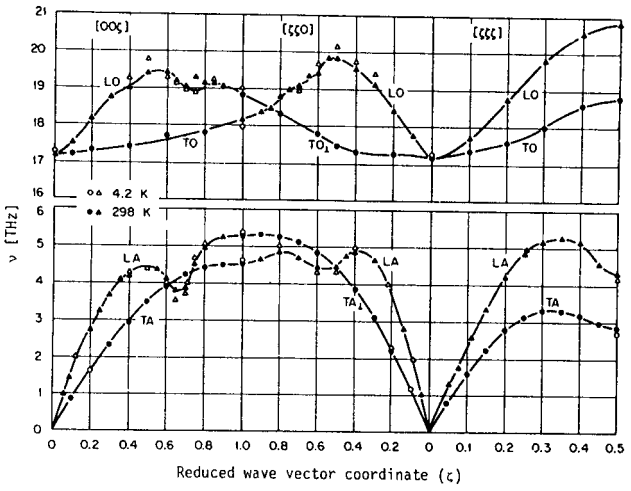

Figure 13 Phonon dispersion of TaC, the dips, for example at (0 0 0.7) andd at (0.6 0.6 0), indicate modes renormalized through the electron phonon coupling, from reference [2].

14a. A possible excitation might consist in the flip of just one spin, like it is shown in figure 14b. This perturbation yields a finite increase in energy of $8JS^2$. However, the temperature dependence of several macroscopic properties like specific heat or magnetization does not correspond to an exponential law, as it has to be expected for a finite excitation energy. Spin waves (magnons) must have a much smaller energy than the single spin flip, like phonons may have lower energy than an ionic vacancy for instance.

The distortion of the magnetic order corresponds to a plane magnetic wave (with propagation vector $\underline{q}$ and frequency ω) and is drawn in Figure 14c. Spins are precessing around the direction of magnetic order (here z) with components :

$$S_p^x = u \cdot exp[i(pqa - \omega t)] \qquad (12.21),$$

$$S_p^y = v \cdot exp[i(pqa - \omega t)] \qquad (12.22),$$

where a designates the lattice constant and b is numbering the spins.

Like in the case of the phonon dispersion one may deduce the magnon relation. In case of a simple chain one yields :

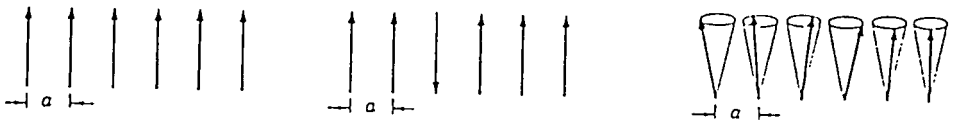

Figure 14 Schematic drawing of a simple ferromagnet : a) ground state, b) one spin being flipped c) in a spin-wave the spins precess on cones (from reference. [4]).

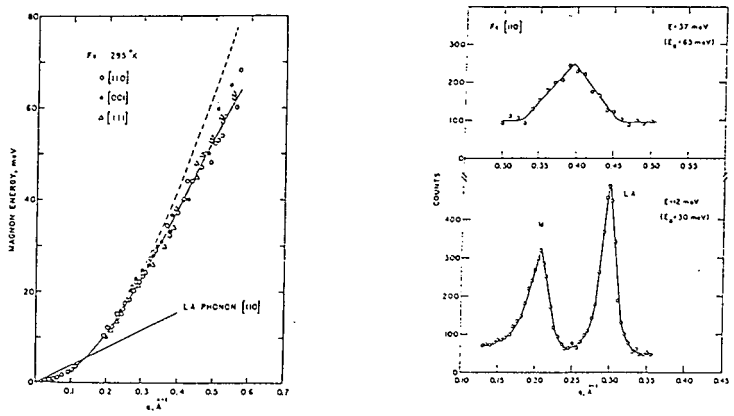

Figure 15 Magnon- and phonon dispersion curves in Fe at room temperature and two $\underline{Q}$-scans at constant energy , reference [5].

$$\hbar\omega(q) = 4JS(1 - cos(qa)) \qquad (12.23),$$

which may be approximated for small $\underline{q}$ by $\hbar\omega(q) = 2JS(qa)^2$, i.e. a quadratic relation. In contrast, an acoustic phonon dispersion is always linear in that $\underline{q}$-range. Equation (12.23) may be extended to the three-dimensional case, in all cubic systems the relation $\hbar\omega(\underline{q}) = 2JS(qa)^2$ remains valid for small q.

Figure 15 shows the magnon dispersion measured in Fe, from which one may obtain the exchange constant J; for comparison the linear dispersion relation of the LA branch is added. One may note, that in the case of Fe the magnon frequencies extend to higher energies than those of the phonons. Due to the special form of the resolution ellipsoid in the triple axis spectrometer, it is favorable to perform scans at constant energy revealing both the phonon and the magnon, which exhibit approximately the same intensities, see right part of figure 15.

Since magnons are bosons, their occupation is given by Bose-statistics like that of the phonons, equation (12.11). Also for the differential cross section one may deduce a formula similar to equation (12.10) valid for phonons :

$$\begin{aligned}(\frac{d^2\sigma}{d\Omega dE'})^{\pm} = \quad & (k'/k) \cdot S \cdot const. \cdot exp(-2W(\underline{Q}))F^2(Q)(1 + \tfrac{Q_z^2}{Q^2}) \cdot \\ & \textstyle\sum_{\underline{\tau}\underline{q}}(n(\omega_{\underline{q}}) + 1/2 \pm 1/2) \cdot \delta(\omega \mp \omega_j(\underline{q})) \cdot \delta(\underline{Q} \mp \underline{q} - \underline{\tau}) \qquad (12.24).\end{aligned}$$

One recognizes the terms for momentum and energy conservation as well as the Bose-factor, which is increased by one in case of magnon creation. Furthermore the intensity is modulated by the same Debye-Waller-factor as the phonons. However, there is no term equivalent to the dynamic structure factor, the intensity is determined just by the spin S, the form factor $F(Q)$ and the direction of the momentum transfer.

Ferromagnetic materials are still of considerable interest due to their enormous technical potential in the context of data storage media. Attempts to optimize the technical properties lead to binary or ternary compounds, where the complexity of the magnetic order is considerably increased. In all cases the study of the magnon dispersion gives an almost unique insight to the microscopic coupling terms.

12.3.2 Antiferromagnetic Excitations

Antiferromagnetic order results from a negative exchange constant J in $U = -2J \sum_p \underline{S}_p \cdot \underline{S}_{p+1}$. The anti-parallel alignment of neighboring spins ($\uparrow\downarrow\uparrow\downarrow\uparrow\downarrow\uparrow\downarrow$), however, leads to a magnetic cell which is larger than the nuclear one. A classical example is given by the antiferromagnetic order observed in MnO at 120 K (Shull et al. 1951). Again one may find excitations in an antiferromagnet, which have lower energy than the simple flip of a single spin. Again each spin deviates from the ordered position by a component given by a plane wave. The calculation of the antiferromagnetic dispersion more closely resembles that of the phonon case :

$$\omega^2(\underline{q}) = (\frac{4JS}{\hbar})^2(1 - cos^2(\underline{q} \cdot a)) \quad \omega(\underline{q}) = -\frac{4JS}{\hbar}|sin(\underline{q} \cdot a)| \qquad (12.25).$$

In contrast to the ferromagnetically ordered structure and in close similarity to the acoustic phonons, the frequency becomes linear in $\underline{q}$ for sufficiently small $\underline{q}$. Figure 16 shows the magnon dispersion observed in $RbMnF_3$ consisting of a single branch and the result of a recent study on the magnetic excitations of $La_{0.5}Sr_{1.5}MnO_4$ with several branches [8]. However, the magnon dispersions studied so far remain still less complex than what can be treated in terms of a phonon dispersion.

In general both dispersion relations (12.23) and (12.25) are not gaped, the magnon energy vanishes for $\underline{q}$ approaching the zone center, like in case of an acoustic phonon. For the acoustic phonon the zone-center limit corresponds to an infinitely small translation of the entire crystal which does not cost any energy, since no force constant is stretched. In case of the magnons the limit corresponds to a rotation of the ordered moment, which in the Heisenberg-model does not involve any energy shift (the interaction depends only on the relative orientation). However, in general this model is not sufficient, there are always interactions favoring the orientation of a certain spin direction. These interactions yield a finite gap in the excitation spectrum, however much smaller than the spin flip energy.

Antiferromagnetic materials have much less technical importance compared to ferromagnetism. However, antiferromagnetic correlations in metallic systems are often essential for the understanding of the electronic properties. For instance the physics of high-temperature cuprate superconductors seems to be determined by the closelyness of the antiferromagnetic order in the insulating parent compounds.

12.3.3 Crystal field excitations for rare earth ions

In the rare earth series one finds unpaired electrons in the 4f-shell, which are strongly

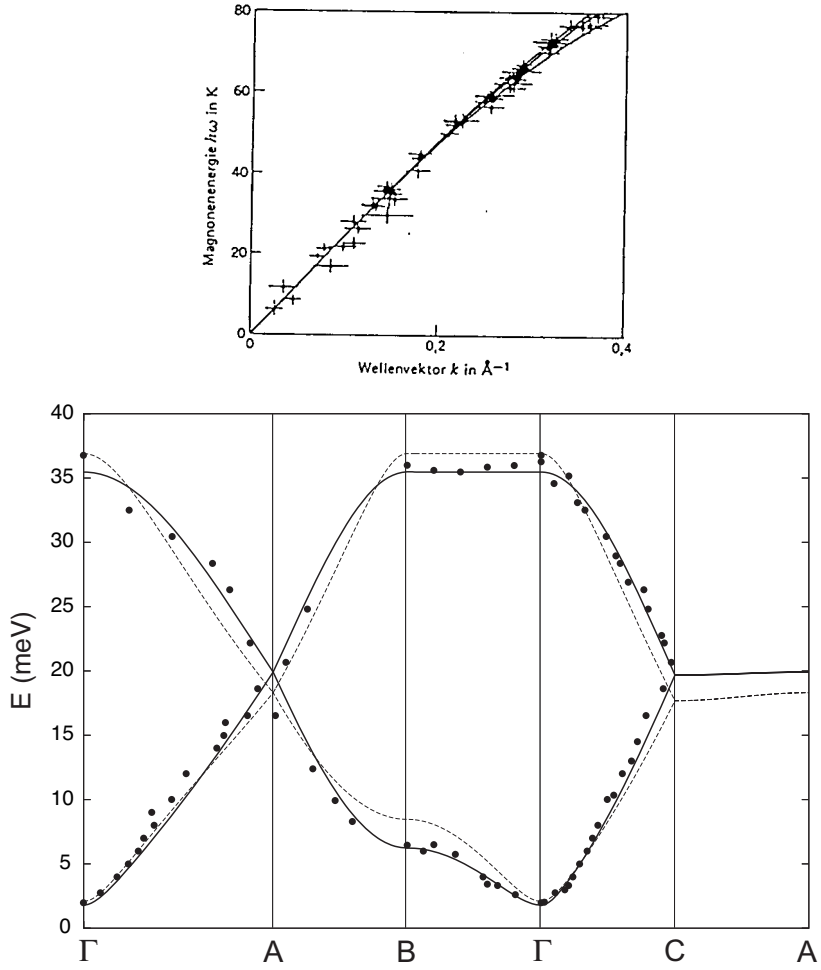

Figure 16 Upper part : Magnon dispersion in $RbMnF_3$ (from reference [4]); lower part : Magnon dispersion in $La_{0.5}Sr_{1.5}MnO_4$ a material related to the colossal magneto-resistivity manganites, points denote experimental magnon frequencies and lines calculations within spin-wave theory [8].

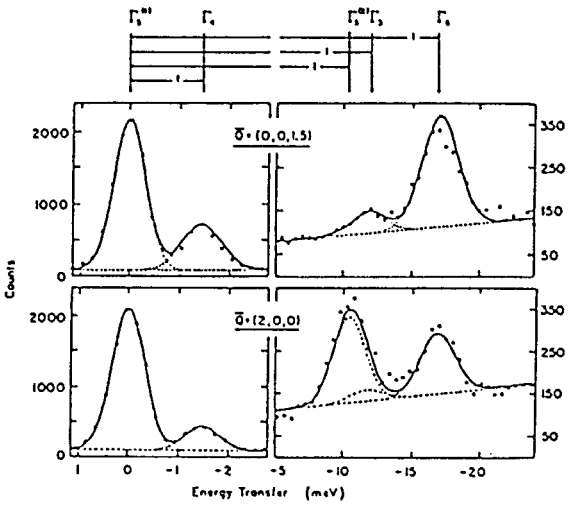

Figure 17 Crystal field scheme and measured energy scans in PrB_3 (T=1.5 K), from reference [6].

localized and therefore screened from the surrounding ions. In consequence the total momentum J remains a good quantum number. For a free ion the the ground state would be $(2J+1)$ times degenerate. In a crystal this degeneracy is partially lifted due to the – weak – Coulomb-fields of the surrounding ionic charges. The transitions between the single levels may be observed by inelastic neutron scattering. (This is valid for the crystal field splittings in transition metals too, but due to the larger overlap of the d-orbitals the excited levels in these compounds are usually to high in energy.) If the rare earth ions are sufficiently diluted, interactions amongst them may be neglected. The level frequencies show then no dispersion and may be studied with time of flight methods on a polycristalline sample.

In figure 17 we show the observed spectrum compared to the crystal field scheme for PrB_3. The levels of Pr^{3+} with a J of 4 may split into not more than 9 levels. The local symmetry of the site occupied by the ion in the lattice determines which levels may exist with which multiplicity. However, the symmetry cannot predict the sequence of the levels, for this purpose one needs a quantitative estimate for the surrounding fields. The single levels are designated according to the irreducible representations of the local symmetry

group by Γ_i. In close resemblance to equations (12.10) and (12.24) the differential cross section arises from the sum of transition probabilities $\Gamma_i \rightarrow \Gamma_j$; these matrix elements may be calculated within point-charge models.

12.4 Conclusions

Inelastic neutron scattering is almost the unique technique to observe lattice vibrations and magnetic excitations throughout the whole Brillouin-zone. The main part of our knowledge on these topics has indeed been achieved by inelastic neutron scattering studies.

Also the subjects of present interest, like high-T_c-superconductors, heavy fermions, quasi-crystals, C_{60} and compounds with colossal magneto-resistivity demand a detailed analysis of their lattice dynamics as well as of their magnetism. Frequently the materials of current interest exhibit a larger complexity; therefore, their study requires a continuous development of the experimental facilities as well as of the analysis methods.

References

1 N.W. Ashcroft and N.D. Mermin, Solid State Physics, Holt-Saunders International Editions, Philadelphia (1976).

2 H. Bilz and W. Kress, Phonon Dispersion Relations in Insulators, Springer Verlag, Berlin Heidelberg New-York (1979).

3 M.T. Dove, Introduction to Lattice Dynamics, Cambridge University Press, Cambridge (1993).

4 C. Kittel, Einführung in die Festkörperphysik, R. Oldenbourg Verlag, München (1983).

5 G. Shirane, V.J. Minkiewiecz and R. Nathans, Journal of Appl. Physics 39, 3833 (1968).

6 A. Furrer, Magnetic Neutron Scattering, World Scientific, Singapore (1995).

7 M. Braden, W. Reichardt, B. Hennion, G. Dhalenne, and A. Revcolevschi Phys. Rev. B 66, 214417 (2002).

8 D. Senff, F. Krger, S. Scheidl, M. Benomar, Y. Sidis, F. Demmel, and M. Braden Phys. Rev. Lett. 96, 257201 (2006).

further suggestions

- P. Brüesch, Phonons: Theory and Experiments I, II, III, Springer Verlag, Berlin Heidelberg New-York (1982).

- Landolt-Börnstein Band 13, Metalle, Phononenzustände, Elektronenustände and Fermiflächen, Springer Verlag, Berlin Heidelberg New-York (1981).

- E. Balcar and S.W. Lovesey, Theory of Magnetic Neutron and Photon Scattering, Oxford Science Publications, Clarendon Press, Oxford (1989).

- G.L. Squires, Thermal Neutron Scattering, Cambridge University Press, Cambridge (1978).

13

Structure of Complex Fluids and Macromolecules

Henrich Frielinghaus

13. Structure of Complex Fluids and Macromolecules

Henrich Frielinghaus

13.1 Introduction

The method small angle neutron scattering (SANS) is widely used in the fields of conventional solid state physics, but more intensively in the field of soft matter research. This field embraces polymer melts, solutions, and rubbers, but also complex fluids such as microemulsions, colloidal dispersions, and micellar solutions. The complex fluids often also contain polymers, i.e. macromolecules. Finally the neighborhood to biological systems brings biophysical subjects close to neutron scattering techniques.

The typical length scale of a SANS experiment lies in the range of 1 to 100 nanometers (or 10 to 1000 Angstroems). The developments of ultra SANS enlarged the spatial region to 10 to 100µm. While the scattering techniques observe structures in the reciprocal space, all these length scales are also covered by microscopy techniques (transmission electron microscopy (TEM) and light microscopy). Advantages of SANS experiments will be made clear.

In the following some important properties of polymers shall be introduced and discussed. Then polymer blends and melts will be introduced connected with their typical scattering pattern. Finally, microemulsions are an interesting system where amphiphilic polymers can be added. These polymers modify the phase behaviour and the microscopic structure, which is studied by SANS experiments.

13.2 Homopolymers

Homopolymers are long linear chain molecules consisting of a single repeat unit, the monomer. While there is a local rigidity and a non-vanishing angular correlation of single carbon-carbon bonds, effective longer chain segments can be defined. The Kuhn segment embraces so many monomers that the angular correlation of these effective segments is lost. In the following we assume the polymer physics we want to describe take place on length scales larger than the Kuhn segment length ℓ_K. Especially, the polymer itself is large compared to the single Kuhn element, of which it contains N_K ($\gg 1$) segments. One important observable of a single polymer is the end-to-end distance, which simply is defined as:

$$\vec{R}_{ee} = \sum_{i=1}^{N_K} \vec{r}_i \qquad (13.1)$$

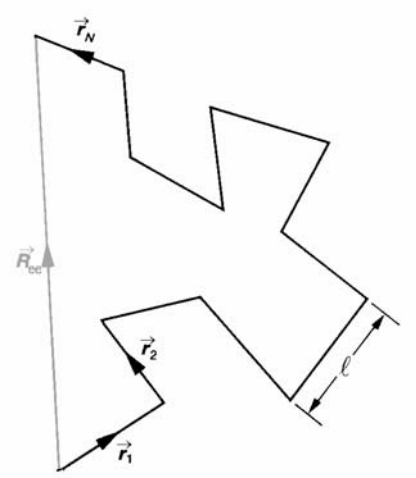

Figure 13.1: Schematic drawing of a chain with independent chain segments. The vectors $\vec{r}_i$ specify the individual segments. The segment length is ℓ_K. The end-to-end vector $\vec{R}_{ee}$ is a measure for the size of the polymer.

The statistical average of this observable is simply zero, since each segment does not have a preferred orientation ($\langle \vec{r}_i \rangle = 0$), and so the whole polymer does not show a preference either. The next higher order moment of this observable is the second moment. We simply can arrange the square of a sum by:

$$\left\langle \vec{R}_{ee}^{\,2} \right\rangle = \sum_{i,j=1}^{N_K} \left\langle \vec{r}_i \cdot \vec{r}_j \right\rangle = \sum_{i=1}^{N_K} \left\langle \vec{r}_i^{\,2} \right\rangle + 2 \cdot \sum_{1 \le i < j \le N_K} \left\langle \vec{r}_i \cdot \vec{r}_j \right\rangle \tag{13.2}$$

The diagonal terms appear N_K times and represent the length of a single Kuhn segment ℓ_K^2. The off-diagonal terms would contribute if angular correlations were present. According to our assumptions this is not the case, and we finally obtain:

$$\left\langle \vec{R}_{ee}^{\,2} \right\rangle = N_K \cdot \ell_K^2 \quad \text{or:} \quad R_{ee} \equiv \sqrt{\left\langle \vec{R}_{ee}^{\,2} \right\rangle} = \sqrt{N_K} \cdot \ell_K \tag{13.3}$$

The radius of gyration is a similar measure for the size of the polymer, which is defined like the moment of inertia normalized to the total mass:

$$\left\langle \vec{R}_g^{\,2} \right\rangle = \frac{1}{N_K + 1} \cdot \sum_{i=0}^{N_K} \left\langle \vec{s}_i^{\,2} \right\rangle \tag{13.4}$$

The single vectors $\vec{s}_i$ specify the distance of a single segment from the centre of mass. It can be shown (as article C1 in reference 4) that the two typical sizes of a polymer are proportional for our assumptions ($N_K \gg 1$):

$$R_g \equiv \sqrt{\left\langle \vec{R}_g^{\,2} \right\rangle} = \sqrt{\tfrac{1}{6} N_K} \cdot \ell_K = \sqrt{\tfrac{1}{6}} \cdot R_{ee} \tag{13.5}$$

In this sense, a polymer with negligible segment rigidity has only one length scale, given by either R_g or R_{ee}. This typical size of the polymer is proportional to the length of a single Kuhn length ℓ_K and the square root of the segment number N_K. In practical equations, often some effective monomer length ℓ_{mon} and the real degree of polymerization N, which is the monomer number in a polymer, are used. For relatively rigid chains the monomer length can be larger than the real geometric length, since the equations hold for sizes on the polymer length scale.

13.3 Scattering of homopolymers

We now consider the scattering of a solution of homopolymers without interactions. The macroscopic scattering cross section $d\Sigma/d\Omega$ as a function of the scattering vector $\vec{Q}$ is defined rigorously as the squared amplitude of the individual phases of all atoms in the whole macroscopic volume V, and thus:

$$\frac{d\Sigma}{d\Omega}(\vec{Q}) = \frac{1}{V} \cdot \left| \sum_j b_j \exp\left(i \vec{Q}_j \vec{R}_j\right) \right|^2 \tag{13.6}$$

The scattering length b_j determines the amplitude of the outgoing wave from a single atom j. with the position R_j. The symbol i is now the imaginary unit. This elementary formula can be expressed in a handier way:

$$\frac{d\Sigma}{d\Omega}(\vec{Q}) = (\Delta\rho)^2 \cdot \phi \cdot \frac{v_K}{N_K} \cdot \left| \sum_j \exp\left(i \vec{Q}_j \vec{R}_j\right) \right|^2 = (\Delta\rho)^2 \cdot \phi \cdot \frac{1}{V_{pol}} \cdot \left| \int_{pol} \exp\left(i \vec{Q} \vec{R}\right) d^3R \right|^2 \tag{13.6}$$

The first assumption is, that we take all monomers of a Kuhn segment as one unit. This unit has a total volume v_K, and so a scattering length density can be defined $\rho_{pol} = (\sum b_j) / v_K$ being a measure of the polymer. In the same way one obtains the scattering length density of the solvent ρ_{sol}. The contrast, i.e. the scattering length density difference, appears when the sum focuses on the solute only. A remaining term considering the solvent as a homogenous matrix results in a delta function $\delta(Q)$, which does not contain information for the typical scattering experiment, and thus is neglected. The concentration ϕ is the volume fraction of the polymer in solution. It is proportional to the number of polymers, and thus the individual sum

in eq. 13.6 over index *j* considers a single homopolymer only. All homopolymers contribute to the scattering independently without interference, which is true for dilute solutions. The second part of eq. 13.6 considers the polymer to be a worm with a finite volume, over which the integration is conducted. The new prefactor contains the volume $V_{pol} = \nu_K \cdot N_K$ of a single polymer. It is important to repeat, that we consider length scales above the Kuhn segment length, and atomic structures within the large molecule are neglected.

The chain statistics we have developed for homopolymers will be applied to this final scattering formula (eq. 13.6) now. For the scattering function $S(Q)$, i.e. the structure factor, we obtain now:

$$\begin{aligned} S(\vec{Q}) &= \frac{\nu_K}{N_K} \cdot \left\langle \left| \sum_j \exp\left(i\vec{Q}_j \vec{R}_j\right) \right|^2 \right\rangle \\ &= \frac{\nu_K}{N_K} \cdot \left\langle \sum_{j,k} \exp\left(i\vec{Q}(\vec{R}_j - \vec{R}_k)\right) \right\rangle \\ &= \frac{\nu_K}{N_K} \cdot \left(\sum_{j,k} 1 + \left\langle \sum_{j,k} i\vec{Q}(\vec{R}_j - \vec{R}_k) \right\rangle + \frac{1}{2} \left\langle \sum_{j,k} \left(i\vec{Q}(\vec{R}_j - \vec{R}_k)\right)^2 \right\rangle + \ldots \right) \end{aligned} \tag{13.7}$$

The vectors $\vec{R}_j$ specify the position of a segment relative to a fixed origin (contrary to $\vec{r}_i$ which is an individual segment vector). In the first transformation the complex conjugate was explicitly used, and all addends were combined in every possible form. The next transformation uses the Taylor expansion of the exponential function. The linear term has an expected value of zero, since again a first order momentum appears. So the quadratic term determines the *Q*-dependence of the structure factor, and one expresses the expansion as an exponential again:

$$S(\vec{Q}) = \frac{\nu_K}{N_K} \cdot \sum_{j,k} \exp\left\langle -\tfrac{1}{2} \left(\vec{Q}(\vec{R}_j - \vec{R}_k)\right)^2 \right\rangle \tag{13.8}$$

For independent chain segments - as we assumed anyhow - it can be shown, that all higher order terms of eq. 13.7 contribute consistently to the final expression of eq. 13.8. The averaging is carried out inside the exponential now, which simplifies the calculation strongly. For a random orientation relatively to the scattering vector *Q*, one obtains:

$$S(\vec{Q}) = \frac{\nu_K}{N_K} \cdot \sum_{j,k} \exp\left(-\tfrac{1}{6} Q^2 \left\langle (\vec{R}_j - \vec{R}_k)^2 \right\rangle\right) \tag{13.9}$$

The inner term $(\vec{R}_j - \vec{R}_k)^2$ specifies a chain part with $|j - k|$ segments. This chain part behaves like an ideal chain, and so its average length follows the formula of eq. 13.3. Furthermore, it

is helpful to express the sum as integrals, which is a good approximation on larger length scales. So one obtains:

$$S(\vec{Q}) = \frac{v_K}{N_K} \cdot \int_0^{N_K} dj \cdot \int_0^{N_K} dk \cdot \exp\left(-\tfrac{1}{6} Q^2 |j-k| \ell_K^2\right)$$
$$= V_{\text{pol}} \cdot f_D(Q^2 R_g^2) \qquad (13.10)$$
$$f_D(x) = \frac{2}{x^2}\left(\exp(-x) - 1 + x\right)$$

The Debye function $f_D(Q^2R_g^2)$ (see Fig. 13.2) is a monotonously decaying function with the maximum at $Q = 0$. There are two important limits of the structure factor. For small scattering vectors a Taylor series yields the Zimm approximation:

$$S^{-1}(\vec{Q}) = V_{\text{pol}}^{-1}(1 + \tfrac{1}{3} Q^2 R_g^2) \qquad (13.11)$$

The extrapolated forward scattering $S^{-1}(Q \to 0)$ is a measure for the single polymer volume. Of course, as described by eq. 13.6, the scattering contrast $(\Delta\rho)^2$ and the concentration ϕ have to be known beforehand. The slope of a Zimm-plot tells about the typical polymer size, i.e. the radius of gyration. At larger scattering angles (the considered length scales are still large compared to the segmental size $Q^{-1} \gg \ell_K$) another important scattering behaviour is obtained:

$$S(\vec{Q}) = 2 \cdot V_{\text{pol}} / (Q^2 R_g^2) \qquad (13.12)$$

Here the self similarity of a chain becomes dominant. On these intermediate scales chain parts still look like perfect chains. The corresponding fractal dimension of ideal chains is 2.

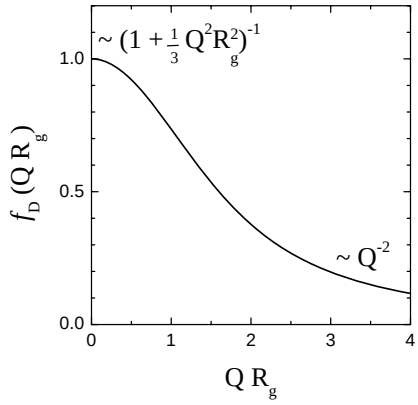

Figure 13.2: The Debye-Function as a function of the scaled scattering vector. Two important limits are given for small and large scattering vectors.

13.4 Scattering of Homopolymer Blends

The formula 13.10 was derived for dilute homopolymers in soultion without interactions. When describing homopolymer blends of two homopolymers, the assumptions of dilution and of negligible interactions do not hold anymore. The concept of the random phase approximation (RPA) bases on the undisturbed chain structure factor (eq. 13.10) and introduces high concentrations and interactions afterwards. Since this short lecture cannot go into details, we simply present the final expression of the RPA:

$$S_{RPA}^{-1}(Q) = \Delta\rho^2 / \frac{d\Sigma}{d\Omega}(Q) = \left(\phi_{pol1} V_{pol1} f_D(Q^2 R_{g1}^2)\right)^{-1} + \left(\phi_{pol2} V_{pol2} f_D(Q^2 R_{g2}^2)\right)^{-1} + \Gamma \qquad (13.13)$$

The reciprocal structure factor of a homopolymer blend is the sum of the reciprocal structure factors of the undisturbed homopolymers plus the Flory-Huggins interaction parameter Γ. In the limit of identical homopolymers (for instance a blend of protonated and deuterated polymers) and negligible interactions basically the undisturbed chain structure factor is obtained. An example of a real polymer blend is depicted in Fig. 13.3. The basic properties of the Debye function are preserved, but of course the Flory-Huggins interaction parameter is obtained by the detailed analysis. The scattering at small scattering vectors is maximal, which means that on large length scales the thermal composition fluctuations are maximal. The extrapolated forward scattering $S(Q=0)$ is the reciprocal susceptibility. The peak width is connected with the correlation length ξ telling over which distance the local composition can be assumed constant. At high temperatures $S(0)$ and ξ are small which is connected with a small or even negative interaction parameter Γ. When the interaction parameter comes close to the critical value $\Gamma = 2/V_{pol}$ the fluctuations become infinitely large, and $S(0)$ and ξ diverge. At this moment the concept of the RPA breaks down, and the system behaves like a 3d-Ising system. This means that the point of criticality is shifted to slightly lower temperatures compared to the RPA estimation. The temperature shift is proportional to the Ginzburg number, which is a measure how strongly fluctuations influence the thermo-dynamics of the system [7].

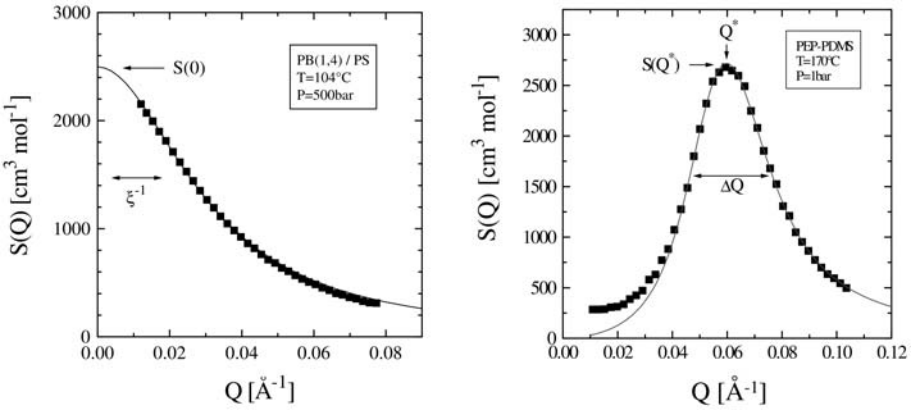

Figure 13.3: The scattering function $S(Q)$ as a function of the scattering vector. On the left the typical scattering of a homopolymer is shown. The sample is a polybutadiene(1,4) / polystyrene blend at 104°C and 500bar. On the right the typical scattering of a diblock copolymer is shown which is a poly-ethylene-propylene-poly-dimethylsiloxane at 170°C and 1bar.

13.4 Scattering of Diblock Copolymers

Diblock copolymers are chainlike molecules with two different kinds of monomers which are placed along the molecule at two different blocks. The RPA is capable to describe the scattering of diblock copolymers at high temperatures. The combination of Debye functions is just slightly more complex as in eq. 13.13, but the interaction parameter is added in the same way [8]. So we simply look on the scattering pattern of a diblock copolymer in Fig. 13.3. At small scattering vectors the ideal intensity vanishes at $Q = 0$ and increases like Q^2, which is due to the chemical connectivity of the two blocks. Fluctuations on large length scales ideally are impossible. Polydispersity of the block length ratio leads to some finite intensity at $Q = 0$. At large scattering vectors mainly chain parts are observed, and the connectivity of the blocks does not play a role anymore. Thus the same Q^{-2} behaviour as for homopolymers is observed. At the intermediate Q^* the pronounced intensity maximum indicates strong fluctuations on length scales $2\pi/Q^*$ similar to the radius of gyration. The peak width again is connected with the reciprocal correlation length, and the maximal intensity is the reciprocal susceptibility. When the temperatures are lowered the fluctuations become much stronger as for homopolymers, and deviations from the RPA concept become much more prominent. The corresponding Ginzburg numbers are much larger.

13.5 Scattering of Homopolymer / Diblock Copolymer blends

For mixtures of A and B homopolymers with an AB diblock copolymer (here polybutadiene and polystyrene) the scattering patterns of the two different systems compete [9]. For small diblock copolymer contents the strong scattering occurs at small scattering angles, while for larger diblock copolymer contents the strong scattering occurs at a finite scattering vector Q^*. For intermediate diblock copolymer contents there appears a wide plateau of strong scattering intensity ranging from zero to finite scatting angles. This high temperature phase is interesting by itself to study the critical behaviour of these extremely strong fluctuations.

At lower temperatures a phase separation occurs. While for the homopolymer-like systems with $Q^* = 0$ a phase separation takes place on macroscopic length scales (macrophase separation), for the diblock-like systems with finite Q^* the phase separation leads to ordered structures (microphase separation). For the intermediate diblock copolymer contents discussed here the system forms a bicontinuous phase structure. This means that the A-rich phase forms a sponge-like structure with space for the B-rich phase. Each of the phases is continuously connected. The diblock copolymer acts as a surfactant and thus inhibits the macrophase separation.

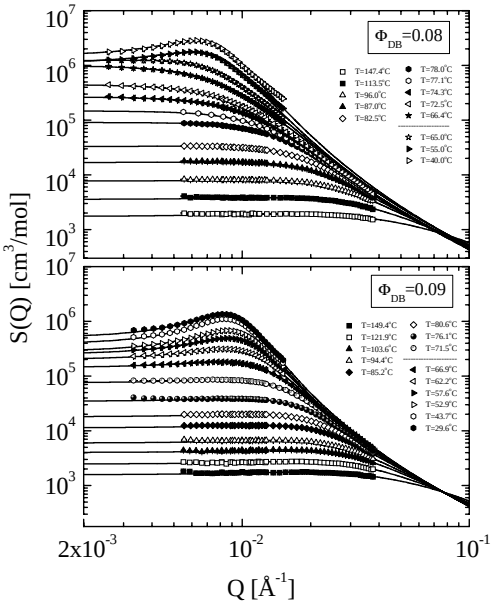

Fig. 13.4: The scattering function of an A/B/AB homopolymer / diblock copolymer blend. At higher temperatures the scattering is less intense, the plateau at small scattering angles is quite broad. At lower temperatures there is a phase transition to the microemulsion phase where a correlation peak appears.

The tailoring of homopolymer domains by small amounts of additives (here: diblock copolymers) is an interesting field of the current research. These systems resemble microemulsions since the mediating component has an A-philic and a B-philic segment. Some systems mimic the microemulsions better others worse. The still open mayor issue is to replace the costly diblock copolymers by less expensive polymers.

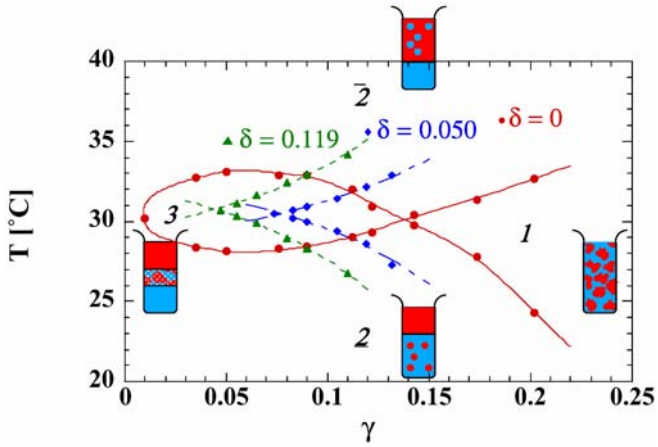

Figure 13.5: A typical fish-phase-diagram (red curve): temperature versus surfactant content for a symmetric water to oil ratio. At high surfactant contents a one-phase microemulsion (1) is observed, while for lower surfactant contents the three-phase coexistance (2) with a microemulsion phase, an excess oil and an excess water phase is found. At low and high temperatures (2 and $\bar{2}$) a two-phase coexistance occurs with excess oil or water phases. When adding aphiphilic diblock copolymers (δ measures the polymer content with respect to the amphiphile) the fish-tail moves to lower surfactant contents. The minimum amount of surfactant of the one-phase region is given by the fish-tail-point and is a measure for the efficiency of the amphiphile. The polymer increases the efficiency dramatically.

13.6 Microemulsions

Microemulsions consist of oil, water and a surfactant. While the microemulsion appears macroscopically homogenous, oil- and water-rich domains form on a microscopic level. The mediating surfactant forms a thin film between these domains. In the following we restrict ourselves to equal amounts of oil and water. A typical phase diagram is shown in Fig. 13.5 in the temperature versus surfactant content γ representation [10]. The most interesting region is the one-phase region (1), where a bicontinuous microemulsion is found. The minimum amount of surfactant is connected to the fish-tail-point, and is a measure for the efficiency of

the surfactant. When adding amphiphilic diblock copolymer, the system becomes more efficient. The polymer amount δ is given in units relative to the total amphiphile, but in absolute units it is less than 0.5%. The dramatically increased efficiency bases on the polymer boosting effect which is described in the following.

By contrast variation measurements it was revealed where the polymer is placed in this four component system. Is was necessary to have each component in a normal protonated and a deuterated version, i.e. normal and heavy water, normal and deuterated decane and normal and deuterated $C_{10}E_4$ surfactant. The minor component polymer was always protonated. The bulk contrast was achieved by using heavy water and protonated components otherwise. Then the water domain is visible against the other components. For the film contrast also deuterated decane was used, and the surfactant film became visible. For the polymer contrast only the protonated polymer was visible. The macroscopic cross section of such a four component system can be written generally as:

$$\begin{aligned}\frac{d\Sigma}{d\Omega}(Q) = {} & (\rho_O - \rho_W)^2 S_{OO} + (\rho_F - \rho_W)^2 S_{FF} + (\rho_P - \rho_W)^2 S_{PP} \\ & + (\rho_O - \rho_W)(\rho_F - \rho_W) S_{OF} + (\rho_F - \rho_W)(\rho_P - \rho_W) S_{FP} \\ & + (\rho_O - \rho_W)(\rho_P - \rho_W) S_{OP}\end{aligned} \qquad (13.14)$$

The first three terms are purely represented by the bulk, film, and polymer contrast (S_{OO}, S_{FF}, S_{PP}). But since the macroscopic cross section is a quadrature of the scattering amplitudes (see eq. 13.6) also cross terms appear. By measuring many contrasts close to the polymer contrast, also the other partial scattering functions (S_{OF}, S_{FP}, S_{OP}) are detectable. These cross terms arise due to a convolution of the real space structures, and thus relative positions of two components are measurable. This valuable information is unavailable by the diagonal terms or a single contrast condition.

For many measurements of macroscopic cross sections at different contrast conditions eq. 13.14 reads $d\vec{\Sigma}/d\Omega = \underline{\underline{\Delta\rho}} \cdot \vec{S}$. Usually, there are many more measurements than the six unknown partial scattering functions, and so the system is over-determined and the experimental noise is reduced. Formally, the inverse matrix of the scattering length densities can be calculated by the Sigular Value Decomposition method, and the partial scattering functions are obtained by $\vec{S} = \underline{\underline{\Delta\rho}}^{-1} \cdot d\vec{\Sigma}/d\Omega$. An example of a cross term S_{FP} is shown in Fig. 13.6. The valuable information of the polymer relative to the surfactant membrane is obtained. The solid line is described by a diblock copolymer decorating the surfactant membrane. Each of the blocks is placed in its pleasant environment and the coils form a mushroom like object.

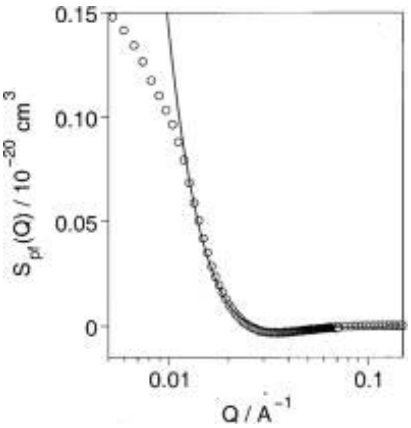

Figure 13.6: The partial polymer-film scattering function as a function of the scattering vector. The fitted function describes a polymer in the presence of a planar wall. The polymer shows a mushroom conformation.

13.7 Bulk Scattering and Phase Diagrams

The bulk scattering also reveals valuable information about the domain structure and finally about the thermodynamics of the microemulsion [11]. An example for the bulk scattering is shown in Fig. 13.7. The macroscopic cross section can be described by the Teubner-Strey theory which bases on a Ginzburg-Landau approach, which considers long wavelength fluctuations of the oil and water domains. The final formula reads:

$$\frac{d\Sigma}{d\Omega}(Q) = \frac{(\Delta\rho_{OW})^2 \cdot 8\pi\phi_W(1-\phi_W)/\xi}{((2\pi/d)^2+\xi^{-2})^2 - 2((2\pi/d)^2-\xi^{-2})Q^2 + Q^4} \tag{13.15}$$

The dominator contains the total fraction of water ϕ_W. Much more interesting are the two structural parameters ξ and d which are obtained as fitting parameters from the measurement. The domain size d is to be understood as the average distance between two consecutive water parts. The correlation length ξ is a measure for the regularity of alternating domains. As indicated in Fig. 13.7 the peak position is mainly given by the domain size d, and the peak width is mainly given by the correlation length ξ. In comparison to diblock copolymers the forward scattering of microemulsions is clearly non-zero. Thermal fluctuations of oil and water can take place easily on large length scales while for the diblock copolymer the bond between the block makes sure that the polymer looks homogenous on large length scales. Many similarities to the polymeric microemulsions become visible (see Fig. 13.4) where the domains become less pure by raising the temperature or the domains even turn to fluctuations at temperatures above the phase boundary.

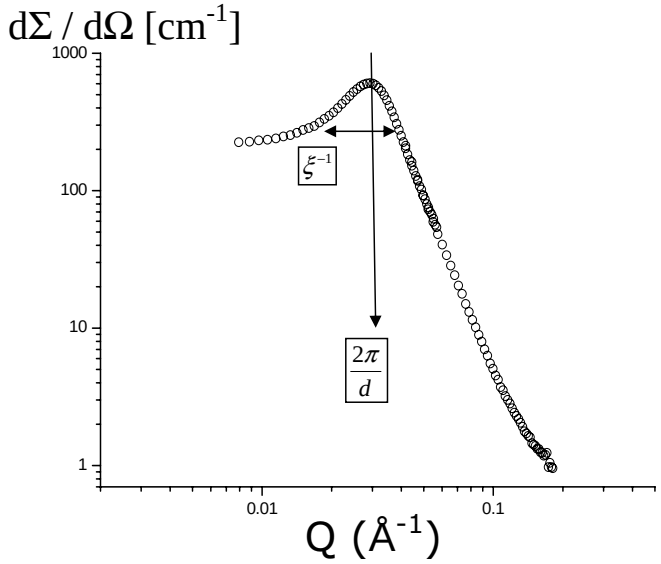

Figure 13.7: A typical scattering pattern of a bicontinuous microemulsion. The peak position is connected to the domain spacing *d*. The peak width is inversely proportional to the correlation length ξ. This kind of data is usually well described by the Teubner-Strey fitting function given in eq. 13.15.

While the structure is described by the concepts above, the thermodynamic properties of a microemulsion shall be discussed now. Phase diagram measurements and SANS measurements can be compared in a unique way. The Helfrich free energy assumes that the free energy of a microemulsion is dominated by the elastic properties of the surfactant film:

$$H = \int dS \left(\tfrac{1}{2} \kappa (c_1 + c_2)^2 + \bar{\kappa} c_1 c_2 \right) \tag{13.16}$$

The integral is conducted along the membrane surface. The two principal curvatures c_1 and c_2 are obtained by a tangential construction of two circles at each membrane point. The curvatures $c_i = 1/R_i$ are the reciprocal radii, and the two circles are perpendicular. The mean curvature $c_1 + c_2$ is connected with the first modulus, the bending rigidity κ. The Gaussian curvature $c_1 c_2$ is connected with the saddle splay modulus $\bar{\kappa}$. The moduli have the following dependence:

$$\begin{aligned} \frac{\kappa_R}{k_B T} &= \frac{\kappa_0}{k_B T} + 0.239 \cdot \ln \gamma + 0.214 \cdot \sigma (R_W^2 + R_O^2) \\ \frac{\bar{\kappa}_R}{k_B T} &= \frac{\bar{\kappa}_0}{k_B T} - 0.265 \cdot \ln \gamma - 0.167 \cdot \sigma (R_W^2 + R_O^2) \end{aligned} \tag{13.17}$$

The logarithmic spatial renormalization ($\ln \gamma$) lets the membrane appear flabbier on larger length scales. The connected intrinsic modulus (κ_0, $\bar{\kappa}_0$) is the extrapolated modulus for high surfactant contents ($\gamma \to 1$). The analytic theory of diblock copolymers [12] scales with the grafting density σ and the end-to-end distances R_{ee} of the oil- and water-soluble blocks. Please note, that for both moduli the correction terms are very similar except for the sign. As a rule of thumb, the saddle splay modulus $\bar{\kappa}_R$ is basically the negative value of the bending rigidity κ_R.

Now, both moduli are connected with experimentally accessible magnitudes. At the fish tail point of the phase diagram (see Fig. 13.5) the renormalized saddle splay modulus $\bar{\kappa}_R$ is a small constant, and, thus, changes of the minimal surfactant amount are connected with the polymer amount: $\Delta\bar{\kappa}_R / k_B T = -0.167 \cdot \sigma(R_W^2 + R_O^2) = +0.265 \cdot \Delta \ln \gamma$. In a real experiment the sensitivity $\hat{\Xi}$ (i.e. one coefficient) is measured besides the linear dependence, and, thus, $\Delta \ln \gamma = -\hat{\Xi} \cdot \sigma(R_W^2 + R_O^2)$. The bending rigidity is accessible through SANS experiments by the following trick: The Gaussian random field theory describes the statistics of a membrane by a random field, which defines the membrane at the zero of the random field. The fluctuations of the random field are controlled by a parameterized spectral density, which exactly has the appearance of eq. 13.15. In this way the structural parameters *d* and ξ are connected with the bending rigidity by $\kappa_R / k_B T = 0.85 \cdot \xi / d$. Again, the linear dependence is observed as a function of the scaled polymer amount by: $\Delta\kappa_R / k_B T = 0.85 \cdot \Delta(\xi / d) = \Xi \cdot \sigma(R_W^2 + R_O^2)$.

While this concept proved correct for amphiphilic diblock copolymers it remains to be tested for the newly synthesized sticker polymers. These polymers have only a short hydrophobic unit of 10 carbon atoms, and a polymeric hydrophilic block (90 ethylene oxide units). If all polymers are anchored at the surfactant membrane the same equations should hold, except for the oil soluble end-to-end distance, which simply can be set to zero. The obtained results are shown in Fig. 13.8. The dependencies are linear as predicted by the theory. The coefficients read $\hat{\Xi} = 1.64$ and $\Xi = 0.256$ which agrees exceptionally well with the coefficients of the diblock copolymers. This means, that the polymer boosting effect is successfully transferred to the new sticker polymers which are much easier to synthesize and therefore much cheaper to produce. This polymer is highly water soluble, which is important for formulations of powders. So this polymer is much better for applications than the initially well characterized diblock copolymer.

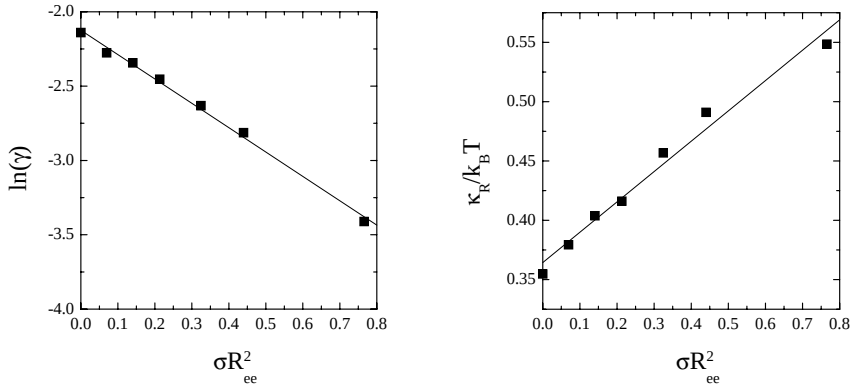

Figure 13.8: The minimum surfactant amount γ as a function of the scaled polymer amount $\sigma \cdot R_{ee}$ for microemulsions with increasing amount of a sticker polymer $C_{12}E_{90}$. The decrease shows that the microemulsion becomes more and more efficient, i.e. the polymer boosting effect is successfully transferred to sticker polymers. On the right the bending rigidity κ_R is plotted as a function of the scaled polymer amount. The increased bending rigidity explains why larger domain structures with a better surface to volume ratio can be formed. On a microscopic scale both diagrams are related through the Helfrich free energy. The polymer effect was described by Lipowsky.

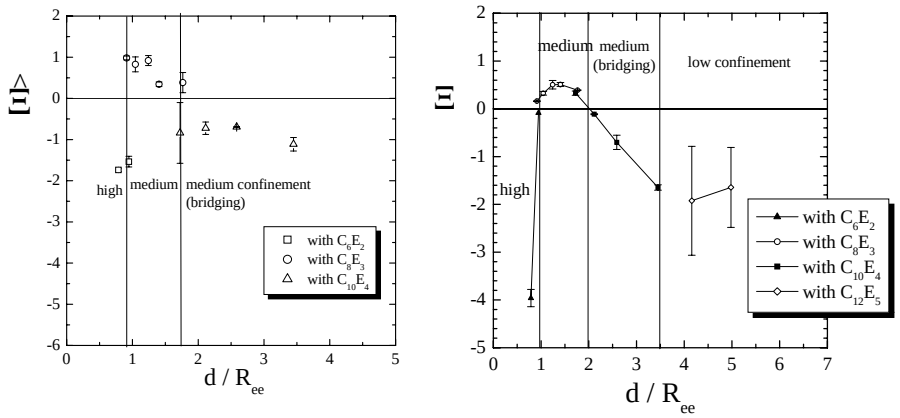

Figure 13.9: The sensitivities of the telechelic polymer on the phase diagram and the bending rigidity for different scaled domain sized d / R_{ee}. At low confinement (large d) a constant limit is reached (for Ξ). At medium confinement there is a region where bridging is continuously switched on (for Ξ) and a region where the sensitivity is almost constant. This constant sensitivity compares well with the confined diblock copolymer. At high confinement a reversed behaviour is found. For this degree of confinement homopolymers, diblock copolymers and telechelic polymers agree. The discontinuous change of $\hat{\Xi}$ at medium confinement might be interesting for applications.

Another aspect of possible additives is addressed with the telechelic polymer. This polymer has two hydrophobic end-groups at each end of the hydrophilic mid-block. So this polymer will connect two spots of the membrane, if both end-groups are anchored safely. This kind of connection can take place between neighbored points, or between opposite points, if the domains are small enough. For the full information of possible conformations, the domain size d has to be changed with respect to the end-to-end distance R_{ee} of the polymer. The sensitivities $\hat{\Xi}$ and Ξ of the saddle splay modulus and the bending rigidity are shown as a function of the scaled domain size d/R_{ee} in Fig. 13.9 (the reciprocal ratio R_{ee}/d can be also interpreted as a degree of confinement). At large domain sizes a constant value is reached (at least for Ξ). Here only neighbored membrane points should be connected, and the dependence on the domain size should vanish. At medium domain sizes a continuous change of Ξ indicates that more and more polymers bridge opposite membrane points. At even lower domain sizes a plateau value of Ξ is reached, which is comparable for diblock copolymers in the same stage (d/R_{ee}). For these medium domain sizes $\hat{\Xi}$ changes discontinuously from negative to positive values. So the bridging does not affect the saddle splay modulus continuously, but the plateau value at lower domain sizes is comparable to diblock copolymers as for Ξ. The plateau value is a sign of medium confinement without differentiating between bridging and connecting neighbored points, since telechelic polymers and diblock copolymers are similar. At the lowest domain sizes a reversed behavior is found. This high confinement stage is universal for homopolymers, diblock copolymers and telechelic polymers. Here the polymer is reflected by the membrane many times, and the anchoring does only play a minor role.

The sudden change of $\hat{\Xi}$ at medium domain sizes is directly connected to the phase behavior, and should be interesting for applications. When dilution of microemulsions plays a role in an industrial process, the polymer supports the emulsification for a concentrated system and a phase separation upon dilution. In metal processing often microemulsions are used, which are cleaned and phase separated after the process in order to be reused for another cycle. The telechelic polymer acts as an intelligent additive which reacts on the environment and supports special purposes. Other polymer architectures may bear many other important properties, which should be uncovered and made suitable for applications. Furthermore, the synthetic polymers mimic biological proteins on cell membranes. The basic research on synthetic polymers thus reveals also valuable information about the functions of biological attachments on membranes, such as the cytoskeleton. Many interesting results are about to come.

13.6 Summary

Many new interesting aspects appear, when certain polymers are added to either polymer blends or microemulsions. All these new polymers are A-philic and B-philic at certain parts, and the architecture can vary. The aim of the polymer additives is always to modify the overall miscibility of the components A and B. Furthermore, the domain size and shape can be influenced by the polymer additive. While the miscibility often can be studies by visual inspection - it is a macroscopic property - the detailed analysis of the nano-scale domain structure is performed best by scattering experiments. The more components are used in the final formulation the more important is the method of contrast variation. This method inevitably leads to neutron scattering. In this way basic research will support the tailoring of next-generation materials.

References

Text books:

[1] R.J. Roe, *Methods of x-ray and neutron scattering in polymer science*. Oxford University Press, Oxford 2000

[2] J.S. Higgins and H.C. Benoit, *Polymers and neutron scattering*. Clarendon Press, Oxford (1994)

IFF Spring Schools:

[3] 33. IFF-Ferienkurs 2002, *Soft Matter - Complex Materials on Mesoscopic Scales*, Schriften des Forschungszentrums Jülich, Jülich 2002

[4] 35th Spring School 2004, *Physics Meets Biology - From Soft Matter to Cell Biology*, Schriften des Forschungszentrums Jülich, Jülich 2004

[5] 38th Spring School 2007, *Probing the Nanoworld - Microscopies, Scattering and Spectroscopies of the Solid State*, Schriften des Forschungszentrums Jülich, Jülich 2007

[6] 22. IFF-Ferienkurs 1991, *Physik der Polymere*, Ferienkurse des Forschungszentrums Jülich, Jülich 1991 (written in German)

Articles:

[7] D. Schwahn *Adv. Polym. Sci.* **183**, 1 (2005)

[8] L. Leibler, *Macromolecules* **13**, 1602 (1980)

[9] V. Pipich, D. Schwahn, L. Willner *J. Chem. Phys.* **123**, 124904 (2005)

[10] H. Endo, M. Mihailescu, M. Monkenbusch, J. Allgaier, G. Gompper, D. Richter, B. Farago, T. Sottmann, R. Strey, I. Grillo, *J. Chem. Phys.* **115**, 580 (2002)

[11] D. Byelov, H. Frielinghaus, O. Holderer, J. Allgaier, D. Richter *Langmuir* **20**, 10433 (2004)

[12] C. Hiergeist, R. Lipowsky *J. Phys. II* **6**, 1465 (1996)

14

Polymer Dynamics

Dieter Richter

14. Polymer Dynamics

D. Richter

14.1 Introduction

In our every day life plastics or polymers play a very important role. Polymeric materials are used, because they are durable, cheaply to produce, easily to process and because they exhibit very versatile and favorable mechanical properties, e.g. depending on temperature or time the same polymer may be viscose, rubber elastic, very tough with high impact strength or even brittle. In the simplest case polymers are long linear chain molecules, build from one repeating unit, the monomer; such polymers are called linear homopolymers.

Since in general rotational isomers may be easily formed at each bond of the chain backbone, long chain polymers possess a very large number of internal degrees of freedom which contribute importantly to the entropic part of the molecules free energy. At length scales somewhat larger than the size of the monomer, the detailed chemical structure of the chain building blocks ceases to be of importance and very general properties determined by the statistical mechanics of the chains prevail, e.g. the conformational entropy follows from the number of possible arrangements of a chain sequence in space. According to the central limit theorem the most probable arrangement is that of a *Gaussian* coil, e.g. the polymer chain performs a random walk in space. If pieces of the chain are now stretched an entropic force arises and acts on these stretched segments endeavouring to restore them to the most probable contorted state. Such forces are the basis of rubber elasticity.

This lecture aims to identify general principles of chain motion on a molecular scale which underlie the macroscopic mechanical properties, and presents concepts and experimental results on these motional mechanisms in space and time. Thereby, we restrict ourselves to melts of homopolymers.

Neutron scattering with its space time sensitivity on a molecular and atomic scale unravels the details of the molecular motions in question. Commencing at the scale of the single bond, where movements take place at a pace as in normal liquids, quasielastic neutron scattering (QENS) provides insight into local relaxation processes. At longer length scales first the entropy driven Rouse motion and at even larger distances the effect of entanglement

constraints due to the mutual interpenetration of chains comes into the observation range. The most powerful technique suitable for these investigations, the neutron spin echo spectroscopy (NSE) operates in the time domain and uncovers a time range from about *2ps* to *200ns* and accesses momentum transfers between 0.01Å^{-1} and 3Å^{-1}. The second important high resolution technique is neutron backscattering providing an energy resolution of about $1\mu eV$ and covering a Q-range $0.1 \le Q \le 2\text{Å}^{-1}$.

This lecture naturally is not able to review exhaustively the contribution of high resolution neutron scattering to the field of polymer melt dynamics, but rather wants in an exemplary way to display important contributions by example. First in Chapter 2 we will discuss neutron results on the local chain dynamics, addressing self and pair correlation functions. These experiments are of importance in connection with the glass transition in polymer melts. Then in Chapter 3 we deal with the entropy driven dynamics, the Rouse motion. Chapter 4 discusses the large scale chain motion eluding to the reptation process and Chapter 5 finally concludes this lecture.

14.2 Local dynamics

The classical relaxation processes in polymers, the α- and β-relaxations, have been studied since more than 50 years by spectroscopic techniques, like dielectric spectroscopy, mechanical spectroscopy and NMR. Fig.14.1 displays a typical outcome of such experiments for the case of polybutadiene (PB) $[\text{-C}_4\ \text{H}_6\text{-}]_n$. The dominant relaxation process, the α-relaxation, is related to the macroscopic flow and freezes at a finite temperature, the glass transition temperature T_g. Aside from this process a secondary relaxation, β_{slow}, departs from the α-relaxation at a temperature about 20% above T_g. This relaxation displays an Arrhenius behaviour and passes unchanged through the glass transition.

As already mentioned, the α-relaxation is behind the viscous flow of polymers. Its relaxation function may be phenomenologically described by a stretched exponential

$$\phi_\alpha(t) = \exp\left\{-\left(\frac{t}{\tau_{KWW}}\right)^{\beta}\right\} \tag{14.1}$$

τ_{KWW} is the Kohlrausch-William-Watts relaxation time and $\beta < 1$ the stretching exponent. τ_{KWW} in good approximation follows a Vogel-Fulcher temperature dependence.

$$\tau_{KWW}(T) \approx \exp\left\{\frac{A}{T - T_0}\right\} \tag{14.2}$$

The temperature offset in the denominator of the exponent leads to a divergence of τ_{KWW} at T_0, a temperature below T_g which, however, may never be reached in equilibrium.

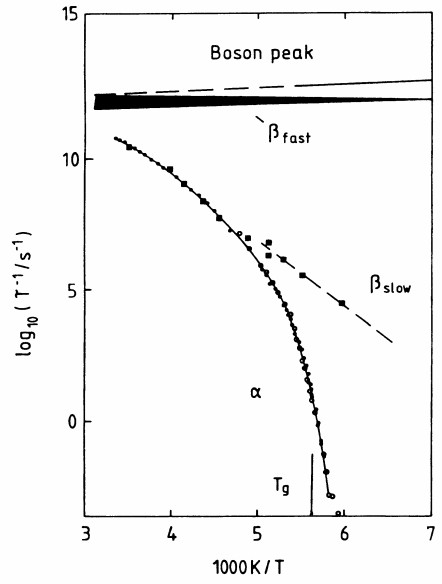

Figure 14.1: Relaxation landscape of PB. α and β_{slow} correspond to the classical relaxation processes and are treated here.

The dielectric β-relaxation is considered to be a result of a partial reorientation of the molecular dipoles in the substance. It is interpreted as a local activated process, where the dipole hops between two positions separated by an activation energy E. The relaxation time follows an Arrhenius behaviour

$$\tau_\beta(E) = \tau_0^\beta \exp\left[\frac{E}{k_B T}\right] \tag{14.3}$$

due to the disorder in the material the activation energies E are distributed around an average value E_0. For the distribution function in general a *Gaussian* is assumed.

$$g(E) \approx \exp\left\{-\left(\frac{E-E_0}{\sigma}\right)^2\right\} \tag{14.4}$$

Empirically it is found that the width $\sigma(T)$ decreases with increasing temperature. Though such processes have been investigated well by spectroscopic techniques, their molecular origin is still unclear. Here QENS with its ability to provide space time resolution on the proper scales contributes to a further exploration of the molecular mechanisms behind these relaxations.

14.2.1 Dynamic structure factors

We commence with the derivation of the dynamic structure factor for the β-process which we consider as a hopping process between two adjacent sites. For such a process the self correlation function has been derived in the lecture on quasielastic scattering, it is given by a sum of two contributions.

$$S_s(Q,t) = \frac{1}{2}\underbrace{\left[1+\frac{\sin(Qd)}{Qd}\right]}_{S^{el}} + \frac{1}{2}\underbrace{\left[1-\frac{\sin(Qd)}{Qd}\right]}_{S^{inel}} \exp\left(-\frac{2t}{\tau(E)}\right) \tag{14.5}$$

Here d is the distance between the two sites and $\tau(E)$ is the jump time corresponding to an activation energy E. The complete scattering function is obtained in averaging Eq.[14.5] with the barrier distribution function $g(E)$ obtained e.g. by dielectric spectroscopy. The Q-dependence of the two contributions to Eq.[14.5] is displayed in Fig.14.2 as a function of Q (d = 1.5Å). From the oscillation of both contributions with Q the jump distance may be obtained. The associated time scale may be found from the time decay of the inelastic part.

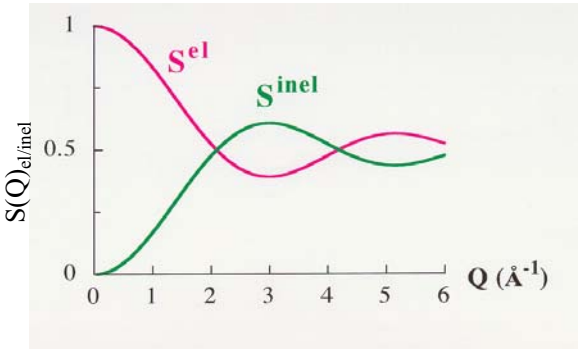

Figure 14.2: Elastic and inelastic contribution to the incoherent scattering function for jump motion between two site. The Figure assumes a jump distance of 1.5Å.

The associated pair correlation function is more difficult to obtain, since now we have to deal with a change of configurations of atoms rather than with single atom jumps. The conceptual difference between the pair and the self correlation function for jump processes may be visualized most easily considering rotational jumps. Let us regard e.g. the 120° rotational jumps of a methyl group around its symmetry axis. An incoherent study would reveal the atomic jumps of the associated hydrogens. The pair correlation function reflects the change of atomic configurations before and after the jump. Since a 120° jump does not change the configuration, a coherent scattering experiment would not reveal anything.

Back to the pair correlation function for the β-process, where we will introduce a simple approximation. We know that for $t = 0$ the pair correlation function is reflected by the static structure factor $S(Q)$. Therefore for $t = 0$ the corresponding pair correlation function for the β-process must reveal $S(Q)$. We now assume that the inelastic scattering is related to uncorrelated jumps of the different atoms. Then all interferences for the inelastic process are destructive and the inelastic form factor should be identical to that of the self correlation function. For the normalized dynamic structure factor for the β-process we arrive at

$$\frac{S(Q,t)_\beta}{S(Q)} = \left\langle \frac{S(Q) - S_{\cdot}^{inel}(Q)}{S(Q)} + \frac{S^{inel}(Q)}{S(Q)} e^{-2t/\tau(E)} \right\rangle_{g(E)} \qquad (14.6)$$

This incoherent approximation does not reveal e.g. symmetry related cancellations, but displays a major feature of the corresponding dynamic structure factor, namely the relative suppression of the inelastic contributions from local jump processes at the maximum of the structure factor. Fig.14.3 displays the situation for polybutadiene. There a β-process corresponding to a jump length of d = 1.5Å has been found. The corresponding inelastic dynamic structure factor is strongly reduced at the position of the first peak, while it contributes strongly at higher Q. Fig.14.3 suggests a Q selectivity for the different relaxation processes: at the structure factor maximum local jump processes should not contribute and the relaxation due to flow should dominate. On the other hand at larger Q, in particular in the minimum of the structure factor, the secondary relaxation should reveal itself.

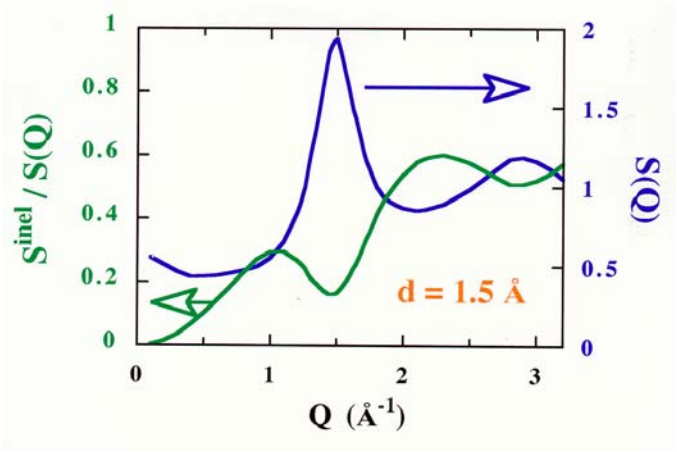

Figure 14.3: Static structure factor $S(Q)$ and normalized inelastic contribution $\frac{S_{inel}}{S(Q)}$ to $S(Q,\omega)/S(Q)$ for PB.

We now assume that the α- and the β-relaxation are statistically independent. Then, in real space the joint correlation function is given by a convolution of the corresponding functions for both separated processes. In Q-space this convolution becomes a product and we may write the total scattering function as a product of the structure factor due to the α- and β-processes.

$$\frac{S(Q,t)}{S(Q)} = S^{\alpha}(Q,t)\,S_{\beta}(Q,t)/S(Q) \tag{14.7}$$

The approximation behind Eq.[14.7] is called Vinyard approximation and approximates the proper pair correlation function by its self counter part. The self correlation function for a diffusive process relates directly to the mean square displacement.

$$S^{self}(Q,t) = \exp\left\{-\frac{Q^2}{6}\left\langle r^2(t)\right\rangle\right\} \tag{14.8}$$

where $\left\langle r^2(t)\right\rangle$ is the mean square displacement of the flowing particle. According to Eq.[14.1] this should be described by a stretched exponential with the consequence

$$\left\langle r^2(t)\right\rangle = \tilde{D}\ t^{\beta}$$

and

$$\tau_{KWW} = Q^{2/\beta}\tilde{D}^{-1/\beta} \tag{14.9}$$

the combination of Eq.[14.8] and [14.9] invokes sublinear diffusion of the polymer segments as the underlying reason for the stretched exponential behaviour. Its signature is a power law dependence of the Kohlrausch-William-Watts relaxation times τ_{KWW} with an exponent *2/β*.

14.2.2 Experimental results

14.2.2.1 Self correlation function

We commence with the secondary relaxation taking polyisobutylene as an example. Fig.14.4 presents the relaxation map of PIB. The solid line corresponds to the dielectric *β*-relaxation, the dashed line named *δ* represents NMR results interpreted as a methyl group rotation. *γ* and *γ'* are theoretically predicted relaxation mechanisms. In the dynamic regime, where the α-relaxation is too slow to contribute, neutron backscattering has been employed, in order to unravel details of the *β*-process in this polymer. Fig.14.5 presents as an example a spectrum taken at T = 270K and Q = 1.7Å^{-1}. The spectrum is characterized by a narrow peak, which nearly coincides with the instrumental resolution function (dashed line) and a broad foot revealing the relaxational behaviour. Such a spectral shape is typical for broad distributions of relaxation times, where only a part of it is resolved in the spectrum.

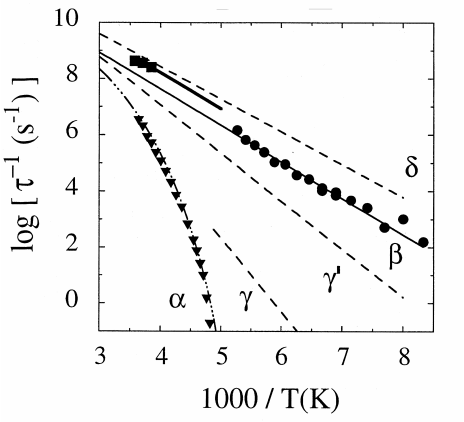

Figure 14.4: Relaxation map for PIB. ▼ marks the α-trace, ● relates to dielectric relaxation experiments on the β-relaxation, ■ results from QENS-experiments.

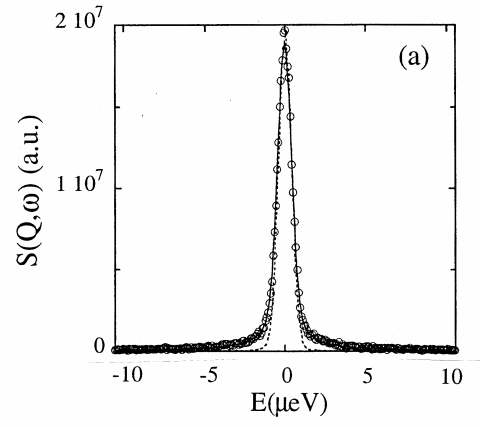

Figure 14.5: Backscattering spectrum from PIB at 270K at a Q-value Q = 1.7Å. The dashed line gives the resolution function, while the solid line displays the fit with the model (see text).

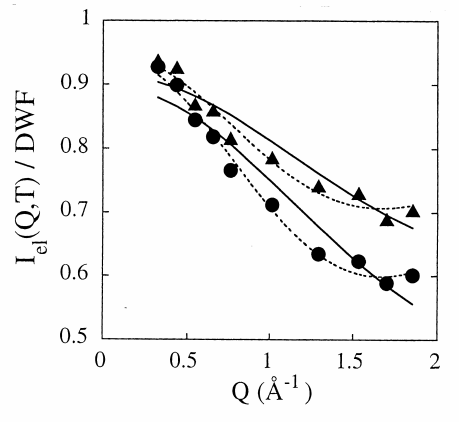

Figure 14.6: EISF for PIB (▲: 250K, ●: 270K). Solid lines: EISF for methylgroup rotation, dashed lines: fit result for a jump distance d = 2.7Å.

Fig.14.6 displays the elastic intensity observed for PIB as a function of Q. The data were corrected for multiple scattering and fitted with Eq.[14.5]. This elastic incoherent structure factor (EISF) (see lecture Quasielastic Scattering) reveals a jump distance d = 2.7Å. For comparison the solid lines display the prediction for methyl group rotation, which was invoked by NMR spectroscopy. Obviously the neutron data point into the direction of a larger motional amplitude.

The squares in Fig.14.4 display the neutron results for the β time scale. Within a factor of 2 they agree with the dielectric spectroscopy results. Since the underlying process has an amplitude of 2.7Å and is also dielectrically active, it cannot be understood as due to a methylgroup rotation alone. A possible interpretation is a combined backbone and methyl motion which is also supported by simulation results.

We now turn to the α-relaxation and ask, whether the sub linear diffusion argument is supported by quasielastic neutron scattering. Fig.14.7 displays Kohlrausch-William-Watts relaxation rates obtained for four different polymers, polyvinylether (PVE) at 340K, polyisobutylene (PIB) at 365K, polybutadiene (PB) at 280K and polyisoprene (PI) at 340K.

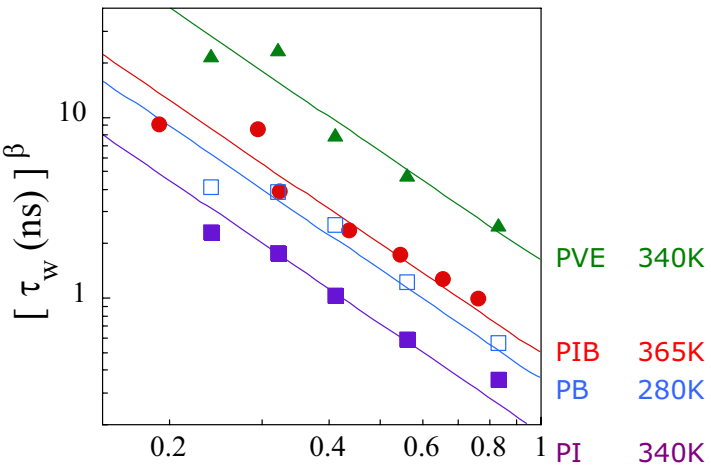

Figure 14.7: $(\tau_{KWW})^{\beta}$ for 4 different polymers as a function of Q. The solid lines display a Q^2 power law.

In order to test Eq.[14.9] the relaxation rates have been exponentiated with the exponent β, obtained from the stretching of the relaxation functions in these polymers in dielectric spectroscopy. According to Eq.[14.9], τ^{β} should be proportional to Q^2. The solid lines in Fig.14.7 display this power law relation. As may be seen, in all cases within experimental error the experimental relaxation times again obtained by backscattering spectroscopy follow the predicted power law behaviour. Thus, the experimental evidence supports a sub linear diffusion process as underlying the α-relaxation. We remark that this result is in disagreement with assertions that the stretched exponential relaxation function of the α-process originates from heterogeneous motional processes, where polymer segments in different parts of the sample would relax at different relaxation rates.

14.2.3 Pair correlation function

The dynamic pair correlation function for polymer relaxation has been studied thoroughly on polybutadiene as a function of temperature and momentum transfer. Fig.14.8 gives a synopsis of these results. The dynamic data presented have been taken at the positions of the first and second peaks in the static structure factor of this polymer. As may be seen from the middle part of Fig.14.8 the first peak of the static structure factor moves strongly with temperature. This peak originates from interchain correlations, where weak v. d. Waals interactions lead to thermal expansion. The second peak relates mainly to intrachain correlations as may be seen from the temperature independence of its position indicative for covalent bonds. The temperature dependent relaxation spectra were rescaled in their time dependence with the characteristic time for viscosity relaxation τ_{η} (actually the time dependent monomeric friction coefficient was used, see next paragraph). By this procedure the time correlation functions at the first peak assemble to a master curve, showing that the dynamics at the interchain distance follows the same relaxational behaviour as the macroscopic flow. On the other hand as evidenced by the lower part of Fig.14.8 at the second structure peak, such a scaling does not reassemble the data points to a master curve. Obviously the dynamics at the second peak at higher Q follows different dynamics.

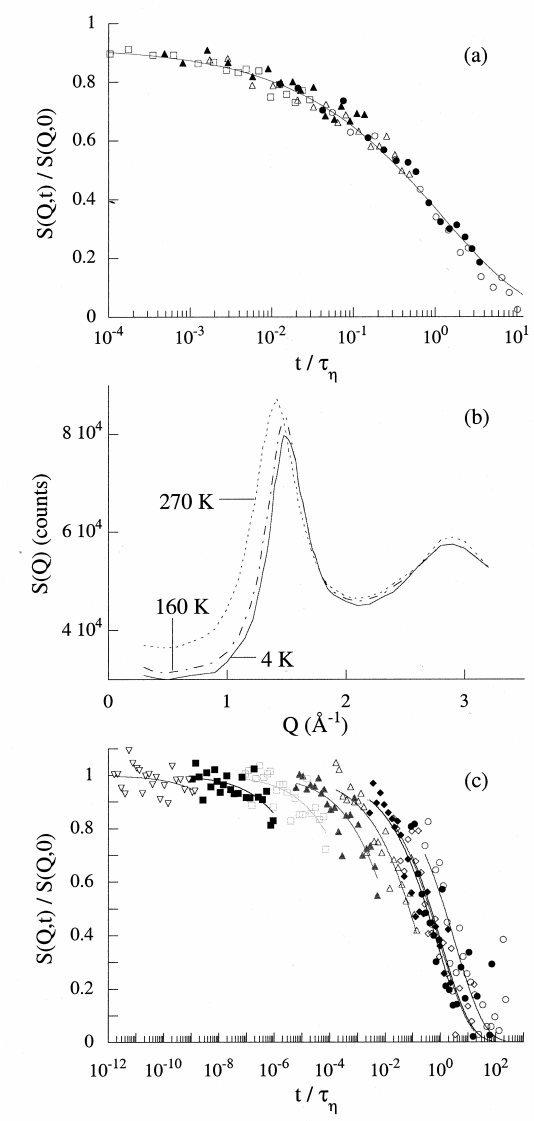

Figure 14.8: NSE spectra from PB taken at the first and second structure factor peak. The time is rescaled with the temperature dependence from flow relaxation. Center: $S(Q)$ for different temperatures.

Fig.14.9 displays the temperature dependence of the corresponding relaxation rates. While the data at the first peak nicely agree with the temperature dependence of the α-relaxation, as already evidenced by the scaling, the relaxation rates taken at the second peak follow an

Arrhenius temperature dependence with a same activation energy as that of the corresponding dielectric β-process.

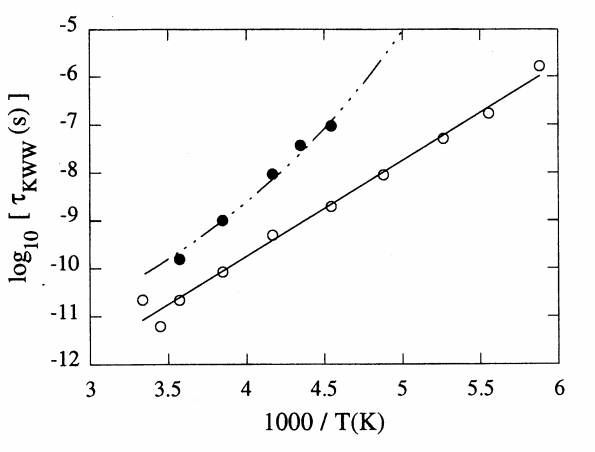

Figure 14.9: Relaxation rates at the first and second structure factor peak of PB in an Arrhenius representation. Solid lines: α- and β traces for this polymers.

An evaluation of the structure factor following Eq. [14.6] and [14.7] reveals a jump distance for the β-process of d = 1.5Å. It also shows that the assumption of statistically independent α- and β-relaxations is supported by the temperature and momentum transfer dependent spectra.

14.3 Entropy driven dynamics – the Rouse regime

As outlined in the introduction, the conformational entropy of a chain acts as a resource for restoring forces for chain conformations, deviating from thermal equilibrium. In this Chapter we deal with these entropy driven dynamics in terms of the Rouse model and present NSE results on the space-time evolution of the Rouse relaxation and finally discuss recent molecular dynamic simulations which have been performed in parallel to NSE experiments, in order to explore the limits of the Rouse picture.

14.3.1 Entropic forces – the Rouse model

As the simplest model for chain relaxation, the Rouse model considers a Gaussian chain in a heat bath. The building blocks of such a *Gaussian* chain are segments consisting of several monomers, so that their end to end distance follows a Gaussian distribution. Their conformations are described by vectors $\underline{a}_n = \underline{r}_n - \underline{r}_{n+1}$ along the chain. Thereby $\underline{r}_n$ is the position vector of the segment *"n"*. The chain is described by a succession of freely connected segments of length ℓ. We are interested in the motion of these segments on a length scale

$\ell < r < R_e$, where $R_e^2 = n\,\ell^2$ is the end to end distance of the chain. The motion is described by a Langevin equation

$$\zeta_0 \frac{d\underline{r}_n}{dt} = \nabla_n F\left(\underline{r}_n\right) + \underline{f}_n(t) \ , \tag{14.10}$$

where ζ_0 is the monomeric friction coefficient. For the stochastic force $\underline{f}_n(t)$ we have $\left\langle \underline{f}_n(t) \right\rangle = 0$ and $\left\langle f_{n\alpha}(t) f_{m\beta}(0) \right\rangle = 2k_B T \ \zeta_0 \delta_{nm} \delta_{\alpha\beta} \delta(t-t')$ α, and β denote the Cartesian components of $\underline{r}$. $F(\underline{r}_n)$ is the free energy of the polymer chain. The force term in Eq.[14.10] is dominated by the conformational entropy of the chain

$$S = k_B \ell n \ W\left(\{\underline{r}_n\}\right)$$

where $W\left(\{\underline{r}_n\}\right)$ is the probability for a chain conformation $\{\underline{r}_n\}$ of a Gaussian chain of *n*-segments.

$$W\left(\{\underline{r}_n\}\right) = \prod_{i=1}^{N} \left\{\frac{3}{2\pi \ \ell^2}\right\}^{3/2} \exp\left\{\frac{-3\ \left(\underline{r}_i - \underline{r}_{i-1}\right)^2}{2\ell^2}\right\} \tag{14.11}$$

With the boundary conditions of force free ends Eq.[14.10] is readily solved by cosine Fourier transformation, resulting in a spectrum of normal modes. These solutions are similar to e.g. the transverse vibrational modes of a linear chain except that relaxational motions are involved instead of periodic vibrations. The dispersion of the relaxation rates $1/\tau_p$ is quadratic in the number of knots *p* along the chain.

$$\frac{1}{\tau_p} = \frac{3k_BT}{\zeta_0 \ell^2}\frac{\pi^2}{N^2}p^2 = W\frac{\pi^2}{N^2}p^2 = \frac{p^2}{\tau_R}\ , \tag{14.12}$$

where τ_R is the Rouse time - the longest time in the relaxations spectrum – and W is the elementary Rouse rate. The mode correlation function for the Rouse modes is obtained as

$$\left\langle x_p^\alpha(t) \quad x_q^\beta(0)\right\rangle = \delta_{\alpha\beta}\delta_{pq}\frac{N\ell^2}{6\pi^2 p^2} \quad \exp\left(-t/\tau_p\right) \tag{14.13}$$

$$\left\langle x_0^\alpha(t) \quad x_0^\beta \quad (0)\right\rangle = \delta_{\alpha\beta}\frac{2k_BT}{N\zeta_0}t$$

Thereby x_p^α is the α-component of the number p normal mode and x_0^α is the centre of mass coordinate. In order to study Brownian motion, the segment correlation functions in the real space $\Delta r_{nm}^2(t) = \left\langle \left(r_m(t) - r_n(0)\right)^2 \right\rangle$ are required. They are obtained by retransformation of the normal coordinates leading to

$$\Delta r_{nm}^2(t) = 6D_R t + |n-m| \quad \ell^2$$
$$+\frac{4N\ell^2}{\pi^2}\sum_{p=1}^{N}\ \frac{1}{p^2}\cos\ \left(\frac{p\pi\ \ m}{N}\right)\cos\ \left(\frac{p\pi\ \ m}{N}\right)\left(1-\exp\ \left(-\frac{p^2 t}{\tau_R}\right)\right) \tag{14.14}$$

in Eq.[14.14] we use the fact that the mean square displacement of the centre of mass provides the diffusion constant. For the special case of the self correlation function *(n = m)* $\Delta r_{nn}(t)$ reveals the mean square displacement of a polymer segment. We obtain

$$\Delta r_{nn}^2(t) = 2\ell^2\left(\frac{3k_BTt}{\pi\zeta_0\ell^2}\right)^{1/2} \tag{14.15}$$

In contrast to normal diffusion Δr_{nn}^2 does not grow linearly, but with the square route of time. For the translational diffusion coefficient $D_R = k_BT/N\zeta_0$ is obtained. D_R is inversely proportional to the number of friction performing segments.

By means of neutron scattering two different correlation functions may be accessed. In the case of coherent scattering, all partial waves emanating from different scattering centres are capable of interference – the *Fourier* transform of the pair correlation function of a single chain is measured. In contrast incoherent scattering, where the interferences from partial waves of different scatterers are destructive, measures the self correlation function. The self correlation function leads directly to the mean square displacement of the diffusing segments. In Gaussian approximation for $t < \tau_R$ we have

$$S_{inc}(Q,t) = \exp\left\{-\frac{2}{\sqrt{\pi}}\left(\frac{k_B T \ell^2}{12\zeta_0} Q^4 t\right)^{1/2}\right\} \tag{14.16}$$

in the case of coherent scattering, which observes the pair correlation function, interferences from scattering waves emanating for various segments complicate the scattering function. With Eq.[14.14] we obtain

$$S(Q,t) = \frac{1}{N}\exp\left[-Q^2 D_R t\right] \sum_{n,m}\exp\left\{-\frac{1}{6}|n-m|\ Q^2\ell^2\right\} \tag{14.17}$$

$$-\frac{2}{3}\frac{R_E^2 Q^2}{\pi^2}\sum_p \frac{1}{p^2}\left\{\cos\left(\frac{p\pi\ m}{N}\right)\cos\left(\frac{p\ \pi n}{N}\right)\left(1-\exp\left(-\frac{tp^2}{\tau_R}\right)\right)\right\}$$

for small Q ($QR_E < 1$) the second and third terms are negligible and $S(Q,t)$ describes the centre of mass diffusion of the chain.

$$S(Q,t) = N\ \exp\left(-D_R t\right) \tag{14.18}$$

For $QR_E > 1$ and $t < \tau_R$ the internal relaxations dominate. Converting the sums in Eq.[14.17] to integrals and after some algebra de Gennes has derived an expression for the dynamic structure factor.

$$S(Q,t) = \frac{12}{Q^2\ell^2}\int_0^\infty du \;\exp\left\{-u - (\Omega_R t)^{1/2}\, h\left(u(\Omega_R t)^{-1/2}\right)\right\} \tag{14.19}$$

$$h(y) = \frac{2}{\pi}\int_0^\infty dx\, \frac{\cos(xy)}{x^2}\left(1-\exp\left(-x^2\right)\right)$$

We observe that in spite of the complicated functional form *S(Q,t),* like the self correlation function, only depends on one variable, the Rouse variable.

$$(\Omega_R t)^{1/2} = \frac{Q^2}{6}\sqrt{\frac{3k_B T\ell^2 t}{\zeta_0}} = \frac{Q^2\ell^2}{6}\sqrt{Wt} \tag{14.20}$$

Since there is no length scale in the problem, for different momentum transfers the dynamic structure factors are predicted to collapse to one master curve, if they are represented as a function of the Rouse variable.

14.3.2 Neutron spin echo results

The self correlation function of a Rouse chain was first observed on polydimethylsiloxane (PDMS). Since a straight forward study of the incoherent scattering by NSE is very difficult – due to spin flip scattering a severe loss of polarization occurs leading to very weak signals – the measurements of the self correlation function were performed on high molecular weight deuterated PDMS chains which contained short protonated labels at random positions. In such a sample the scattering essentially originates from the contrast between the protonated sequence and a deuterated environment and therefore is coherent. On the other hand the sequences are randomly distributed, so that there is no constructive interference of partial waves arising from different sequences. Under these conditions the scattering experiments measures the self correlation function.

In Fig.14.10 the corresponding NSE spectra are plotted against the scaling variable of the Rouse model. The results for the different momentum transfers follow a common straight line. In Gaussian approximation for the case of the self correlation function the scattering function directly measures the mean square segment displacement, which according to Eq.[14.15] obeys a square root law in time. This behaviour may be directly read off from Fig.14.10.

The pair correlation function arising from the segment motion within one given chain is observed, if some protonated chains are dissolved in a deuterated matrix. Fig.14.11 displays the observed spectra from polyethylethylene (90% dPEE, 10% hPEE) at a molecular weight of M_W = 20.000. The solid lines give the prediction of the dynamic structure factor of Eq.[14.19]. Obviously very good agreement is achieved.

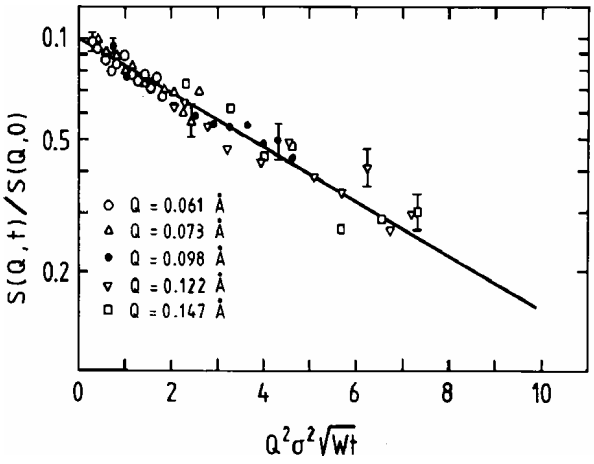

Figure 14.10: Self correlation for a PDMS melt T = 100C. The data at different momentum transfers are plotted us the scaling variable of the Rouse model ($\sigma \equiv \ell$).

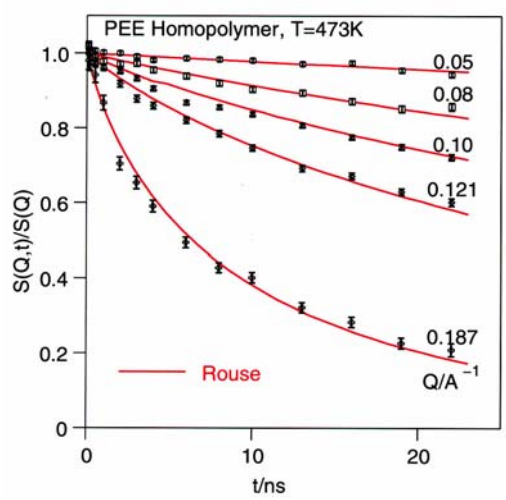

Figure 14.11: Single chain structure factor from a PEE melt at 473K. The solid lines represent a joint fit with the Rouse model.

We now use these data, in order to investigate the scaling prediction inherent in Eq.[14.19]. Fig.14.12 presents a plot of the data of Fig.14.11, now as a function of the Rouse scaling variable (Eq.[14.20]).

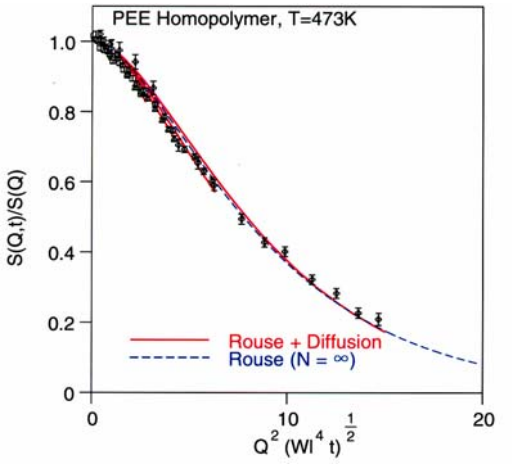

Figure 14.12: Single chain structure factor from PEE melts as a function of the Rouse scaling variable.

The data follow with satisfying precision the scaling prediction. The small deviations are related to the translational diffusion of the chains. This becomes evident from Fig.14.13, where the obtained relaxation rates $\Gamma(Q)$ are plotted versus Q in a double logarithmic fashion.

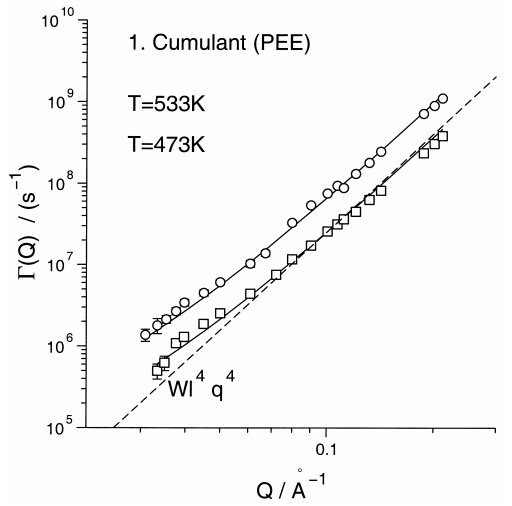

Figure 14.13: Relaxation rates from PEE melts vs. Q for two different temperatures.

The dashed line gives the Rouse prediction $\Gamma \propto W\ell^4 Q^4$. While at larger momentum transfers the experimental results follow very well this prediction, towards lower Q, a systematic relative increase of the relaxation rate is observed. Including the diffusion, we have

$$\Gamma(Q) = Q^2 \left[D + Q^2 \frac{W\ell^4}{6} \right] \tag{14.21}$$

the solid lines in Fig.14.13 represents the prediction of Eq.[14.21]. Perfect agreement is obtained.

14.3.3 Computer simulation

In order to learn about the limits of the Rouse model, recently a detailed quantitative comparison of molecular dynamics (MD) computer simulations on a 100 C-atom polyethylene chain (PE) with NSE experiments on PE chains of similar molecular weight has been performed. Both, the experiment and the simulation were carried out at T = 509K. Simulations were undertaken, both for an explicit *(ea)* as well as for an united *(ua)* atom model. In the latter the *H*-atoms are not explicitly taken into account but reinserted when calculating the dynamic structure factor. The potential parameters for the MD-simulation were either based on quantum chemical calculations or taken from literature. No adjusting parameter was introduced. Fig.14.14 compares the results from the MD-simulation (solid and broken lines) with the NSE-spectra. The time axis thereby is scaled with the centre of mass diffusion coefficient, in order to correct for the slightly different overall time scales of experiment and simulation. From Fig.14.14 quantitative agreement between both results is evident. Fig.14.15 compares the same experimental data, which agreed quantitatively with the simulations with a best fit to the Rouse model (Eq.[14.17]. Here a good description is observed for small Q-values ($Q \leq 0.14$Å^{-1}), while at higher Q important deviations appear. Similarly also the simulations cannot be fit in detail with a Rouse structure factor.

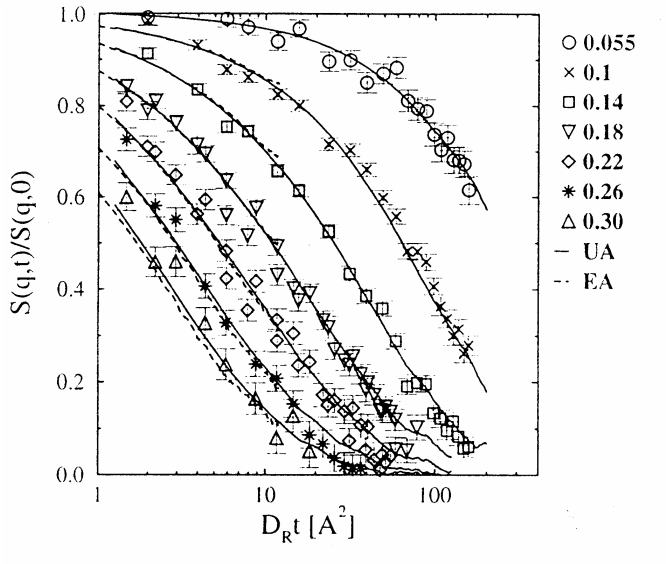

Figure 14.14: NSE data from PE melts vs. computer simulations (see text).

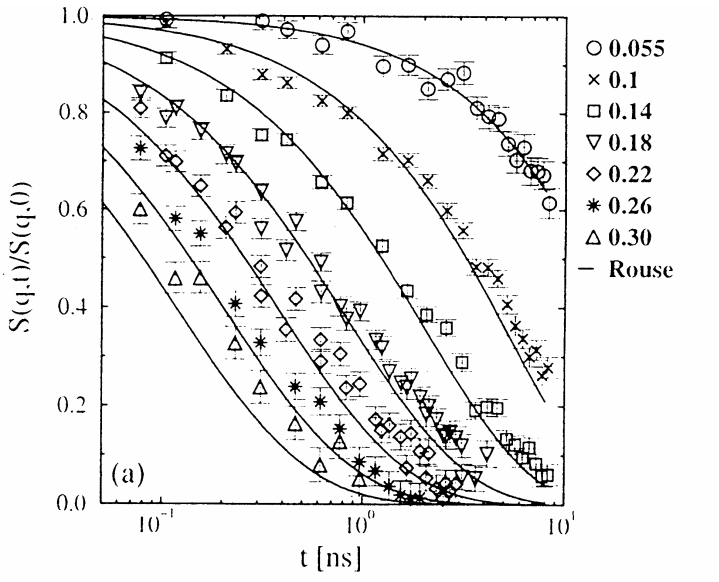

Figure 14.15: NSE data from PE melts in comparison to a best fit with the Rouse model (see text).

Having obtained very good agreement between experiment and simulation, the simulations which contain complete information about the atomic trajectories may be further exploited, in order to rationalize the origin for the discrepancies with the Rouse model. A number of deviations evolve.

1. According to the Rouse model the mode correlators (Eq.[14.13] should decay in a single exponential fashion. A direct evaluation from the atomic trajectories shows that the 3 contributing Rouse modes decay with stretched exponentials displaying stretching exponents β of *(1:$\beta = 0.96$ and 2,3:$\beta = 0.86$)*

2. A detailed scrutiny of the *Gaussian* assumption (see e.g. (Eq.[14.16] and [14.17]) reveals that for $t < \tau_R$ deviations occur.

3. While the Rouse model predicts a linear time evolution of the mean squared centre of mass coordinate (Eq.[14.17]), within the time window of the simulation *($t < 9ns$)* a sublinear diffusion in form of a stretched exponential with the stretching exponent of $\beta = 0.83$ is found. A detailed inspection of the time dependent mean squared amplitudes reveals that the sublinear diffusion mainly originates from motions at short times $t < \tau_R = 2ns$.

The prediction of a time dependent centre of mass diffusion coefficient has recently been corroborated by NSE-experiments on short chain polybutadienes. Fig.14.16 displays the mean square centre of mass displacement from simulation compared to the same quantity obtained from the dynamic structure factor at various *Q*-values. Both the simulation as well as the experimental data consistently lead to a weaker than linear time dependence of the mean square centre of mass displacement.

The overall picture emerging from this combined simulational and experimental effort is, that for chains, which should be ideal Rouse chains, the model is capable of quantitatively describing the behaviour only on time scales of the order of the Rouse time or larger and therefore on length scales of the order of the radius of gyration of the chains or larger and in the regime, where the chains actually show Fickian diffusion. The self diffusion behaviour for times smaller than the Rouse time and the relaxation of the internal modes of the chains show

small but systematic deviations from the Rouse prediction. The origin of these discrepancies are traced to interchain interactions.

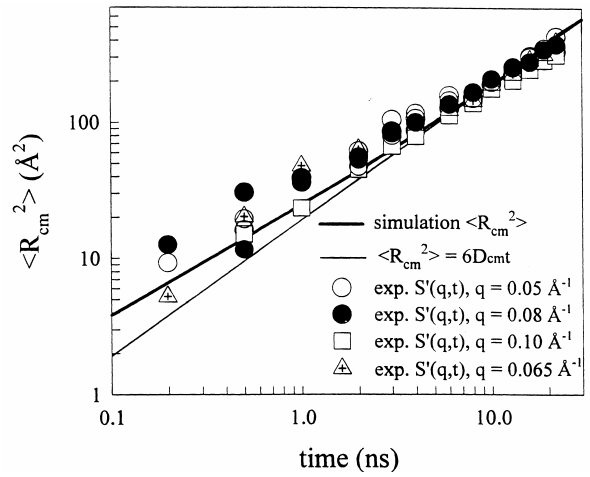

Figure 14.16: Mean square center of mass displacement for PB chains in the melt obtained from $\left\langle r^2(t)\right\rangle = -\frac{6}{Q^2}\,\ell n\, S(Q,t)$. Solid line: simulation result; dashed line $\left\langle r^2(t)\right\rangle = D_e t$.

14.4 Topological interactions - Reptation

The reptation model of de Gennes, Doi and Edwards proceeds from the intuitive concept that the motions of a chain in a melt are heavily impeded in directions lateral to their own profile by the other chains encircling them. The dominant diffusive motion proceeds along the chain profile. A chain twists and turns through a melt like a snake. The lateral restrictions are modelled by a tube with a diameter *d*, parallel to the chain profile, whereby *d* relates to the plateau modulus of the melt. The restrictions of the motion through other chains are not effective on a monomer scale, but rather permits lateral excursions on intermediate length scales *(d ≅ 50....Å)*. The experimental observations for viscosity and diffusion can be made directly comprehensible in this simple intuitive model.

As it concerns the motion of an individual polymer, large scale lateral diffusion is quenched during the life time τ_d of the tube constrains. Initially for short times the chain relaxes according to the Rouse picture until the mean square displacement reaches about the tube

diameter *d*. At that time (τ_e) the chain has explored the lateral confinement $\tau_e \cong \frac{N_e^2}{\pi^2} W$; with ($d^2 = N_e \ell^2$). For longer times $t \leq \tau_R$ the Rouse modes relax along the tube (local reptation). Thereafter longitudinal creep governed by the Rouse diffusion coefficient D_R along the tube dominates. This process takes place until the chain has left its original confinement at a time $\tau_d \cong \frac{1}{W} N^3$. Beyond that time normal diffusion takes over.

For the mean square segment displacement the reptation mechanism invokes a sequence of power laws in the time variable. For short times $t < \tau_e$ Rouse motion prevails and $\Delta r^2 \propto t^{1/2}$ holds. Then in the regime of local reptation we deal with Rouse modes occurring along a contorted Gaussian tube. The segment displacement along the tube follows a $t^{1/2}$ law, in real space considering the random walk nature of the tube, this transforms to a $t^{1/4}$ law. After all Rouse modes have relaxed, Rouse diffusion along the contorted tube takes place. A similar argument as before leads to a power law $\Delta r^2 \propto t^{1/2}$ and only for times longer than τ_d, the lifetime of the tube constraints, $\Delta r^2 \propto t$ holds.

The tube constraints also provoke a strong retardation for the single chain relaxations causing a near plateau regime in the time dependent single chain correlation function. Neglecting the initial free Rouse process de Gennes has formulated a tractable expression for the dynamic structure factor which is valid for $t > \tau_e$, i.e. once confinement effects become important. In the large *Q* limit the dynamic structure factor assumes the form

$$\frac{S(Q,t)}{S(Q,0)} = \left\{ 1 - \exp\left[-\left(\frac{Qd}{6} \right)^2 \right] \right\} \exp\left(t/\tau_0 \right) \; erfc\left(\sqrt{t/\tau_0} \right) + \frac{8}{\pi^2} \exp\left(-\left(\frac{Qd}{6} \right)^2 \right) \sum_{n_{odd}} \frac{1}{n^2} \exp\left(-n^2 t/\tau_d \right) \tag{14.22}$$

For short times *S(Q,t)* decays mainly due to local reptation (first term), while for longer times (and low *Q*) the second term resulting from the creep motion dominates. The two time scales are given by $\tau_0 = \frac{36}{W \ell^4 Q^4}$ *and* $\tau_d = \frac{3N^3 \ell^2}{\pi^2 W d^2}$. Since the ratio of these time scales is proportional to N^3 for long chains at intermediate times $\tau_e < t < \tau_d$ a pronounced plateau in

S(Q,t) is predicted. Such a plateau is a signature for confined motion and relates not only to the reptation concept. Besides the reptation model also other entanglement models have been broad forward. We discuss them briefly by categories.

1. In generalized Rouse models, the effect of topological hindrance is described by a memory function. In the border line case of long chains the dynamic structure factor can be explicitly calculated in the time domain of the NSE experiment. In this class fall entanglement models by Ronca, Hess, Chaterjee and Loring.

2. Rubber like models take entanglements literally as temporary cross links. Such an approach has been brought forward recently by des Cloiseaux. He assumes that the entanglement points between chains are fixed as in a rubber and that under the boundary condition of fixed entanglements the chains perform Rouse motion. This rubber like model is conceptually closest to the idea of a temporary network.

3. Recently in a mode coupling approach a microscopic theory describing the polymer motion in entangled melts has been developed. While these theories describe well the different time regimes for segmental motion, unfortunately as a consequence of the necessary approximations up to now a dynamic structure factor could not yet been derived.

14.4.1 Experimental observations

Fig.14.17 presents measurements on alternating polyethylene propylene copolymer melts at 496K. The dynamic structure factors are plotted linearly against time and qualitatively obey the expectation set by the reptation or other confinement models. For short times $S(Q,t)$ shows fast relaxation which is transformed into a slightly sloping plateau above about 15ns. The broken line demonstrates the expected relaxation in the Rouse model.

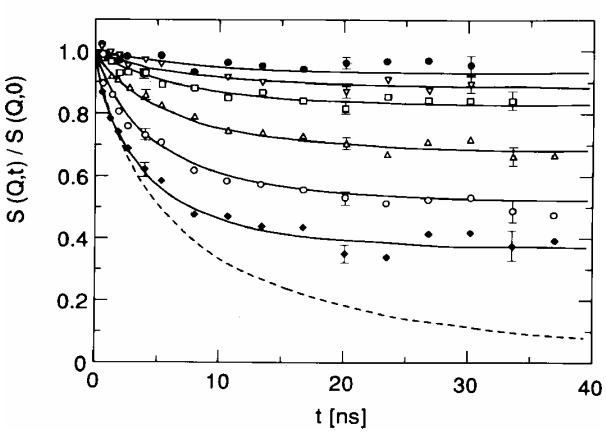

Figure 14.17: Dynamic structure factor of a PEP melt for different Q-values. Solid lines: Ronca model; dashed line: Rouse model at the largest Q-value.

In Fig.14.18 the same data are plotted versus the scaling variable of the Rouse model (Eq.[14.20]). In contrast to Fig.14.12 the scaled data do not follow a common curve but are rather split into Q dependent branches after an initial common course. This splitting is a consequence of the existence of a dynamic length scale which invalidates the Rouse scaling properties. We note, that this length is of purely dynamical character and cannot be observed in static experiments. In order to distinguish between different models measurements up to Fourier times 3 or 4 times larger than τ_e are not enough. Here, the recent development of an ultra high resolution NSE spectrometer (IN15 at the ILL in Grenoble opened new ground in pushing the time limit of NSE up to about 200ns).

Fig.14.19 displays recent experimental results on a polyethylene melt (M_w = 36.000) which were carried over a time regime of 170ns. The data are compared with the dynamic structure factors of the reptation model as well as the models of de Cloizeaux and Ronca. It is apparent that these data clearly favour the reptation model which appears to be the only so far existing model yielding a dynamic structure factor which is in quantitative agreement with this NSE data. The model of Ronca produces a plateau which is too flat. From Fig.14.19 it is also apparent that the Rubber like model of de Cloizeaux leads to an inconsistent Q dependence which is most apparent at the larger Q values. We note that the fits were preformed varying

only one single parameter, the tube diameter d, while the Rouse rate was determined from earlier NSE data taken at short times. With this one parameter it is possible to achieve quantitative agreement both with respect to the Q and the time dependence of the dynamic structure factor.

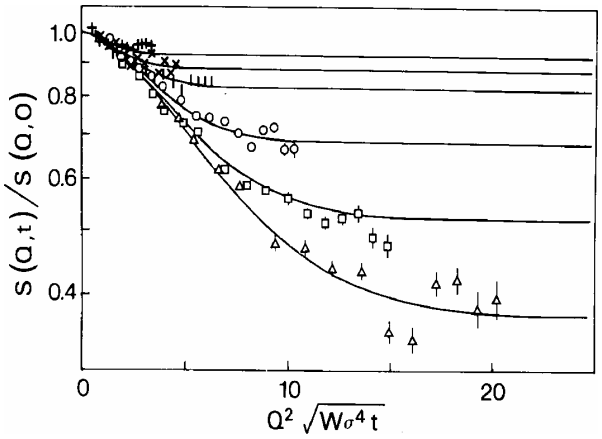

Figure 14.18: Data from Fig.14.17 in a scaling representation as a fact of the Rouse variable ($\sigma \equiv \ell$)

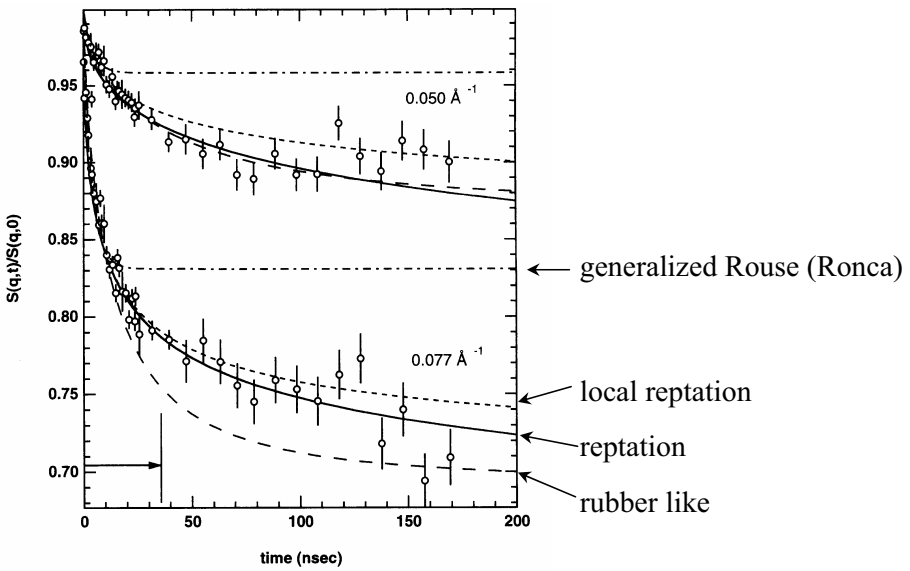

Figure 14.19: NSE data from PE melts at 509K compared to various models.

Finally, one may test whether only local reptation or also the creep motion along the tube is important on this experimental time scale. Local reptation corresponds to $\tau_d = \infty$ and indeed (Fig.14.19) at low Q a difference between local reptation only and the global reptation mechanism appears to become distinguishable indicating the presence of τ_d. Here future experimental work will have to set in. As it stands NSE spectroscopy accessing quantitatively the dynamic structure factor has by now seen clear and unambiguous signature of reptation in a flexible linear polymer chain. The data cover a region of the time domain where reptation is in principle applicable. Compared with other phenomenological approaches reptation is by now the only approach providing a consistent description of all NSE data. It implies that reptation must emerge from any successful microscopic theory of polymer relaxation.

14.5 Summary

High resolution neutron spectroscopy permits to access the molecular motions simultaneously in space and time. Restricting itself to the dynamics of homopolymers melts this lecture attempted to transmit a flavour of what can be achieved in particular by NSE. Choosing different time and length scales, we covered the range of molecular motions, commencing at the scale of a few bonds to large scale motions reaching the scale of the entire chain.

In the regime of the 'classical relaxations' of polymers neutron spectroscopy informs on the geometrical evolution of the motions in question. We have seen, that the α-relaxation may be understood as a sublinear diffusion process while the β-relaxation is in good agreement with a local jump process of a few angstrom distances. Both processes may be considered with good approximation as statistically independent. At scales where the detailed chemical structure of the monomers ceases to be of importance, NSE measurements have by and large confirmed the predictions of the entropy governed Rouse dynamics both for the self and the pair correlation function. Recently, an in depth comparison of specially designed NSE experiments with computer simulation also pointed out the limits of this approach.

The dynamics of polymer melts under the influence of topological interactions which result from the mutually interpenetrating chains poses high demands both conceptually and also experimentally. NSE experiments on the single chain dynamic structure factor of long chain melts, established experimentally the essential prediction of local reptation namely the tube

confinement of the relaxation of large scale Rouse modes. Presently there exists no other theory providing a dynamic structure factor, which is in agreement with this data.

References

A. Review Articles and books

[1] M. Doi, S.F. Edwards, The Theory of Polymer Dynamics, Clarendon Press, Oxford (1986)

[2] B. Ewen, D. Richter, Advances in Polymer Science 134, Springer, Berlin (1997)

[3] D. Richter, Polymer Dynamics by Neutron Spin Echo Spectroscopy in "Scattering in Polymeric and Colloidal Systems" Ed by Wyn Brown and Kell Mortensen, Gordon and Breach, London (2000)

[4] D. Richter, Visoelasticity and microscopic motion in dense polymer systems, Review article in Diffusion in Condensed Matter, Eds: J. Kärger, P. Heitjans, R. Haberlandt (Vieweg, Braunschweig (1998))

B. Experimental work

[5] A. Arbe, U. Buchenau, L. Willner, D. Richter, Study of the Dynamic Structure Factor in the β-Relaxation Regime of Polybutadiene, Phys. Rev. Lett. **76**, 1872 (1996)

[6] A. Arbe, D. Richter, J. Colmenero, B. Farago, The Merging of the α- and β-Relaxations in Polybutadiene; A Neutron Spin Echo and Dielectric Study, Phys. Rev. E. **54**, 3853 (1996)

[7] A. Arbe, J. Colmenero, M. Monkenbusch, D. Richter, Dynamics of glass-forming polymers: homogeneous vs. heterogeneous scenario, Phys. Rev. Lett. **81**, 590 (1998)

[8] D. Richter, M. Monkenbusch, A. Arbe, J. Colmenero, R. Faust, Space Time Observation of the α-Process in Polymers by Quasielastic Neutron Scattering, J. Phys. Condens. Matter **11**, A297 (1999)

[9] A. Arbe, J. Colmenero, B. Frick, M. Monkenbusch, D. Richter, Investigation of the dielectric β-process in Polyisobutylene by incoherent quasielastic neutron scattering, Macromolecules **29**, 4926 (1998)

[10] D. Richter, M. Monkenbusch, J. Allgaier, A. Arbe, J. Colmenero, B. Farago, Y. Cheol Bae, R. Faust, From Rouse Dynamics to Local Relaxation - A Neutron Spin Echo Study of Polyisobutylene Melts, J. Chemical Physics 111, 6107 (1999)

[11] W. Paul, G.D. Smith, D.Y. Yoon, B. Farago, S. Rathgeber, A. Zirkel, L. Willner, D. Richter, Chain Motion in an Unentangled Polymer Melt: A Critical Test of the Rouse Model by Molecular Dynamics Simulations and Neutron Spin Echo Spectroscopy, Phys. Rev. Lett. **80**, 2346 (1998)

[12] P. Schleger, B. Farago, A. Kollmar, C. Lartigue, D. Richter, Clear Evidence of reptation in polyethylene from neutron spin echo spectroscopy, Phys. Rev. Lett. **81**, 124 (1998)

[13] H. Montes, M. Monkenbusch, L. Willner, S. Rathgeber, L.J. Fetters, D. Richter, Neutron Spin Echo Investigations of Concentration fluctuations dynamics in melts of diblock-copolymers, J. Chemical Physics **110**, 10188 (1999)

C Theoretical Work

[14] G. Ronca, Frequency spectrum and dynamic correlations of concentrated polymer liquids, J. Chem. Phys. **79**, 1031 (1983)

[15] A. Chatterjee, R. Loring, Calculation of the dynamic structure factor in polymer melts, J. Chem. Phys. **101**, 1595 (1994)

[16] J. des Cloizeaux, Dynamic form function of a long polymer constrained by entanglement in a polymer melt, J. Phys. I. (France) **3**, 1523 (1993)

[17] K.S. Schweizer, G. Szamel, Crossover to entangled dynamics in polymer solutions and melts, J. Chem. Phys. **103**, 1934 (1995)

15

Magnetism

Thomas Brückel

15. Magnetism

Thomas Brückel, IFF, FZ-Jülich

15.1 Introduction

Magnetism is a very active and challenging subject of solid state science since it represents a typical many-body problem and a complex application of quantum-mechanics, statistical physics and electromagnetism. During the last decades, new discoveries have emerged in this field due to the synthesis of new classes of magnetic materials, due to improved or new powerful techniques or due to advancements in solid state theory. Let us mention a few examples of materials of current interest: the high temperature superconductors and the colossal magneto-resistance manganite compounds, both of which have structures derived from the perovskite structure, the rare-earth nickel-born carbide compounds with a coexistence of magnetism and superconductivity, the large class of Kondo systems and heavy fermion compounds, spin glasses and spin liquids or new and rather complex hard magnetic materials, just to mention a few. Besides bulk materials, magnetism of thin films and surfaces became a topic of great current interest, mainly due to the improved preparation techniques. Driven by pure curiosity, scientists have discovered many fundamental effects of thin film devices, such as the oscillating interlayer coupling or the giant magneto-resistance effects. Within less than ten years from their initial discovery, these effects found their applications for example in read heads of computer hard disks. A promising new field of application emerges, so-called magneto-electronics with spin transistors or magnetic random access memories MROM. This should serve us as an excellent example, how curiosity driven fundamental research can find new applications of an effect known since 2500 years (the discovery of the magnetism of magnetite) which are able to change our modern life. This progress is largely due to new experimental methods and again we just want to mention a few: developments in the field of polarised neutron scattering, such as the ^{3}He-polarisation filter or zero-field neutron polarimetry, the development of the spin resonance techniques, resonant nuclear scattering of synchrotron radiation or magnetic x-ray diffraction. Finally, all this experimental progress would be in vain without the improvements of the theory, which provide us with a deeper understanding of correlated electron systems. Probably the most powerful technique that has emerged during the last years is the density functional theory which allows one to calculate

the ground state of metallic magnets. Numerical methods such as Monte-Carlo simulation allows us to test models of complex disordered magnetic systems.

After having motivated the interest in solid state magnetism, let us come back to the basic magnetic properties. Quite generally, a magnetic system can be described by its magnetisation, which denotes the total magnetic moment per unit volume. The magnetisation of a sample can vary in space and time: $\underline{M}(\underline{r},t)$. The magnetisation is coupled to the conjugate magnetic field $\underline{H}(\underline{r},t)$. If the excitation $\underline{H}$ is very small, the response will, to a good approximation, be linear. In the framework of this linear response theory, we can define a magnetic susceptibility χ by:

$$\underline{M} = \underline{\underline{\chi}} \cdot \underline{H} \tag{15.1}$$

Here, $\underline{\underline{\chi}}$ is written as a tensor to describe anisotropic magnetic response. In isotropic systems, $\underline{M}$ will align parallel to $\underline{H}$ and χ reduces to a scalar quantity. More generally, for a spatially and temporally varying magnetic field, we can write:

$$\underline{M}(\underline{r},t) = \iint d^3r'\,dt'\,\underline{\underline{\chi}}(\underline{r}-\underline{r}',t-t')\cdot\underline{H}(\underline{r}',t') \tag{15.2}$$

Every material shows a magnetic response. Most materials are diamagnetic with a negative susceptibility χ, which expresses Lenz's rule that the induced magnetisation $\underline{M}$ is anti-parallel to the magnetic field H. Of greater interest are materials, in which χ is positive. Here, two classes of materials have to be distinguished: localised electron systems (e. g. ionic compounds) and itinerant electron systems (metals). Localised electron systems with $\chi > 0$ have open shells with unpaired electrons. Spin- S, orbital- L, and total- angular momentum J for the free ion are determined by Hund's rules. These values can be modified by solid state effects such as the crystalline field or spin transfer into covalent bonds. In itinerant electron systems, the conduction electrons carry the magnetic moment. Within a simple band picture, magnetism arises from an unequal population of spin-up and spin-down bands. At elevated temperatures, systems with $\chi > 0$ show paramagnetic behaviour with strongly fluctuating magnetic moments. As the temperature is lowered interaction between the moments becomes more and more important. In general magnetic dipole-dipole interactions play only a minor

role, compared to the stronger exchange interactions, which result from Coulomb interaction and the Pauli principle. In ionic compounds, we observe direct exchange, if the orbitals of two magnetic ions overlap or super-exchange and double exchange, if the interaction is mediated via an intervening anion. In itinerant electron systems, the interaction is mediated by the conduction electrons and has an oscillating character. This indirect coupling of magnetic moments by conduction electrons is referred to the Rudermann-Kittel-Kasaya-Yosida (RKKY) interaction. If the energy equivalent kT is in the order of the interaction energy, a phase transition from the paramagnetic high temperature state to a magnetically long-range ordered low temperature state can eventually take place. Systems with spontaneous macroscopic magnetisations such as ferromagnets (FM) and ferrimagnets have to be distinguished from antiferromagnets (AF), for which the zero-field magnetisation vanishes. The microscopic arrangement of spin- and orbital- magnetic moments, the so-called magnetic structure, can be rather complex, especially in the case of antiferromagnets.

Neutron scattering is a most powerful technique for the investigation of magnetism due to the magnetic dipole interaction between the magnetic moments of the electrons in the sample and the nuclear magnetic moment of the neutron. We have seen in chapter 3 that for elastic events, the neutron scattering cross section is directly related to the Fourier transform of the magnetic moment density distribution. For the inelastic case, one can show that the double differential cross section for magnetic neutron scattering is connected with the most fundamental quantity, the Fourier transform of the linear response function or susceptibility (15.2) $\chi(\underline{r},t)$ in microscopic space and time variables $\underline{r}$ and t, respectively. In contrast to macroscopic methods it allows one to study magnetic structures, fluctuations and excitations with a spatial and energy resolution well adapted to atomic dimensions. Traditionally neutron scattering is the method to study magnetism on an atomic level, only recently complemented by the new technique of magnetic x-ray scattering.

In what follows, we will give a few examples for applications of neutron scattering in magnetism. Obviously it is completely impossible to give an representative overview within the limited time, nor is it possible to reproduce the full formalism. Therefore we will just quote a few results and concentrate on the most simple examples. Even so polarisation analysis experiments are extremely important in the field, we will not discuss these rather complex experiments and refer to chapter 4.

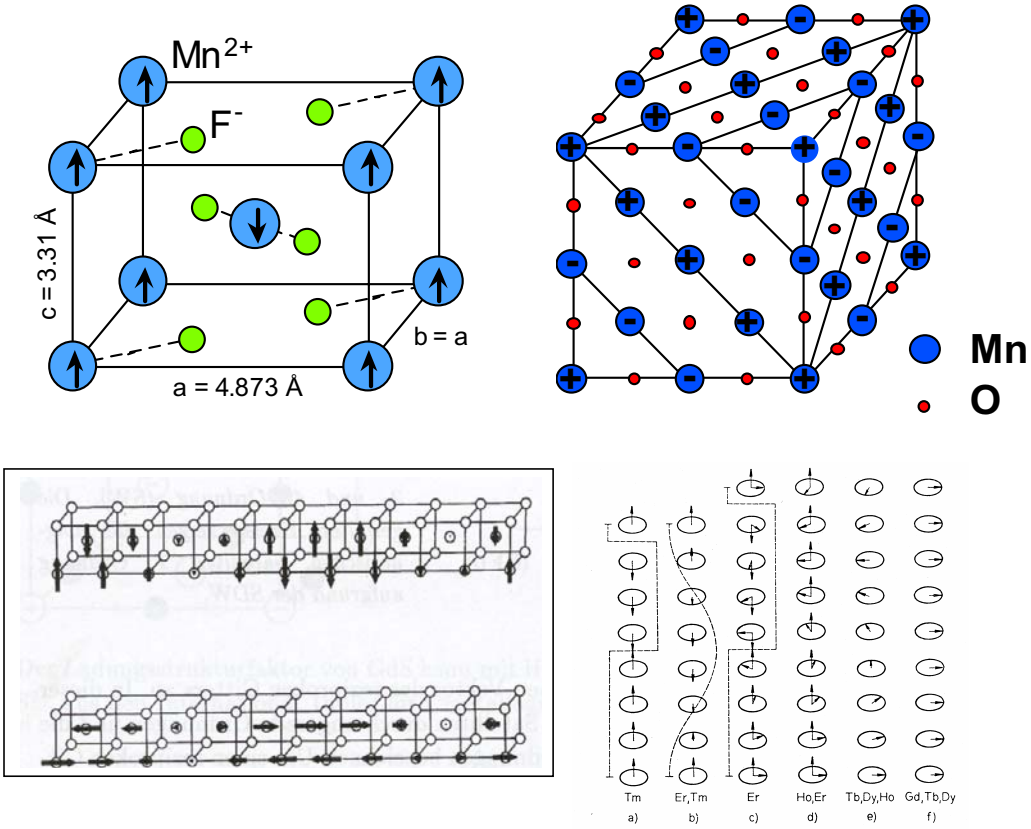

Fig. 15.1: Some examples of magnetic structures: a) The collinear antiferromagnetic structure of MnF_2. The spin moments at the corners of the tetragonal unit cell point along the c-direction, the spin moment in the centre of the unit cell is antiparallel to the moments at the corners. b) The MnO-type magnetic structure on a fcc lattice. Spins within 111 planes are parallel, adjacent planes are coupled antiferromagnetically. c) The spin density wave of chromium, which can be described by an amplitude variation along one of the cubic 001 axis. The spin density wave can be longitudinal or transversally polarised. d) Schematic representation of the magnetic structures of the hexagonal rare-earth metals. Spins in the hexagonal basal plane are always parallel. The figure shows, how successive planes along the c-directions are coupled. One can distinguish a simple ferromagnetic phase, a c-axis modulated phase, helix and cone phases. In reality, the magnetic structures are much more complex with spin slip or multi-k structures. A recent review is given by [1].

16.1 Magnetic Structure Determination

As mentioned in the introduction, the magnetic structure of a substance exhibiting magnetic long range order can be very complex. In general a magnetic structure can be described by its Fourier-components in the form

$$\underline{m}_{l,j} = \sum_{\underline{q}} \underline{m}_{\underline{q}j} \cdot \exp\left(-i\underline{q} \cdot \underline{R}_l\right) \tag{15.3}$$

where $\underline{m}_{l,j}$ denotes the moment of atom j in cell l and $\underline{q}$ is the so called magnetic propagation vector. Some examples for magnetic structures are given in figure 15.1.

Magnetic neutron scattering is the classical method to determine magnetic structures. As neutral particles, neutrons penetrate deep into most materials and allow to study bulk properties. Thermal neutrons have wavelengths in the vicinity of 1 Å, which is well adapted to studies with atomic resolution. Neutrons carry a magnetic dipole moment

$$\underline{\mu}_n = -\gamma\mu_N \cdot \underline{\sigma} \tag{15.4}$$

with the gyromagnetic ratio $\gamma = -1.913$ of the neutron and the nuclear magneton $\mu_N = 5.051 \cdot 10^{-27}\,\mathrm{J/T}$. This magnetic moment of the neutron can interact with the magnetic field created by the spin or orbital angular momentum of unpaired electrons within the solid, see chapter 3. If we restrict ourselves to elastic scattering of unpolarised neutrons, the purely magnetic scattering cross section is given by

$$\left(\frac{d\sigma}{d\Omega}\right)_{el,mag} = \left(\frac{\gamma r_0}{2}\right)^2 \left|\left\langle M_\perp(\underline{Q})/\mu_B \right\rangle\right|^2 = \left(\frac{\gamma r_0}{2}\right)^2 \left|\left\langle 2S_\perp(\underline{Q}) + L_\perp(\underline{Q}) \right\rangle\right|^2 \tag{15.5}$$

with $\frac{\gamma r_0}{2} = 2.696\,\mathrm{fm}$. $\mathrm{M}_\perp(\underline{\mathrm{Q}})$ is the component of the Fourier transform of the sample magnetisation perpendicular to the scattering vector. $\underline{\mathrm{S}}(\mathrm{Q})$ and $\underline{\mathrm{L}}(\mathrm{Q})$ are the Fourier transform of the spin- and orbital- angular momentum density, respectively. The index $\perp$ denotes the component of the corresponding quantity perpendicular to the scattering vector. Neutrons

only "see" this component and not the component of the magnetisation along the scattering vector Q (compare chapter 3). This directional dependence allows one to determine the spin direction, while the magnetic propagation vector can be determined from the position of the magnetic Bragg reflections. Finally, the magnitude of the magnetic moment can be determined by comparing the intensities of the magnetic Bragg reflections with the intensities of nuclear reflections. The scattering amplitude of neutrons by a single fixed nucleus is given by the scattering lengths tabulated in [2]. As an example, the scattering length for cobalt amounts to 2.49 fm, which is comparable to the equivalent magnetic scattering amplitude for spin = 1/2 of 2.696 fm. The formalism for magnetic neutron scattering is detailed by Squires [3] and Lovesey [4], the determination of magnetic structures is described by Rossat-Mignod [5].

Here we want to discuss the most simple example, the determination of the magnetic structure of MnF_2. For simplicity, we will neglect the scattering of the fluorine atoms completely. Then our problem reduces to magnetic Bragg diffraction from a tetragonal body centred antiferromagnet. In the so called antiferromagnetic order of type I, shown in figure 15.2, all spins at the corners of the unit cell are parallel, while the spin in the centre is anti-parallel to the spins at the corners. We assume that due to some anisotropy, e.g. the crystal field effects, all moments are aligned along ±c.

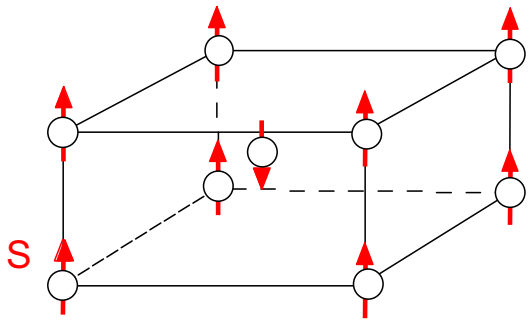

Fig. 15.2: Magnetic structure of a type I antiferromagnet on a body-centred tetragonal lattice. In the figure is assumed that c is the easy axis, i.e. all spins are aligned along c.

The scattering power density can be calculated as a convolution of an infinite three dimensional lattice, which describes the position of the origin of all unit cells, with the scattering power density of a pair of atoms located at the origin and at the centre of the unit cell. Therefore, when calculating the scattered intensity as the Fourier transform of the scattering power density, it is given as a product of the Fourier transform of the lattice and the Fourier transform of the scattering power density of a pair of atoms. The Fourier transform of the lattice is the well known Laue function (compare chapter 3). It gives rise to the Bragg reflections at integer h, k, l. The intensity of these Bragg reflections is being modulated by the Fourier transform of the scattering power density within the unit cell (here of the atom pair), the so called *elastic structure factor*. The structure factor for the pure nuclear scattering is given by:

$$\begin{aligned} S_N(h,k,l) &= b(1+e^{2\pi i(h\cdot\frac{1}{2}+k\cdot\frac{1}{2}+l\cdot\frac{1}{2})}) \\ &= b(1+(-1)^{h+k+l}) = \begin{cases} 0 & h+k+l \quad uneven \\ 2b & h+k+l \quad even \end{cases} \end{aligned} \tag{15.6}$$

The body centring gives rise to an extinction of all reflections with index h+k+l uneven, while all reflections with h+k+l even have the same intensity. In complete analogy to (15.6), the magnetic structure factor can be calculated. We only have to take into account that the spin direction in the centre is opposite to the spin directions at the corners, which can be described by a different sign for the two spins:

$$\begin{aligned} S_M(h,k,l) &= \gamma_n r_o f_m S(1-e^{2\pi i(h\cdot\frac{1}{2}+k\cdot\frac{1}{2}+l\cdot\frac{1}{2})}) \\ &= \gamma_n r_o f_m S(1-(-1)^{h+k+l}) = \begin{cases} 2\gamma_n r_o f_m S & h+k+l \; uneven. \\ 0 & h+k+l \; even \end{cases} \end{aligned} \tag{15.7}$$

The magnetic structure is „anti body centred“: all reflections with index h+k+l even vanish, while reflections with h+k+l uneven are present. In the diffraction pattern, a magnetic Bragg reflection appears right between two nuclear ones. The intensity of the magnetic reflections decreases with increasing momentum transfer due to the magnetic form factor (see chapter 3), while the nuclear reflections have constant intensity, if we neglect the temperature factor – see figure 15.3.

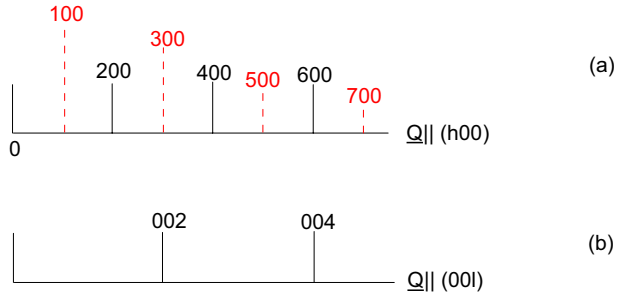

Fig. 15.3: Schematic plot of a neutron diffraction diagram for the antiferromagnet of fig. 15.2. Top: along the (h00) direction; bottom: along (00l). Magnetic Bragg reflections are indicated by the broken lines. The height of the lines is representative for the scattered intensity.

We can determine the direction of the magnetic moments with the help of the directional factor in eq. (15.5). If one measures along the tetragonal a or b directions, one obtains the magnetic Bragg reflections of figure 15.3 a. However, if one measures along c, S || Q holds, i.e. all magnetic reflections of type 0 0 l are extinct and one obtains the diffraction pattern depicted in figure 15.3 b. In this simple case, one can directly deduce the spin direction along c from the extinction of the 0 0 l reflections. Finally one can obtain the magnitude of the spin moment by comparing the intensities of the magnetic Bragg reflections with the intensities of the nuclear ones.

16.2 Magnetic Form Factors; Magnetisation Densities

For the magnetic structure determination we used a predetermined form factor, e.g. from Hartree-Fock calculations of electronic wave functions for the free atom [6]. Each atomic site was characterised by just one integral variable, the atomic magnetic moment. A scattering experiment can, however, give much more information, if sufficient Fourier components can be measured. We can then obtain the magnetisation density within each atom, which will show deviations from the density of the free atom due to solid state effects. Magnetisation density can be transferred to neighbouring atoms by covalent bonds. In metallic magnetic systems, the "magnetic" electrons are itinerant and the magnetisation density is strongly de-localised. We learned in chapter 3 that the magnetic form factor is the Fourier transform of

the magnetisation density of one atom. Therefore magnetic form factor measurements give us all the important information about such solid state effects.

To illustrate the kind of information we can obtain from such measurements let us quote some recent studies of high temperature superconductors or molecular magnets. There are theories of high temperature superconductivity, which propose a magnetic coupling mechanism for the Cooper-pairs. While no long range ordered magnetic structure is observed in the super-conducting state, dynamic magnetic fluctuations have been searched for with neutron scattering [7,8]. If one wants to detect, which atomic sites are susceptible to magnetism, one can study the magnetisation density induced in the material by an external magnetic field [9]. Molecular magnets are another active field of current interest, due to their very high potential for applications, but also due to fundamental interest. These are organic compounds, where the magnetism is not due to intra-atomic exchange ("Hund's rules"), as in the case of 3d or 4f metal ions, but due to the specific arrangement of bonds. The magnetisation density is distributed over many atomic sites. A neutron study of it's distribution can give us insight to the mechanism giving rise to the magnetic coupling and thus guide us in the search for new, optimised materials [10].

The most efficient way to measure weak magnetic signals is to use the interference between magnetic and nuclear scattering. Using this interference effect, we can even determine the phase of the magnetic structure factors, in addition to their magnitude. In this special case we have then solved the phase problem of crystallography.

We have learned in chapter 4 that this interference term can only be measured with polarised neutrons and cancels for unpolarised neutron diffraction. An interference between nuclear and magnetic scattering can only occur, if both types of scattering are allowed, i.e. the interference can only appear in the "non-spin flip" channel, if the nuclear as well as the magnetic structure factor are non- vanishing. To maximise the magnetic signal, one chooses a diffraction geometry as in figure 15.4, for which the magnetisation is perpendicular to the diffraction plane. This condition can be enforced by applying a strong magnetic field along this direction.

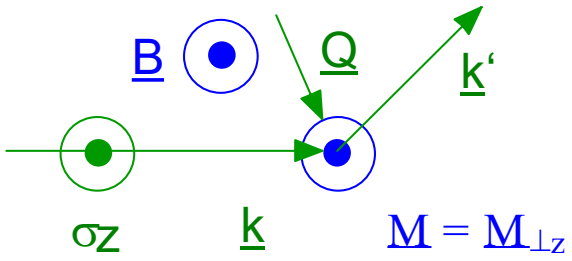

Fig. 15.4: Scattering geometry for measuring the interference term between nuclear- and magnetic scattering with polarised neutrons, but without polarisation analysis.

The relevant cross sections to measure the interference term in this geometry are:

$$\left(\frac{d\sigma}{d\Omega}\right)_{++} = \left|b(\underline{Q}) - \frac{\gamma_n r_o}{2\mu_B} M(\underline{Q})\right|^2 = b^2 - 2\frac{\gamma_n r_o}{2\mu_B} bM + \left(\frac{\gamma_n r_o}{2\mu_B}\right)^2 M^2 \qquad (15.8)$$

b,M real

$$\left(\frac{d\sigma}{d\Omega}\right)_{--} = \left|b(\underline{Q}) + \frac{\gamma_n r_o}{2\mu_B} M(\underline{Q})\right|^2 = b^2 + 2\frac{\gamma_n r_o}{2\mu_B} bM + \left(\frac{\gamma_n r_o}{2\mu_B}\right)^2 M^2 \qquad (15.9)$$

Besides the magnitude square of the amplitude for nuclear- and magnetic- scattering, respectively, these cross sections contain one term, in which a product of the magnetic- and nuclear- amplitudes appears. This interference term is especially useful, if the amplitude of magnetic scattering is much smaller than the amplitude of nuclear scattering:

$$\left|\frac{\gamma_n r_o}{2\mu_B} M\right| << |b| \qquad (15.10)$$

This is for example the case, if an external magnetic field induces a weak magnetisation in the paramagnetic state, when the ration between magnetic- and nuclear- amplitude is often below 10^{-3}. This implies that the contribution from magnetic scattering to the total signal is in the order of 10^{-6} or less, and thus no longer measurable. However, if we take data in two measurements, once with the neutron polarisation parallel and once anti-parallel to the magnetic field, we can determine the so-called *flipping ratio*:

$$R(\underline{Q}) = \frac{(d\sigma/d\Omega)_{++}}{(d\sigma/d\Omega)_{--}} = \frac{1 - \frac{\gamma_n r_o}{\mu_B}\frac{M}{b} + \ldots}{1 + \frac{\gamma_n r_o}{\mu_B}\frac{M}{b} + \ldots} \approx 1 - 4\frac{\gamma_n r_o}{2\mu_B}\frac{M(\underline{Q})}{b(\underline{Q})} \qquad (15.11)$$

Note that the polarisation of the scattered beam is known a priori (only non-spin flip processes can occur), so that the experiment is being done with a polarised beam, but without polarisation analysis. The flipping ration (15.11) depends linearly on the magnetic structure factor, instead of quadratic as the scattered intensity. Therefore much smaller values of the magnetic structure factor can be determined. If the nuclear structure factor is known (e.g. from a prior neutron diffraction experiment), these measurements of the flipping ratio give access to a highly precise determination of the phase and magnitude of the magnetic structure factor.

An example is given by the measurement of the form factor of chromium. Cr is the archetypal itinerant antiferromagnet. Therefore the magnetisation density is very de-localised. As a consequence, the magnetic form factor drops extremely rapidly with increasing momentum transfer. In a recent synchrotron x-ray experiment, we could demonstrate that this form factor is spin only [11]. However, in a polarised neutron diffraction experiment we could show [12], that a magnetisation induced in the paramagnetic state by an external magnetic field is much more localised around the individual atoms. Therefore, the field-induced form factor decreases much slower, compare figure 15.6. It has a large contribution (60 %) of orbital angular momentum, quite in contrast to the form factor in the ordered state. By means of a Fourier transform or with the so-called *Maximum Entropy Method* a magnetisation density distribution within the unit cell can be reconstructed (compare figure 15.7). Such data are of utmost importance to test and improve modern band theories, such as the fully relativistic *density functional theory* and thus to obtain a better understanding of the metallic state.

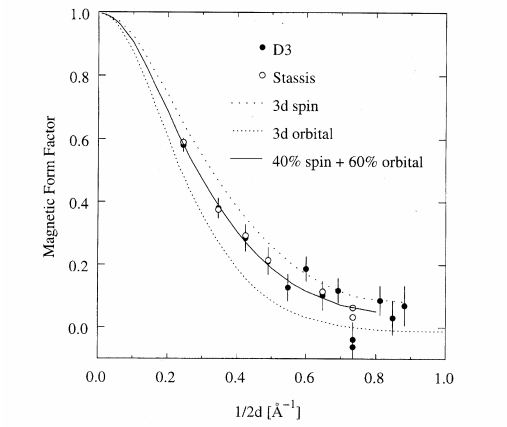

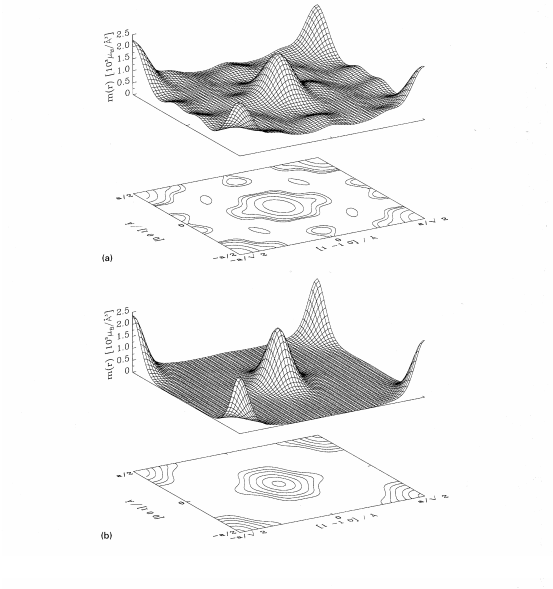

Fig. 15.6: Induced magnetic form factor of Cr for a field of 4.6 T. Open and filled circles are experimental values, the Lines are calculations for spin-, Orbital- and total moment.

Fig. 15.7: Projection of the induced magnetisation density distribution onto the <110> plane. above: Fourier transform Below: Maximum entropy reconstruction

16.3 Magnetic Phase Transitions

Phase transitions can occur between different magnetic phases as a function of various thermodynamic parameters, such as magnetic field, temperature or pressure. Here we will restrict ourselves to the most simple case of a transition from a low temperature ferromagnetic (FM) or antiferromagnetic (AF) phase to a high temperature paramagnetic (PM) phase. First, we will discuss this phenomenon qualitatively, then introduce the quantitative description and finally show just one example of a neutron diffraction study.

The magnetic long range order discussed in section 15.2 can only be stable, as long as the thermal energy k_BT is small enough compared to the exchange interactions giving rise to magnetic order. At sufficiently high temperatures, entropy wins and the magnetic moments

fluctuate in space and time. A phase transition has occurred at a critical temperature, called *Curie temperature* T_C for ferromagnets or *Néel temperature* T_N for antiferromagnets, from a long range ordered state at low temperatures to a paramagnetic high temperature phase. The two phases are characterised by an *order parameter*, such as the magnetisation for ferromagnets or the sublattice magnetisation for antiferromagnets. In the paramagnetic phase this order parameter vanishes, while in the low temperature phase it increases towards a saturation value, when the temperature is lowered. Depending on whether the order parameter changes discontinuously or continuously at the critical temperature, the phase transition is of *first-* or *second- order*, respectively. At least for local moment systems, the magnetic interactions and moments are still present in the paramagnetic phase. Therefore above the critical temperature, magnetic correlations persist. This magnetic short range order fluctuates in time and extends over regions with characteristic linear dimensions, called the *correlation length*. When we decrease the temperature in the paramagnetic phase towards the transition temperature, the correlation length increases. Larger and larger regions develop which show short range order characteristic for the low temperature phase. The larger these correlated regions, the slower the fluctuation-dynamics. At the critical temperature of a second order phase transition, the correlation length and the magnetic susceptibility diverges, while the dynamics exhibits a critical slowing down.

Besides the magnetic phase transitions, there exist also structural phase transitions. However, experiments on magnetic model systems provided the basis for our modern understanding of this complex co-operative effect. Th reason is that magnetic model systems can often be described by some very simple Hamiltonian, such as the Heisenberg (15.12), the x-y (15.13) or the Ising model (15.14), depending whether the system is isotropic, has a strong planar- or a strong uniaxial anisotropy, respectively:

Heisenberg: $$H = \sum_{i,j} J_{ij} \underline{S}_i \cdot \underline{S}_j \qquad (15.12)$$

x-y: $$H = \sum_{i,j} J_{ij} \left(S_{ix} S_{jx} + S_{iy} S_{jy} \right) \qquad (15.13)$$

Ising: $$H = \sum_{ij} J_{ij} S_{iz} S_{jz} \qquad (15.14)$$

Here, J_{ij} denotes the exchange constant between atoms i and j, $S_{i\alpha}$ is the component α (=x, y or z) of the spin operator $\underline{S}_i$ of atom i. If the Hamiltonian depends on three- (Heisenberg-model, 15.12), two- (x-y-model, 15.13) or one- (Ising-model, 15.14) components of the spin operator, one can define a three-, two- or one dimensional order parameter. Moreover, there are crystal structures, where the magnetic atoms are aligned along well separated chains or planes, so that besides the usual three dimensional lattice, there exist magnetic model systems in one and two space dimensions. Finally, depending on whether the system shows covalent or metallic bonding, the exchange interactions can be short- or long ranged, respectively.

The experimental investigation of continuous (second order) phase transitions in many magnetic model systems revealed a quite surprising behaviour in a critical region (a temperature range around the ordering temperature with a width of by and large 10 % of the ordering temperature) close to the phase transition: independent of the precise nature of the system under investigation, the phase transition shows universal behaviour. These experimental results laid the foundations for the formulation of a modern theory of second order phase transitions, the *renormalisation group theory*.

If we define a *reduced temperature* as

$$\tau = \frac{T - T_C}{T_C} \tag{15.15}$$

then all relevant thermodynamical parameters show a power-law behaviour close to the second order phase transition:

specific heat:	$c_H \propto \tau^{-\alpha}$	(15.16)
order parameter ($T<T_C$):	$m \propto (-\tau)^{\beta}$	(15.17)
susceptibility:	$\chi \propto \tau^{-\gamma}$	(15.18)
correlation length:	$\xi \propto \tau^{-\nu}$	(15.19)

The surprising discovery was that all systems can be classified into *universality classes*. Within a given universality class, the values of the *critical exponents* α, β, γ and ν are the

same and do not depend on the detailed nature of the system. Moreover, the critical exponents for a given system are not independent, but fulfil certain *scaling relations*, see e.g. [13]. To which universality class a system belongs is determined by three criteria:

Dimensionality of the order parameter n

Space dimensionality d

Range of the interactions (long- or short ranged)

Table 15.1 lists values of the critical exponents for some universality classes.

n	1	1	2	3
d	2	3	3	3
α	0	0.106	-0.01	-0.121
β	0.125	0.326	0.345	0.367
γ	1.75	1.238	1.316	1.388
ν	1	0.631	0.669	0.707

Tab. 15.1: Values of the critical exponents for a few universality classes according to [13].

As an example we have selected a rather unusual magnetic phase transition, which turns out to be of first order (discontinuous) and thus cannot be classified by the above criteria. Let us briefly discuss the AF-PM phase transition of MnS_2 [14].

The magnetic semiconductor MnS_2 orders with the type-III antiferromagnetic structure on the fcc lattice with the wave vector $\underline{q}$=(1,1/2,0) (compare (15.3)). The antiferromagnetic phase transition at T_N = 48.2 K is found to be of first order, quite in contrast to the classical behaviour for such a compound. We performed a neutron scattering study in a search for the driving mechanism. Figure 15.8 shows a contour plot of the magnetic diffuse scattering in the (001) plane in the paramagnetic phase about 17K above T_N. One can clearly see, how the magnetic diffuse scattering is concentrated at the positions (1,1/2,0), (1,3/2,0), (3/2,1,0) etc, where in the long range ordered phase the magnetic Bragg reflections appear. However, a closer examination shows that the positions at which the diffuse scattering is centred, are not the rational positions listed above.

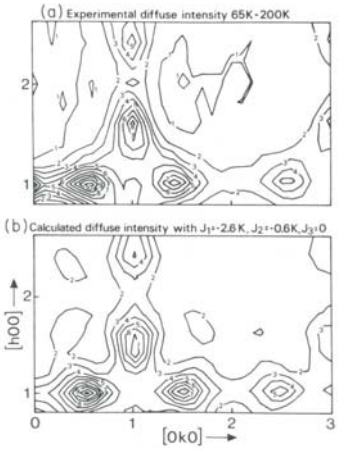

Fig. 15.8: Contour plot of the magnetic diffuse scattering intensity of MnS_2 in the (001) plane at 65 K. Above: measurement; below: calculation

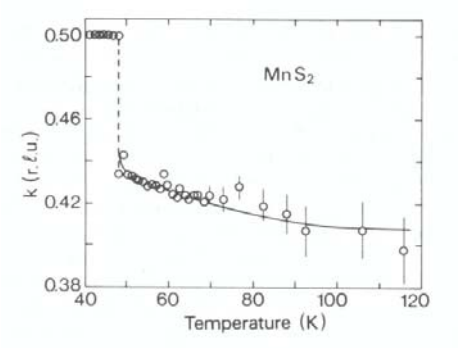

Fig. 15.9: Temperature variation of the incommensurate component.

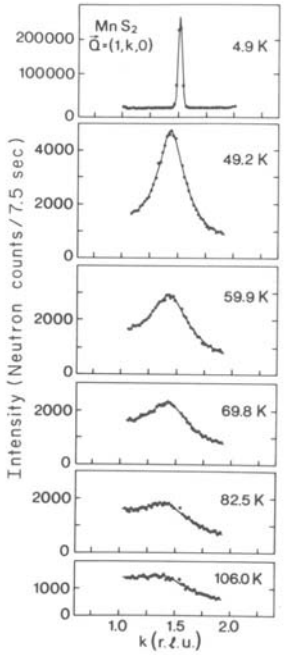

Fig. 15.10: Magnetic diffuse neutron scattering of MnS_2 in reciprocal lattice scans parallel to the modulation vector.

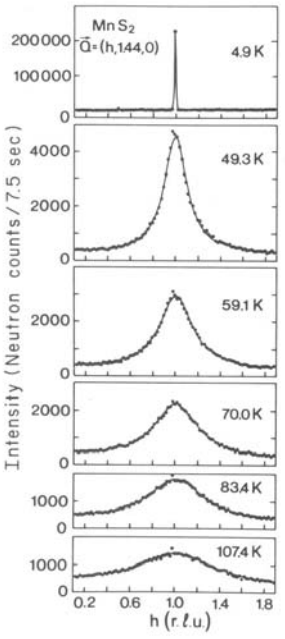

Fig. 15.11: Magnetic diffuse neutron scattering of MnS_2 in reciprocal lattice scans perpendicular to the modulation vector.

Figures 15.10 and 15.11 show the magnetic diffuse neutron scattering of MnS_2 at different temperatures above T_N and the magnetic Bragg peak at 4.9 K (topmost figure). We can clearly observe, how with decreasing temperature the diffuse scattering becomes sharper in reciprocal space and how the peak intensity increases strongly. However, for scans along (1,k,0) the diffuse scattering is not centred at the low temperature Bragg position, while it is centred for the perpendicular scans in the (h,k,0) plane. The magnetic short range order is "*incommensurate*" with the lattice. This means that the periodicity observed in the diffuse magnetic scattering is not just a simple rational multiple of the chemical unit cell periodicity. Figure 15.9 shows the temperature variation of the incommensurate component of the vector at which the diffuse scattering is centred. Note the jump characteristic for a first order transition. Figure 15.9 demonstrates that we can understand the paramagnetic-antiferromagnetic phase transition in MnS_2 as a transition from incommensurate short range order to commensurate long range order. Now it is well established that such "*lock-in-transitions*" are of first order, which explains the unusual behaviour of MnS_2. The problem remains which interaction leads to the shift of the diffuse peak as compared to the Bragg reflection. This question can be solved with model calculations, such as the ones depicted in figure 15.8 [14]. It turns out that an anisotropy term in the Hamiltonian can give rise to the observed effect.

Finally we want to show an example for a true "classical" second order transition, the PM-AF transition in MnF_2. In this case, we have performed the measurements with high energy synchrotron x-rays due to the better reciprocal space resolution as compared to neutrons [15]. Figure 15.12 shows a double logarithmic plot of the reduced sublattice magnetisation m ($m = M/M_S$, where M_S is the saturation value of the magnetisation) versus the reduces temperature τ, defined in eq. (15.15). In this plot, the data points nicely line up along a straight line, corresponding to a power law behaviour as expected from (15.7). The critical exponent β of the sub-lattice magnetisation can be obtained to great precision: $\beta = 0.333\ (3)$, corresponding roughly to the exponent expected for an Ising system (n=1, d=3) according to table 15.1. However, the calculated and measured value do not quite coincide, at least to within two standard deviations, which demonstrates that the precise values of the critical exponents are still not very well established.

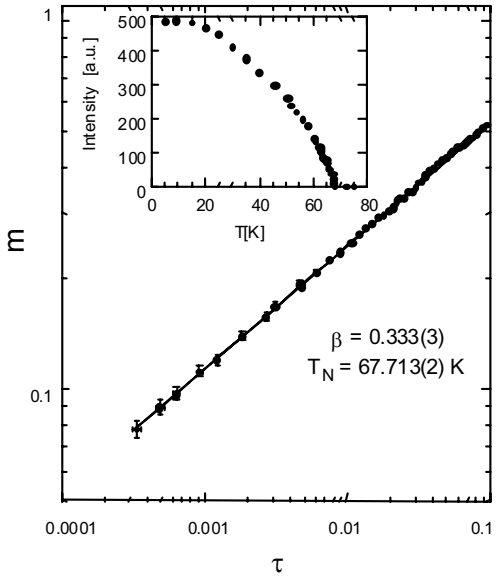

Fig. 15.12: Magnetic Bragg diffraction from MnF_2. The inset shows the temperature dependence of the intensity of the magnetic 300 reflection from 5 to 80K. In the main graph is plotted the reduced sub-lattice magnetisation as a function of reduced temperature on a double logarithmic scale together with a fit employing a power-law function.

16.4 Summary

We have given a few examples of the applications of neutron scattering in magnetism. We have seen how neutrons can be used to investigate the magnetisation density distribution on an atomic level. Besides the rather new technique of magnetic x-ray scattering, no other method can provide the same information on magnetic structure and magnetisation density. Neutrons are ideally suited to study magnetic phase transitions, which are model examples of co-operative phenomena in many body systems. Unfortunately, we were not able to cover other subjects, such as the important fields of magnetic excitations or thin film magnetism. Neutron scattering is the technique to measure spin wave dispersion relations used to determine magnetic interaction parameters (exchange interaction, anisotropy) – see chapter on excitations. In itinerant systems, the transition from collective spin wave like excitations to single particle like "Stoner" excitations could be observed with neutrons. Currently, more "exotic" excitations are in the centre of attention, such as the "resonance peak" in high

temperature superconductors, or excitations in low dimensional magnets. Finally, thin film magnetism is of high current interest due to it's applications in "magnetoelectronics". In this field, neutrons provide the crucial information about the magnetic structure and morphology of thin film devices, compare chapter on reflectometry. While we could not give a comprehensive review, the Jülich group is active in all these fields and we refer to our web page [16] for further information.

References

[1] J. Jensen & A. R. Mackintosh, "Rare Earth Magnetism", Clarendon Press, Oxford (1991)

[2] V. F. Sears, Neutron News 3 (1992) 26

[3] G. L. Squires, "Thermal Neutron Scattering", Cambridge University Press, Cambridge (1978)

[4] S. W. Lovesey, "Theory of Neutron Scattering from Condensed Matter", Clarendon Press, Oxford (1987)

[5] J. Rossat-Mignod, "Magnetic Structures" in: K. Sköld, D. L. Price: "Neutron Scattering", Academic Press, New York (1987)

[6] A. J. Freeman & R. E. Watson, Acta Cryst. 14 (1961), 231

[7] Th. Brückel, H.Capellmann, W. Just, O. Schärpf, S. Kemmler-Sack, R. Kiemel & W. Schäfer; Europhysics Letters 4 (1987) 1189

[8] B. Keimer et al, Physica B 234-236 (1997), 821

[9] J.X. Boucherle et al; Physica B192 (1993), 25

[10] Y.Pontillon et al, Physica B 267-268 (1999), 51

[11] J. Strempfer, Th. Brückel, W. Caliebe, A. Vernes, H. Ebert, W. Prandl & J.R. Schneider; Eur. Phys. J. B14 (2000), 63

[12] J. Strempfer, Th. Brückel, G. J. McIntyre, F. Tasset, Th. Zeiske, K. Burger, W. Prandl, Physica B 267 - 268 (1999), 56

[13] M.F. Collins "Magnetic Critical Scattering", Oxford University Press, Oxford 1989

[14] T. Chattopadhyay, Th. Brückel & P. Burlet; Phys. Rev. B44 (1991), 7394

[15] J. Strempfer, Th. Brückel, U. Rütt, J.R. Schneider, K.-D. Liss & Th. Tschentscher; Acta Cryst. A52 (1996), 438

[16] http://www.fz-juelich.de/iff/Institute/ism/

Schriften des Forschungszentrums Jülich
Reihe Materie und Material / Matter and Materials

1. **Physik der Nanostrukturen**
   Vorlesungsmanuskripte des 29. IFF-Ferienkurses vom 9. bis 20.3.1998
   (1998), ca. 1000 Seiten
   ISBN: 978-3-89336-217-2

2. **Magnetische Schichtsysteme**
   Vorlesungsmanuskripte des 30. IFF-Ferienkurses vom 1. bis 12.3.1999
   (1999), ca. 1300 Seiten, zahlreiche z.T. farb. Abb.
   ISBN: 978-3-89336-235-6

3. **Femtosekunden und Nano-eV: Dynamik in kondensierter Materie**
   Vorlesungsmanuskripte des 31. IFF-Ferienkurses vom 13. bis 24.3.2000
   (2000), ca. 1000 Seiten, zahlreiche z. T. farb. Abb.
   ISBN: 978-3-89336-205-9 (Hardcover)

4. **Massenspektrometrische Verfahren der Elementspurenanalyse**
   Kurzfassungen der Vorträge und Poster des 5. Symposiums und des
   12. ICP-MS-Anwendertreffens vom 18. bis 21. September 2000 in Jülich
   zusammengestellt von H.-J. Dietze, J. S. Becker (2000), XVI, 109 Seiten
   ISBN: 978-3-89336-267-7

5. **Neutron Scattering**
   Lectures of the Laboratory Course
   held at the Forschungszentrum Jülich from 26 September to 6 October 2000
   herausgegeben von Th. Brückel, G. Heger, D. Richter (2000), 382 Seiten
   ISBN: 978-3-89336-269-1

6. **Baryon Excitations**
   Lectures of the COSY Workshop
   held at the Forschungszentrum Jülich from 2 to 3 May 2000
   edited by T. Barnes and H.-P. Morsch (2000), 203 pages
   ISBN: 978-3-89336-273-8

7. **Neue Materialien für die Informationstechnik**
   Vorlesungsmanuskripte des 32. IFF-Ferienkurses vom 05. bis 16.03.2001
   herausgegeben von R. Waser (2001), ca. 1200 Seiten, zahlreiche z. T. farb. Abb.
   ISBN: 978-3-89336-279-0

8. **Deutsche Neutronenstreutagung 2001**
   Kurzfassungen der Vorträge und Poster der
   Deutschen Neutronenstreutagung 2001 vom 19. bis 21. Februar 2001 in Jülich
   zusammengestellt von Th. Brückel (2001), XVI, 186 Seiten
   ISBN: 978-3-89336-280-6

Schriften des Forschungszentrums Jülich
Reihe Materie und Material / Matter and Materials

9. **Neutron Scattering**
   Lectures of the 5th Laboratory Course
   held at the Forschungszentrum Jülich from 18 September to 28 September 2001
   edited by Th. Brückel, G. Heger, D. Richter, R. Zorn (2001), 418 pages
   ISBN: 978-3-89336-288-2

10. **Soft Matter. Complex Materials on Mesoscopic Scales**
    Lecture manuscripts of the 33rd IFF winter school on March 04 - 14 2002
    edited by J. K. G. Dhont, G. Gompper, D. Richter (2002),
    c. 1000 pages, many partly coloured illustrations
    ISBN: 978-3-89336-297-4 (Hardcover)

11. **Proceedings of the symposium on threshold meson production in pp and pd interaction**
    Extended COSY-11 Collaboration Meeting Cracow, 20 - 24 June 2001
    edited by P. Moskal, M. Wolke (2002), 274 pages
    ISBN: 978-3-89336-307-0

12. **Polarized Neutron Scattering**
    Lectures of the 1st Summer School held at the Forschungszentrum Jülich
    from 10 to 14 September 2002
    edited by Th. Brückel, W. Schweika (2002), 360 pages
    ISBN: 978-3-89336-314-8

13. **Beam Cooling and Related Topics**
    255th International WE-Heraeus-Seminar, Bad Honnef, May 13 - 18, 2001
    Proceedings
    edited by D. Prasuhn (2002), PDF-Datei auf CD
    ISBN: 978-3-89336-316-2

14. **Fundamentals of Nanoelectronics**
    34th Spring School of the Department of Solid State Research,
    10 - 21 March 2003, Jülich, Germany
    edited by S. Bluegel, M. Luysberg, K. Urban, R. Waser (2003), c. 1000 pages
    ISBN: 978-3-89336-319-3 (Hardcover)

15. **Neutron Scattering**
    Lectures of the Laboratory course held at the Forschungszentrum Jülich
    edited by Th. Brückel, G. Heger, D. Richter, R. Zorn (2003), 375 pages
    New, revised edition of Materie und Material / Matter and Materials Volume 9
    ISBN: 978-3-89336-324-7

16. **Proceedings of the 1st Summer School 2002 and Workshop on COSY Physics**
    28. August - 4. September 2002
    Organizing Committee: K. Brinkmann, M. Büscher, et al. (2003), CD-ROM
    ISBN: 978-3-89336-331-5

Schriften des Forschungszentrums Jülich
Reihe Materie und Material / Matter and Materials

17. **Resource-orientated Analysis of Metallic Raw Materials: Findings of CRC 525 for Aluminium**
    edited by W. Kuckshinrichs, P. N. Martens (2003), CD-ROM
    ISBN: 978-3-89336-342-1

18. **The Physics of Spallation Processes: Theory, Experiments and Applications**
    by F. Goldenbaum (2004), V, 174 pages
    ISBN: 978-3-89336-346-9

19. **Physics meets Biology: From Soft Matter to Cell Biology**
    Lecture manuscripts of the 35th IFF Spring School from March 22 – April 2, 2004, Jülich, Germany
    edited by G. Gompper, U. B. Kaupp, J. K. G. Dhont, D. Richter, R. G. Winkler (2004), c. 900 pages
    ISBN: 978-3-89336-348-3

20. **Advanced Cold Moderators ACoM-6**
    Proceedings of the 6th International Workshop on Advanced Cold Moderators held at Forschungszentrum Jülich from 11 to 13 September 2002
    edited by H. Conrad (2004), 223 pages
    ISBN: 978-3-89336-363-6

21. **Proceedings of the second symposium on threshold meson production in pp and pd interaction**
    Extended COSY-11 Collaboration Meeting, Cracow, 1-3 June 2004
    ed. by P. Moskal (2004), c. 300 pages
    ISBN: 978-3-89336-366-7

22. **Ferroelectric Tunnel Junctions**
    by J. Rodríguez Contreras (2004), VIII, 162 pages
    ISBN: 978-3-89336-368-1

23. **Development of Ellipsometric Microscopy as a Quantitative High-Resolution Technique for the Investigation of Thin Films at Glass-Water and Silicon-Air Interfaces**
    by F. Linke (2004), 135 pages
    ISBN: 978-3-89336-373-5

24. **Caucasian-German School and Workshop on Hadron Physics**
    Organizing Committee: M. Büscher, A. Kacharava, M. Nioradze, F. Rathmann, H. Ströher (2004), CD-ROM
    ISBN: 978-3-89336-375-9

25. **6th ANKE Workshop on Strangeness Production on Nucleons and Nuclei**
    Organizing Committee: M. Büscher, V. Kleber, Y. Valdau (2004), CD-ROM
    ISBN: 978-3-89336-376-6

Schriften des Forschungszentrums Jülich
Reihe Materie und Material / Matter and Materials

26. **Magnetism goes Nano**
Lecture manuscripts of the 36th IFF Spring School February 14 – 25, 1005, Jülich, Germany
edited by S. Blügel, T. Brückel, C. M. Schneider (2005), c. 1000 pages
ISBN: 978-3-89336-381-0

27. **Hochfrequenzeigenschaften gepulster, supraleitender Halbwellenresonatoren zur Beschleunigung leichter Ionen**
von R. Stassen (2005), VI, 128 Seiten
ISBN: 978-3-89336-394-0

28. **Neutron Scattering**
Lectures of the Laboratory course held at the Forschungszentrum Jülich
edited by Th. Brückel, G. Heger, D. Richter, R. Zorn (2005), c. 500 pages
New, revised edition of Materie und Material / Matter and Materials Volume 15
ISBN: 978-3-89336-395-7

29. **K^+-Meson Production in Nuclei**
by M. Büscher (2005), 1 CD-ROM
ISBN: 978-3-89336-398-8

30. **STORI'05**
6 th International Conference on Nuclear Physics at Storage Rings
23–26 May 2005, Jülich – Bonn
edited by D. Chiladze, A. Kacharava, H. Ströher (2005), c. 400 pages
ISBN: 978-3-89336-404-6

31. **Wetting and Interdiffusion:**
Establishment of a Bio-compatible System and Studies of its Dynamics
by A.-K. Prechtel (2005), 139 pages
ISBN: 978-3-89336-421-3

32. **Computational Condensed Matter Physics**
Lecture manuscripts of the 37th IFF Spring School March 06 – 17, 2006, Jülich, Germany
edited by S. Blügel, G. Gompper, E. Koch, H. Müller-Krumbhaar, R. Spatschek, R. G. Winkler (2006), c. 1000 pages
ISBN: 978-3-89336-430-5

33. **Spin in Hadron Physics**
2nd Caucasian-German School and Workshop on Hadron Physics
Organizing Committee: A. Kacharava … (2006), CD-ROM
ISBN: 978-3-89336-453-4

Schriften des Forschungszentrums Jülich
Reihe Materie und Material / Matter and Materials

34. **Probing the Nanoworld**
Microscopies, Scattering and Spectroscopies of the Solid State
Lecture manuscripts of the 38th IFF Spring School March 12 – 23, 2007
Jülich, Germany
edited by K. Urban, C. M. Schneider, T. Brückel, S. Blügel, K. Tillmann, W. Schweika, M. Lentzen, L. Baumgarten (2007), c. 1000 pages
ISBN: 978-3-89336-462-6

35. **Future Perspectives of European Materials Research**
edited by G. Schumacher, St. Preston, A. Smith, St. Reschke (2007), c. 80 pages
ISBN: 978-3-89336-477-0

36. **Physics of more than 11 years of COSY-11 – history, status, achievements, plans**
edited by J. Przerwa, D. Grzonka, P. Klaja, P. Moskal, W. Oelert (2007), 127 pages
ISBN: 978-3-89336-483-1

37. **ANKE/PAX Workshop on SPIN PHYSICS, Ferrara 2007**
Organizing Committee: G. Ciullo, A. Kacharava, P. Lenisa, F. Rathmann, H. Ströher (2007), CD-ROM
ISBN: 978-3-89336-487-9

38. **Neutron Scattering**
Lectures of the JCNS Laboratory Course held at Forschungszentrum Jülich and the research reactor FRM II of TU Munich
edited by Th. Brückel, G. Heger, D. Richter, R. Zorn (2007), c. 500 pages
New, revised edition of Materie und Material / Matter and Materials Volume 28
ISBN: 978-3-89336-489-3

Forschungszentrum Jülich
in der Helmholtz-Gemeinschaft

Band/Volume 38
ISBN 978-3-89336-489-3

Materie und Material
Matter and Materials